

AD-A275 255



ESL-TR-91-41

2

NUMERICAL ANALYSIS OF DYNAMIC DIRECT TENSION AND DIRECT COMPRESSION TESTS

J.W. TEDESCO, M.L. HUGHES, B.P. O'NEIL

AUBURN UNIVERSITY
DEPARTMENT OF CIVIL ENGINEERING
AUBURN AL 36849

JANUARY 1993

FINAL REPORT

FEBRUARY 1990 - APRIL 1991

APPROVED FOR PUBLIC RELEASE:
DISTRIBUTION UNLIMITED

DTIC
ELECTE
FEB 0 2 1994
S B D

ENGINEERING RESEARCH DIVISION

Air Force Civil Engineering Support Agency

Civil Engineering Laboratory

Tyndall Air Force Base, Florida 32403



94-03376



94 1 31 246

NOTICE

PLEASE DO NOT REQUEST COPIES OF THIS REPORT FROM HQ AFCESA/RA (AIR FORCE CIVIL ENGINEERING SUPPORT AGENCY). ADDITIONAL COPIES MAY BE PURCHASED FROM:

**NATIONAL TECHNICAL INFORMATION SERVICE
5285 PORT ROYAL ROAD
SPRINGFIELD, VIRGINIA 22161**

FEDERAL GOVERNMENT AGENCIES AND THEIR CONTRACTORS REGISTERED WITH DEFENSE TECHNICAL INFORMATION CENTER SHOULD DIRECT REQUESTS FOR COPIES OF THIS REPORT TO:

**DEFENSE TECHNICAL INFORMATION CENTER
CAMERON STATION
ALEXANDRIA, VIRGINIA 22314**

EXECUTIVE SUMMARY

A. OBJECTIVE: The objective of this research project was to develop a construction management program module to support the Combat Readiness and Infrastructure Support Icon Software (CRISIS) Manager, developed by the United States Air Force Academy (USAFA), in enhancing the decision-making process for Airbase Operability (ABO), with respect to construction operations. The system is to serve as an aid for expeditious evaluation of alternatives and for efficient utilization of resources.

B. BACKGROUND: Following an attack, the Wing Commander's first priority and the Base Civil Engineer's primary mission is to rapidly restore and sustain an aircraft launch and recovery capability. This involves execution of construction scenarios, which seek to efficiently use existing resources, in a multi-decision-variables environment created by the overall damage picture. It calls, therefore, for providing the users with an appropriate decision-support tool. Integrating CRISIS ABO graphics capabilities with a Database Management System (DBMS) offers such a tool.

C. SCOPE: This research combined topics from three main disciplines: (1) airbase operability; (2) information systems for construction management; and (3) graphics-databases interfacing in computerized systems. Within this framework, three complementary components were developed: (1) functional description of a pilot system, including the system rationale and fundamentals, conceptual configuration and internal structures, file classes and interfacing mechanism; (2) two test cases, derived from typical peacetime and wartime scenarios, presented through their input, algorithms and output; and (3) stand-alone demonstration-system software, accompanied by documentation to explain its operation and to illustrate the potential benefits of the system as a practical consulting tool.

D. METHODOLOGY: Two methods were considered. Either the overall picture of construction-related decision-making processes could be addressed through analytical simulation of base recovery operations, producing an abstract, general solution and, at the most, a prototype shell; or, particular cases derived from typical airbase scenarios could be generated, through which problems would be observed and around which a working pilot system be developed. In this project the second method was chosen, mainly due to: (1) schedule and budget constraints; (2) limitations in obtaining information about current practices; and (3) the top priority attributed to producing the basis for a practical tool.

E. RESULTS: The proposed system, CDM, is based on the setting-up of an automatic, bi-directional linkage between design information and construction management information. It operates as a multi-environment system, in which CRISIS serves as a source of airbase physical data and as a visual display medium of the processed data, and a DBMS maintains the construction databases and employs programs for data processing and manipulation. CDM features an efficient interfacing mechanism between these two components, and utilizes graphic instruments to facilitate decision-making.

F. CONCLUSIONS: The complexity and unique nature of airbase recovery environment, the importance of efficient utilization of resources, the need to provide the decision-maker with proper guidance, and the potential of the design-construction integration concept substantiate the use of advanced graphics-databases interfacing technology to develop a decision-support tool for construction-related operations on an airbase. A decision-support system, based on the pilot system developed as part of this research and on the philosophy introduced along with that system, can be a valuable tool for the decision-maker, assisting in the generation of alternative solutions for peacetime- or wartime-related problems, and providing comparative and indicative evaluations of these alternatives, as guidance for the selection of a good solution in a typically time- and resource-tight environment. The system could be further developed, to be used as well for monitoring repair and maintenance operations.

G. RECOMMENDATIONS: Further research and development should include: (1) upgrading the system, to better reflect conditions, by amplifying and expanding the currently simplified models; (2) augmenting the system by adding other typical scenarios, with the ultimate goal of expanding it into a general task-oriented system/shell; and (3) exploring the advantages that other relational DBMS might offer, along with incorporation of USAF flat-file databases and/or military/commercial Construction Management packages.

PREFACE

This report was prepared by the Department of Civil Engineering, Auburn University, Auburn, Alabama, under Contract No. F08635-90-C-0120 for Engineering and Services Laboratory, Headquarters, Air Force Civil Engineering Support Agency (HQ AFCESA/RACS), Tyndall AFB, Florida.

This report summarizes the results of work to simulate high strain rate direct tension and direct compression experiments conducted on a Split-Hopkinson pressure bar through a comprehensive numerical analysis. The work was initiated in February 1990 and completed in March 1991. Dr. Joseph W. Tedesco served as principal investigator at Auburn University. Capt. S. T. Kuennen served as the project officer for HQ AFCESA/RACS.

This report has been reviewed by the Public Affairs Office and is releasable to the National Information Service (NTIS). At NTIS it will be available to the general public, including foreign nationals.

This report has been reviewed and is approved for publication.



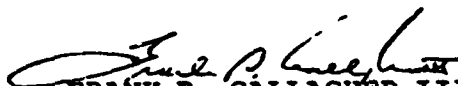
STEVEN T. KUENNEN, Capt, USAF
Project Officer



NEIL H. FRAVEL, Lt Col, USAF
Chief, Engineering
Research Division



LOREN M. WOMACK, GM-14
Chief, Air Base Structural
Materials Branch



FRANK P. GALLAGHER III, Col, USAF
Director, Engineering and
Services Laboratory

DTIC QUALITY INSPECTED 2

(The reverse of this page is blank.)

Accession For	
NTIS GRA&I	<input checked="" type="checkbox"/>
DTIC TAB	<input type="checkbox"/>
Unannounced	<input type="checkbox"/>
Justification	
By	
Distribution/	
Availability Codes	
Dist	Avail and/or Special
A-1	

TABLE OF CONTENTS

Section	Title	Page
I	INTRODUCTION	1
	A. OBJECTIVE	1
	B. BACKGROUND	1
	1. SHPB Experimental Study	2
	2. Numerical Analysis	3
	C. SCOPE	4
II	DIRECT TENSION TESTS	5
	A. INTRODUCTION	5
	B. STATIC ANALYSIS	8
	1. The FEM Model	8
	2. Linear Analysis	8
	3. Nonlinear Analysis	9
	C. DYNAMIC ANALYSIS	11
	1. Results of Nonlinear Analysis (Square-Notch, Load Case 1)	12
	2. Results of Nonlinear Analysis (Square-Notch, Load Case 2)	13
	3. Results of Nonlinear Analysis (Square-Notch, Load Case 3)	13
	4. Summary of Square-Notch Results	14
	5. Results of Nonlinear Analysis (Saddle-Notch, Load Case 1)	14

TABLE OF CONTENTS (CONTINUED)

	6.	Results of Nonlinear Analysis (Saddle-Notch, Load Case 2)	16
	7.	Results of Nonlinear Analysis (Saddle-Notch, Load Case 3)	16
	8.	Summary of Saddle-Notch Results	17
III		DIRECT COMPRESSION TESTS	19
	A.	INTRODUCTION	19
	B.	FEM ANALYSIS	19
	1.	FEM Model	19
	2.	Dynamic Analysis	19
	C.	RESULTS OF NONLINEAR DYNAMIC ANALYSES	21
	1.	Load Case 1	21
	2.	Load Case 2	22
	3.	Load Case 3	23
	4.	Summary of Direct Compression Results	23
IV		DISCUSSION OF RESULTS	26
	A.	DIRECT TENSION TESTS	26
	1.	Linear Static Analysis	26
	2.	Nonlinear Static Analysis	26
	3.	Nonlinear Dynamic Analysis	27
	B.	DIRECT COMPRESSION TESTS	29

TABLE OF CONTENTS CONTINUED

1.	Load Case 1	29
2.	Load Case 2	30
3.	Load Case 3	31
V	CONCLUSIONS AND RECOMMENDATIONS	32
A.	CONCLUSIONS	32
1.	Direct Tension Tests	32
2.	Direct Compression Results	33
B.	RECOMMENDATIONS	33
REFERENCES	35
APPENDIX A: FIGURES FOR SECTIONS I-IV	37
APPENDIX B: REANALYSIS OF DIRECT COMPRESSION TESTS	257

LIST OF FIGURES

Figure	Title	Page
1	Illustration of AFCESA 51 mm SHPB	39
2	Details of AFCESA SHPB in tension mode of operation	40
3	Details of AFCESA SHPB in compression mode of operation	41
4	Direct tension specimens	42
5	Operational schematic of the SHPB	43
6	Square notch test data trace for load case 1	44
7	Square notch test data trace for load case 2	45
8	Square notch test data trace for load case 3	46
9	FEM model of square-notch specimen and portion of the SHPB	47
10	FEM model of saddle-notch specimen and portion of the SHPB	48
11	Longitudinal stress (σ_z) distribution in cross section at the incident end of specimen, linear static analysis	49
12	Longitudinal stress (σ_z) distribution in cross section at the transmitter end of specimen, linear static analysis	50
13	Longitudinal stress (σ_z) distribution in cross section at root of notch, linear static analysis	51
14	Longitudinal stress (σ_z) distribution in cross section at root of notch, linear static analysis	52
15	Longitudinal stress (σ_z) distribution in cross section at the incident end of specimen, linear static analysis	53
16	Longitudinal stress (σ_z) distribution in cross section at the transmitter end of specimen, linear static analysis	54
17	Longitudinal stress (σ_z) distribution in cross section through apex of notch, linear static analysis	55
18	Uniaxial stress-strain relation used in concrete model	56
19	Three dimensional tension failure envelope of concrete model	57
20	Loading sequence for static nonlinear analysis	58
21	Cracking sequence for square-notch specimen, static nonlinear analysis	59

22	Longitudinal stress (σ_z) distribution in cross section at the notch, static nonlinear analysis	60
23	Cracking sequence for saddle-notch specimen, static nonlinear analysis	61
24	Longitudinal stress (σ_z) distribution in cross section at the notch, static nonlinear analysis	62
25	Typical loading function used in dynamic analysis	63
26	Time history for longitudinal stress (square-notch, Load Case 1)	64
27	Time history for longitudinal stress (square-notch, Load Case 1)	65
28	Time history for longitudinal stress (square-notch, Load Case 1)	66
29	Time history for longitudinal stress (square-notch, Load Case 1)	67
30	Time history for longitudinal stress (square-notch, Load Case 1)	68
31	Time history for longitudinal strain (square-notch, Load Case 1)	69
32	Time history for longitudinal strain (square-notch, Load Case 1)	70
33	Time history for longitudinal strain (square-notch, Load Case 1)	71
34	Time history for longitudinal strain (square-notch, Load Case 1)	72
35	Time history for longitudinal strain (square-notch, Load Case 1)	73
36	Profiles for longitudinal stress (square-notch, Load Case 1)	74
37	Profiles for longitudinal stress (square-notch, Load Case 1)	75
38	Profiles for longitudinal stress (square-notch, Load Case 1)	76
39	Profiles for longitudinal stress (square-notch, Load Case 1)	77

40	Profiles for longitudinal strain (square-notch, Load Case 1)	78
41	Profiles for longitudinal strain (square-notch, Load Case 1)	79
42	Profiles for longitudinal strain (square-notch, Load Case 1)	80
43	Profiles for longitudinal strain (square-notch, Load Case 1)	81
44	Cracking sequence for square-notch specimen; Load Case 1: a) $t=266 \mu \text{ sec}$, b) $t=269 \mu \text{ sec}$, c) $t=270 \mu \text{ sec}$, d) $t=300 \mu \text{ sec}$	82
45	Time history for longitudinal stress (square-notch, Load Case 2)	83
46	Time history for longitudinal stress (square-notch, Load Case 2)	84
47	Time history for longitudinal stress (square-notch, Load Case 2)	85
48	Time history for longitudinal stress (square-notch, Load Case 2)	86
49	Time history for longitudinal stress (square-notch, Load Case 2)	87
50	Time history for longitudinal strain (square-notch, Load Case 2)	88
51	Time history for longitudinal strain (square-notch, Load Case 2)	89
52	Time history for longitudinal strain (square-notch, Load Case 2)	90
53	Time history for longitudinal strain (square-notch, Load Case 2)	91
54	Time history for longitudinal strain (square-notch, Load Case 2)	92
55	Profiles for longitudinal stress (square-notch, Load Case 2)	93
56	Profiles for longitudinal stress (square-notch, Load Case 2)	94

57	Profiles for longitudinal stress	
	(square-notch, Load Case 2)	95
58	Profiles for longitudinal stress	
	(square-notch, Load Case 2)	96
59	Profiles for longitudinal strain	
	(square-notch, Load Case 2)	97
60	Profiles for longitudinal strain	
	(square-notch, Load Case 2)	98
61	Profiles for longitudinal strain	
	(square-notch, Load Case 2)	99
62	Profiles for longitudinal strain	
	(square-notch, Load Case 2)	100
63	Cracking sequence for square-notch specimen; Load Case 2:	
	a) $t=258 \mu \text{ sec}$, b) $t=260 \mu \text{ sec}$, c) $t=265 \mu \text{ sec}$,	
	d) $t=295 \mu \text{ sec}$	101
64	Time history for longitudinal stress	
	(square-notch, Load Case 3)	102
65	Time history for longitudinal stress	
	(square-notch, Load Case 3)	103
66	Time history for longitudinal stress	
	(square-notch, Load Case 3)	104
67	Time history for longitudinal stress	
	(square-notch, Load Case 3)	105
68	Time history for longitudinal stress	
	(square-notch, Load Case 3)	106
69	Time history for longitudinal strain	
	(square-notch, Load Case 3)	107
70	Time history for longitudinal strain	
	(square-notch, Load Case 3)	108
71	Time history for longitudinal strain	
	(square-notch, Load Case 3)	109
72	Time history for longitudinal strain	
	(square-notch, Load Case 3)	110
73	Time history for longitudinal strain	
	(square-notch, Load Case 3)	111

74	Profiles for longitudinal stress (square-notch, Load Case 3)	112
75	Profiles for longitudinal stress (square-notch, Load Case 3)	113
76	Profiles for longitudinal stress (square-notch, Load Case 3)	114
77	Profiles for longitudinal stress (square-notch, Load Case 3)	115
78	Profiles for longitudinal strain (square-notch, Load Case 3)	116
79	Profiles for longitudinal strain (square-notch, Load Case 3)	117
80	Profiles for longitudinal strain (square-notch, Load Case 3)	118
81	Profiles for longitudinal strain (square-notch, Load Case 3)	119
82	Cracking sequence for square-notch specimen; Load Case 3: a) $t=255 \mu \text{ sec}$, b) $t=258 \mu \text{ sec}$, c) $t=264 \mu \text{ sec}$, d) $t=267 \mu \text{ sec}$	120
83	Definition sketch for square-notch specimen	121
84	Definition sketch for saddle-notch specimen	122
85	Time history for longitudinal stress (saddle-notch, Load Case 1)	123
86	Time history for longitudinal stress (saddle-notch, Load Case 1)	124
87	Time history for longitudinal stress (saddle-notch, Load Case 1)	125
88	Time history for longitudinal stress (saddle-notch, Load Case 1)	126
89	Time history for longitudinal stress (saddle-notch, Load Case 1)	127
90	Time history for longitudinal stress (saddle-notch, Load Case 1)	128
91	Time history for longitudinal strain (saddle-notch, Load Case 1)	129

92	Time history for longitudinal strain (saddle-notch, Load Case 1)	130
93	Time history for longitudinal strain (saddle-notch, Load Case 1)	131
94	Time history for longitudinal strain (saddle-notch, Load Case 1)	132
95	Time history for longitudinal strain (saddle-notch, Load Case 1)	133
96	Time history for longitudinal strain (saddle-notch, Load Case 1)	134
97	Profiles for longitudinal stress (saddle-notch, Load Case 1)	135
98	Profiles for longitudinal stress (saddle-notch, Load Case 1)	136
99	Profiles for longitudinal stress (saddle-notch, Load Case 1)	137
100	Profiles for longitudinal strain (saddle-notch, Load Case 1)	138
101	Profiles for longitudinal strain (saddle-notch, Load Case 1)	139
102	Profiles for longitudinal strain (saddle-notch, Load Case 1)	140
103	Cracking sequence for saddle-notch specimen; Load Case 1: a) $t=274 \mu \text{ sec}$, b) $t=275 \mu \text{ sec}$, c) $t=277 \mu \text{ sec}$, d) $t=326 \mu \text{ sec}$	141
104	Time history for longitudinal stress (saddle-notch, Load Case 2)	142
105	Time history for longitudinal stress (saddle-notch, Load Case 2)	143
106	Time history for longitudinal stress (saddle-notch, Load Case 2)	144
107	Time history for longitudinal stress (saddle-notch, Load Case 2)	145
108	Time history for longitudinal stress (saddle-notch, Load Case 2)	146

109	Time history for longitudinal stress (saddle-notch, Load Case 2)	147
110	Time history for longitudinal strain (saddle-notch, Load Case 2)	148
111	Time history for longitudinal strain (saddle-notch, Load Case 2)	149
112	Time history for longitudinal strain (saddle-notch, Load Case 2)	150
113	Time history for longitudinal strain (saddle-notch, Load Case 2)	151
114	Time history for longitudinal strain (saddle-notch, Load Case 2)	152
115	Time history for longitudinal strain (saddle-notch, Load Case 2)	153
116	Profiles for longitudinal stress (saddle-notch, Load Case 2)	154
117	Profiles for longitudinal stress (saddle-notch, Load Case 2)	155
118	Profiles for longitudinal stress (saddle-notch, Load Case 2)	156
119	Profiles for longitudinal strain (saddle-notch, Load Case 2)	157
120	Profiles for longitudinal strain (saddle-notch, Load Case 2)	158
121	Profiles for longitudinal strain (saddle-notch, Load Case 2)	159
122	Cracking sequence for saddle-notch specimen; Load Case 2: a) $t=351 \mu \text{ sec}$, b) $t=356 \mu \text{ sec}$, c) $t=362 \mu \text{ sec}$, d) $t=425 \mu \text{ sec}$	160
123	Time history for longitudinal stress (saddle-notch, Load Case 3)	161
124	Time history for longitudinal stress (saddle-notch, Load Case 3)	162
125	Time history for longitudinal stress (saddle-notch, Load Case 3)	163

126	Time history for longitudinal stress (saddle-notch, Load Case 3)	164
127	Time history for longitudinal stress (saddle-notch, Load Case 3)	165
128	Time history for longitudinal stress (saddle-notch, Load Case 3)	166
129	Time history for longitudinal strain (saddle-notch, Load Case 3)	167
130	Time history for longitudinal strain (saddle-notch, Load Case 3)	168
131	Time history for longitudinal strain (saddle-notch, Load Case 3)	169
132	Time history for longitudinal strain (saddle-notch, Load Case 3)	170
133	Time history for longitudinal strain (saddle-notch, Load Case 3)	171
134	Time history for longitudinal strain (saddle-notch, Load Case 3)	172
135	Profiles for longitudinal stress (saddle-notch, Load Case 3)	173
136	Profiles for longitudinal stress (saddle-notch, Load Case 3)	174
137	Profiles for longitudinal stress (saddle-notch, Load Case 3)	175
138	Profiles for longitudinal strain (saddle-notch, Load Case 3)	176
139	Profiles for longitudinal strain (saddle-notch, Load Case 3)	177
140	Profiles for longitudinal strain (saddle-notch, Load Case 3)	178
141	Cracking sequence for saddle-notch specimen; Load Case 3: a) $t=351 \mu \text{ sec}$, b) $t=355 \mu \text{ sec}$, c) $t=363 \mu \text{ sec}$, d) $t=444 \mu \text{ sec}$	179
142	Direct compression test data trace for Load Case 1	180
143	Direct compression test data trace for Load Case 2	181

144	Direct compression test data trace for Load Case 3	182
145	FEM model of direct compression specimen and portion of SHPB	183
146	Time history for longitudinal stress (direct compression, Load Case 1)	184
147	Time history for longitudinal stress (direct compression, Load Case 1)	185
148	Time history for longitudinal stress (direct compression, Load Case 1)	186
149	Time history for longitudinal stress (direct compression, Load Case 1)	187
150	Time history for longitudinal strain (direct compression, Load Case 1)	188
151	Time history for longitudinal strain (direct compression, Load Case 1)	189
152	Time history for longitudinal strain (direct compression, Load Case 1)	190
153	Time history for longitudinal strain (direct compression, Load Case 1)	191
154	Time history for circumferential strain (direct compression, Load Case 1)	192
155	Time history for circumferential strain (direct compression, Load Case 1)	193
156	Time history for circumferential strain (direct compression, Load Case 1)	194
157	Time history for radial strain (direct compression, Load Case 1)	195
158	Time history for radial strain (direct compression, Load Case 1)	196
159	Time history for radial strain (direct compression, Load Case 1)	197
160	Profiles for longitudinal stress (direct compression, Load Case 1)	198
161	Profiles for longitudinal stress (direct compression, Load Case 1)	199

162	Profiles for longitudinal stress (direct compression, Load Case 1)	200
163	Profiles for longitudinal stress (direct compression, Load Case 1)	201
164	Profiles for longitudinal stress (direct compression, Load Case 1)	202
165	Profiles for longitudinal strain (direct compression, Load Case 1)	203
166	Profiles for longitudinal strain (direct compression, Load Case 1)	204
167	Profiles for longitudinal strain (direct compression, Load Case 1)	205
168	Profiles for longitudinal strain (direct compression, Load Case 1)	206
169	Profiles for longitudinal strain (direct compression, Load Case 1)	207
170	Cracking sequence for direct compression specimen; Load Case 1: a) $t=279 \mu \text{ sec}$, b) $t=281 \mu \text{ sec}$, c) $t=282 \mu \text{ sec}$, d) $t=284 \mu \text{ sec}$	208
171	Time history for longitudinal stress (direct compression, Load Case 2)	209
172	Time history for longitudinal stress (direct compression, Load Case 2)	210
173	Time history for longitudinal stress (direct compression, Load Case 2)	211
174	Time history for longitudinal stress (direct compression, Load Case 2)	212
175	Time history for longitudinal strain (direct compression, Load Case 2)	213
176	Time history for longitudinal strain (direct compression, Load Case 2)	214
177	Time history for longitudinal strain (direct compression, Load Case 2)	215
178	Time history for longitudinal strain (direct compression, Load Case 2)	216

179	Time history for radial strain (direct compression, Load Case 2)	217
180	Time history for radial strain (direct compression, Load Case 2)	218
181	Time history for radial strain (direct compression, Load Case 2)	219
182	Profiles for longitudinal stress (direct compression, Load Case 2)	220
183	Profiles for longitudinal stress (direct compression, Load Case 2)	221
184	Profiles for longitudinal stress (direct compression, Load Case 2)	222
185	Profiles for longitudinal stress (direct compression, Load Case 2)	223
186	Profiles for longitudinal stress (direct compression, Load Case 2)	224
187	Profiles for longitudinal strain (direct compression, Load Case 2)	225
188	Profiles for longitudinal strain (direct compression, Load Case 2)	226
189	Profiles for longitudinal strain (direct compression, Load Case 2)	227
190	Profiles for longitudinal strain (direct compression, Load Case 2)	228
191	Profiles for longitudinal strain (direct compression, Load Case 2)	229
192	Cracking sequence for direct compression specimen; Load Case 2: a) $t=272 \mu \text{ sec}$, b) $t=276 \mu \text{ sec}$, c) $t=278 \mu \text{ sec}$, d) $t=284 \mu \text{ sec}$	230
193	Time history for longitudinal stress (direct compression, Load Case 3)	231
194	Time history for longitudinal stress (direct compression, Load Case 3)	232
195	Time history for longitudinal stress (direct compression, Load Case 3)	233

196	Time history for longitudinal stress (direct compression, Load Case 3)	234
197	Time history for longitudinal strain (direct compression, Load Case 3)	235
198	Time history for longitudinal strain (direct compression, Load Case 3)	236
199	Time history for longitudinal strain (direct compression, Load Case 3)	237
200	Time history for longitudinal strain (direct compression, Load Case 3)	238
201	Time history for circumferential strain (direct compression, Load Case 3)	239
202	Time history for circumferential strain (direct compression, Load Case 3)	240
203	Time history for circumferential strain (direct compression, Load Case 3)	241
204	Time history for radial strain (direct compression, Load Case 3)	242
205	Time history for radial strain (direct compression, Load Case 3)	243
206	Time history for radial strain (direct compression, Load Case 3)	244
207	Profiles for longitudinal stress (direct compression, Load Case 3)	245
208	Profiles for longitudinal stress (direct compression, Load Case 3)	246
209	Profiles for longitudinal stress (direct compression, Load Case 3)	247
210	Profiles for longitudinal stress (direct compression, Load Case 3)	248
211	Profiles for longitudinal stress (direct compression, Load Case 3)	249
212	Profiles for longitudinal strain (direct compression, Load Case 3)	250

213	Profiles for longitudinal strain (direct compression, Load Case 3)	251
214	Profiles for longitudinal strain (direct compression, Load Case 3)	252
215	Profiles for longitudinal strain (direct compression, Load Case 3)	253
216	Profiles for longitudinal strain (direct compression, Load Case 3)	254
217	Cracking sequence for direct compression specimen; Load Case 3: a) $t=216 \mu \text{ sec}$, b) $t=218 \mu \text{ sec}$, c) $t=226 \mu \text{ sec}$, d) $t=236 \mu \text{ sec}$	255
218	Definition sketch for direct compression specimen	256
219	Illustration of rigid link (master nodes and slave nodes)	266
220	Time history for longitudinal stress (direct compression, Load Case 1)	267
221	Time history for longitudinal stress (direct compression, Load Case 1)	268
222	Time history for longitudinal stress (direct compression, Load Case 1)	269
223	Time history for longitudinal stress (direct compression, Load Case 1)	270
224	Time history for longitudinal stress (direct compression, Load Case 1)	271
225	Time history for longitudinal stress (direct compression, Load Case 1)	272
226	Time history for longitudinal stress (direct compression, Load Case 1)	273
227	Time history for longitudinal stress (direct compression, Load Case 1)	274
228	Time history for longitudinal stress (direct compression, Load Case 1)	275
229	Time history for longitudinal stress (direct compression, Load Case 1)	276

230	Time history for longitudinal stress (direct compression, Load Case 1)	277
231	Definition sketch for direct compression specimen	278
232	Profiles for longitudinal stress (direct compression, Load Case 1)	279
233	Profiles for longitudinal stress (direct compression, Load Case 1)	280
234	Profiles for longitudinal stress (direct compression, Load Case 1)	281
235	Profiles for longitudinal stress (direct compression, Load Case 1)	282
236	Profiles for longitudinal stress (direct compression, Load Case 1)	283
237	Definition sketch for direct compression specimen	284
238	Cracking sequence for direct compression specimen; Load Case 1: a) $t=300\ \mu\text{sec}$, b) $t=525\ \mu\text{sec}$, c) $t=550\ \mu\text{sec}$, d) $t=600\ \mu\text{sec}$	285
239	Time history for longitudinal stress (direct compression, Load Case 2)	286
240	Time history for longitudinal stress (direct compression, Load Case 2)	287
241	Time history for longitudinal stress (direct compression, Load Case 2)	288
242	Time history for longitudinal stress (direct compression, Load Case 2)	289
243	Time history for longitudinal stress (direct compression, Load Case 2)	290
244	Time history for longitudinal stress (direct compression, Load Case 2)	291
245	Time history for longitudinal stress (direct compression, Load Case 2)	292
246	Time history for longitudinal stress (direct compression, Load Case 2)	293
247	Time history for longitudinal stress (direct compression, Load Case 2)	294

248	Time history for longitudinal stress (direct compression, Load Case 2)	295
249	Time history for longitudinal stress (direct compression, Load Case 2)	296
250	Time history for longitudinal strain (direct compression, Load Case 2)	297
251	Time history for longitudinal strain (direct compression, Load Case 2)	298
252	Time history for longitudinal strain (direct compression, Load Case 2)	299
253	Time history for longitudinal strain (direct compression, Load Case 2)	300
254	Time history for longitudinal strain (direct compression, Load Case 2)	301
255	Time history for longitudinal strain (direct compression, Load Case 2)	302
256	Time history for longitudinal strain (direct compression, Load Case 2)	303
257	Time history for longitudinal strain (direct compression, Load Case 2)	304
258	Time history for longitudinal strain (direct compression, Load Case 2)	305
259	Time history for longitudinal strain (direct compression, Load Case 2)	306
260	Time history for longitudinal strain (direct compression, Load Case 2)	307
261	Profiles for longitudinal stress (direct compression, Load Case 2)	308
262	Profiles for longitudinal stress (direct compression, Load Case 2)	309
263	Profiles for longitudinal stress (direct compression, Load Case 2)	310
264	Profiles for longitudinal stress (direct compression, Load Case 2)	311

265	Profiles for longitudinal stress (direct compression, Load Case 2)	312
266	Profiles for longitudinal strain (direct compression, Load Case 2)	313
267	Profiles for longitudinal strain (direct compression, Load Case 2)	314
268	Profiles for longitudinal strain (direct compression, Load Case 2)	315
269	Profiles for longitudinal strain (direct compression, Load Case 2)	316
270	Profiles for longitudinal strain (direct compression, Load Case 2)	317
271	Cracking sequence for direct compression specimen; Load Case 2: a) $t=265 \mu\text{sec}$, b) $t=289 \mu\text{sec}$, c) $t=292 \mu\text{sec}$, d) $t=300 \mu\text{sec}$	318
272	Time history for longitudinal stress (direct compression, Load Case 3)	319
273	Time history for longitudinal stress (direct compression, Load Case 3)	320
274	Time history for longitudinal stress (direct compression, Load Case 3)	321
275	Time history for longitudinal stress (direct compression, Load Case 3)	322
276	Time history for longitudinal stress (direct compression, Load Case 3)	323
277	Time history for longitudinal stress (direct compression, Load Case 3)	324
278	Time history for longitudinal stress (direct compression, Load Case 3)	325
279	Time history for longitudinal stress (direct compression, Load Case 3)	326
280	Time history for longitudinal stress (direct compression, Load Case 3)	327
281	Time history for longitudinal stress (direct compression, Load Case 3)	328

282	Time history for longitudinal stress (direct compression, Load Case 3)	329
283	Time history for longitudinal strain (direct compression, Load Case 3)	330
284	Time history for longitudinal strain (direct compression, Load Case 3)	331
285	Time history for longitudinal strain (direct compression, Load Case 3)	332
286	Time history for longitudinal strain (direct compression, Load Case 3)	333
287	Time history for longitudinal strain (direct compression, Load Case 3)	334
288	Time history for longitudinal strain (direct compression, Load Case 3)	335
289	Time history for longitudinal strain (direct compression, Load Case 3)	336
290	Time history for longitudinal strain (direct compression, Load Case 3)	337
291	Time history for longitudinal strain (direct compression, Load Case 3)	338
292	Time history for longitudinal strain (direct compression, Load Case 3)	339
293	Time history for longitudinal strain (direct compression, Load Case 3)	340
294	Profiles for longitudinal stress (direct compression, Load Case 3)	341
295	Profiles for longitudinal stress (direct compression, Load Case 3)	342
296	Profiles for longitudinal stress (direct compression, Load Case 3)	343
297	Profiles for longitudinal stress (direct compression, Load Case 3)	344
298	Profiles for longitudinal stress (direct compression, Load Case 3)	345

299	Profiles for longitudinal strain (direct compression, Load Case 3)	346
300	Profiles for longitudinal strain (direct compression, Load Case 3)	347
301	Profiles for longitudinal strain (direct compression, Load Case 3)	348
302	Profiles for longitudinal strain (direct compression, Load Case 3)	349
303	Profiles for longitudinal strain (direct compression, Load Case 3)	350
304	Cracking sequence for direct compression specimen; Load Case 3: a) $t = 230 \mu\text{sec}$, b) $t = 249 \mu\text{sec}$, c) $t = 255 \mu\text{sec}$, d) $t = 275 \mu\text{sec}$	351

LIST OF TABLES

Number	Title	Page
1	Concrete Material Properties	5
2	Summary of SHPB Square-Notch Results	7
3	Concrete Model Parameters	10
4	Load Function Parameters	11
5	Maximum Strain Rates for Square-Notch Tests	14
6	Maximum Longitudinal Stresses for Square-Notch Tests	15
7	Summary of Square-Notch Specimen Failures	15
8	Maximum Strain Rates for Saddle-Notch Tests	17
9	Maximum Longitudinal Stress for Saddle-Notch Tests	18
10	Summary of Saddle-Notch Specimen Failures	18
11	Summary of SHPB Direct Compression Results	20
12	Load Function Parameters for Direct Compression Analyses	21
13	Maximum Strain Rates for Direct Compression Tests	24
14	Maximum Longitudinal Stress for Direct Compression Tests	24
15	Summary of Direct Compression Specimen Failures	25
16	Maximum Stresses, Load Case 1	260
17	Maximum Stresses and Strains, Load Case 2	261
18	Maximum Stresses and Strains, Load Case 3	262

SECTION I

INTRODUCTION

A. OBJECTIVE

A comprehensive numerical analysis of direct tension and direct compression tests of plain concrete, performed at strain rates between 1 and 10^2 on a Split-Hopkinson Pressure Bar (SHPB), was conducted. The objectives of the study were to ascertain the states of stress in the concrete specimens at failure and to identify the modes of failure.

B. BACKGROUND

The effect of increasing strain rate on the strength properties of many materials has been recognized for a number of years. Efforts to experimentally test materials at high strain rates using bar impact began approximately 75 years ago. Most materials, with the exception of some work-hardened aluminum alloys, experience some increase in strength with increases in load or strain rate. These increases in strength begin to appear in the strain rate range of 10/second to 10^3 /second. Mortar and concrete compressive tests are easier to conduct than tensile tests and some experimental compressive strength properties in the strain rate range of 10^{-7} /second to approximately 10^3 /second have been determined. However, in the intermediate strain rate range of 10^{-1} /second to 10/second, testing is difficult and compressive data is scarce.

In the study of conventional weapons' effects upon structures, loading pulses having rise times in the vicinity of 1.0 millisecond may impose strain rates in the range of 10/second up to 10^3 /second on materials and structures. Therefore, the understanding of material response to high-amplitude, short-duration, impulse loads is essential in the analysis and design of protective shelters (Reference 1). Moreover, very little data are available on the strength of concrete and mortar at strain rates associated with close-range conventional weapons explosions, thus prompting several recent research efforts in that area (References 2,3).

Tensile strength testing of concrete and mortar is difficult, even in the low or quasi-static strain rate range. To emphasize this statement the American Society of Testing Materials (ASTM) does not recognize a standard method for testing mortar or concrete in direct tension. The splitting cylinder method, an

indirect tensile test, is recognized by ASTM as a concrete tensile strength test in the low strain rate range.

The direct tension test has seldom been used to evaluate the tensile strength of concrete. This is because of the difficulties of holding the specimens to achieve axial tension and the uncertainties of secondary stresses induced by the holding devices. Recently, however, direct tension tests on plain concrete specimens, using a Split Hopkinson Pressure Bar (SHPB), have been successfully conducted at strain rates between 10/second and 10^3 /second (Reference 4). However, a critical shortcoming with experiments performed on the SHPB is the inability to ascertain the stress condition in the material specimen at failure. Therefore, in an effort to analyze the dynamic stress distribution in high rate SHPB direct tension and direct compression tests, a comprehensive finite element method (FEM) study was conducted (Reference 5) through implementation of the ADINA (Reference 6) computer programs.

Numerous plots of stress histories and stress profiles were generated in the FEM analyses. Many of these plots are very similar in appearance and are presented consecutively. Therefore, for the reader's convenience, all figures have been placed in Appendix A.

1. SHPB Experimental Study

An illustration of the SHPB device used in the experimental study (Reference 4) is shown in Figure 1. The device is operated by the Air Force Civil Engineering Support Agency (AFCEA), Tyndall AFB, Florida. The pressure bars are constructed of PH 13-8 MO stainless steel. Each pressure bar is 51 mm in diameter. The principles of operation of the SHPB, shown schematically for a tensile mode of operation in Figure 2, are as follows (Reference 7):

a. The striker bar impacts Bar 2, which creates a stress wave in both the striker bar and Bar 2.

b. The stress pulse in the striker bar reflects from its free end and is unloaded, giving a finite-length pulse equal to twice the transit time of the striker bar.

c. The finite length pulse in Bar 2 impinges on the specimen, sandwiched between Bar 1 and Bar 2. The incident or loading pulse is recorded by Strain Gage SG2.

d. A portion of the incident pulse is reflected from the specimen and is recorded by the Strain Gage SG2. A portion of the incident pulse is also transmitted into Bar 1 and recorded by the Strain Gage SG1.

e. The three stress or strain pulses, that is, incident, reflected, and transmitted, may be used to determine high strain-rate strength, strain rates, and dynamic stress-strain curves.

The SHPB illustrated in Figure 1, originally used as a compressive SHPB at Southwest Research, Inc. (Reference 8) was modified for tension and compression at AFCESA. The transmitter bar (denoted as Bar 2 in Figure 2) of the original compressive device was threaded at the free end and a tup was screwed into the threaded end. A sliding sleeve striker bar was placed on Bar 2, enclosed in an outer tube, and projected against the tup, thus sending a direct tensile pulse toward the specimen. This modification is shown schematically in Figure 2. The tensile loading, or incident pulse, and the associated reflected pulse are recorded at the Strain Gage SG2 of Figure 2. The transmitted tensile pulse is recorded at Strain Gage SG1.

When the AFCESA SHPB is operated in compression, the arrangement is as shown in Figure 3. This arrangement is used for the direct compression tests. In these tests, the loading compression pulse and reflected pulse, traveling in Bar 1, are recorded at Strain Gage SG1, and the transmitted pulse is recorded at Strain Gage SG2 on Bar 2.

2. Numerical Analysis

High strain rate mechanical testing is complicated by the effects of stress wave propagation. At strain rates above 10^3 /second it is difficult to achieve uniform loading conditions over the gage length of a standard tensile specimen because there may be insufficient time to dampen the often complex stress waves generated during the test. The complex geometry associated with grips, specimen design, screw threads, etc., makes analysis of stress wave propagation in such a test virtually intractable.

The SHPB has evolved into a useful high-rate test apparatus because the stress waves generated in long cylinders are relatively simple and are capable of precise analysis. In addition, specimen dimensions have been reduced significantly to minimize delays associated with stress wave propagation. However, several significant shortcomings are associated with SHPB experiments. First, it is not possible to accurately determine the stress condition in the

specimen at failure from the available data, and second, it is frequently not possible to ascertain the mode of failure in the specimen. A comprehensive numerical analysis was conducted on various direct tension and direct compression SHPB experiments to gain some insight into those phenomena.

Because of the dynamic nature of the impulse loading associated with the SHPB experiments, and the highly nonlinear behavior of the concrete test specimens, the finite element method (FEM) of analysis was employed in the research effort. The analyses were conducted on two-dimensional, axisymmetric models comprised of nine-node isoparametric finite elements (Reference 9). Both linear and nonlinear analyses were performed.

C. SCOPE

Two different types of SHPB experiments were simulated in the FEM analysis: (1) direct tension tests, and (2) direct compression tests. In the direct tension study, both a square-notch and a saddle-notch specimen were analyzed, each 51 mm in length and diameter. In the direct compression tests, the specimen was a regular 51 mm diameter cylinder, 51 mm long. For all numerical analyses, the FEM model included portions of the incident and transmitter bars, in addition to the specimen. Three different load cases for each specimen were investigated.

SECTION II

DIRECT TENSION TESTS

A. INTRODUCTION

The direct tension test has seldom been used to evaluate the tensile strength of concrete. This is because of the difficulties of holding the specimens to achieve axial tension and the uncertainties of secondary stresses induced by the holding devices. Recently, however, direct tension tests using a Split Hopkinson Pressure Bar (SHPB) have been successfully conducted (Reference 10). Two types of tensile specimens were tested, a square-notch specimen (Figure 4a) and saddle-notch specimen (Figure 4b). Both specimens are 51 mm in diameter and length. The quasi-static material properties for the concrete specimens are presented in Table 1. All specimens were cemented to the ends of the SHPB with

TABLE 1. CONCRETE MATERIAL PROPERTIES

Concrete Property	Value
E, Young's Modulus (GPa)	37.93
f'_c , Compressive Stress (MPa)	57.7
f'_t , Tensile Stress (MPa)	4.53
γ , Density (kg/m ³)	2405.0

a nonepoxy concrete cement. The bar surfaces and specimen surfaces were cleaned in a manner similar to that used for surface cleaning before the placement of foil-resistant strain gages.

The principles of operation of the compressive SHPB (Figure 15) are detailed in References 10 and 11, and these same principles apply to the direct tension SHPB. The configuration of the SHPB arrangement employed in the direct tension study reported in Reference 10 is also illustrated in Figure 5. The tensile loading mechanism consists of a hollow cylindrical striker bar sliding on the compressive transmitter bar (Bar 2) of the SHPB. The striker bar impacts a tup threaded into the end of what becomes the tensile incident bar (Bar 2).

A tensile stress wave then propagates toward the specimen, cemented between the two bars.

SHPB direct tension tests were conducted for three different loading conditions (Reference 4). The stress versus time histories for these cases are illustrated in Figures 6, 7, and 8. It is assumed that the dynamic tensile strength at the notch, f_{tn} , is proportional to the transmitted stress, σ_T , through the expression

$$f_{tn} = \sigma_T A_r \quad (1)$$

in which

$$A_r = \frac{D_b^2}{D_n^2} \quad (2)$$

where A_r is the area ratio, D_b is the diameter of the Hopkinson Bar, and D_n is the diameter of the specimen at the notch.

Additionally, the loading rate, $\dot{\sigma}$, and the strain rate, $\dot{\epsilon}$, in the specimen can be estimated from the expressions (Reference 12)

$$\dot{\sigma} = \frac{f_m}{\tau} \quad (3)$$

and

$$\dot{\epsilon} = \frac{\dot{\sigma}}{E_s} \quad (4)$$

where τ is the time lag between the start of the reflected stress wave and the maximum transmitted stress, and E_s is the modulus of elasticity of the specimen material. A summary of the results obtained from the SHPB square-notch tests is presented in Table 2.

Table 2. SUMMARY OF SHPB SQUARE NOTCH RESULTS

Load Case Number	Incident Stress σ_I (MPa)	Transmitted Stress σ_T (MPa)	Dynamic		Loading Rate $\dot{\sigma}$ (MPa/sec)	Strain Rate $\dot{\epsilon}$ (sec ⁻¹)
			Tensile Stress f_{tn} (MPa)			
1	26.5	4.5	9.31		6.01*10 ⁵	4.9
2	67.0	4.0	7.59		1.48*10 ⁶	5.3
3	75.0	4.1	7.93		2.08*10 ⁶	5.8

B. STATIC ANALYSES

1. The FEM Model

To provide an accurate numerical simulation of the SHPB direct tension tests, a detailed FEM model of the specimens and portions of the incident and transmitter bars was constructed. A partial illustration of the axisymmetric FEM model for the square-notch analyses is presented in Figure 9. A similar representation of the saddle-notch model is presented in Figure 10. A 1321 mm segment of the incident and transmitter bars were each modeled with 1594 nine-node axisymmetric elements. The FEM model of the square-notch specimen, presented in Figure 9, is comprised of 348 nine-node, axisymmetric elements. The FEM model of the saddle-notch specimen, illustrated in Figure 10, is comprised of 408 nine-node, axisymmetric elements. For each analysis, the incident and transmitter bars were joined with the appropriate specimen to provide a continuous FEM model. The longitudinal axis of the model is the z-axis, and the transverse axis is the y-axis. The loading is applied uniformly at the free end of the incident bar.

2. Linear Analysis

To ascertain the stress distribution along various cross sections through the specimen, and to identify and quantify areas of stress concentration, a linear static analysis was conducted. The concrete material properties used in the static analysis are presented in Table 1. A load of 29 MPa was applied at the free end of the incident bar.

The distribution of the longitudinal stress, σ_z , in the square-notch specimen along a cross section next to the incident bar is presented in Figure 11. A similar plot of the σ_z stress distribution at the transmitter end of the specimen is depicted in Figure 12. Plots of the σ_z stress distribution along cross sections of the specimen taken through the roots of the notch are presented in Figures 13 and 14.

The distribution of the longitudinal stress, σ_z , in the saddle-notch specimen along the cross section next to the incident bar is presented in Figure 15. Plots of the σ_z stress distribution along cross sections of the specimen taken through the base of the notch and the apex of the notch are presented in Figures 16 and 17, respectively.

Figures 11 through 17 indicate a nonlinear stress distribution in both specimens. The nonlinearity is more pronounced at the sections through the notches. For the square-notch specimen, a stress concentration factor of 2.93 was calculated at the root of the notch (Figures 13 and 14). For the saddle-notch specimen, a stress concentration factor of 1.93 was calculated at the apex of the notch (Figure 17). Regions of stress concentration are also indicated at the outer surfaces of the specimens at cross sections immediately adjacent to the incident bar (Figures 11 and 15) and transmitter bar (Figure 12). This effect is attributed to the fact that the specimens are rigidly attached to the bars, thus creating a Poisson effect.

3. Nonlinear Analysis

A static nonlinear material analysis was conducted to identify possible failure mechanisms in the specimens. The concrete material model employed in the nonlinear analysis is a hypoelastic model based on a uniaxial stress-strain relation (Figure 18) that is generalized to take biaxial and triaxial conditions into account (Reference 14). The model employs three basic features to describe the material behavior: (1) a nonlinear stress-strain relation including strain softening to allow for weakening of the material under increasing compressive stresses; (2) a failure envelope that defines cracking in tension and crushing in compression; and (3) a strategy to model post-cracking and crushing behavior of the material.

To establish the uniaxial stress-strain law accounting for multiaxial stress conditions, an appropriate failure envelope must be employed. Since failure of the specimen is tension-dominated, the tension failure envelope depicted in Figure 19 was used in the concrete model. To identify whether the material has failed, the principal stresses are used to locate the current stress state in the failure envelope. The tensile strength of the material in a principal direction does not change with the introduction of tensile stresses in other principal directions. The pertinent material parameters for the failure envelope and the uniaxial stress-strain relation are summarized in Table 3.

The loading was applied monotonically over 16 load steps at the free end of the incident bar, as illustrated in Figure 20. In the square-notch, first cracking appeared at the root of the notch after Load Step 4, as illustrated in Figure 21, at a load of approximately 1 MPa. Failure of the specimen occurred by fracture through the notched portion of the cross section after Load Step 8

TABLE 3. CONCRETE MODEL PARAMETERS

Parameter	Value
E_0 , Initial tangent modulus (GPa)	37.93
σ_t , Uniaxial cut-off tensile strength (MPa)	4.53
σ_c , Uniaxial maximum compressive strength (MPa)	57.7
σ_u , Uniaxial ultimate compressive strength (MPa)	28.9
e_c , Uniaxial compressive strain at σ_c	0.002
e_u , Uniaxial compressive strain at σ_u	0.003
σ_{p1} , σ_{p2} , σ_{p3} , Principal stress in directions 1,2,3, respectively	Figure 19
σ'_t , Uniaxial cut-off tensile stress under multiaxial conditions	Figure 19
σ'_c , Uniaxial compressive failure stress under multiaxial conditions	Figure 19

at an approximate loading of 2 MPa. The failure sequence for the square-notch specimen is illustrated in Figure 21. The profile of the longitudinal stress, σ_z , along the cross section through the notch immediately prior to failure is presented in Figure 22.

In the saddle-notch, first cracking appeared after Load Step 6 at the outside surface of the specimen at cross sections located next to the incident and transmitter bars (Figure 23a). Failure of the specimen occurred by fracture through the cross section at the apex of the notch after Load Step 7 at an approximate load of 1.5 MPa. The failure sequence for the saddle-notch specimen is presented in Figure 23. The profile of the longitudinal stress, σ_z , along the cross section through the apex of the notch immediately prior to failure is presented in Figure 24.

There are several interesting observations in the aftermath of the nonlinear analysis. First, the saddle-notch specimen exhibits cracking in the cross sections adjacent to the incident and transmitter bars, while the square-notch specimen does not. Second, both the square-notch and the saddle-notch specimens fail on the cross section through their respective notches. The

square-notch specimen fails at the cross section through the root of the notch (Figure 21d) and the saddle-notch fails at the cross section through the apex of the notch (Figure 23b). Interestingly enough, however, the failure load for the saddle-notch specimen is slightly less than that for the square-notch specimen. Nevertheless, the modes of failure manifested in the nonlinear analysis support the results obtained in the linear static analysis.

C. DYNAMIC ANALYSIS

Dynamic nonlinear material analyses were conducted on the SHPB direct tension specimens previously described. The nonlinear material model is the same as described for the nonlinear static analyses. The loading conditions for the dynamic analyses were determined from the SHPB data curves of the incident, reflected, and transmitted stress versus time histories presented in Figure 6, 7, and 8. The loading function used in the numerical analyses, representative of the incident stress time history, is depicted in Figure 25. The rise time, t_1 , the duration of the ramp loading, t_2 , the total time of duration, t_3 , and the stress level, P_0 , for the three load cases are summarized in Table 4.

TABLE 4. LOAD FUNCTION PARAMETERS

Load Case Number	Rise Time t_1 (μsec)	Ramp Time t_2 (μsec)	Total Time t_3 (μsec)	Stress Level P_0 (MPa)
1	45	145	190	26.5
2	45	145	190	67
3	35	135	170	75

For problems in which an elastic body is subjected to a short-duration impulse loading, propagation of stress/strain waves through the body must be considered in formulating the solution. Modal analyses generally do not yield cost-effective, accurate results for wave propagation problems. Therefore, a direct numerical integration procedure must be utilized.

In the present study, the Newmark method of implicit time integration with a consistent mass formulation is employed. The time step selected for temporal

integration in a wave propagation problem is critical to the accuracy and stability of the solution. Since the Newmark method is unconditionally stable, selection of the time step can be based entirely upon accuracy considerations. In a wave propagation problem, the maximum time step is related to wave speed in the material and element size. The maximum time step is selected so that the stress wave propagates the distance between element integration points within that time increment. The maximum time step is defined by

$$(\Delta t)_{\max} = \frac{L_e \sqrt{2}}{c} \quad (5)$$

where L_e is the length of an element in the direction of wave propagation, and c is the velocity of wave propagation, given by

$$c = \sqrt{\frac{E}{\rho}} \quad (6)$$

in which ρ is the mass density of the material. It has been determined from previous experience (Reference 15, 16, and 17) that a time step of

$$\Delta t \leq \frac{1}{3} (\Delta t)_{\max} \quad (7)$$

yields accurate results. In the present study a time step of $\Delta t = 0.1 \mu\text{sec}$ was used for all dynamic analyses.

1. Results of Nonlinear Analysis (Square-Notch, Load Case 1)

Time histories for the longitudinal stress, σ_z , at five locations in the specimen are illustrated in Figures 26 through 30. Time histories for the longitudinal strain, ϵ_z , at the corresponding locations are illustrated in Figures 31 through 35. Profiles for the longitudinal stress at four cross sections in the specimen at selected times are presented in Figures 36 through 39. Profiles for the longitudinal strain at the corresponding cross sections and times are presented in Figures 40 through 43.

The cracking sequence for the specimen, from the initiation of the first crack until failure is illustrated in Figure 44. First cracking occurs simultaneously along the axis of symmetry at the interface of the specimen and the incident bar and at the root of the notch (Figure 44a), at time $t = 266 \mu\text{sec}$.

This result is also evident in the stress time histories presented in Figures 27, 28, and 29. At time $t = 269 \mu\text{sec}$, cracking at the incident end of the specimen has become more extensive (Figure 44b). At time $t = 270 \mu\text{sec}$, cracking is extensive in both the incident end of the cross section as well as in the vicinity of the notch (Figure 44c). Finally, at time $t = 300 \mu\text{sec}$, the specimen fails at the cross section through the notch (Figure 44d).

2. Results of Nonlinear Analysis (Square-Notch, Load Case 2)

Time histories for the longitudinal stress, σ_z , at five locations in the specimen are illustrated in Figures 45 through 49. Time histories for the longitudinal strain, ϵ_z , at the corresponding locations are illustrated in Figures 50 through 54. Profiles for the longitudinal stress at four cross sections in the specimen at selected times are presented in Figures 55 through 58. Profiles for the longitudinal strain at the corresponding cross sections and times are presented in Figures 59 through 62.

The cracking sequence for the specimen, from the initiation of the first crack until failure, is illustrated in Figure 63. The first crack occurs along the axis of symmetry at the interface of the specimen and the incident bar (Figure 63a), at time $t = 258 \mu\text{sec}$. This result is also evident in the stress time history presented in Figure 46. Cracks do not appear in the notch until time $t = 260 \mu\text{sec}$, as shown in Figure 63b. At this same time, however, cracking at the incident end of the specimen has become more extensive. At time $t = 265 \mu\text{sec}$, cracking is extensive in both the incident end of the cross section as well as in the vicinity of the notch (Figure 63c). Finally, at $t = 295 \mu\text{sec}$, the specimen fails simultaneously at the notch and at the incident end (Figure 63d).

3. Results of Nonlinear Analysis (Square-Notch, Load Case 3)

Time histories for the longitudinal stress, σ_z , at five locations in the specimen are illustrated in Figures 64 through 68. Time histories for the longitudinal strain, ϵ_z , at the corresponding locations are illustrated in Figures 69 through 73. Profiles for the longitudinal stress at four cross sections in the specimen at selected times are presented in Figures 74 through 77. Profiles for the longitudinal strain at the corresponding cross sections and times are presented in Figures 78 through 81.

The cracking sequence for the specimen, from the initiation of the first crack until failure, is illustrated in Figure 82. The first crack occurs

along the axis of symmetry at the interface of the specimen and the incident bar (Figure 82a), at time $t = 255 \mu\text{sec}$. This result is also evident in the stress time history presented in Figure 65. Cracks do not appear in the notch until time $t = 258 \mu\text{sec}$, as shown in Figure 82b. However, cracking at the incident end of the specimen has become more extensive. At time $t = 264 \mu\text{sec}$, cracking is extensive in both the incident end of the cross section as well as in the vicinity of the notch (Figure 82c). Finally, at time $t = 267 \mu\text{sec}$, the specimen fails by fracture at the incident end (Figure 82d).

4. Summary of Square-Notch Results

The maximum strain rates, $\dot{\epsilon}_z$, predicted at five locations in the specimen (identified as Points A, B, C, D, and E in Figure 83) are summarized in Table 5. The maximum longitudinal stresses, σ_z , predicted at these same

TABLE 5. MAXIMUM STRAIN RATES FOR SQUARE-NOTCH TESTS

Location (see Figure 83)	Strain Rate, $\dot{\epsilon}_z$ (sec) ⁻¹		
	Load Case 1	Load Case 2	Load Case 3
A	6.073	4.712	7.966
B	5.776	3.744	7.825
C	356.140	174.593	95.728
D	8.957	12.229	8.975
E	8.793	9.115	10.180

locations, are presented in Table 6. A summary of the predicted failure in the specimens is presented in Table 7.

5. Results of Nonlinear Analysis (Saddle-Notch, Load Case 1)

The definition sketch for stress and strain time history locations in the saddle-notch specimens is presented in Figure 84. Time histories for the longitudinal stress, σ_z , at six locations in the specimen are illustrated in Figures 85 through 90. Time histories for the longitudinal strain, ϵ_z , at the corresponding locations are illustrated in Figures 91 through 96. Profiles for the longitudinal stress at three cross sections in the specimen at selected times are presented in Figures 97 through 99. Profiles for the longitudinal strain at the corresponding cross sections and times are presented in Figures 100 through 102.

TABLE 6. MAXIMUM LONGITUDINAL STRESSES FOR
SQUARE-NOTCH TESTS

Location (see Figure 83)	$(\sigma_z)_{\max}$ (MPa)		
	Load Case 1	Load Case 2	Load Case 3
A	4.51	4.11	4.37
B	4.03	4.01	3.95
C	4.52	4.47	4.37
D	4.53	4.36	4.09
E	4.90	4.13	4.06
Transmitter Bar	4.49	5.52	3.97

TABLE 7. SUMMARY OF SQUARE-NOTCH SPECIMEN FAILURES

LOAD CASE	First Cracking		Failure	
	Location (see Figure 83)	Time (μ sec)	Description	Time (μ sec)
1	B, C and D	266	Fracture at notch	300
2	B	260	Simultaneous fracture at notch and incident end of specimen	295
3	B	255	Fracture at incident end of specimen	267

The cracking sequence for the specimen, from the initiation of the first crack until fracture is illustrated in Figure 103. First cracking occurs at the radial surface of the specimen at the incident end (Figure 103a) at time $t = 274 \mu\text{sec}$. This result is also evident in the stress time history presented in Figure 86. At time $t = 275 \mu\text{sec}$, cracks develop in the apex of the notch and cracking at the incident end of the specimen becomes more extensive (Figure 103b). At time $t = 277 \mu\text{sec}$, more extensive cracking is observed at the incident end of the specimen as well as in the vicinity of the notch (Figure 103c). Finally at $t = 326 \mu\text{sec}$, the specimen fractures simultaneously at the incident end and at the apex of the notch (Figure 103d).

6. Results of Nonlinear Analysis (Saddle Notch, Load Case 2)

Time histories for the longitudinal stress, σ_z , at six locations in the specimen are illustrated in Figures 104 through 109. Time histories for the longitudinal strain, ϵ_z , at the corresponding locations are illustrated in Figures 110 through 115. Profiles for the longitudinal stress at three cross sections in the specimen at selected times are presented in Figures 116 through 118. Profiles for the longitudinal strain at the corresponding cross sections and times are presented in Figures 119 through 121.

The cracking sequence for the specimen, from the initiation of the first crack until fracture, is illustrated in Figure 122. Initial cracking occurs on the radial surface of the specimen at the incident end (Figure 122a) at time $t = 351 \mu\text{sec}$. This result is also evident in the stress time history presented in Figure 105. At time $t = 356 \mu\text{sec}$, cracks develop in the apex of the notch and cracking at the incident end of the specimen becomes more extensive (Figure 122b). At time $t = 362 \mu\text{sec}$, more extensive cracking is observed at the incident end of the specimen and in the vicinity of the notch. Also, at this time, significant cracking has developed at the transmitter end of the specimen (Figure 122c). Finally, at $t = 425 \mu\text{sec}$, the specimen fractures at the incident end (Figure 122d).

7. Results of Nonlinear Analysis (Saddle-Notch, Load Case 3)

Time histories for the longitudinal stress, σ_z , at six locations in the specimen are illustrated in Figures 123 through 128. Time histories for the longitudinal strain, ϵ_z , at the corresponding locations are illustrated in Figures 129 through 134. Profiles for the longitudinal stress at three cross sections in the specimen at selected times are presented in Figures 135 through

137. Profiles for the longitudinal strain at the corresponding cross sections and times are presented in Figures 138 through 140.

The cracking sequence for the specimen, from the initiation of the first crack until fracture, is illustrated in Figure 141. Initial cracking occurs on the radial surface of the specimen at the incident end (Figure 141a) at time $t = 351 \mu\text{sec}$. This result is also evident in the stress time history presented in Figure 124. At time $t = 355 \mu\text{sec}$, cracks develop in the apex of the notch and cracking at the incident end of the specimen becomes more extensive (Figure 141b). At time $t = 363 \mu\text{sec}$, more extensive cracking is observed at the incident end of the specimen and in the vicinity of the notch. Also, at this time, significant cracking has developed at the transmitter end of the specimen (Figure 141c). Finally, at $t = 444 \mu\text{sec}$, the specimen fails at the incident end.

8. Summary of Saddle-Notch Results

The maximum strain rates, $\dot{\epsilon}_z$, predicted at six locations in the specimen (identified at Points A, B, C, D, E, and F in Figure 84) are summarized in Table 8. The maximum longitudinal stresses, σ_z , predicted at these same locations are presented in Table 9. A summary of the predicted failures in the specimens is presented in Table 10.

TABLE 8. MAXIMUM STRAIN RATES FOR SADDLE-NOTCH TESTS

Location (see Figure 84)	Strain Rate, $\dot{\epsilon}_z$ (sec) ⁻¹		
	Load Case 1	Load Case 2	Load Case 3
A	6.500	9.815	9.306
B	1000.0	6.876	8.576
C	2.386	4.640	5.448
D	15.000	13.185	28.798
E	8.882	6.161	9.299
F	9.348	10.449	11.338

TABLE 9. MAXIMUM LONGITUDINAL STRESS FOR
SADDLE-NOTCH TESTS

Location (see Figure 84)	$(\sigma_z)_{\max}$ (MPa)		
	Load Case 1	Load Case 2	Load Case 3
A	3.65	3.10	3.48
B	3.06	3.05	3.12
C	2.89	3.00	1.85
D	3.66	3.62	3.61
E	3.58	3.65	3.37
F	3.67	3.43	3.36
Transmitter Bar	3.85	3.92	3.87

TABLE 10. SUMMARY OF SADDLE-NOTCH SPECIMEN FAILURES

Load Case	First Cracking		Failure	
	Location (see Figure 84)	Time (μ sec)	Description	Time (μ sec)
1	B	273	failed at incident end and apex of notch	326
2	B	351	failed at incident end	425
3	B	351	failed at incident end	444

SECTION III

DIRECT COMPRESSION TESTS

A. INTRODUCTION

In recent years, several significant studies employing the Split Hopkinson Pressure Bar (SHPB) technique to evaluate the compressive strength properties of concrete at high strain rates have been conducted (References 18, 19, and 20). The compressive SHPB is generally recognized by experts to provide accurate material properties data in the strain rate range from 10^2 /second to 10^4 /second (References 21 and 22). The details of the SHPB in the compressive mode of operation are illustrated in Figure 3.

SHPB direct compression tests were conducted on cylindrical concrete specimens, 51 mm in diameter and length (Reference 4). Three different loading conditions were investigated. The stress versus time histories for these load cases are presented in Figures 142, 143, and 144. A summary of the results obtained from the SHPB experiments is presented in Table 11.

B. FEM ANALYSIS

1. FEM Model

The FEM model employed for the direct compression analyses was similar to that used for the direct tension simulations. An important assumption employed in the numerical simulations is that the pressure bars and specimen are modeled as a continuous medium. A partial illustration of the axisymmetric direct compression FEM model is presented in Figure 145. A 1321 mm segment of the incident and transmitter bars were each modeled with 1594 nine-node axisymmetric elements. The FEM model of the specimen is comprised of 358 nine-node, axisymmetric elements. The longitudinal axis of the model is the z-axis, and the transverse axis is the y-axis. All loadings were applied uniformly at the free end of the incident bar.

2. Dynamic Analysis

Both linear and nonlinear dynamic analyses were conducted. However, only the results of the nonlinear analysis are summarized in this report. The nonlinear concrete material model employed in the direct tension analyses was also used for the direct compression studies. The pertinent parameters for the nonlinear material model are summarized in Table 3.

TABLE 11. SUMMARY OF SHPB DIRECT COMPRESSION RESULTS

Load Case No.	Incident Stress σ_I (MPa)	Transmitted Stress σ_T (MPa)	Dynamic Compressive Strength (MPa)	Loading Rate $\dot{\sigma}$ (MPa/sec)	Strain Rate $\dot{\epsilon}$ (sec ⁻¹)
1	- 77	-61.6733	68.62	2.84×10^6	17
2	- 80	-63.4877	66.07	3.00×10^6	25
3	-240	- 2.71958	106.21	9.38×10^6	200

The loading conditions for the dynamic analysis were determined from the SHPB data curves of the incident, reflected, and transmitted stress versus time histories presented in Figures 142, 143, and 144. The loading function used in the numerical analyses, representative of the incident stress time history, is depicted in Figure 25. The rise time, t_1 , the duration of the ramp loading, t_2 , the total time of duration, t_3 , and the stress level, P_0 , are summarized in Table 12. All three load cases were investigated in the nonlinear analysis. Only Load Case 1 was investigated in the linear analysis.

TABLE 12. LOAD FUNCTION PARAMETERS FOR
DIRECT COMPRESSION ANALYSES

Load Case Number	Rise Time $t_1(\mu\text{sec})$	Ramp Time $t_2(\mu\text{sec})$	Total Time $t_3(\mu\text{sec})$	Stress Level $P_0(\text{MPa})$
1	27	227	252	- 77
2	25	250	275	- 80
3	25	250	275	-240

C. RESULTS OF NONLINEAR DYNAMIC ANALYSES

1. Load Case 1

Time histories for the longitudinal stress, σ_z , at three locations in the specimen and in the transmitter bar are illustrated in Figures 146 through 149. Time histories for the longitudinal strain, ϵ_z , at the corresponding locations are illustrated in Figures 150 through 153. Time histories for the circumferential strain, ϵ_x , and the radial strain, ϵ_y , at three locations in the specimen are illustrated in Figures 154 through 156, and Figures 157 through 159, respectively.

Profiles for the longitudinal stress, σ_z , at five transverse cross sections in the specimen at selected times are presented in Figures 160 through 164. Profiles for the longitudinal strain, ϵ_z , at the corresponding cross sections and times are presented in Figures 165 through 169.

The failure sequence for the specimens is illustrated in Figure 170. First cracking occurs simultaneously at both the incident and transmitter ends, on the radial surface of the specimen, at time $t = 279 \mu\text{sec}$ (Figure 170a). These are tension cracks, attributed to the radial constraint provided at the pressure bar/specimen interfaces. At time $t = 281 \mu\text{sec}$ (Figure 170b), localized crushing of the concrete at these same locations is observed. At time $t = 282 \mu\text{sec}$ (Figure 170c), material crushing becomes more extensive at the transmitter end of the specimen. Finally, at time $t = 284 \mu\text{sec}$ (Figure 170c), specimen failure by material crushing occurs. It is noted that approximately 25% of the specimen remains intact. This observation suggests that the specimen is not completely pulverized at failure.

2. Load Case 2

Time histories for the longitudinal stress, σ_z , at three locations in the specimen and in the transmitter bar are illustrated in Figures 171 through 174. Time histories for the longitudinal strain, ϵ_z , at the corresponding locations are illustrated in Figures 175 through 178. Time histories for the circumferential strain, ϵ_y , at three locations in the specimen are illustrated in Figures 179 through 181.

Profiles for the longitudinal stress, σ_z , at five transverse cross sections in the specimen at selected times are presented in Figures 182 through 186. Profiles for the longitudinal strain, ϵ_z , at the corresponding cross sections and times are presented in Figures 187 through 191.

The failure sequence for the specimen, from initiation of the first crack until fracture, is illustrated in Figure 192. First cracking occurs simultaneously at both the incident and transmitter ends, on the radial surface of the specimen at time $t = 272 \mu\text{sec}$ (Figure 192a). At time $t = 276 \mu\text{sec}$ (Figure 192b), more localized crushing is observed at these same locations. At time $t = 278 \mu\text{sec}$ (Figure 192c), significant material crushing is observed in the specimen extending from the incident end to slightly past the specimen mid-length. Crushing at the transmitter end remains very localized, however. Finally, at time $t = 284 \mu\text{sec}$ (Figure 192d), specimen failure by material crushing occurs. However, approximately 15% of the specimen remains intact. Similar to Load Case 1, this observation suggests that the specimen is not completely pulverized at failure.

3. Load Case 3

Time histories for the longitudinal stress, σ_z , at three locations in the specimen and in the transmitter bar are illustrated in Figures 193 through 196. Time histories for the longitudinal strain, ϵ_z , at the corresponding locations are illustrated in Figures 197 through 200. Time histories for the radial strain, ϵ_x , and the circumferential strain, ϵ_y , at three locations in the specimen are illustrated in Figures 201 through 203 and Figures 204 through 206, respectively.

Profiles for the longitudinal stress, σ_z , at five transverse cross sections in the specimen at selected times are presented in Figures 207 through 211. Profiles for the longitudinal strain, ϵ_z , at the corresponding cross sections and times are presented in Figures 212 through 216.

The failure sequence for the specimen, from initiation of the first crack until fracture, is illustrated in Figure 217. First cracking occurs at the incident end, on the radial surface of the specimen, at time $t = 216 \mu\text{sec}$ (Figure 217a). It is noted that these cracks are tension-induced. At time $t = 218 \mu\text{sec}$ (Figure 217b), the tensile cracking in this vicinity has become more extensive. At time $t = 226 \mu\text{sec}$ (Figure 217c), the tensile cracking has propagated through a substantial portion of the cross section at the incident end of the specimen. At the same time increment, tensile cracking is observed to initiate at the transmitter end, on the radial surface of the specimen. Finally, at time $t = 236 \mu\text{sec}$ (Figure 217d), the specimen experiences a tension failure on a transverse plane at the transmitter end of the specimen.

4. Summary of Direct Compression Results

The maximum strain rates, $\dot{\epsilon}_x$, predicted at three locations in the specimen (identified as points A, B and C in Figure 218) and in the transmitter bar for all three load cases are summarized in Table 13. The maximum longitudinal stress, σ_z , predicted at these same locations are presented in Table 14. A summary of the predicted failure modes for the specimens is presented in Table 15.

TABLE 13. MAXIMUM STRAIN RATES FOR
DIRECT COMPRESSION TESTS

Location (see Figure 218)	Strain Rate, $\dot{\epsilon}_z$ (sec ⁻¹)		
	Load Case 1	Load Case 2	Load Case 3
A	-22.769	-33.742	-110.839
B	-42.111	-46.743	-112.655
C	-45.885	-60.253	- 10.224
Transmitter			
Bar	- 4.281	- 5.709	- 1.483

TABLE 14. MAXIMUM LONGITUDINAL STRESS FOR
DIRECT COMPRESSION TESTS

Location (see Figure 218)	$(\sigma_z)_{\max}$ (MPa)		
	Load Case 1	Load Case 2	Load Case 3
A	-65.4129	-64.4723	-33.0677
B	-58.3562	-58.4841	-14.6697
C	-63.9065	-62.4872	- 2.68633
Transmitter			
Bar	-61.6733	-63.4877	- 2.71958

TABLE 15. SUMMARY OF DIRECT COMPRESSION SPECIMEN FAILURES

Load		First Cracking		Failure
Case	Location (see Figure 218)	Time (μ sec)	Description	Time (μ sec)
1	E and G	279	Crushing Failure	284
2	E	272	Crushing Failure	284
3	E	216	Tension Failure	236

SECTION IV

DISCUSSION OF RESULTS

A. DIRECT TENSION TESTS

1. Linear Static Analysis

Linear static analyses were conducted on the direct tension specimens to ascertain the stress distribution through various cross sections and to identify areas of stress concentration in the specimen.

Profiles for the longitudinal stress, σ_z , at four cross sections in the square-notch specimen are presented in Figures 11 through 14. Similar plots for the longitudinal stress profiles in the saddle-notch specimen are presented in Figures 15 through 17.

The results of the linear static analyses indicate a non-uniform distribution of the longitudinal stress, σ_z , at all cross sections. The non-uniformity is exaggerated at the sections through the notches. For the square-notch specimen, a stress concentration factor of 2.93 was calculated at the root of the notch (Figures 13 and 14). For the saddle-notch specimen, a stress concentration factor of 1.93 was calculated at the apex of the notch. Regions of stress concentration are also indicated at the radial surfaces of these specimens at cross sections immediately adjacent to the incident bar (Figures 11 and 15) and the transmitter bar (Figure 12). This phenomena is attributed to the Poisson effect, since the specimen is rigidly attached to the bars.

Close scrutiny of the linear static results suggests that failure of the specimen should occur at cross sections through the notches. Also, cracking of the specimens at cross sections in the vicinity of the incident and transmitter bars is also suggested by the results of the linear static analyses.

2. Nonlinear Static Analysis

A static nonlinear material analysis was conducted to identify possible failure mechanisms in the specimens. The concrete material model employed in the nonlinear analyses has been discussed in Section II. The pertinent material parameters implemented in the concrete model are summarized in Table 3.

The loading was applied monotonically over 16 load steps at the free end of the incident bar as illustrated in Figure 20. The failure sequence for the square-notch specimen is presented in Figure 21. First cracking appears at the root of the notch after Load Step 4, and failure of the specimen is manifested by fracture through the notched portion of the cross section.

The failure sequence for the saddle-notch specimen is presented in Figure 23. First cracking occurs at the radial surfaces of the specimen at the cross sections adjacent to the incident and transmitter bars. However, failure of the specimen occurs by fracture through the cross section at the apex of the notch.

The failures predicted by the nonlinear analysis are consistent with the linear analysis results. The saddle-notch specimen exhibits cracking in the cross sections adjacent to the incident and transmitter bars. Linear static analysis results indicated stress concentrations at these locations. The fact that this same phenomena was not observed in the square-notch specimen is attributed to the fact that the stress concentration in the vicinity of the square-notch is more severe than that in the saddle-notch. Consequently, failure in the square-notch specimen occurs in the notched cross section before cracks can develop in any other location.

3. Nonlinear Dynamic Analysis

Dynamic nonlinear material analyses were conducted on the SHPB direct tension specimens described in Section II. The nonlinear material model is the same as that employed in the nonlinear static analyses. The loading conditions of the dynamic analyses are summarized in Figure 25 and Table 4, and are represented as Load Case 1, Load Case 2, and Load Case 3.

The predicted failure sequences for the square-notch specimens are presented in Figures 44, 63 and 82 for Load Cases 1, 2, and 3, respectively, and are summarized in Table 7. For Load Case 1, failure occurs by fracture through the notched cross section. However, significant cracking at both the incident and transmitter ends of the specimen is noted (Figure 44). For Load Case 2, failure occurs by simultaneous fracture at cross sections through the notch and at the incident end of the specimen (Figure 63). For Load Case 3, failure occurs by fracture of the cross section at the incident end of the specimen (Figure 82). The failure patterns predicted by the FEM analyses are consistent with those

observed in the SHPB experiments. These results indicate that the mode of failure is highly sensitive to the rate of loading.

In all three cases, the specimens failed or fractured during the rise time of the loading (incident) pulse. This early failure is evident in the strain gage traces presented in Figures 6, 7, and 8. For Load Case 1 (Figure 6), the transmitted pulse is inverted and illustrates that the peak of the transmitted pulse occurs in the rise time of the reflected pulse. The occurrence of failure early in the incident pulse precludes the use of the reflected pulse to calculate the strain rate in the specimen. However, the peak reflected stress is indicative of the concrete tensile strength and the slope of the transmitted time curve is a measure of the strain rate, assuming a linear elastic material. The strain rates for the SHPB experiments were calculated by dividing the slope of the straight line segment of the transmitted stress by the quasi-static elastic modulus. These experimentally determined strain rates, which are presented in Table 2, are in good agreement with those predicted by the FEM analyses, which are presented in Table 5.

An interesting aspect of the SHPB experiments is the occurrence of oscillations at the trailing end of the transmitted pulse (refer to Figures 6, 7, and 8). Upon fracture of the specimen, an unloading pulse is transmitted toward the specimen/transmitter bar interface. Due to the characteristic impedance mismatch at this interface, a portion of the pulse is trapped between the segment of the specimen which is cemented to the transmitter bar and the fracture plane through the notch. This pulse oscillates back and forth within the broken specimen, but decays rather rapidly. The shape of the oscillation is different in each load case. For the lower strain rate test, Load Case 1, the specimen fractured at the notch giving rise to a comparatively larger oscillation (Figure 6) than was exhibited in the other two load cases. For the intermediate strain rate test, Load Case 2, the specimen fractured at both the notch and the incident end of the specimen resulting in a different signature at the end of the transmitted pulse (Figure 7). The specimen in the high strain rate test, Load Case 3, fractured at the incident end, resulting in a longer length of fractured specimen which remained attached to the transmitter bar. This in turn yielded a different pattern at the end of the transmitted pulse (Figure 8).

It is doubtful that this experimentally observed phenomenon has any significant influence on the tensile strength of the concrete. However, it does

serve as a check on the ability of the FEM simulations to accurately predict the true behavior of the experiments. Indeed, the results obtained from the FEM analyses do indicate the presence of these oscillations at the trailing end of the transmitted pulses, as illustrated in Figures 26, 27, and 28 for Load Case 1, Figures 45, 46, and 47 for Load Case 2, and Figures 64, 65, and 66 for Load Case 3.

The predicted failure sequences for the saddle-notch specimens are presented in Figures 103, 122, and 141 for Load Cases 1, 2, and 3, respectively, and are summarized in Table 10. For Load Case 1, the specimen fractures simultaneously at the incident end and at the apex of the notch (Figure 103). For Load Case 2, failure occurs by fracture of the cross section at the incident end of the specimen (Figure 122). A similar failure is predicted for Load Case 3 (Figure 141), fracture at the incident end of the specimen. Once again, the failure patterns predicted by the FEM analyses are consistent with those observed in the SHPB experiments. And, as expected, the mode of failure is highly sensitive to the rate of loading.

Similar to what was predicted in the square-notch tests, the saddle-notch specimens fractured during the rise time of the loading for all three cases. The strain rates in the specimen at failure, predicted by the numerical analysis, are summarized in Table 8. These values are in good agreement with the experimentally determined strain rates.

B. DIRECT COMPRESSION TESTS

1. Load Case 1

The predicted failure sequence for Load Case 1 is presented in Figure 170 and summarized in Table 15. Failure occurs by material crushing in approximately 75% of the specimen. At the time of failure the specimen is, for the most part, still intact. This observation suggests relatively large fragmentation pieces. This predicted result is consistent with that observed in the SHPB experiment for this load case.

The longitudinal stress histories, σ_z , are presented in Figures 146 through 148. The corresponding longitudinal strain histories, ϵ_z , are presented in Figures 150 through 153. These stress and strain histories support the compressive failure sequence illustrated in Figure 170. However, an interesting

result is disclosed in the longitudinal stress profiles presented in Figures 160 and 164, which represent the stress condition through cross sections at the incident end and transmitter end of the specimen, respectively. It is observed in these profiles, that the longitudinal stress is uniform throughout the cross section except at the radial surface of the specimen, where a 50% decrease in stress is noted. This phenomenon is also evident in the longitudinal strain profiles presented in Figures 165 and 169. This idiosyncrasy is attributed to the Poisson effect. Since the specimen and the bars are modeled as a continuous medium, the specimen is restrained from lateral movement in the vicinity of the specimen/bar interfaces. This condition in the numerical model (continuous medium) significantly prejudices the results obtained in the high rate load case.

2. Load Case 2

The predicted failure sequence for Load Case 2 is presented in Figure 192 and summarized in Table 15. Failure occurs by material crushing in approximately 85% of the specimen. At the time of failure the specimen is still intact. This observation suggests relatively large fragmentation pieces. This predicted result is consistent with that observed in the SHPB experiment for this load case.

The longitudinal stress histories, σ_z , are presented in Figures 171 through 174. The corresponding longitudinal strain histories, ϵ_z , are presented in Figures 175 through 179. Time histories for the radial strain, ϵ_y , at three locations in the specimen are presented in Figures 179 through 181. These stress and strain histories support the predicted compressive failure sequence illustrated in Figure 192. The longitudinal stress profiles at five cross sections within the specimen are illustrated in Figures 182 through 186. It is observed from these profiles that the longitudinal stress distribution is uniform throughout the specimen, except at the incident (Figure 132) and transmitter ends (Figure 196). It is observed in these profiles that there is a significant reduction in stress (approximately 50%) at the radial surface of the specimen. This observation is corroborated by the longitudinal strain profiles presented in Figures 187 and 191. This observation is similar to that reported for Load Case 1, and is also attributed to the Poisson effect.

3. Load Case 3

The predicted failure sequence for Load Case 3 is presented in Figure 217 and summarized in Table 15. The failure for this load case is tension-induced. First cracking initiates at the incident end, on the radial surface of the specimen (Figure 217a). With time, the tensile cracking in this region becomes more extensive (Figure 217b). As the stress wave propagates through the specimen, tensile cracking develops at the transmitter end of the specimen (Figure 217c). The specimen finally fails in a tension mode at the incident end (Figure 217d).

The failure mode exhibited in Load Case 3 is directly attributed to the boundary constraints imposed at the specimen/bar interfaces. Since the specimen is constrained from lateral movement at these locations, secondary tensile stresses due to the Poisson effect develop, which eventually perpetrate failure. Time histories for the longitudinal stress, σ_z , illustrated in Figures 193, 194, and 195 depict tension stresses with magnitudes reaching the tension cut-off limit (3.67 MPa). Moreover, profiles for the longitudinal stress, presented in Figures 207 through 211, clearly define the tensile stress state in the specimen. Unfortunately, the state of stress and failure mode exhibited in this load case are not representative of the actual behavior, but are conditions prejudiced by the assumption of a continuous medium. Indeed, the model does not accurately represent the SHPB experiment at this high strain rate. Therefore, the direct compression tests for all three load cases were reanalyzed with modified boundary conditions at the specimen/bar interfaces. The results of the reanalyses are presented in Appendix B.

SECTION V

CONCLUSIONS AND RECOMMENDATIONS

A. CONCLUSIONS

1. Direct Tension Tests

The results of the linear analyses indicate high stress concentration factors in the vicinity of the notches. In the square-notch test, a stress concentration factor of 2.93 was calculated at the root of the notch. For the saddle-notch specimen, a stress concentration factor of 1.93 was calculated at the apex of the notch. Regions of stress concentration, albeit much lower than those determined in the notches, are also indicated in the radial surfaces of the specimen next to the incident bar and transmitter bar. The results of the linear analyses suggest failures on a transverse plane passing through the notch of the respective specimens.

The results from the nonlinear static analyses support the inferences of failure projected by the linear analyses. Failure of the square-notch specimen occurred by fracture through the root of the notch. First cracking appears at the root of the notch. The failure sequence is illustrated in Figure 21. Failure of the saddle-notch specimen occurred by fracture through the apex of the notch. However, first cracking appears in the cross sections adjacent to the incident and transmitter bars. The failure sequence is illustrated in Figure 23.

In the dynamic nonlinear analyses, the predicted mode of failure depends on the rate of loading for both the square-notch and saddle-notch specimens. For a low strain rate, failure occurs in the immediate vicinity of the notch as illustrated in Figure 44 and Table 7 for the square-notch, and Figure 103 and Table 10 for the saddle-notch. For an intermediate strain rate, the square-notch specimen experiences a simultaneous failure at the notch and at the incident end (Figure 63 and Table 7), whereas the saddle-notch specimen fails at the incident end (Figure 122 and Table 10). For a high strain rate both the square-notch (Figure 82 and Table 7) and the saddle-notch (Figure 141 and Table 10) specimens experience fracture at the incident end. Regardless of the rate of loading, however, failure invariably occurs during the rise time of the loading, before multiple reflections can develop within the specimen.

2. Direct Compression Results

The FEM model employed in the direct compression study did not accurately represent the SHPB tests for the high load rate case (Load Case 3). However, the model did accurately represent the SHPB experiment of the low load rates (Load Cases 1 and 2). The results predicted for these cases are consistent with those observed in the experiment. The predicted failure sequence for Load Case 1 is illustrated in Figure 170. The specimen fails in a crushing mode, but remains relatively intact. It is interesting to note that during the failure sequence the specimen exhibits relatively significant radial tension strains (ϵ_r), which are illustrated in Figures 157 and 158. The extent to which these tensile strains influence the failure has not been discerned.

The predicted failure sequence for Load Case 2 is illustrated in Figure 192. Similar to Load Case 1, the specimen fails in a crushing mode, but is not completely pulverized. This observation suggests relatively large pieces of fragmentation, which is consistent with behavior exhibited in the SHPB experiments. Significant radial tensile strains are also exhibited in this load case (Figures 179 and 190).

The predicted results for Load Case 3 are tension dominated due to the boundary constraints imposed at the specimen/bar interfaces. The assumption of a continuous medium (that is, a continuous model of the bars and the specimen) accurately represents the direct tension tests, but grossly misrepresents the direct compression tests, at least at the highest load rate. At such rates (for example Load Case 3), the secondary tensile stresses in the vicinity of the specimen/bar interfaces build up to the tensile strength of the concrete and precipitate a tension failure prior to arrival of any significant compressive stress wave. Refer to Appendix B for reanalyses of the direct compression tests.

B. RECOMMENDATIONS

The failures predicted in the direct tension tests are highly sensitive to the rate of loading. This observation is also supported by the results of the SHPB experiments. Moreover, the material model employed in the FEM analyses predicated failure upon the static tensile strength of concrete. Therefore, it is recommended that additional analyses be conducted at a wide range of load rates to quantify the relationship between load rate and the mode of failure. Additional numerical analyses should be conducted using a material model having

higher tensile strengths to investigate material strain rate effects on the mode of failure.

Finally, with respect to the direct tension tests, the notches in the specimens analyzed in this study were relatively shallow. It is recommended that specimens with deeper notches be analyzed, both experimentally and numerically, to quantify the effect of notch depth on the mode of failure.

The results obtained for the numerical simulation of the direct compression tests were prejudiced by the boundary constraints imposed at the bar/specimen interfaces. This assumption in the FEM model instigated a tension dominated failure in the high load rate case (Load Case 3), thus rendering the results inconsequential. It is therefore recommended that the direct compression analyses be redone with an FEM model which accurately represents the discontinuity between the specimen and the bars. This can be accomplished by imposing contact surfaces at the specimen/bar interfaces or by implementing the appropriate constraint equations at these same locations. Refer to Appendix B for the results of the reanalysis of the direct compression tests with modified boundary conditions at the specimen/bar interfaces.

Furthermore, it has been suggested by other investigators that confining pressure can significantly influence the failure mode of concrete at high strain rates. However, it is very difficult to simulate confinement in SHPB experiments. Therefore, it is recommended that FEM analysis of SHPB direct compression tests with varying intensities of confining pressure be conducted to investigate its effects on ultimate strength and mode of failure.

REFERENCES

1. Fundamental of Protective Design for Conventional Weapons, Department of the Army, Waterways Experiment Station, Corps of Engineers, Vicksburg, MS, July 1984.
2. Ross, C.A., Kuennen, S.T., and Tedesco, J.W., "Experimental and Numerical Analysis of High Strain-Rate Concrete Tensile Tests," Micromechanics of Failure of Quasi-Brittle Materials, Elsevier Science Publishing Co., New York, NY, pp. 353-364, 1990.
3. Ross, C.A., Kuennen, S.T., and Strickland, W.S., "High Strain Rate Effects on Tensile Strength of Concrete," Fourth International Symposium on the Interaction of Non-nuclear Munitions with Structures, Panama City Beach, FL, April 17-21, 1989.
4. Ross, C.A., Split-Hopkinson Pressure Bar Tests, ESL-TR-88-82, Air Force Engineering and Services Center, Tyndall AFB, FL, 1989.
5. Tedesco, J.W., Numerical Analysis of Dynamic Splitting-Tensile and Direct Tension Tests, ESL-TR-89-45, Air Force Engineering and Services Center, Tyndall AFB, FL, Contract FO8635-88-C-0195, 1990.
6. ADINA - A Finite-Element Program for the Automatic Dynamic Incremental Nonlinear Analysis, ARD 87-1, ADINA R&D, Inc. Watertown, MA, 1987.
7. Ross, C.A., Thompson, P.Y., and Tedesco, J.W., "Split-Hopkinson Pressure Bar Tests on Concrete and Mortar in Tension and Compression," ACI Materials Journal, V. 86, No. 5, pp. 475-485, September-October 1989.
8. Ross, C.A., Nash, P.T., and Friesenhahn, G.J., Pressure Waves in Soils Using a Split-Hopkinson Pressure Bar, ESL-TR-86-29, Engineering Services Laboratory, HQ Air Force Engineering and Services Center, Tyndall AFB, FL, July 1986.
9. ADINA, Theory and Modeling Guide, ARD 84-4, ADINA R&D, Inc., Watertown, MA, December 1984.
10. Malvern, L.E. and Ross, C.A., Dynamic Response of Concrete and Concrete Structures, First Annual Technical Report, AFOSR, Contract F49620-83-K007, 1984.
11. Nicholas, T., "Material Behavior at High Strain Rates," Chapter 8 in Impact Dynamics, Zukas, J.R., Editor, John Wiley & Sons, New York, NY, pp. 277-332, 1982.

12. Tedesco, J.W., Ross, C.A., and Brunair, R.M., "Numerical Analysis of Dynamic Split-Cylinder Tests," Computers and Structures, Vol. 32, No. 3, pp. 609-624, 1989.
13. Tedesco, J.W., Stress Wave Propagation in Layered Media, Final Report, AFOSR, Contract F49620-85-C-0013, 1988.
14. Bathe, K.J., Walczak, J., Welch, A., and Mistry, N., "Nonlinear Analysis of Concrete Structures," Computers and Structures, Vol. 32, No. 314, pp. 563-590, 1989.
15. Tedesco, J.W., Hayes, J.R., and Landis, D.W., "Dynamic Response of Layered Structures Subject to Blast Effects of Non-nuclear Weaponry," Computers and Structures, Vol. 26, No. 1, pp. 79-86, 1987.
16. Tedesco, J.W. and Landis, D.W., "Wave Propagation Through Layered Systems," Computers and Structures, Vol. 32, No. 3, pp. 625-638, 1989.
17. Tedesco, J.W. and McGill, P.B., "Dynamic Response of Prestressed Concrete Armor Units to Pulsating Loads", Journal of Ocean Engineering, Vol. 18, No. 3, pp. 175-189, 1991.
18. Malvern, L.E., Jenkins, D.A., Tianxi, T. and Ross, C.A., "Dynamic Compressive Testing of Concrete," Proceedings of the Second Symposium on the Interaction of Non-nuclear Munitions with Structures, Panama City Beach, FL, April 15-18, 1985, pp. 397-402.
19. Malvern, L.E. and Ross, C.A., Dynamic Response of Concrete and Concrete Structures, Second Annual Technical Report, AFOSR, Contract F49620-83-K007, February 1985.
20. Malvern, L.E. and Ross, C.A., Dynamic Response of Concrete and Concrete Structures, Final Report, AFOSR, Contract F49620-83-K007, May 1986.
21. Lindholm, U.S., "Some Experiments with the Split-Hopkinson's Pressure Bar," J. Mech. Phys. Solids, Vol. 12, pp. 317-335, 1964.
22. Kolsky, H., "An Investigation of the Mechanical Properties of Materials at Very High Strain Rates of Loading", Proceedings of the Physical Society, Section B, Vol. 62, pp. 676-700, 1949.

APPENDIX A: FIGURES FOR SECTIONS I-IV

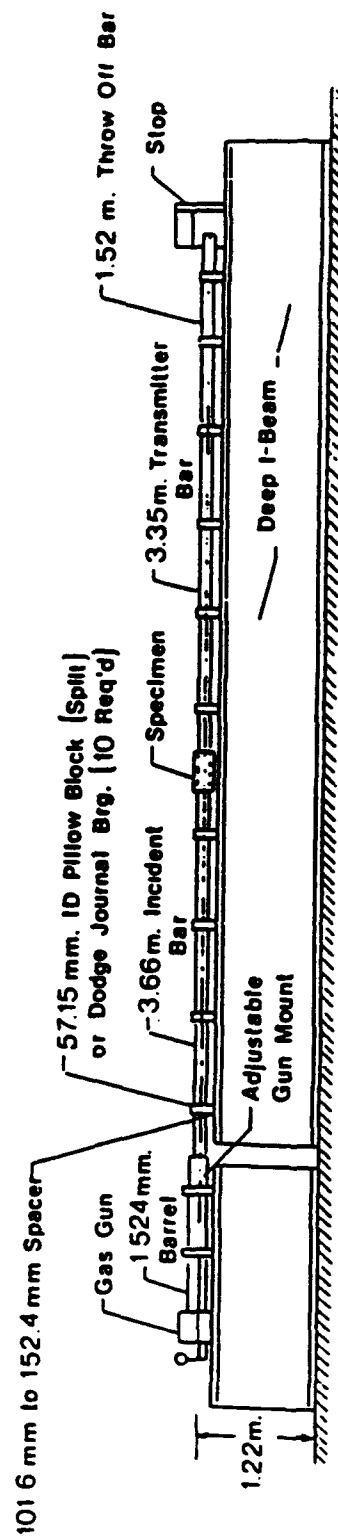


Figure 1. Illustration of AFCEA 51 mm SHPB.

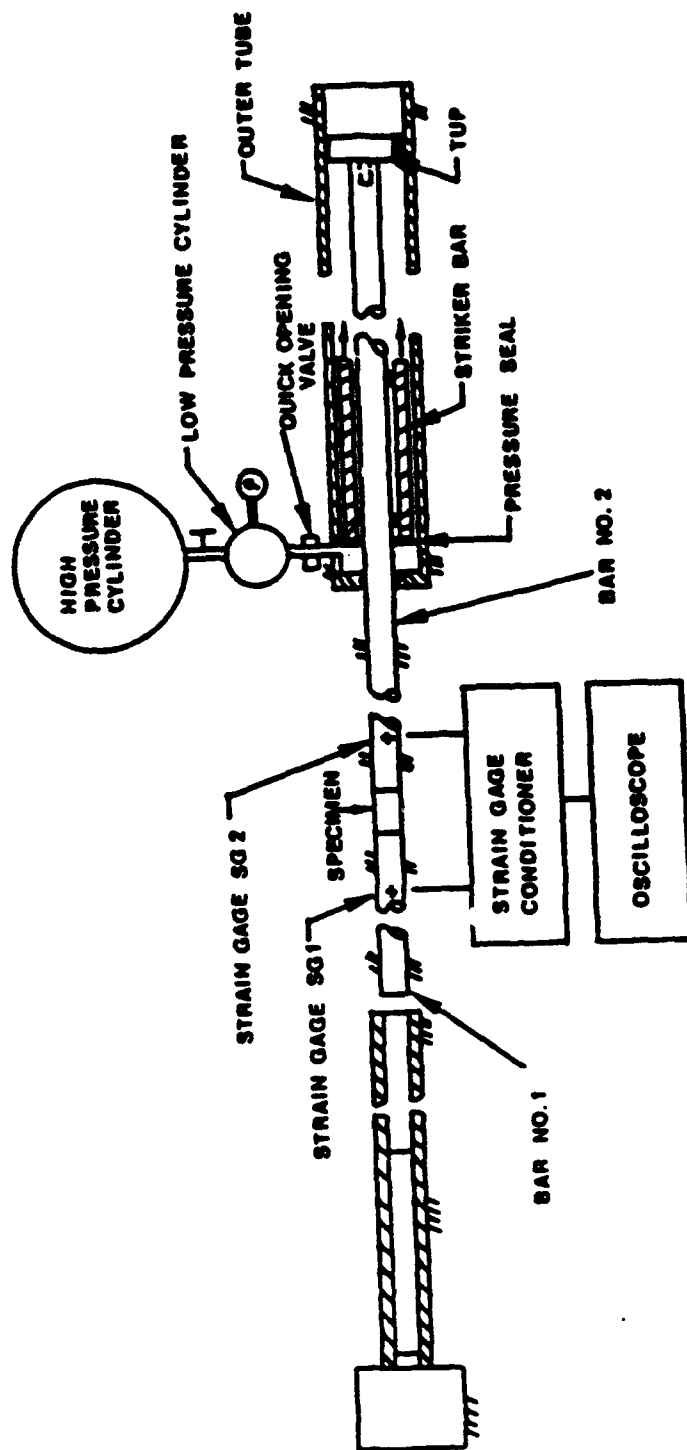


Figure 2. Details of AFCESA SHPB in tension mode of operation.

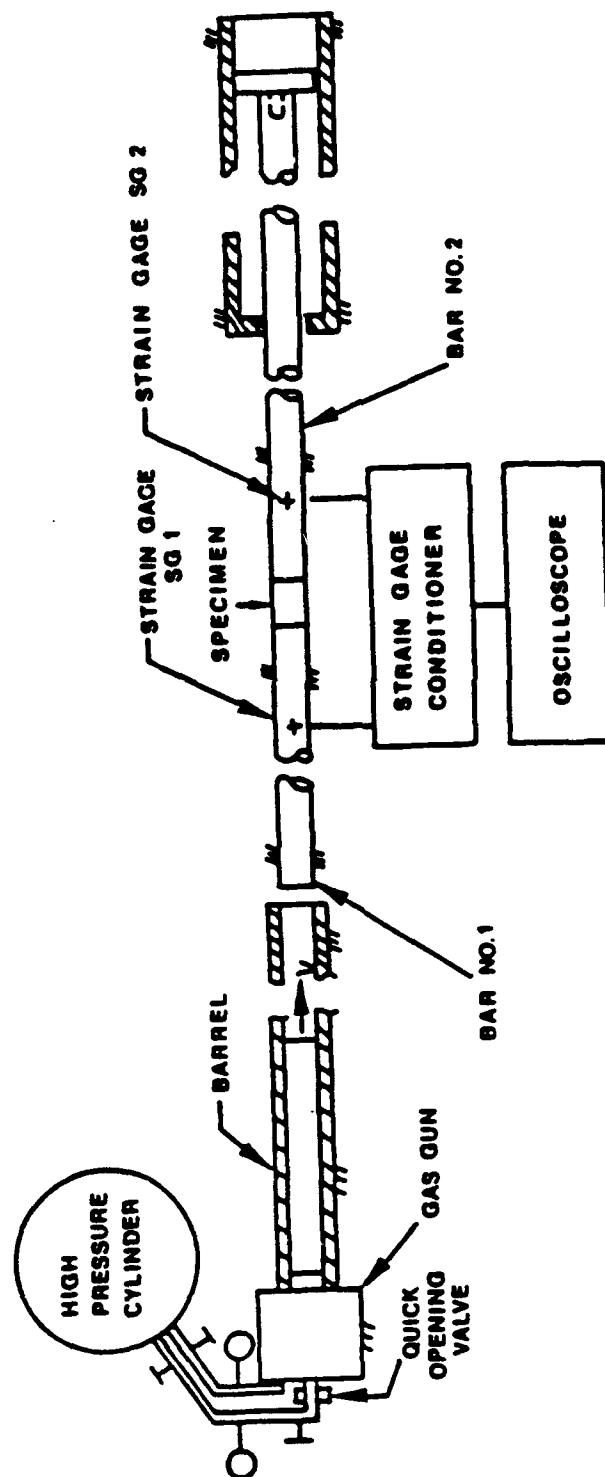


Figure 3. Details of AFCESA SHPB in compression mode of operation.

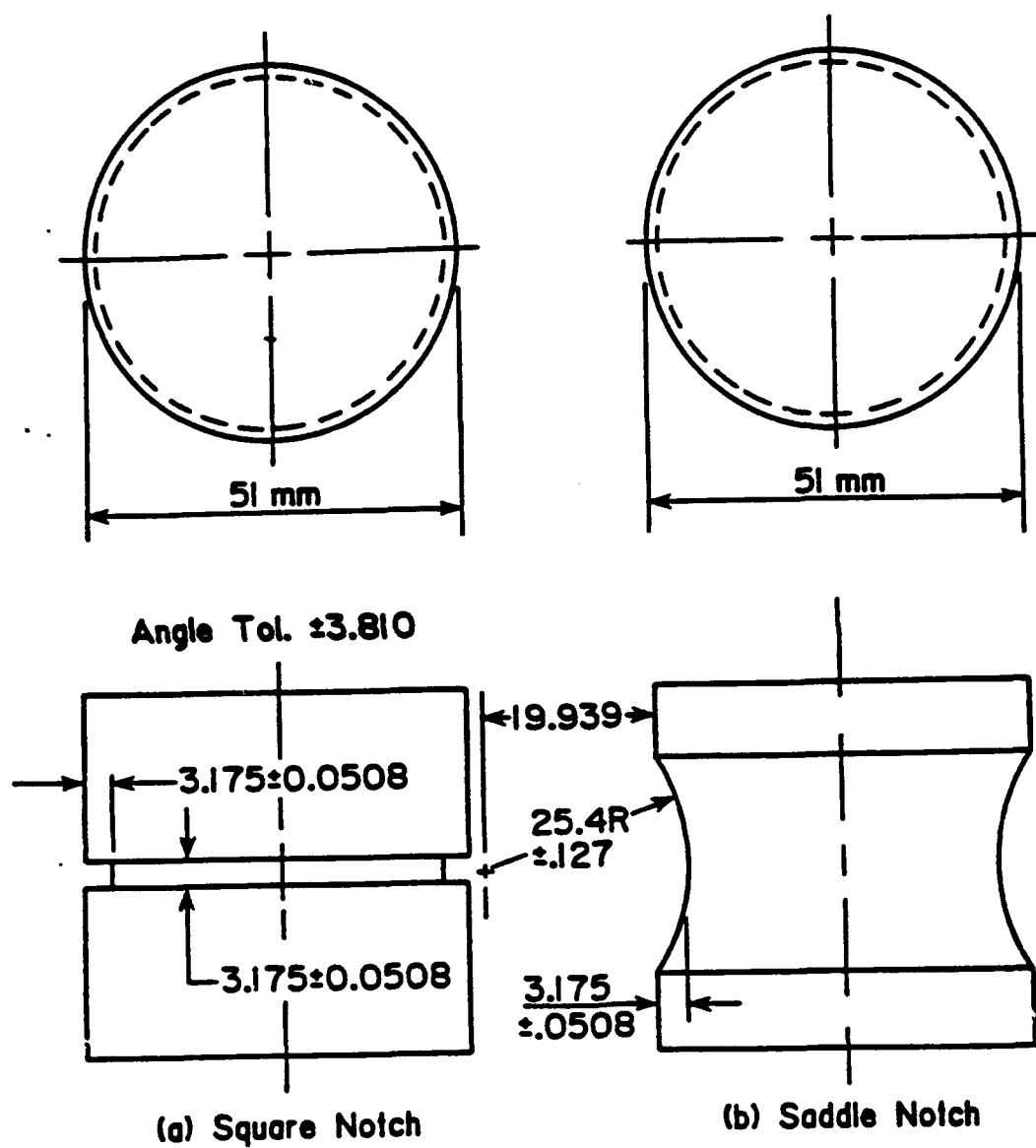


Figure 4. Direct tension specimens.

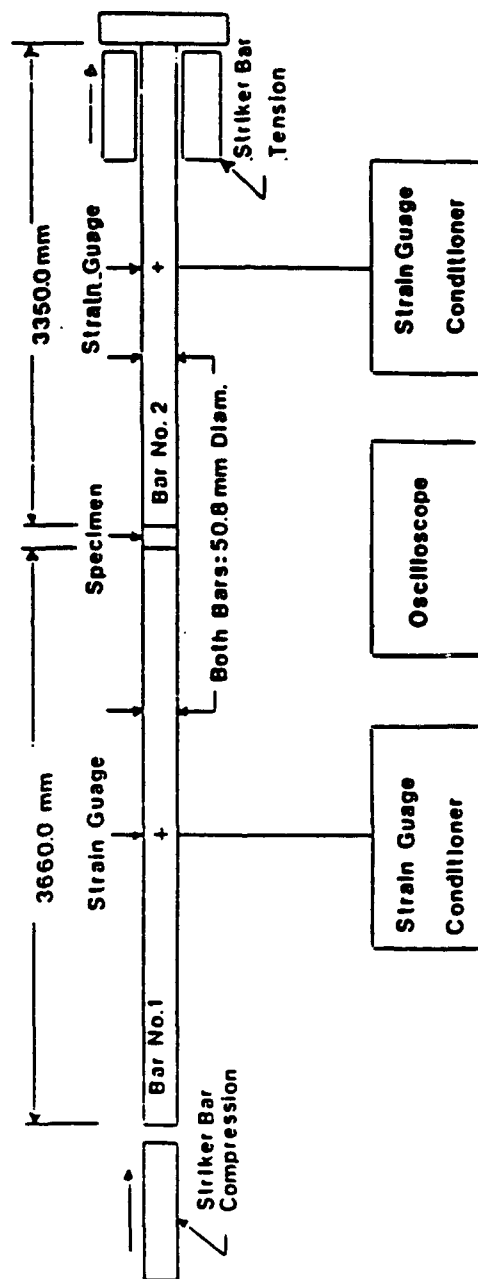


Figure 5. Operational schematic of the SHPB.

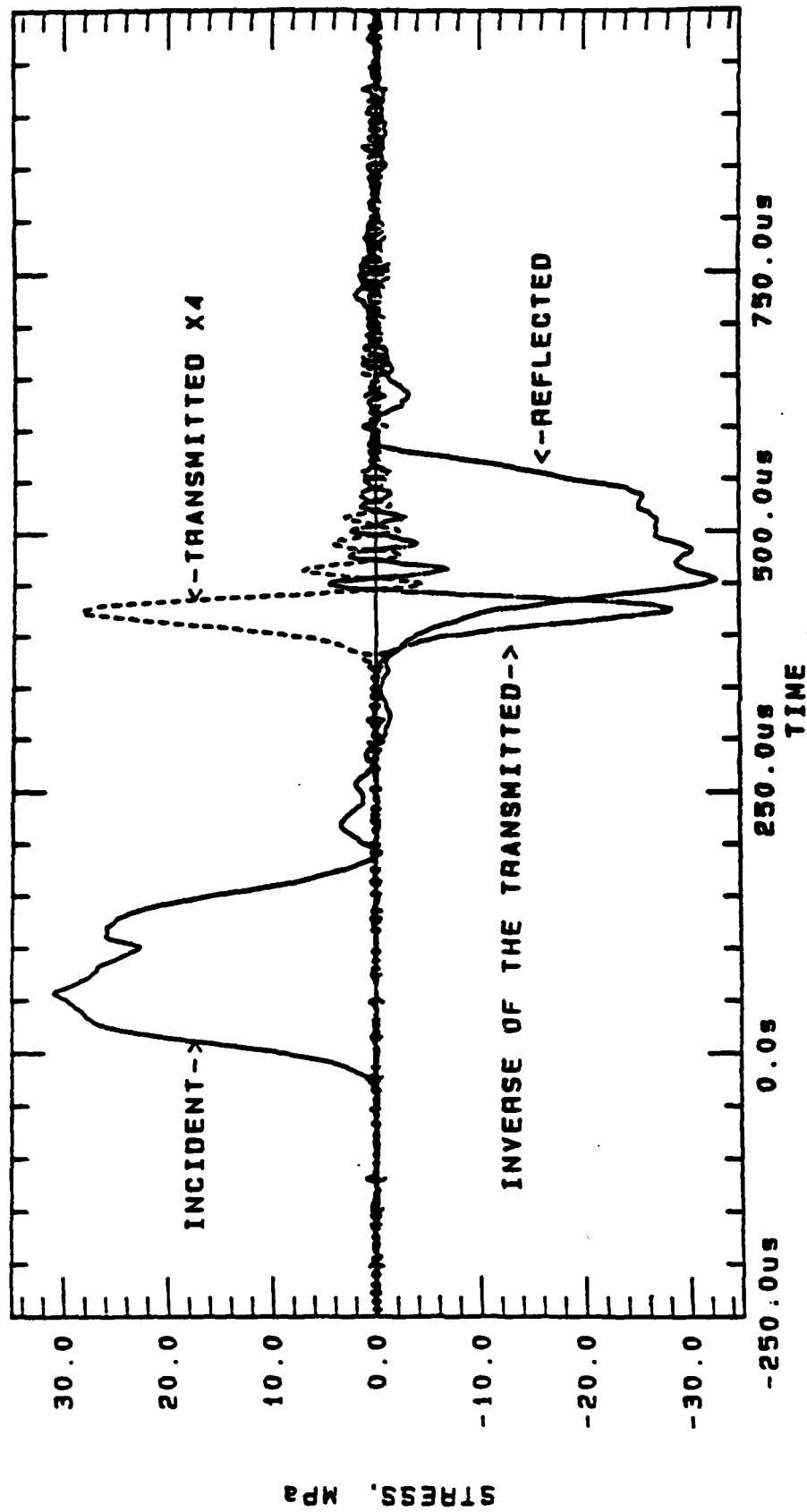


Figure 6. Square notch test data trace for load case 1.

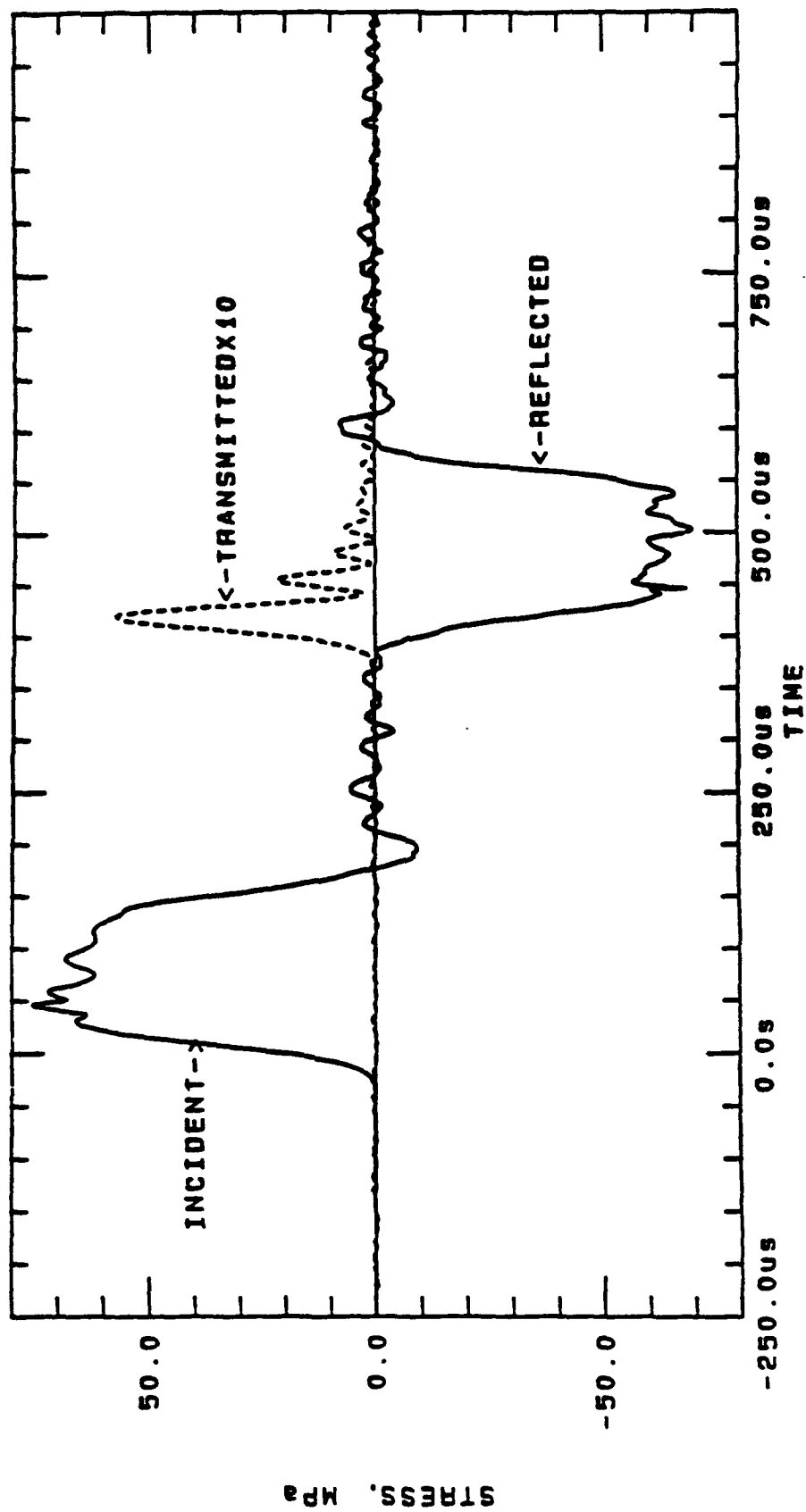


Figure 7. Square notch test data trace for load case 2.

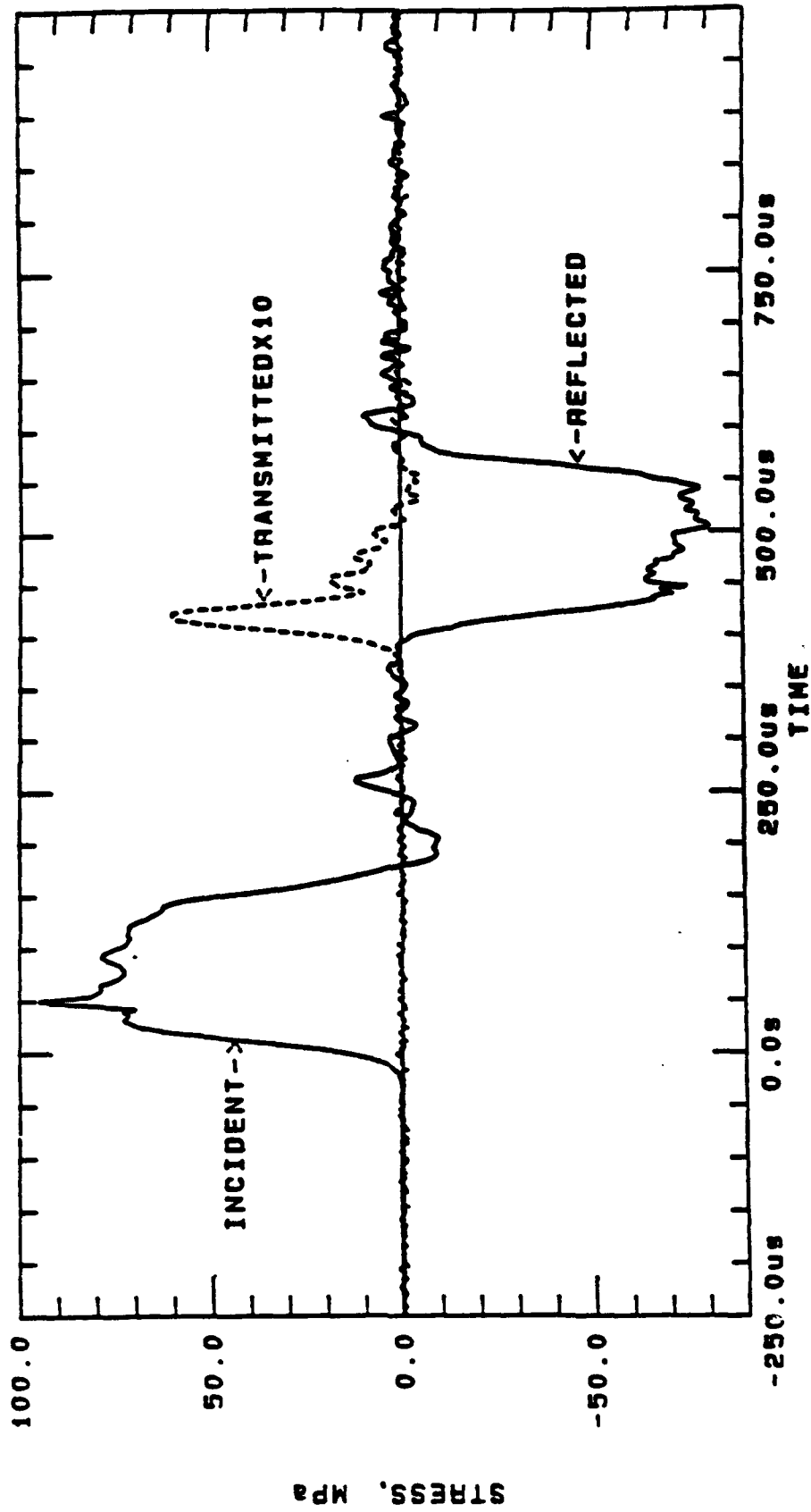


Figure 8. Square notch test data trace for load case 3.

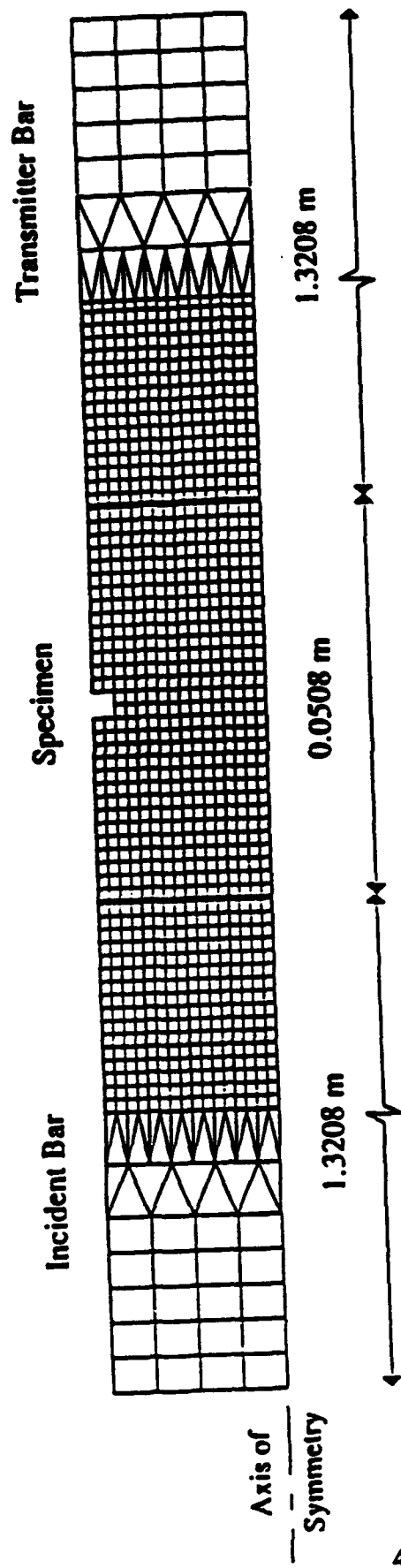


Figure 9. FEM model of square-notch specimen and portion of the SHPB.

Transmitter Bar

Specimen

Incident Bar

Axis of
Symmetry

Symmetry

1.3208 m

0.0508 m

1.3208 m

Figure 10. FEM model of saddle-notch specimen and portion of the SHPB.

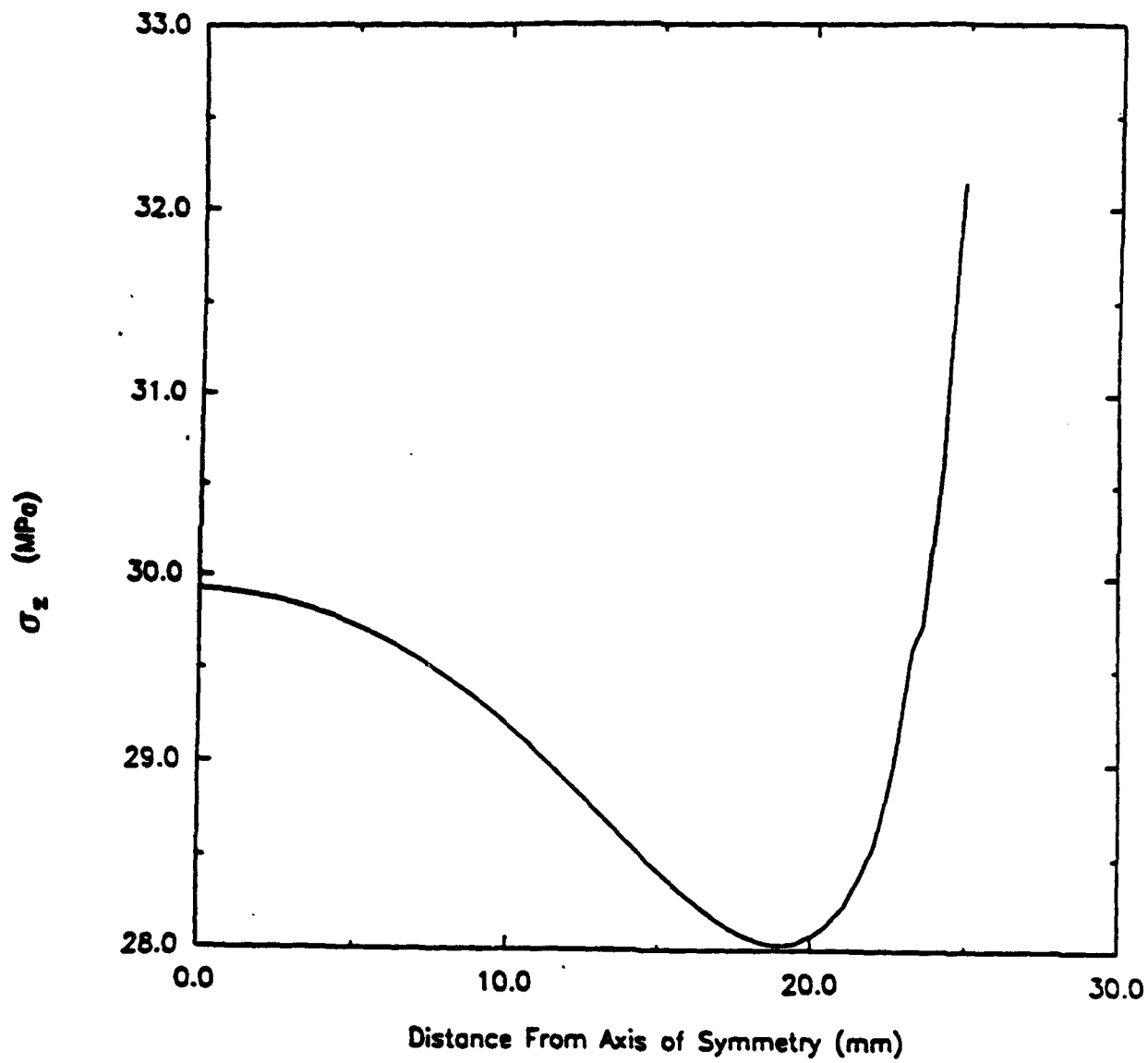


Figure 11. Longitudinal stress (σ_z) distribution in cross section at the incident end of specimen, linear static analysis.

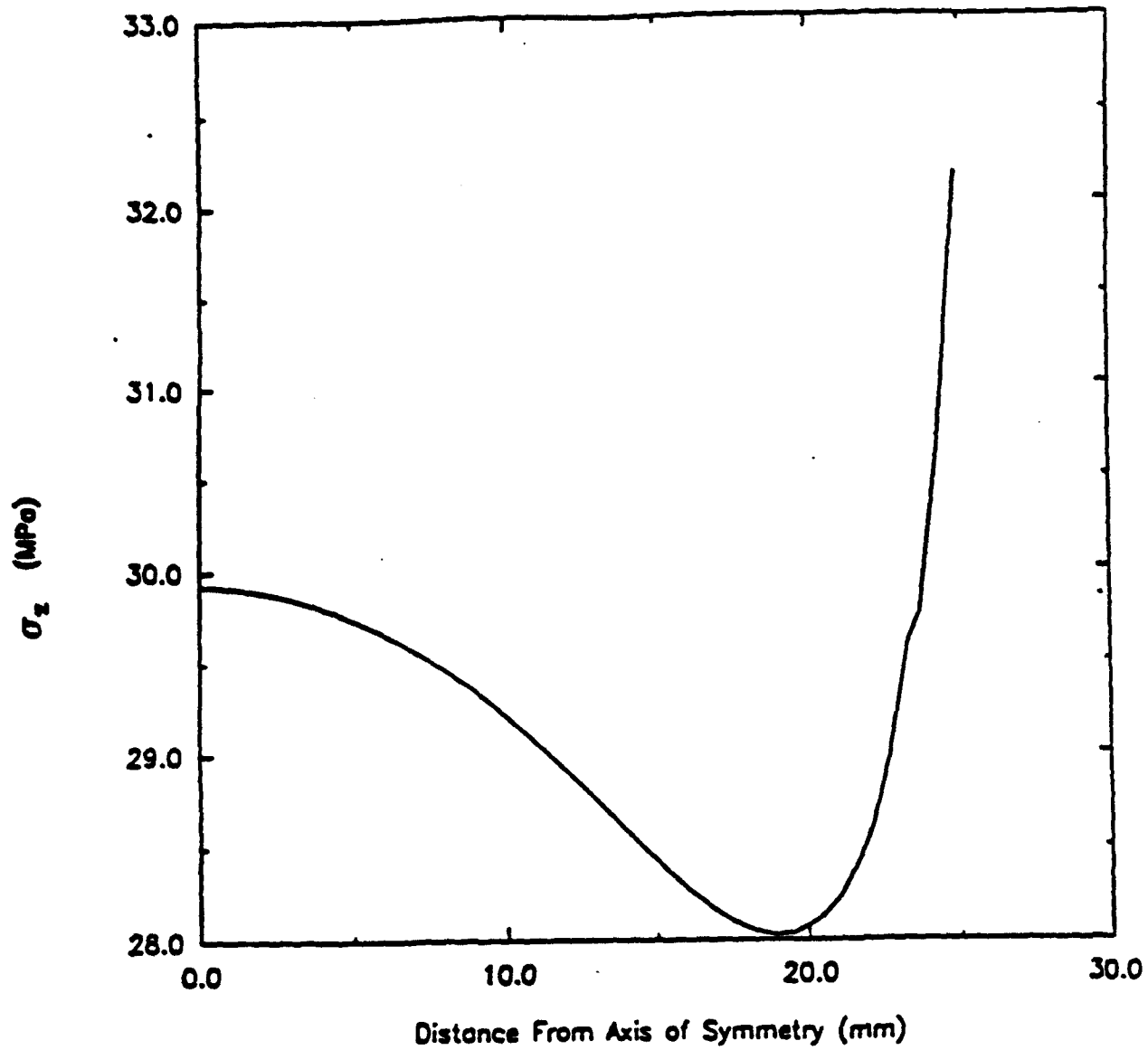


Figure 12. Longitudinal stress (σ) distribution in cross section at the transmitter end of specimen, linear static analysis.

Incident Bar

Transmitter Bar

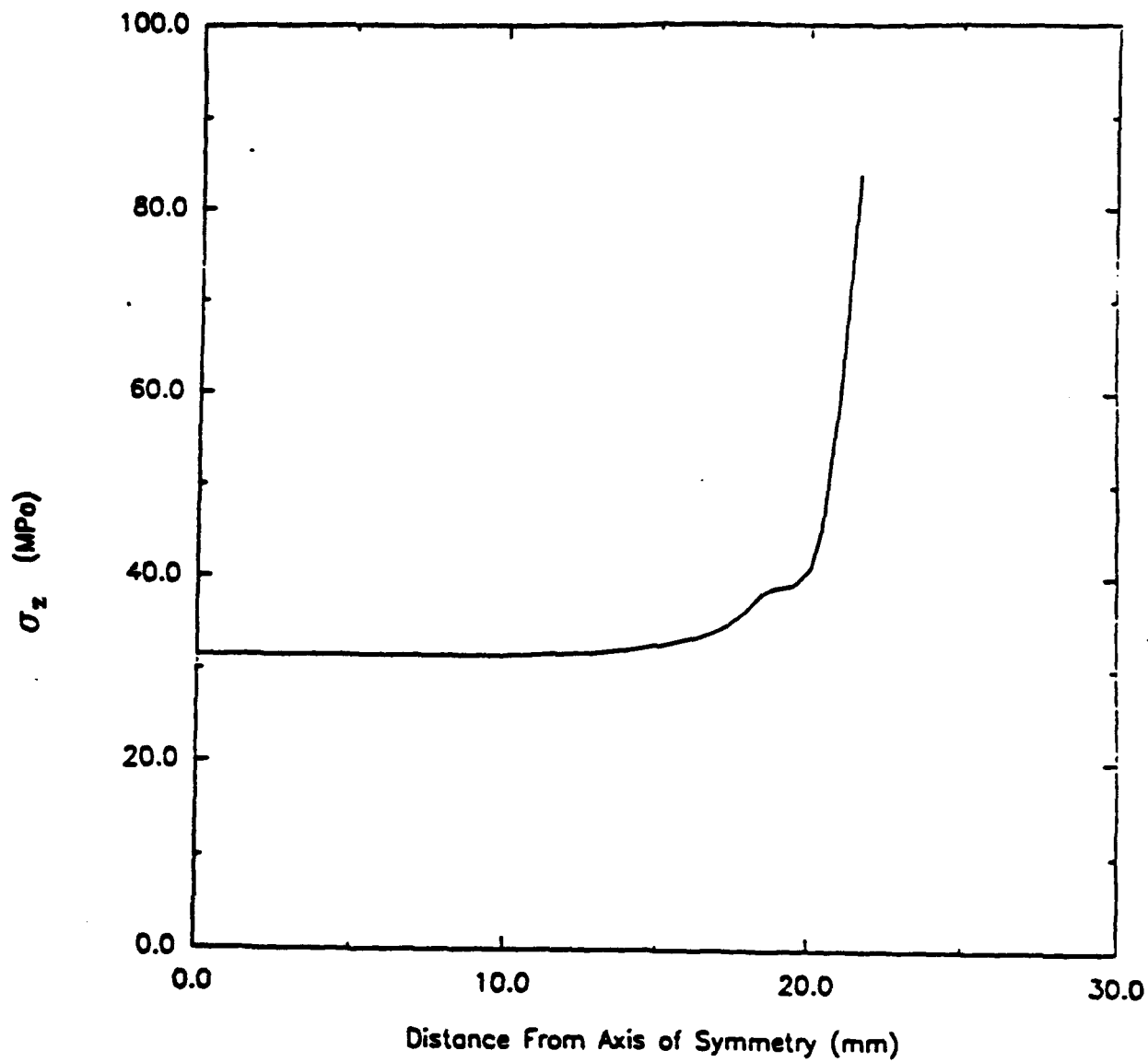


Figure 13. Longitudinal stress (σ_z) distribution in cross section at root of notch, linear static analysis.

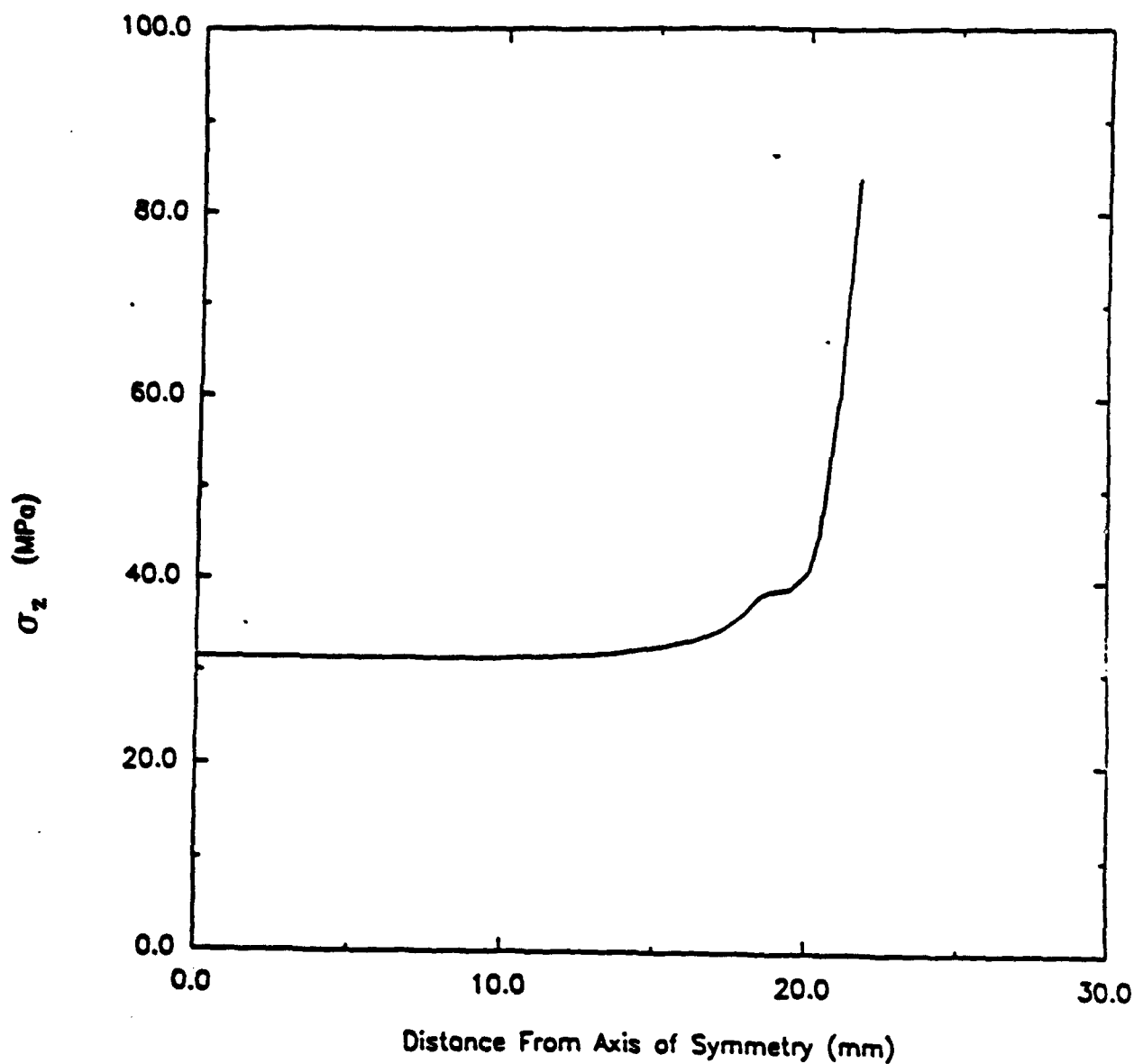


Figure 14. Longitudinal stress (σ_z) distribution in cross section at root of notch, linear static analysis.

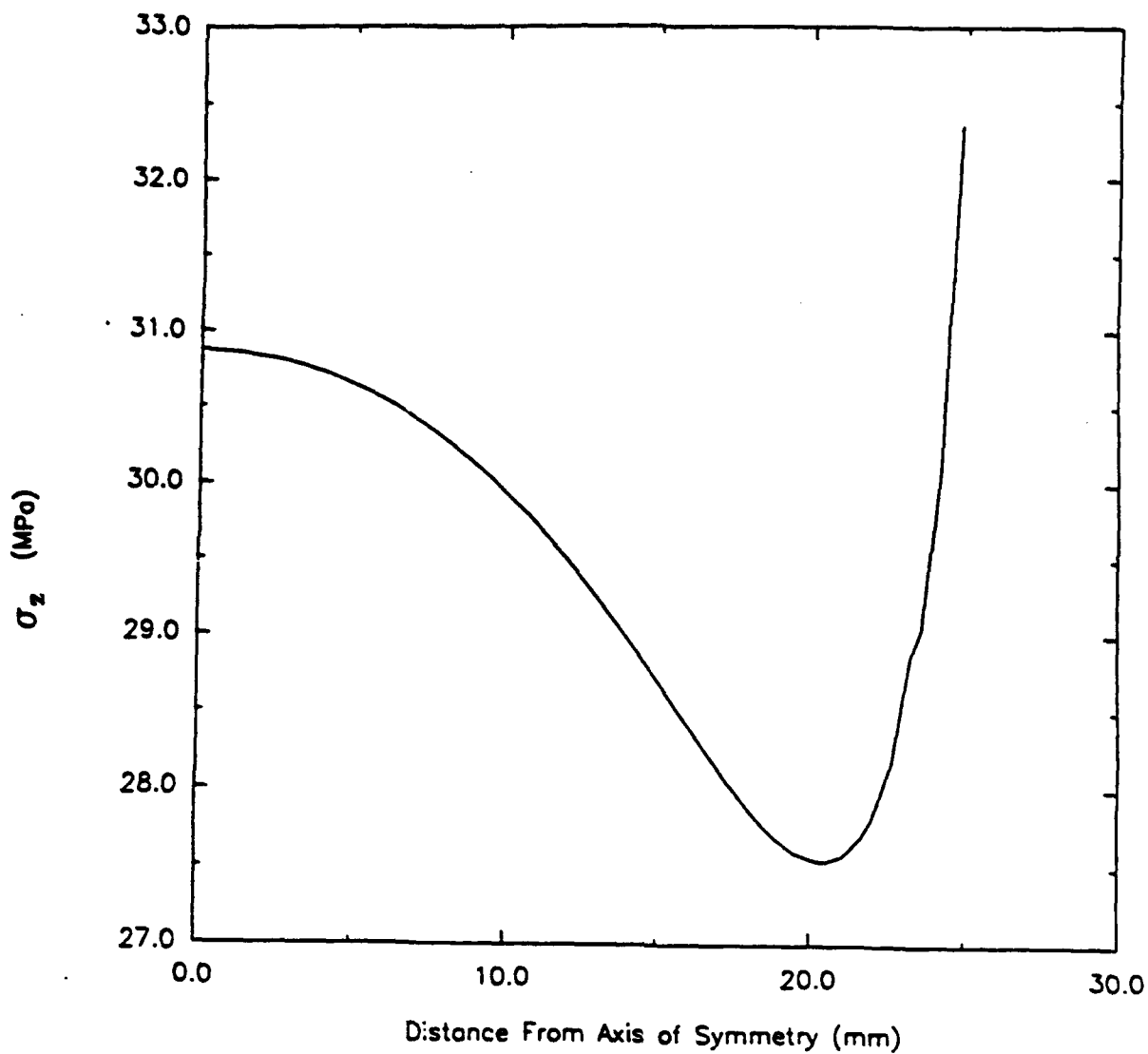


Figure 15. Longitudinal stress (σ_z) distribution in cross section at the incident end of specimen, linear static analysis.

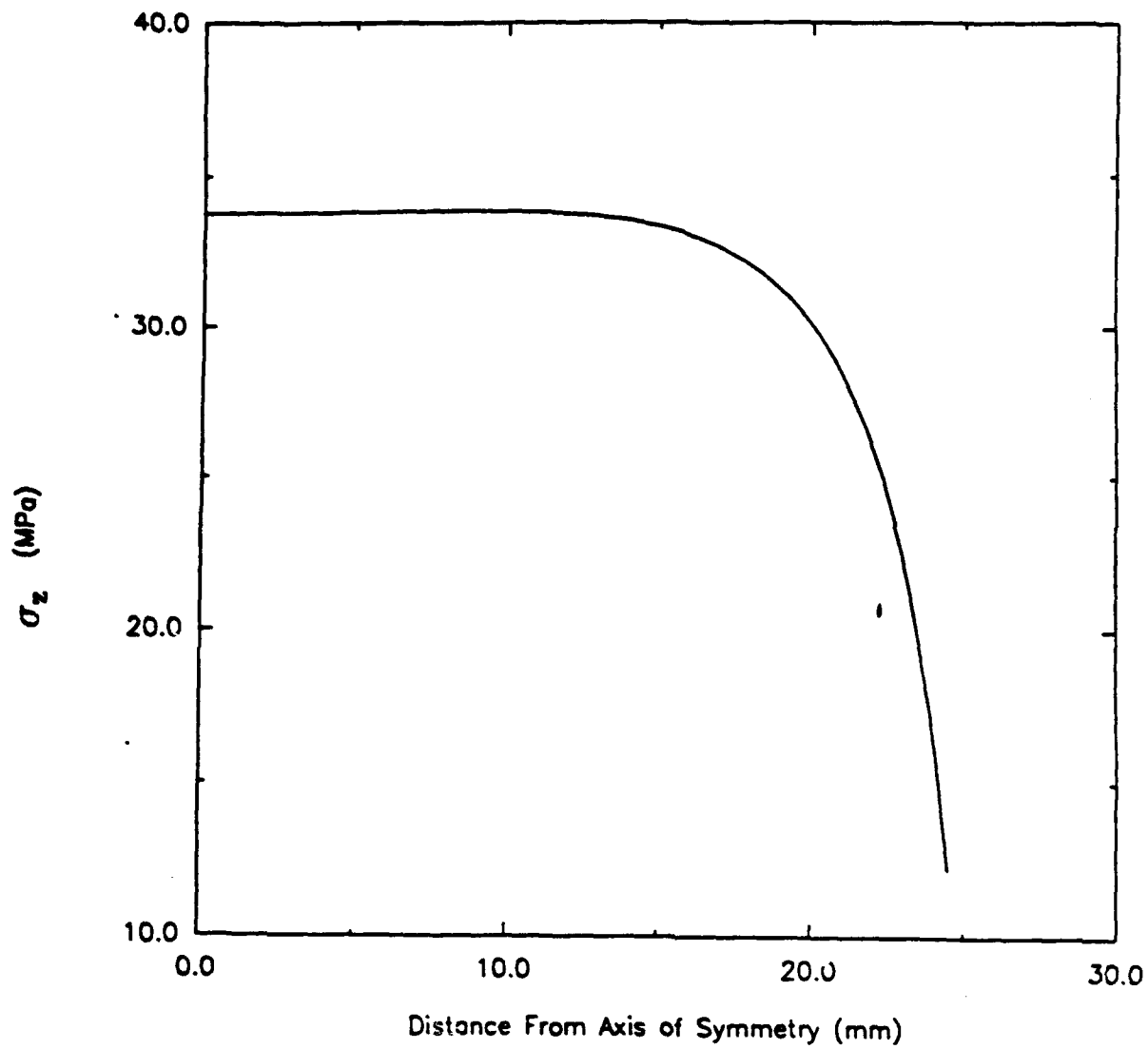
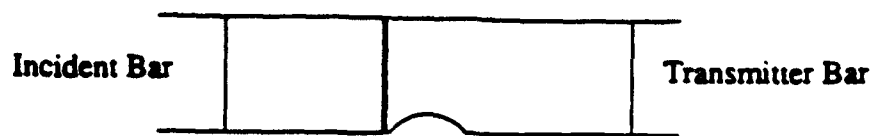


Figure 16. Longitudinal stress (σ_z) distribution in cross section at the transmitter end of specimen, linear static analysis.

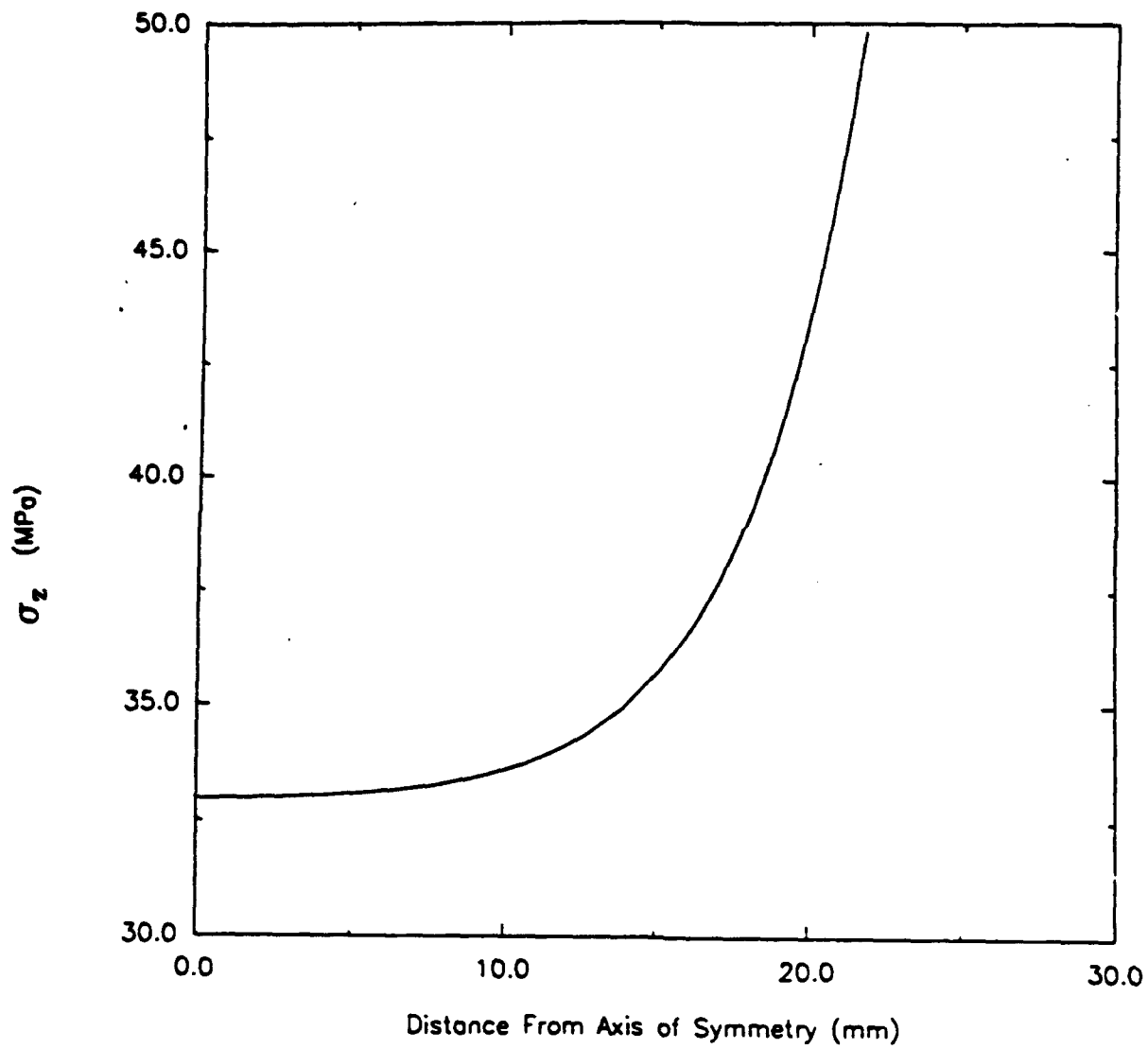
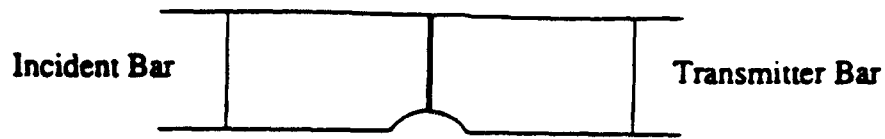


Figure 17. Longitudinal stress (σ) distribution in cross section through apex of notch, linear static analysis.

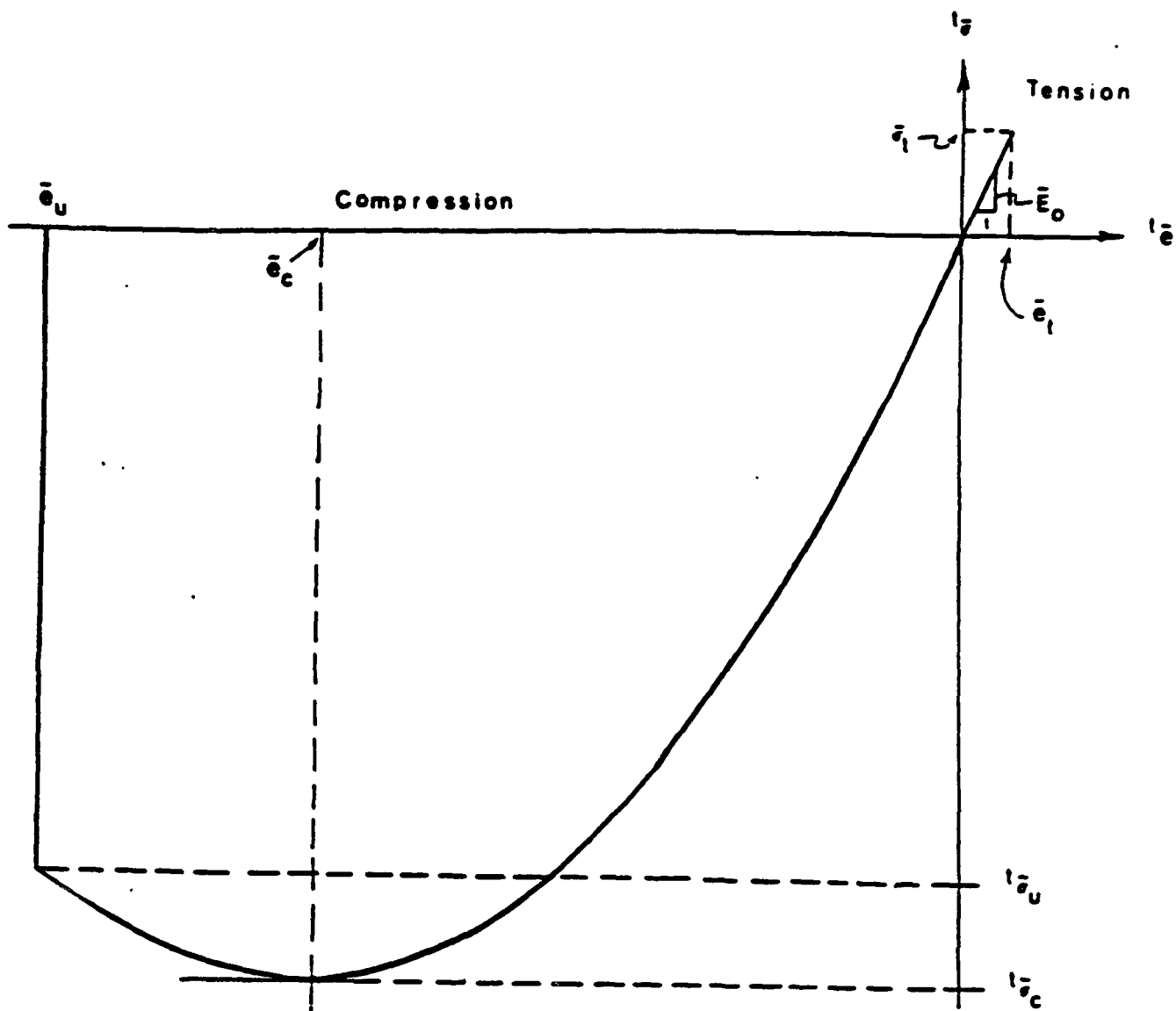


Figure 18. Uniaxial stress-strain relation used in concrete model.

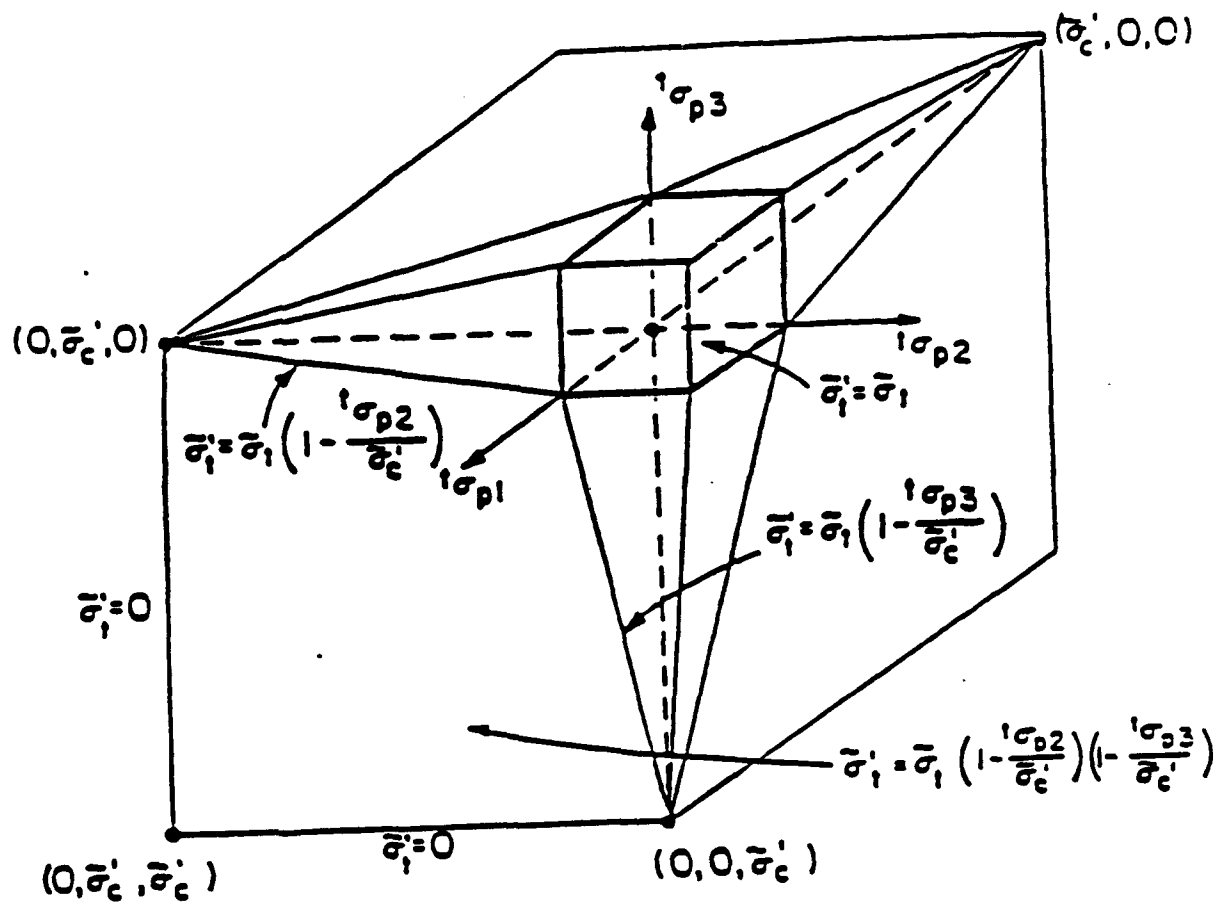


Figure 19. Three dimensional tension failure envelope of concrete model.

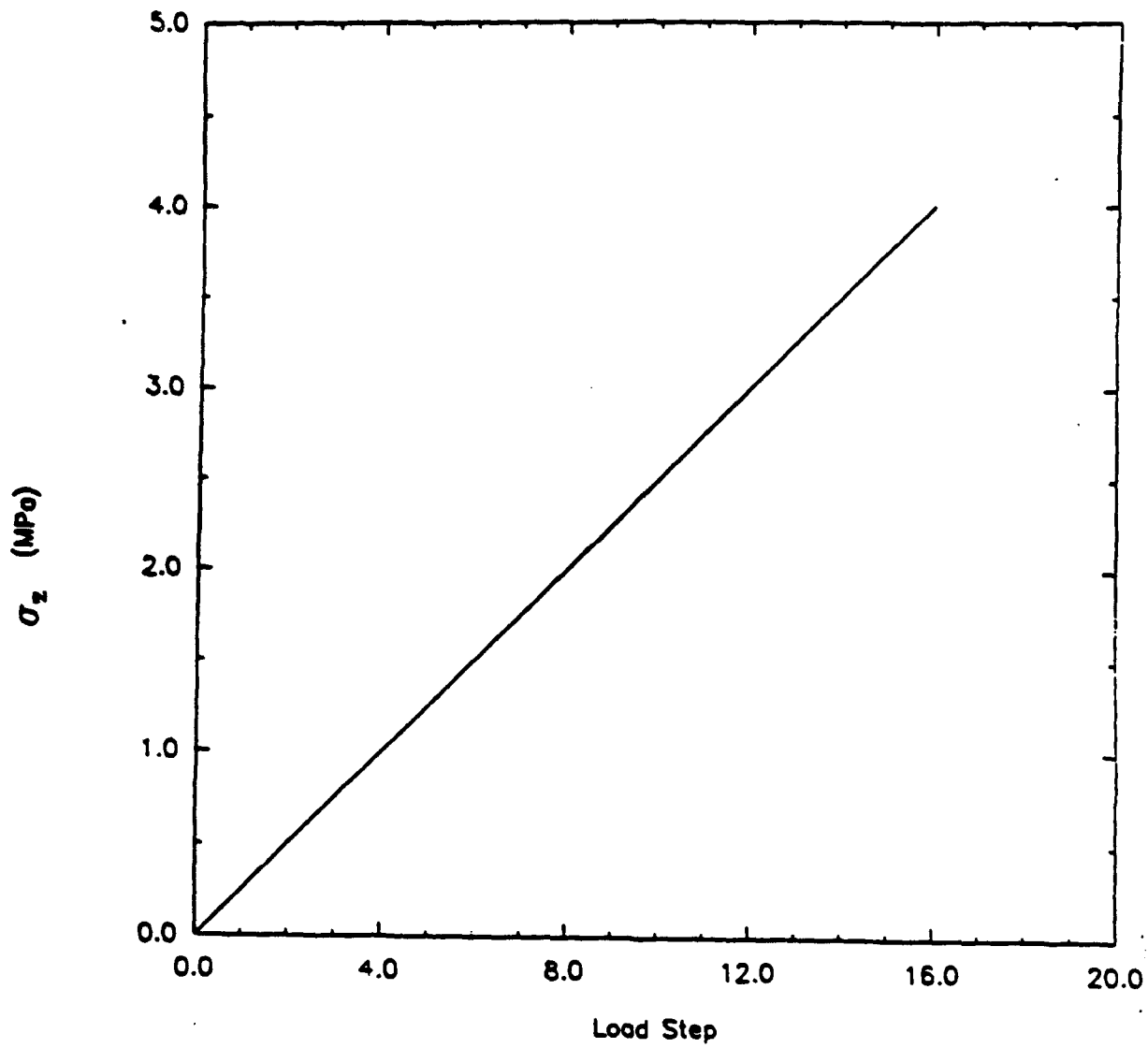
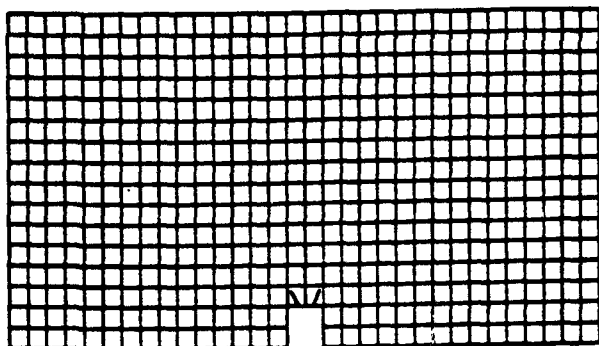
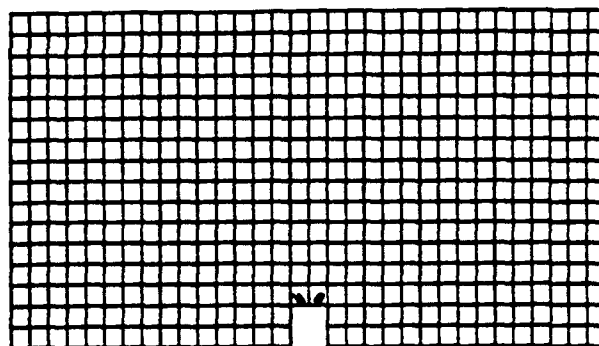


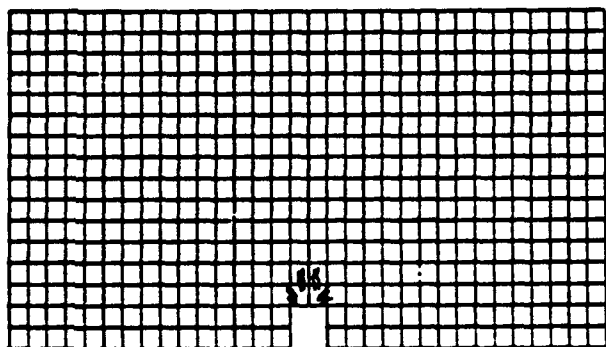
Figure 20. Loading sequence for static nonlinear analysis.



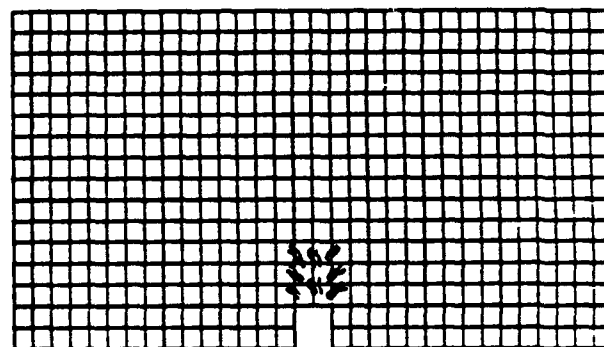
(a)



(b)



(c)



(d)

Figure 21. Cracking sequence for square-notch specimen, static nonlinear analysis.

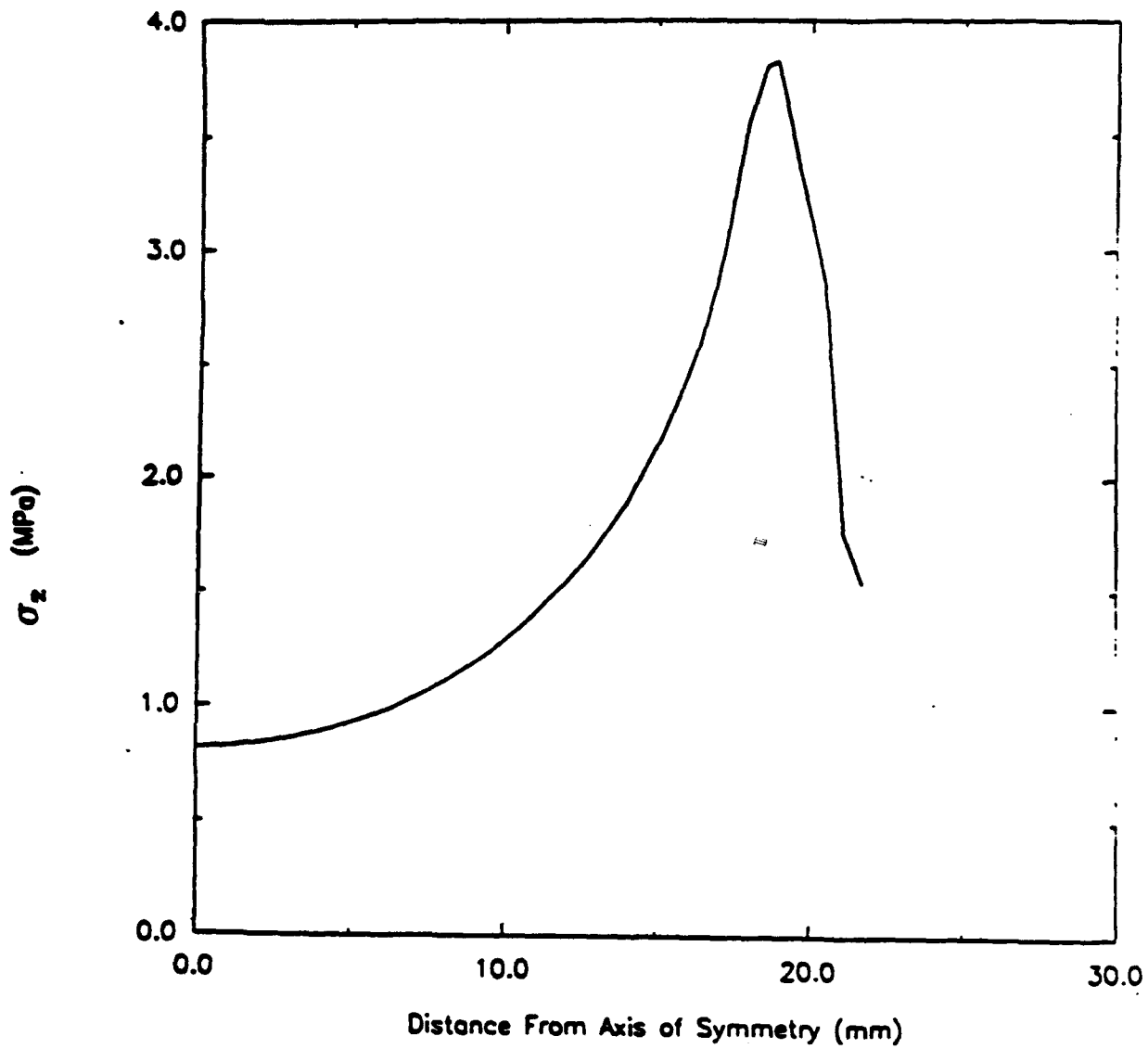
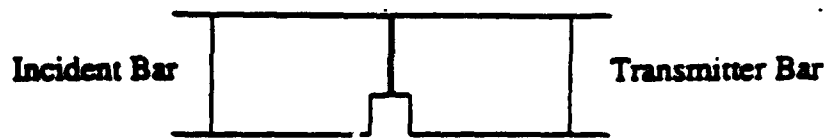
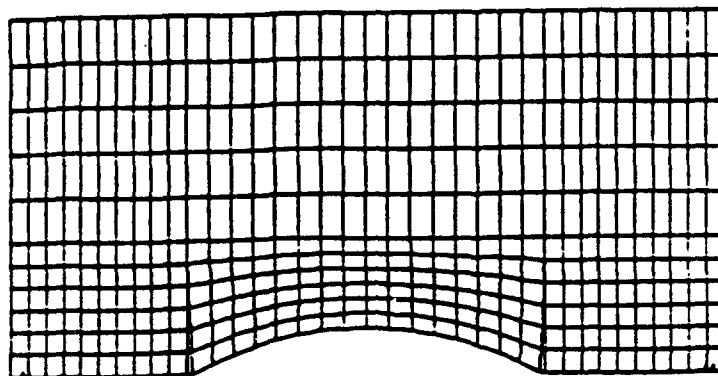
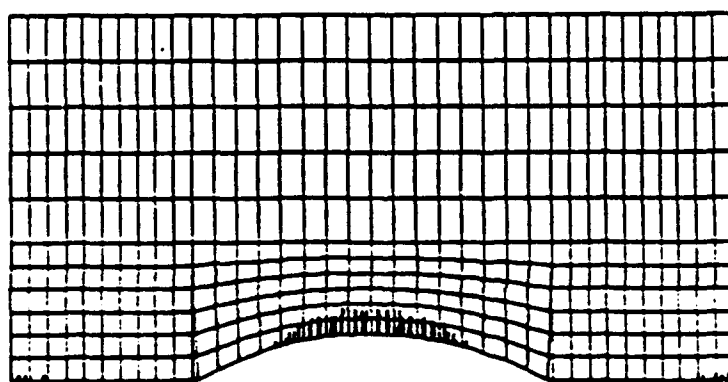


Figure 22. Longitudinal stress (σ) distribution in cross section at the notch, static nonlinear analysis.



(a)



(b)

Figure 23. Cracking sequence for saddle-notch specimen, static nonlinear analysis.

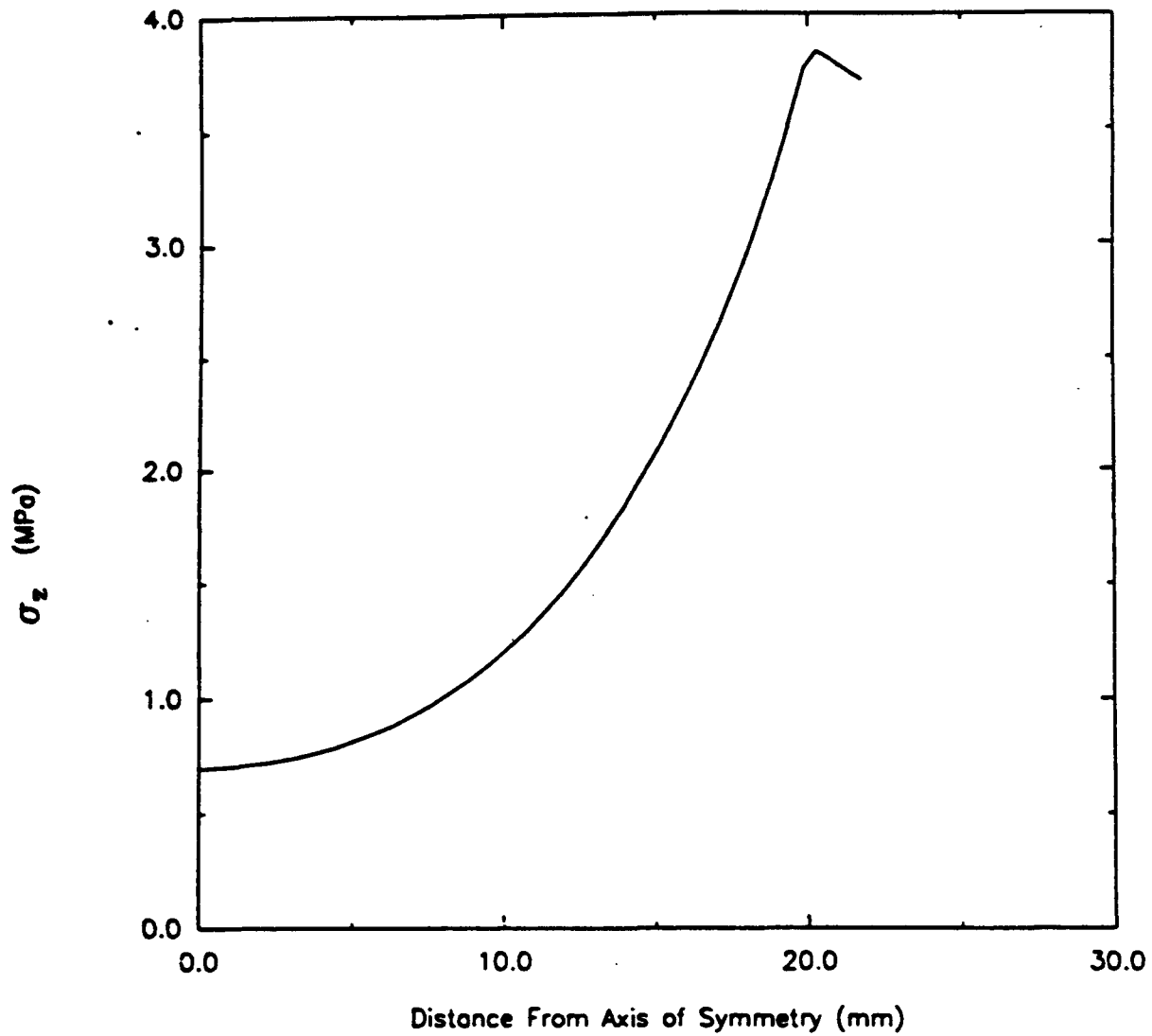
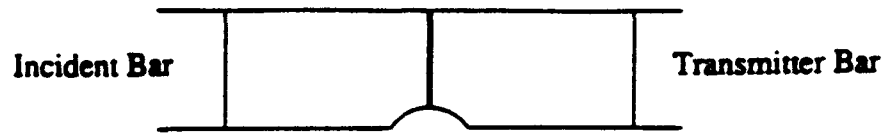


Figure 24. Longitudinal stress (σ) distribution in cross section at the notch, static nonlinear analysis.

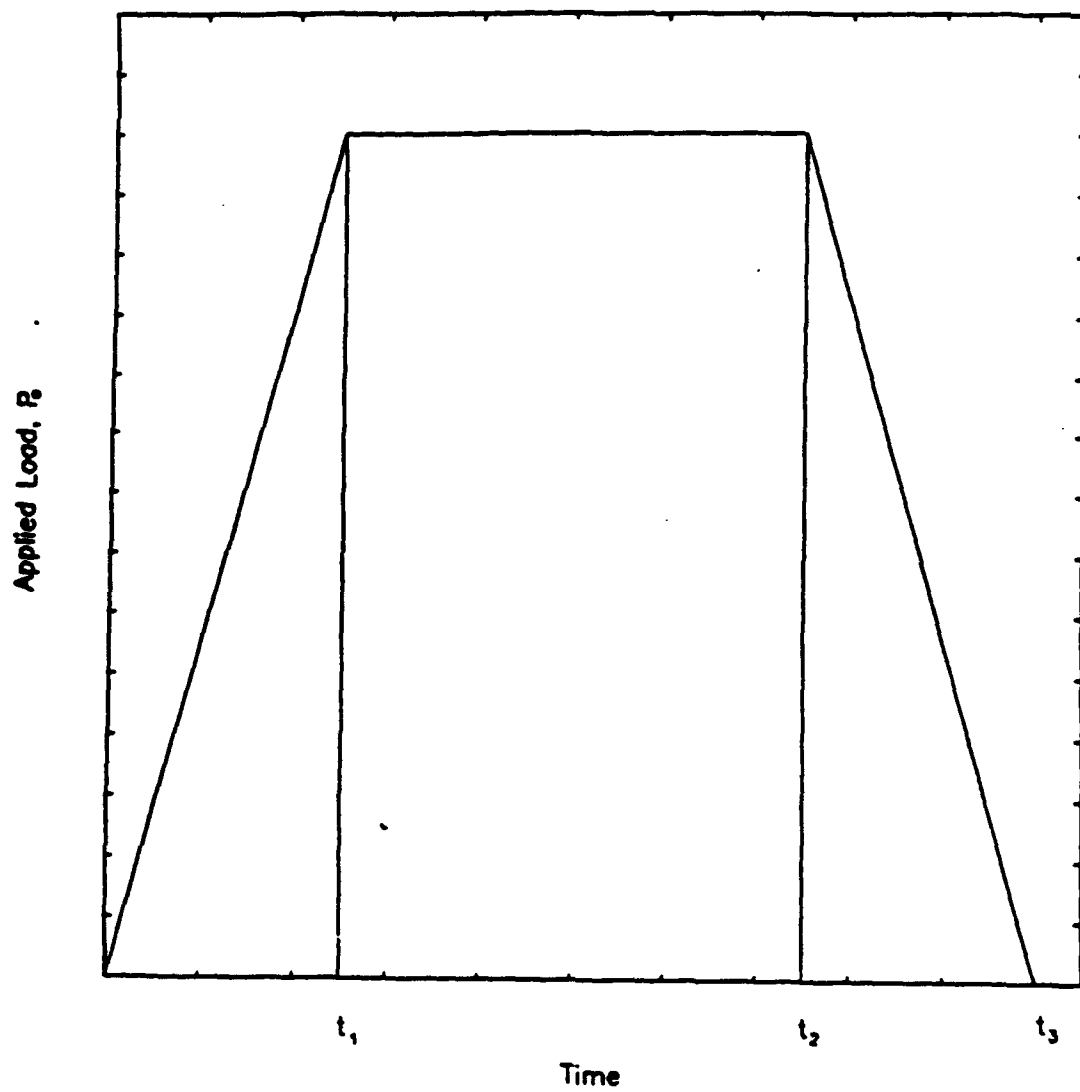


Figure 25. Typical loading function used in dynamic analysis.

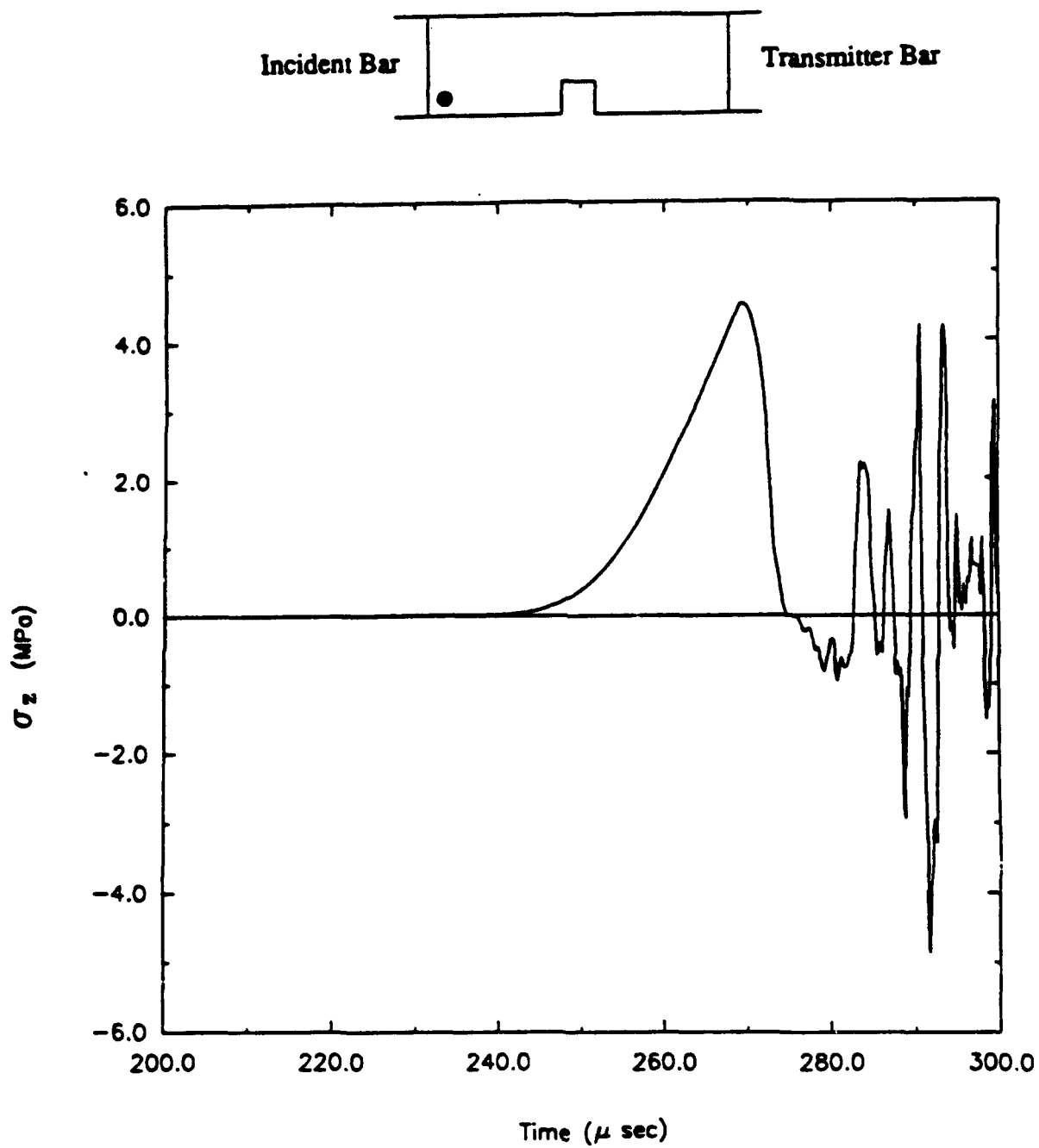


Figure 26. Time history for longitudinal stress (square-notch, Load Case 1).

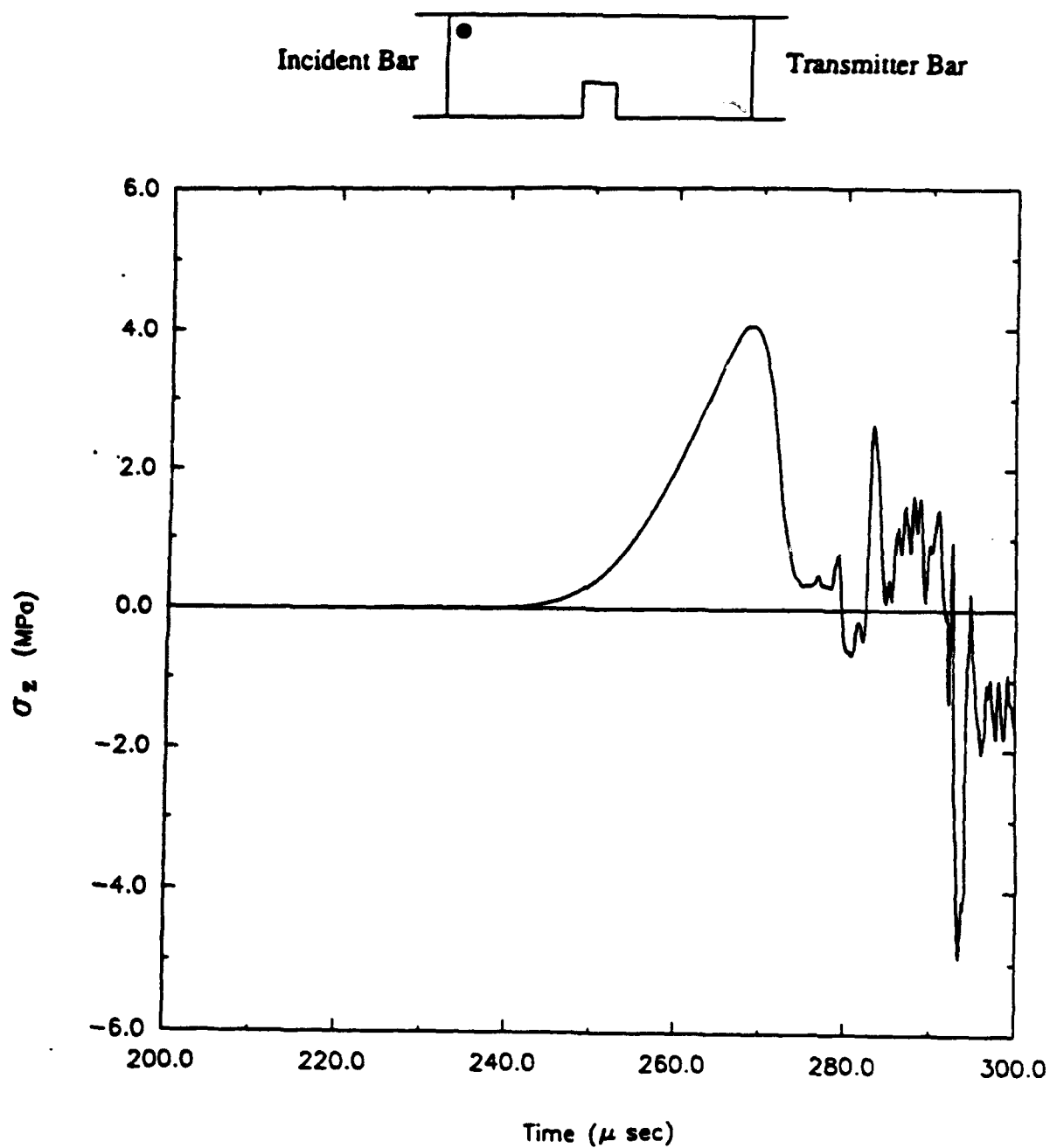


Figure 27. Time history for longitudinal stress (square-notch, Load Case 1).

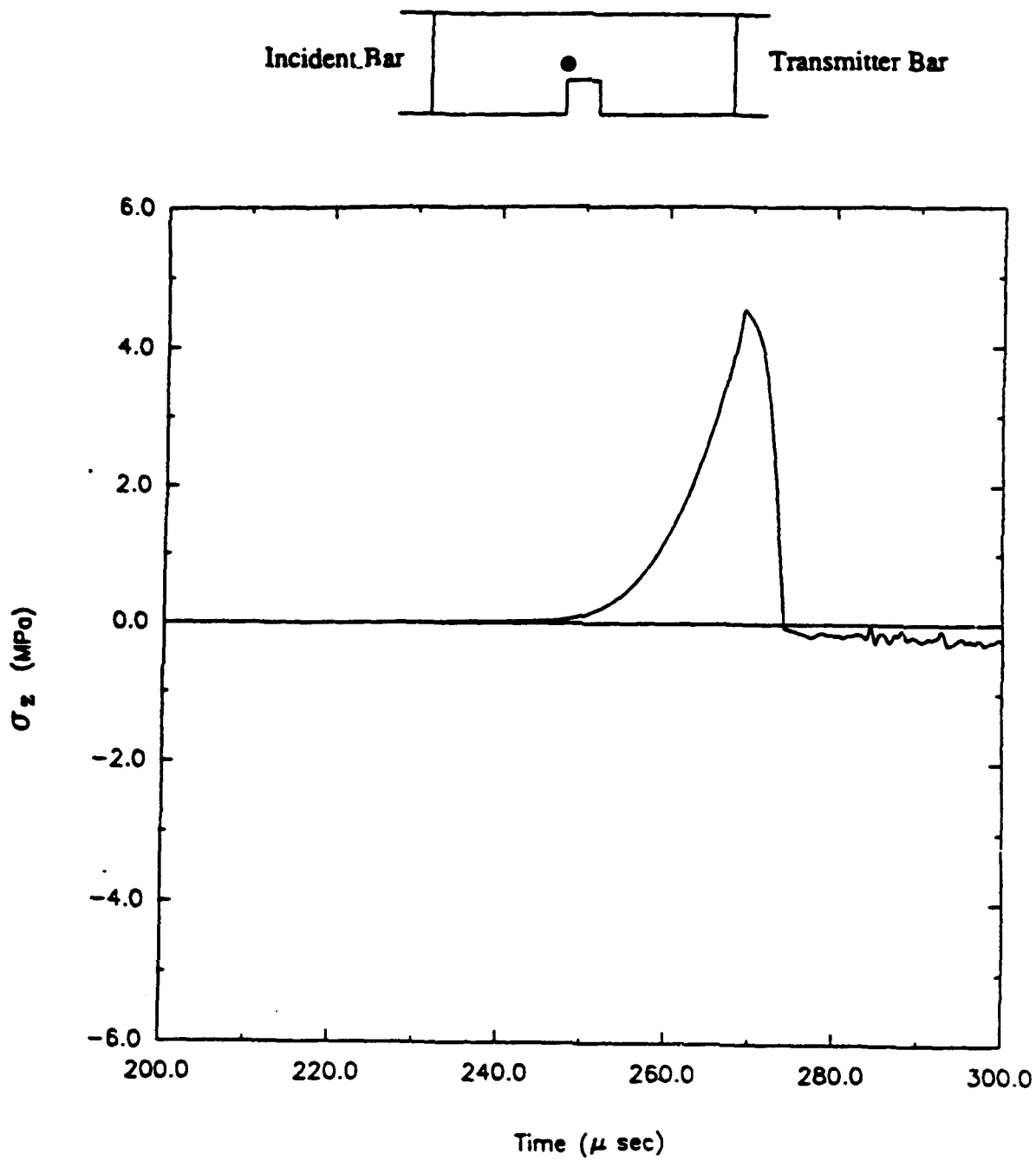


Figure 28. Time history for longitudinal stress (square-notch, Load Case 1).

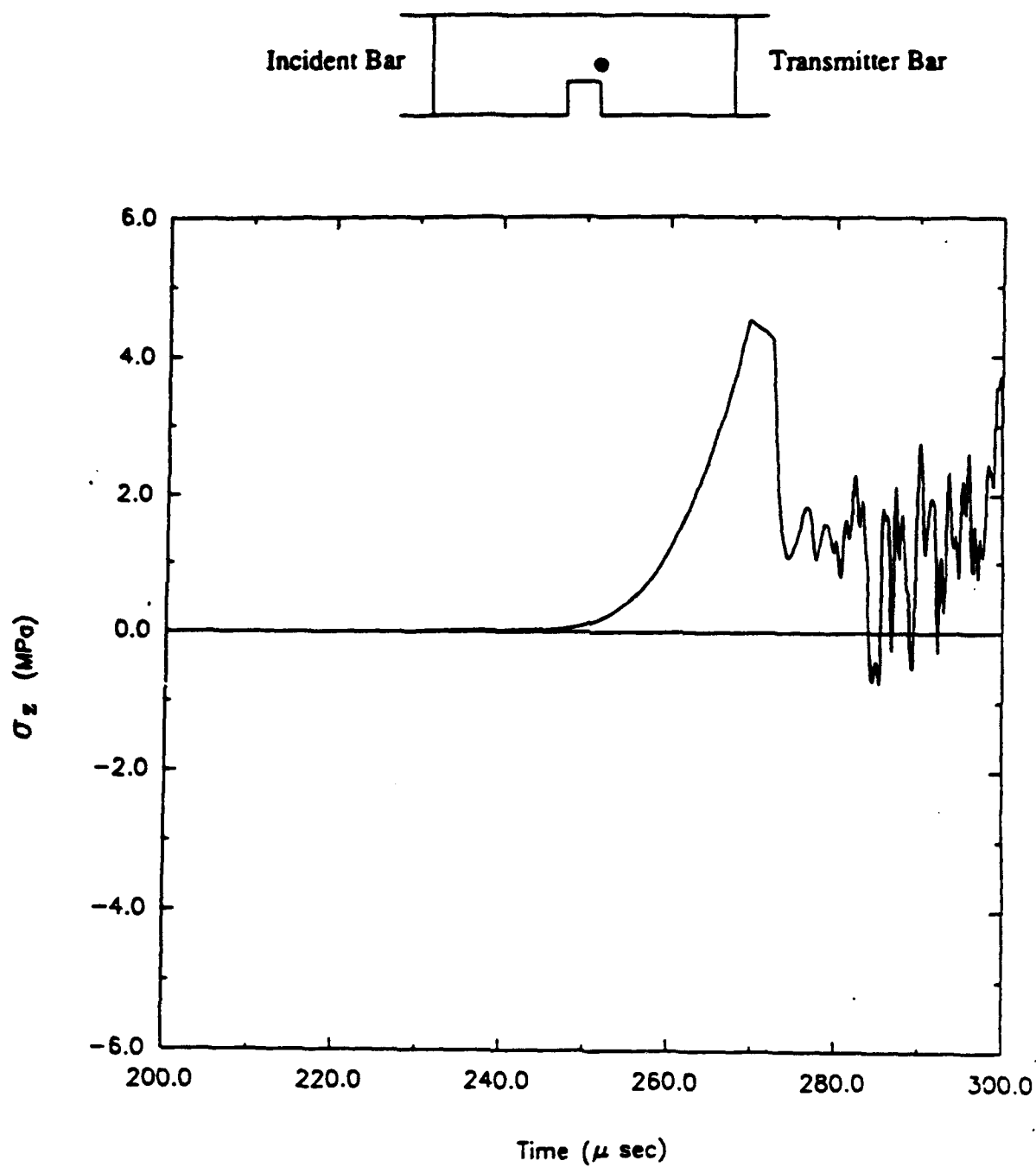


Figure 29. Time history for longitudinal stress (square-notch, Load Case 1).

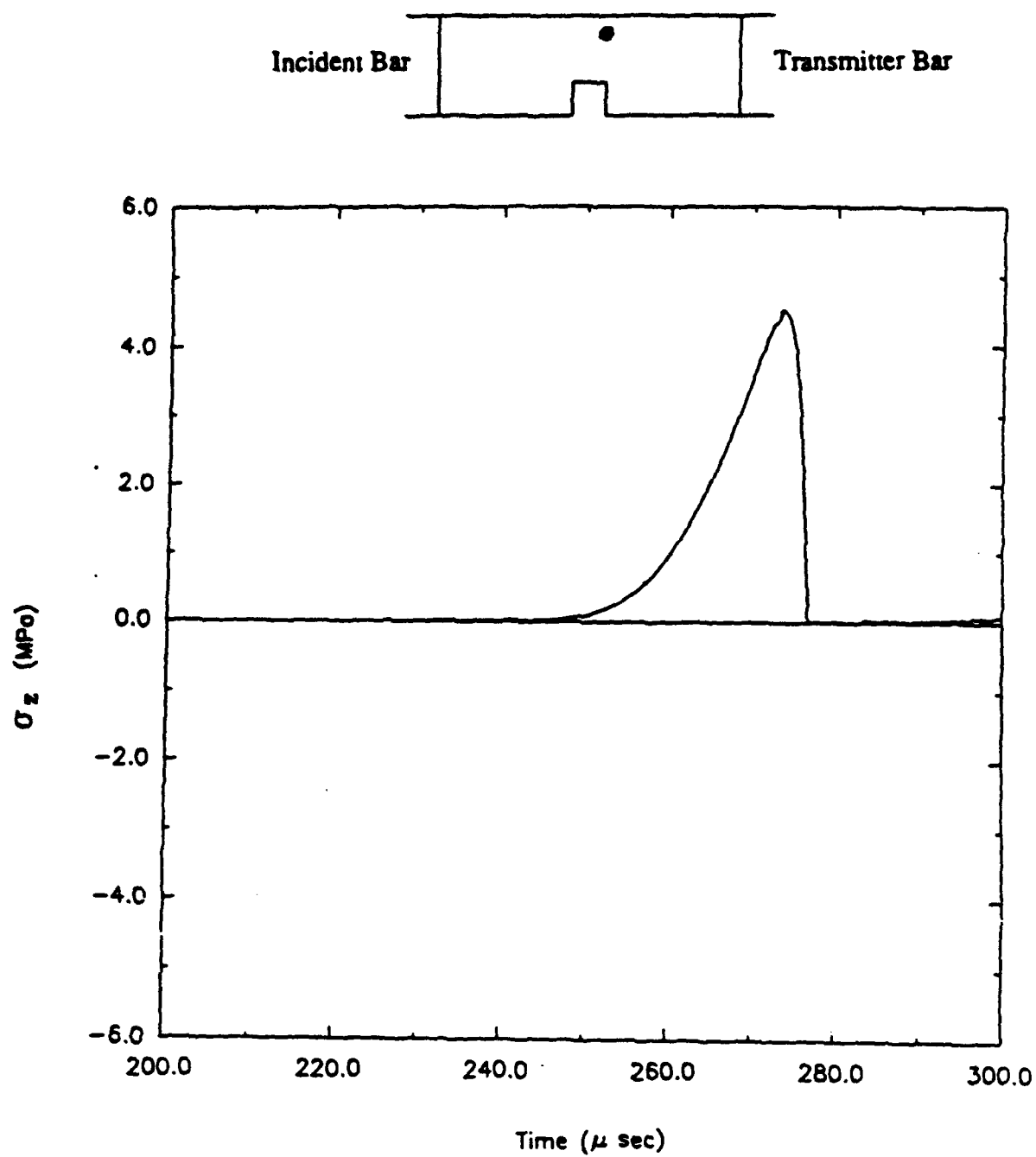


Figure 30. Time history for longitudinal stress (square-notch, Load Case 1).

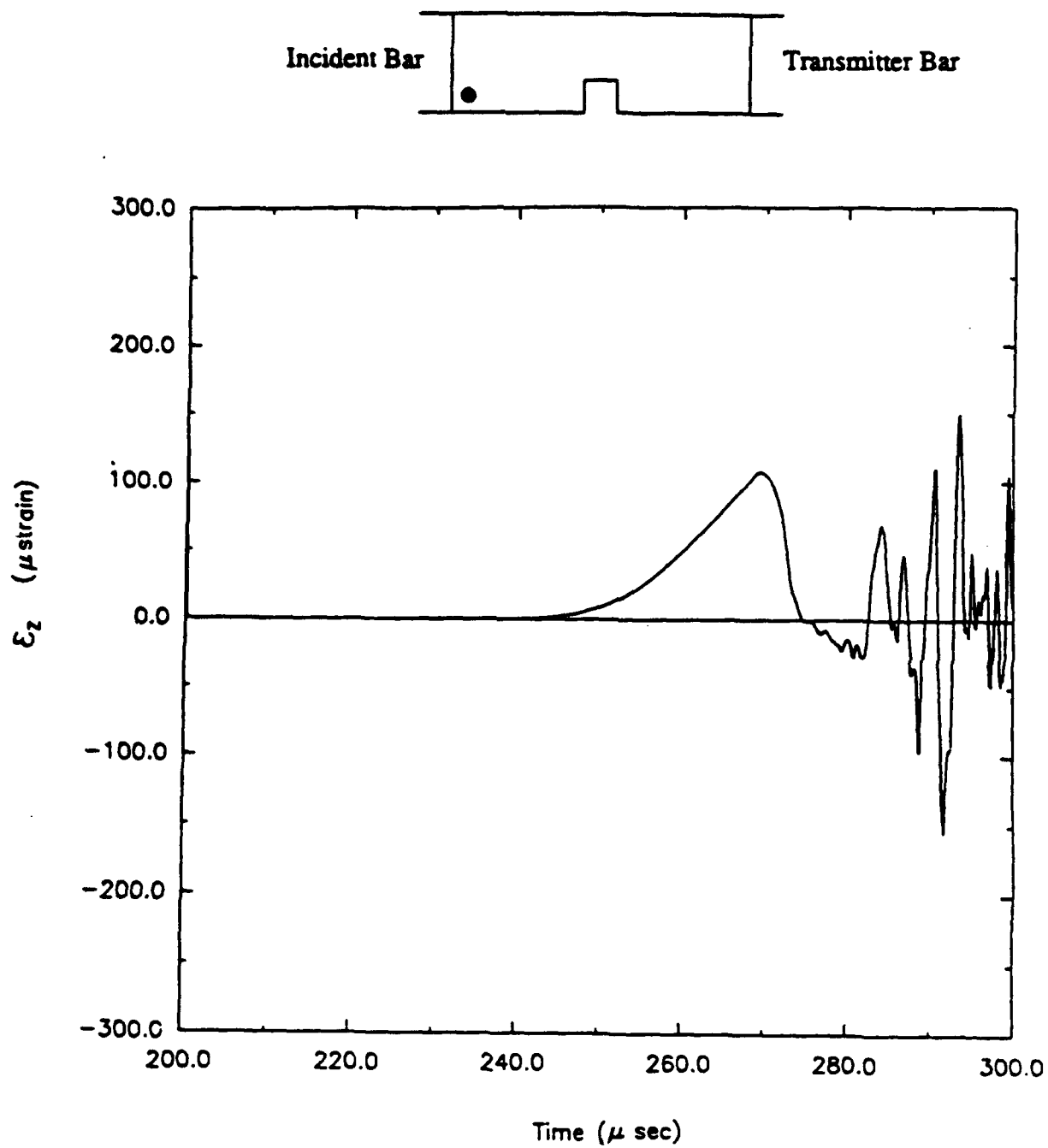


Figure 31. Time history for longitudinal strain (square-notch, Load Case 1).

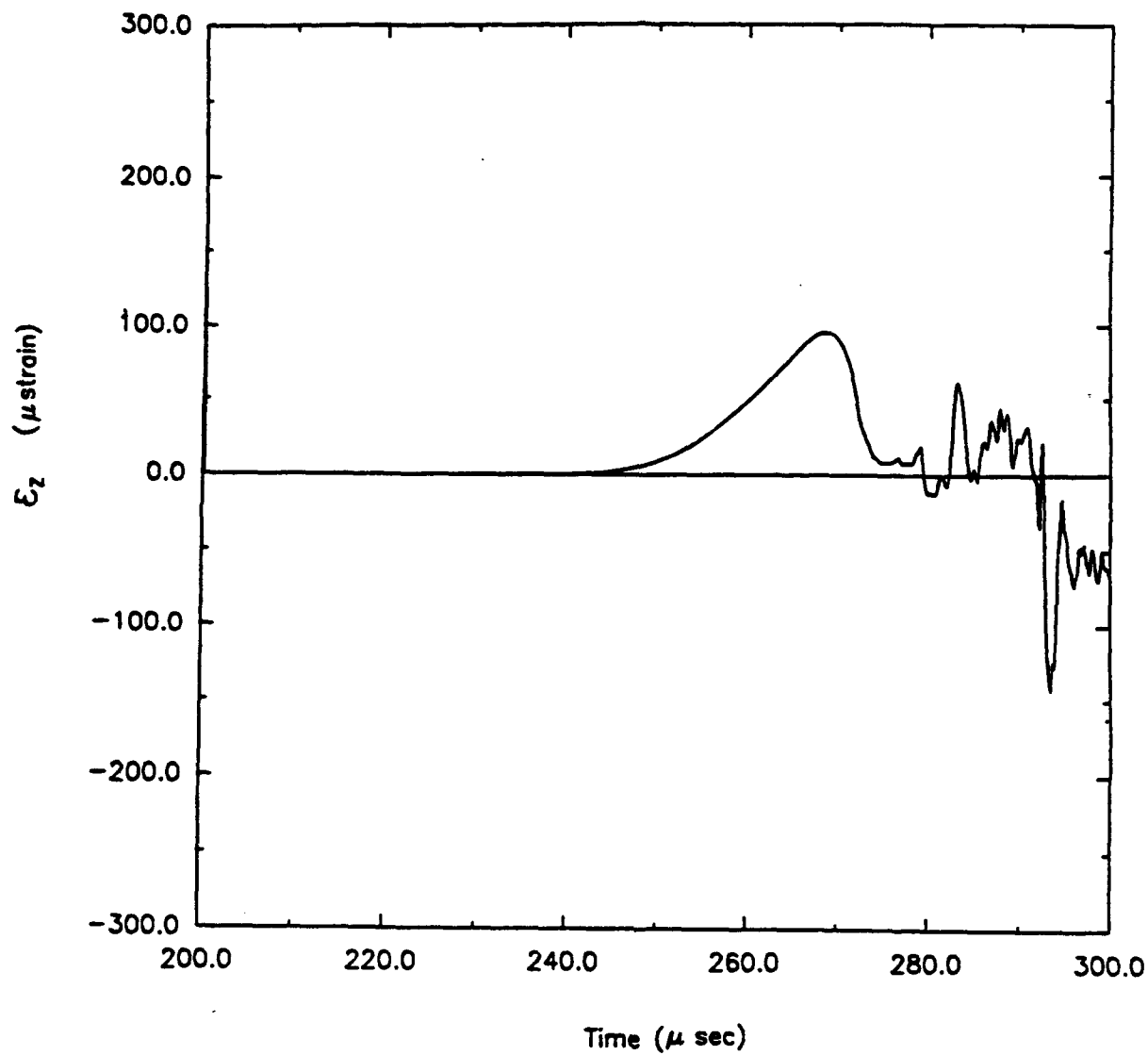


Figure 32. Time history for longitudinal strain (square-notch, Load Case 1).

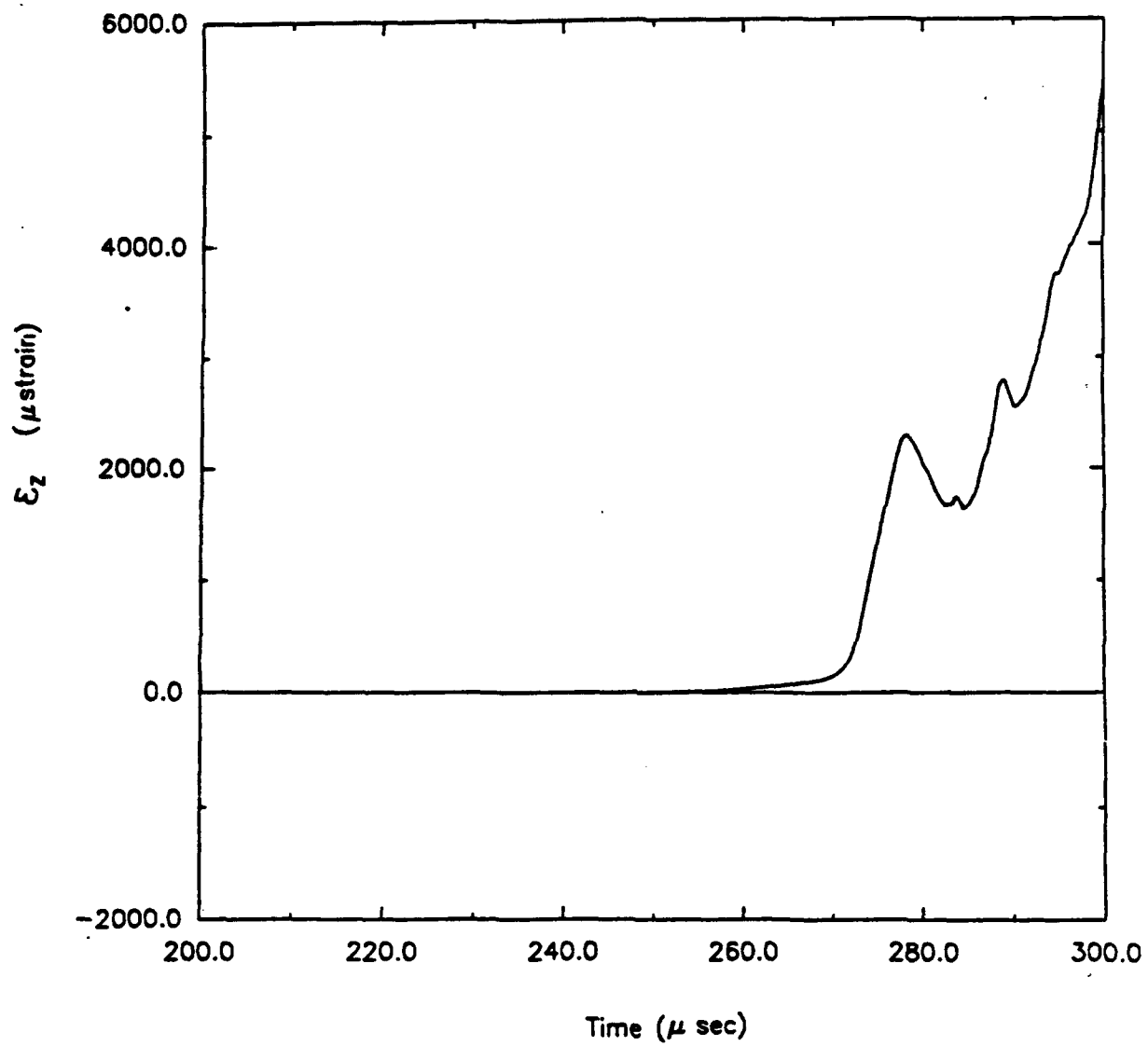
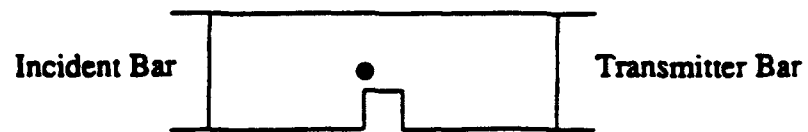


Figure 33. Time history for longitudinal strain (square-notch, Load Case 1).

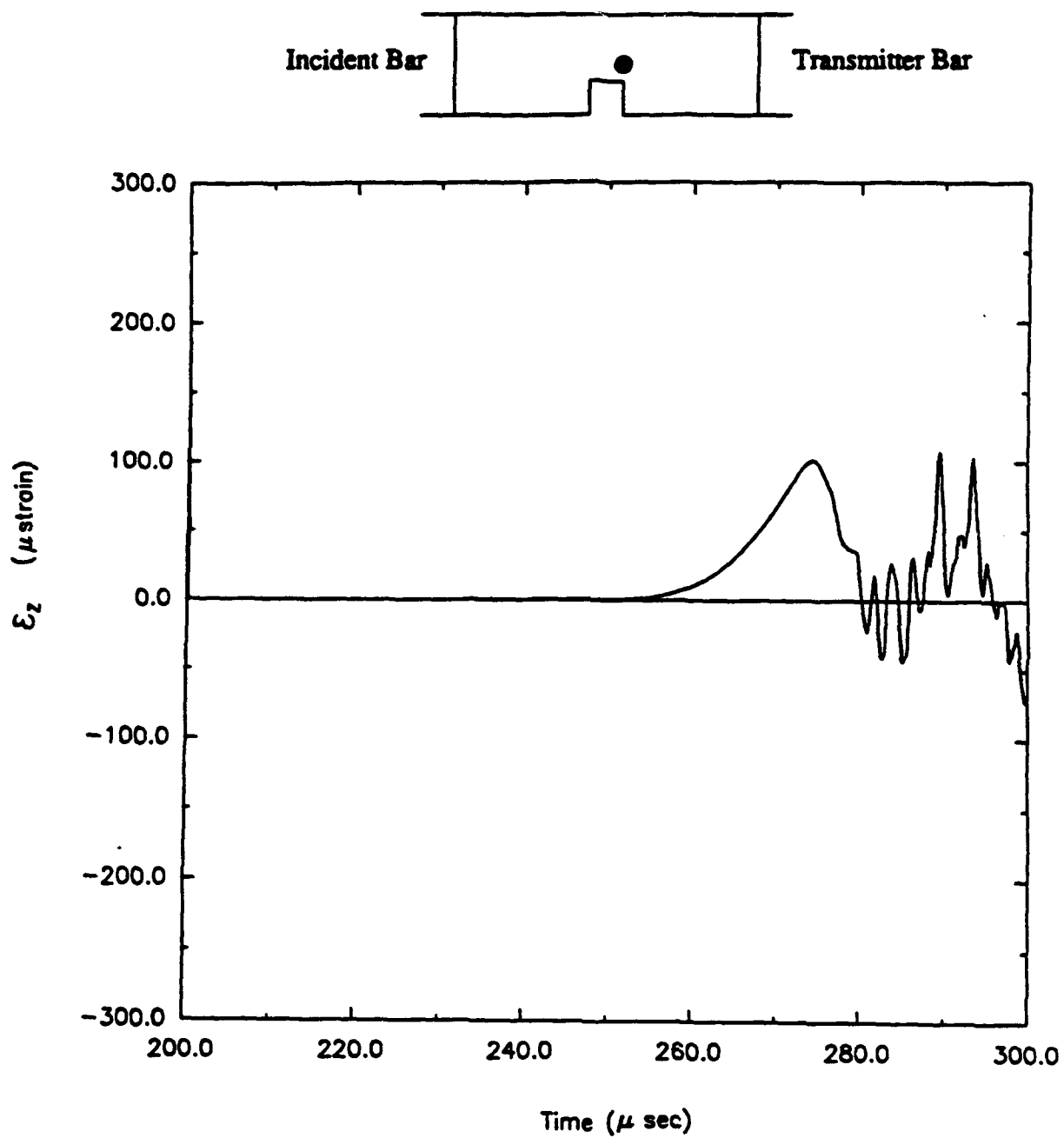


Figure 34. Time history for longitudinal strain (square-notch, Load Case 1).

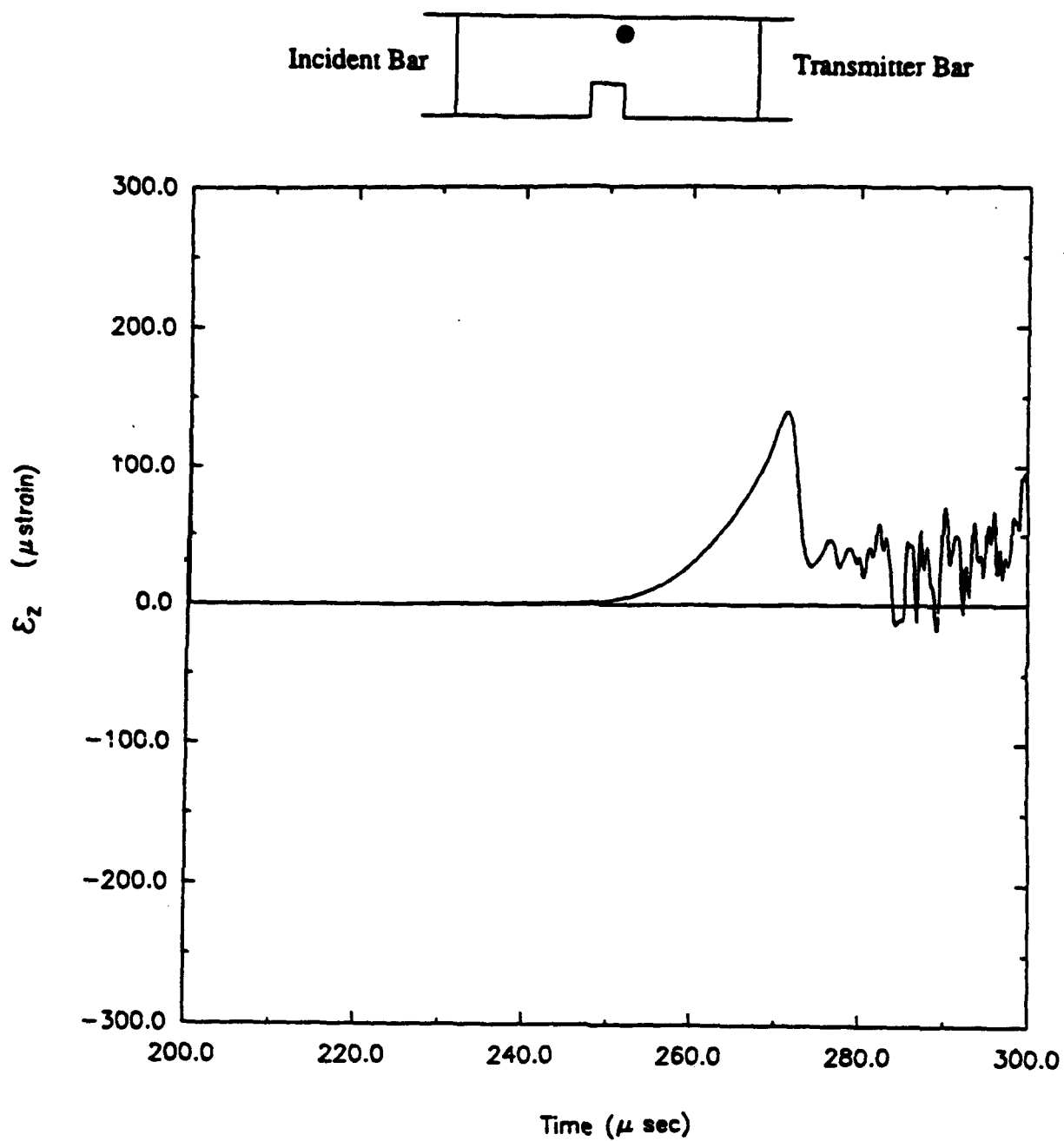


Figure 35. Time history for longitudinal strain (square-notch, Load Case 1).

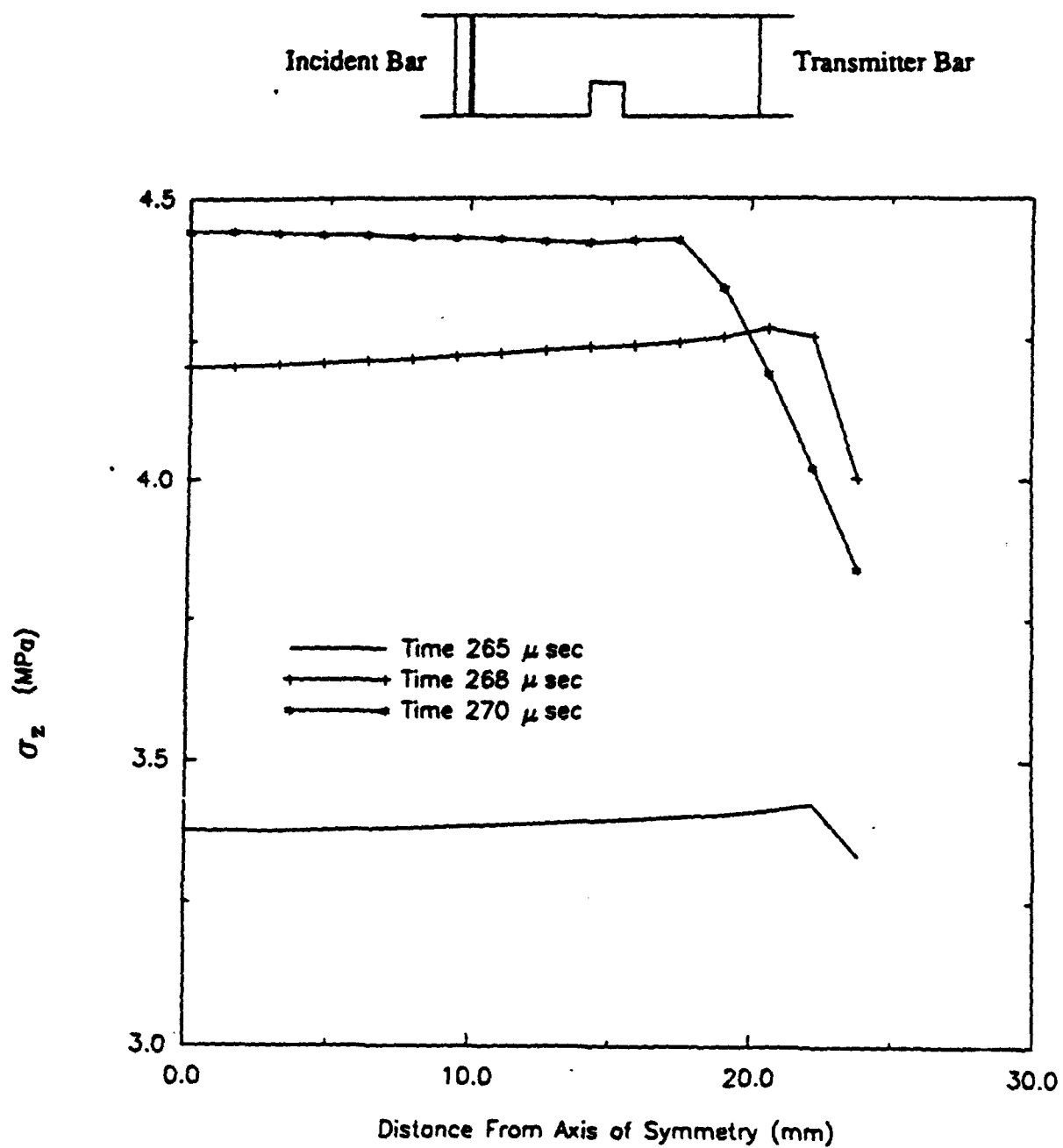


Figure 36. Profiles for longitudinal stress (square-notch, Load Case 1).

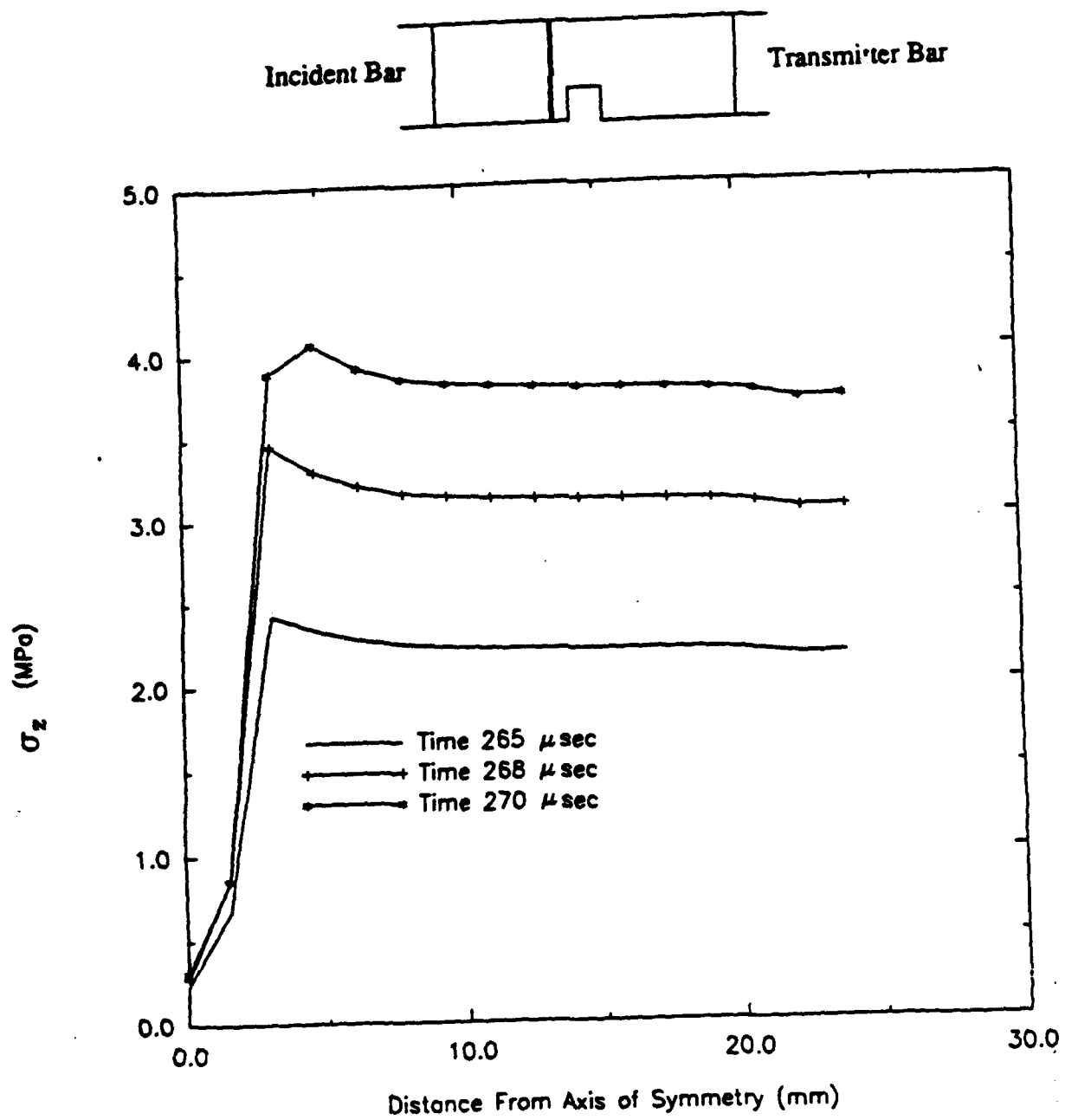


Figure 37. Profiles for longitudinal stress (square-notch, Load Case 1).

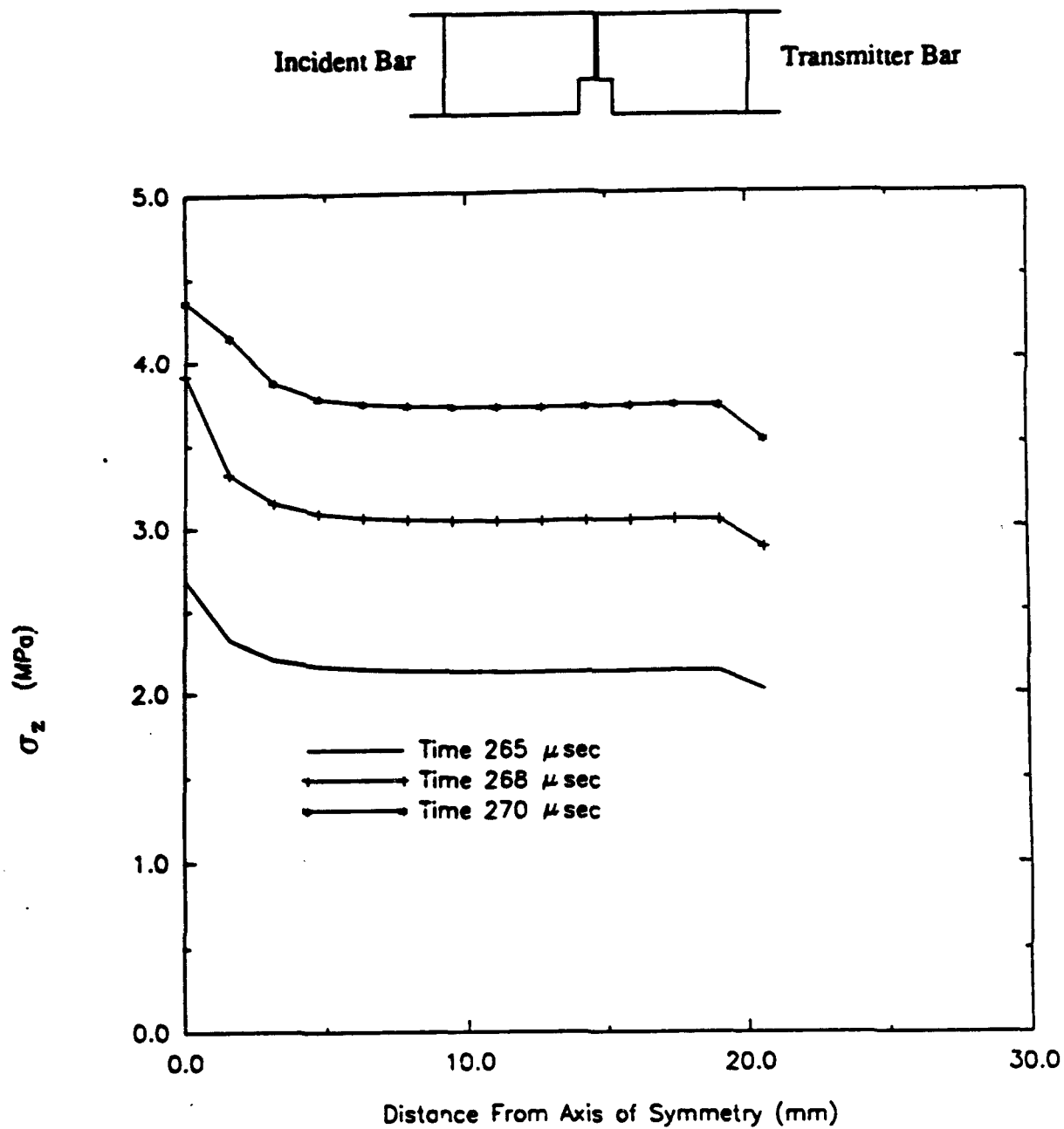


Figure 38. Profiles for longitudinal stress (square-notch, Load Case 1).

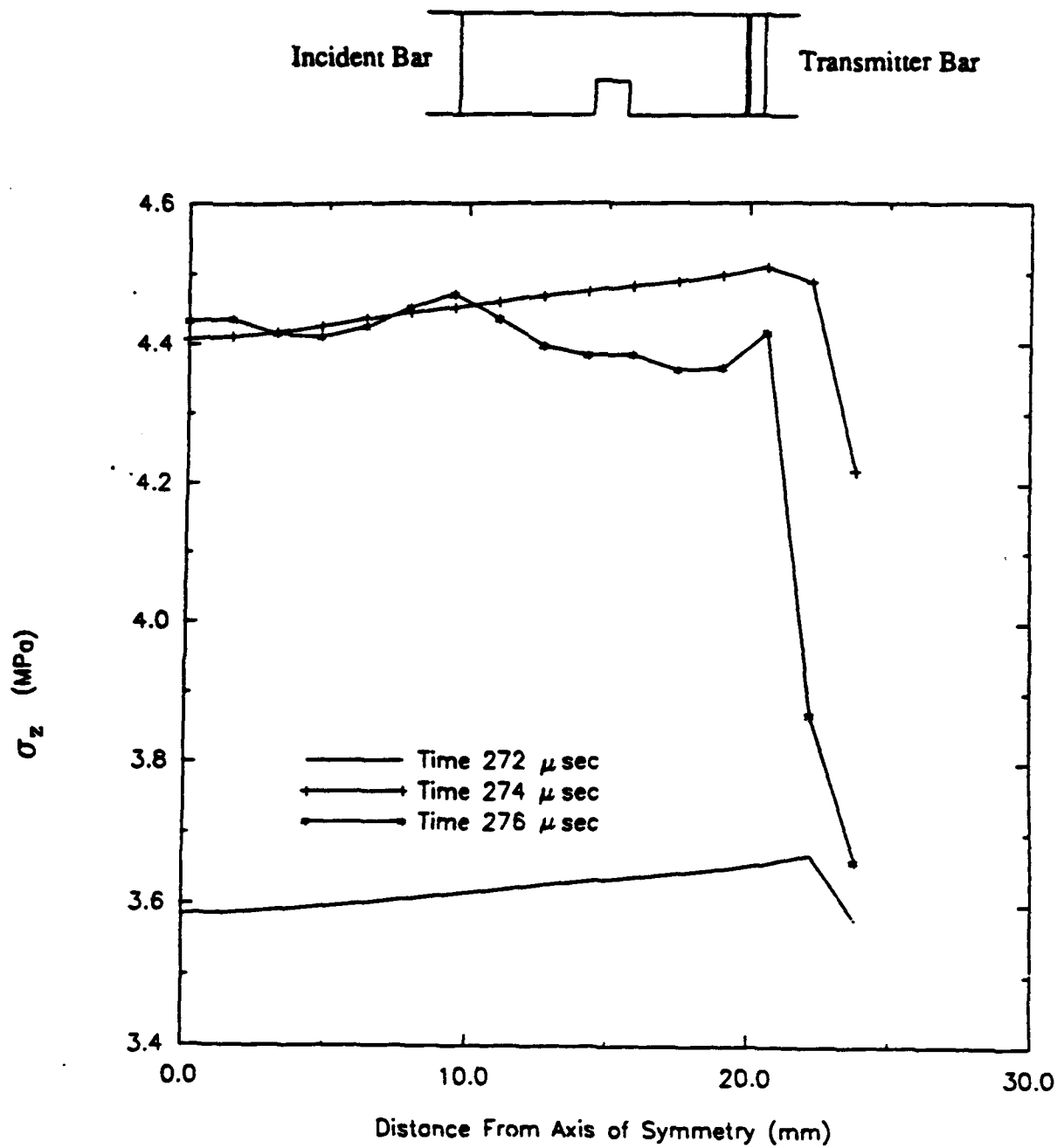


Figure 39. Profiles for longitudinal stress (square-notch, Load Case 1).

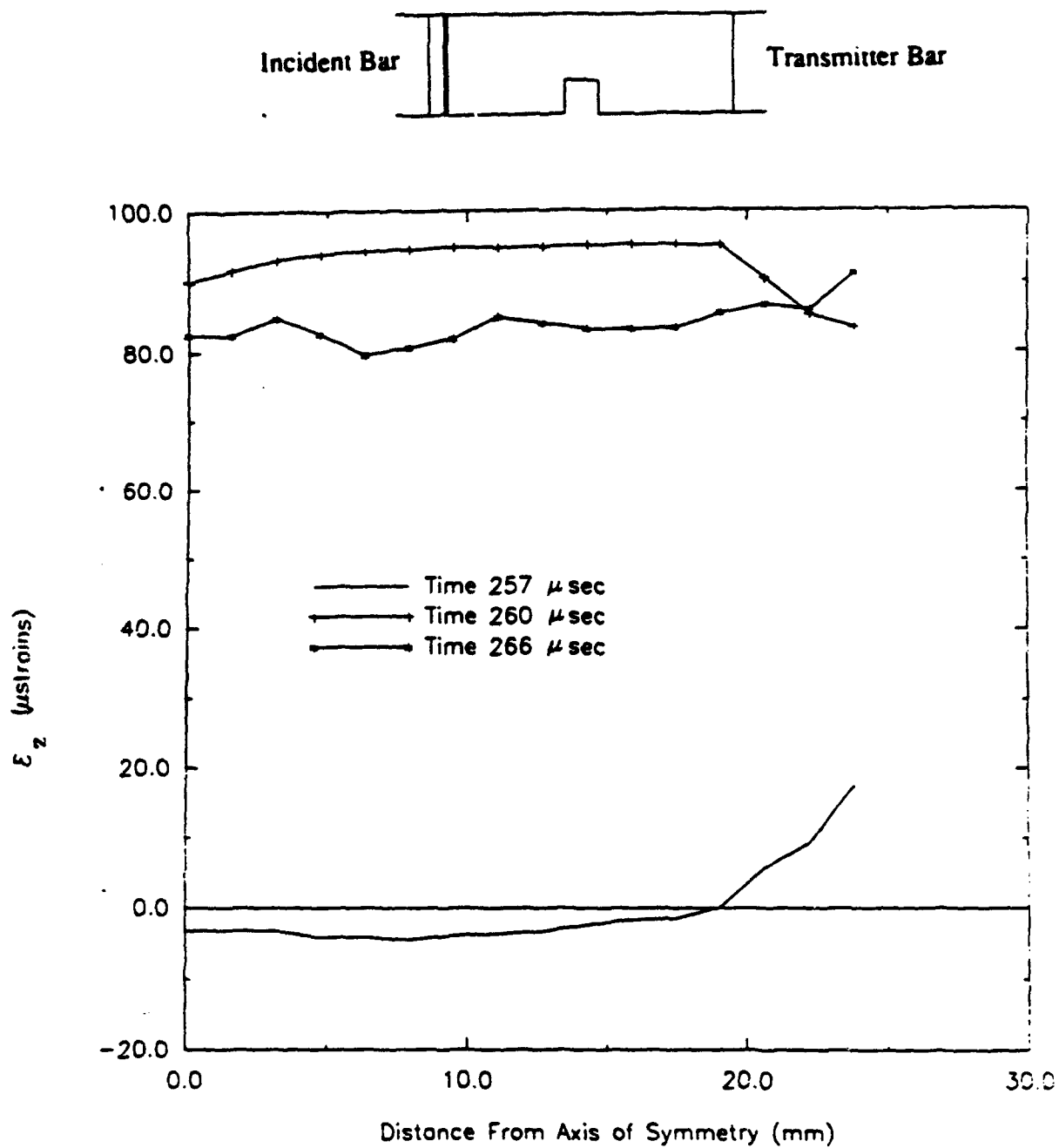


Figure 40. Profiles for longitudinal strain (square-notch, Load Case 1).

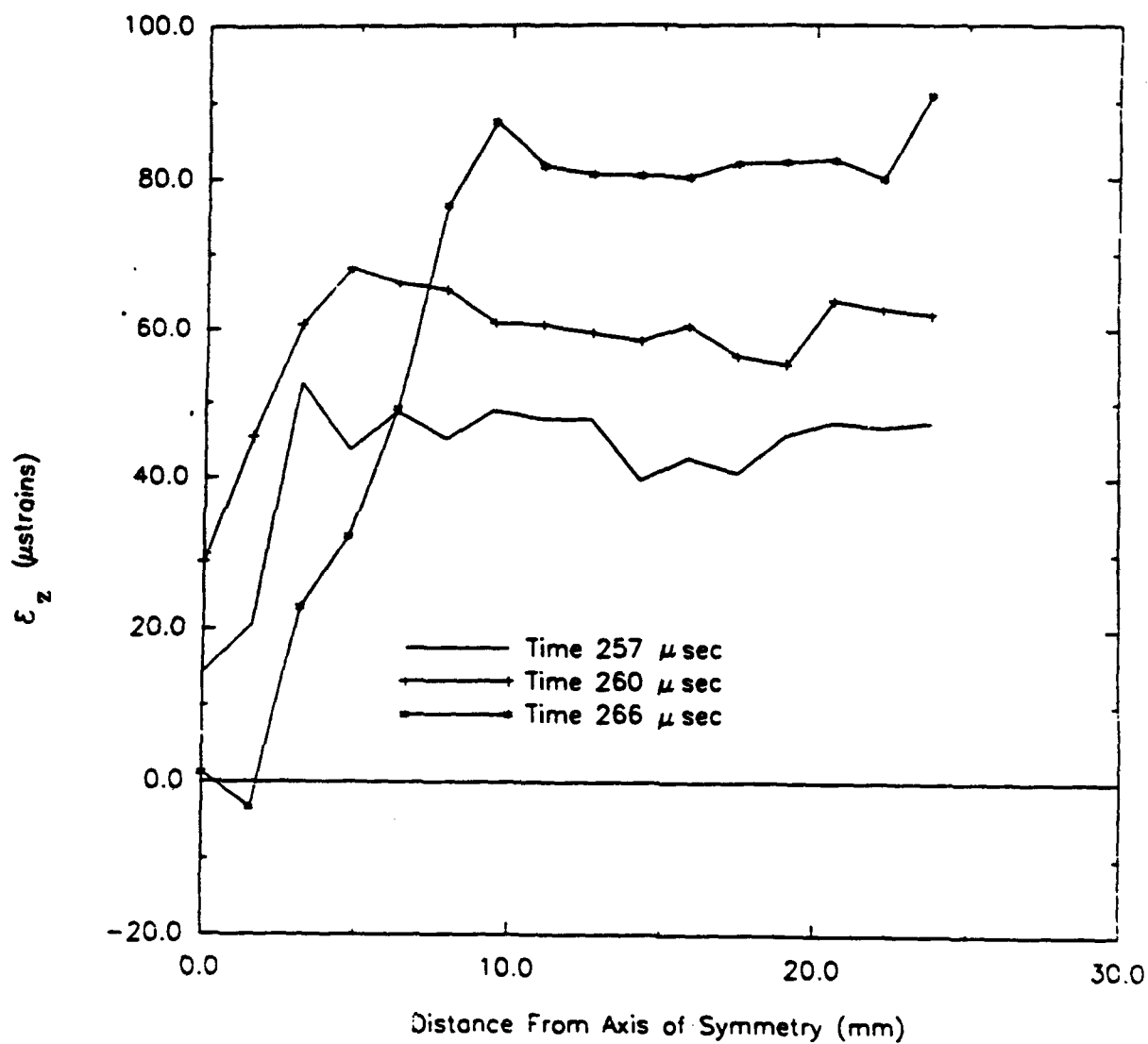


Figure 41. Profiles for longitudinal strain (square-notch, Load Case 1).

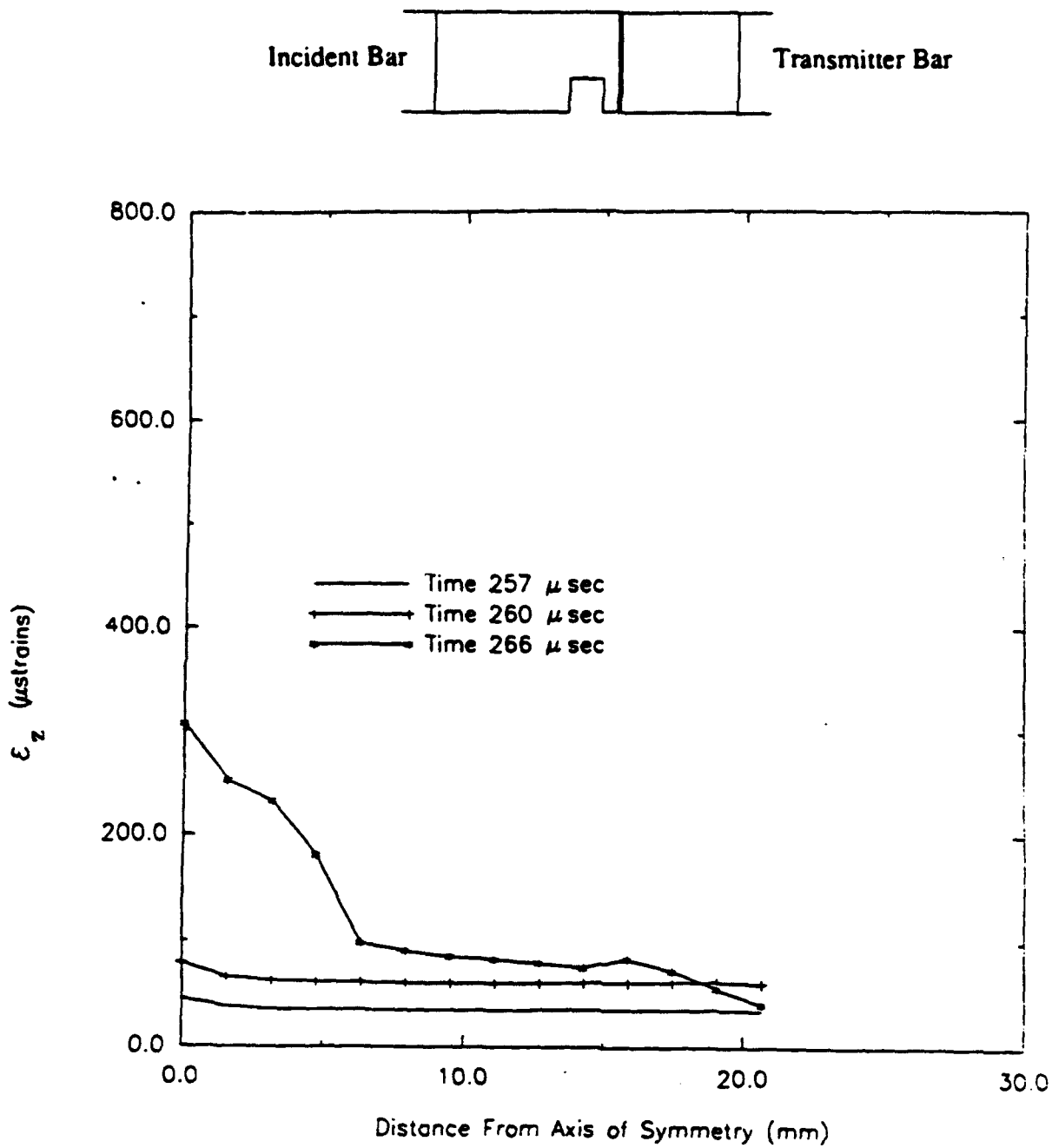


Figure 42. Profiles for longitudinal strain (square-notch, Load Case 1).

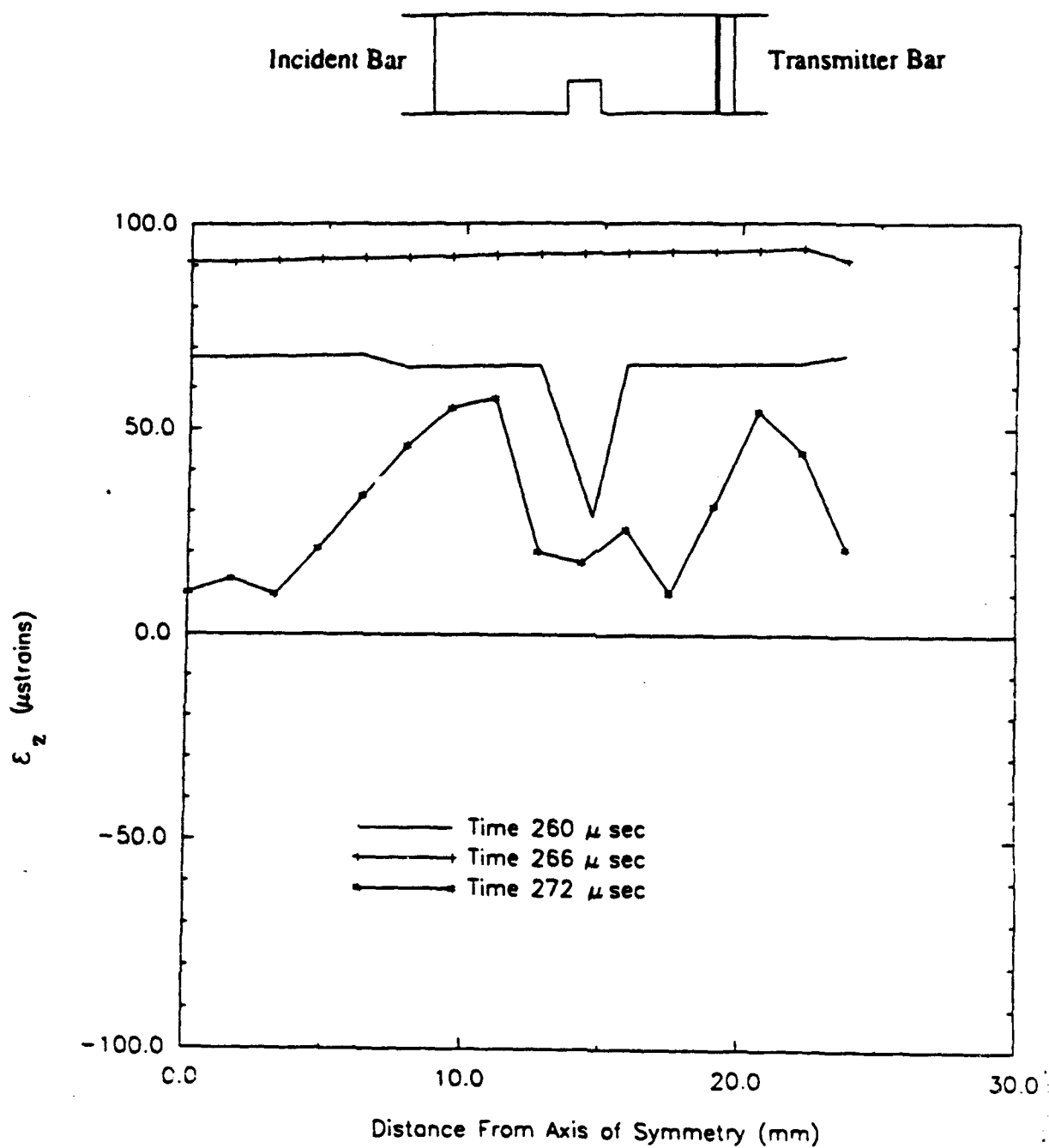
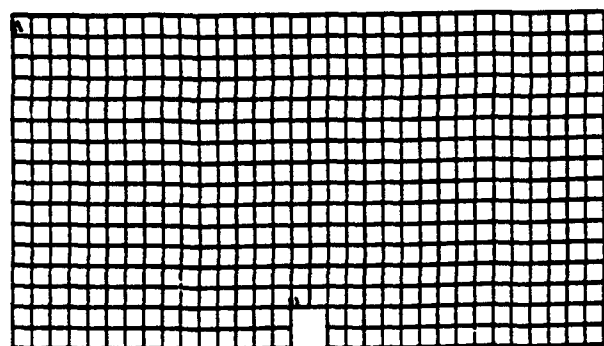
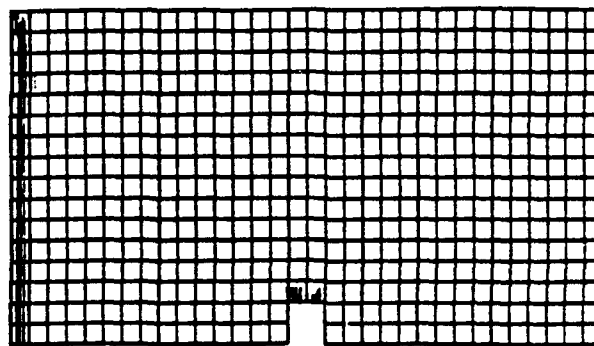


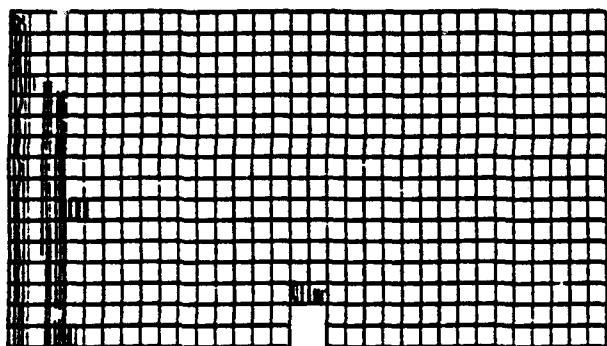
Figure 43. Profiles for longitudinal strain (square-notch, Load Case 1).



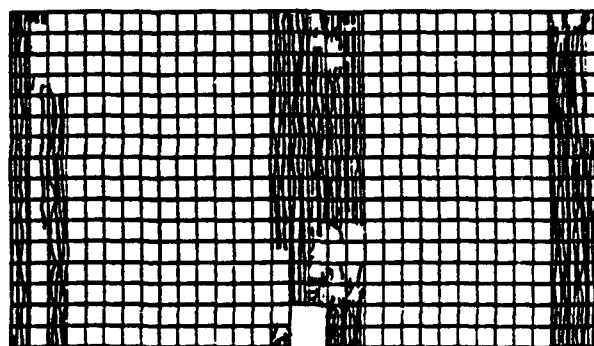
(a)



(b)



(c)



(d)

Figure 44. Cracking sequence for square-notch specimen; Load Case 1:
a) $t=266 \mu \text{ sec}$, b) $t=269 \mu \text{ sec}$, c) $t=270 \mu \text{ sec}$, d) $t=300 \mu \text{ sec}$.

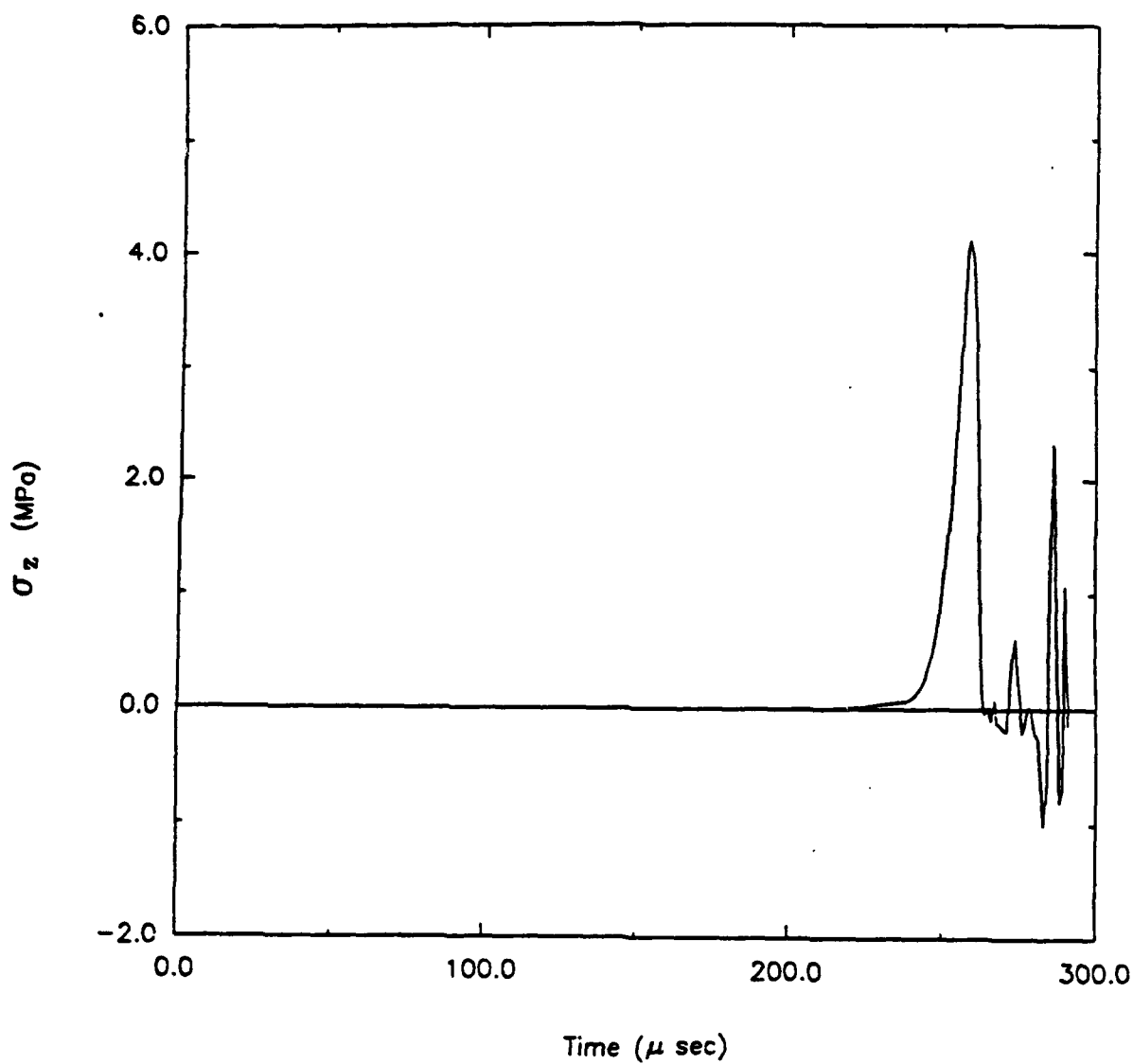


Figure 45. Time history for longitudinal stress (square-notch, Load Case 2).

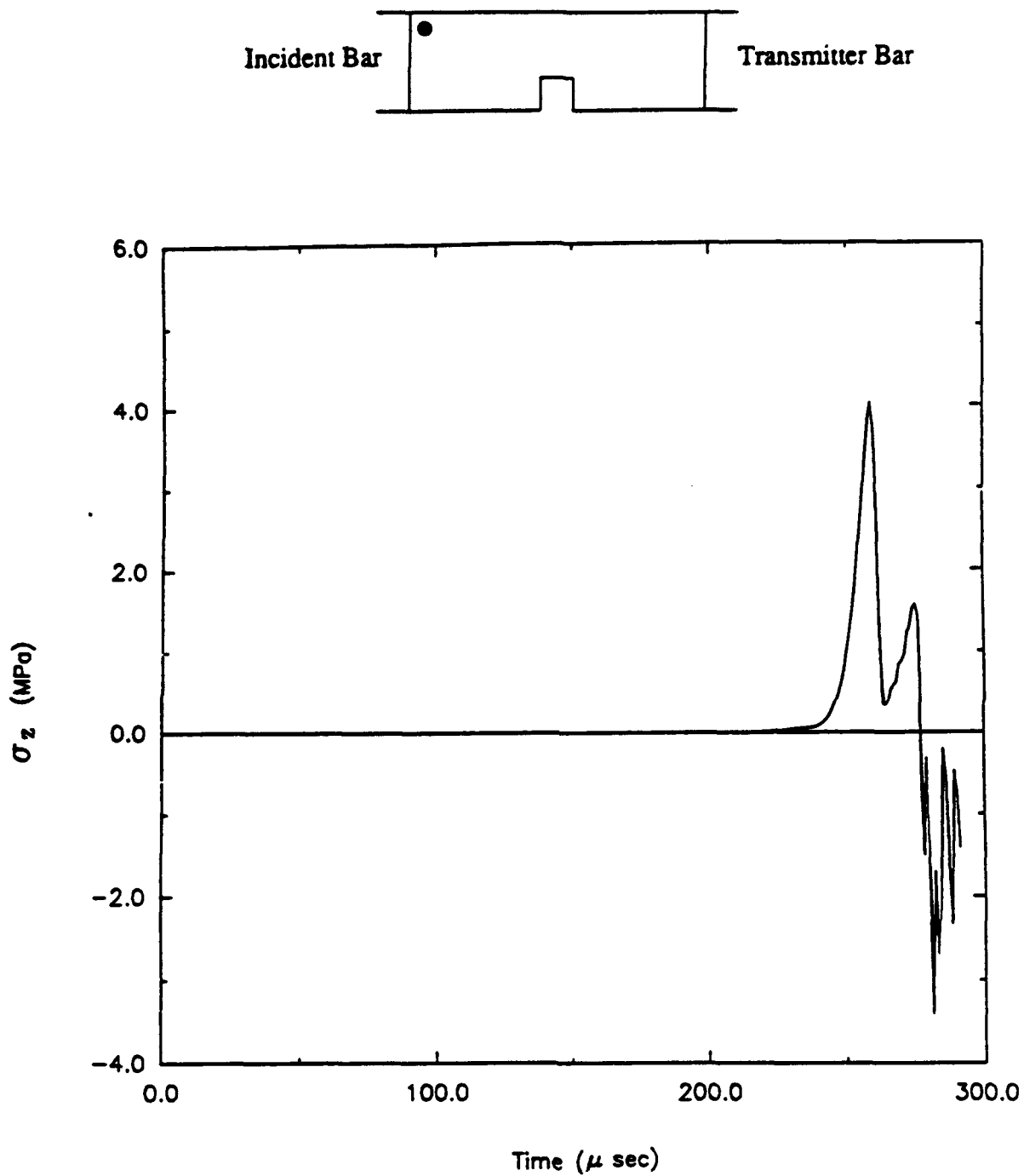


Figure 46. Time history for longitudinal stress (square-notch, Load Case 2).

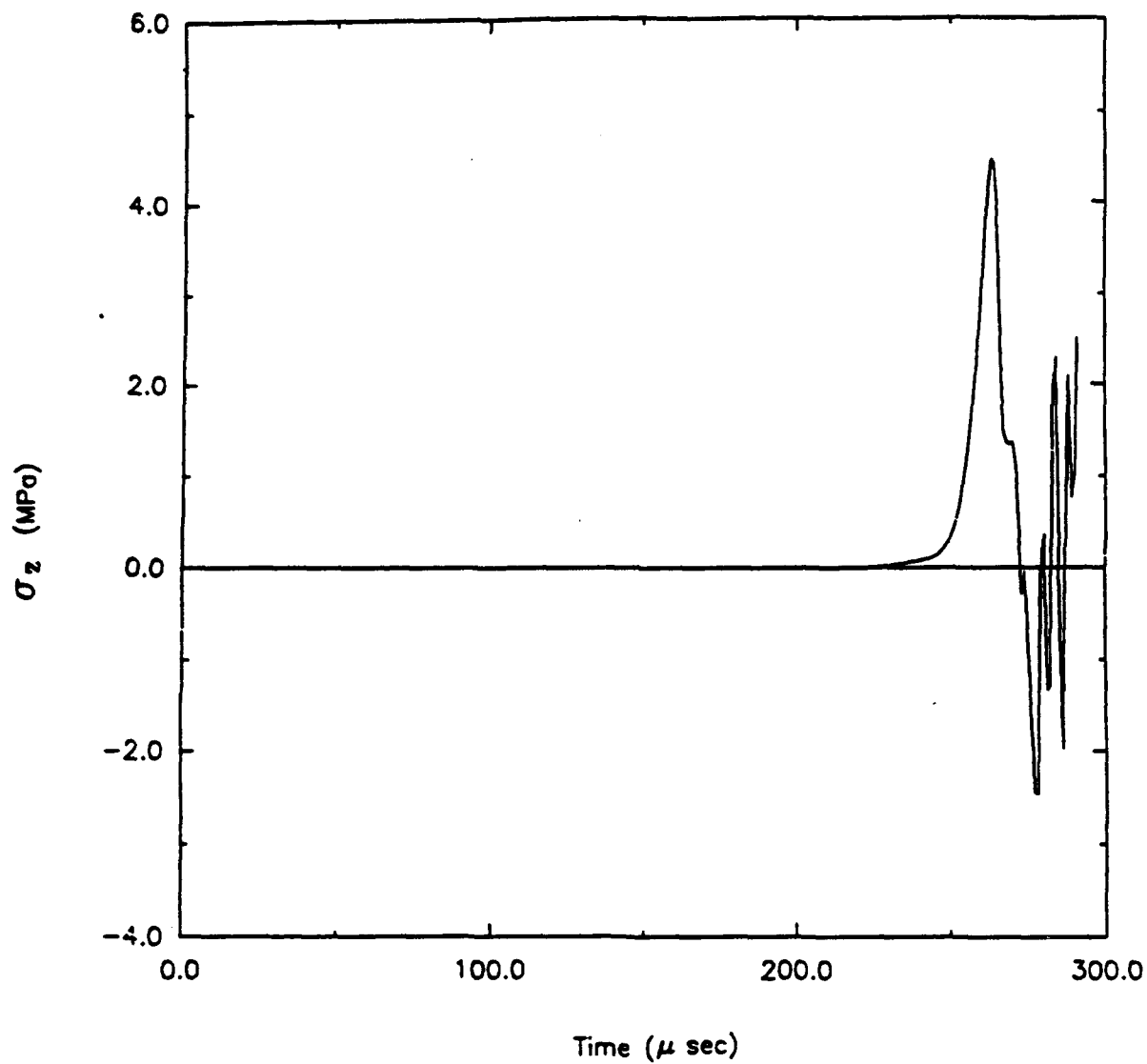


Figure 47. Time history for longitudinal stress (square-notch, Load Case 2).

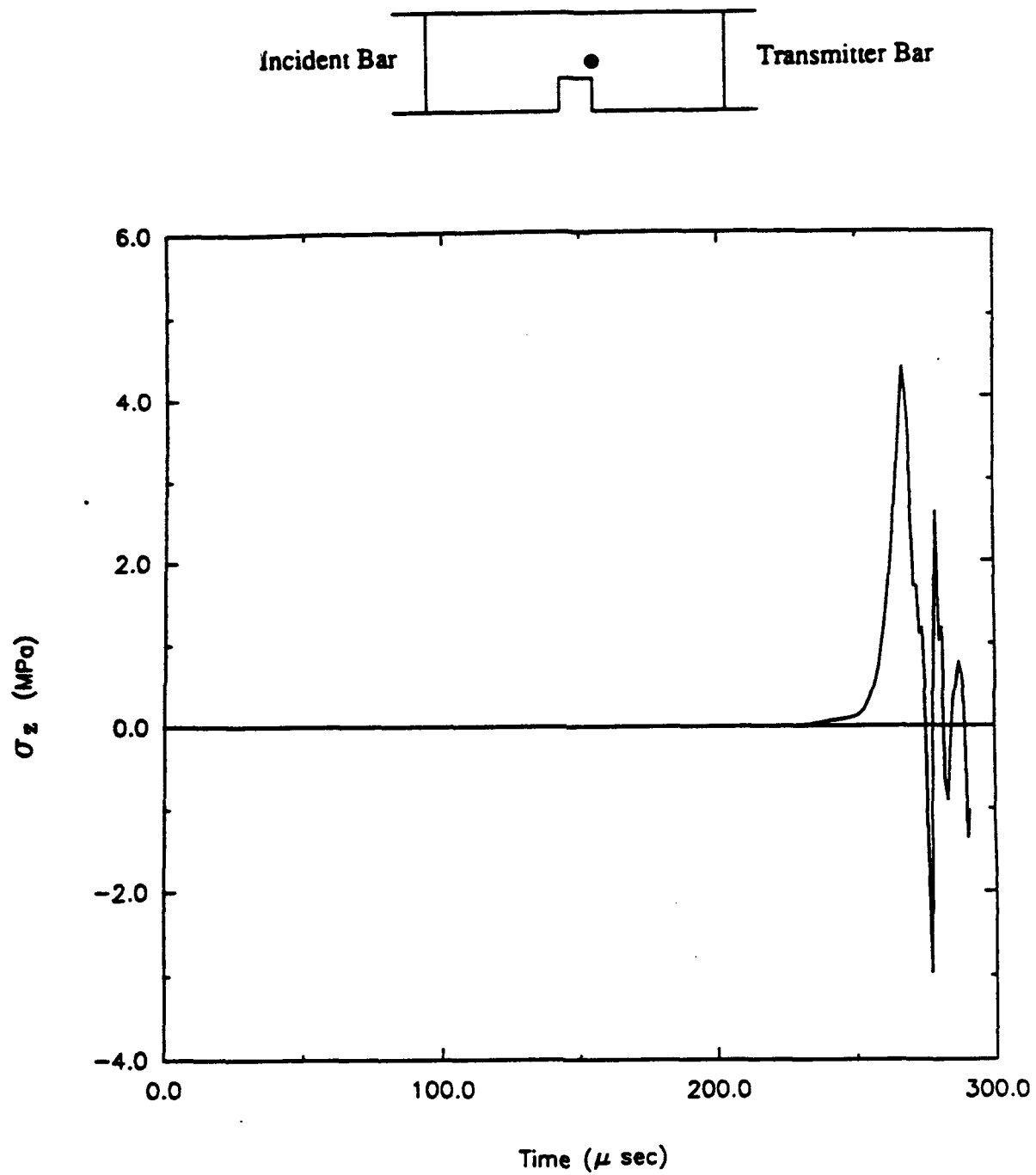


Figure 48. Time history for longitudinal stress (square-notch, Load Case 2).

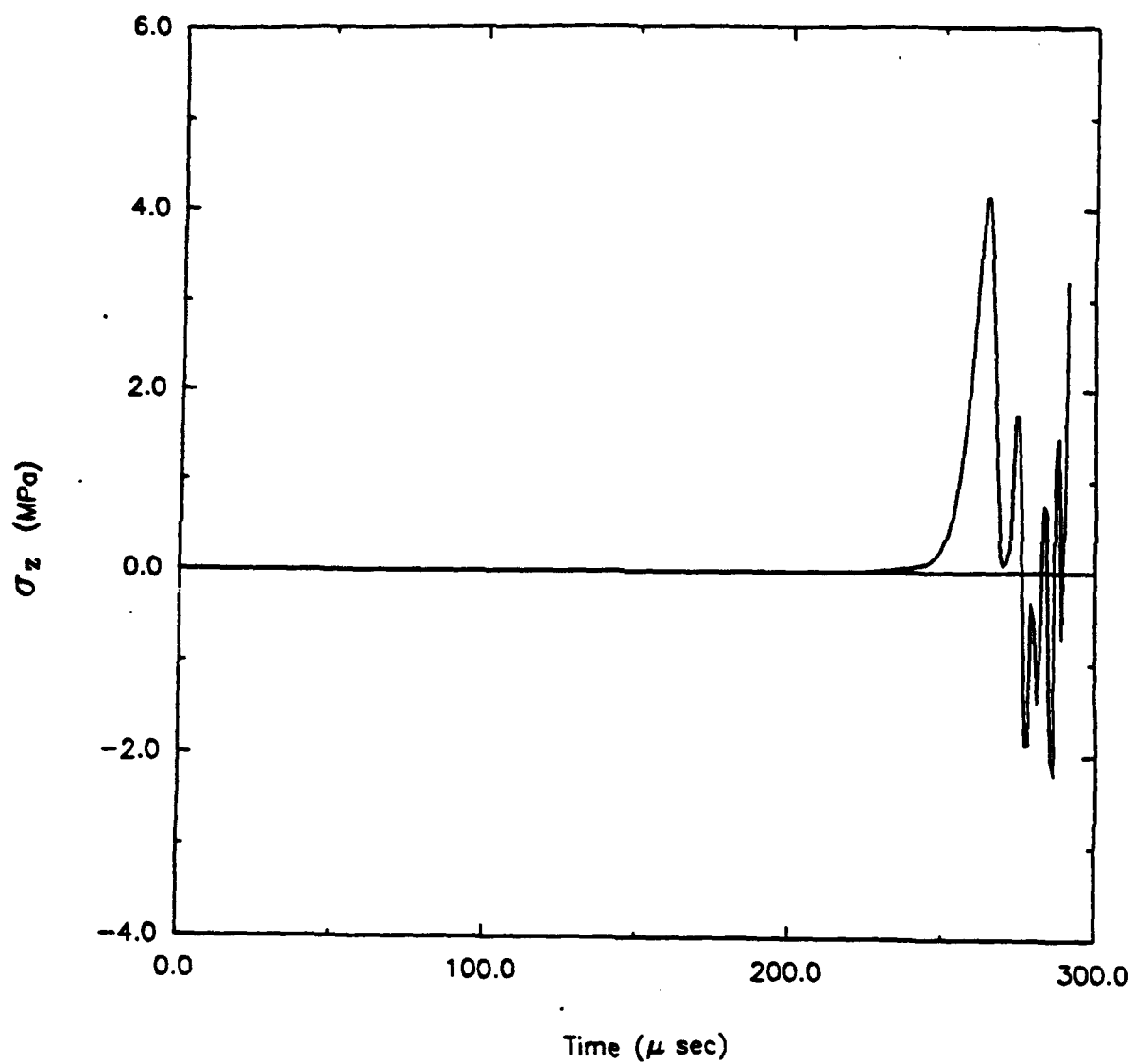
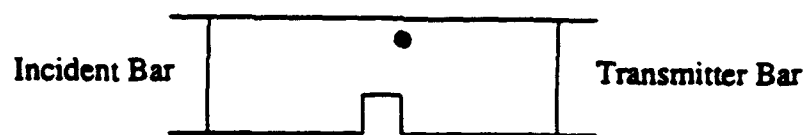


Figure 49. Time history for longitudinal stress (square-notch, Load Case 2).

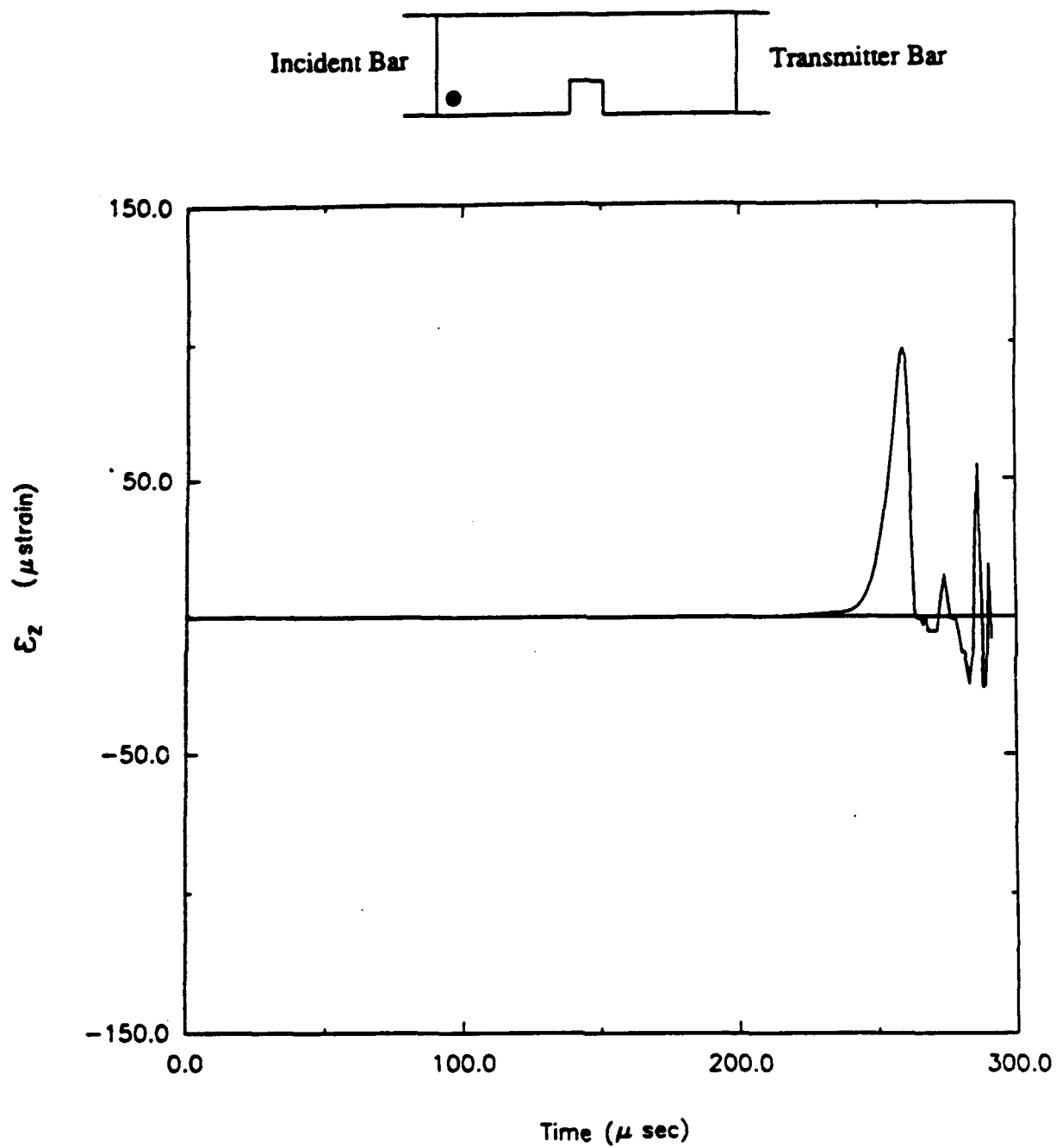


Figure 50. Time history for longitudinal strain (square-notch, Load Case 2).

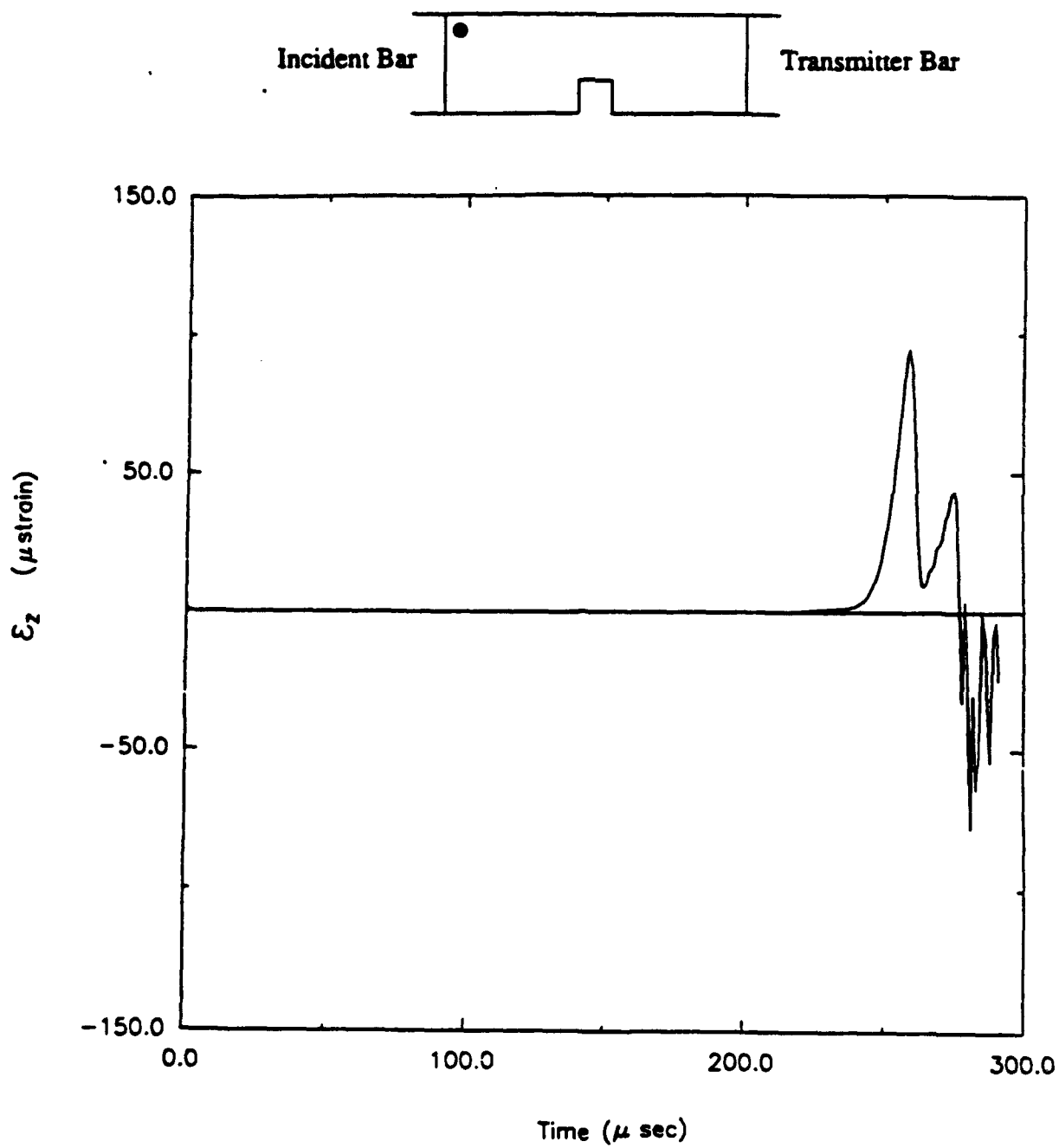


Figure 51. Time history for longitudinal strain (square-notch, Load Case 2).

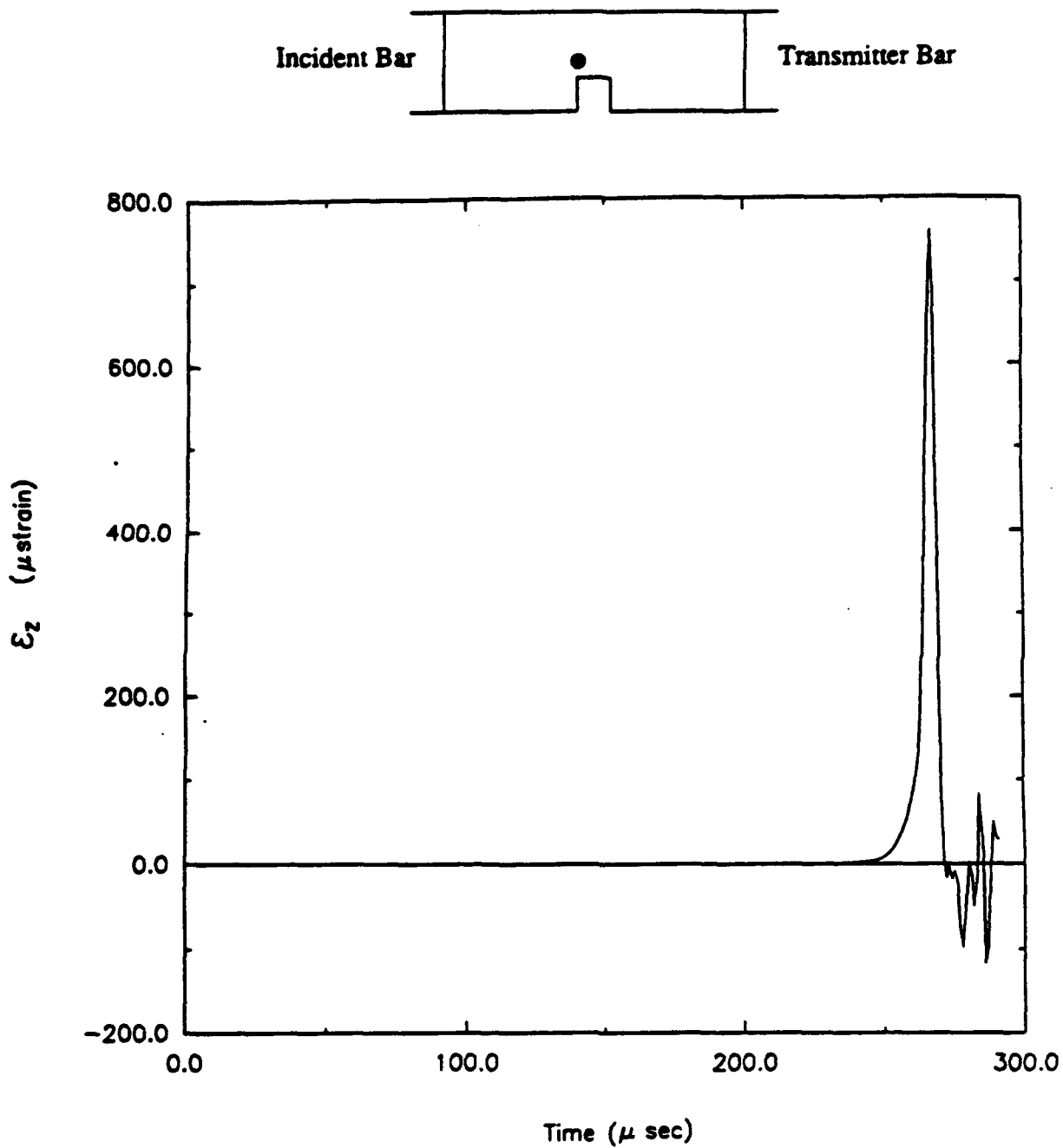


Figure 52. Time history for longitudinal strain (square-notch, Load Case 2).

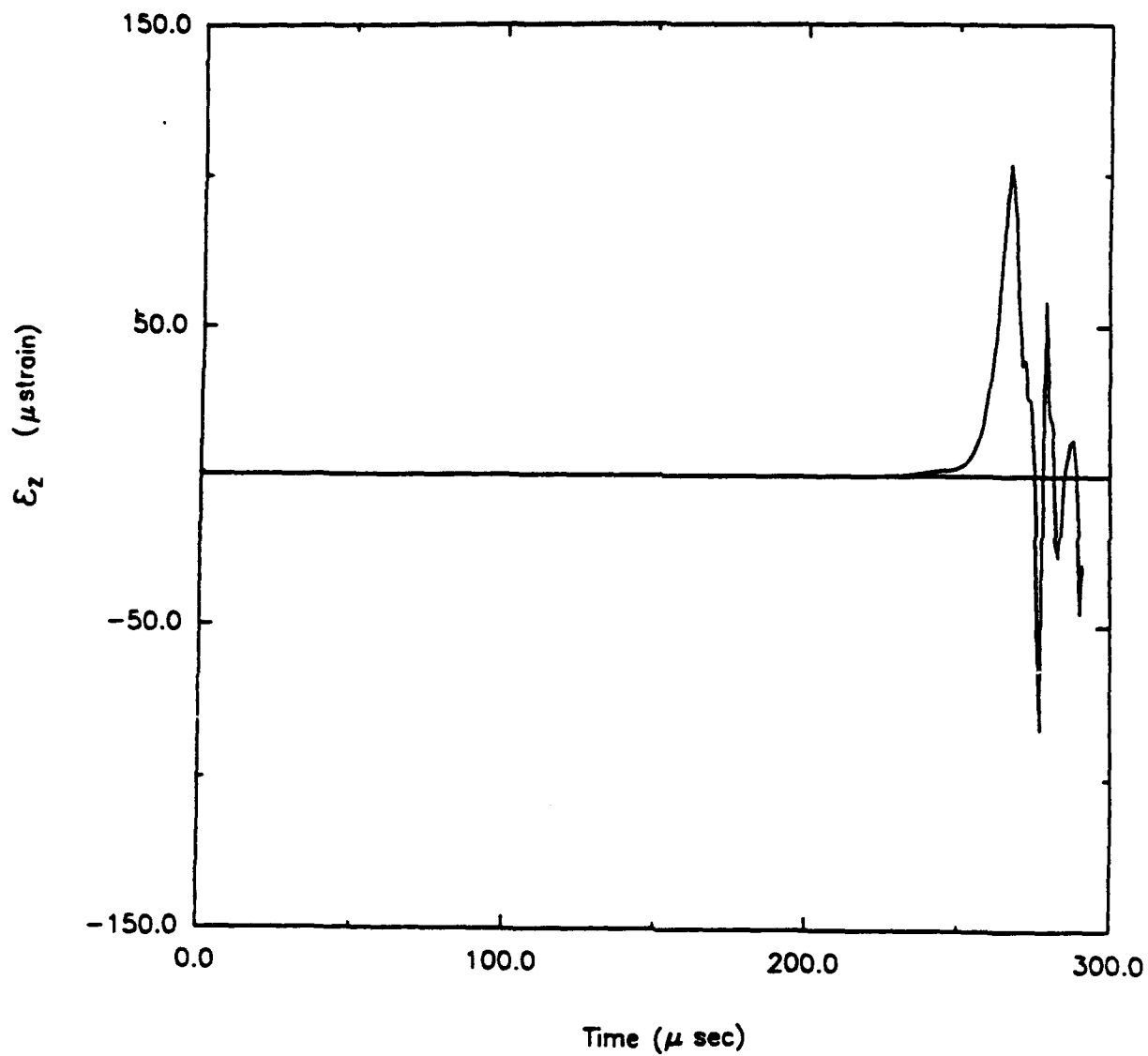
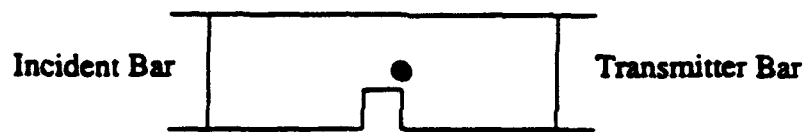


Figure 53. Time history for longitudinal strain (square-notch, Load Case 2).

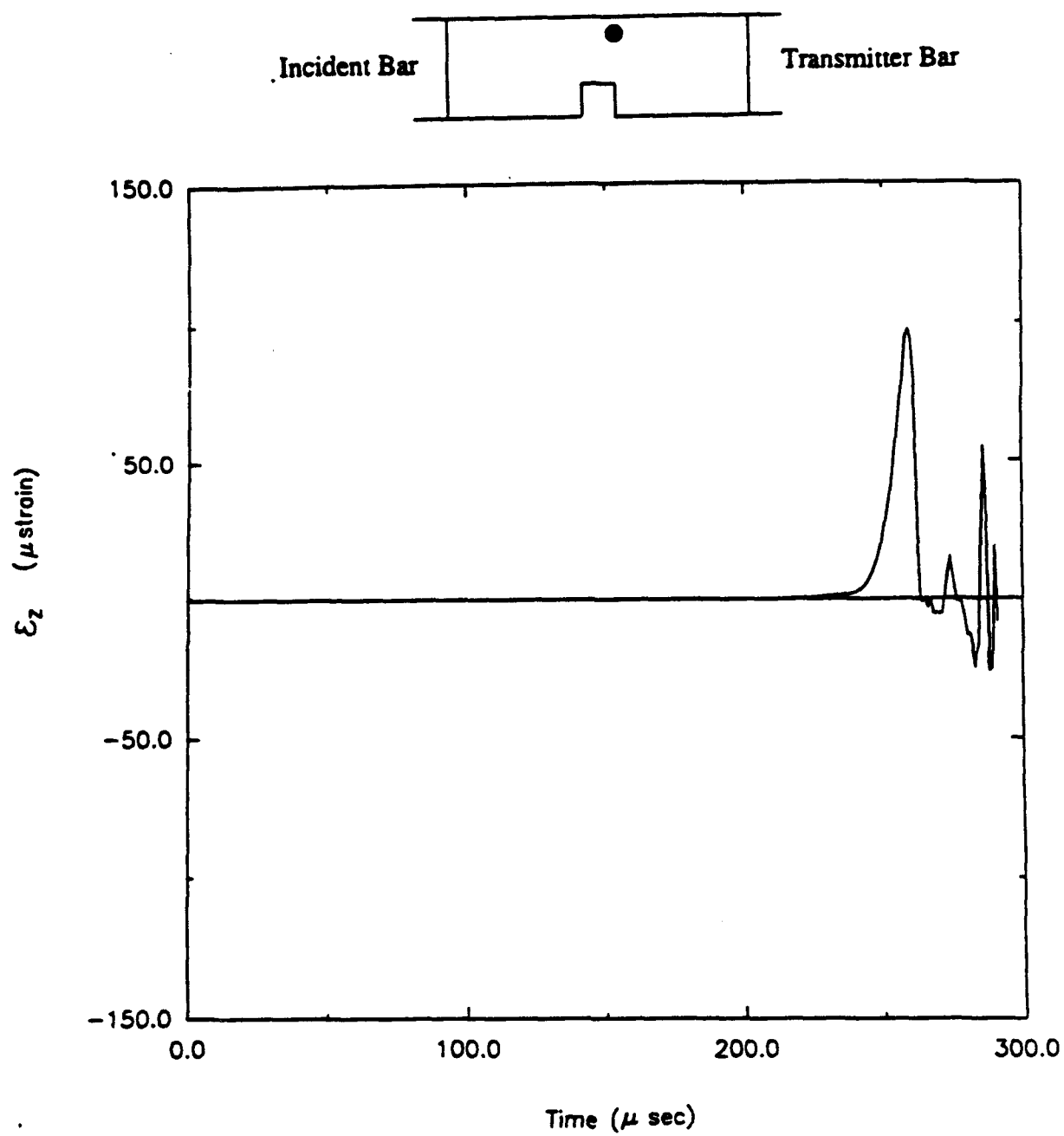


Figure 54. Time history for longitudinal strain (square-notch, Load Case 2).

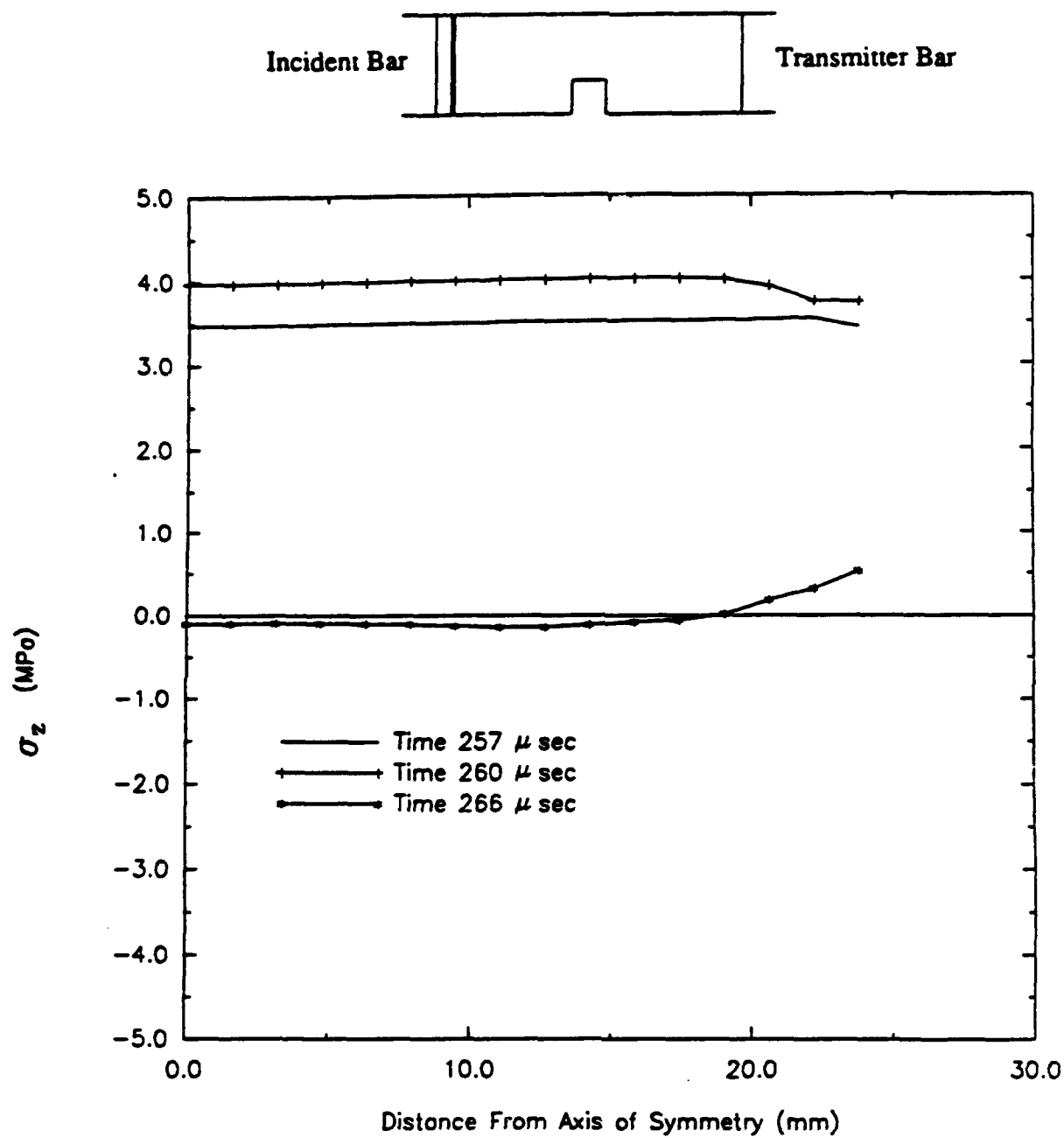


Figure 55. Profiles for longitudinal stress (square-notch, Load Case 2).

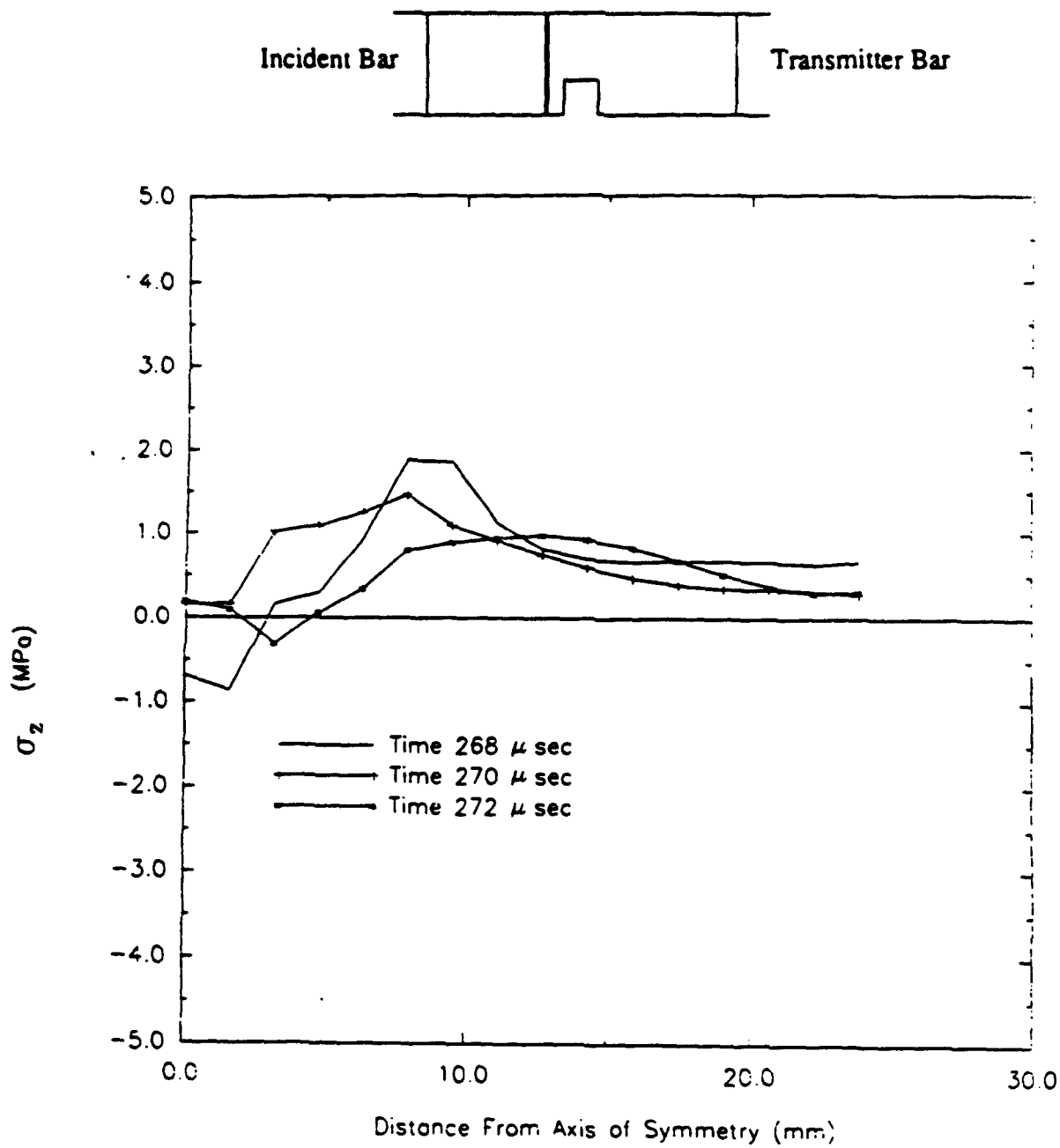


Figure 56. Profiles for longitudinal stress (square-notch, Load Case 2).

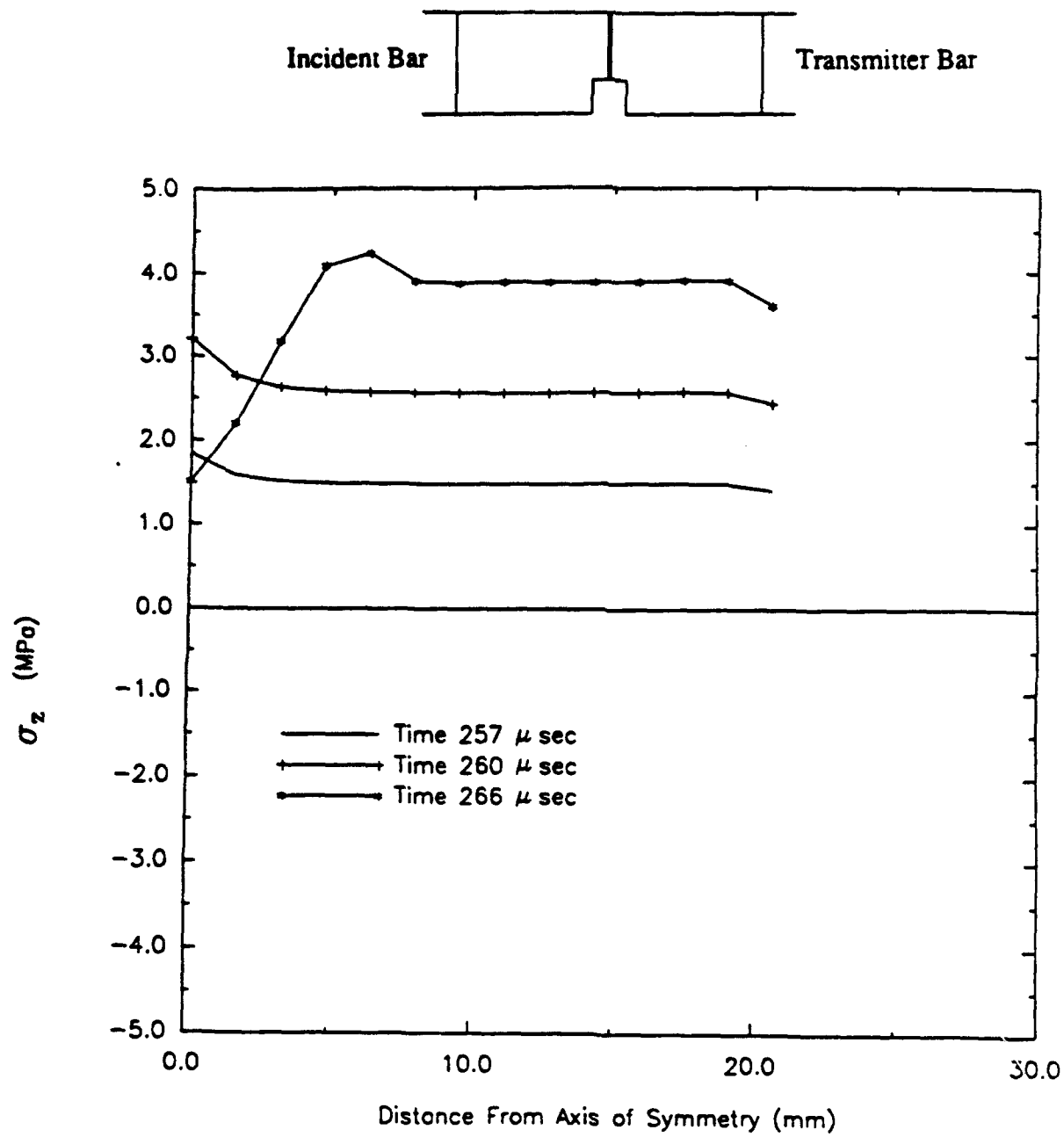


Figure 57. Profiles for longitudinal stress (square-notch, Load Case 2).

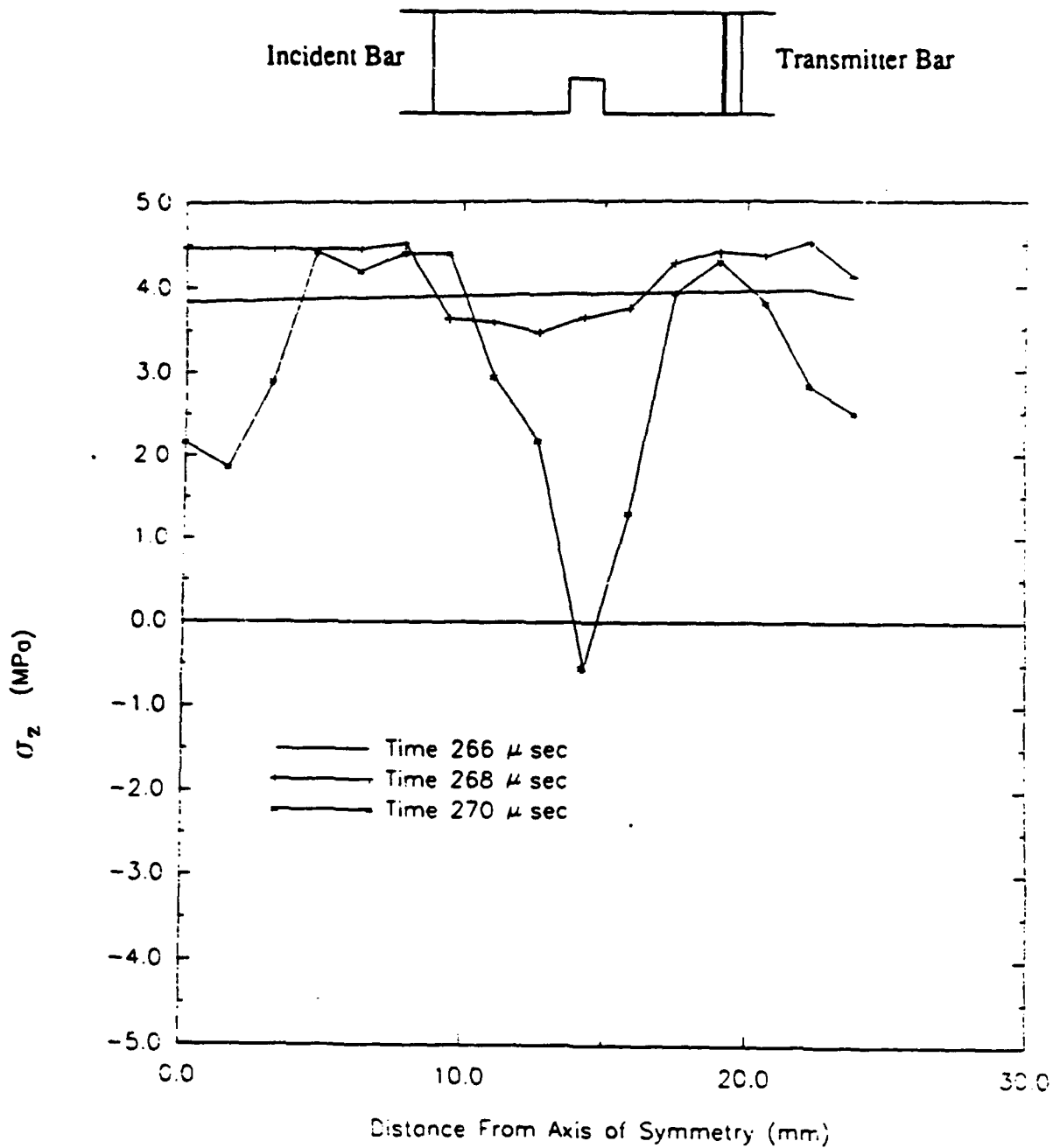


Figure 58. Profiles for longitudinal stress (square-notch, Load Case 2).

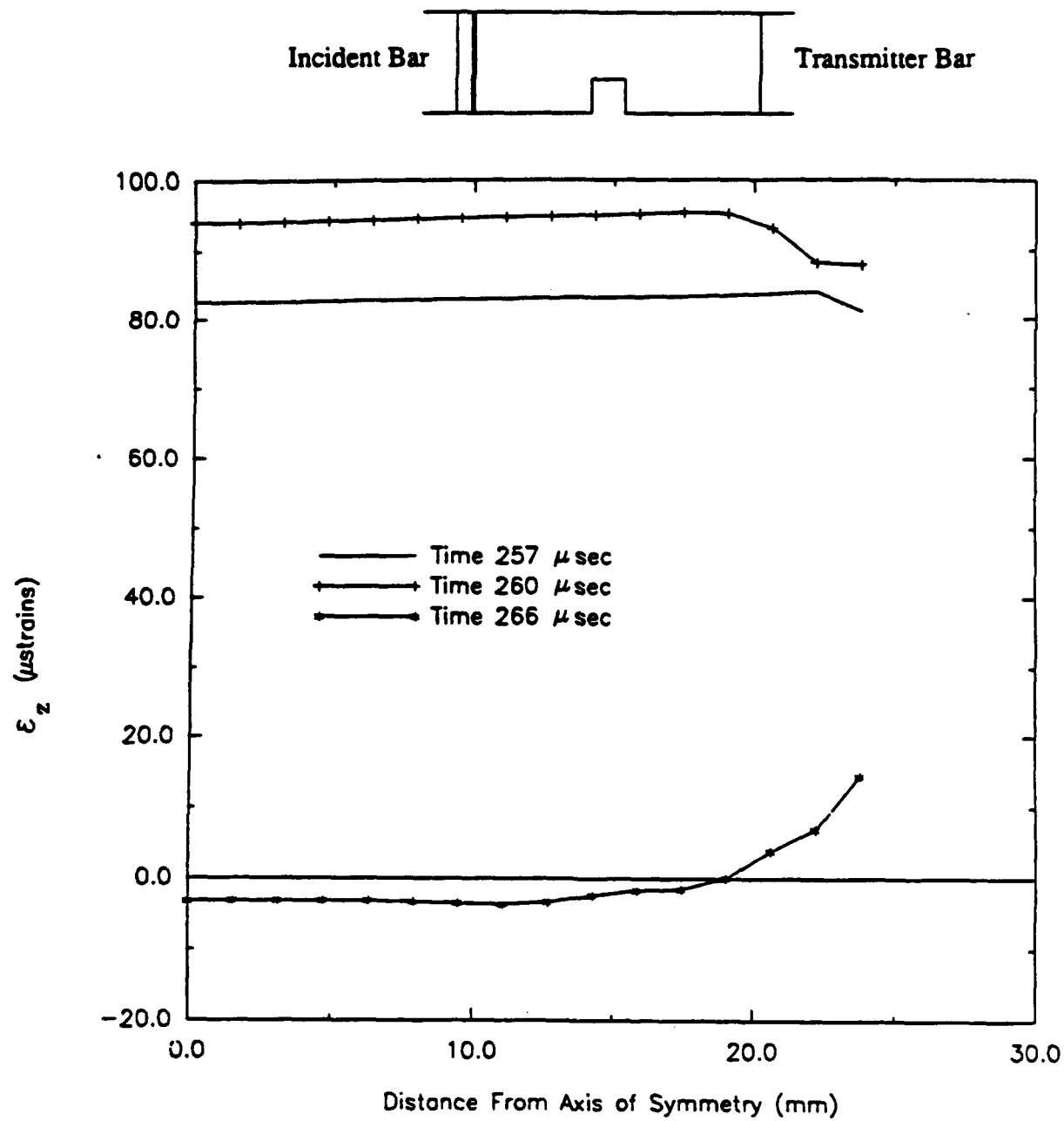


Figure 59. Profiles for longitudinal strain (square-notch, Load Case 2).

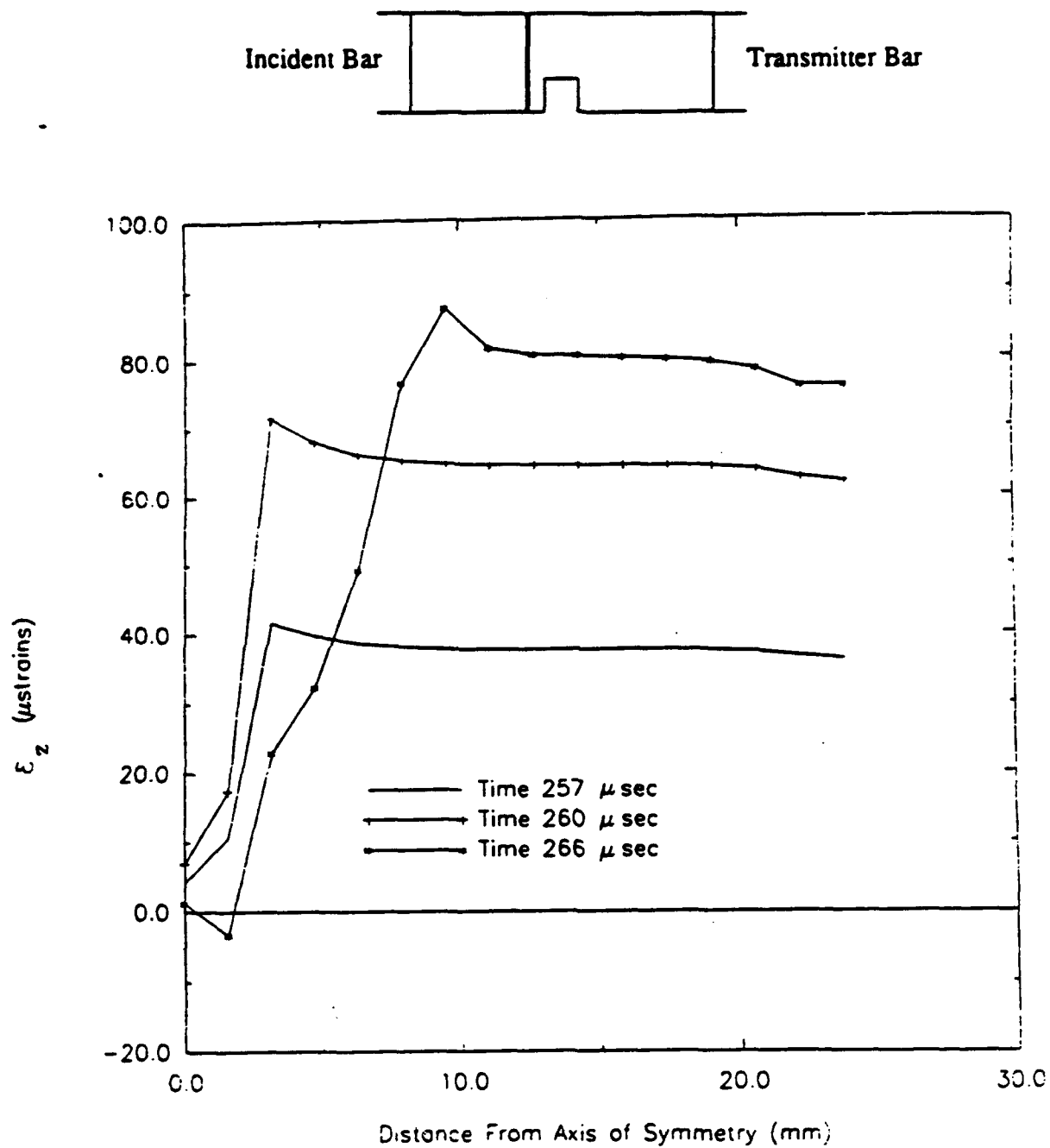


Figure 60. Profiles for longitudinal strain (square-notch, Load Case 2).

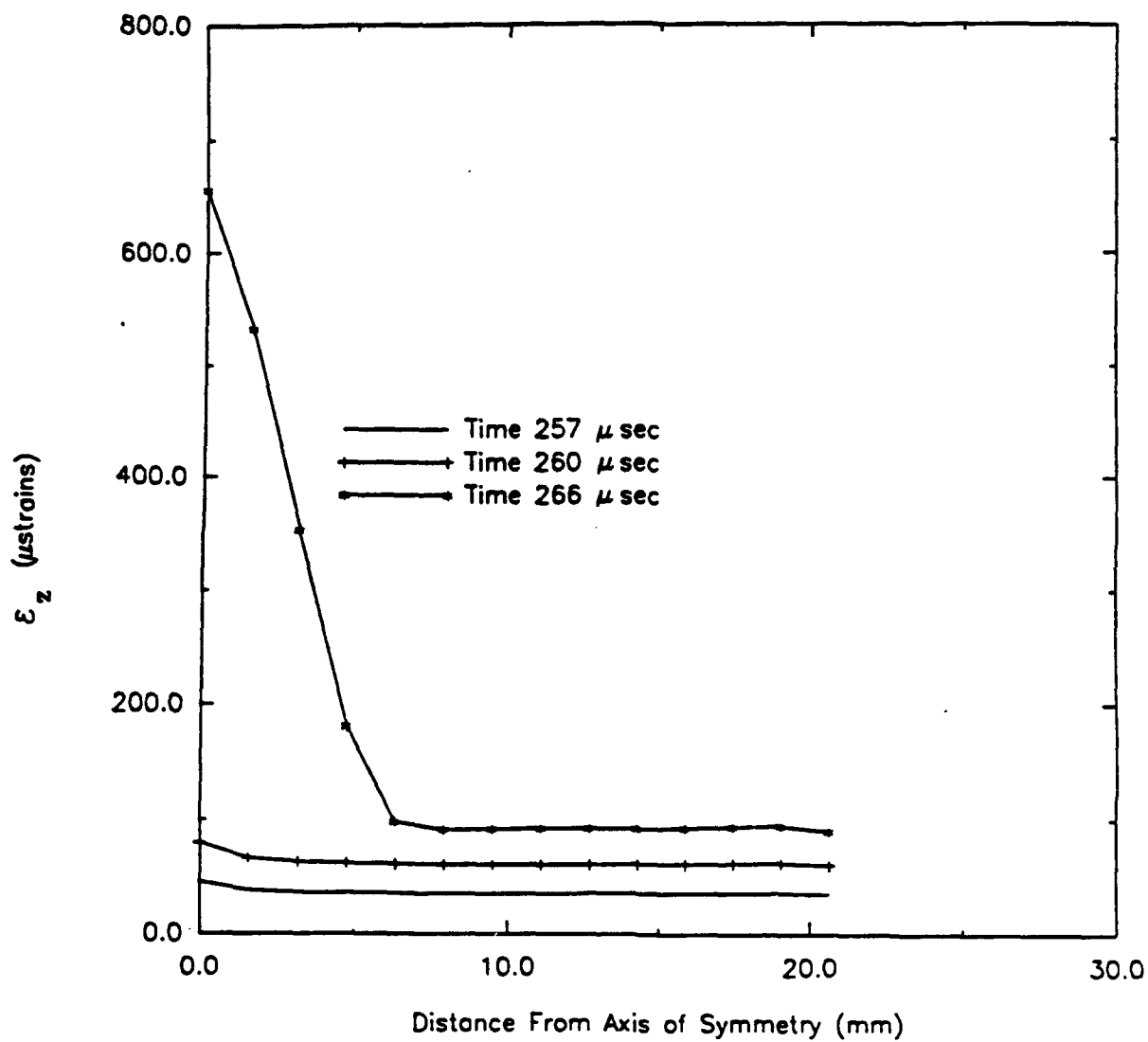
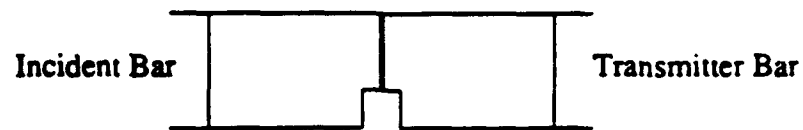


Figure 61. Profiles for longitudinal strain (square-notch, Load Case 2).

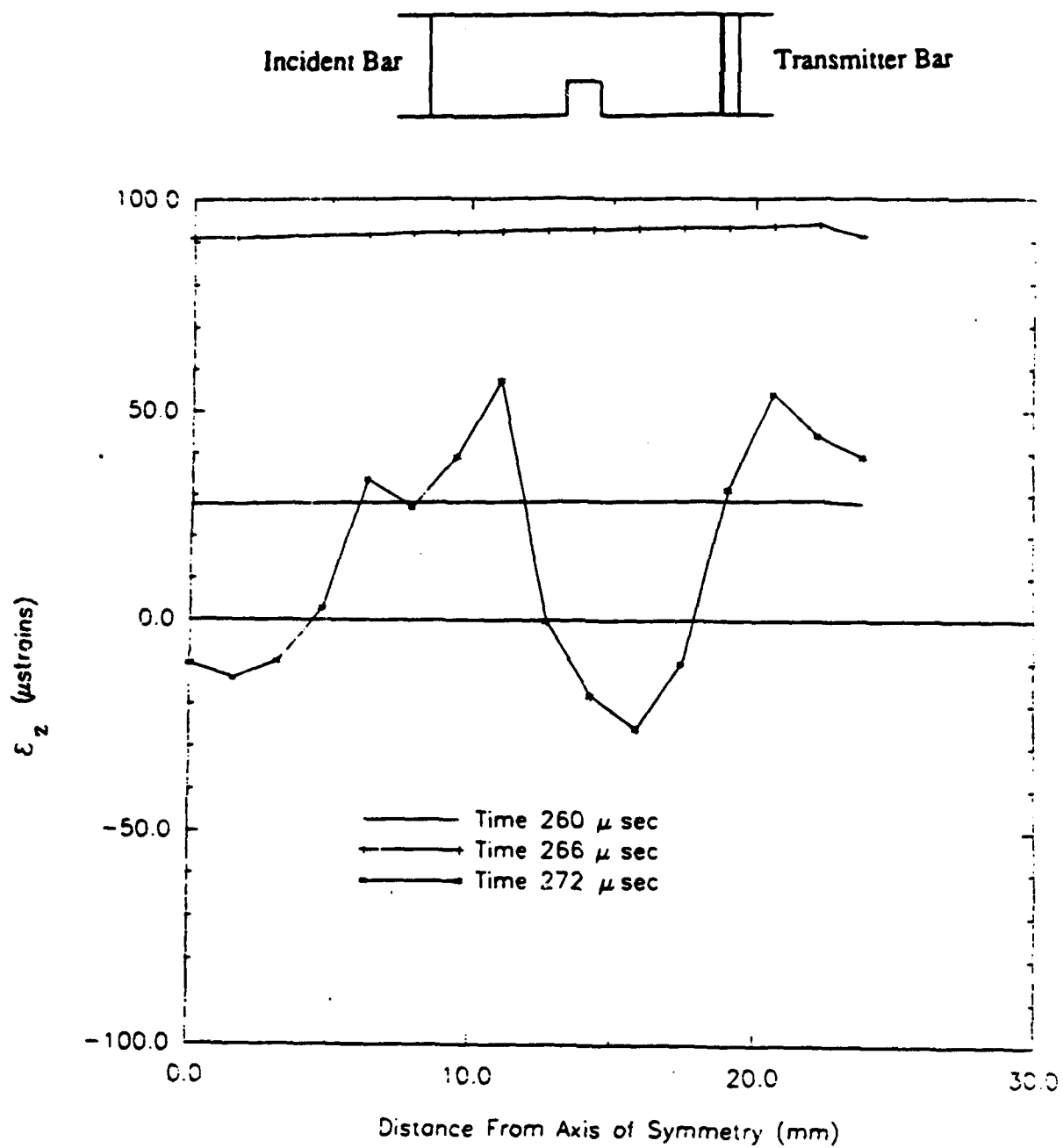
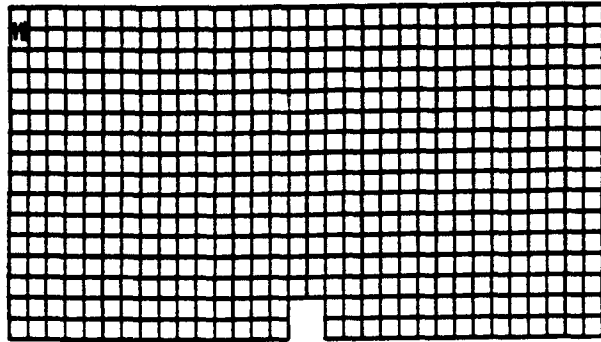
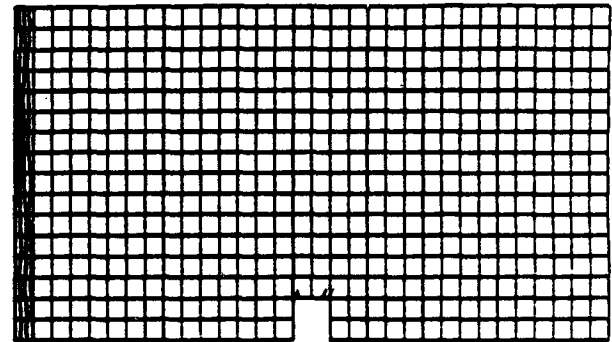


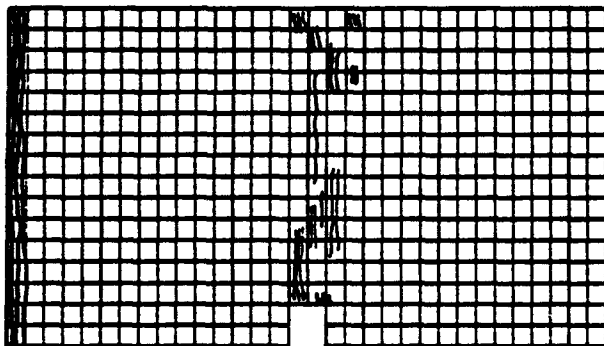
Figure 62. Profiles for longitudinal strain (square-notch, Load Case 2).



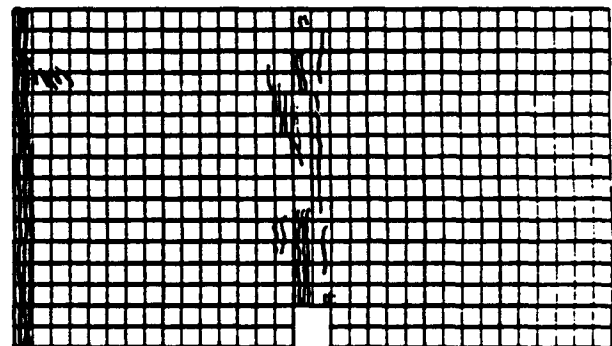
(a)



(b)



(c)



(d)

Figure 63. Cracking sequence for square-notch specimen; Load Case 2:
a) $t=258 \mu \text{ sec}$, b) $t=260 \mu \text{ sec}$, c) $t=265 \mu \text{ sec}$, d) $t=295 \mu \text{ sec}$.

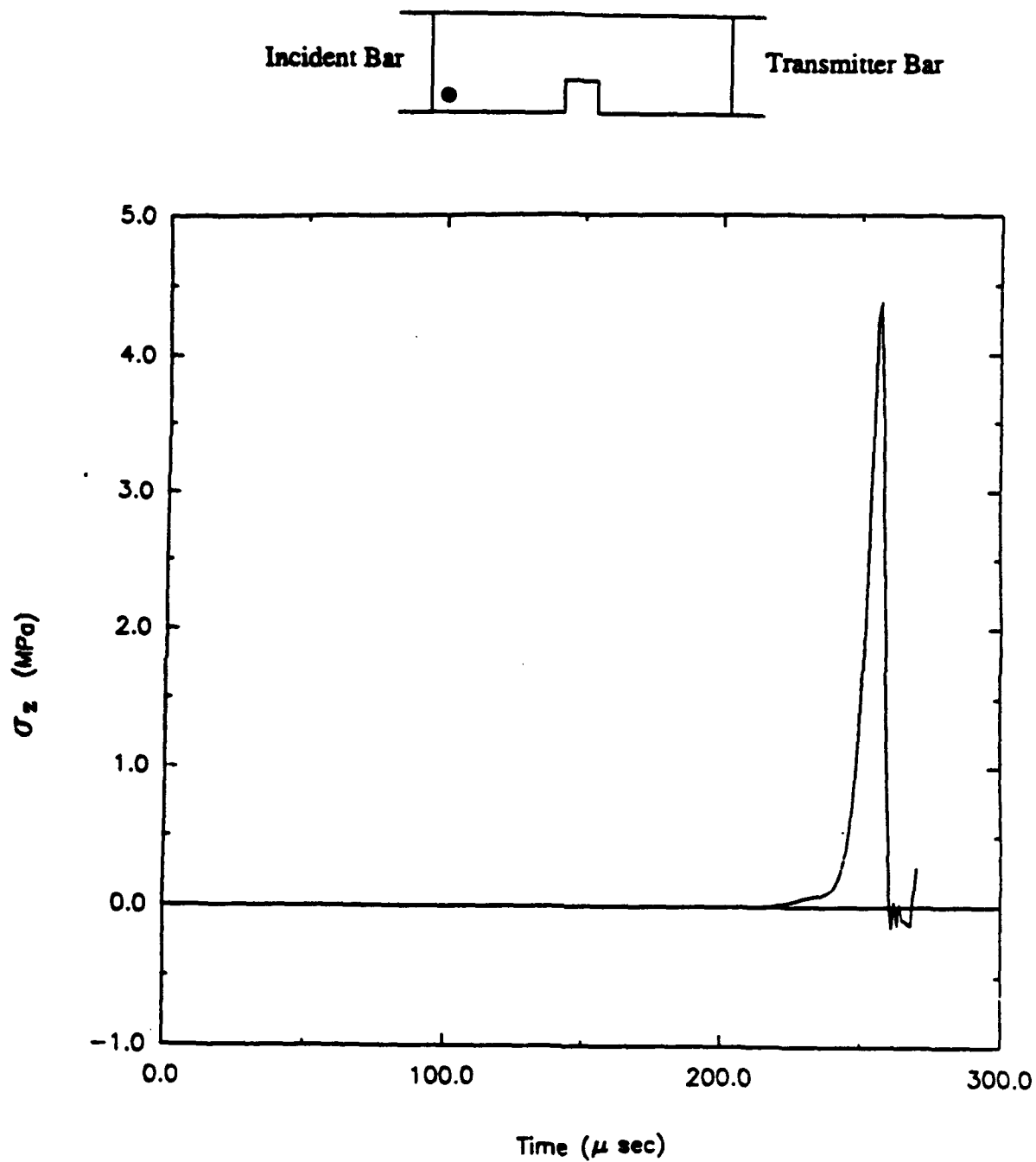


Figure 64. Time history for longitudinal stress (square-notch, Load Case 3).

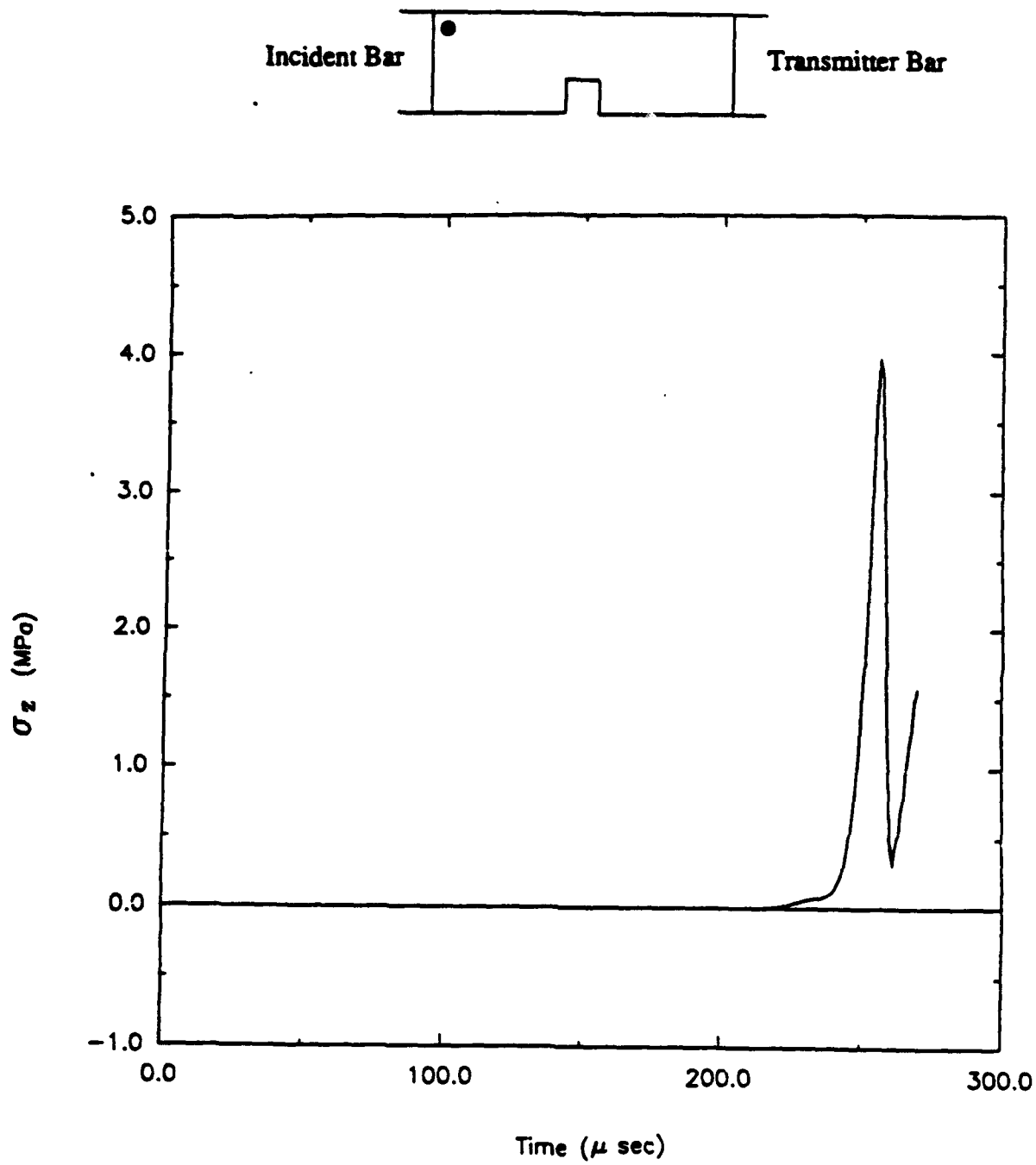


Figure 65. Time history for longitudinal stress (square-notch, Load Case 3).

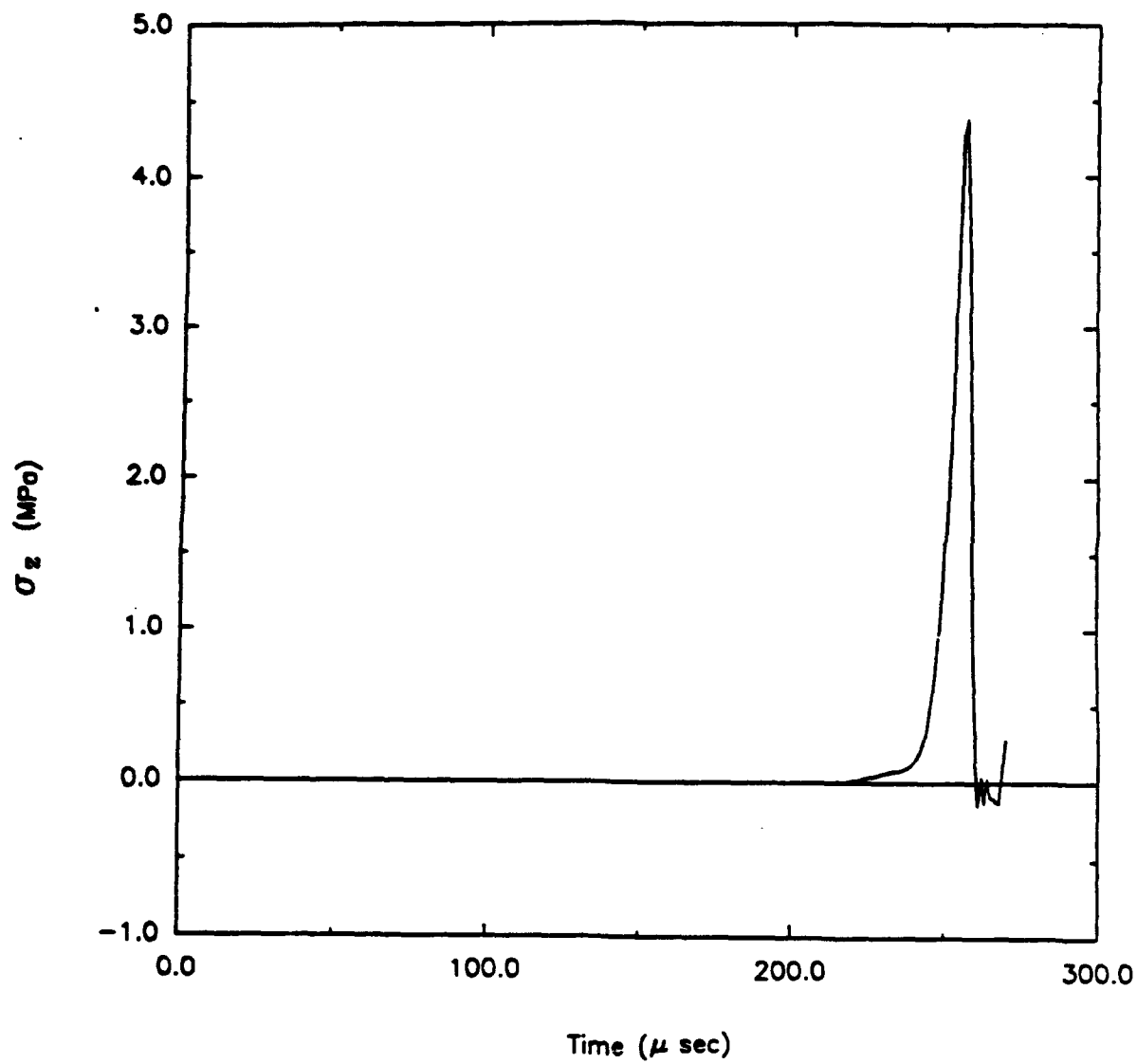


Figure 66. Time history for longitudinal stress (square-notch, Load Case 3).

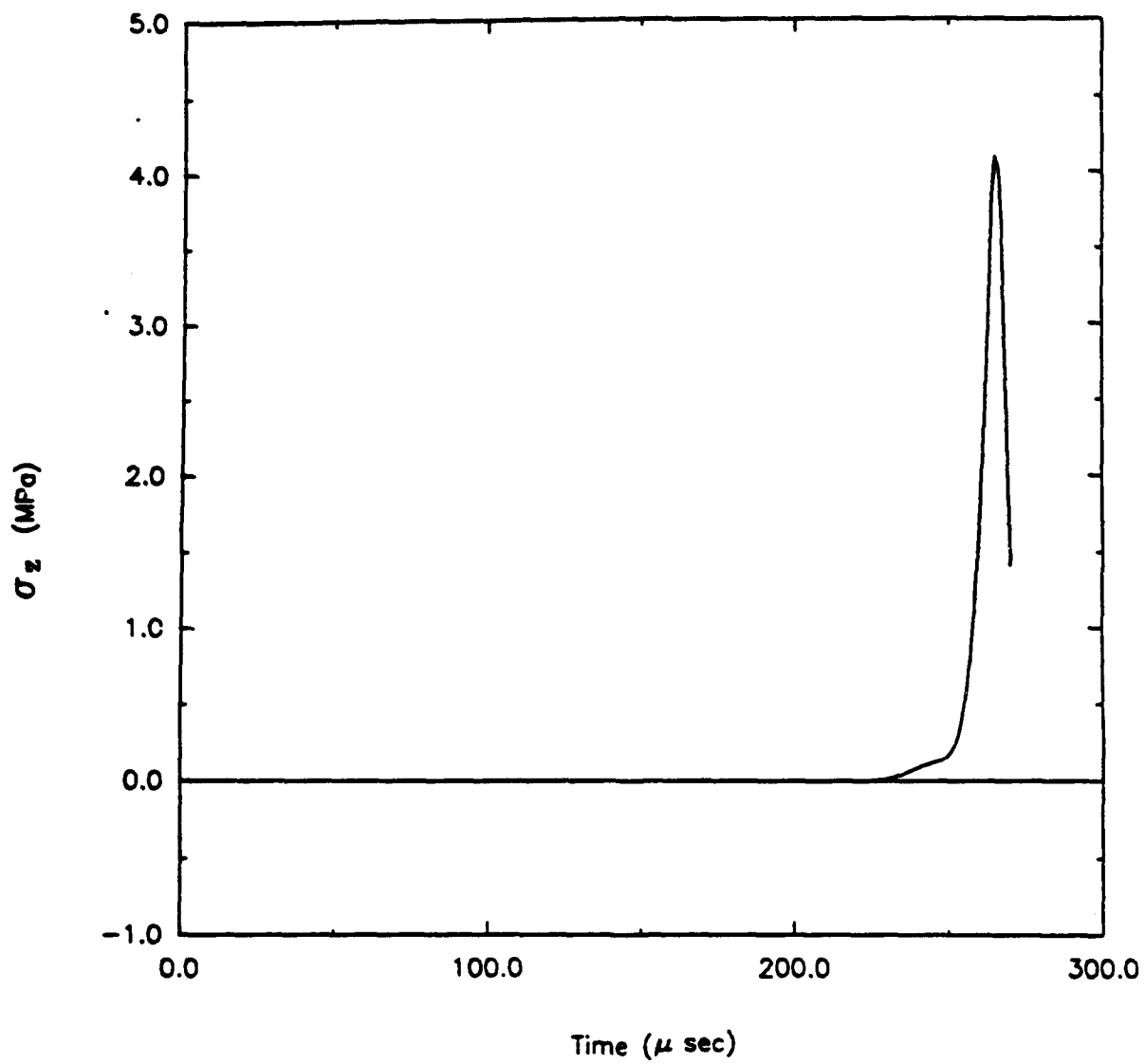
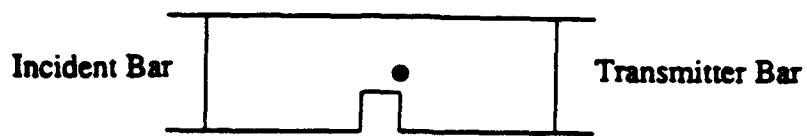


Figure 67. Time history for longitudinal stress (square-notch, Load Case 3).

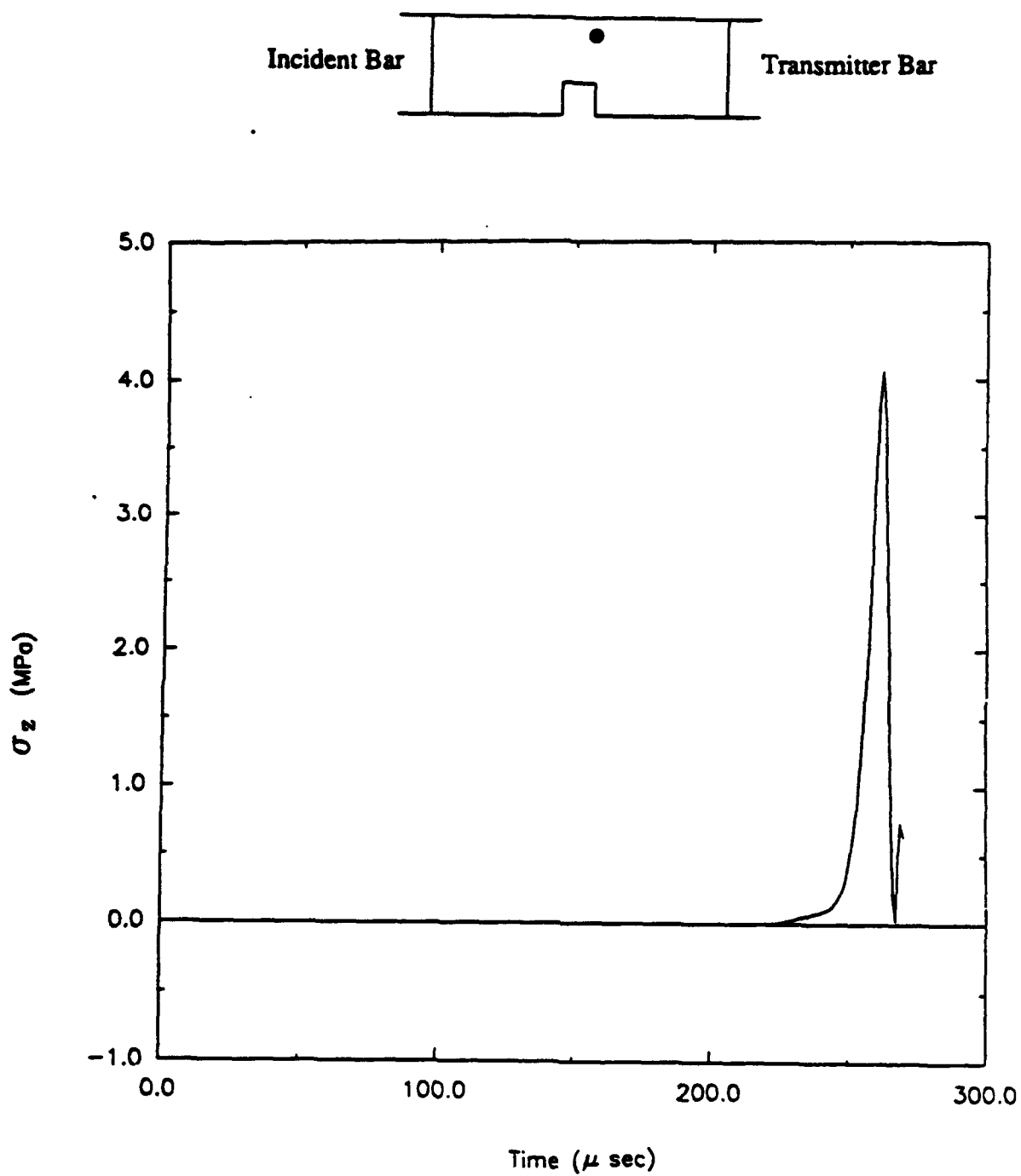


Figure 68. Time history for longitudinal stress (square-notch, Load Case 3).

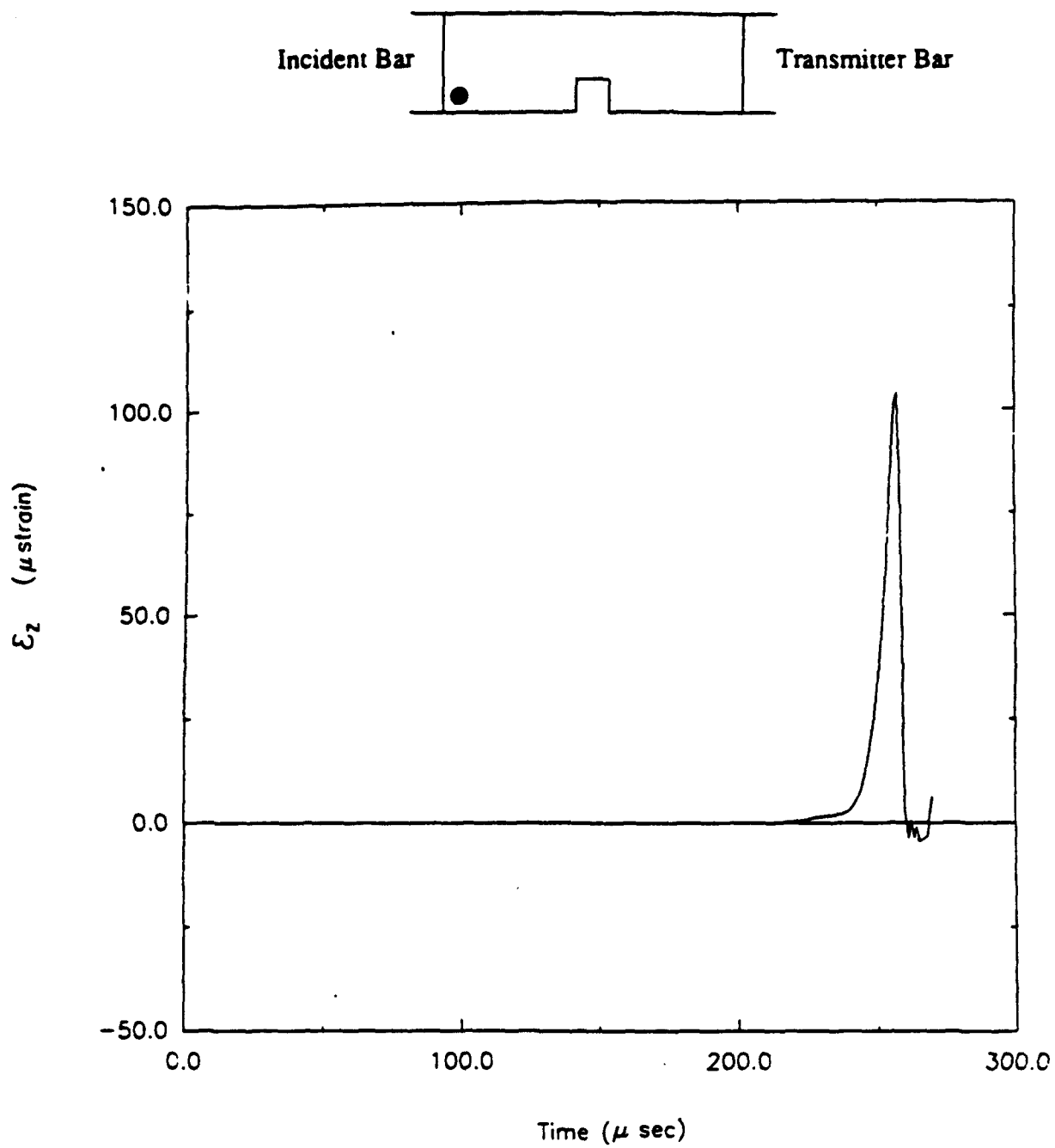


Figure 69. Time history for longitudinal strain (square-notch, Load Case 3).

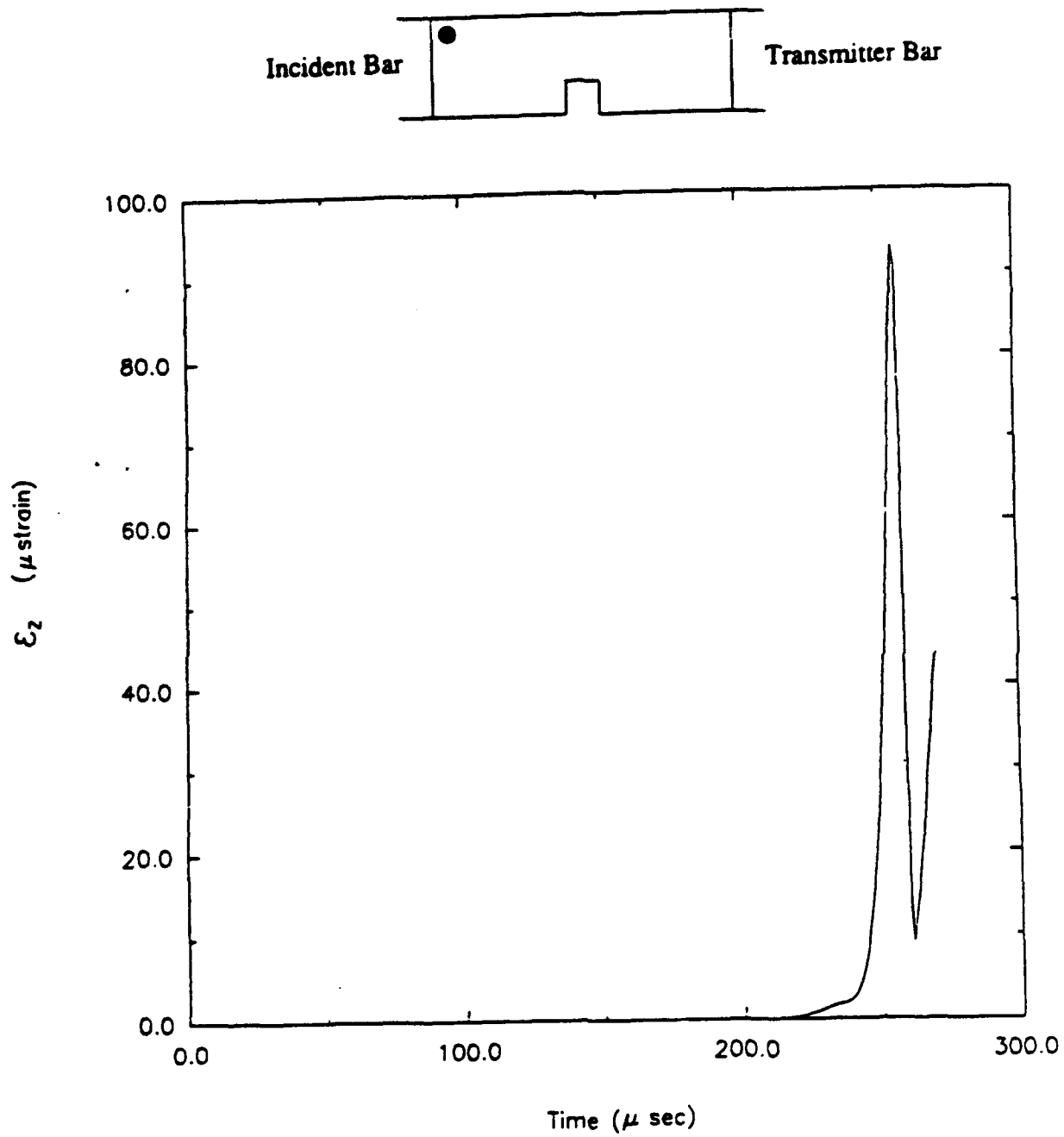


Figure 70. Time history for longitudinal strain (square-notch, Load Case 3).

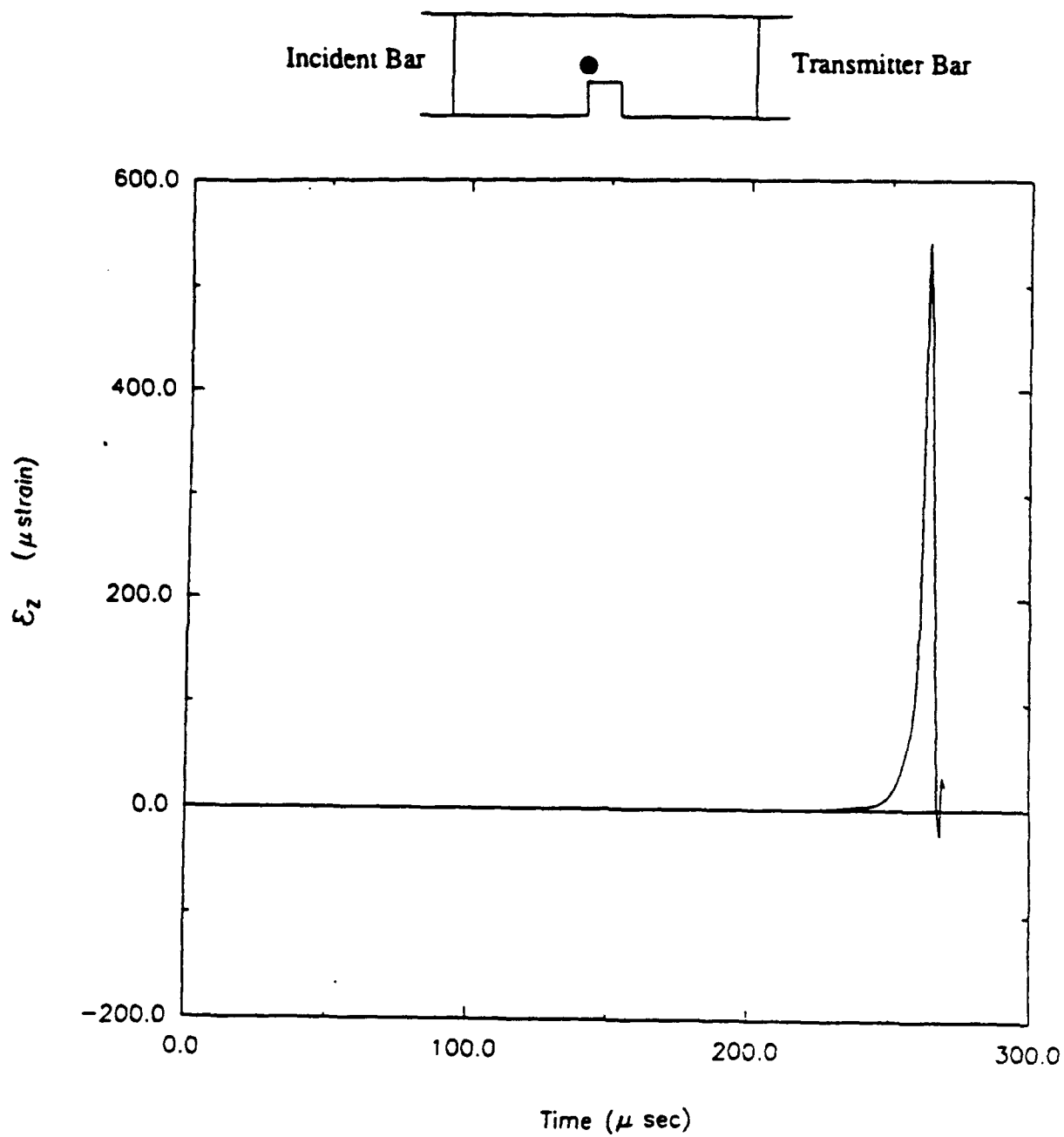


Figure 71. Time history for longitudinal strain (square-notch, Load Case 3).

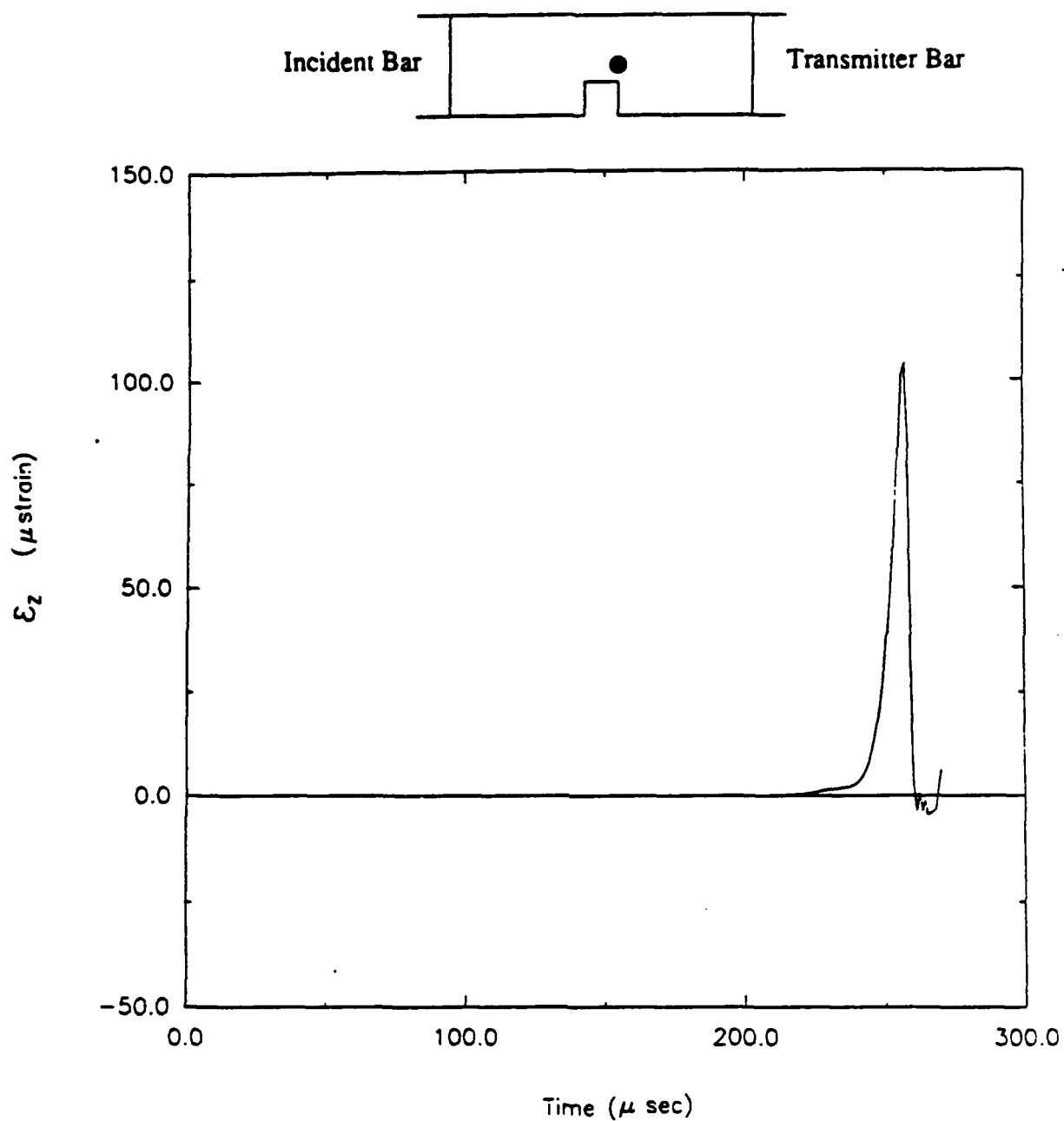


Figure 72. Time history for longitudinal strain (square-notch, Load Case 3).

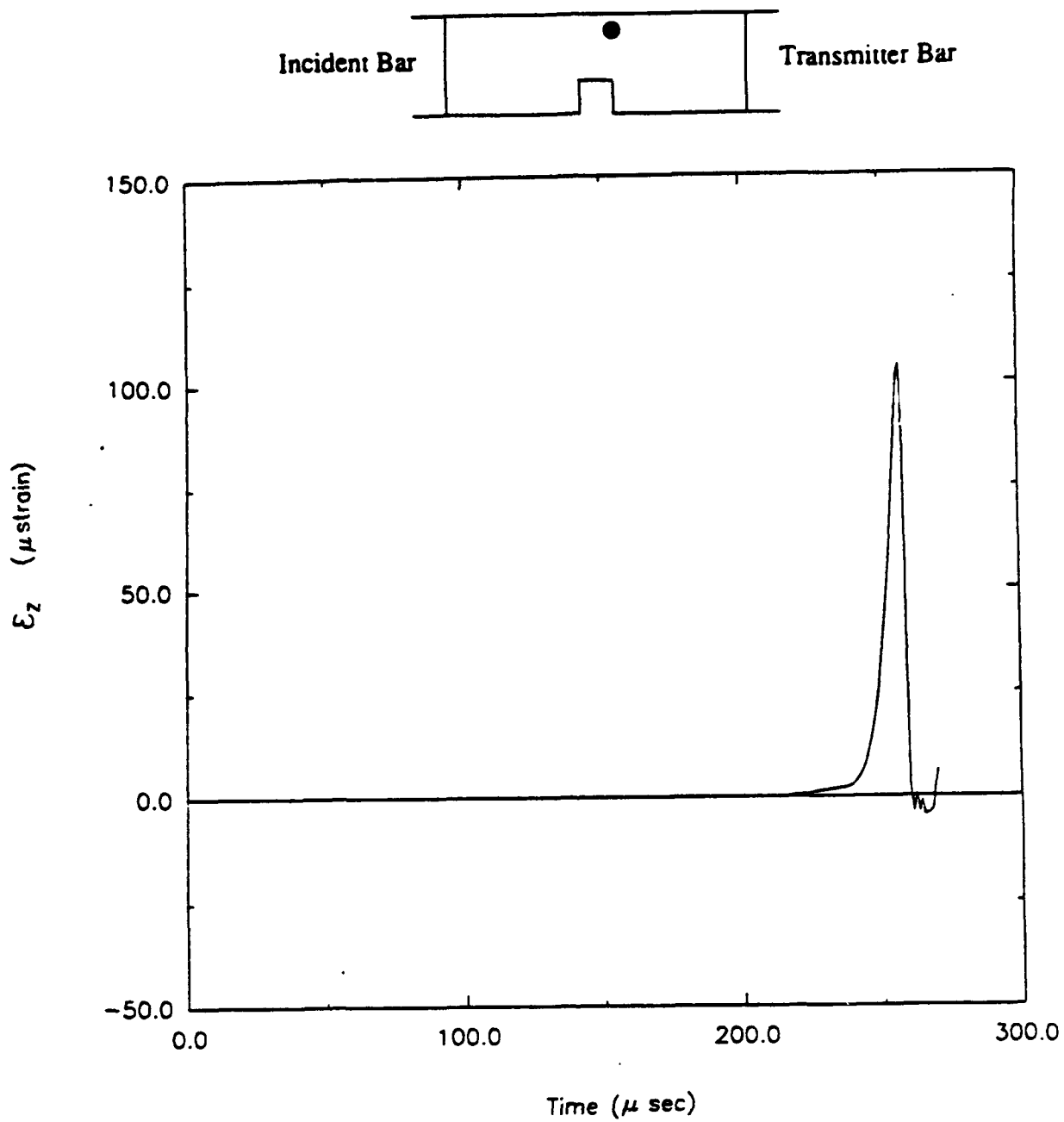


Figure 73. Time history for longitudinal strain (square-notch, Load Case 3).

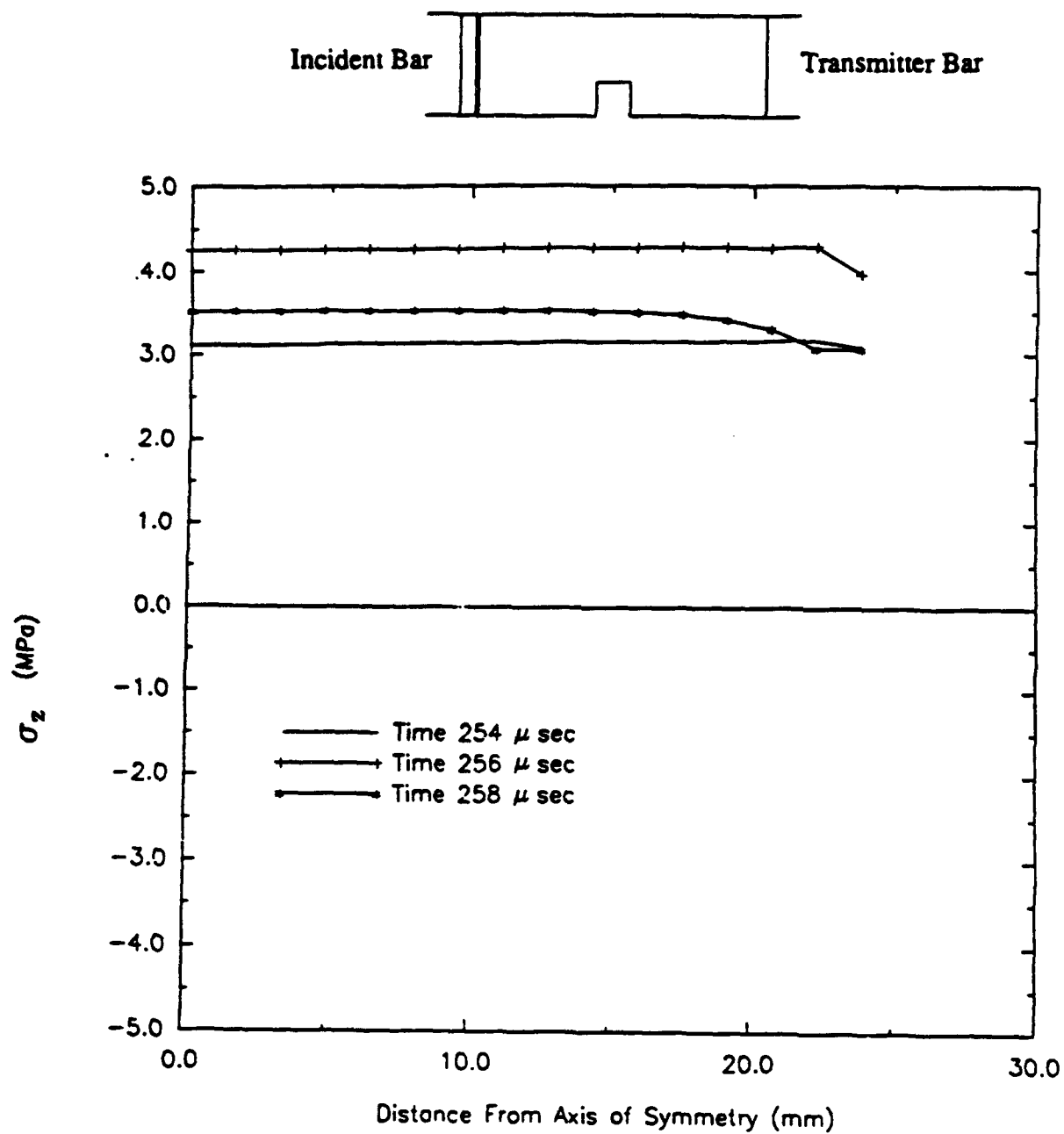


Figure 74. Profiles for longitudinal stress (square-notch, Load Case 3).

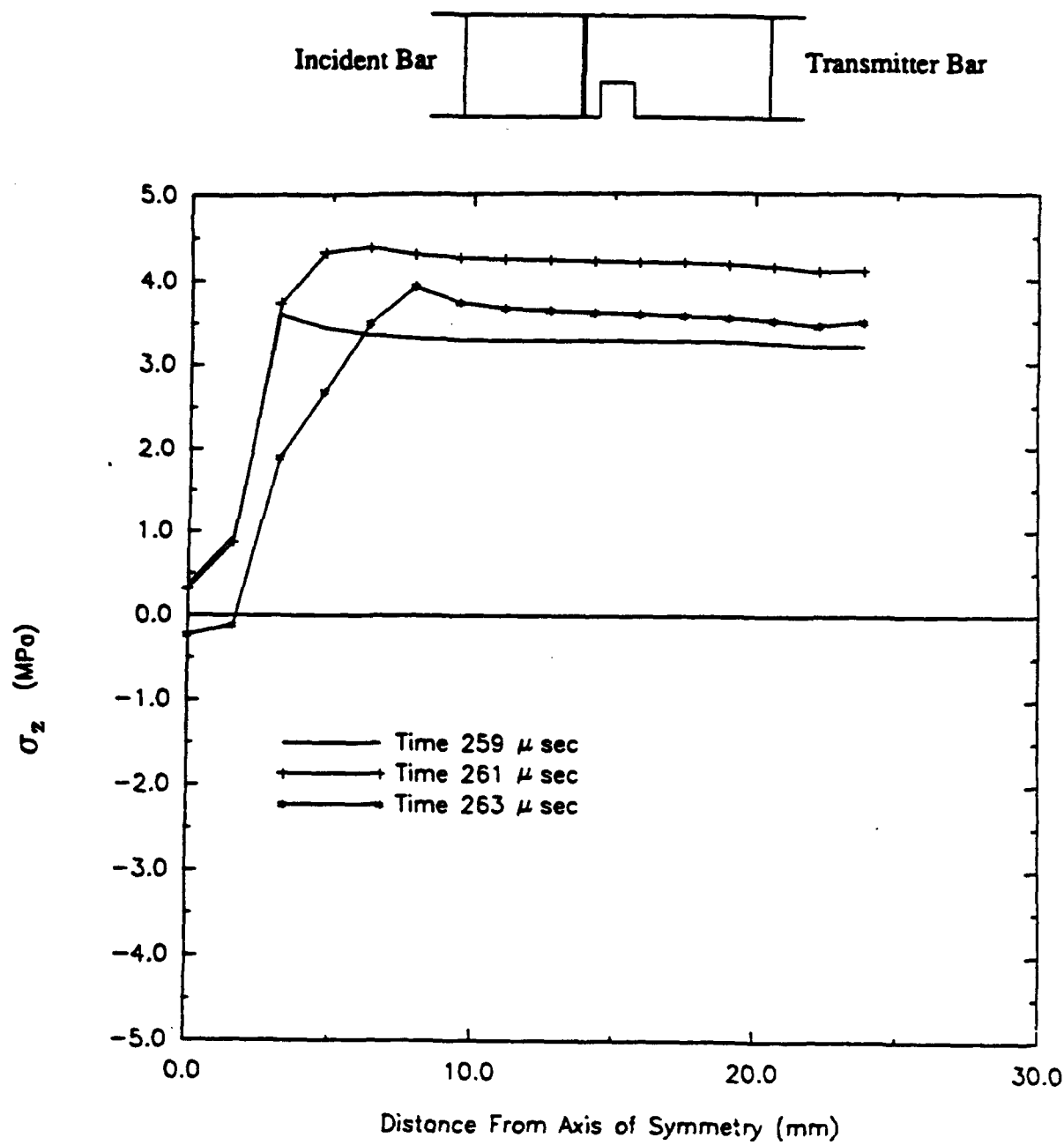


Figure 75. Profiles for longitudinal stress (square-notch, Load Case 3).

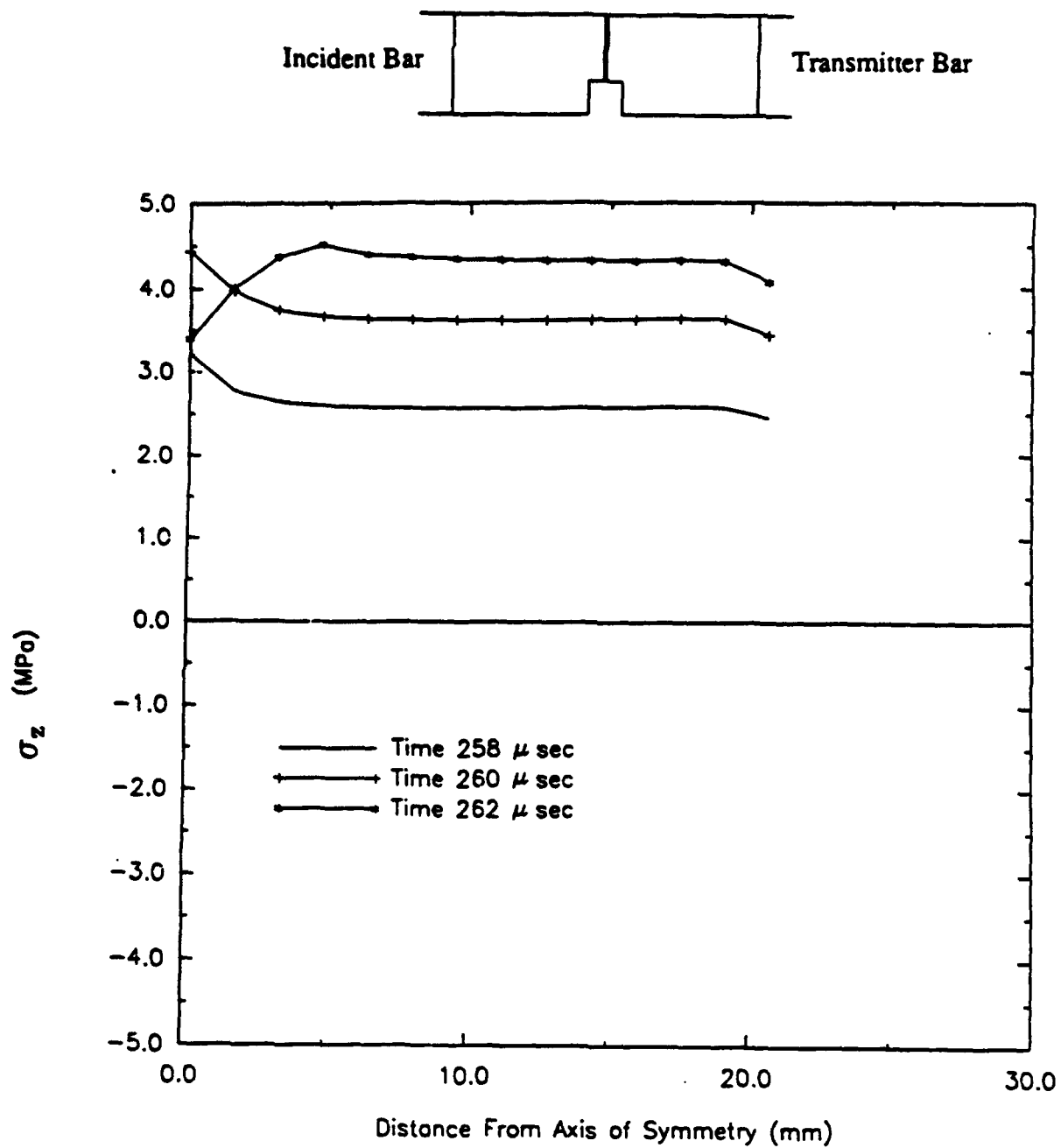


Figure 76. Profiles for longitudinal stress (square-notch, Load Case 3).

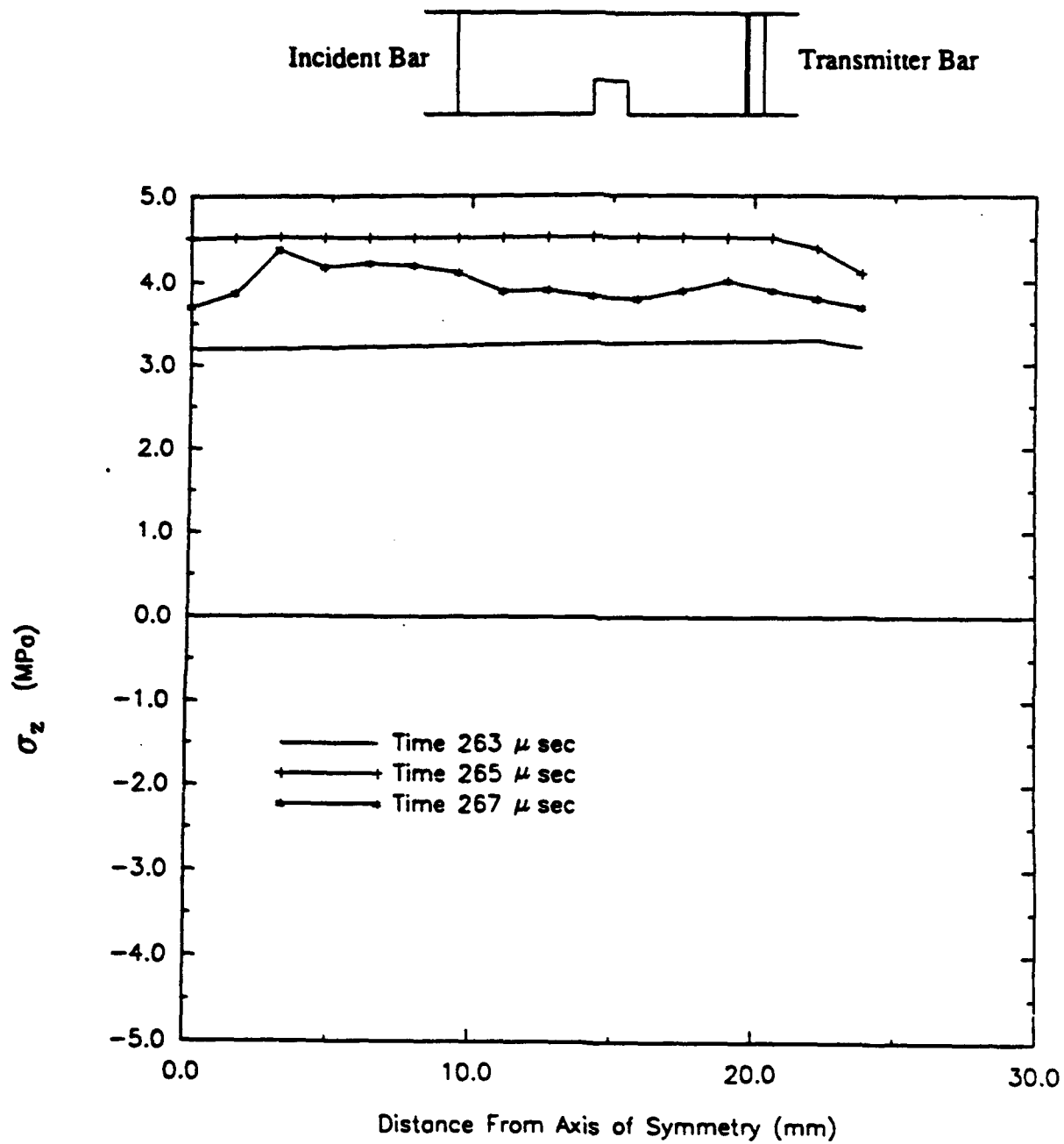


Figure 77. Profiles for longitudinal stress (square-notch, Load Case 3).

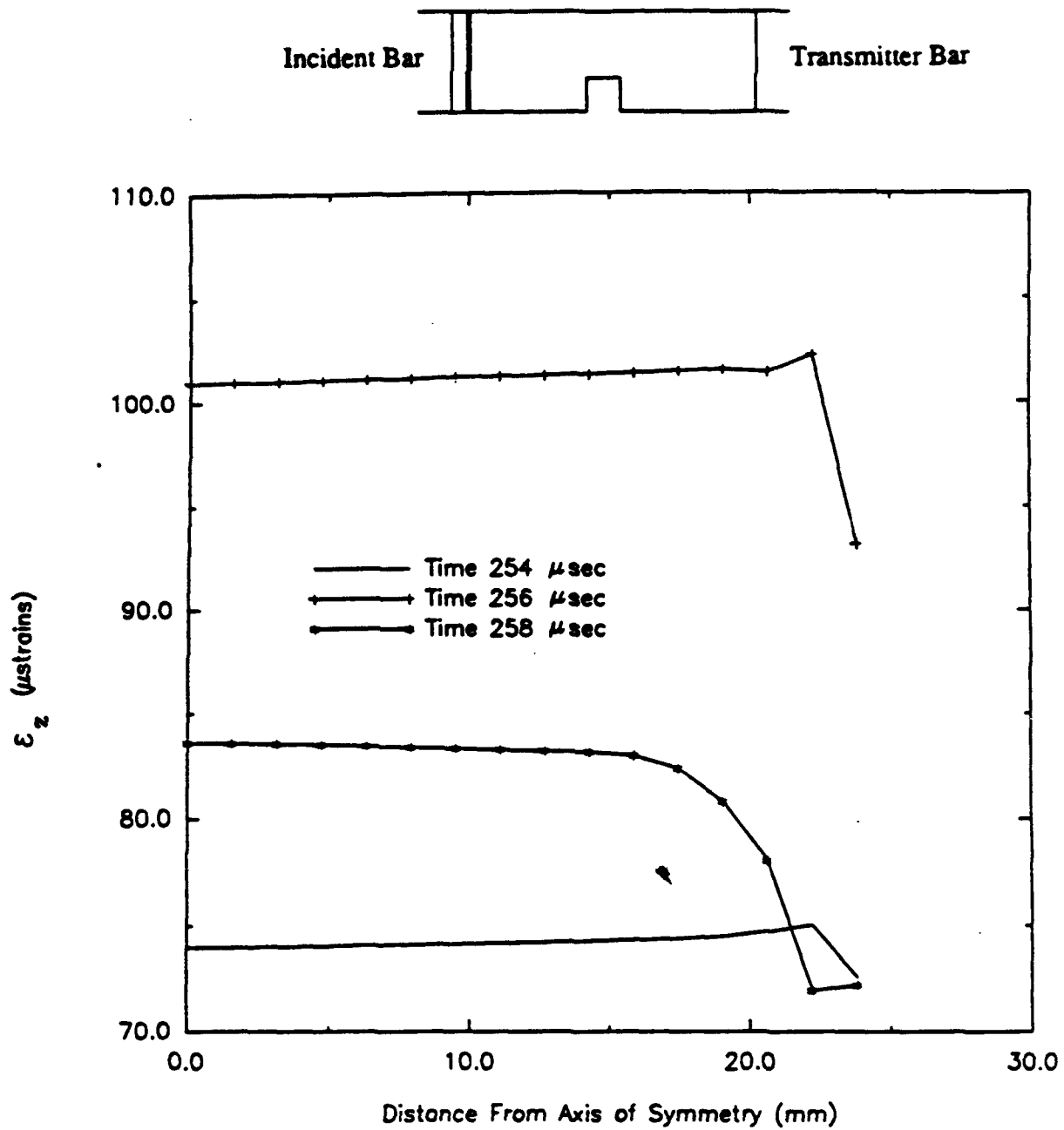


Figure 78. Profiles for longitudinal strain (square-notch, Load Case 3).

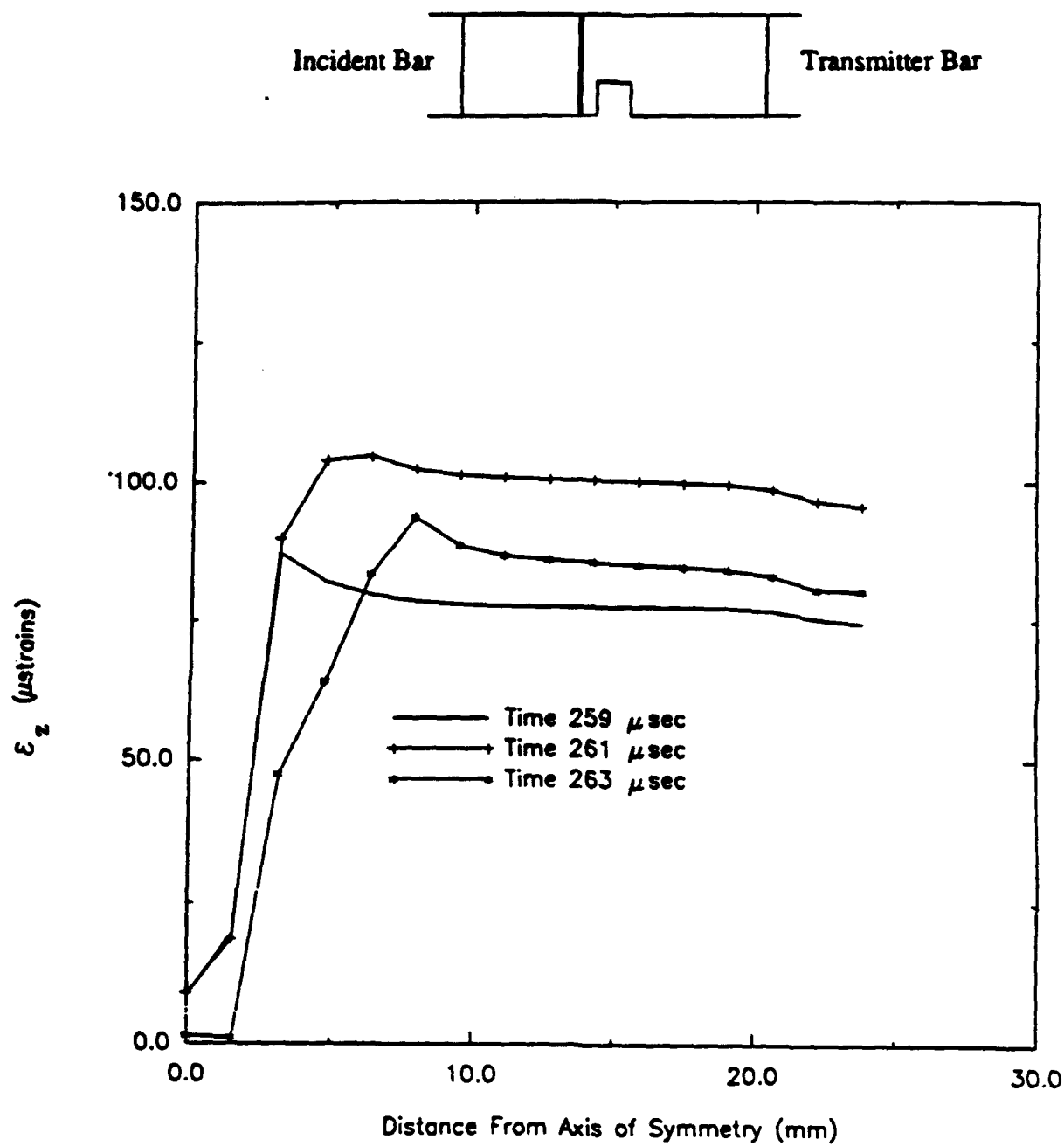


Figure 79. Profiles for longitudinal strain (square-notch, Load Case 3).

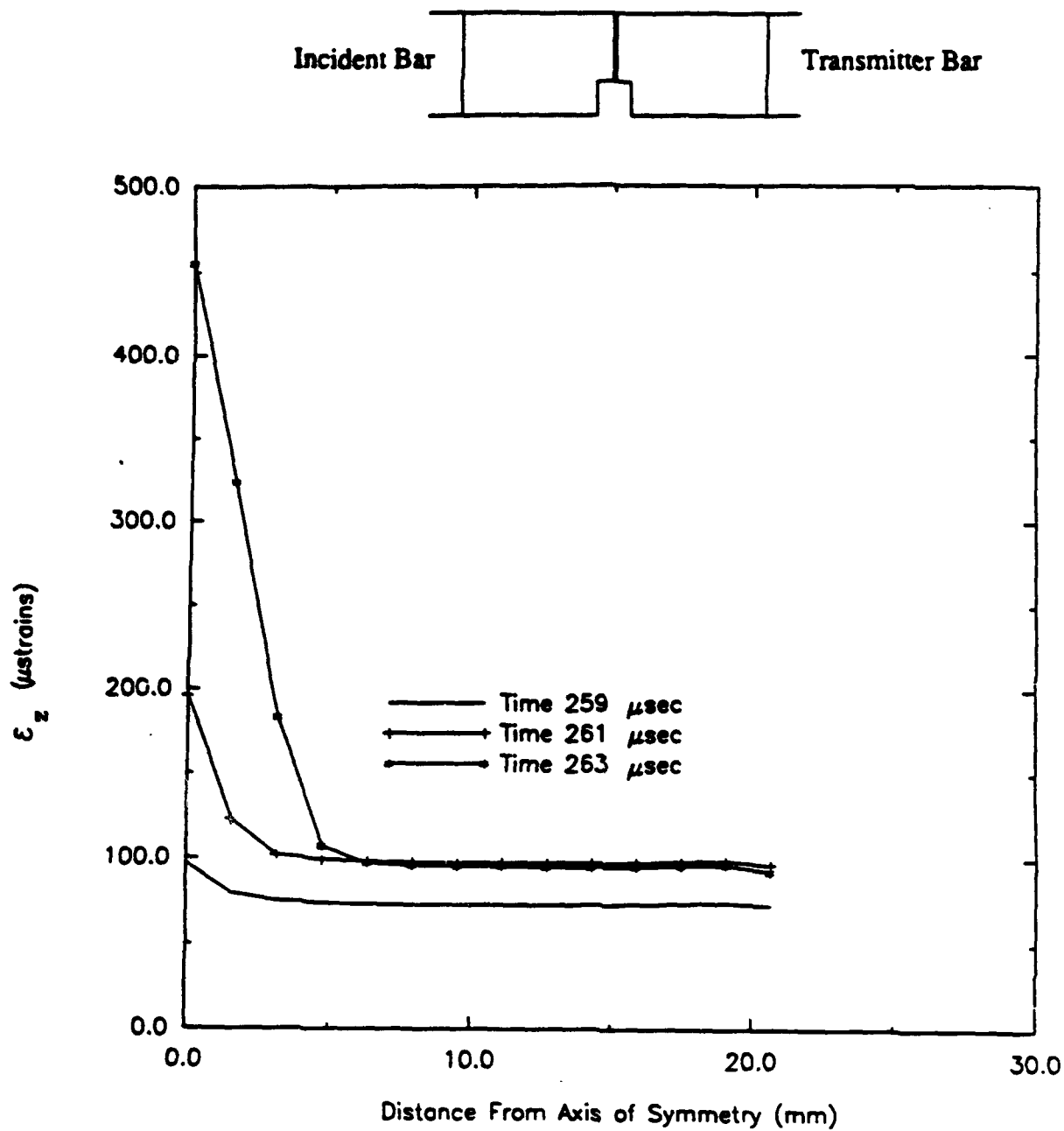


Figure 80. Profiles for longitudinal strain (square-notch, Load Case 3).

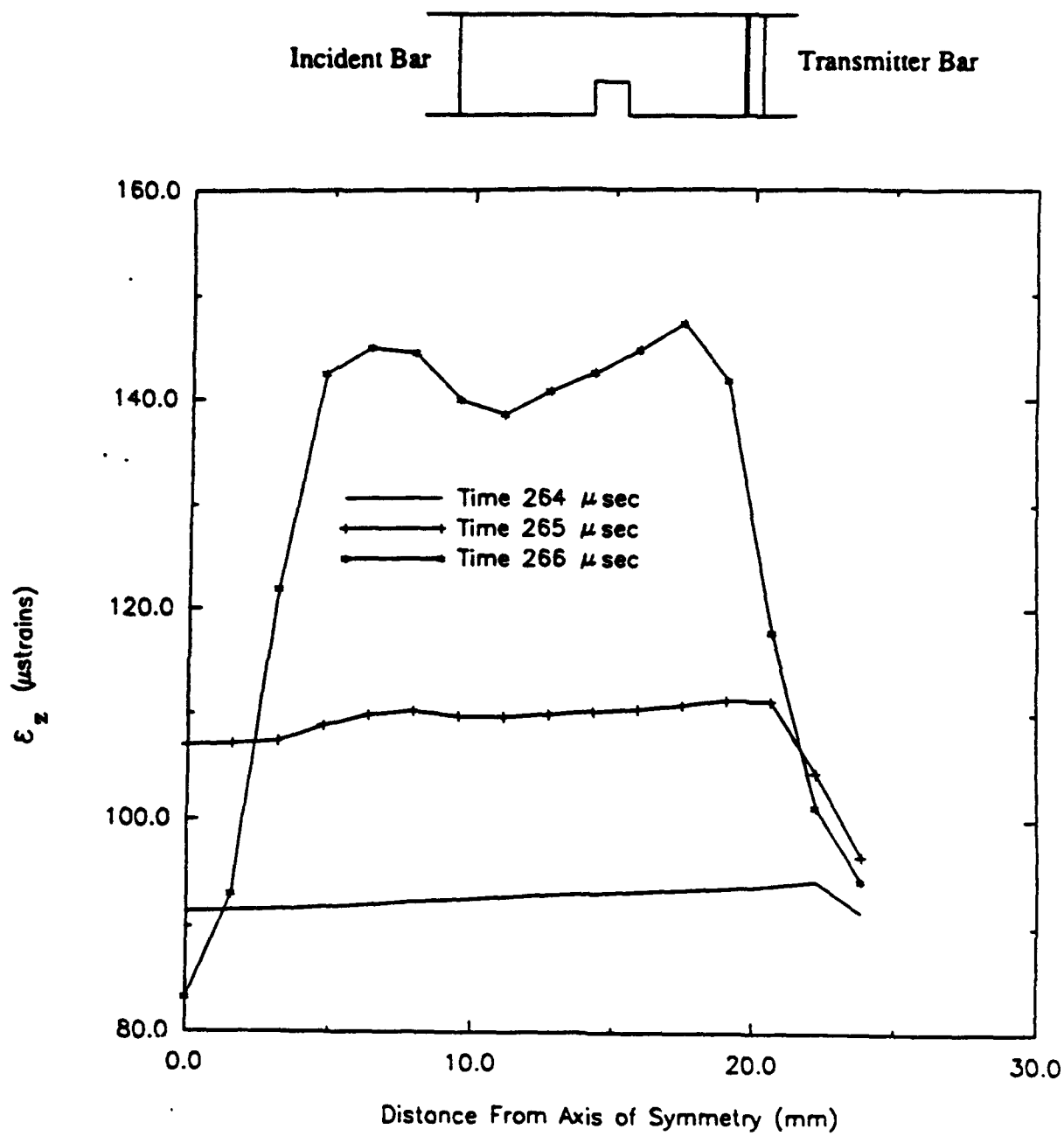
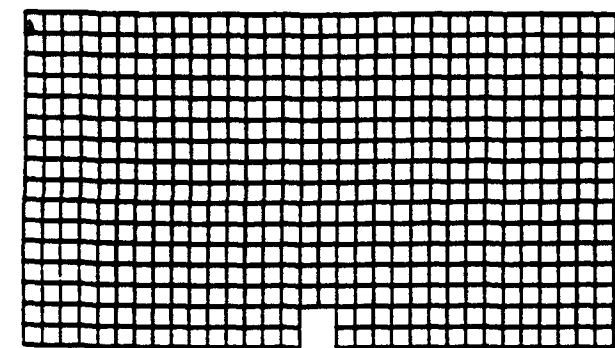
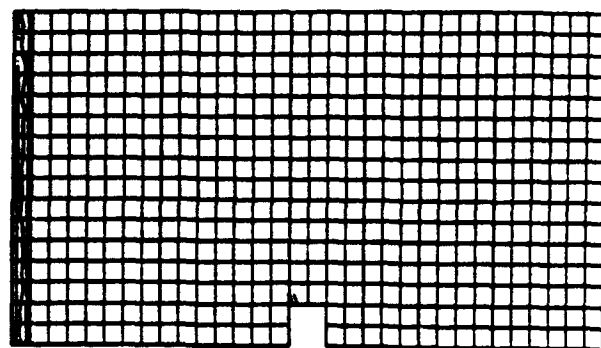


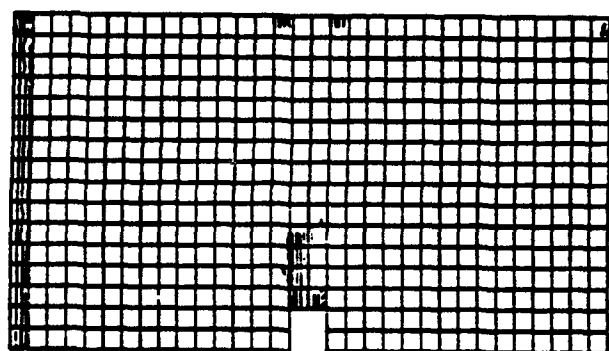
Figure 81. Profiles for longitudinal strain (square-notch, Load Case 3).



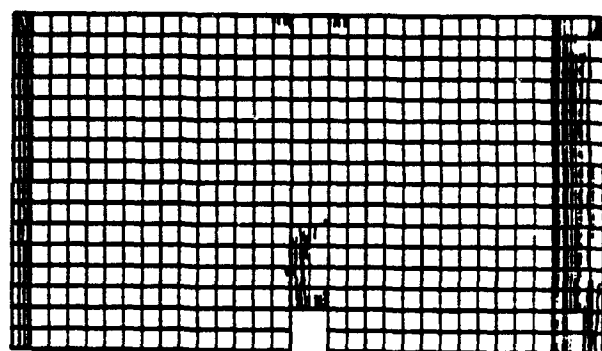
(a)



(b)



(c)



(d)

Figure 82. Cracking sequence for square-notch specimen; Load Case 3:
a) $t=255 \mu \text{ sec}$, b) $t=258 \mu \text{ sec}$, c) $t=264 \mu \text{ sec}$, d) $t=267 \mu \text{ sec}$.

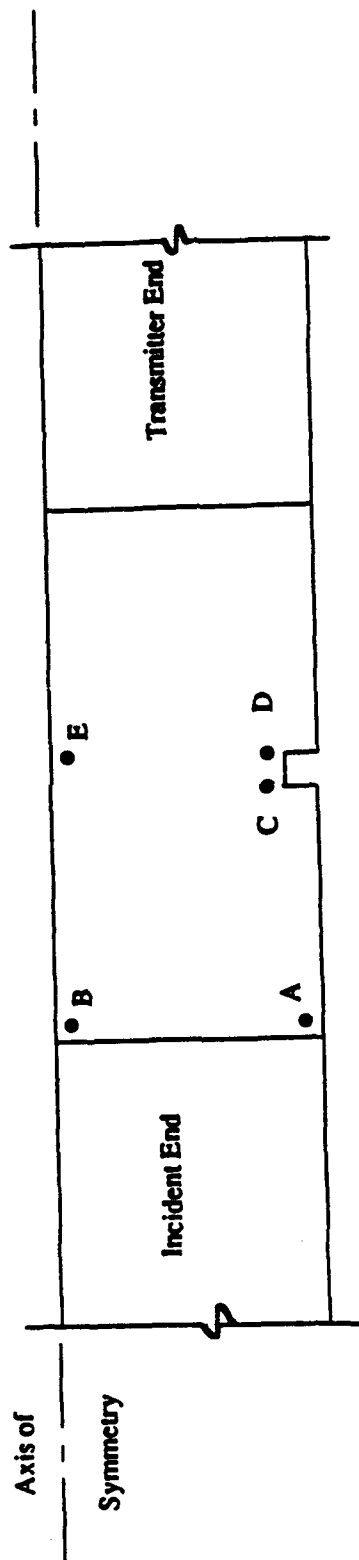


Figure 83. Definition sketch for square-notch specimen.

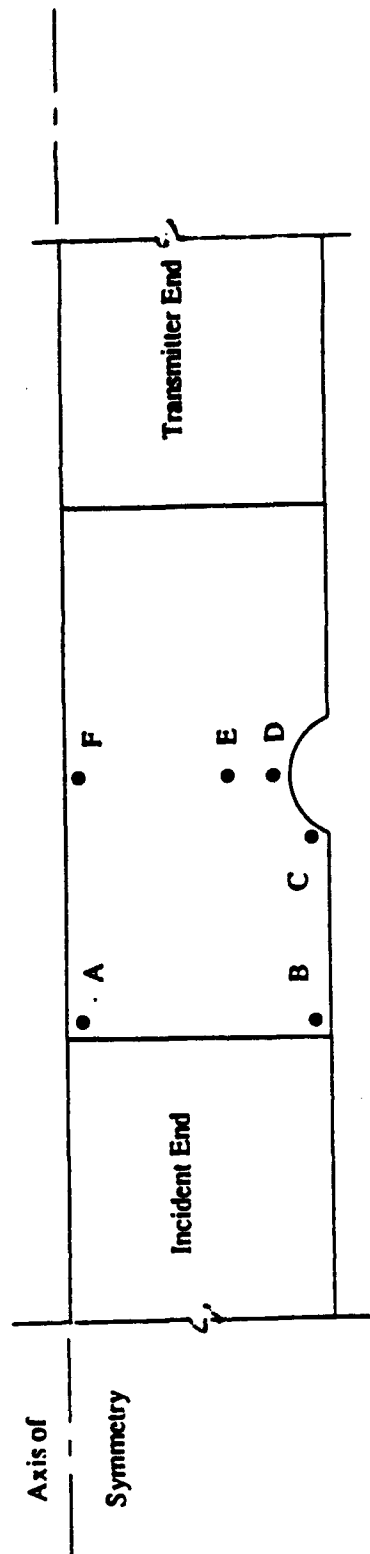


Figure 84. Definition sketch for saddle-notch specimen.

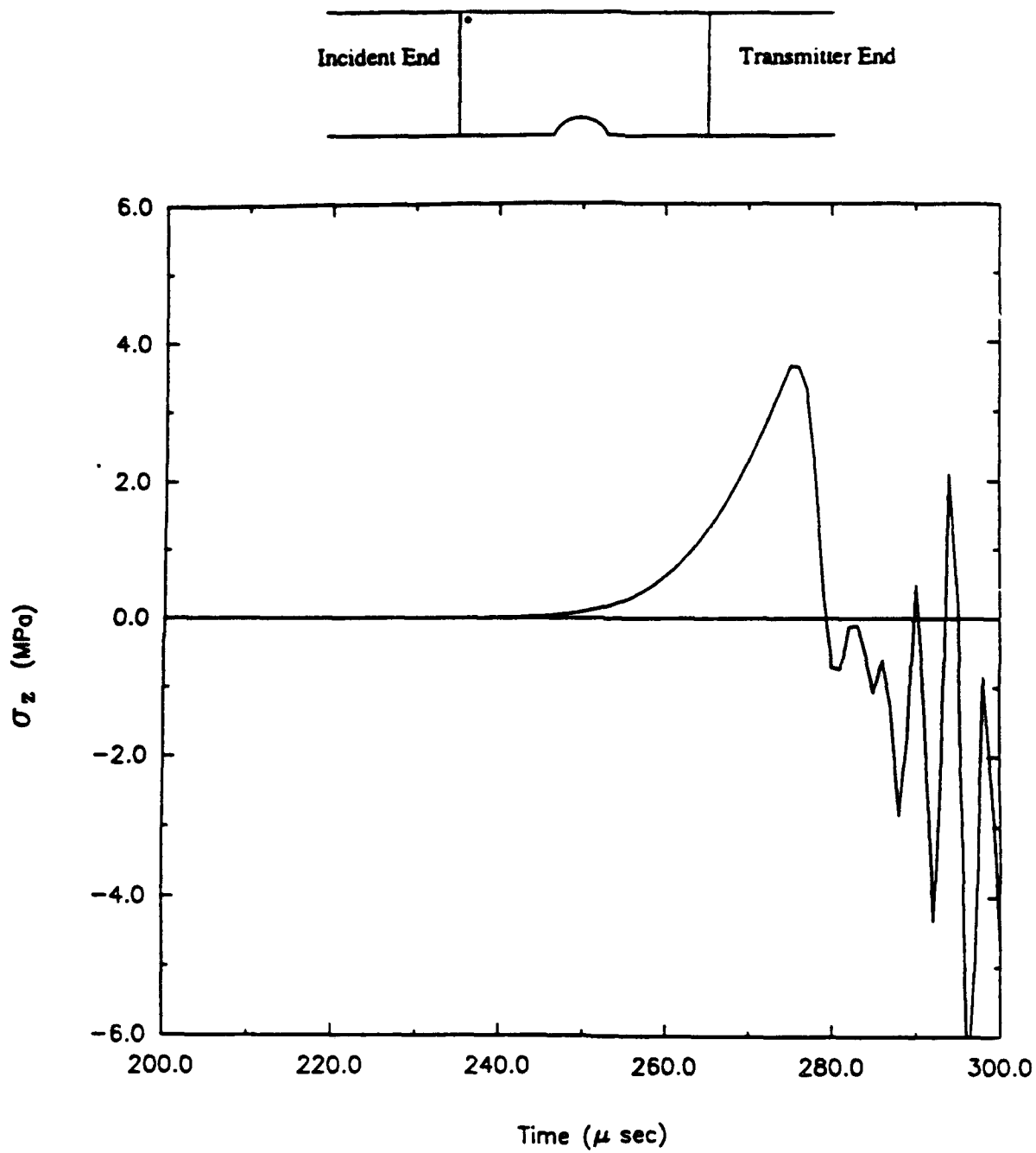


Figure 85. Time history for longitudinal stress (saddle-notch, Load Case 1).

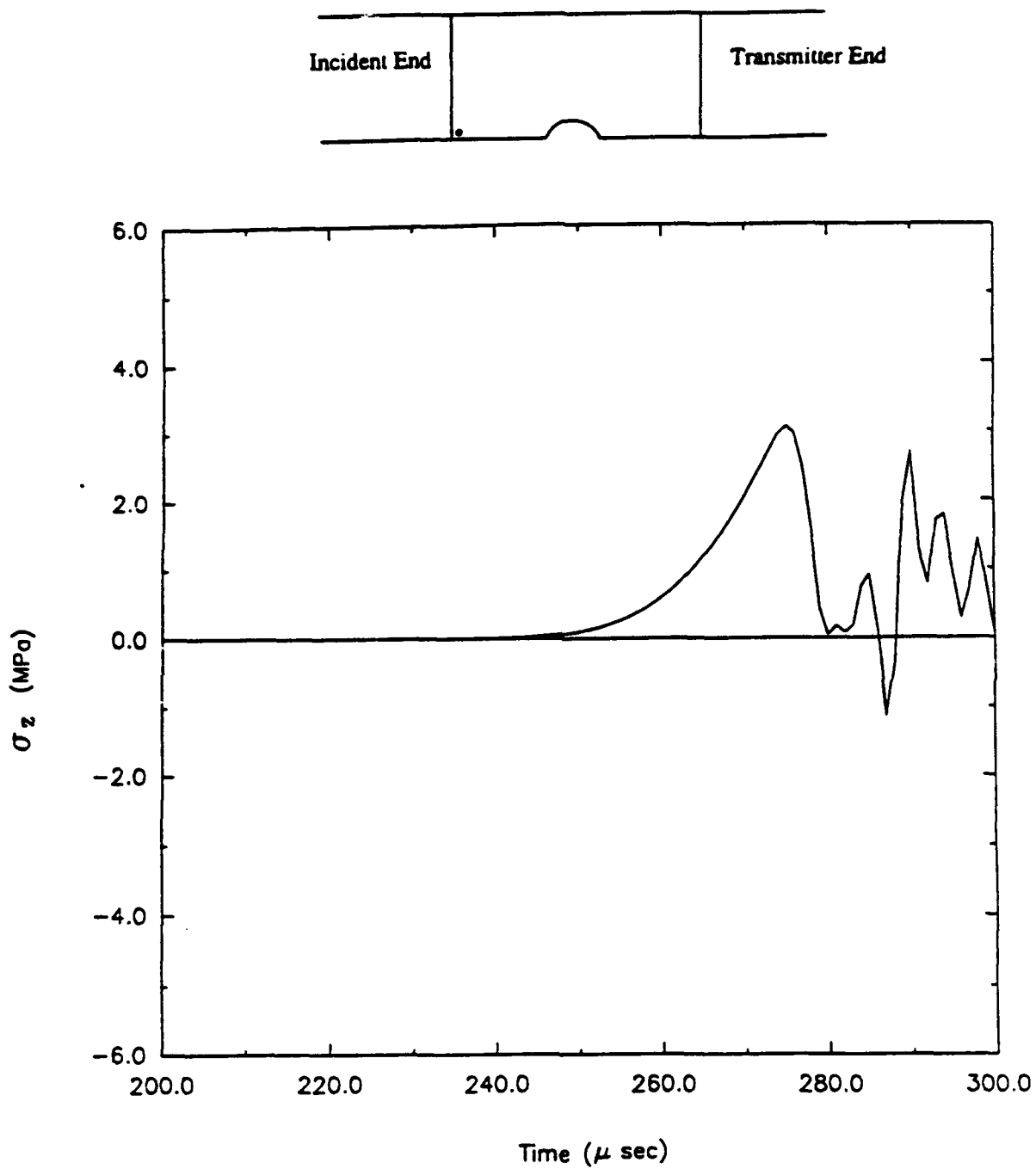


Figure 86. Time history for longitudinal stress (saddle-notch, Load Case 1).

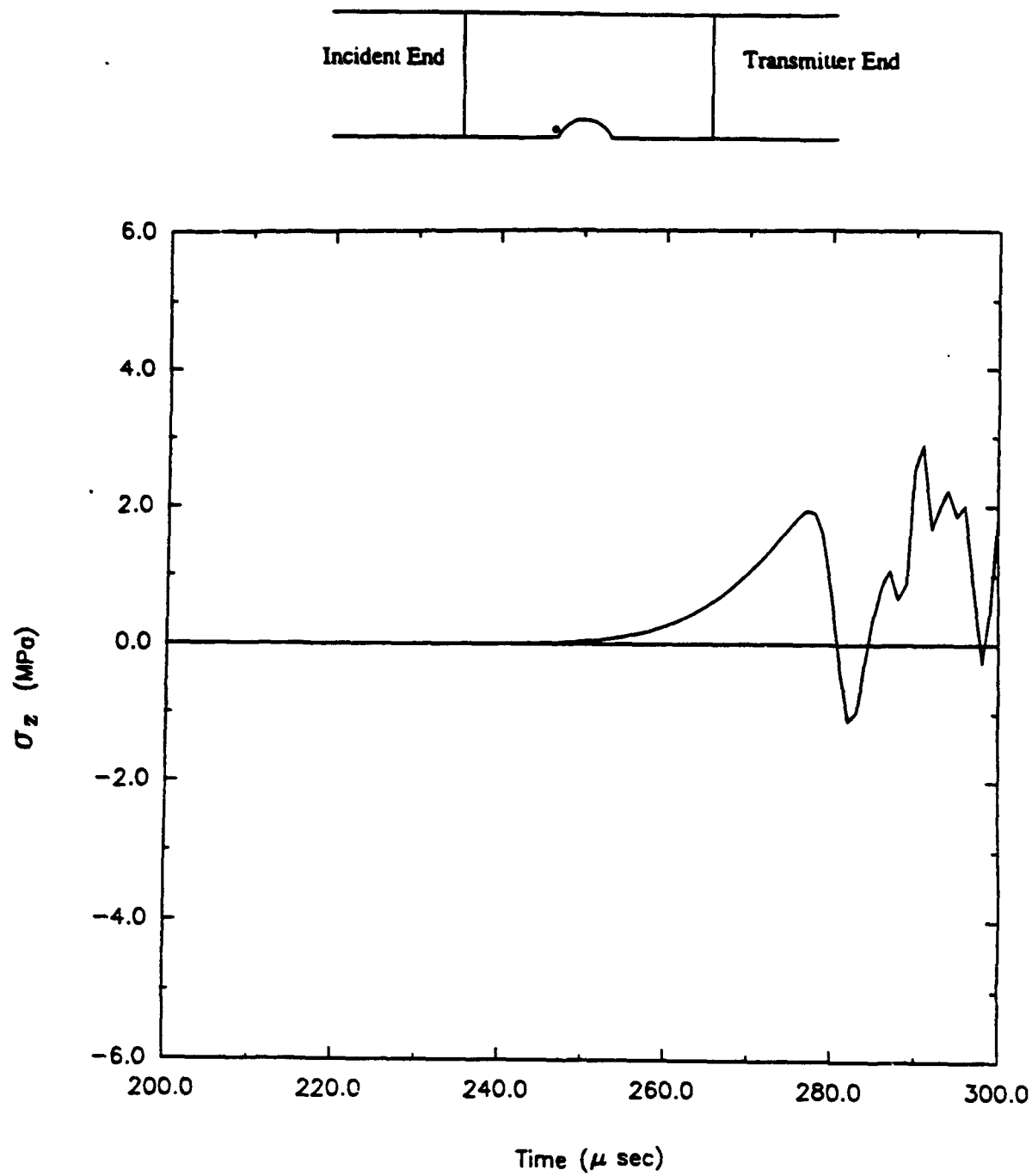


Figure 87. Time history for longitudinal stress (saddle-notch, Load Case 1).

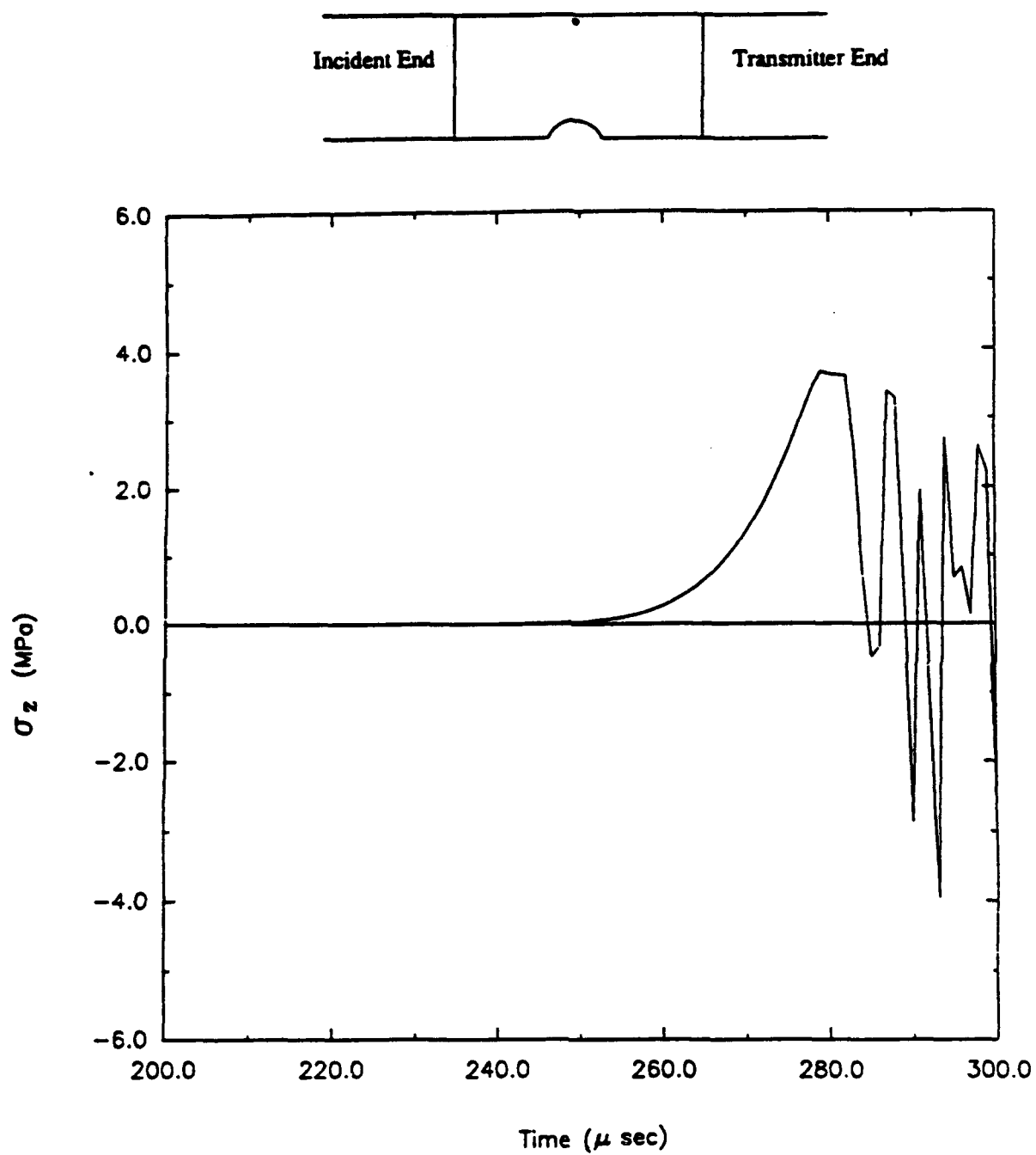


Figure 88. Time history for longitudinal stress (saddle-notch, Load Case 1).

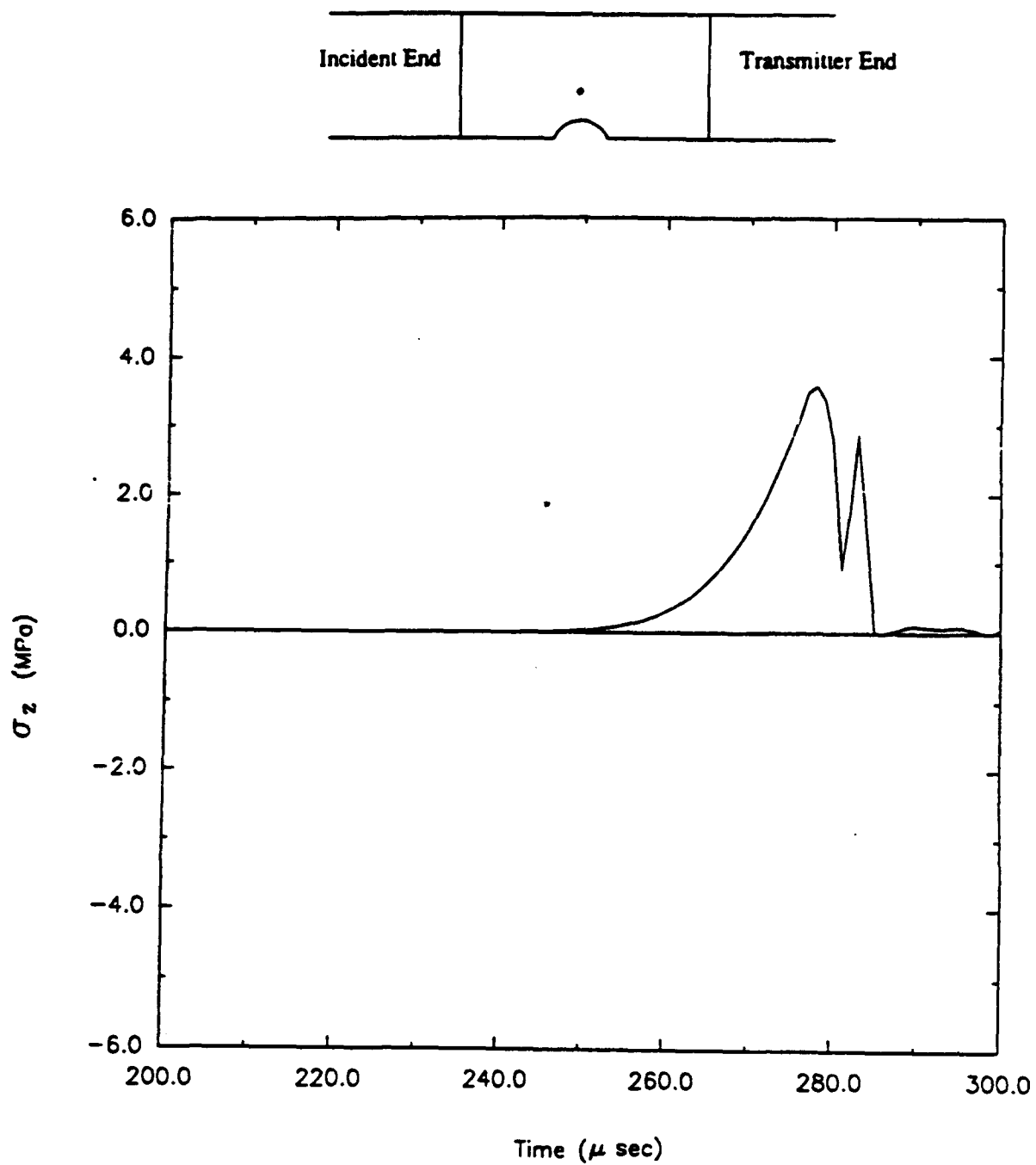


Figure 89. Time history for longitudinal stress (saddle-notch, Load Case 1).

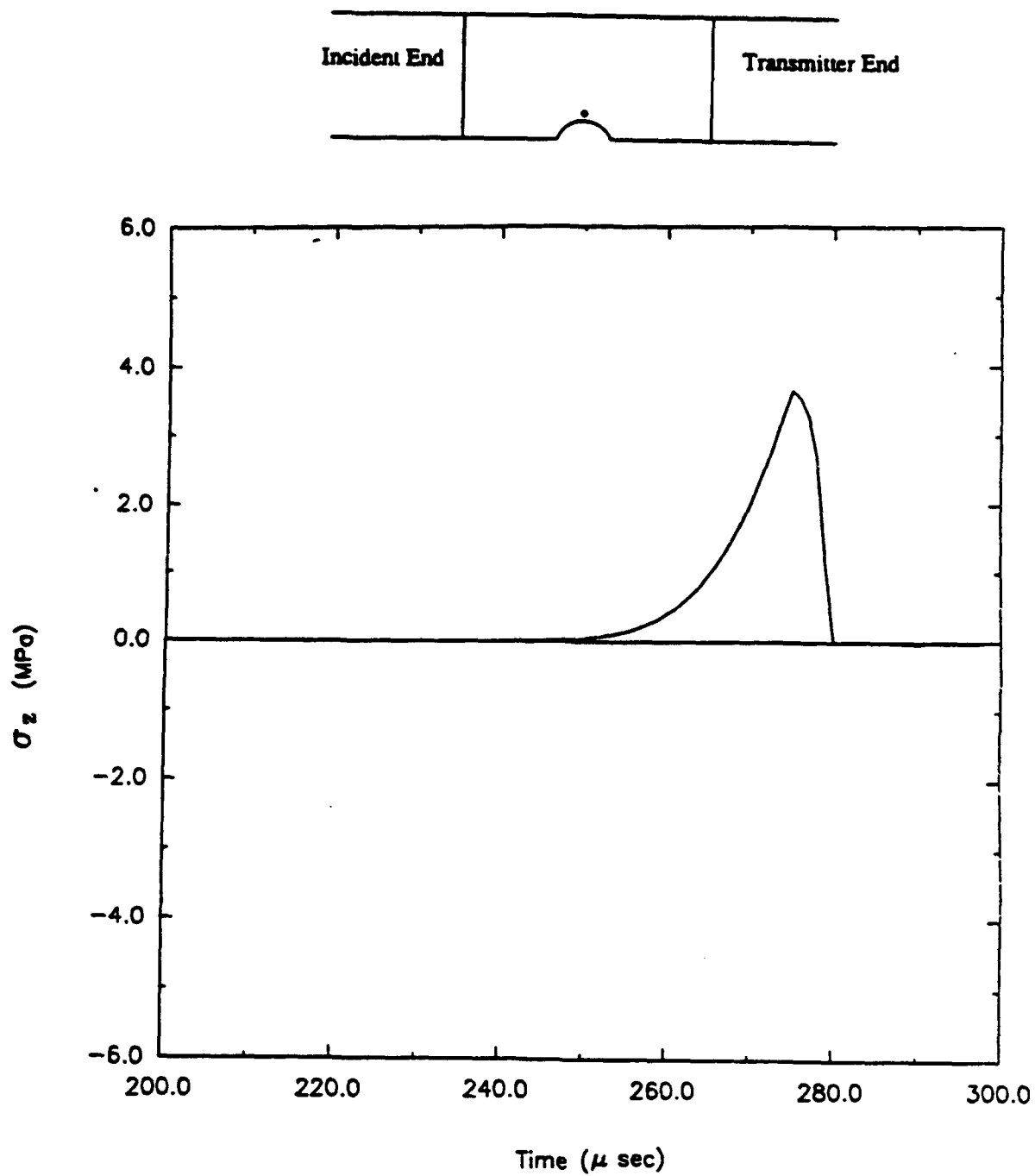


Figure 90. Time history for longitudinal stress (saddle-notch, Load Case 1).

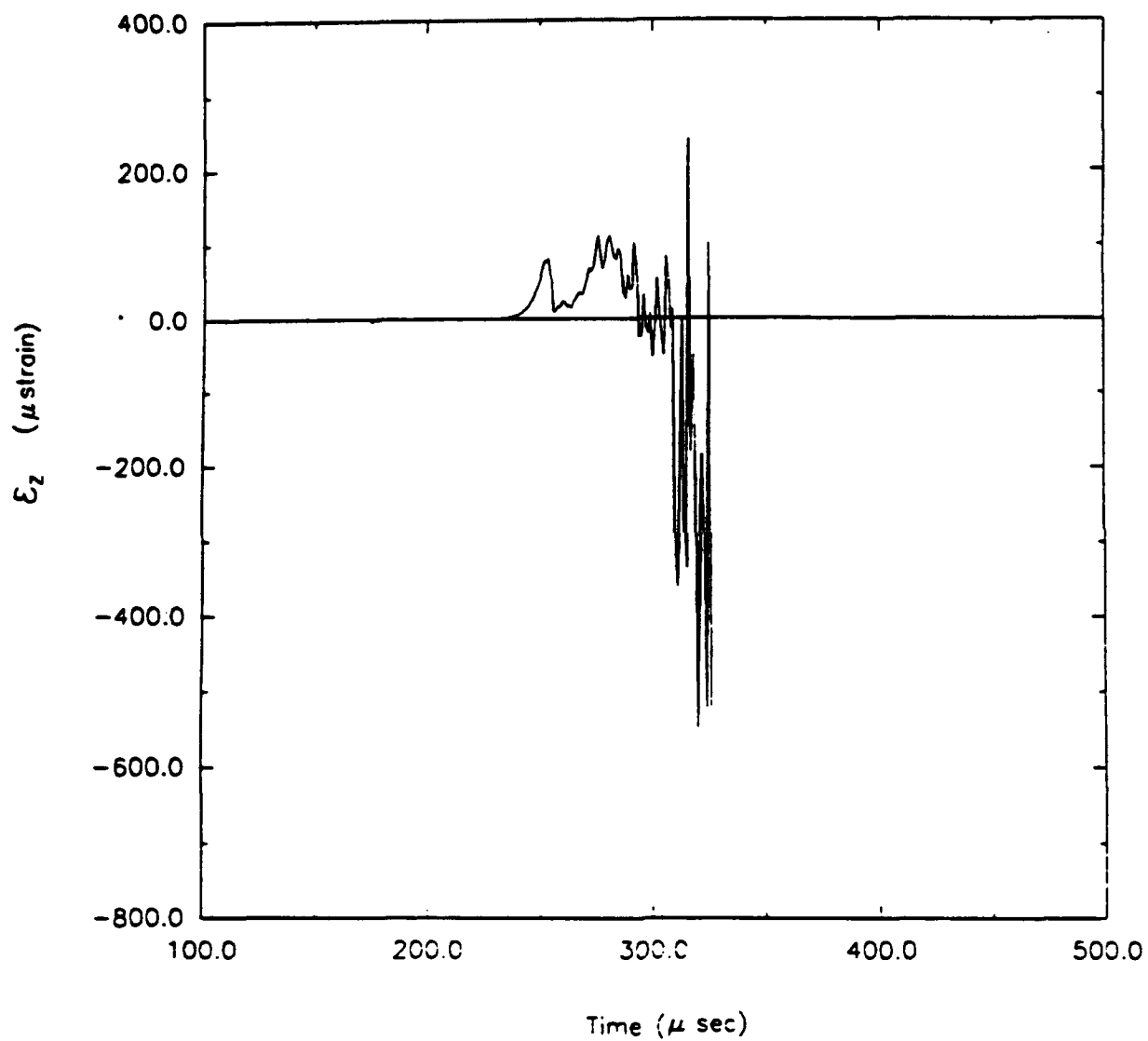
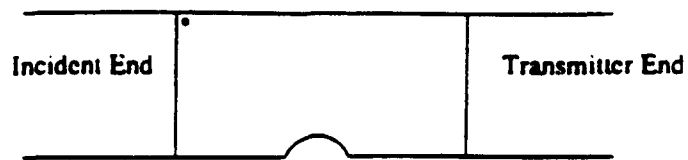


Figure 91. Time history for longitudinal strain (saddle-notch, Load Case 1).

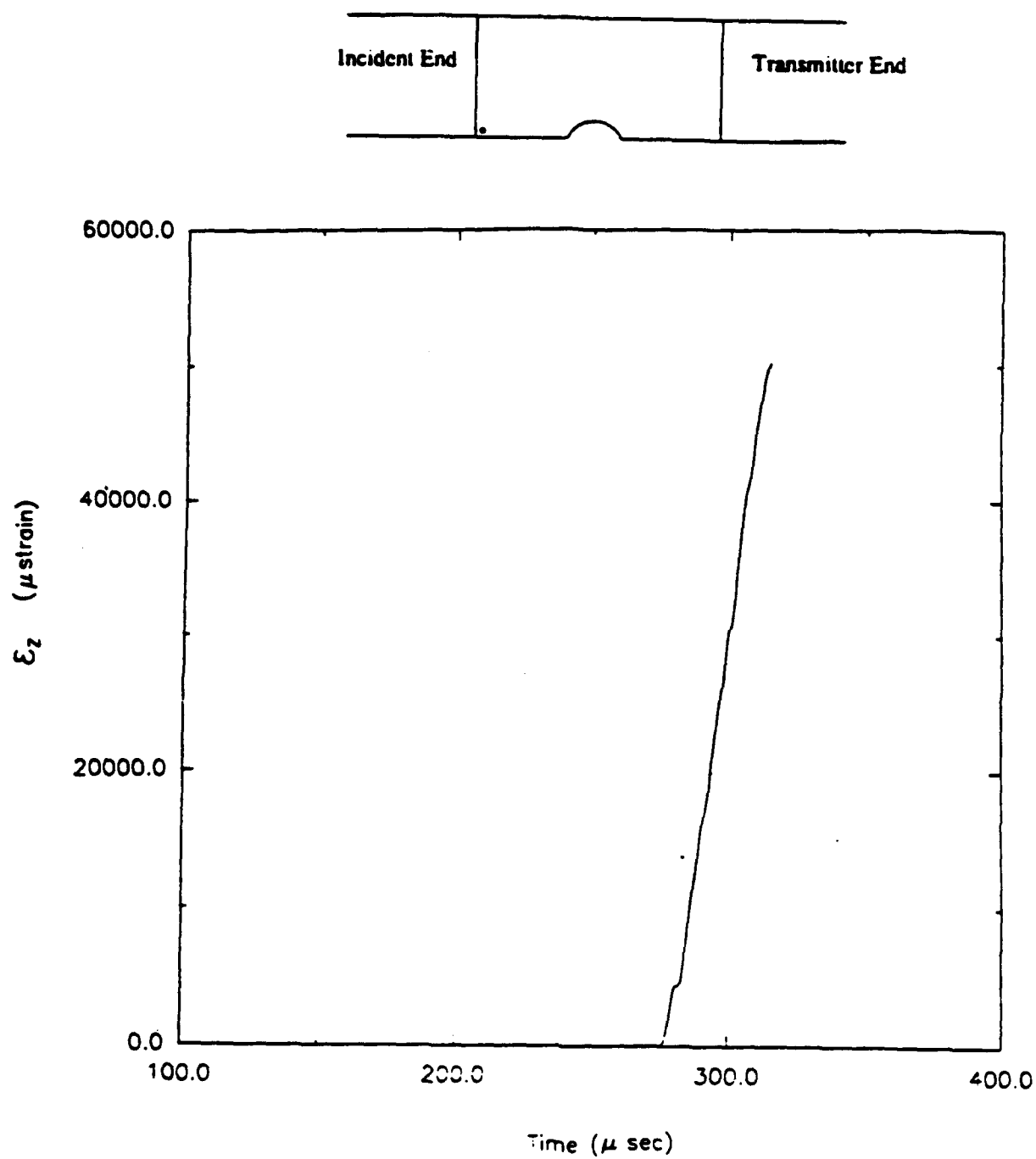


Figure 92. Time history for longitudinal strain (saddle-notch, Load Case 1).

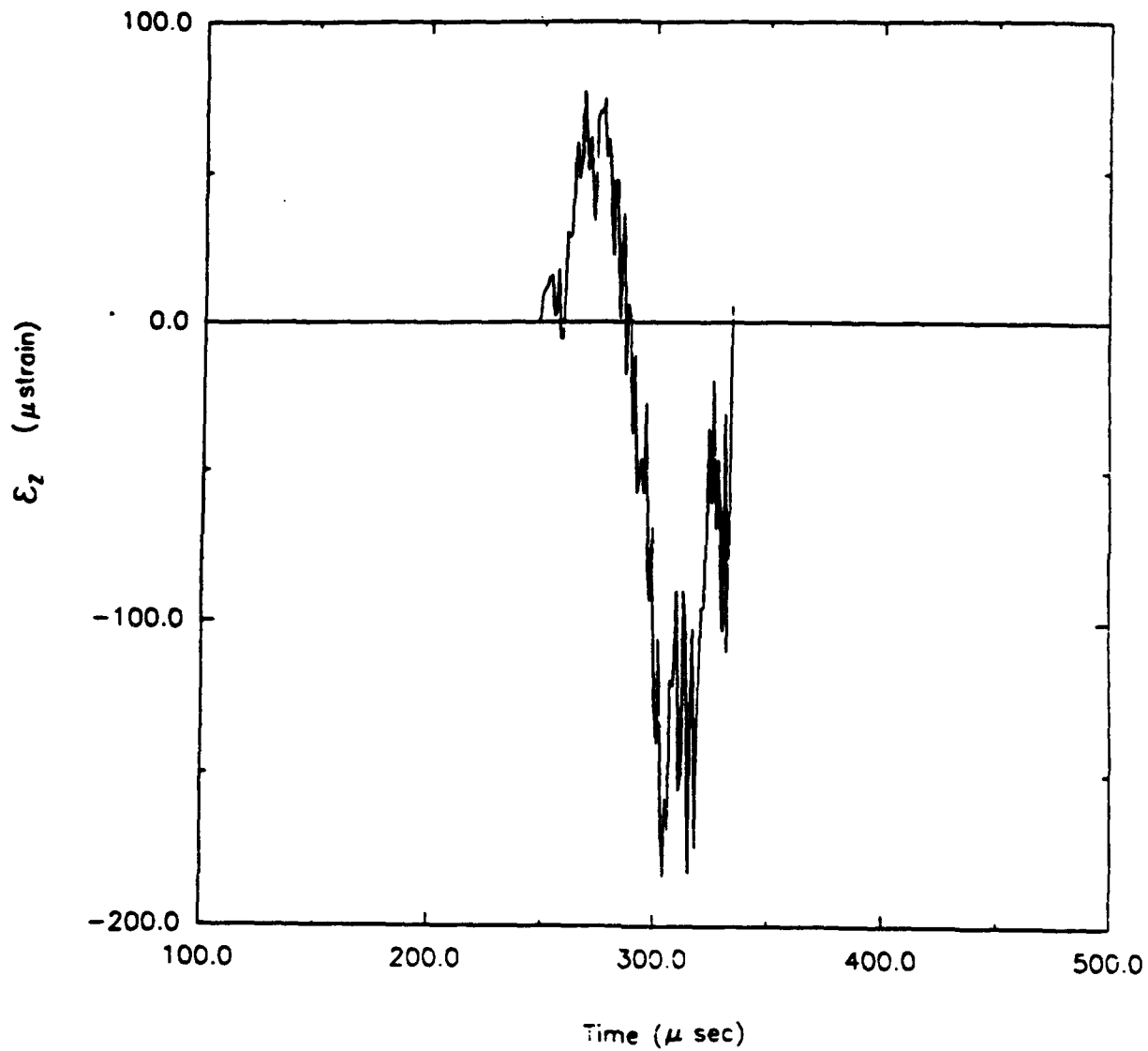
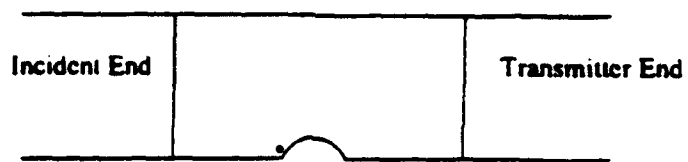


Figure 93. Time history for longitudinal strain (saddle-notch, Load Case 1).

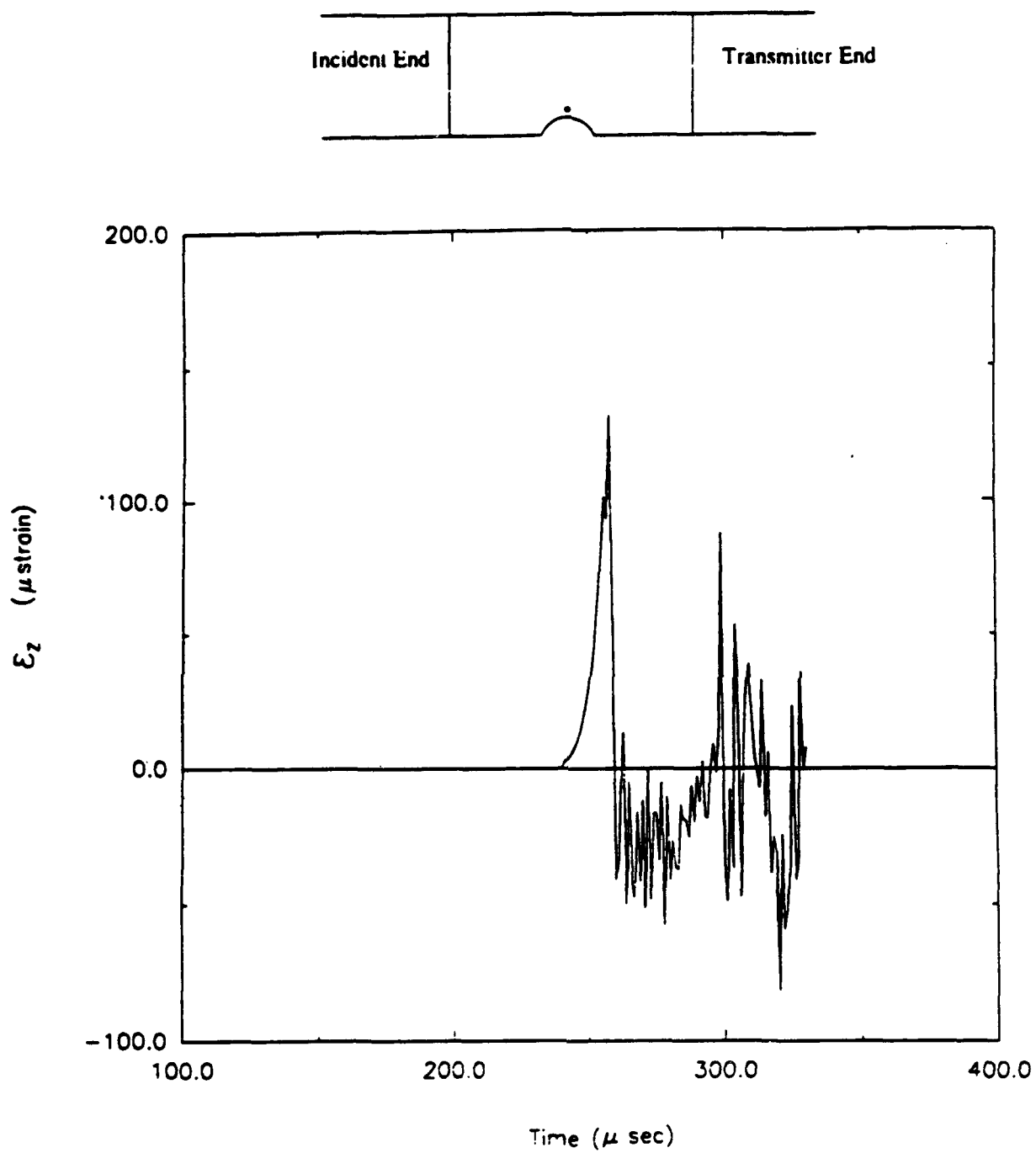


Figure 94. Time history for longitudinal strain (saddle-notch, Load Case 1).

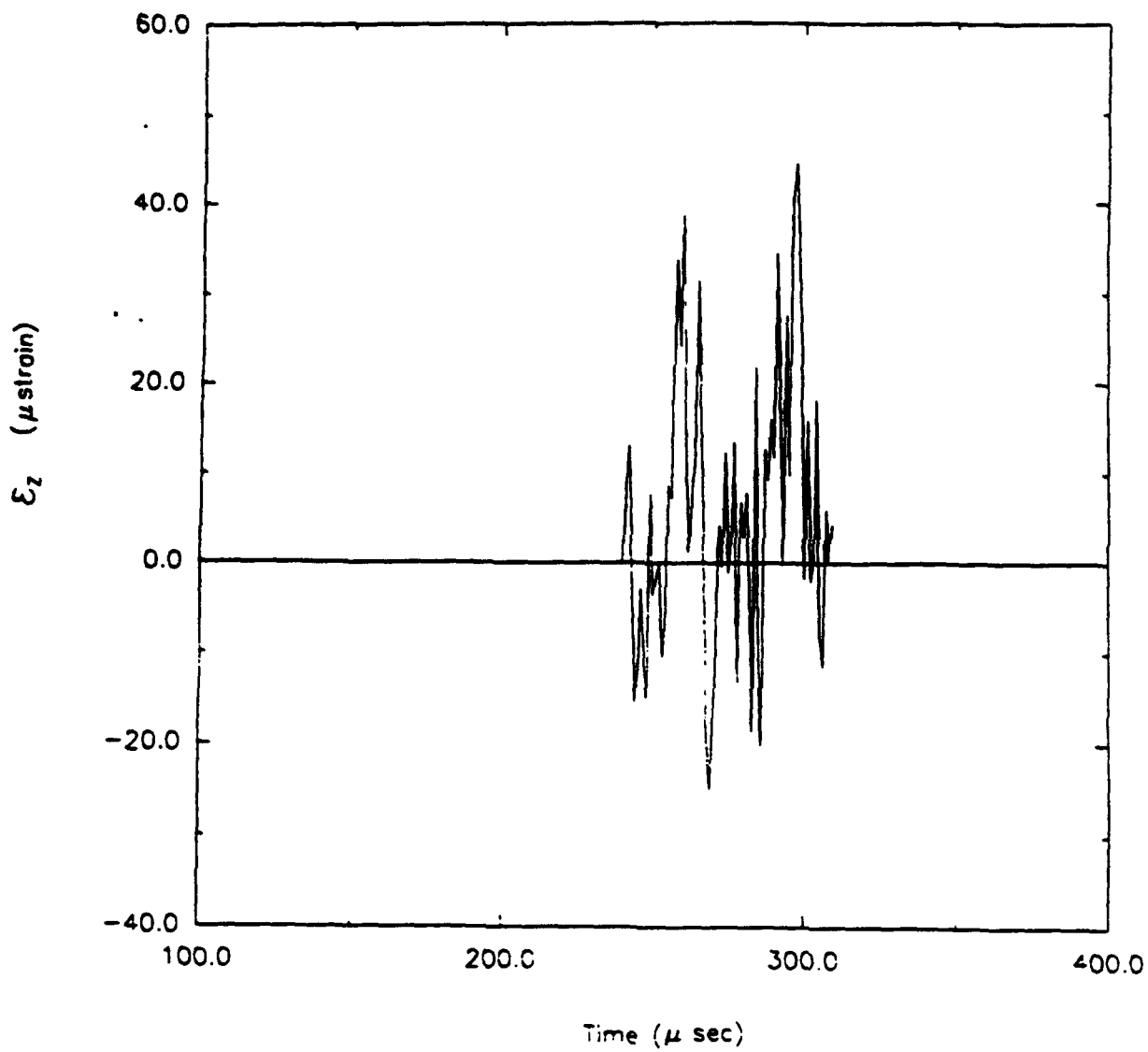
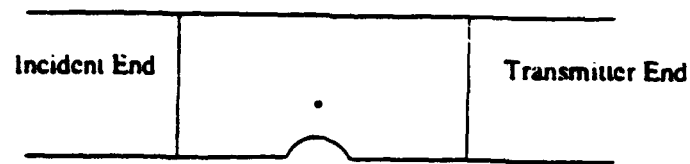


Figure 95. Time history for longitudinal strain (saddle-notch, Load Case 1).

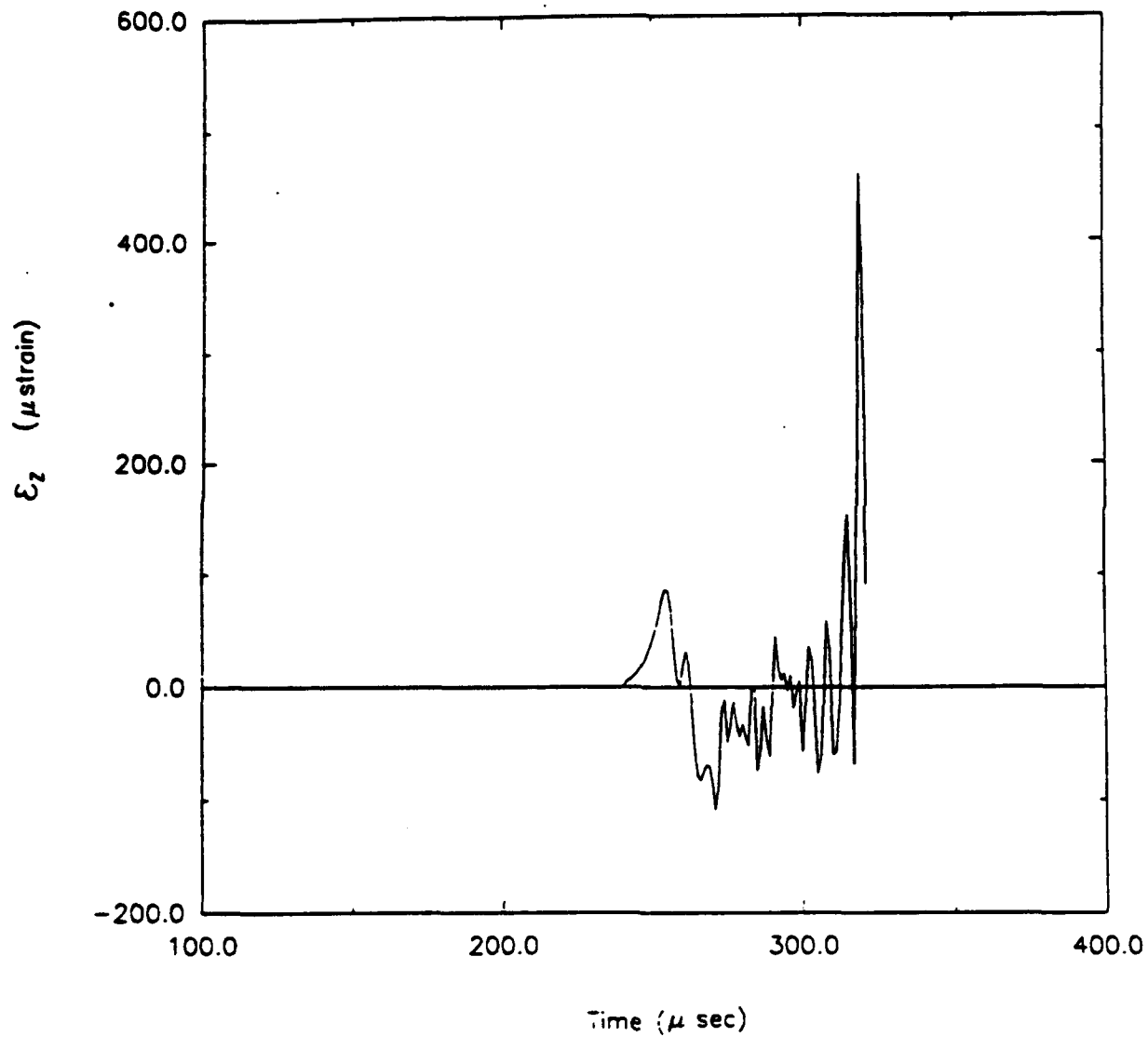
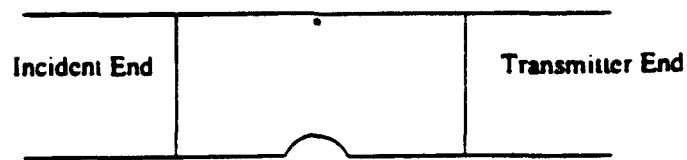


Figure 96. Time history for longitudinal strain (saddle-notch, Load Case 1).

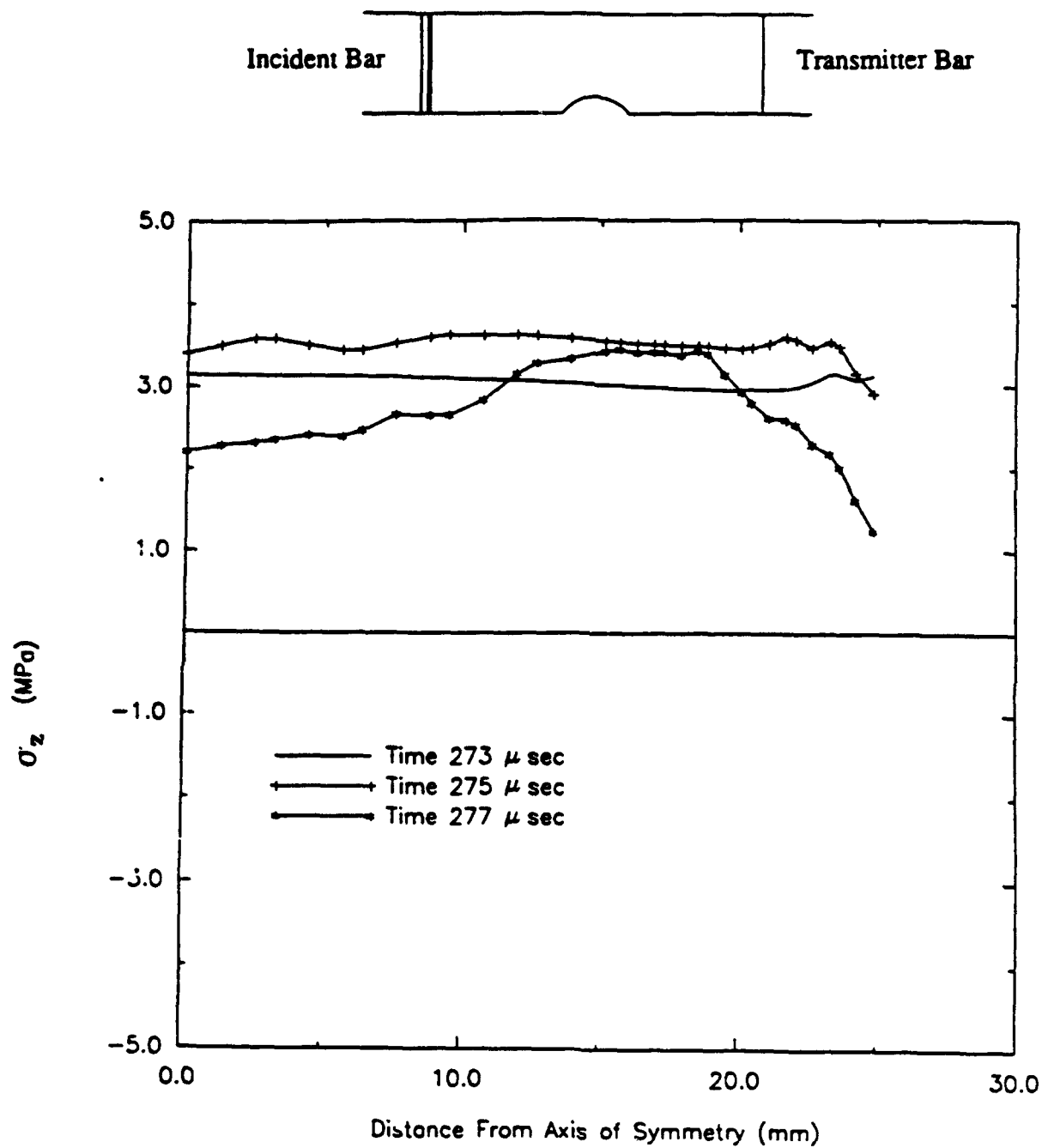


Figure 97. Profiles for longitudinal stress (saddle-notch, Load Case 1).

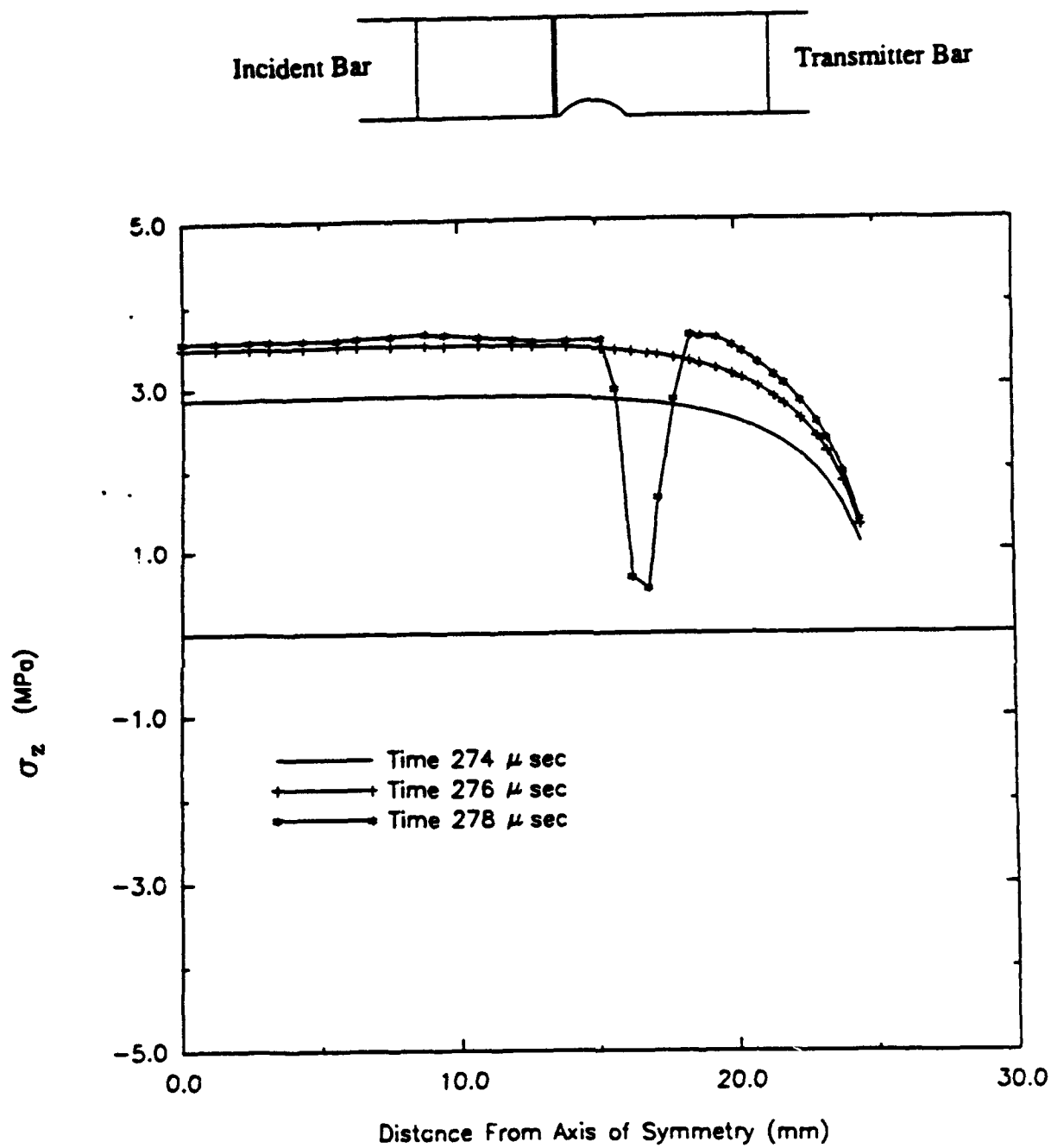


Figure 98. Profiles for longitudinal stress (saddle-notch, Load Case 1).

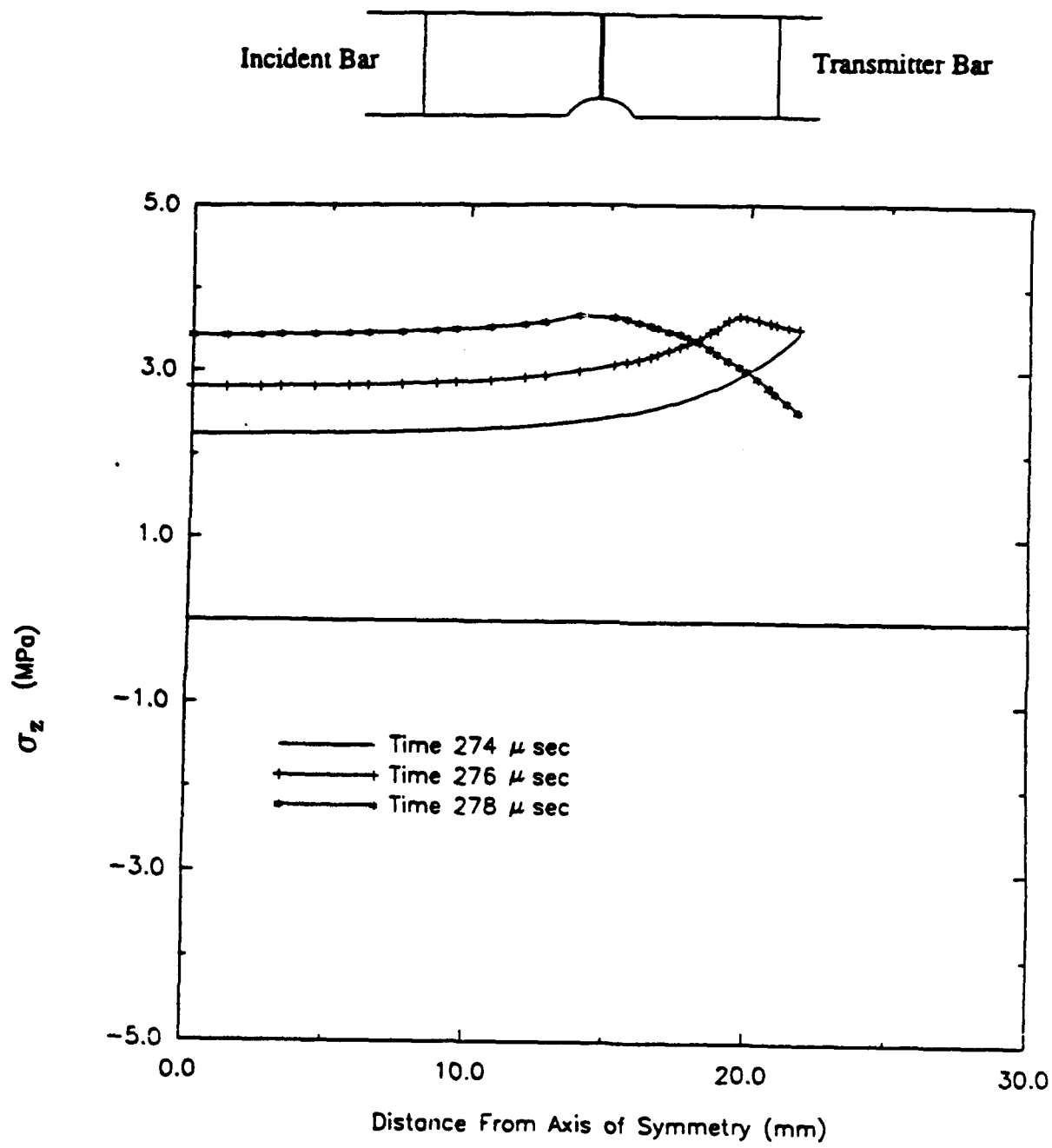


Figure 99. Profiles for longitudinal stress (saddle-notch, Load Case 1).

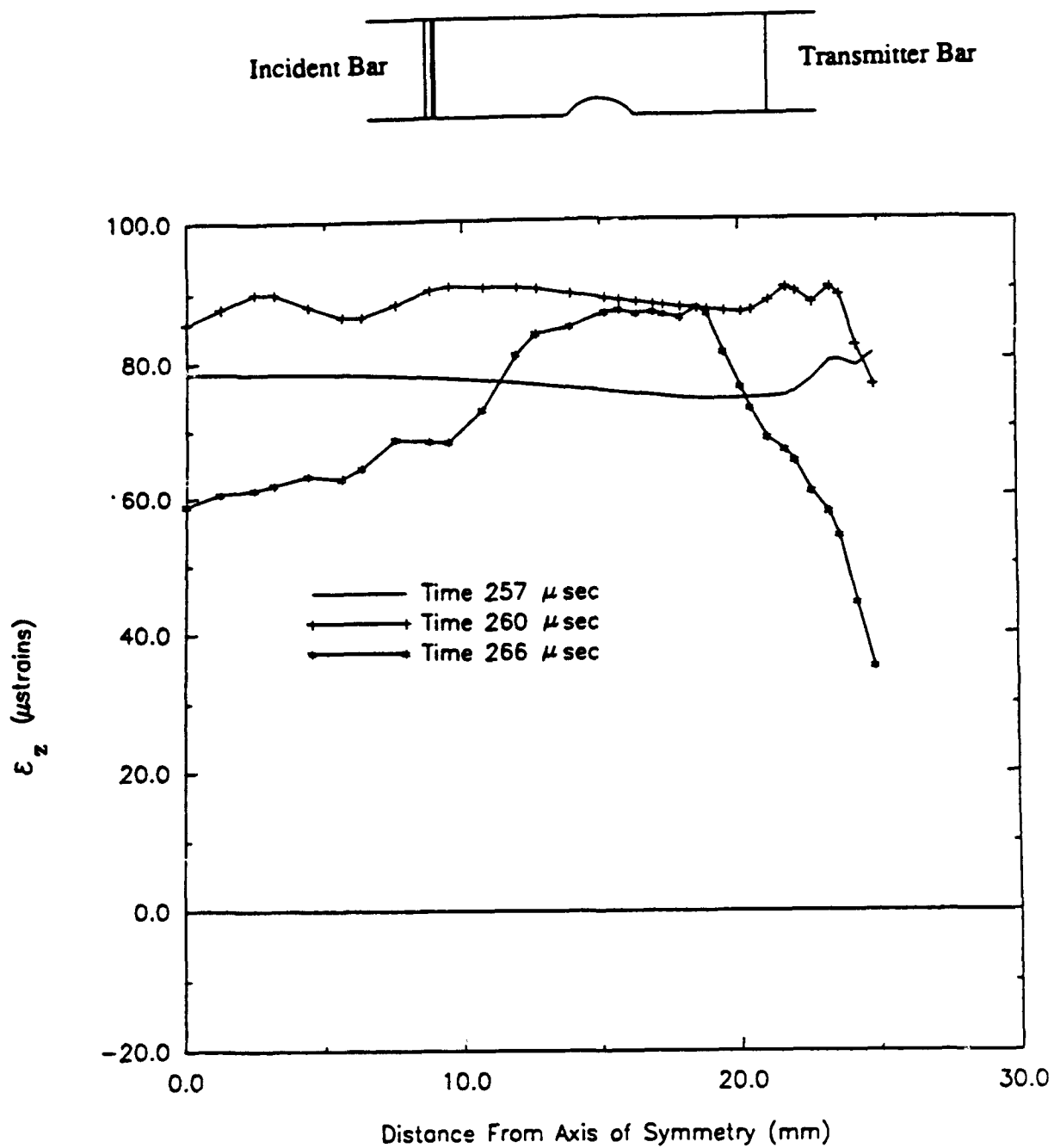


Figure 100. Profiles for longitudinal strain (saddle-notch, Load Case 1).

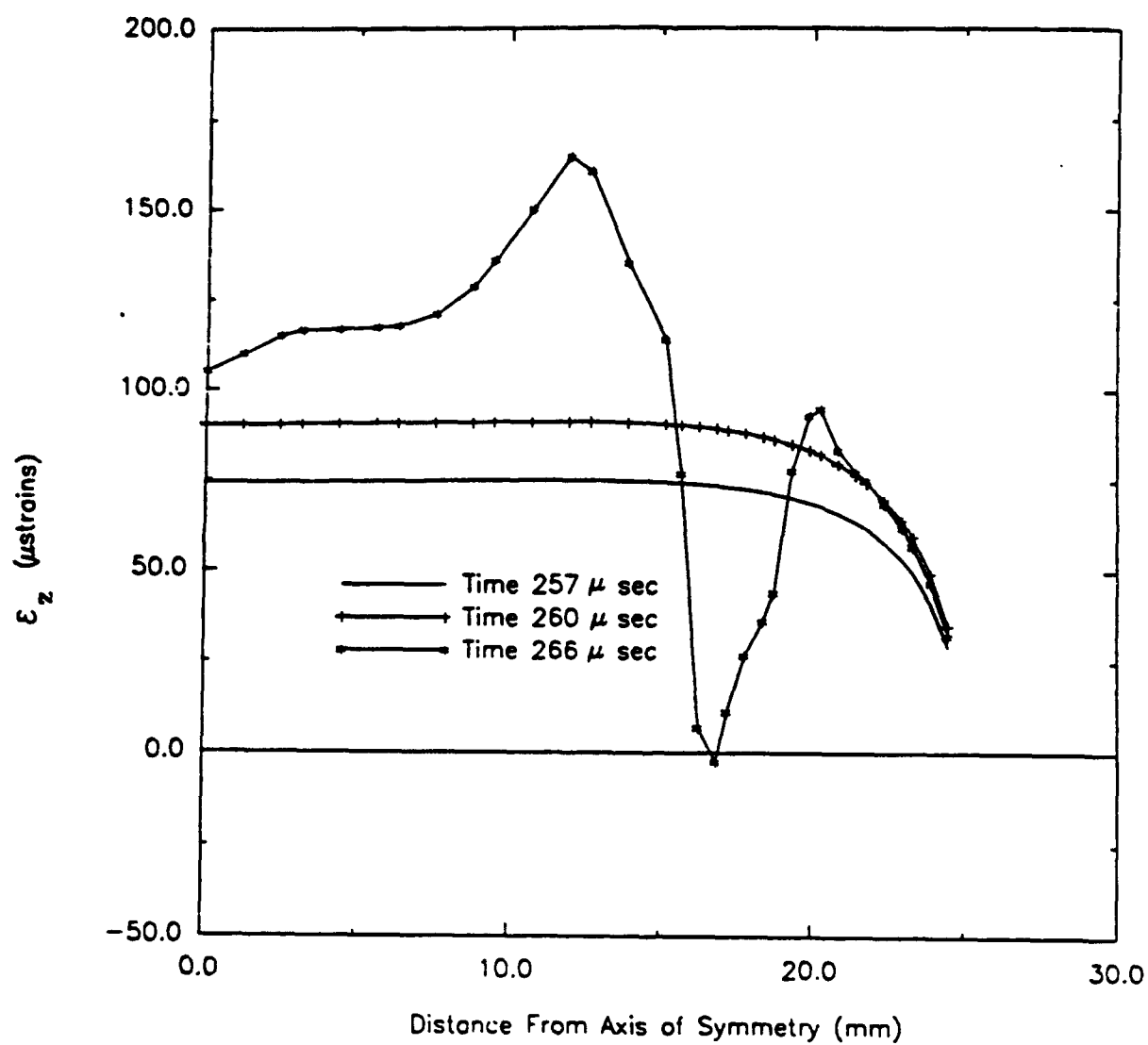
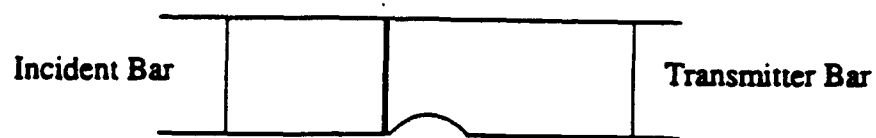


Figure 101. Profiles for longitudinal strain (saddle-notch, Load Case 1).

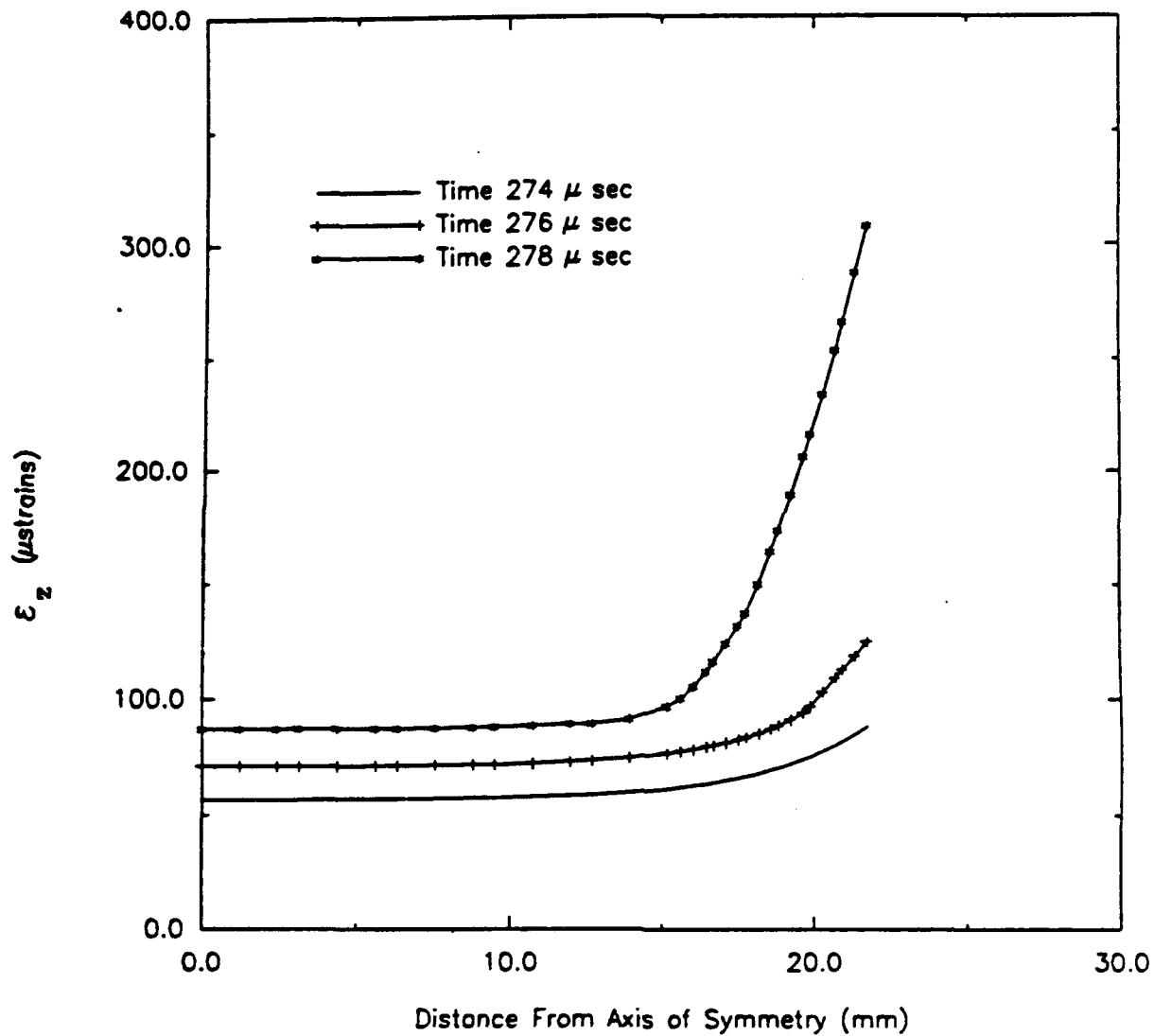
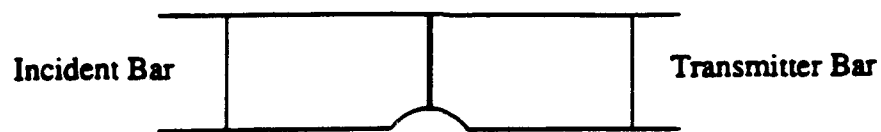
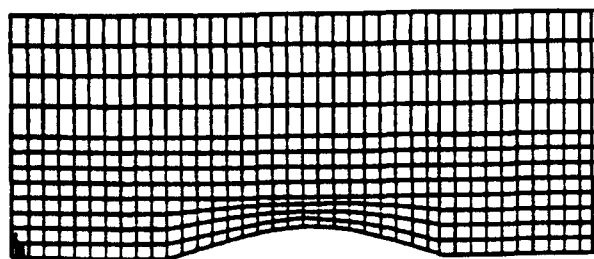
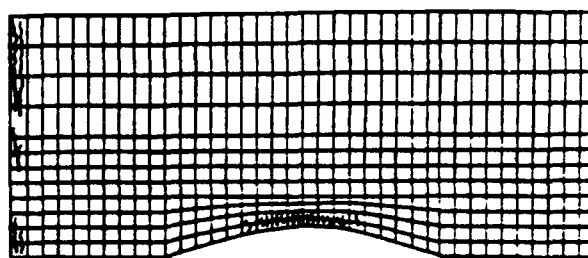


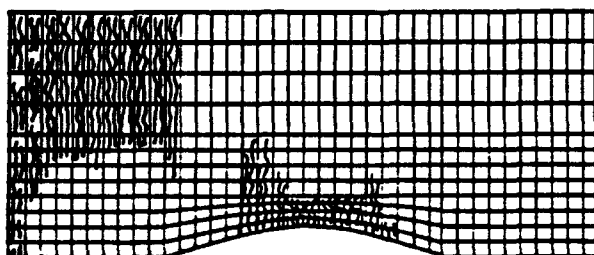
Figure 102. Profiles for longitudinal strain (saddle-notch, Load Case 1).



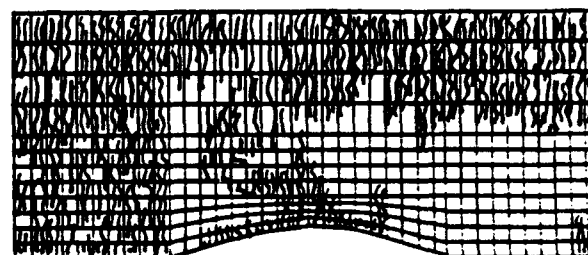
(a)



(b)



(c)



(d)

Figure 103. Cracking sequence for saddle-notch specimen; Load Case 1:
a) $t=274 \mu \text{ sec}$, b) $t=275 \mu \text{ sec}$, c) $t=277 \mu \text{ sec}$, d) $t=326 \mu \text{ sec}$.

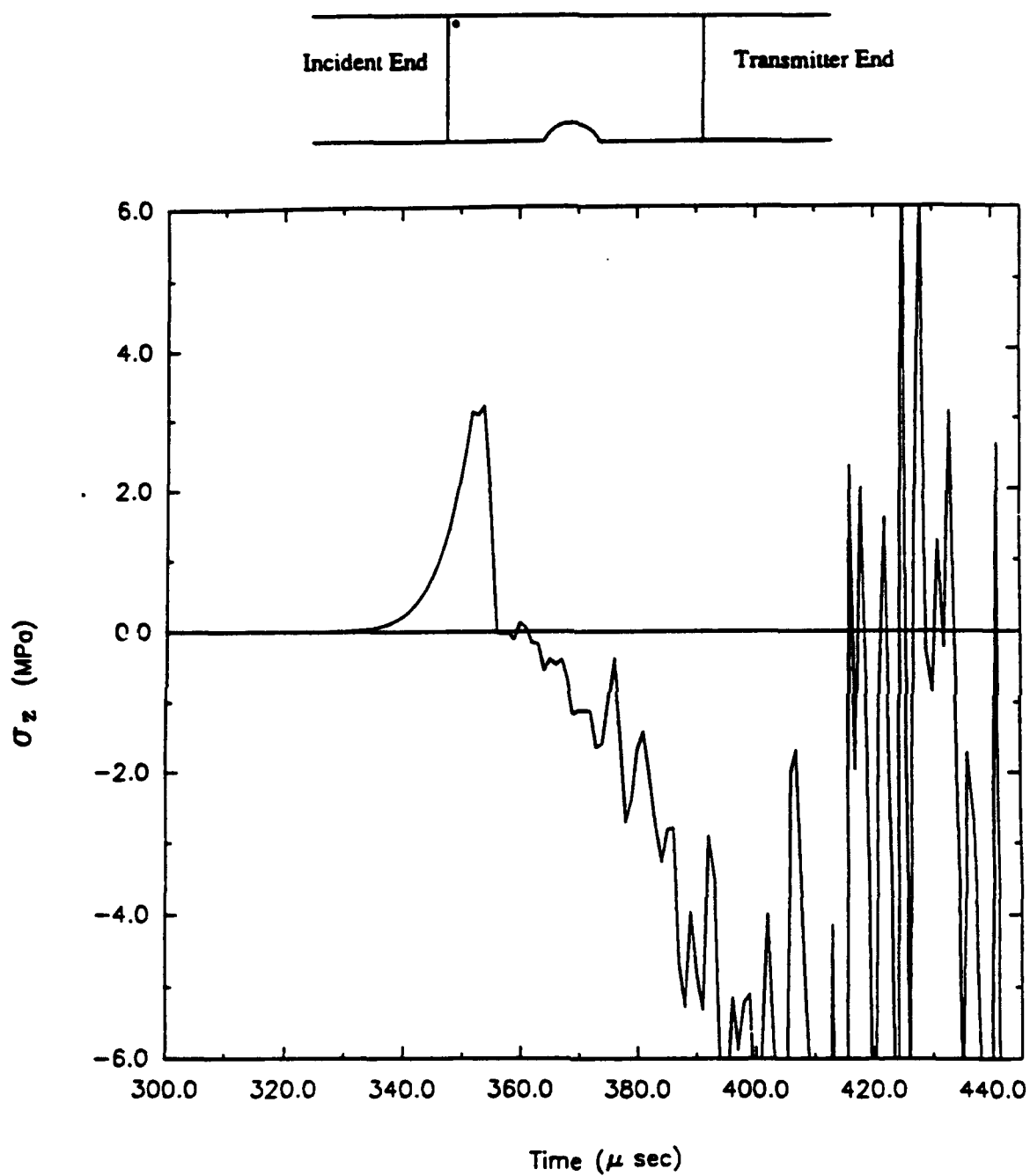


Figure 104. Time history for longitudinal stress (saddle-notch, Load Case 2).

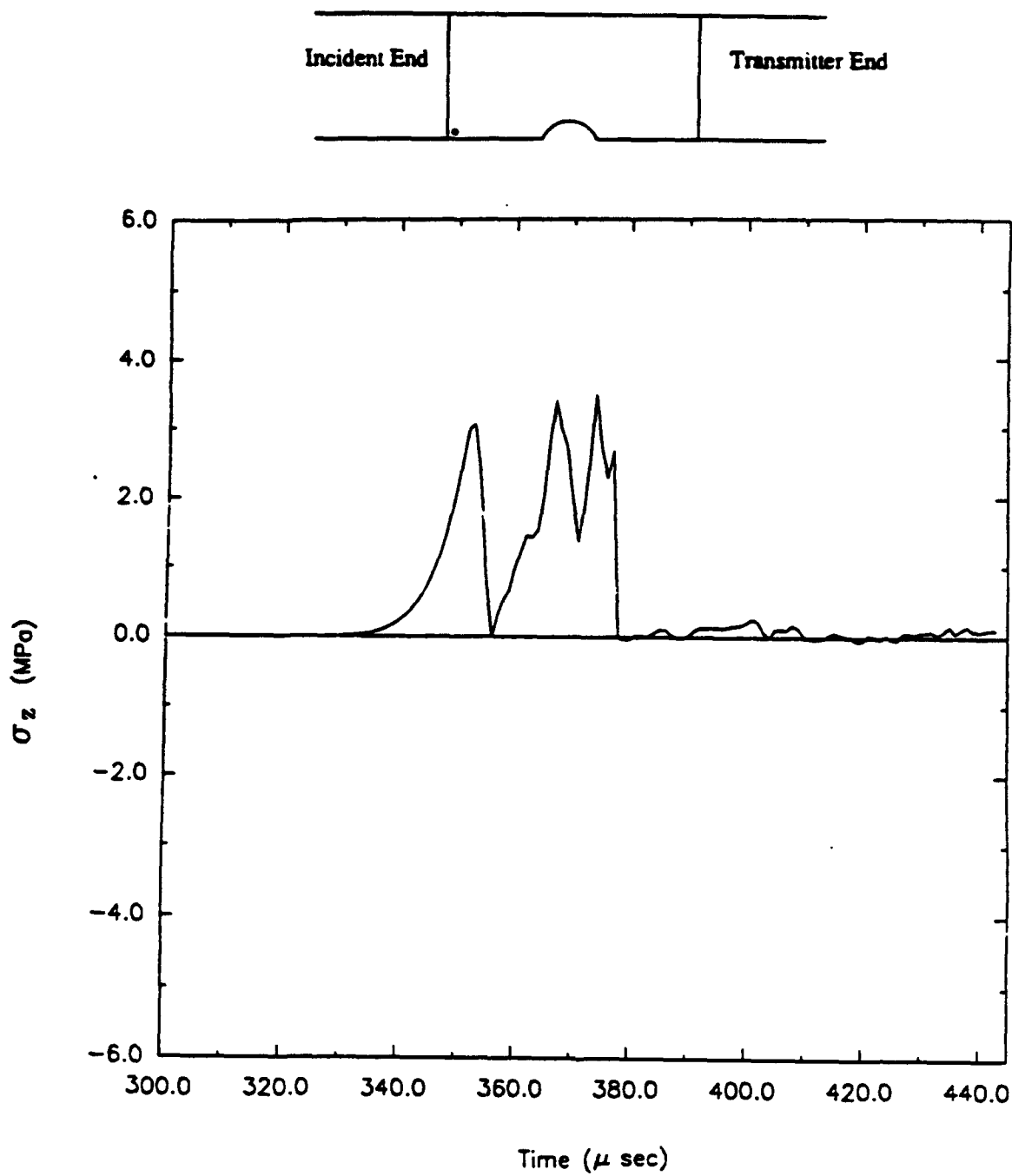


Figure 105. Time history for longitudinal stress (saddle-notch, Load Case 2).

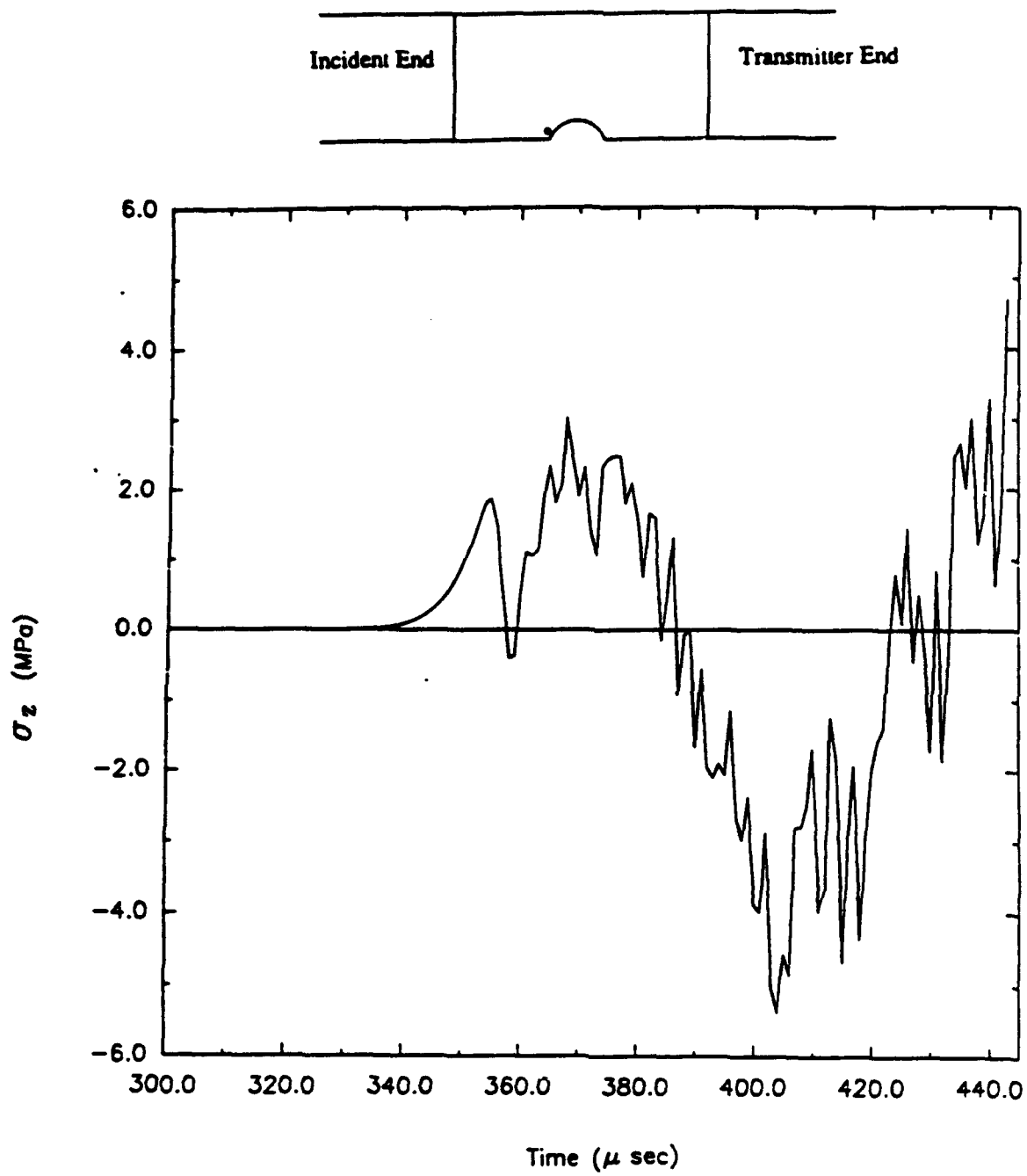


Figure 106. Time history for longitudinal stress (saddle-notch, Load Case 2).

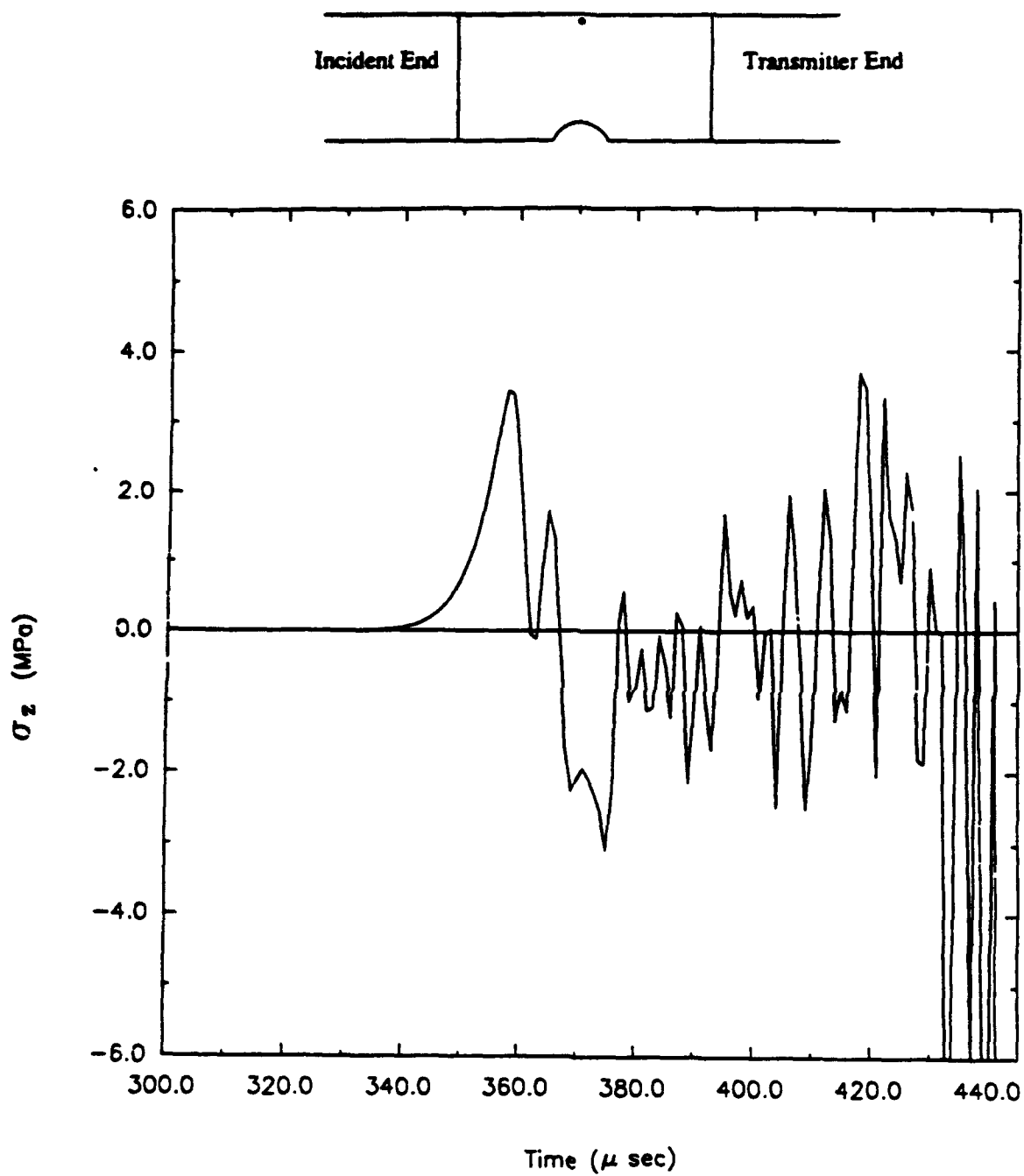


Figure 107. Time history for longitudinal stress (saddle-notch, Load Case 2).

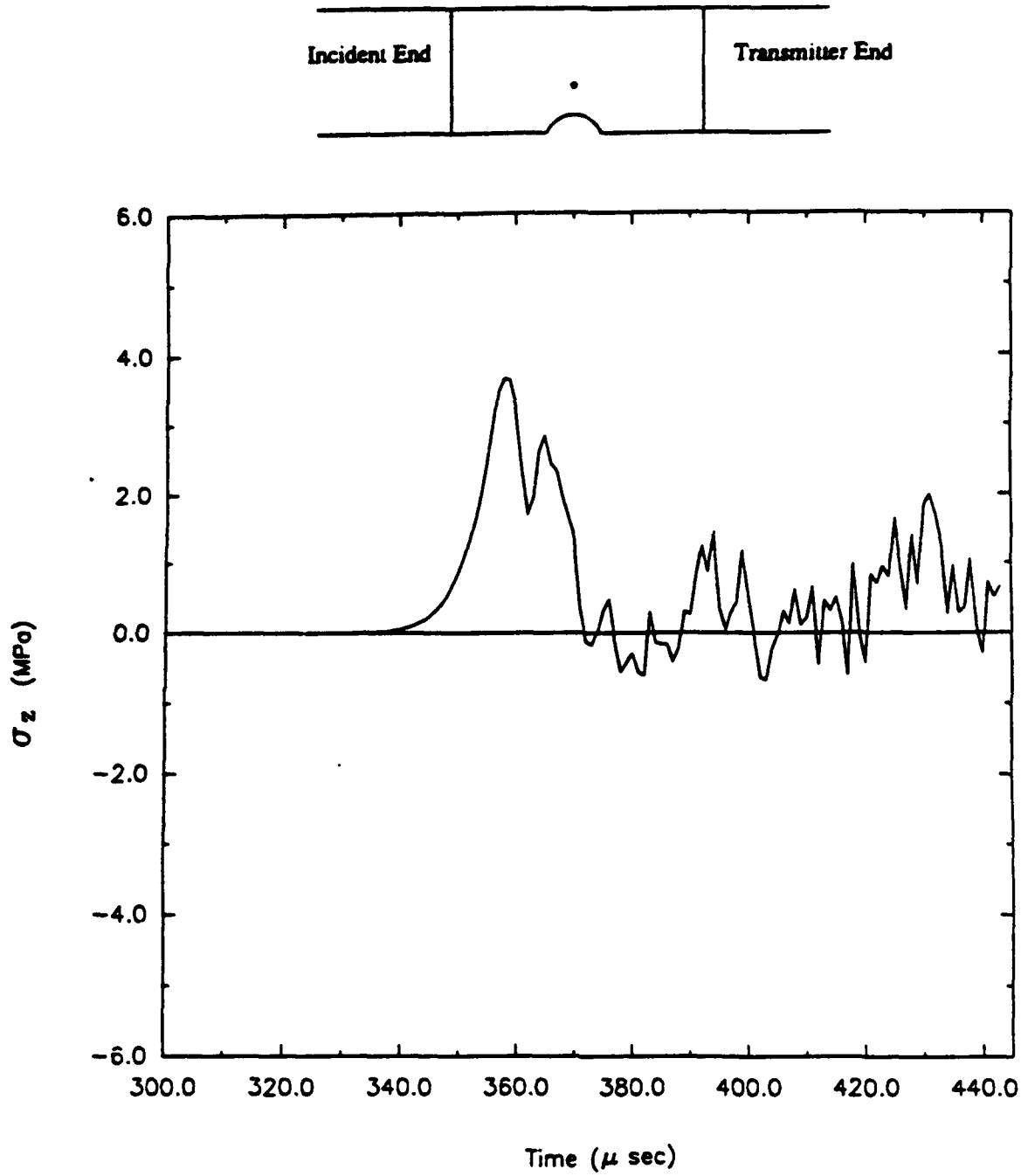


Figure 108. Time history for longitudinal stress (saddle-notch, Load Case 2).

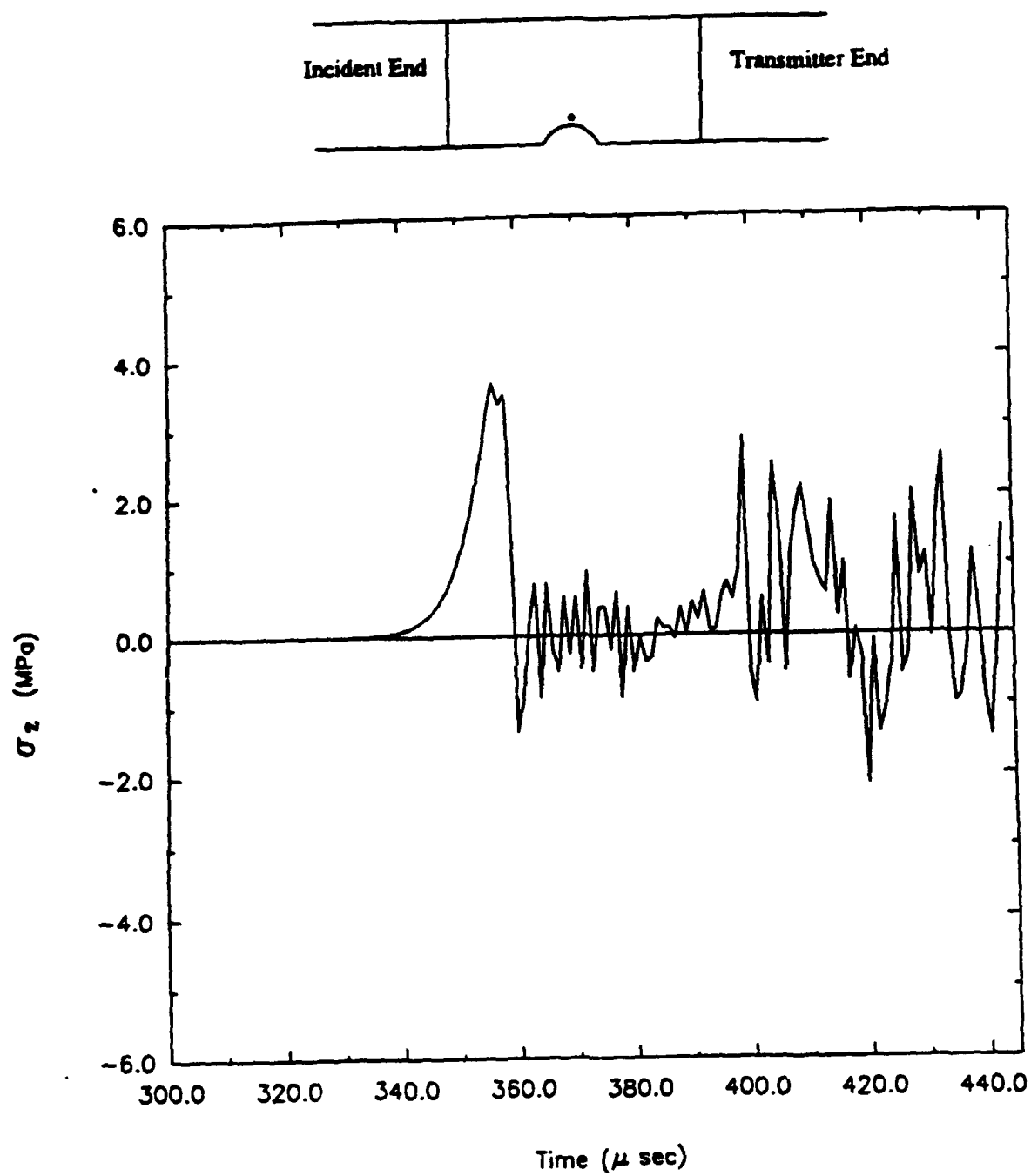


Figure 109. Time history for longitudinal stress (saddle-notch, Load Case 2).

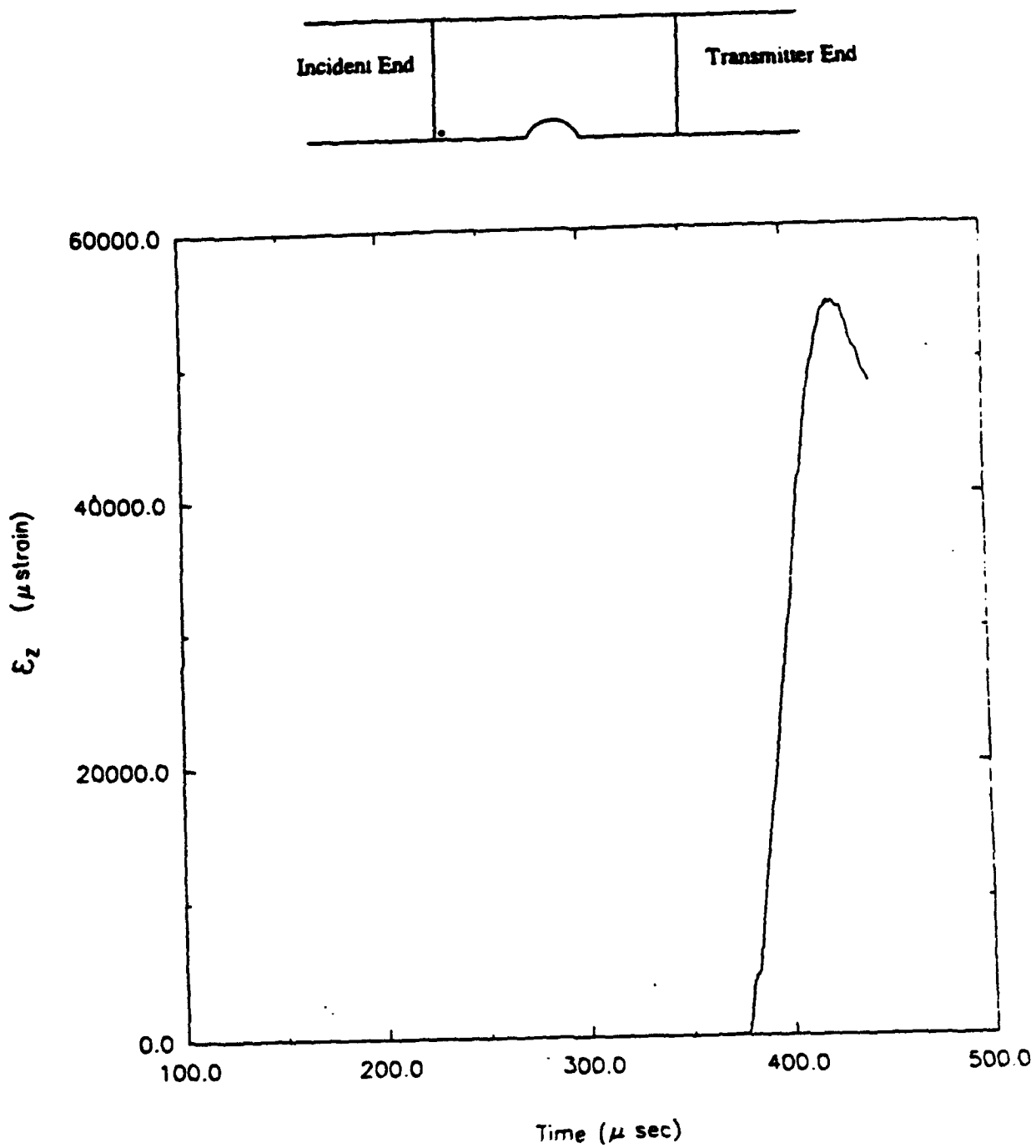


Figure 110. Time history for longitudinal strain (saddle-notch, Load Case 2).

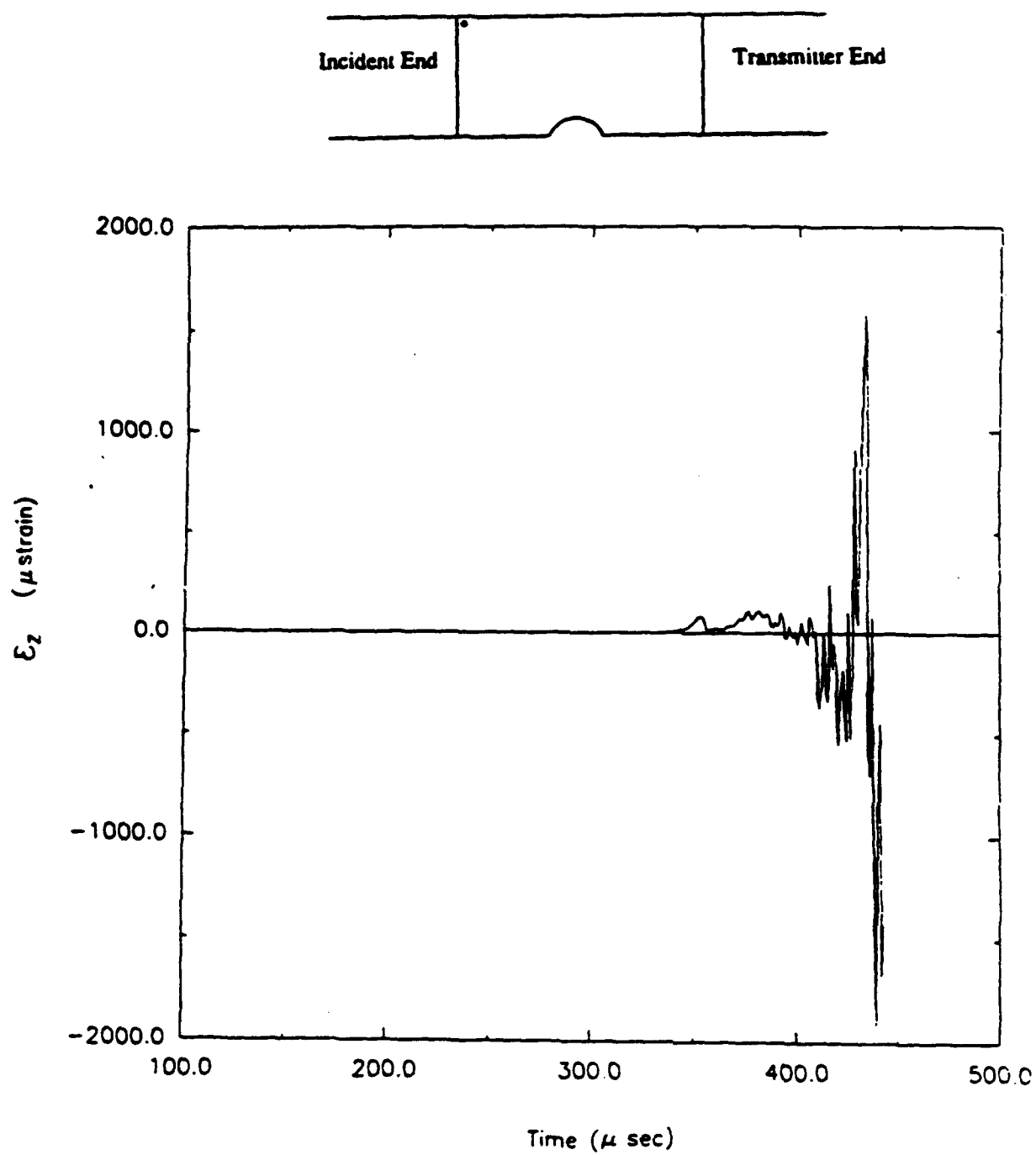


Figure 111. Time history for longitudinal strain (saddle-notch, Load Case 2).

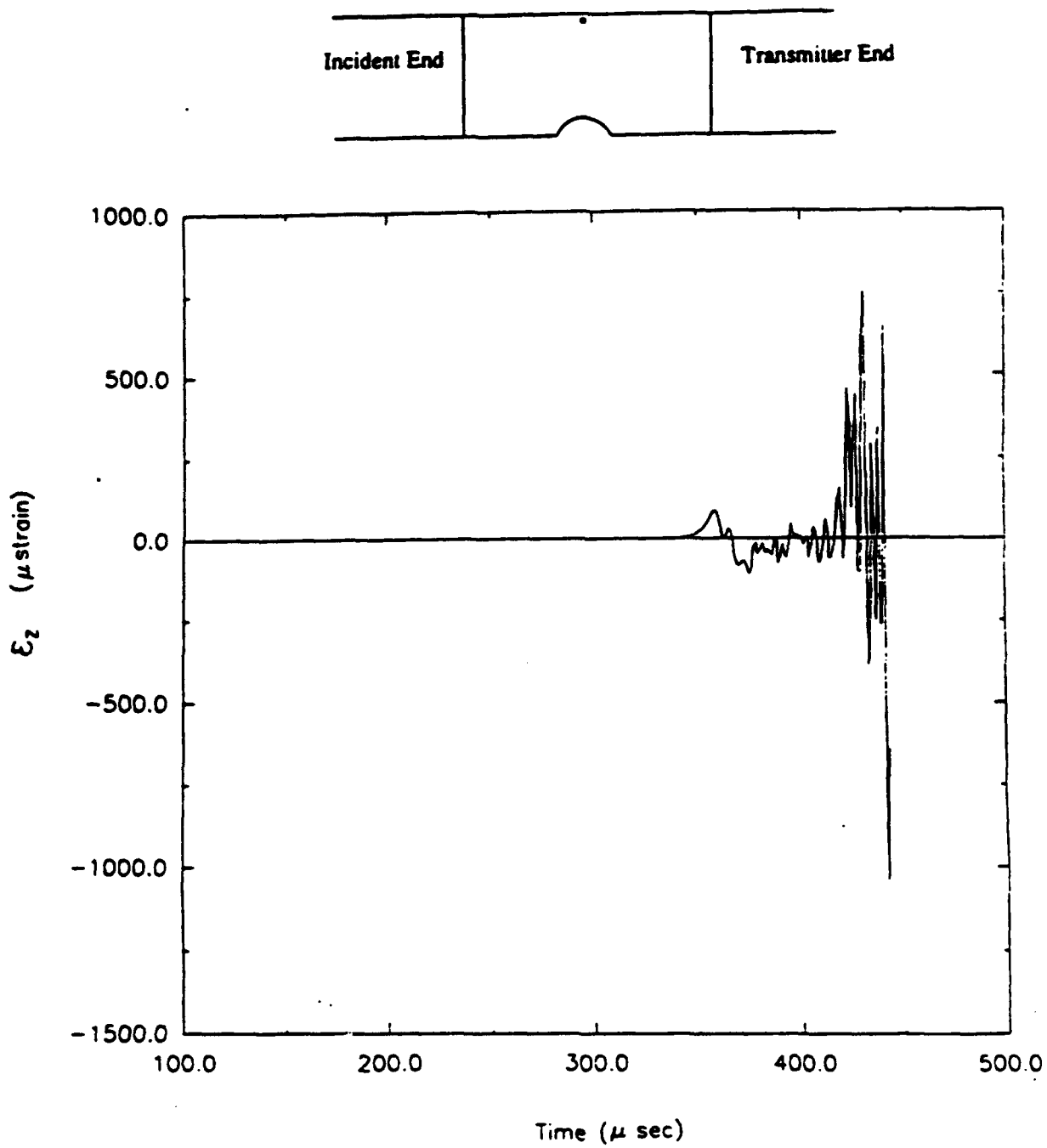


Figure 112. Time history for longitudinal strain (saddle-notch, Load Case 2).

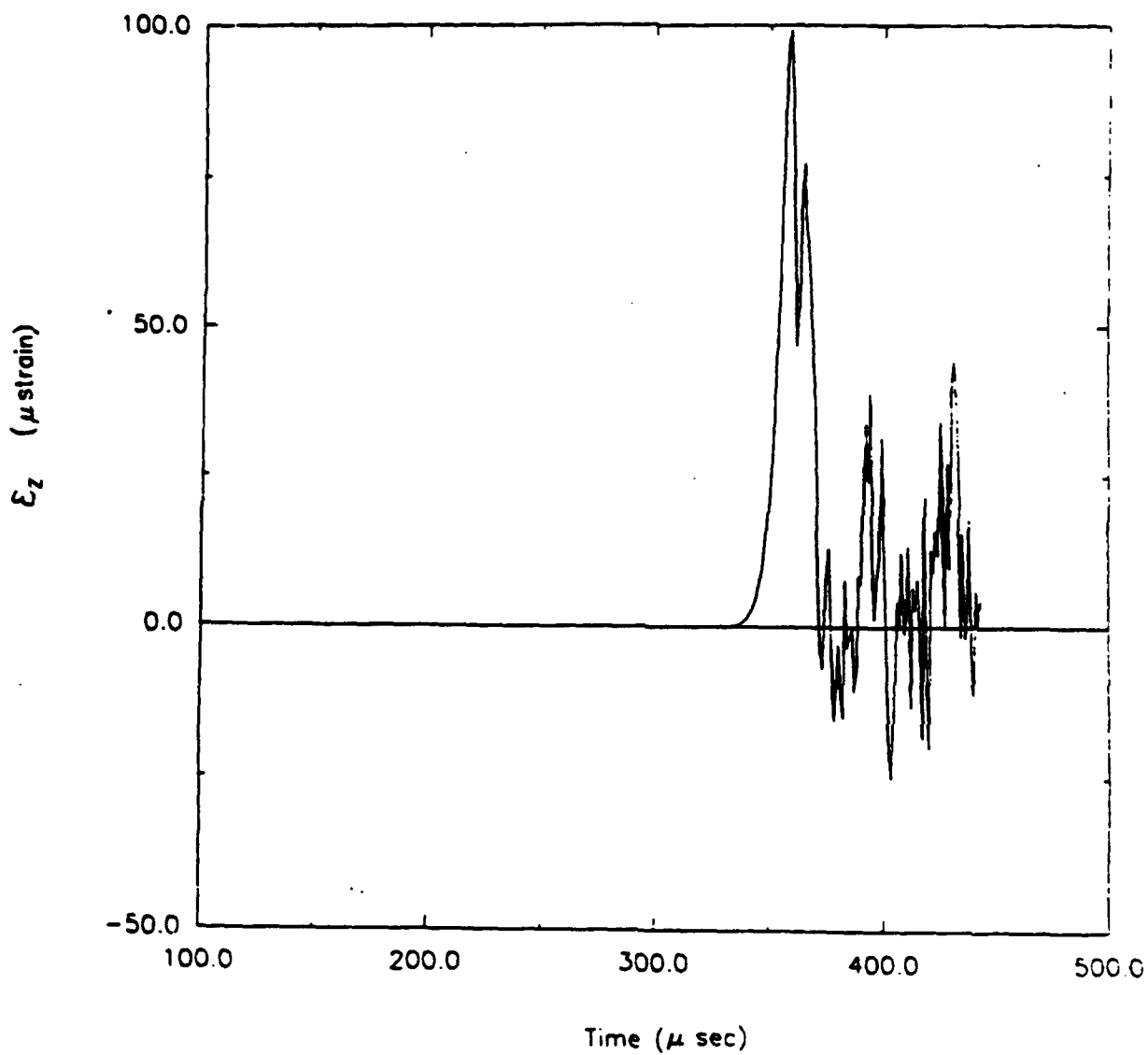


Figure 113. Time history for longitudinal strain (saddle-notch, Load Case 2).

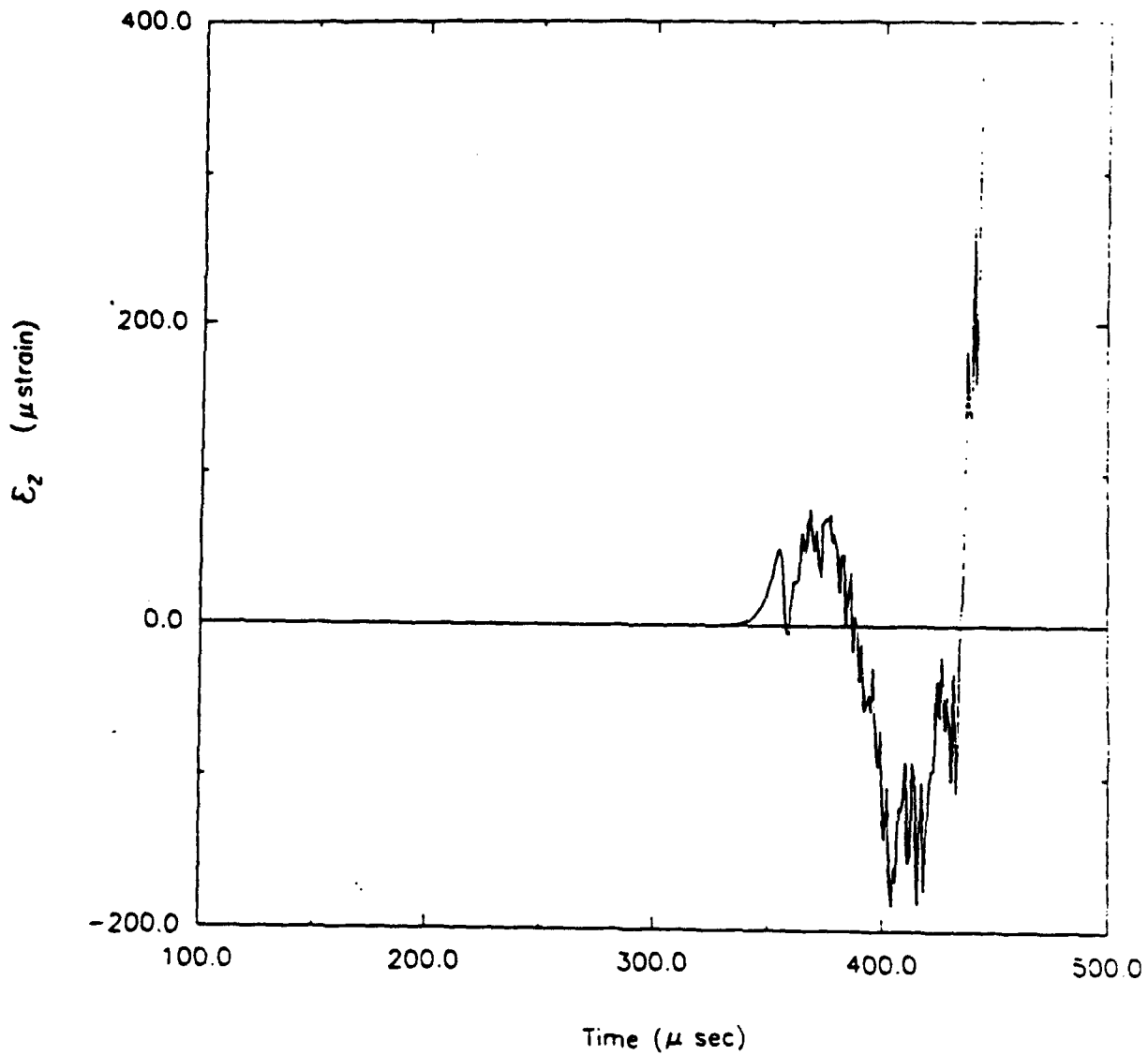
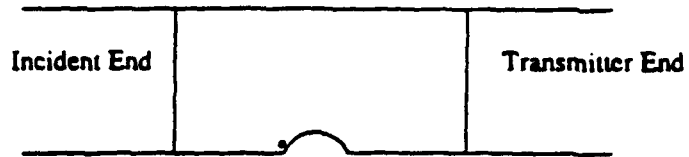


Figure 114. Time history for longitudinal strain (saddle-notch, Load Case 2).

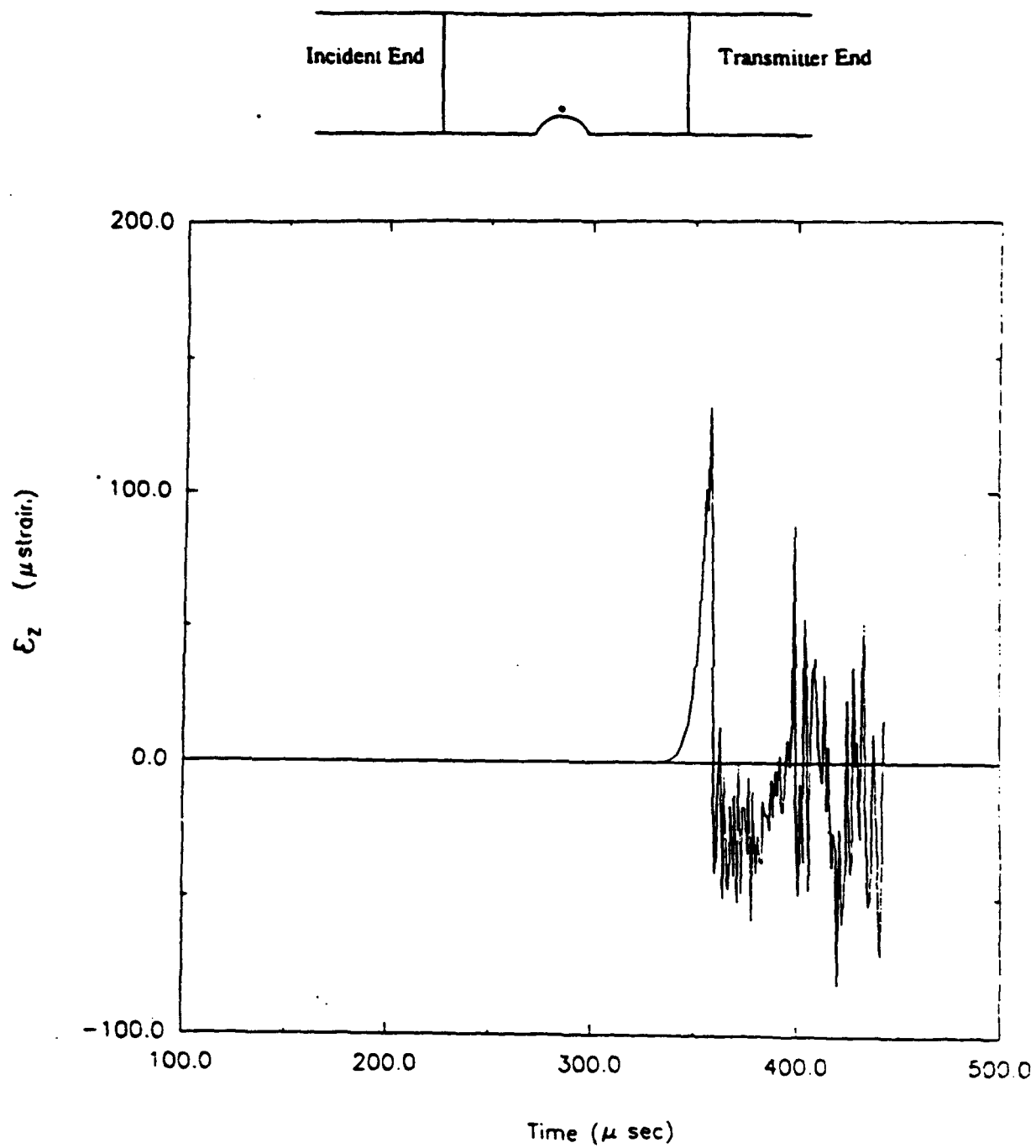


Figure 115. Time history for longitudinal strain (saddle-notch, Load Case 2).

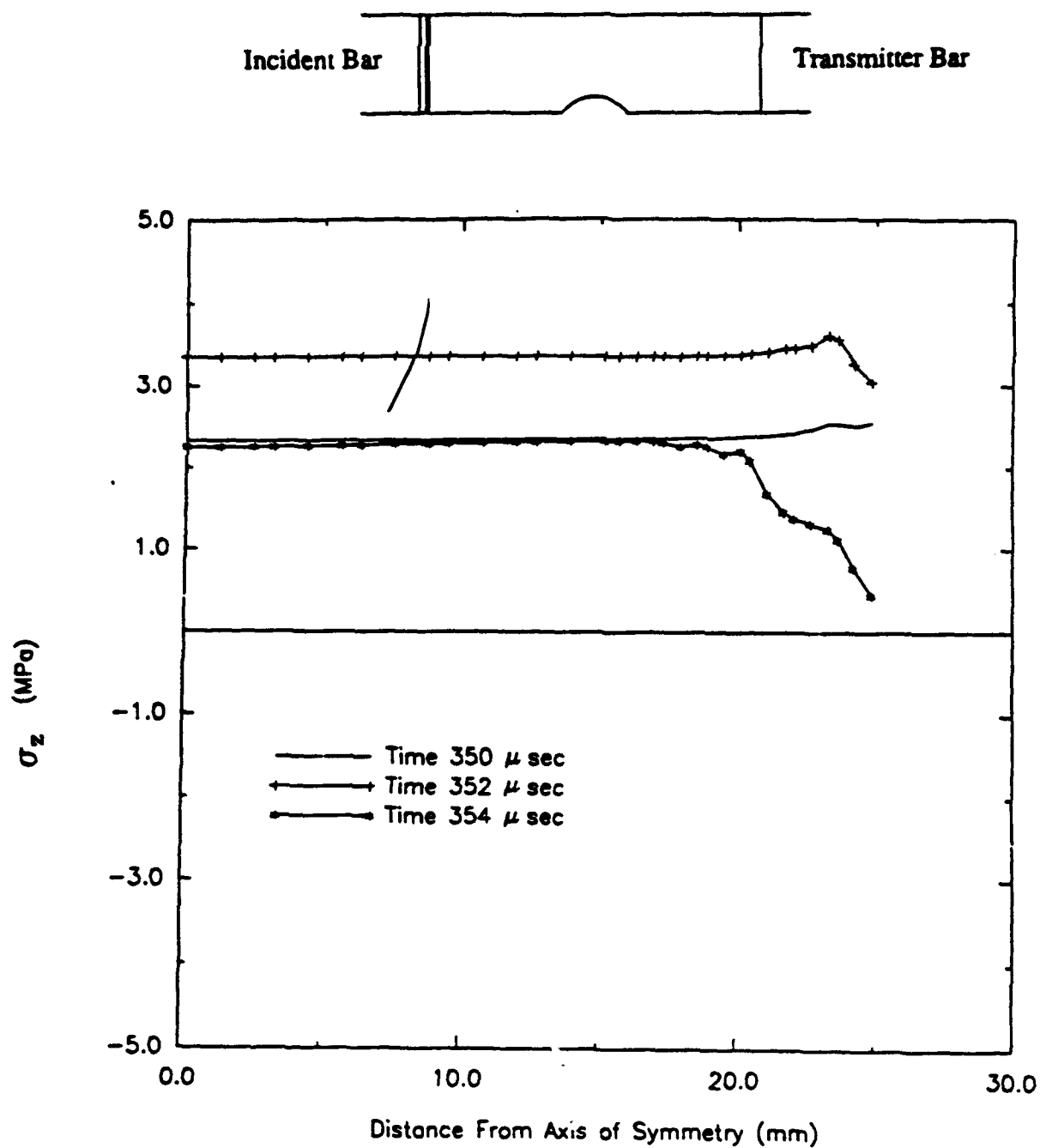


Figure 116. Profiles for longitudinal stress (saddle-notch, Load Case 2).

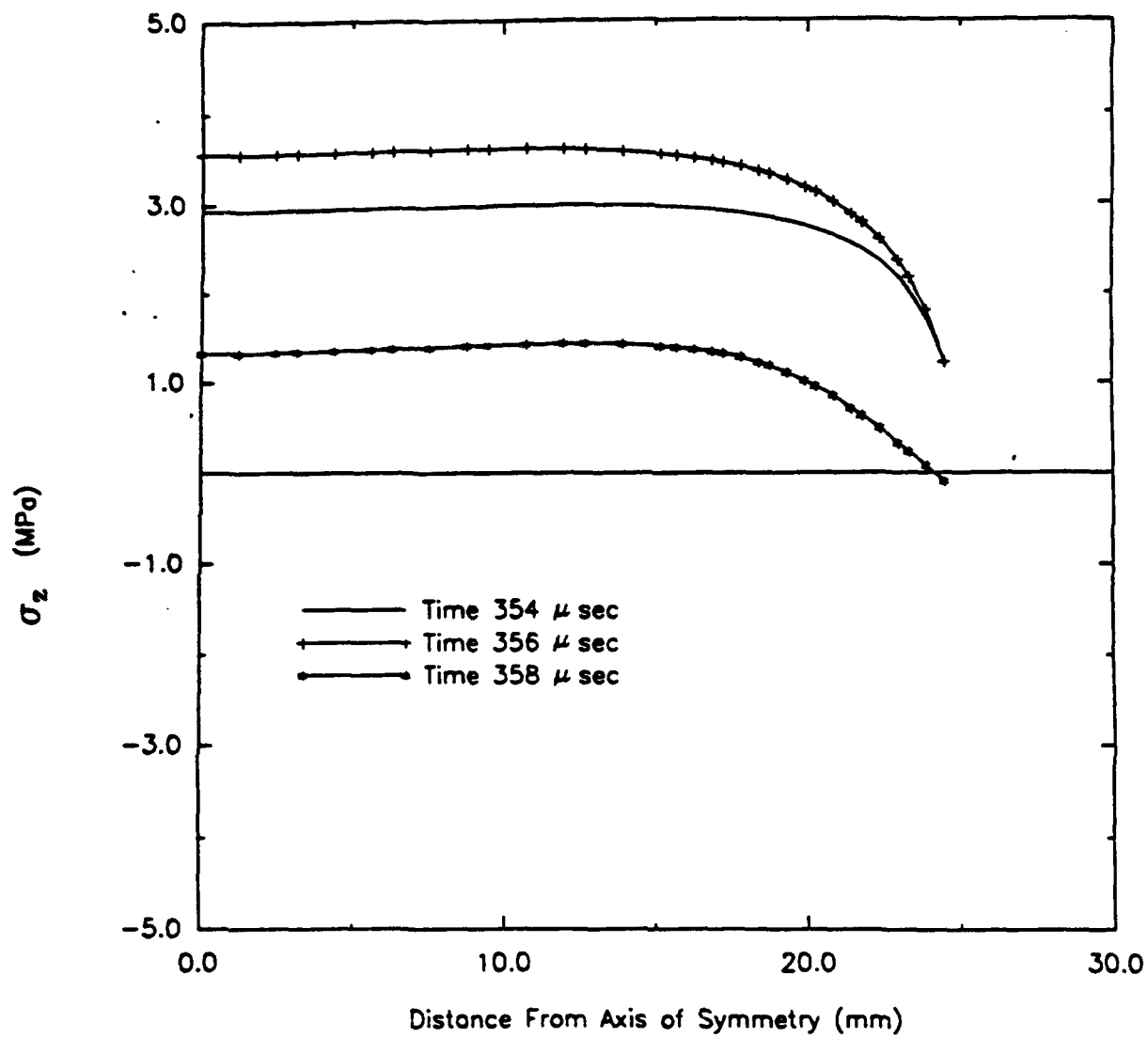
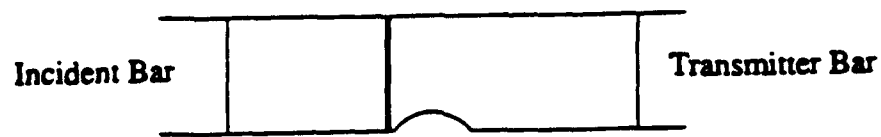


Figure 117. Profiles for longitudinal stress (saddle-notch, Load Case 2).

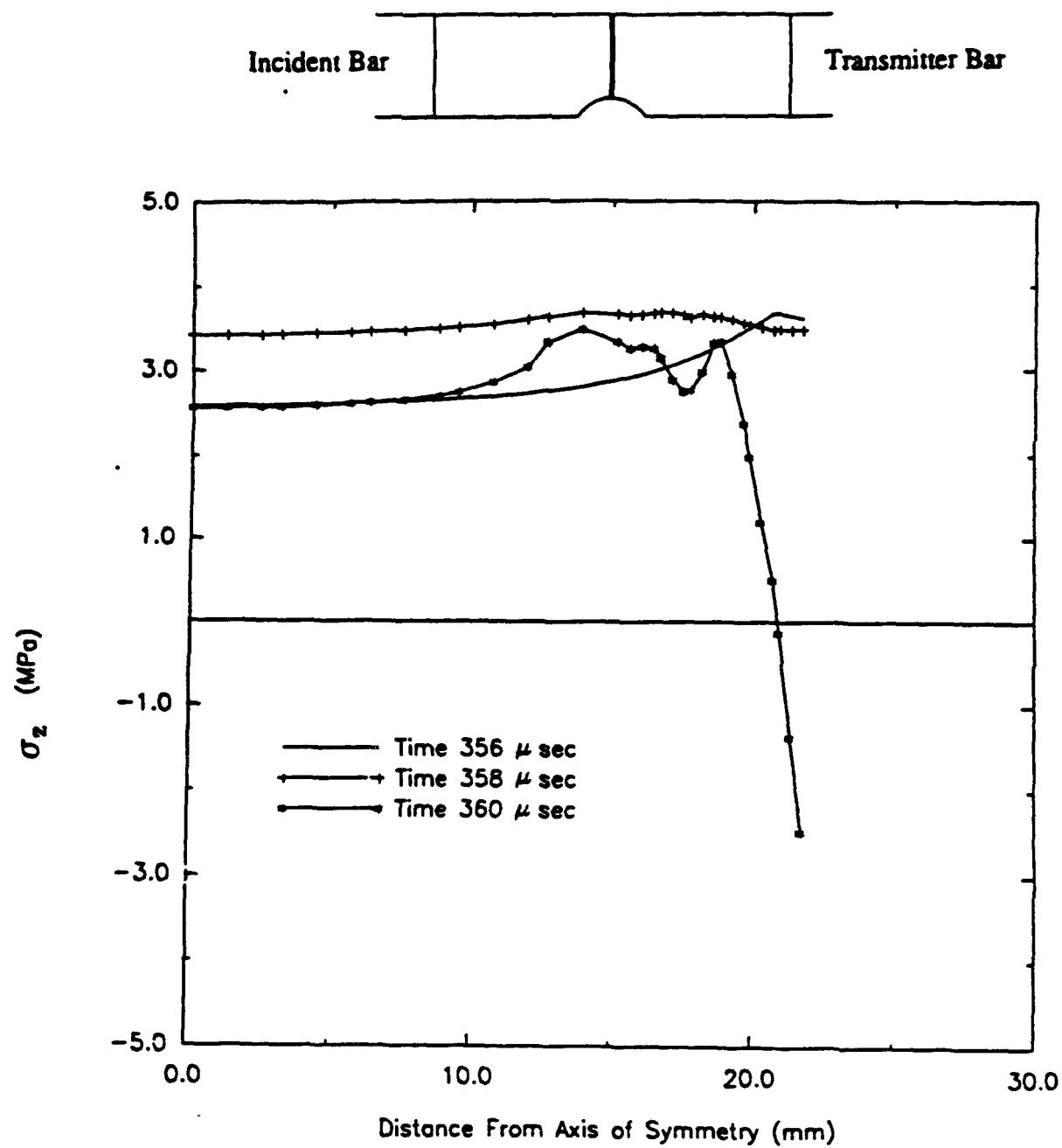


Figure 118. Profiles for longitudinal stress (saddle-notch, Load Case 2).

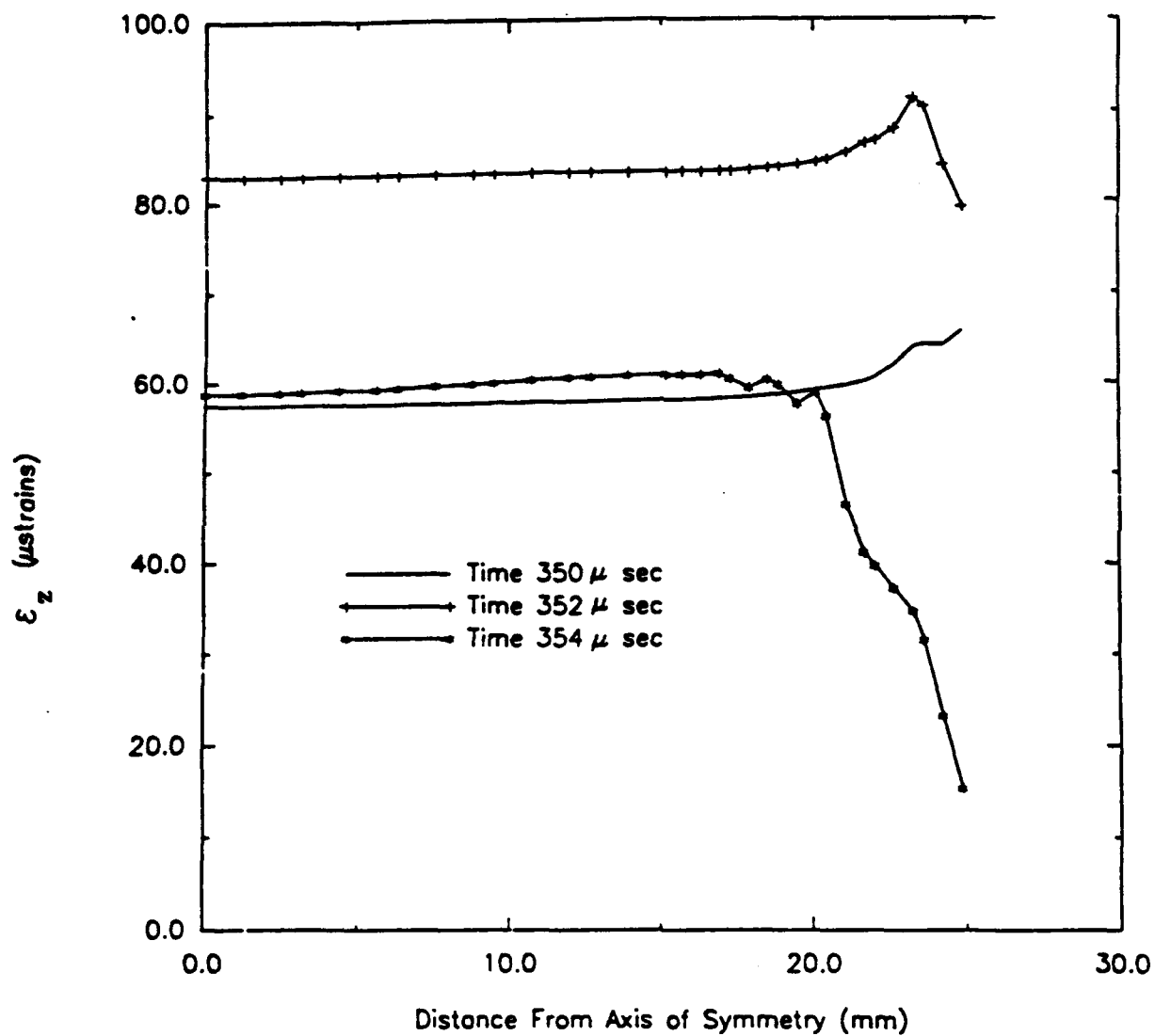


Figure 119. Profiles for longitudinal strain (saddle-notch, Load Case 2).

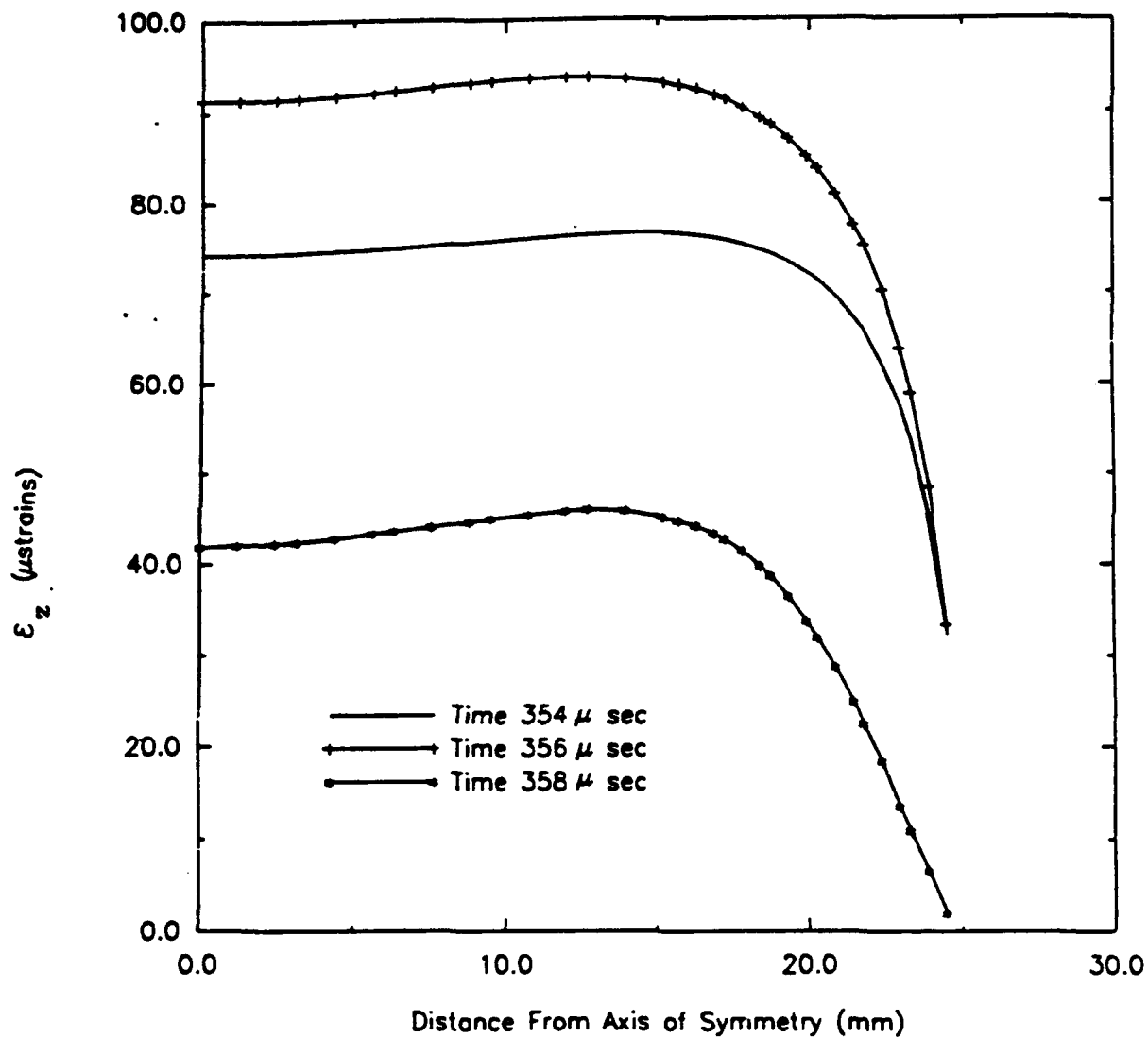
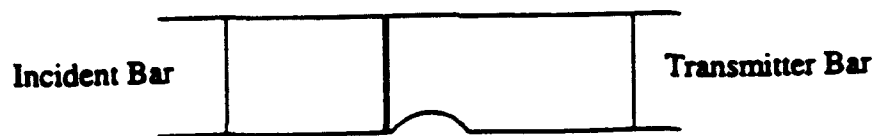


Figure 120. Profiles for longitudinal strain (saddle-notch, Load Case 2).

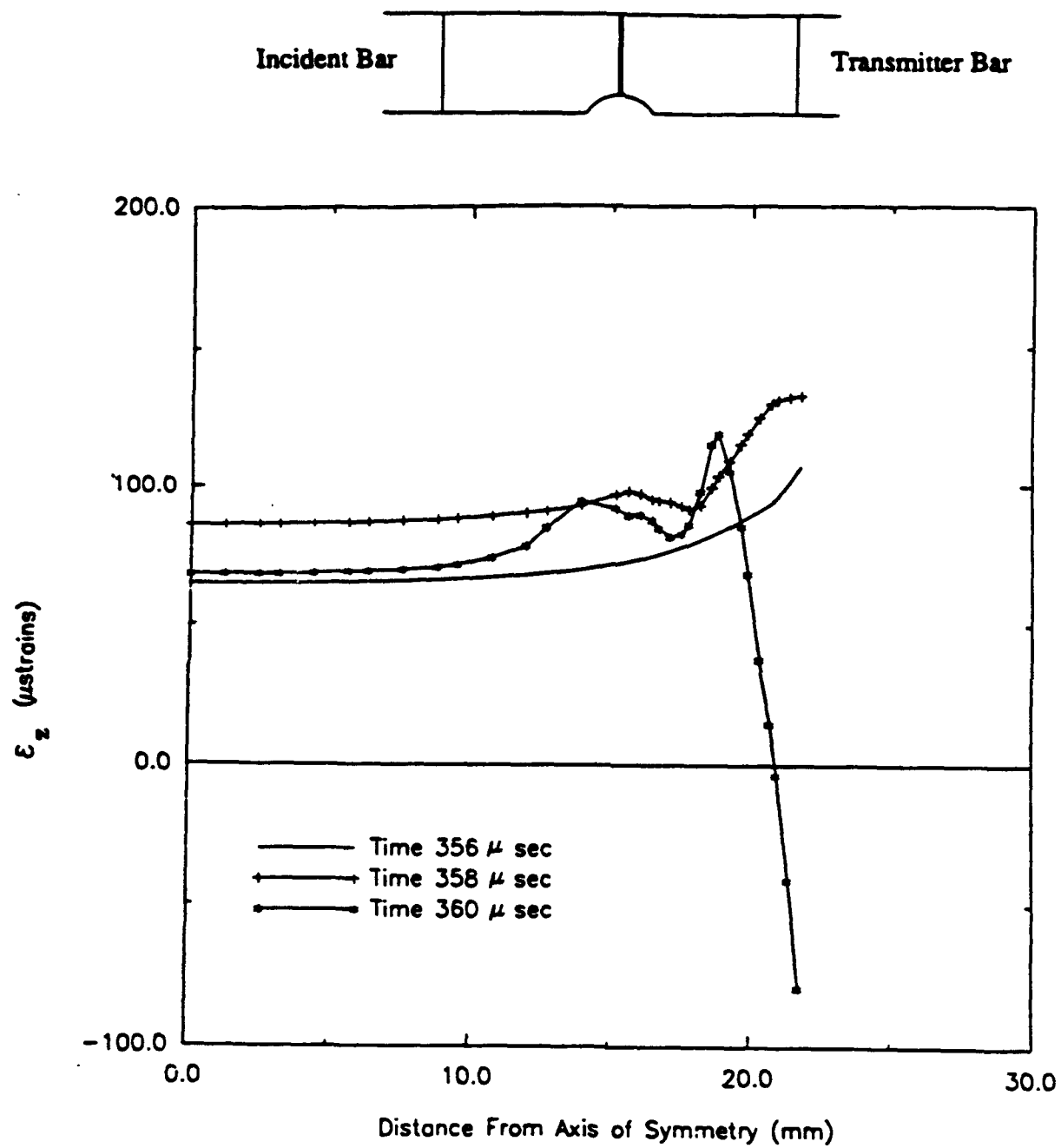
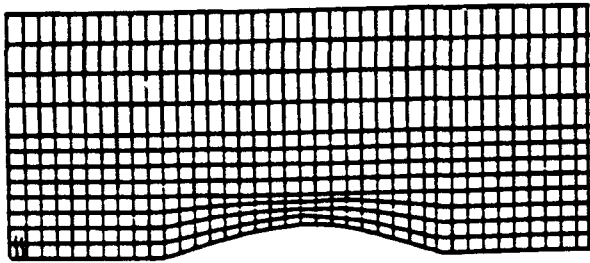
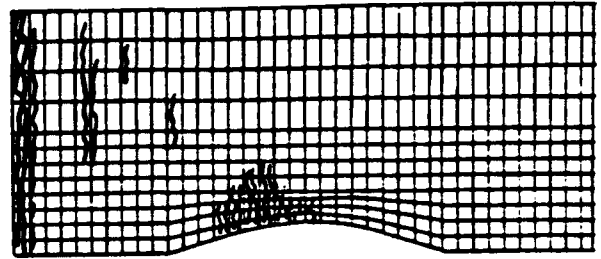


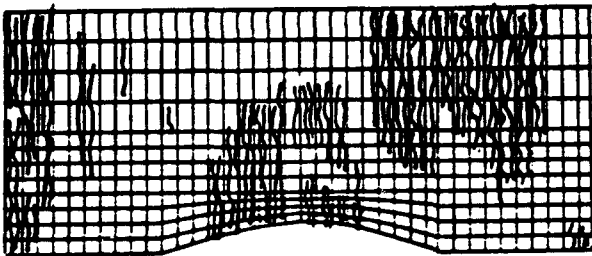
Figure 121. Profiles for longitudinal strain (saddle-notch, Load Case 2).



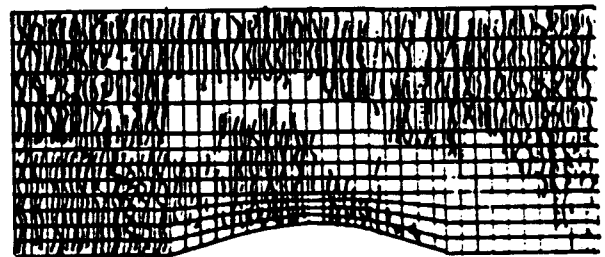
(a)



(b)



(c)



(d)

Figure 122. Cracking sequence for saddle-notch specimen; Load Case 2:
a) $t=351 \mu \text{ sec}$, b) $t=356 \mu \text{ sec}$, c) $t=362 \mu \text{ sec}$, d) $t=425 \mu \text{ sec}$.

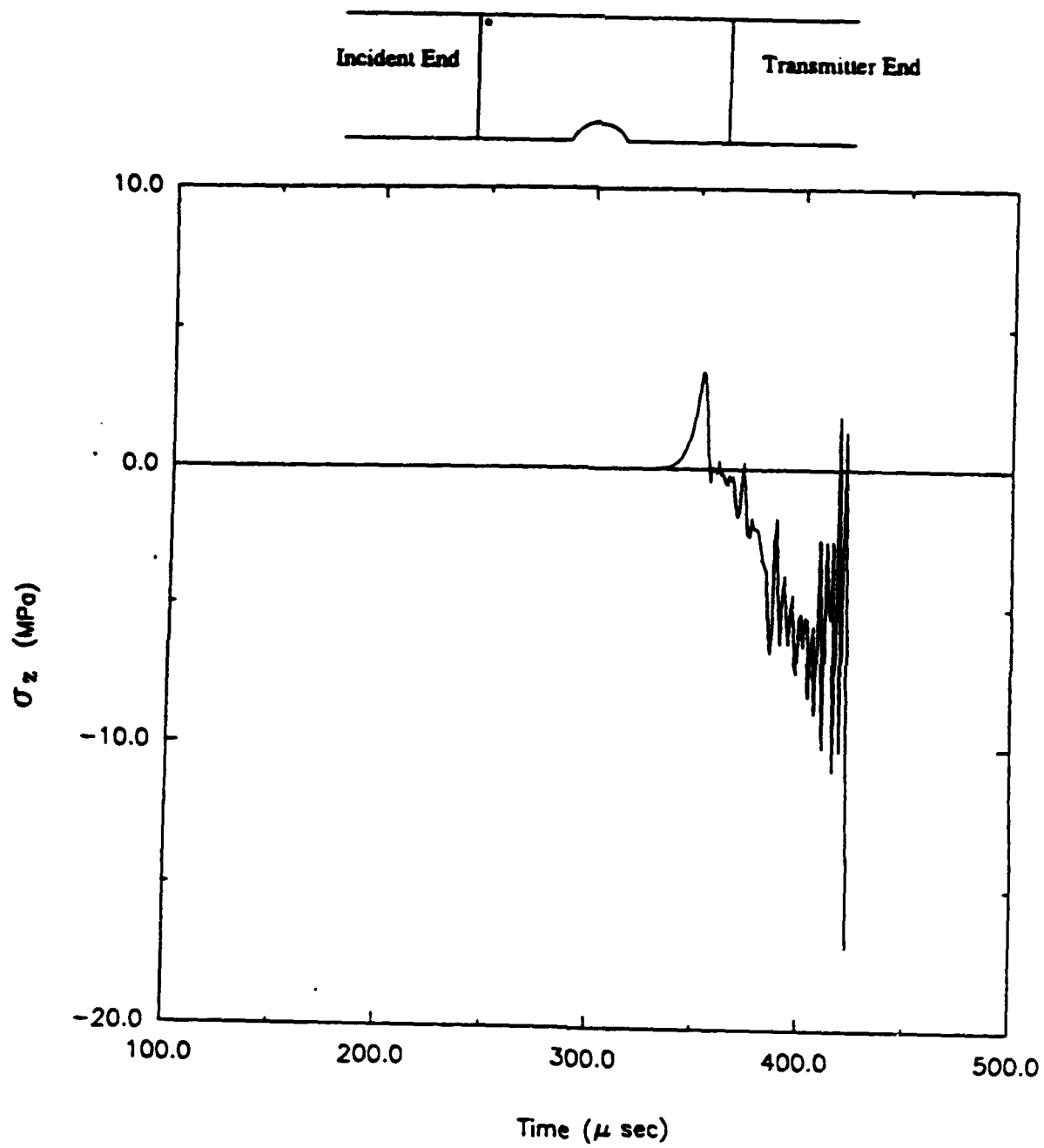


Figure 123. Time history for longitudinal stress (saddle-notch, Load Case 3).

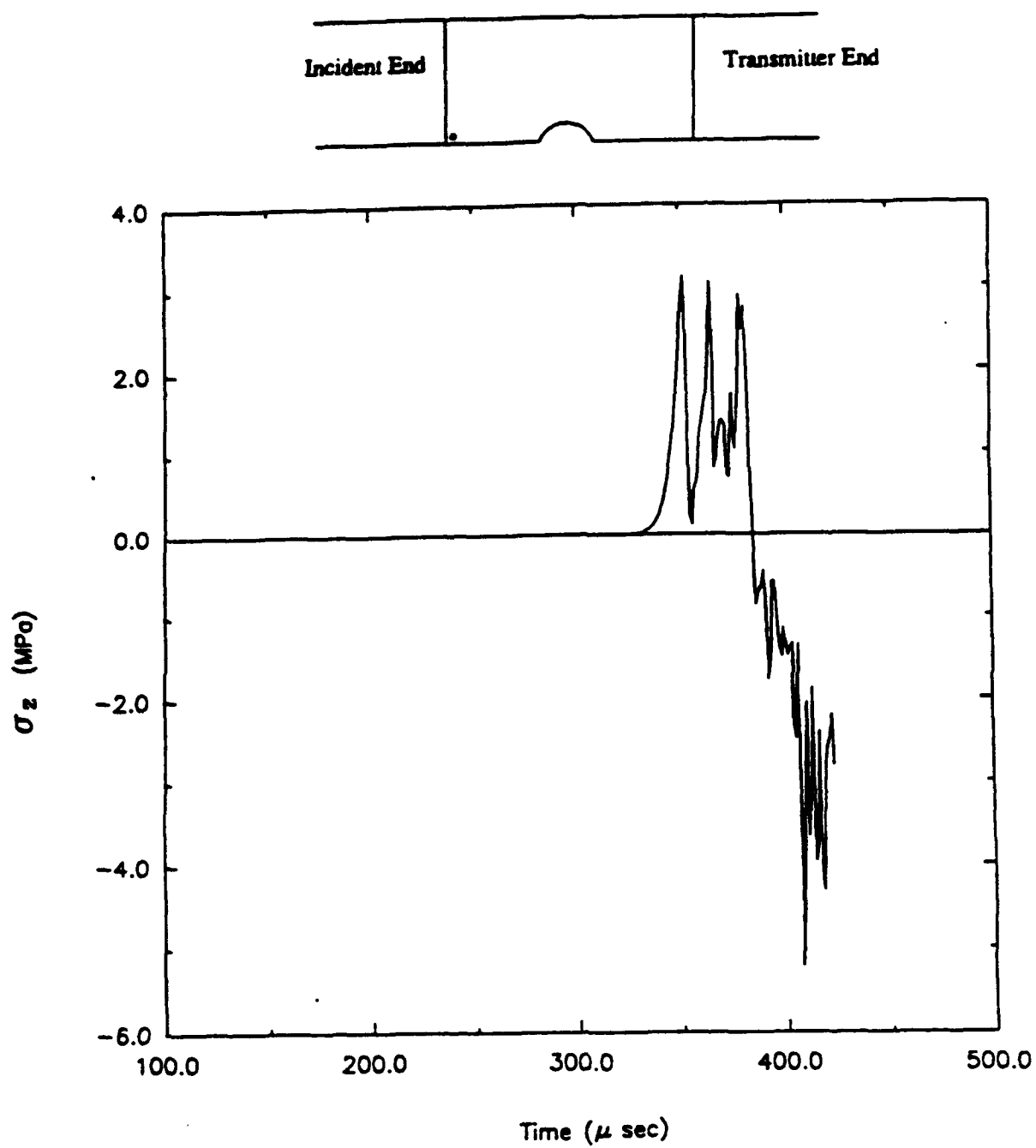


Figure 124. Time history for longitudinal stress (saddle-notch, Load Case 3).

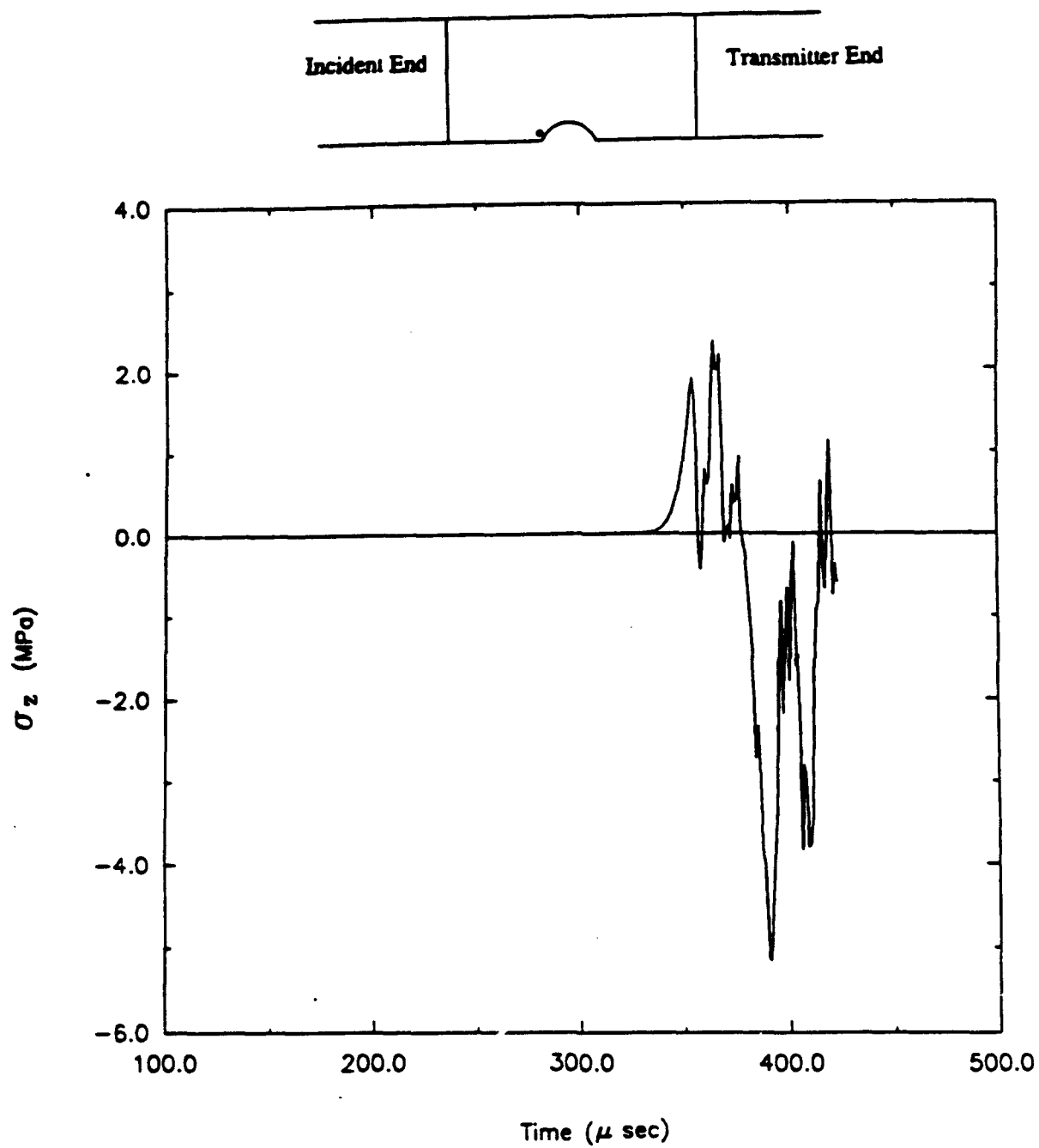


Figure 125. Time history for longitudinal stress (saddle-notch, Load Case 3).

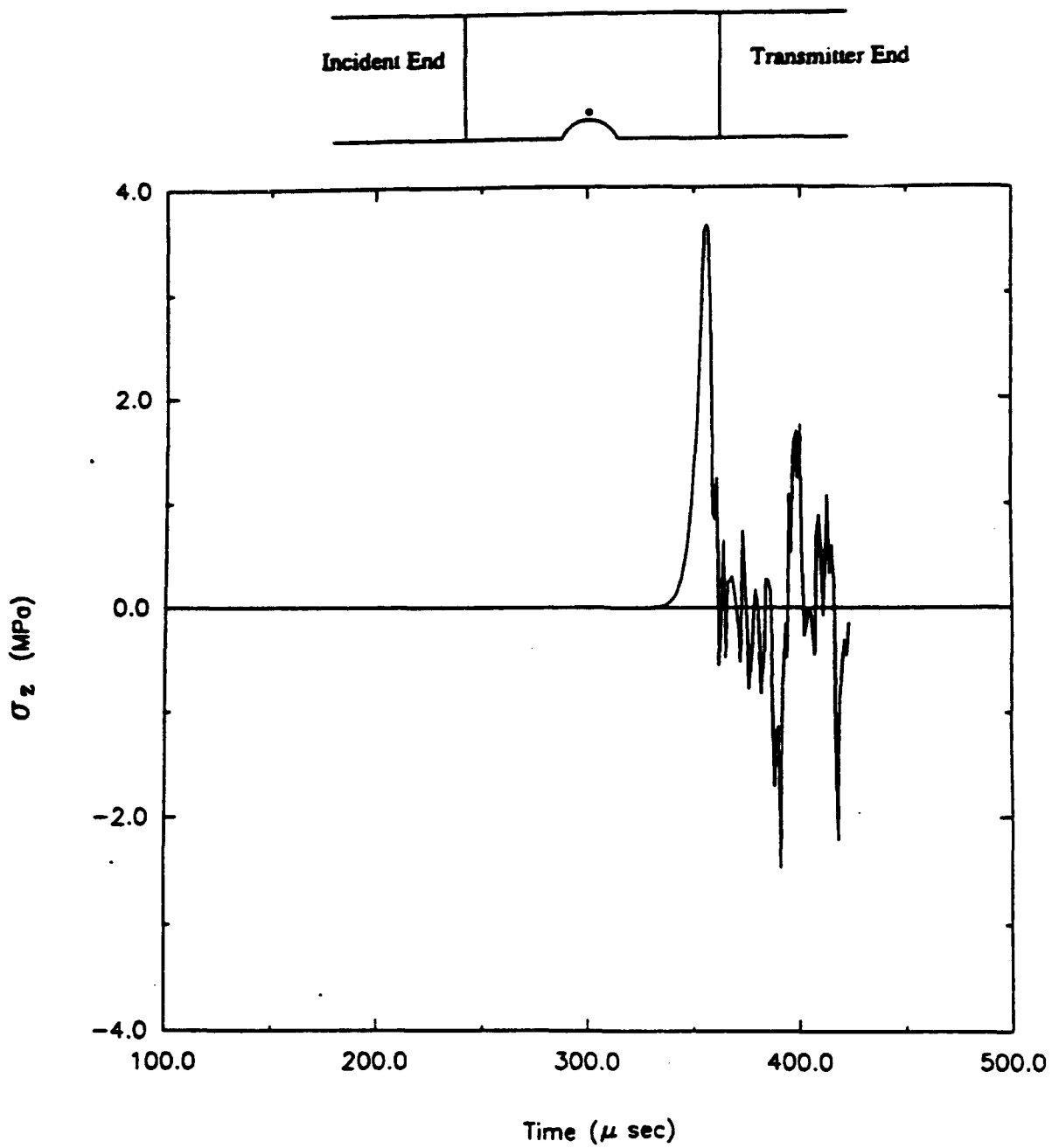


Figure 126. Time history for longitudinal stress (saddle-notch, Load Case 3).

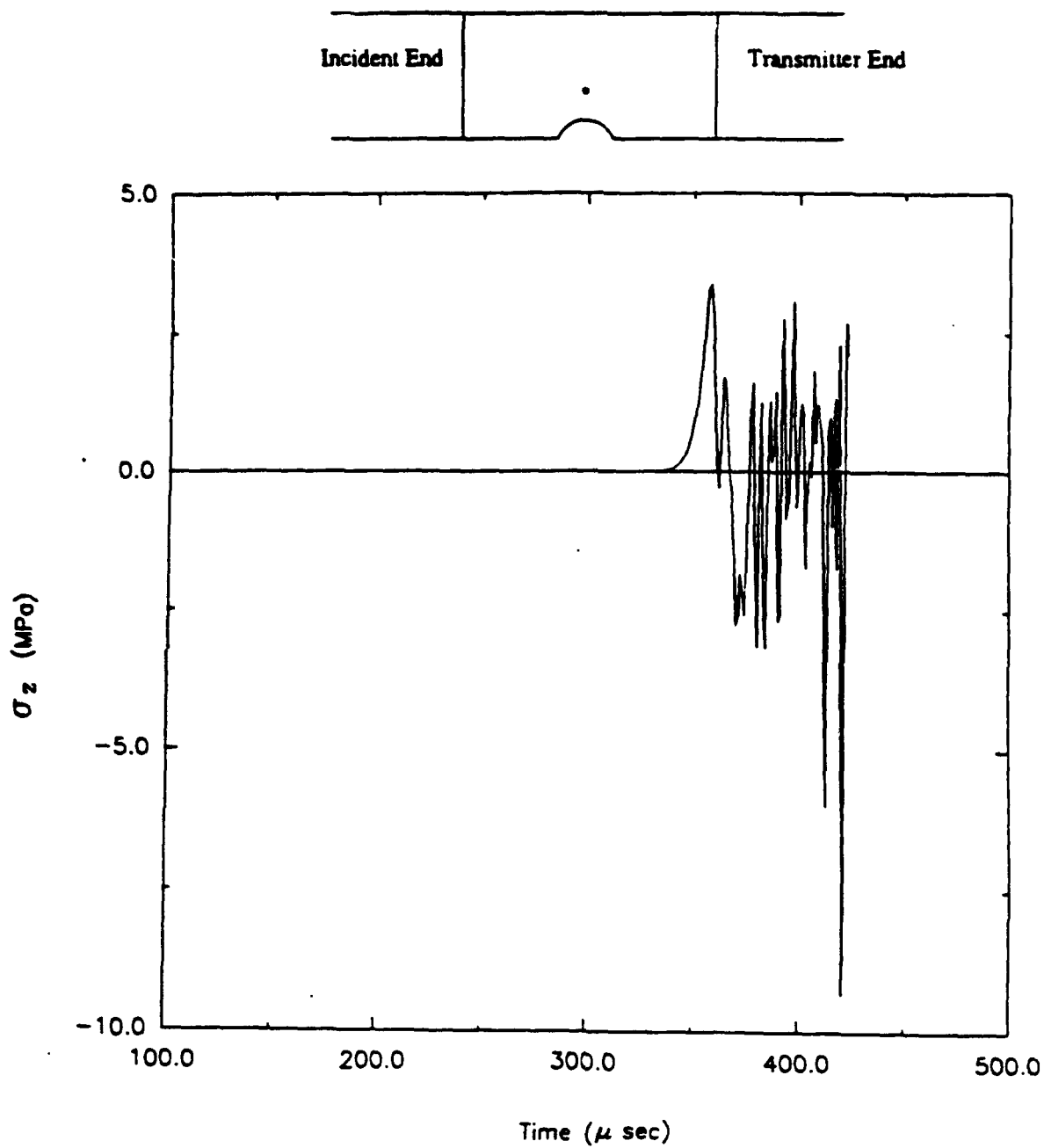


Figure 127. Time history for longitudinal stress (saddle-notch, Load Case 3).

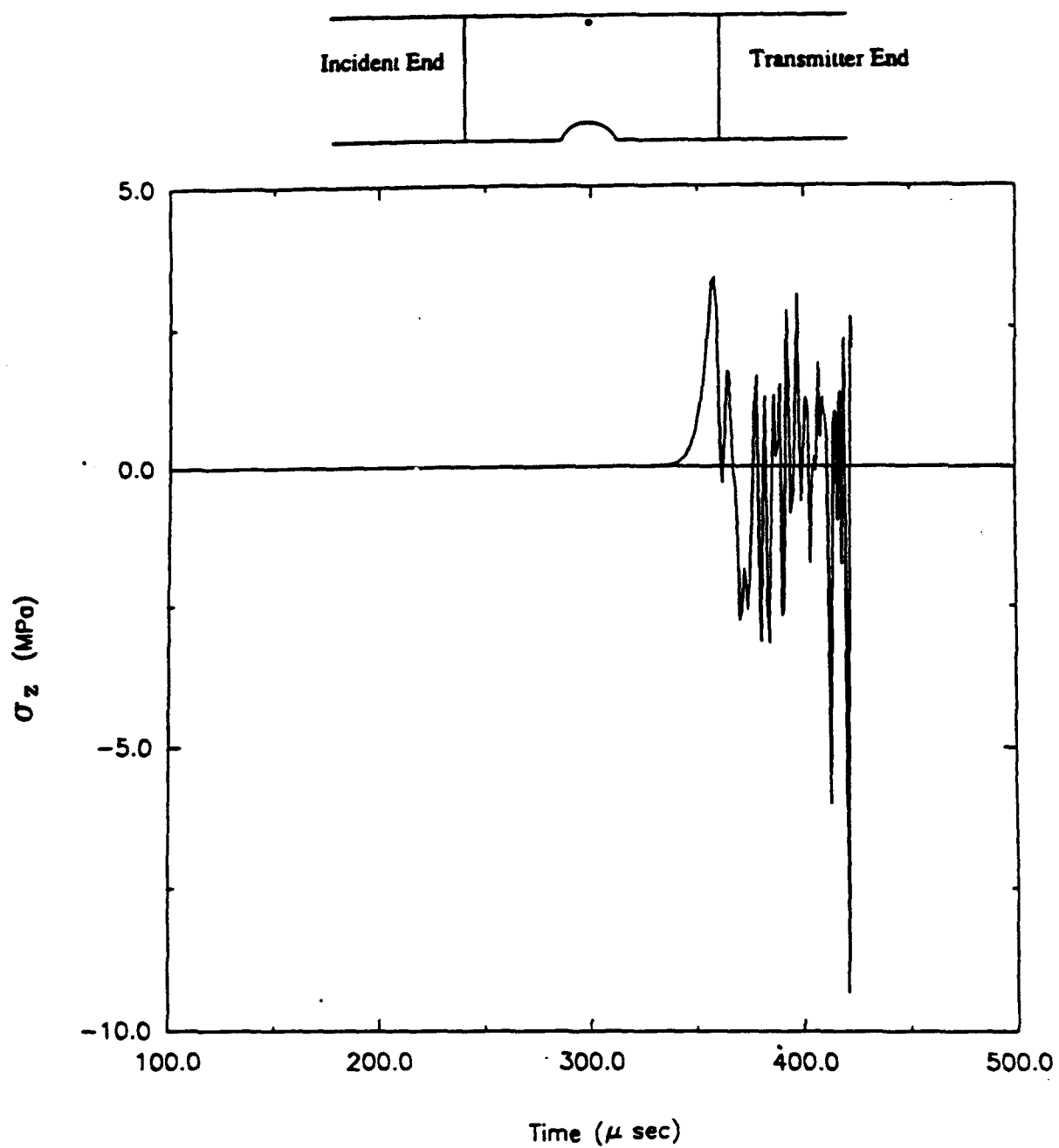


Figure 128. Time history for longitudinal stress (saddle-notch, Load Case 3).

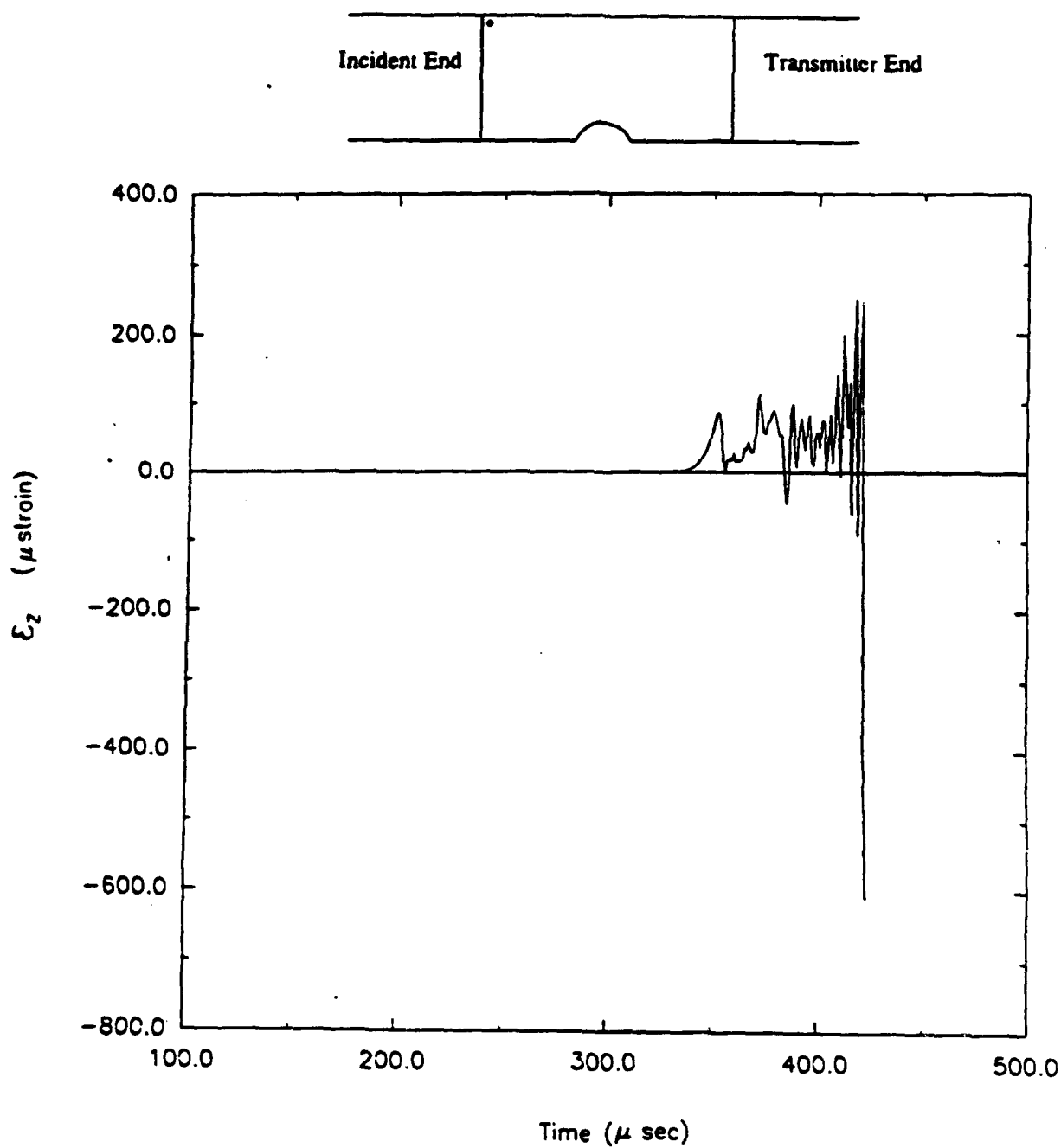


Figure 129. Time history for longitudinal strain (saddle-notch, Load Case 3).

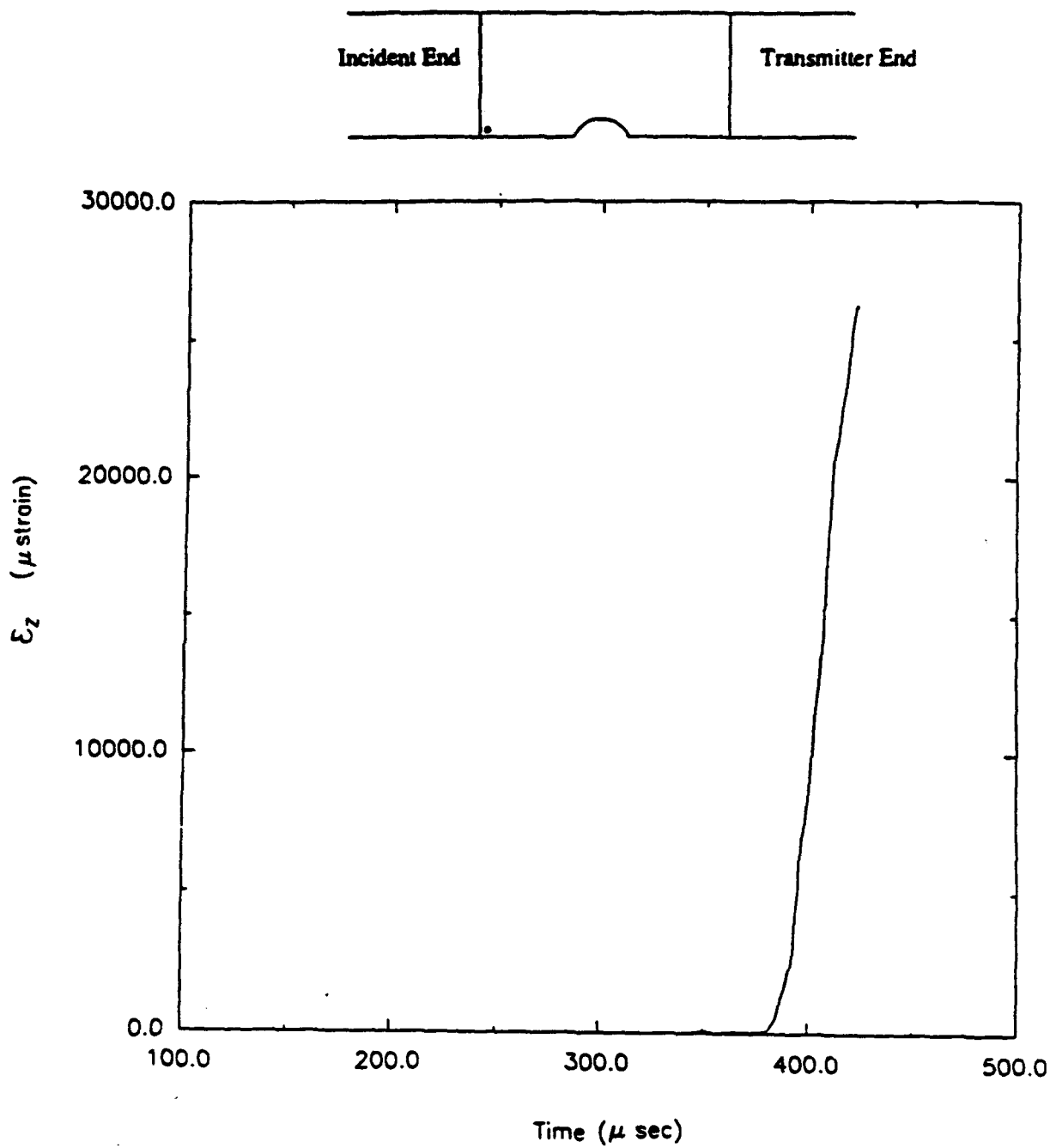


Figure 130. Time history for longitudinal strain (saddle-notch, Load Case 3).

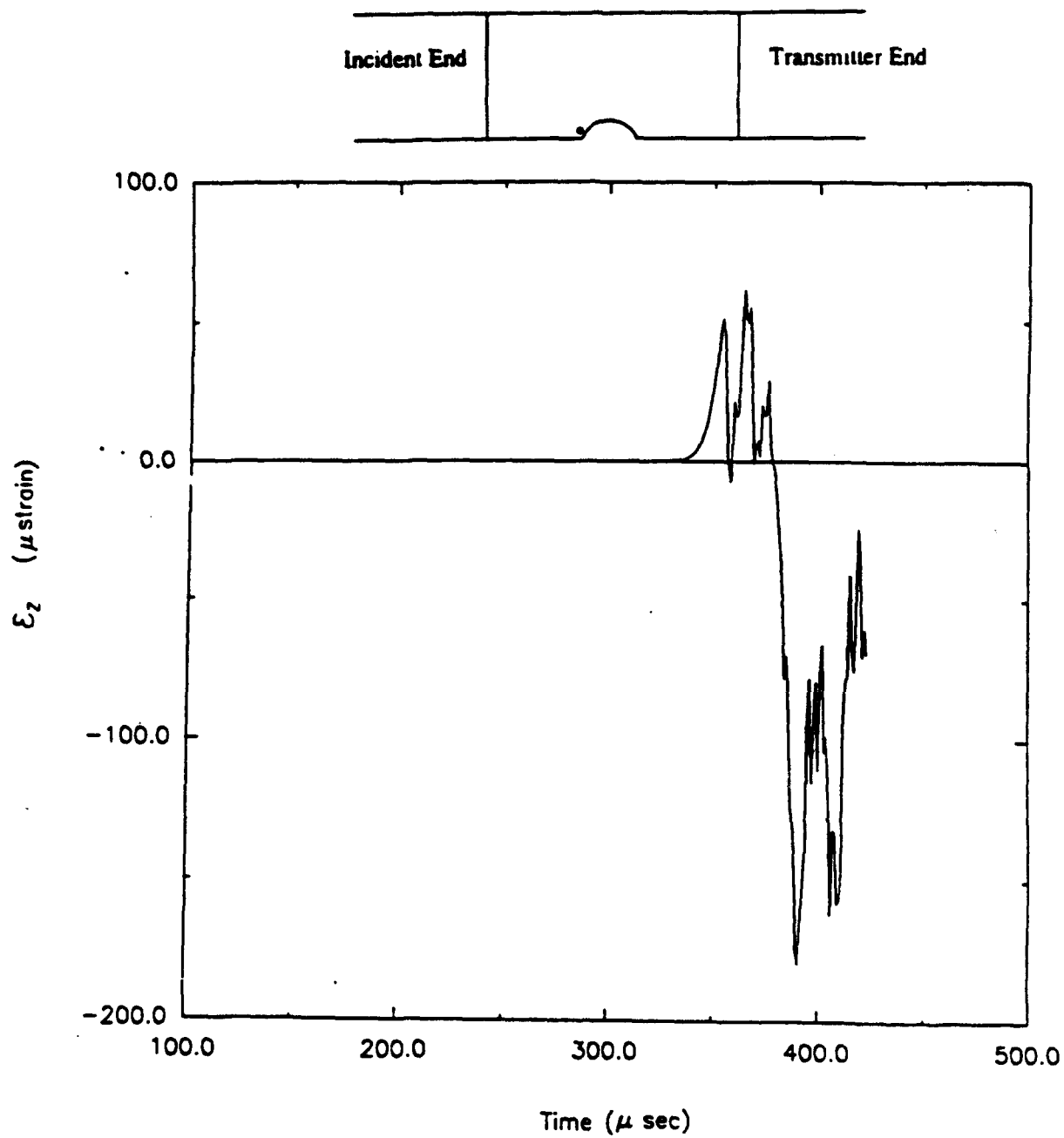


Figure 131. Time history for longitudinal strain (saddle-notch, Load Case 3).

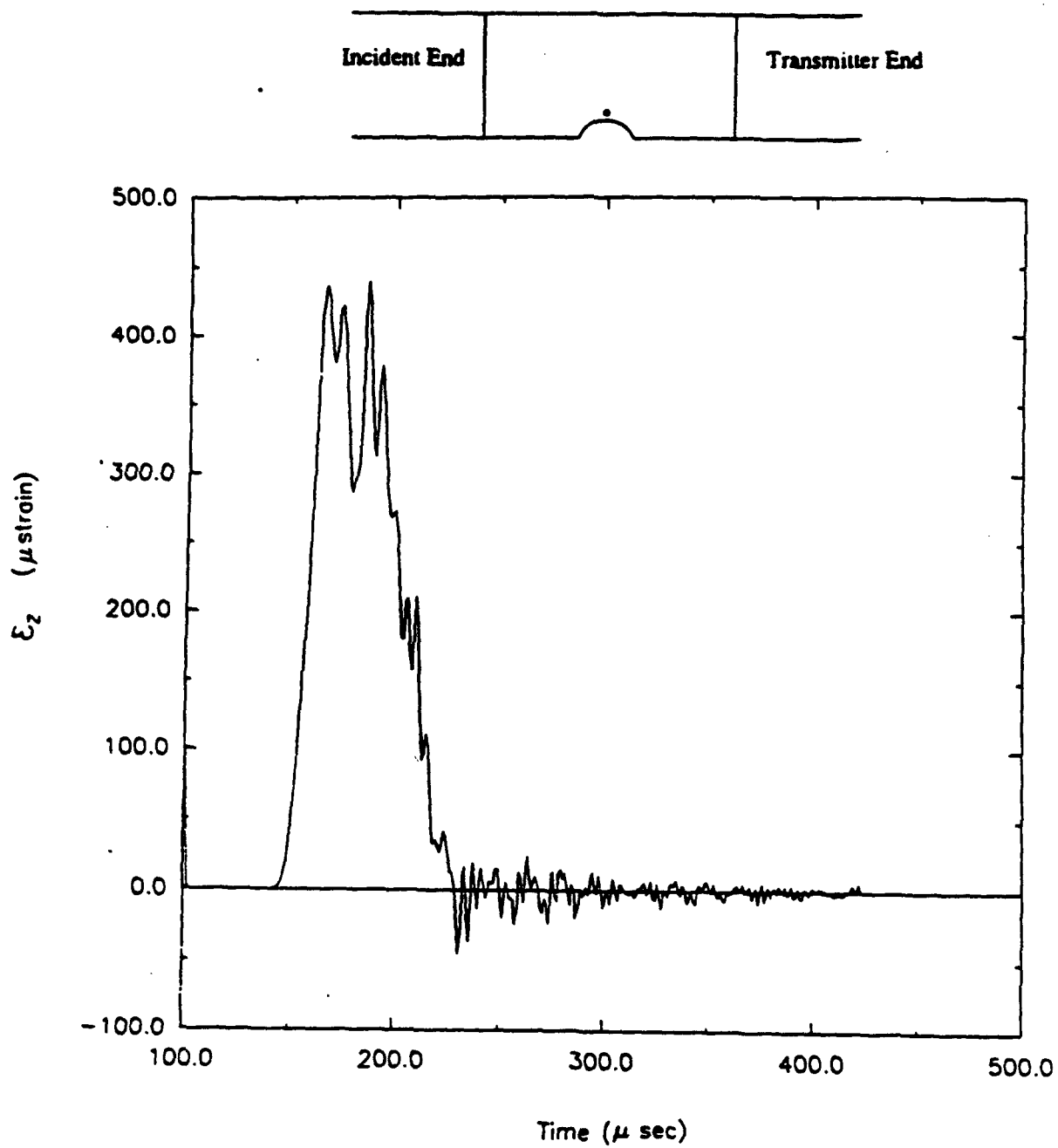


Figure 132. Time history for longitudinal strain (saddle-notch, Load Case 3).

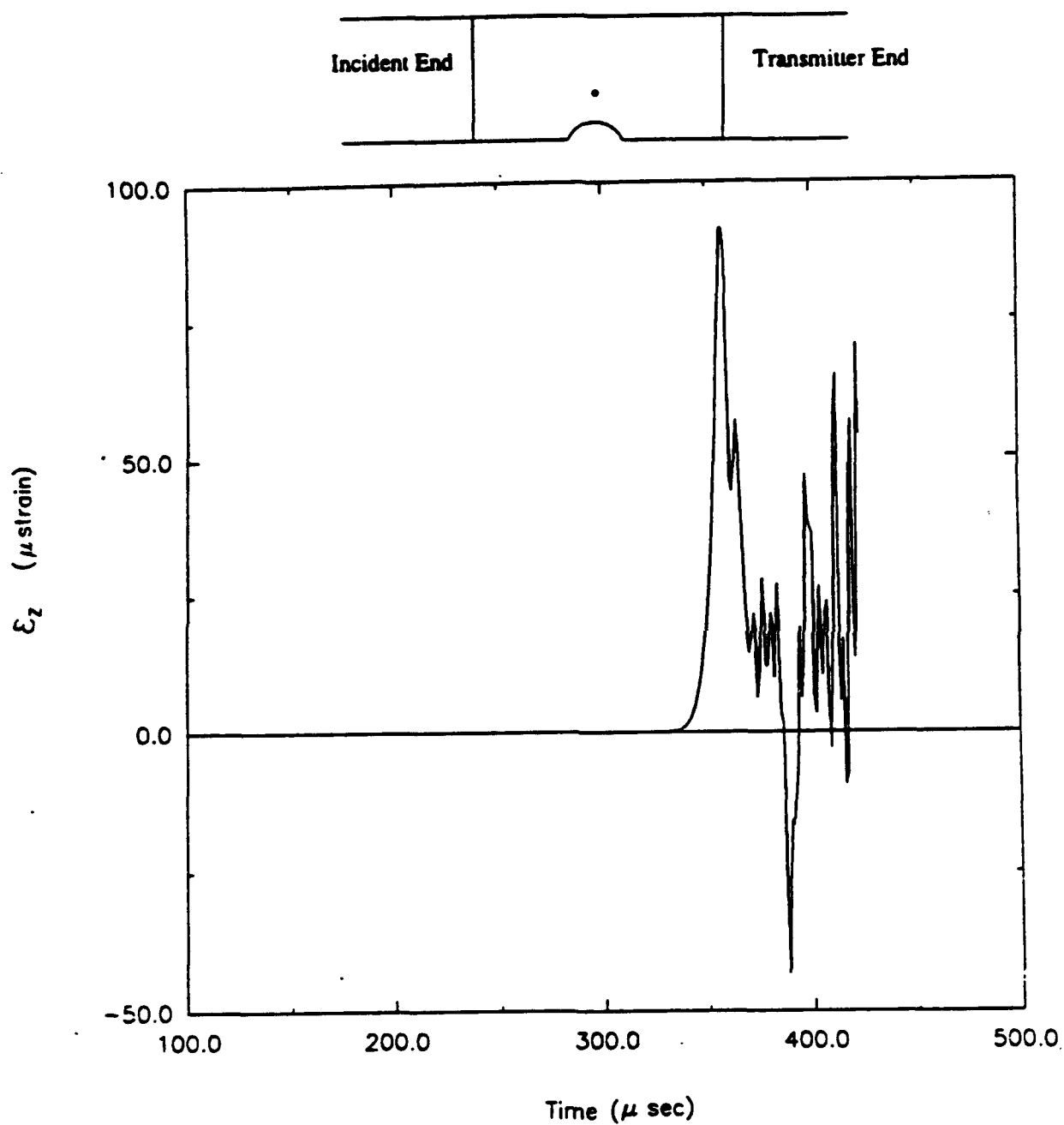


Figure 133. Time history for longitudinal strain (saddle-notch, Load Case 3).

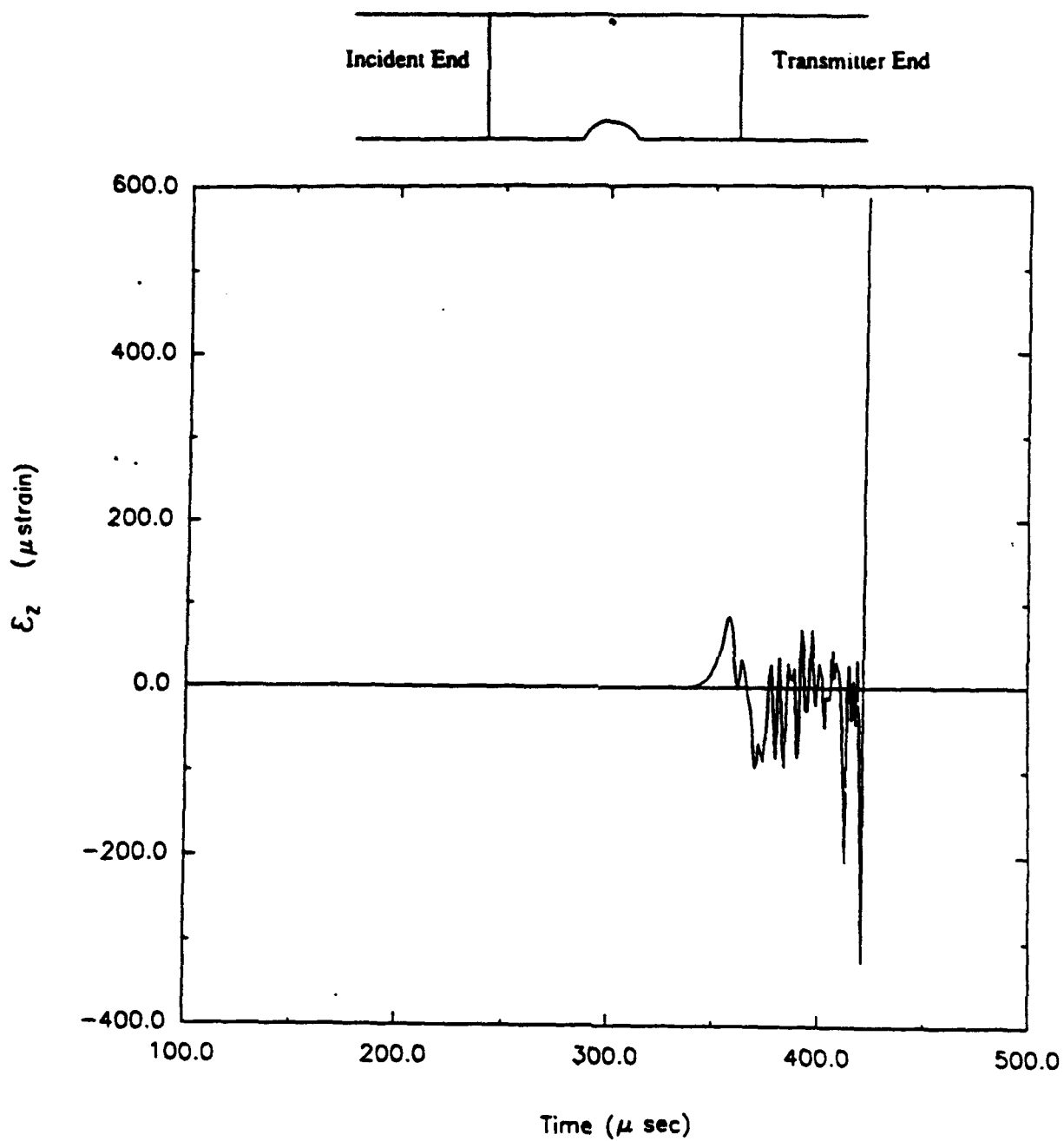


Figure 134. Time history for longitudinal strain (saddle-notch, Load Case 3).

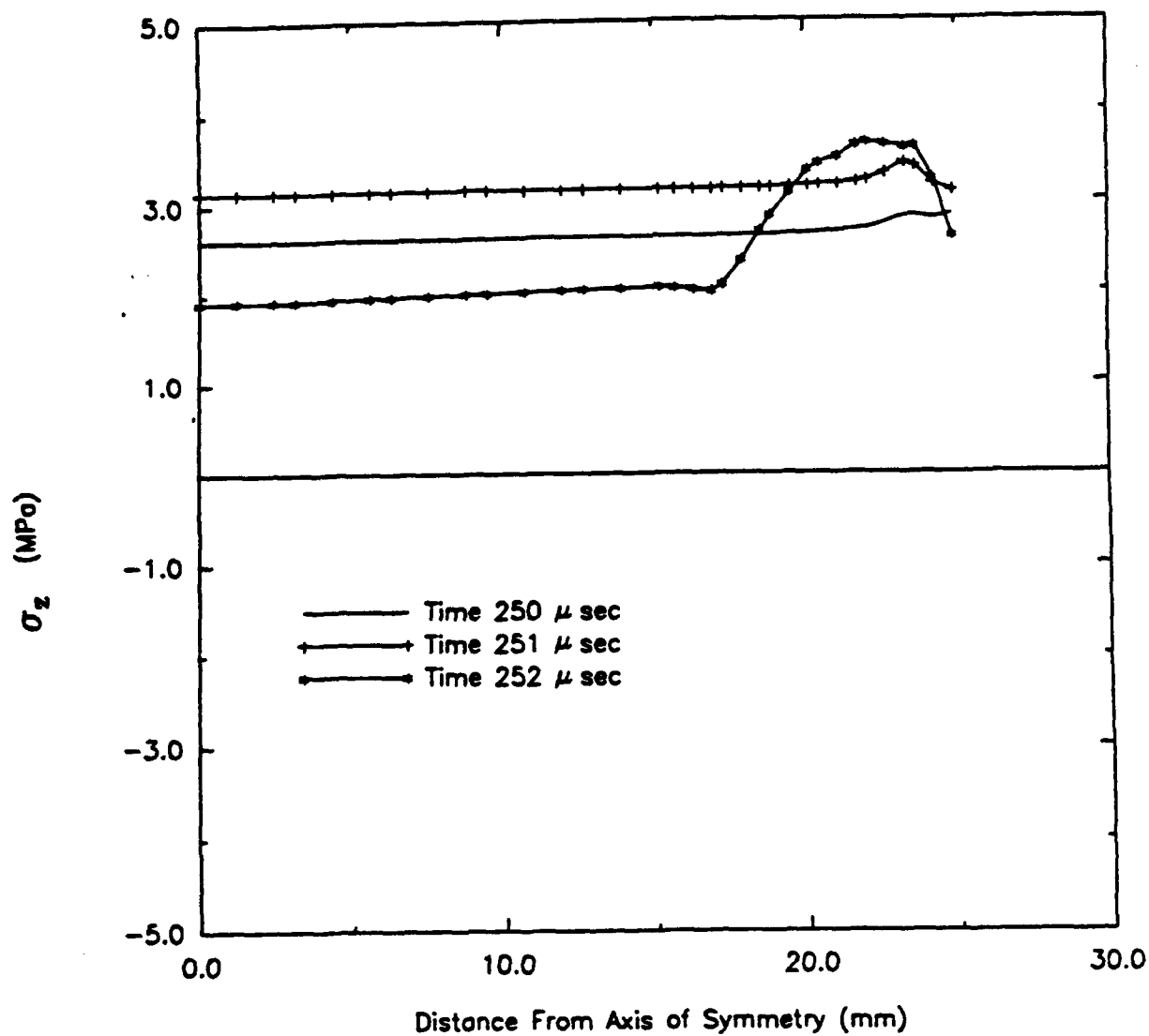
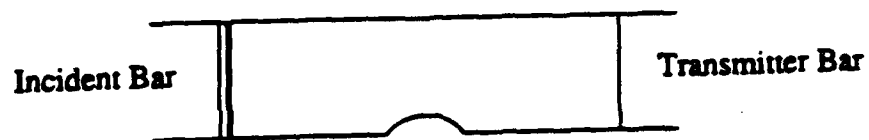


Figure 135. Profiles for longitudinal stress (saddle-notch, Load Case 3).

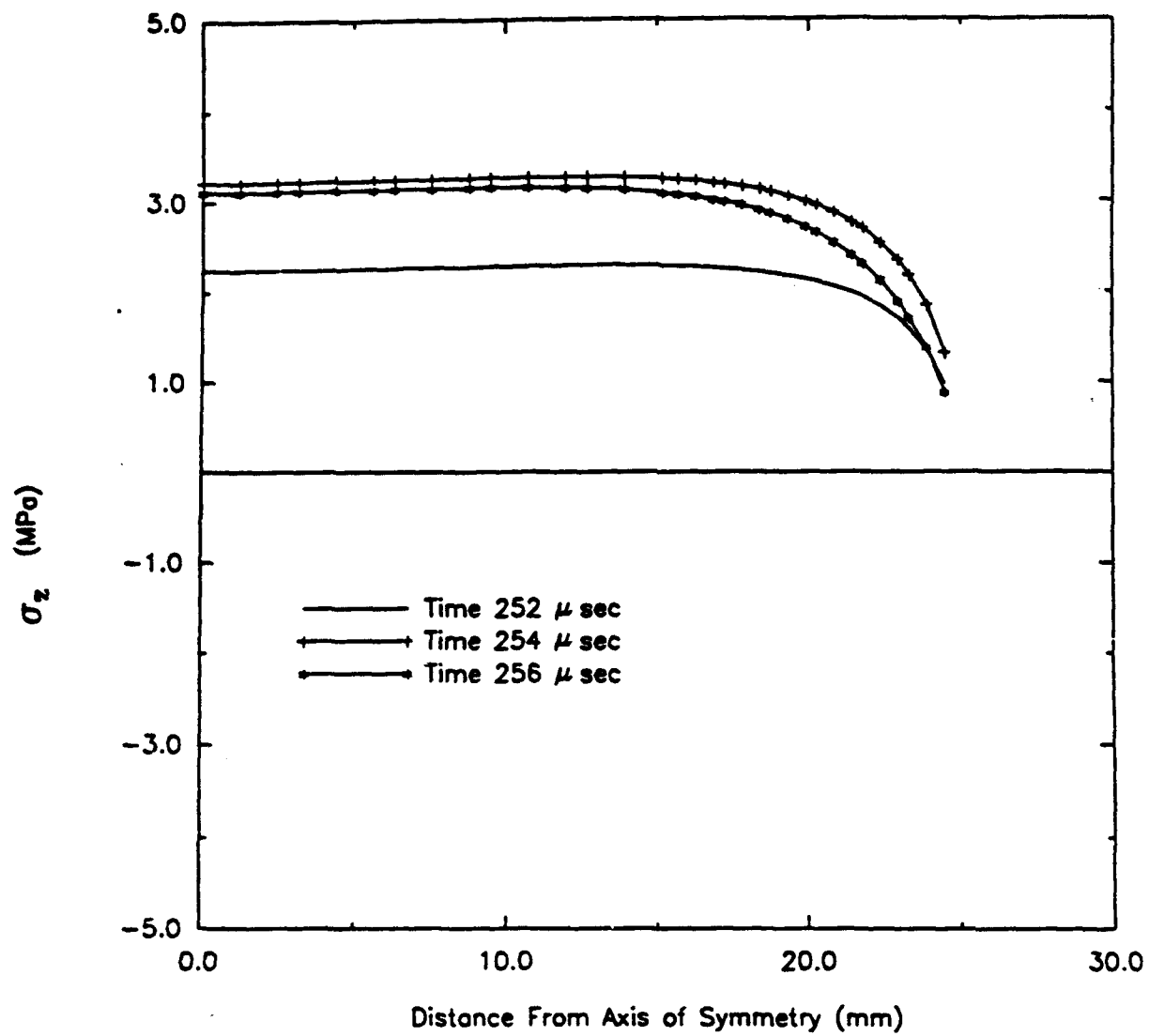


Figure 136. Profiles for longitudinal stress (saddle-notch, Load Case 3).

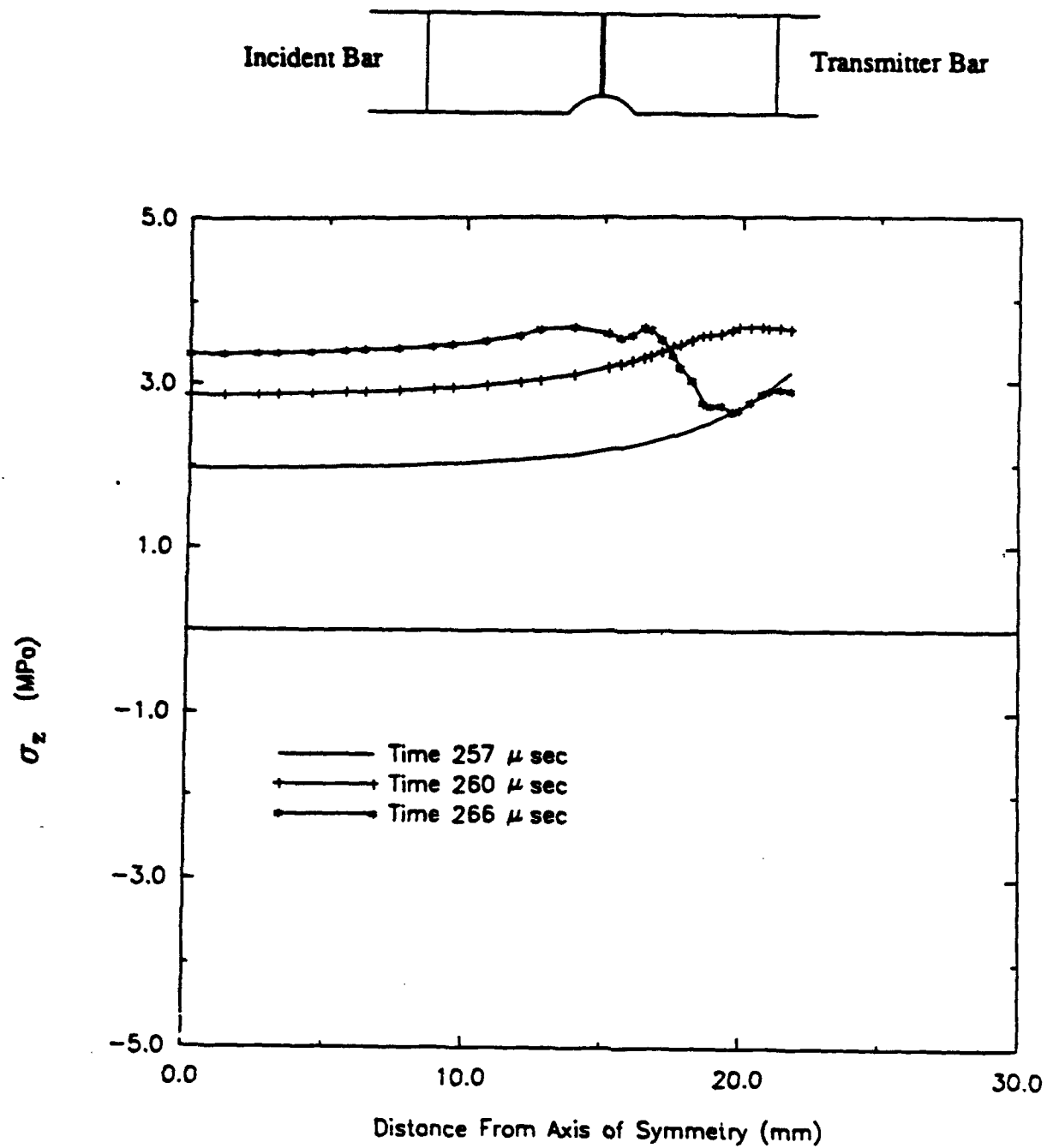


Figure 137. Profiles for longitudinal stress (saddle-notch, Load Case 3).

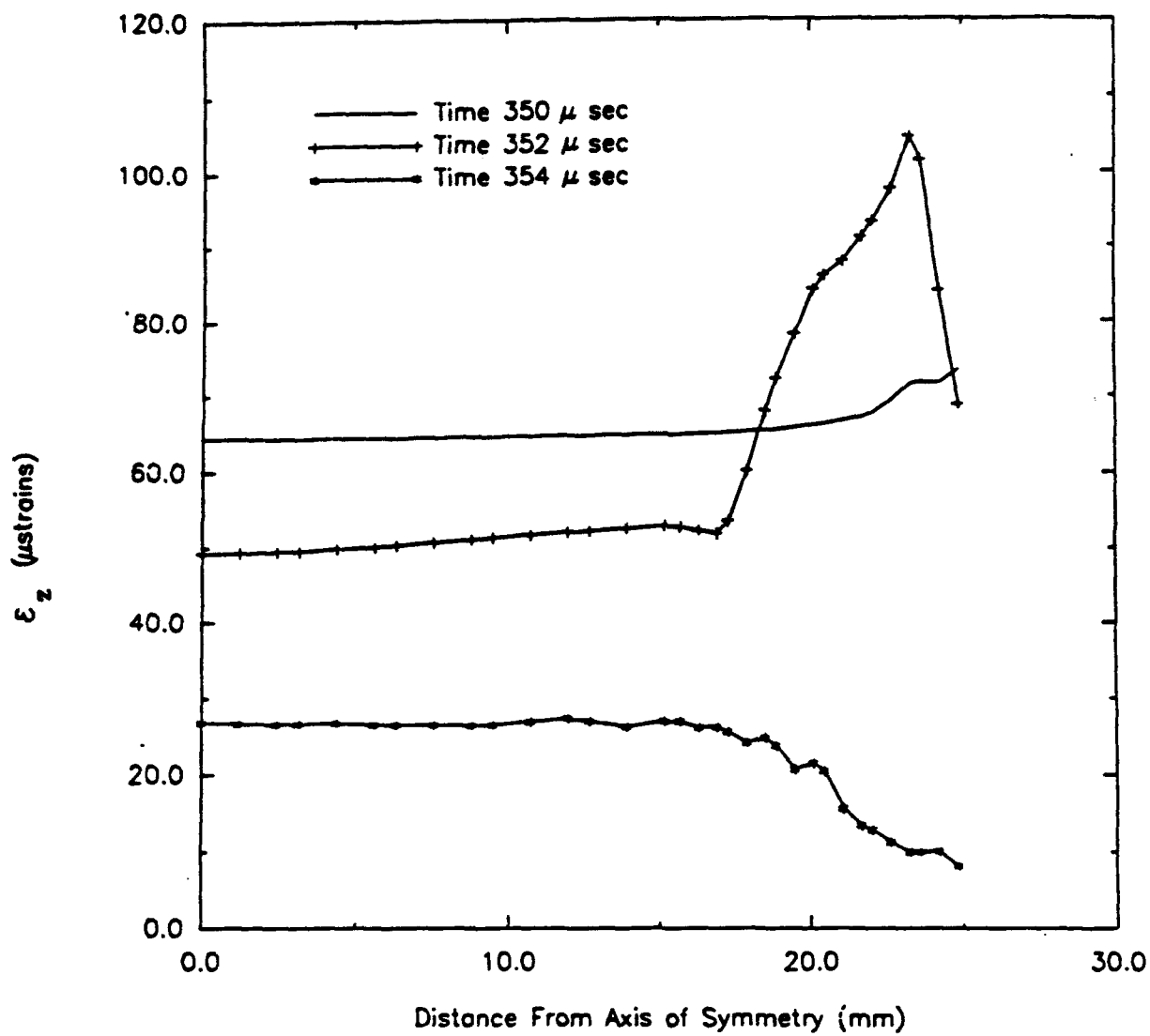
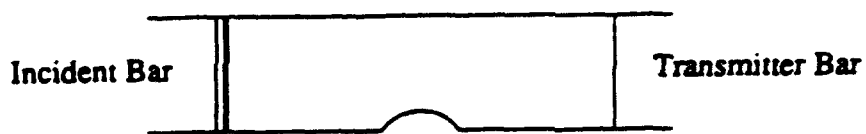


Figure 138. Profiles for longitudinal strain (saddle-notch, Load Case 3).

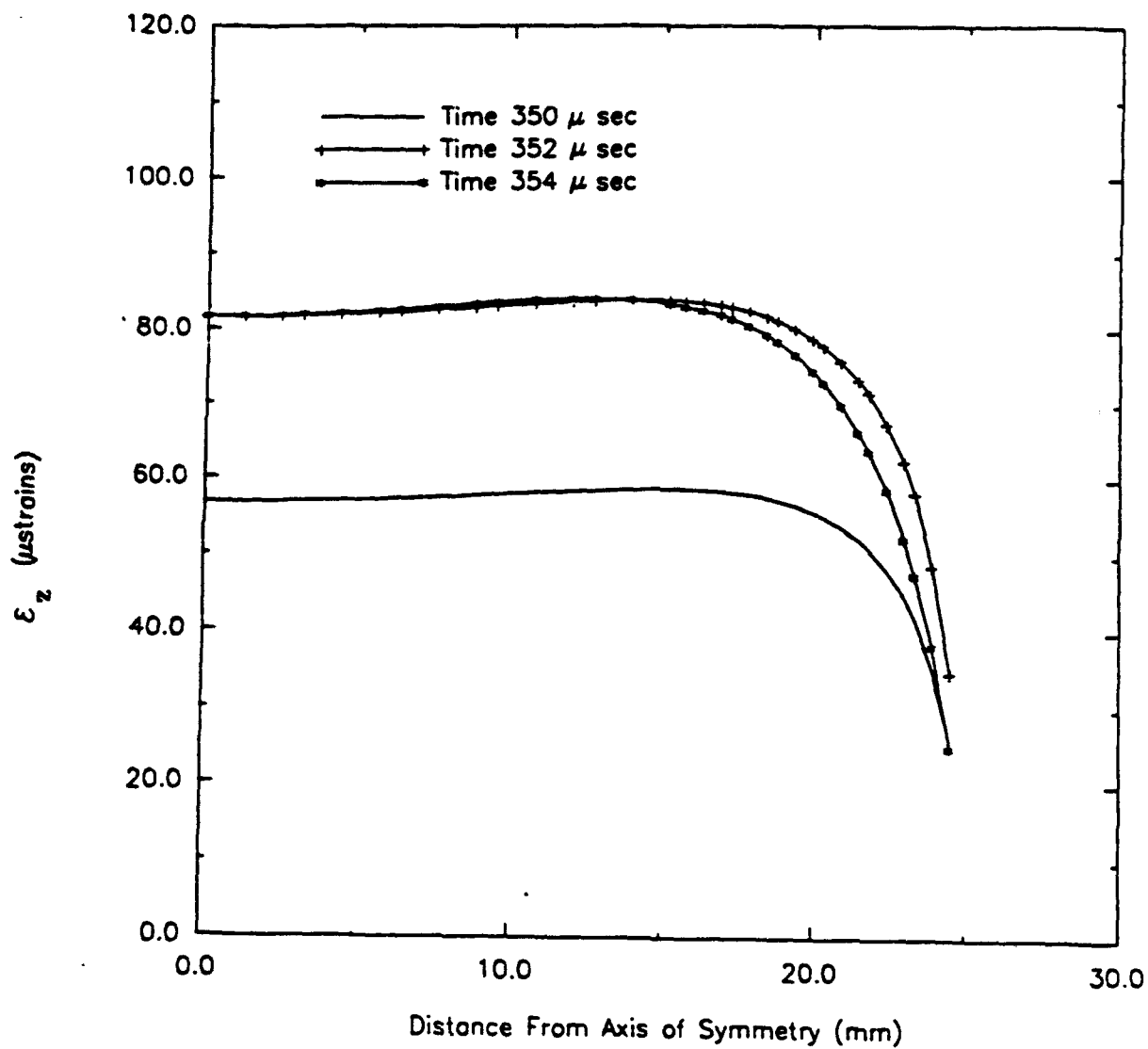
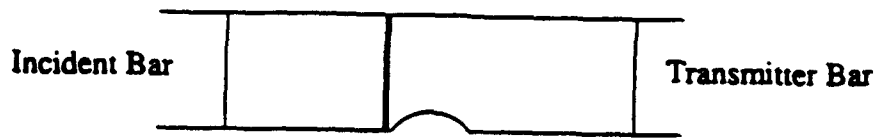


Figure 139. Profiles for longitudinal strain (saddle-notch, Load Case 3).

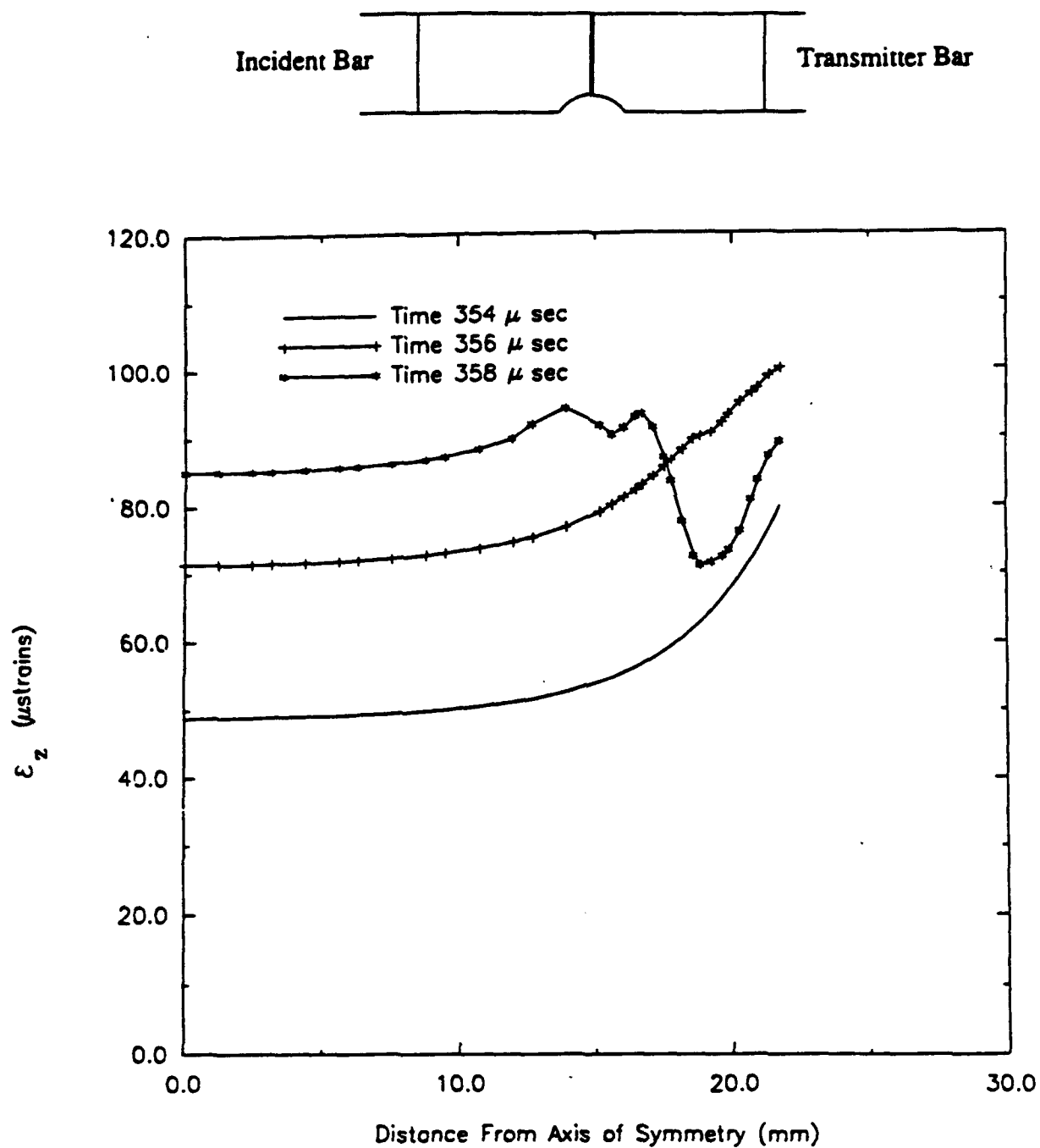
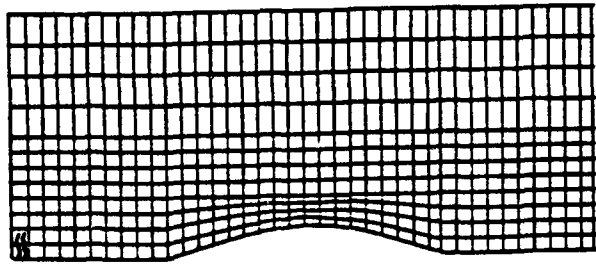
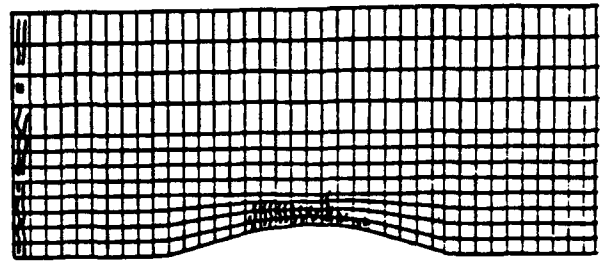


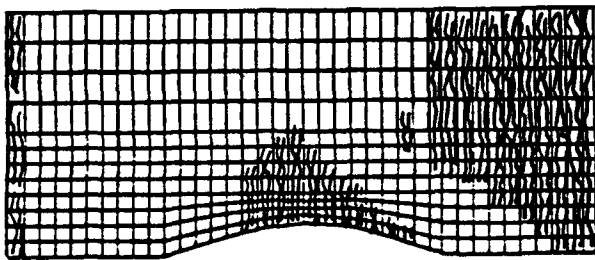
Figure 140. Profiles for longitudinal strain (saddle-notch, Load Case 3).



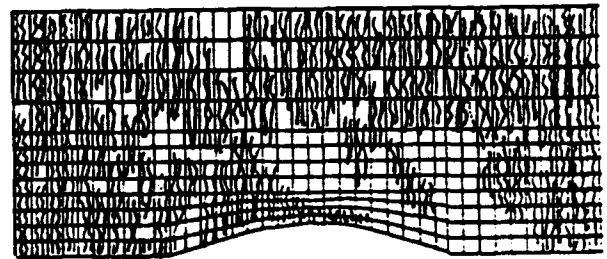
(a)



(b)



(c)



(d)

Figure 141. Cracking sequence for saddle-notch specimen; Load Case 3:
a) $t=351 \mu \text{ sec}$, b) $t=355 \mu \text{ sec}$, c) $t=363 \mu \text{ sec}$, d) $t=444 \mu \text{ sec}$.

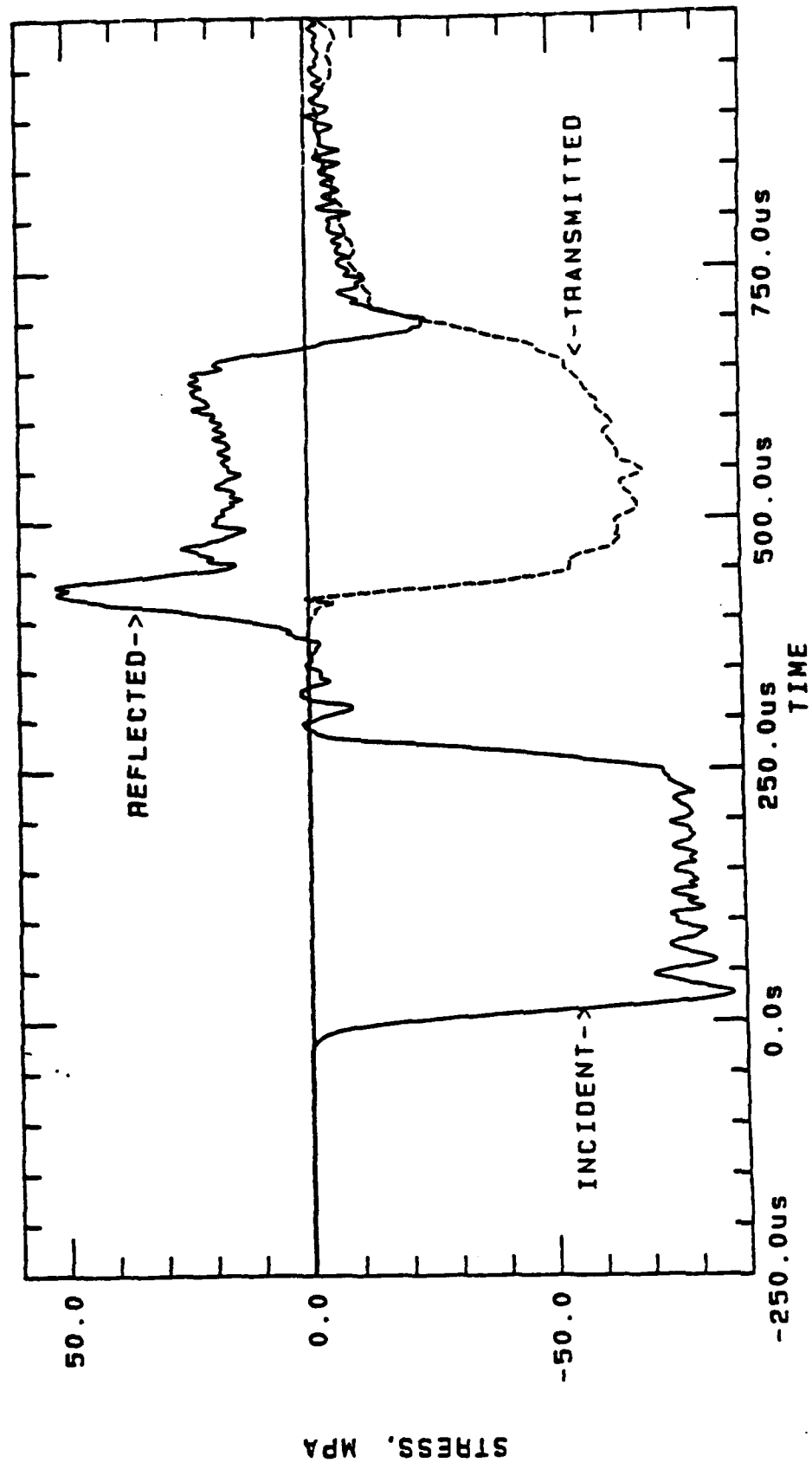


Figure 142. Direct compression test data trace for Load Case 1.

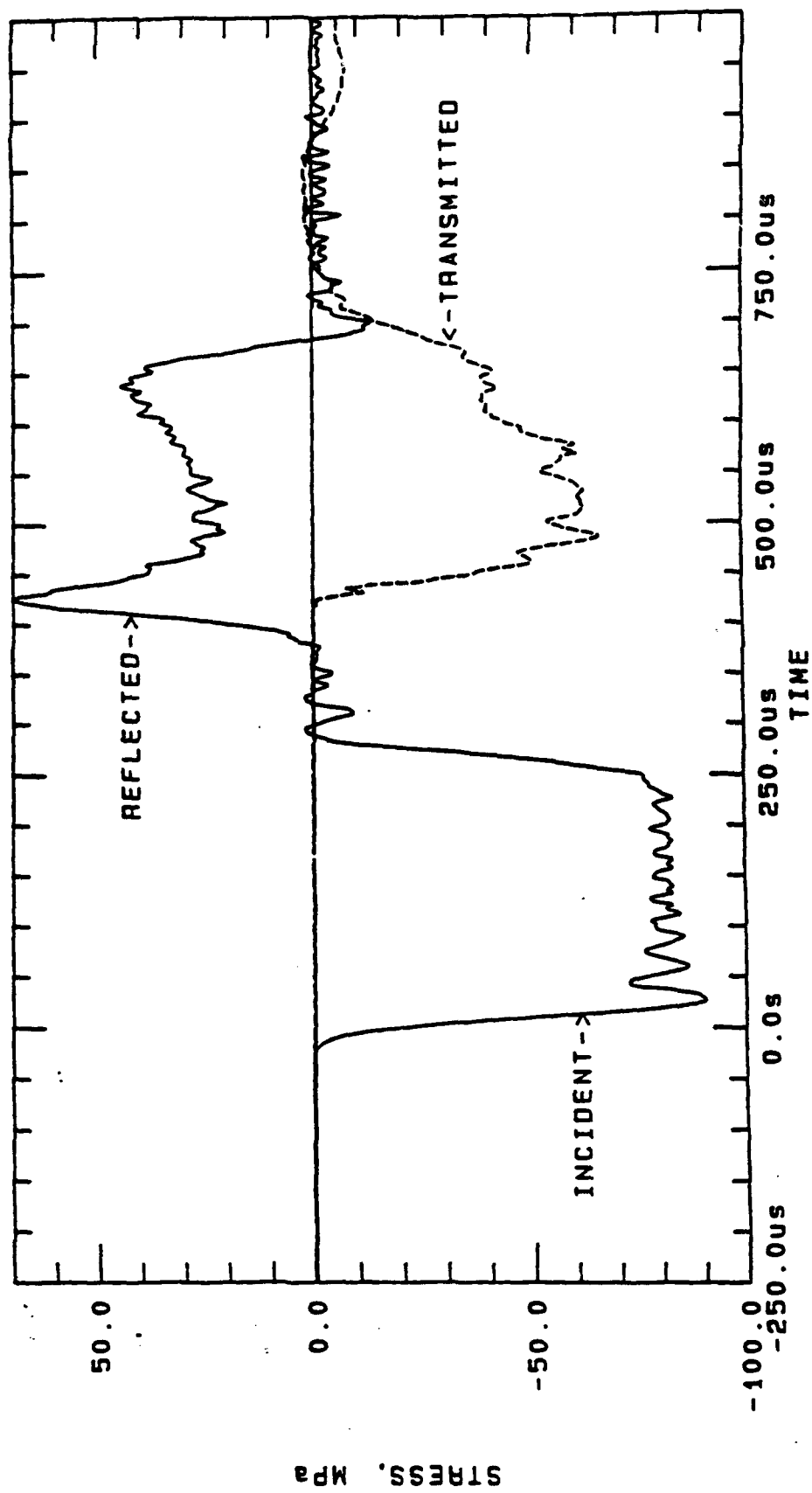


Figure 143. Direct compression test data trace for Load Case 2.

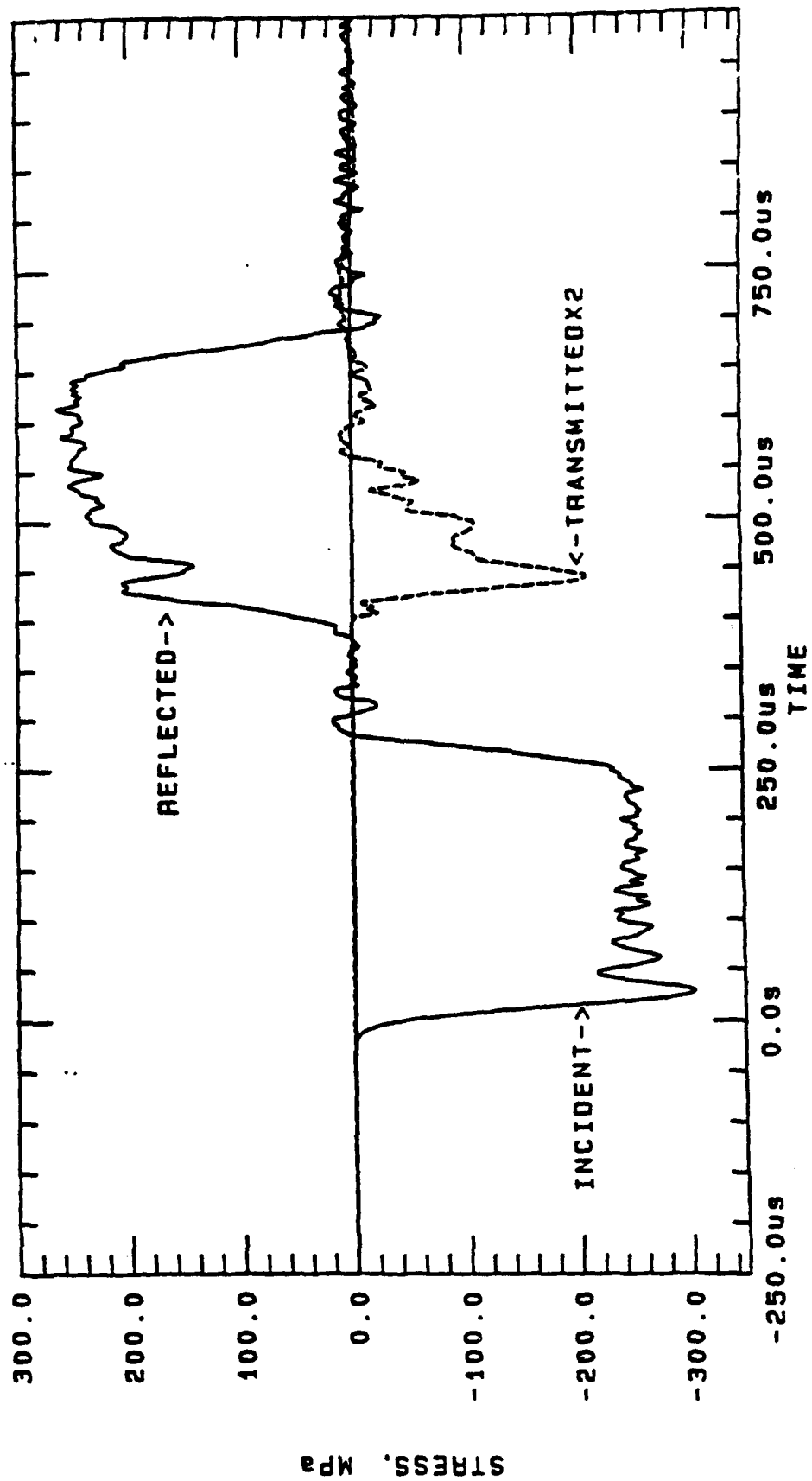


Figure 144. Direct compression test data trace for Load Case 3.

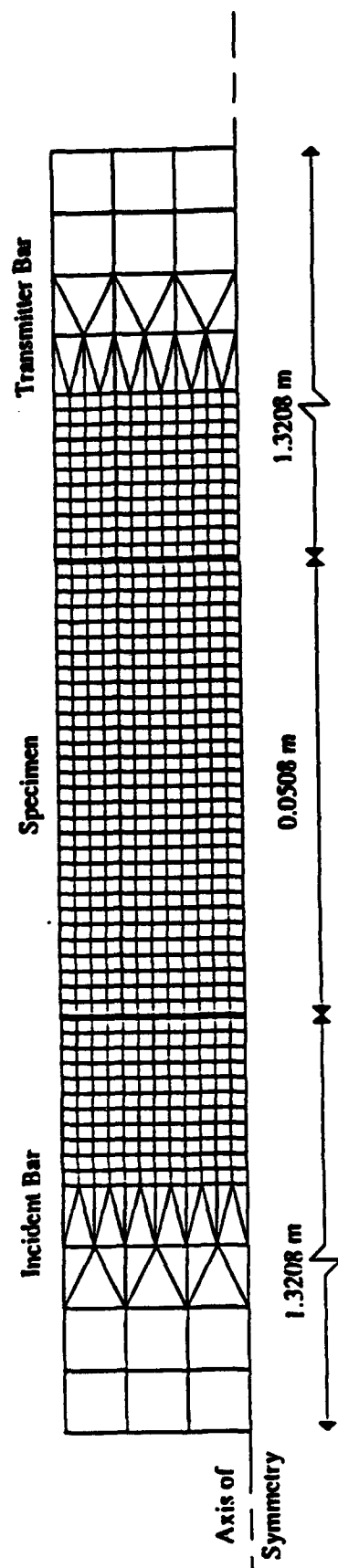
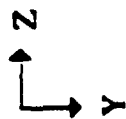


Figure 145. FEM model of direct compression specimen and portion of SHPB.

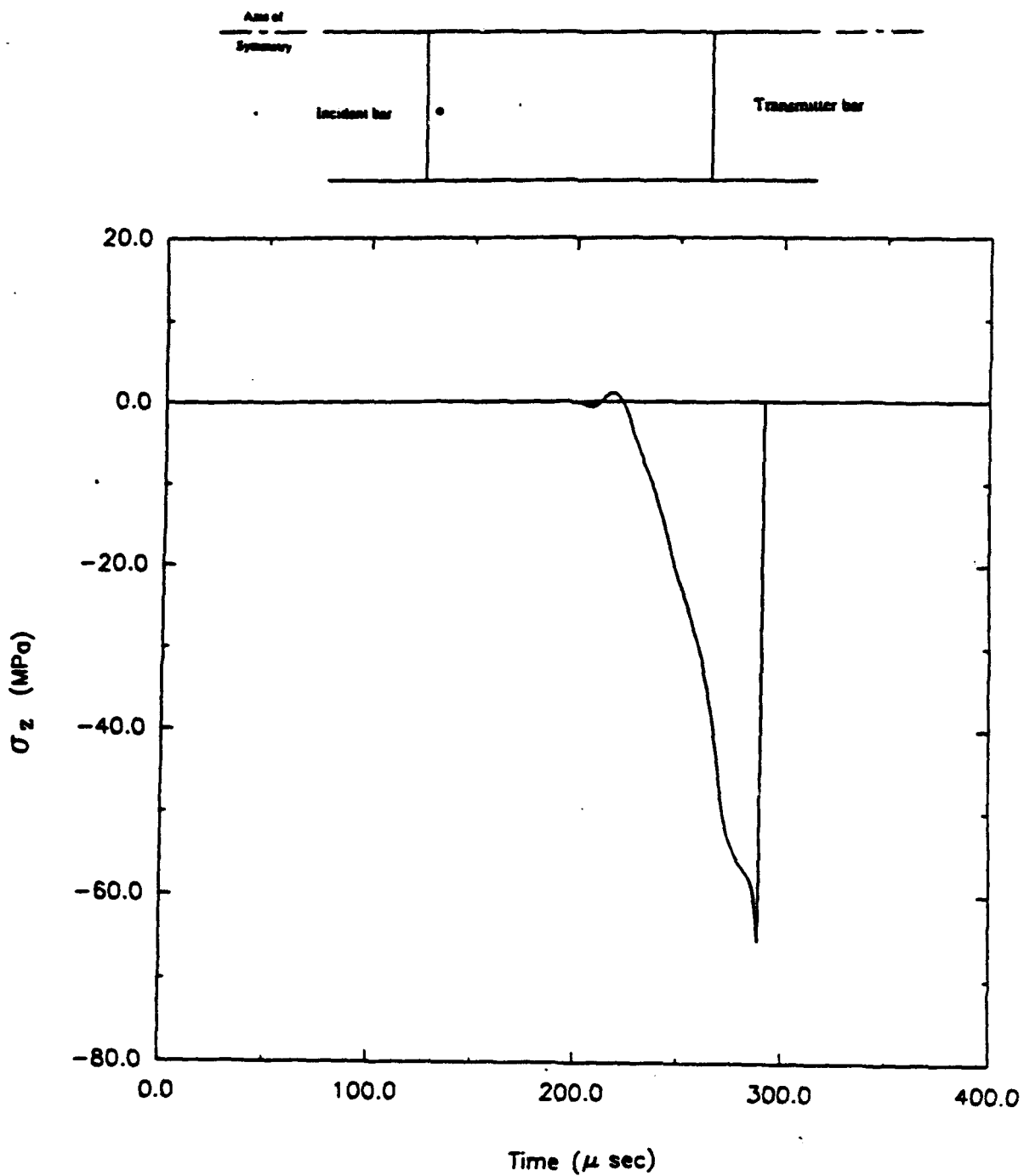


Figure 146. Time history for longitudinal stress (direct compression, Load Case 1).

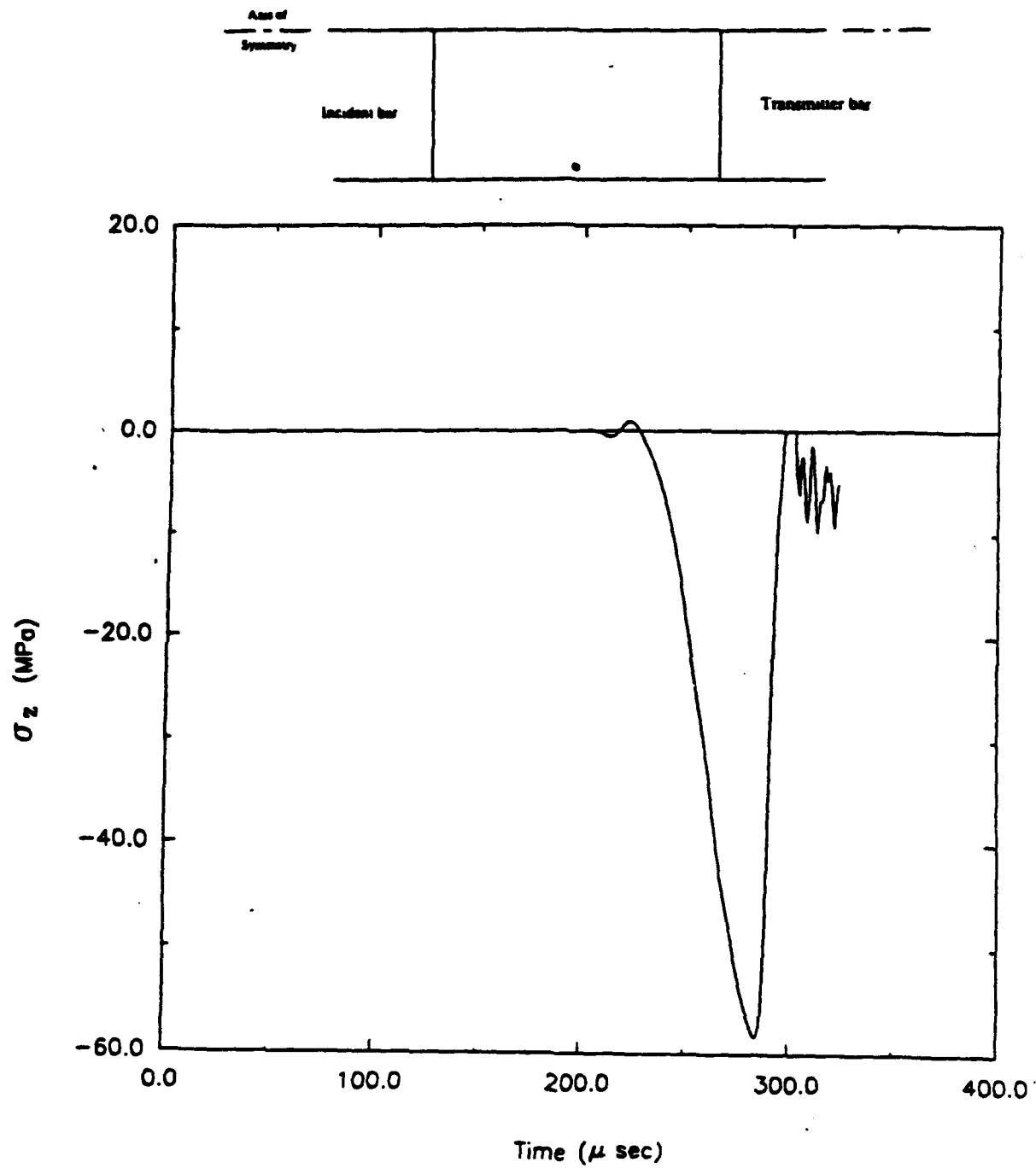


Figure 147. Time history for longitudinal stress (direct compression, Load Case 1).

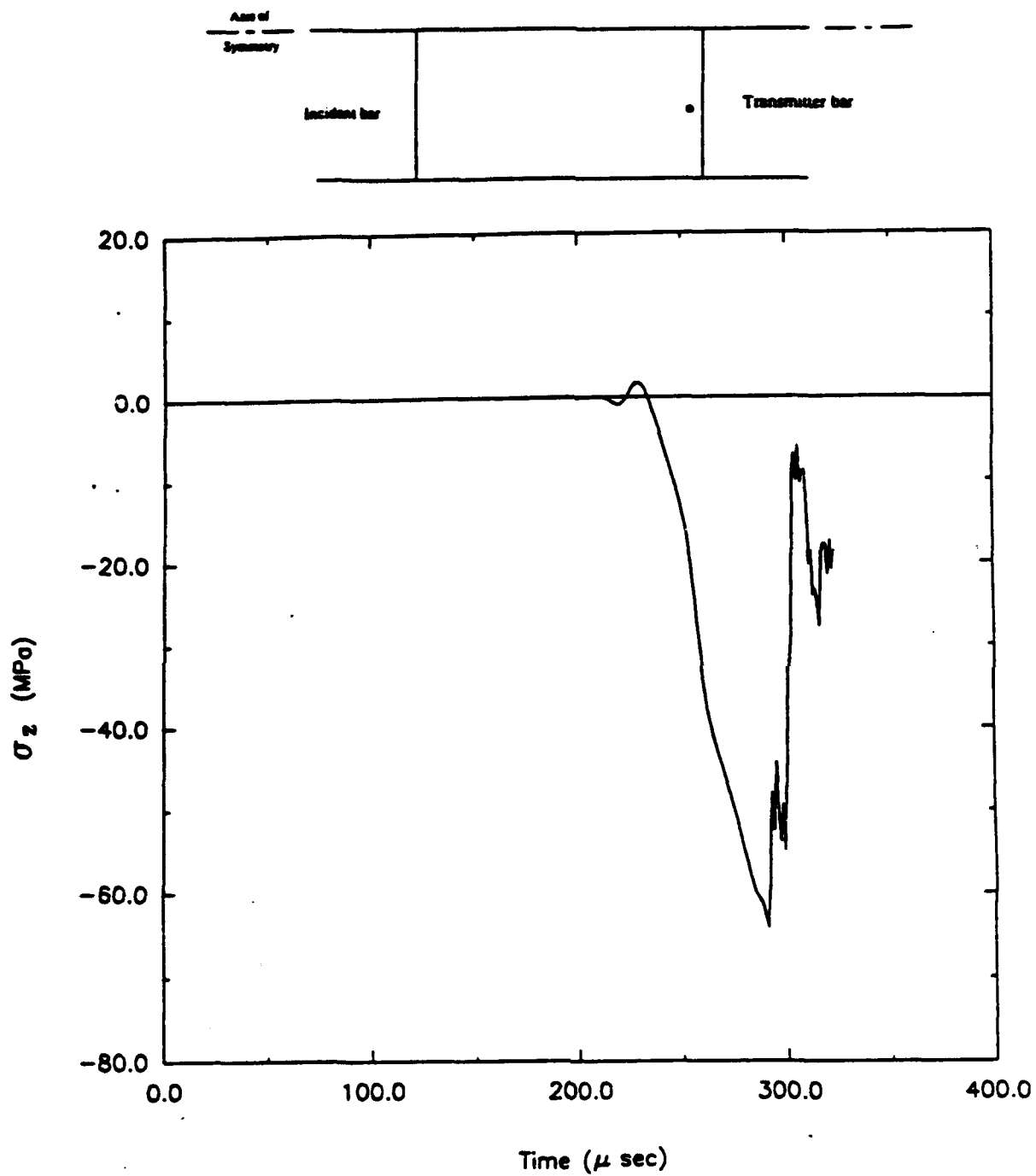


Figure 148. Time history for longitudinal stress (direct compression, Load Case 1).

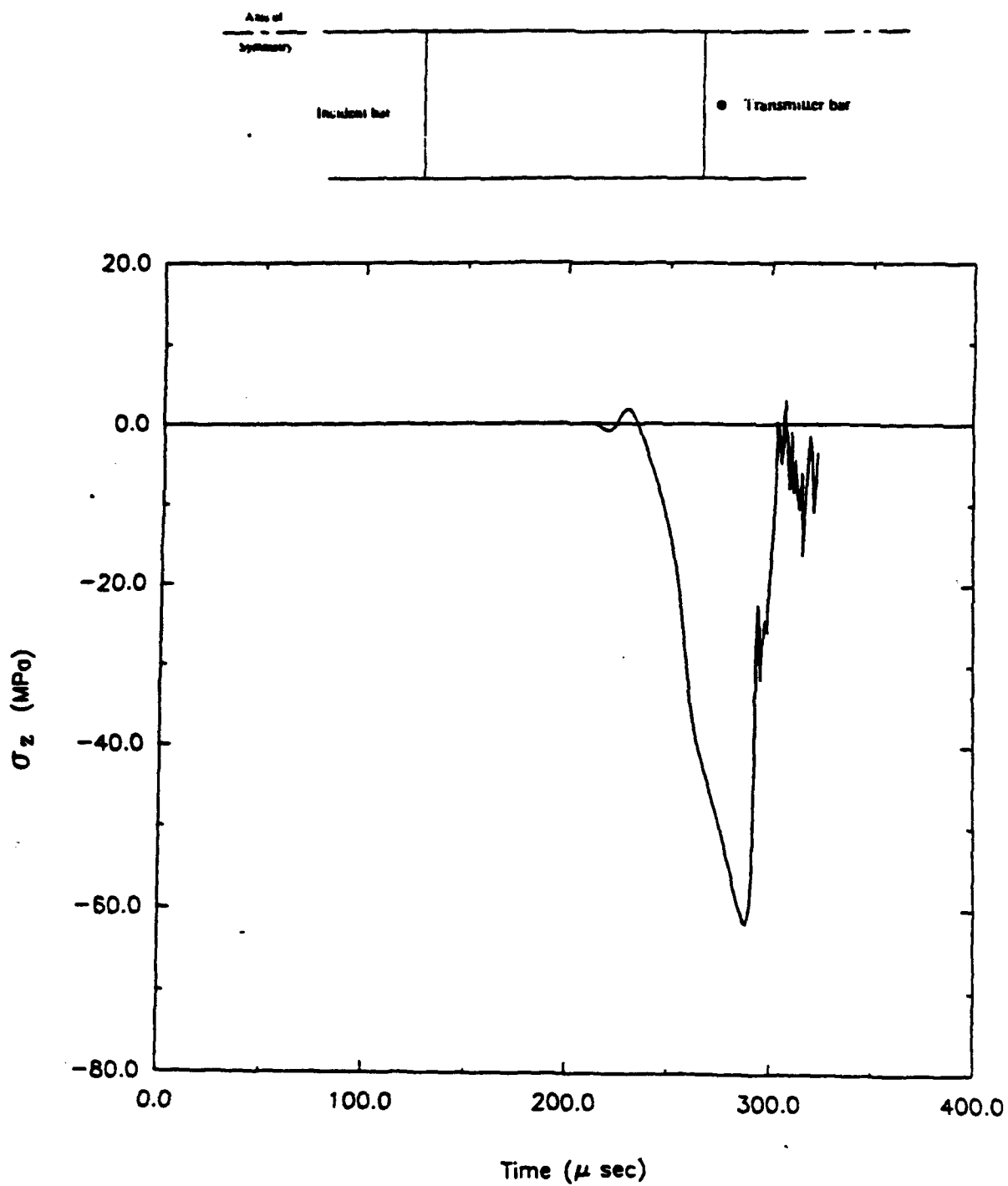


Figure 149. Time history for longitudinal stress (direct compression, Load Case 1).

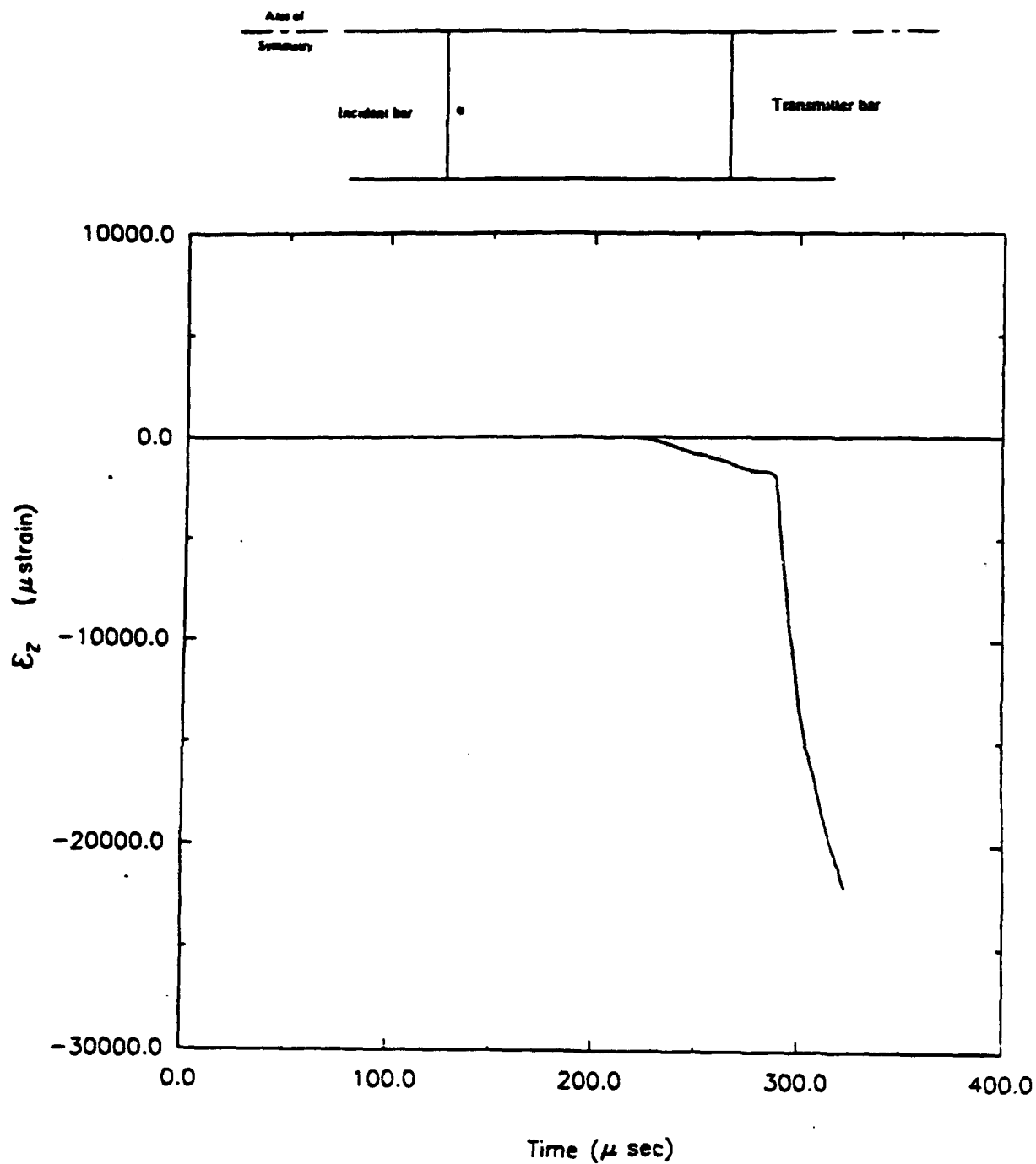


Figure 150. Time history for longitudinal strain (direct compression, Load Case 1).

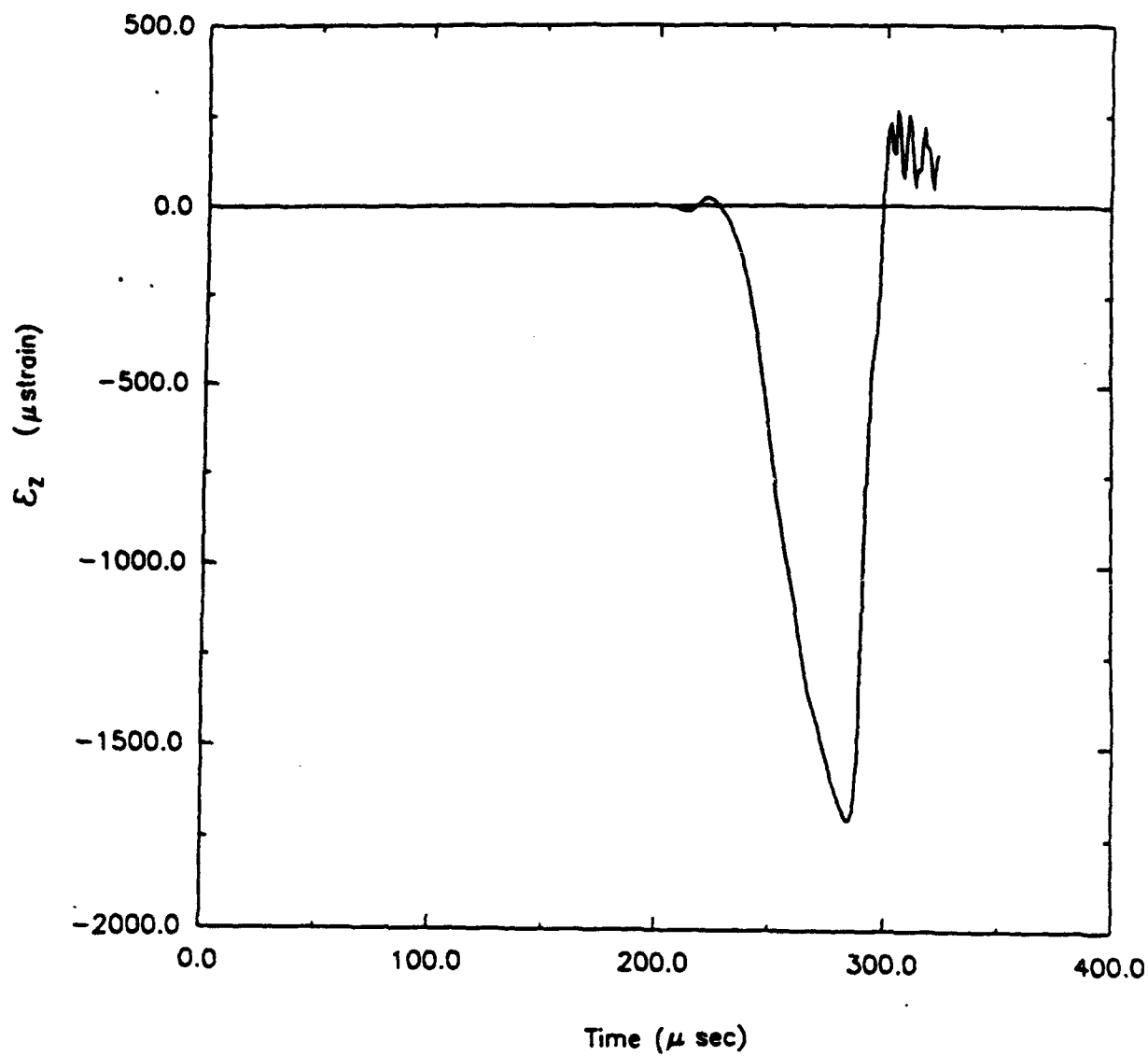
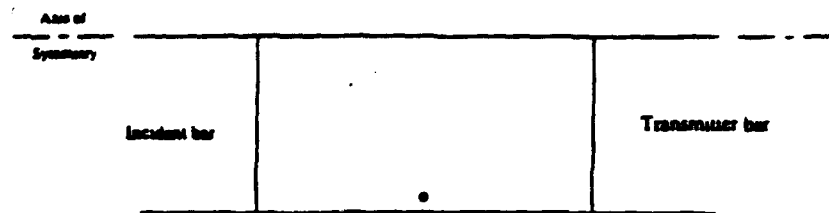


Figure 151. Time history for longitudinal strain (direct compression, Load Case 1).

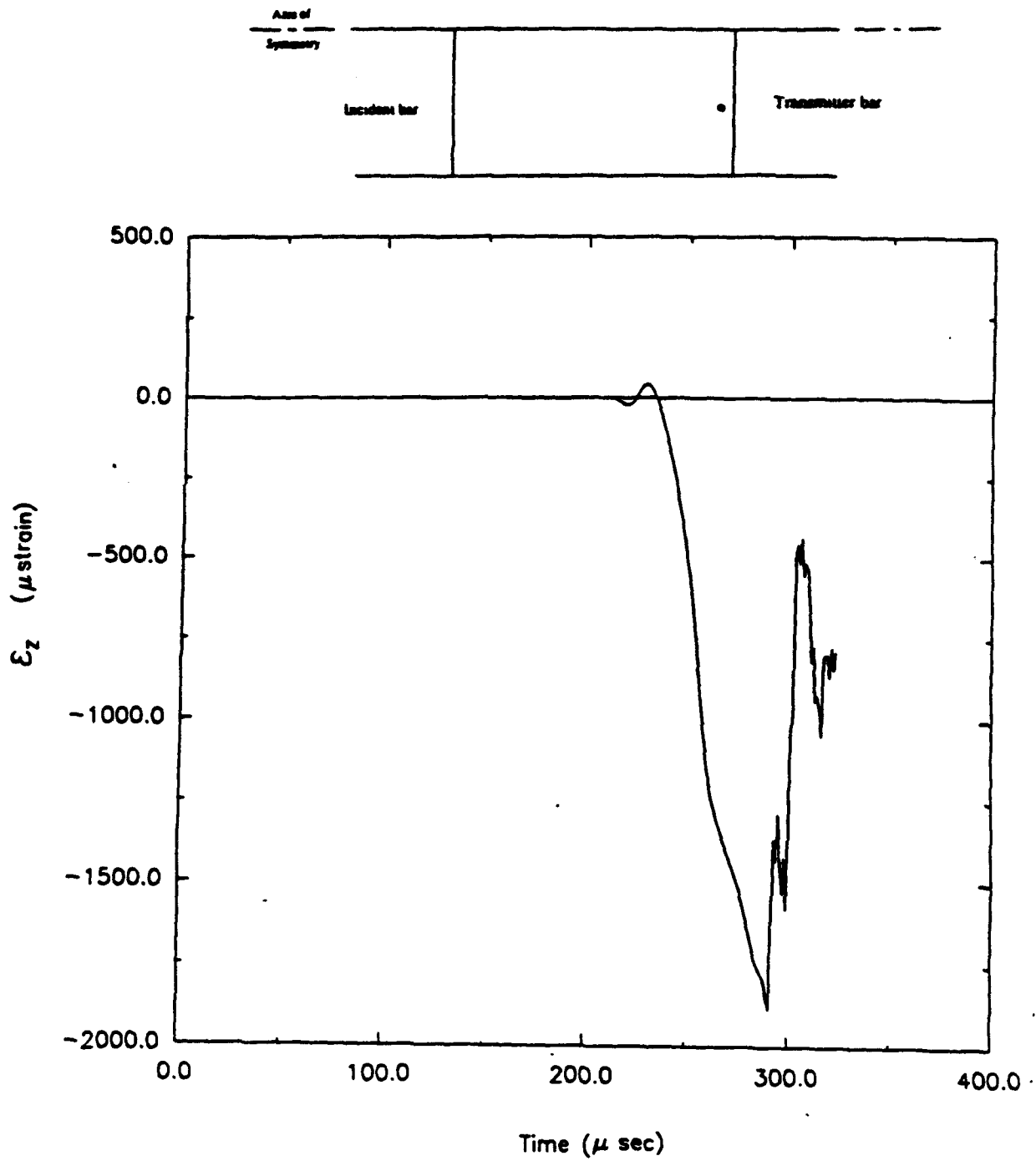


Figure 152. Time history for longitudinal strain (direct compression, Load Case 1).

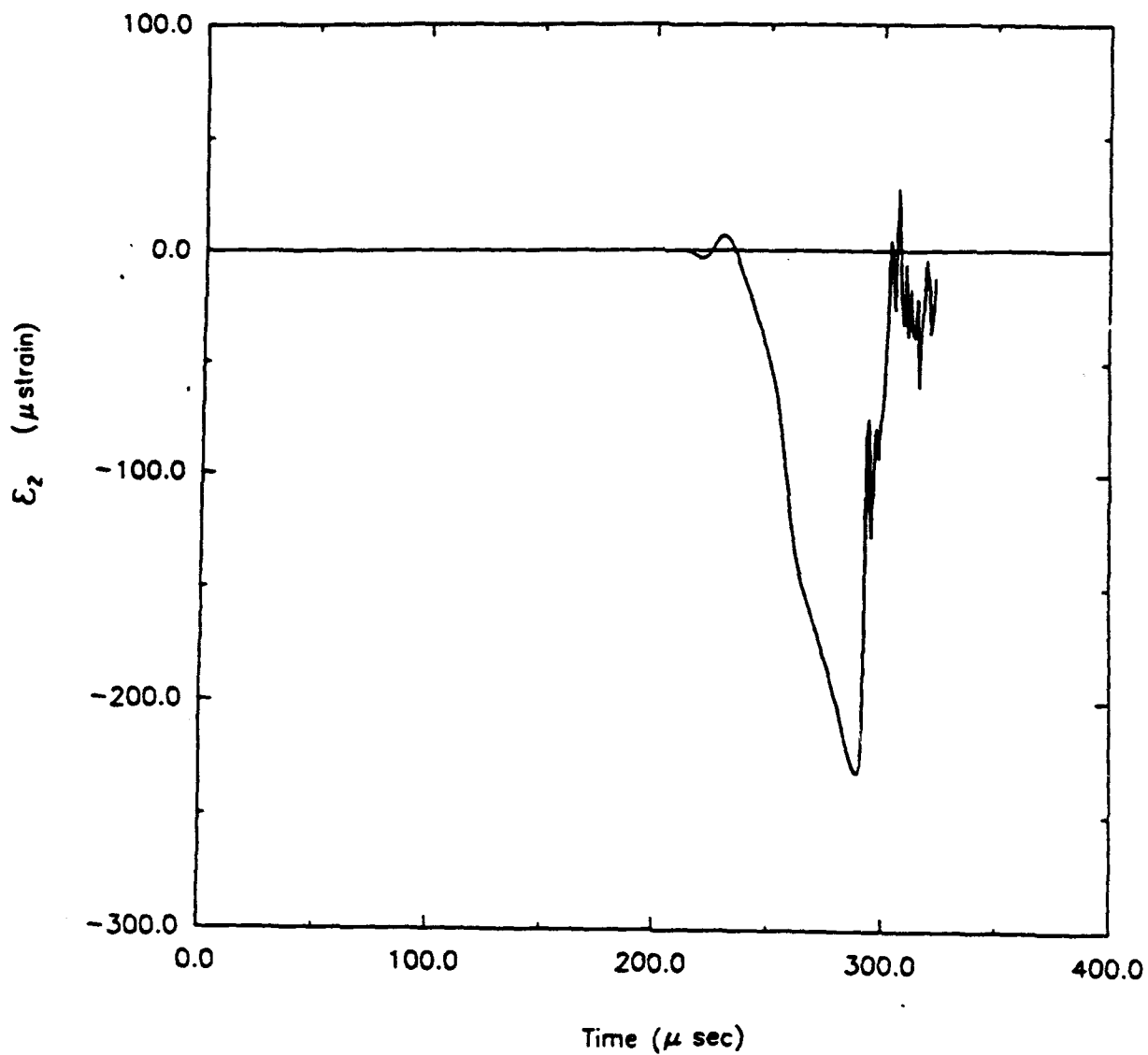
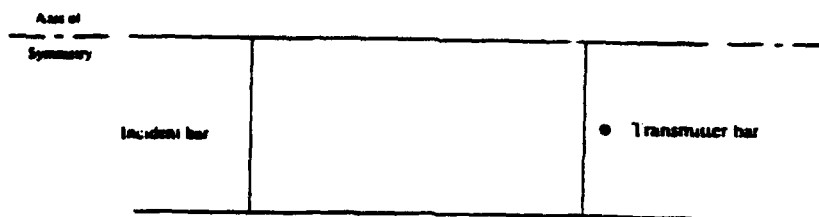


Figure 153. Time history for longitudinal strain (direct compression, Load Case 1).

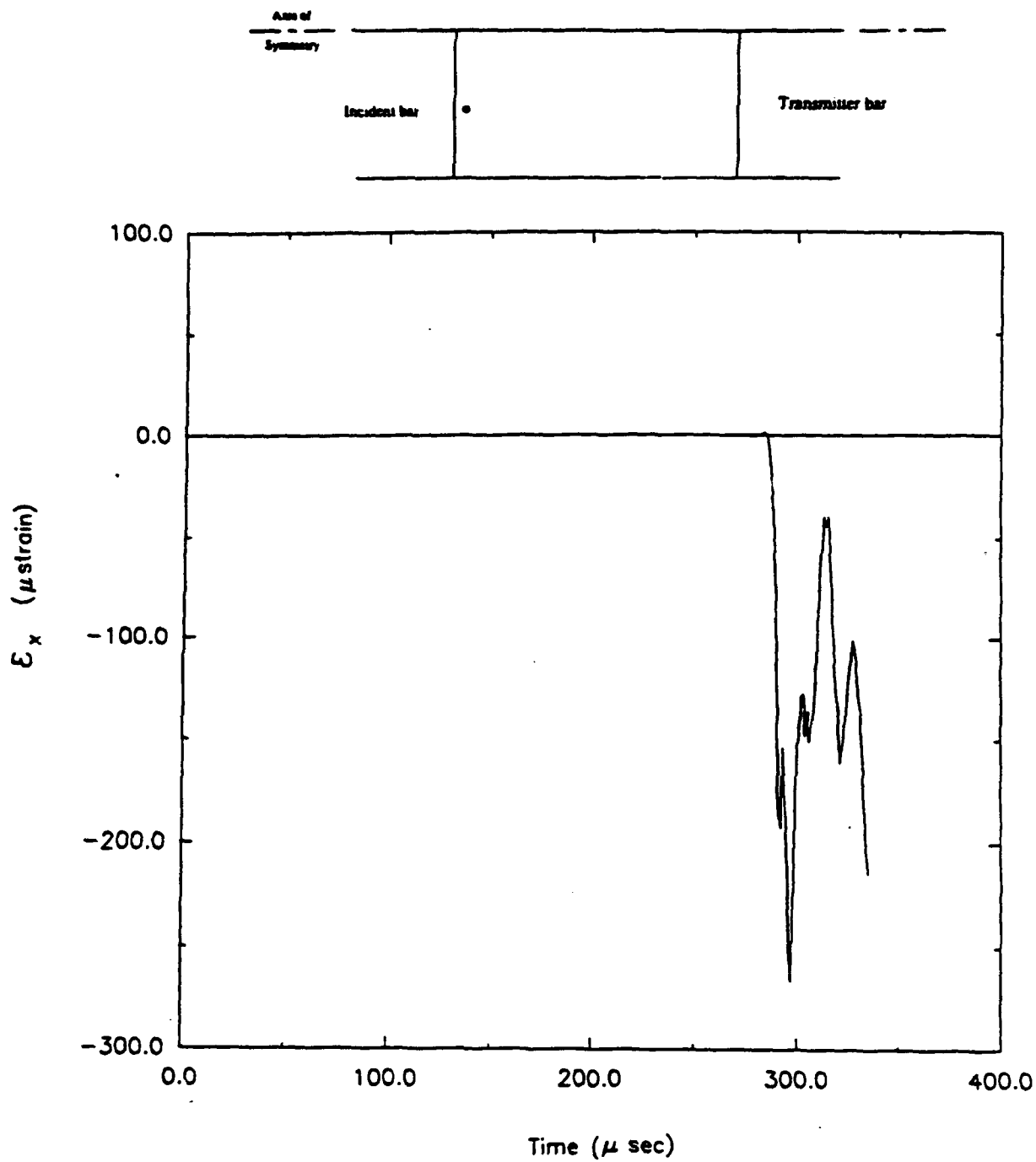


Figure 154. Time history for circumferential strain (direct compression, Load Case 1).

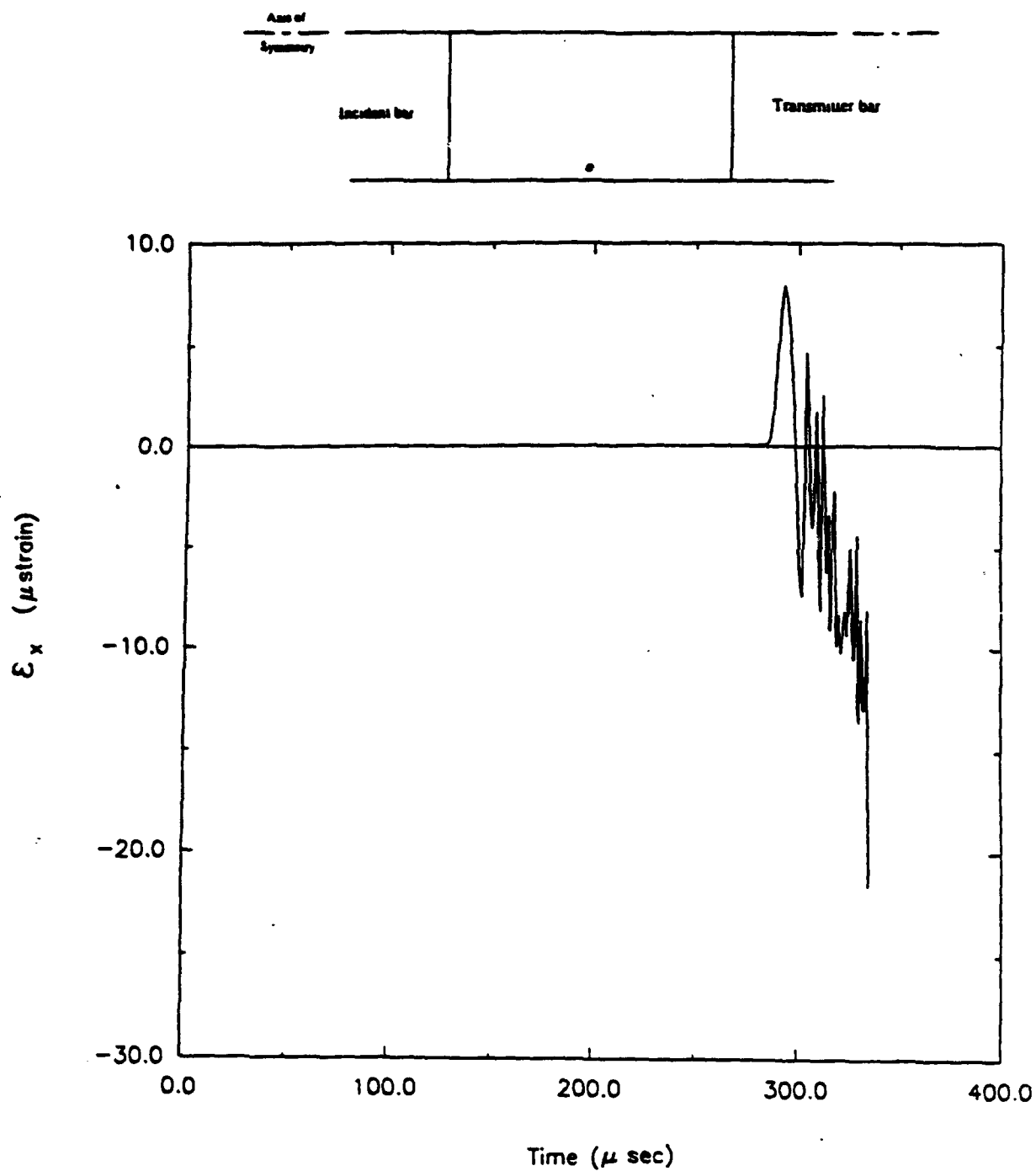


Figure 155. Time history for circumferential strain (direct compression, Load Case 1).

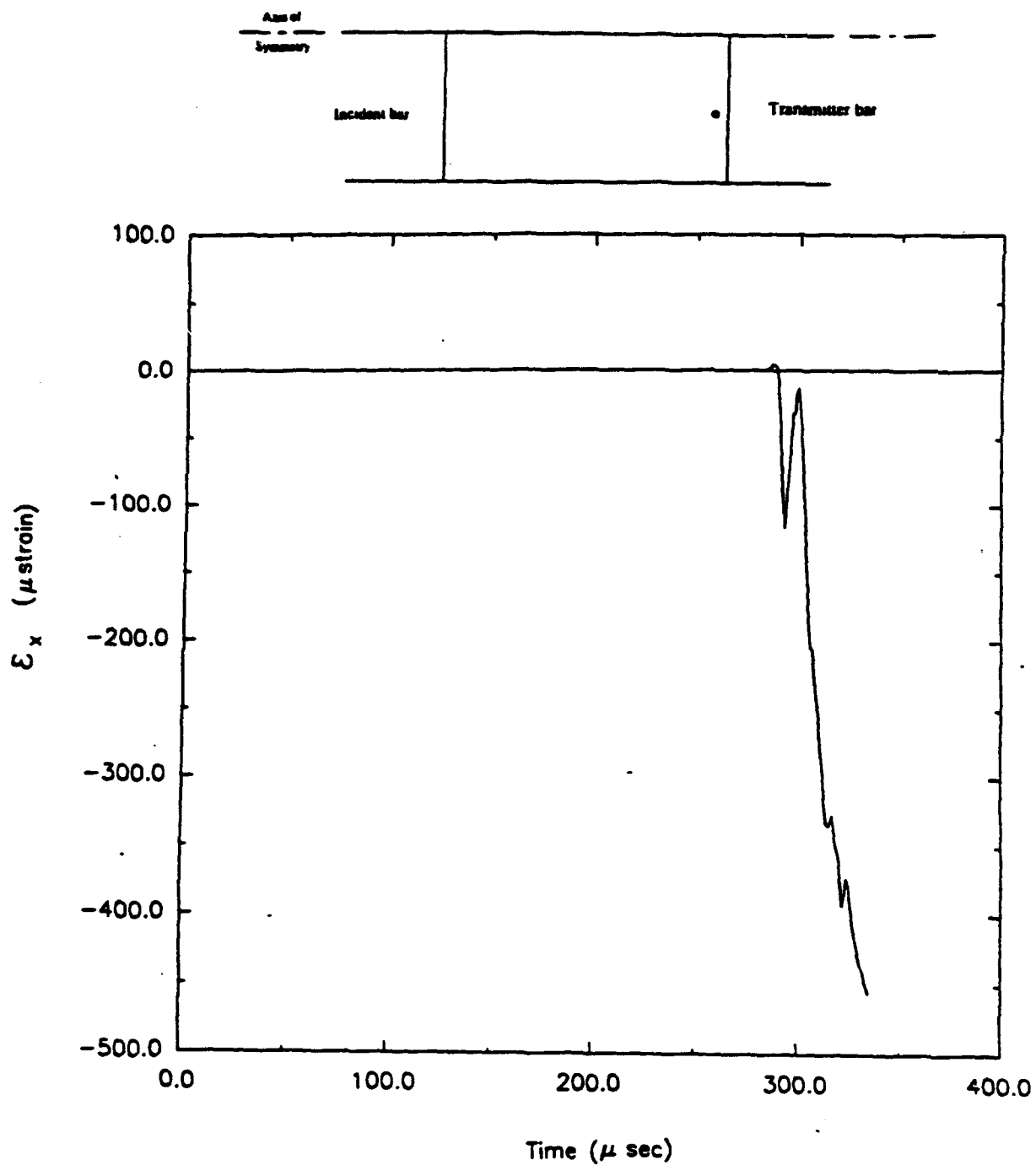


Figure 156. Time history for circumferential strain (direct compression, Load Case 1).

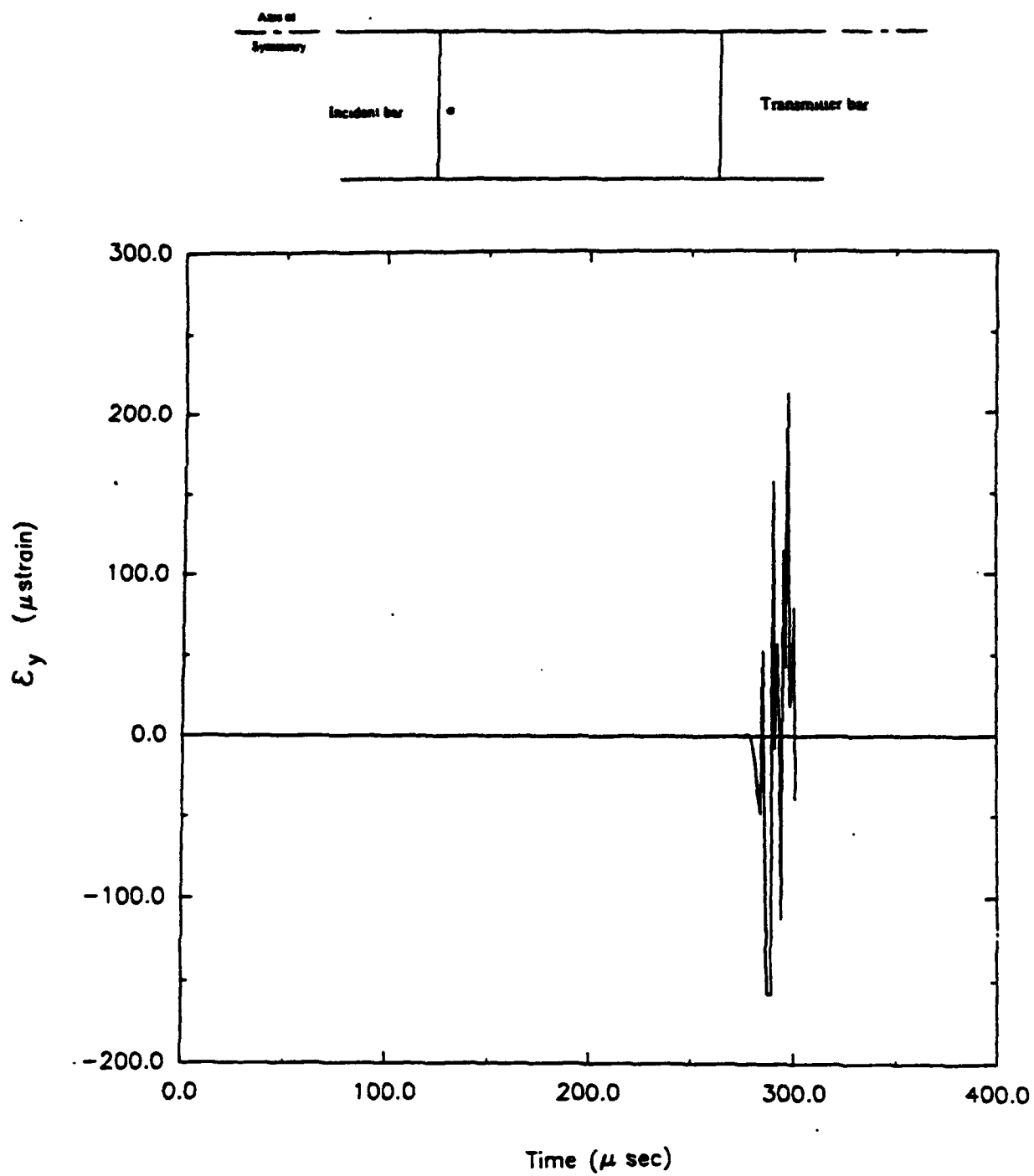


Figure 157. Time history for radial strain (direct compression, Load Case 1).

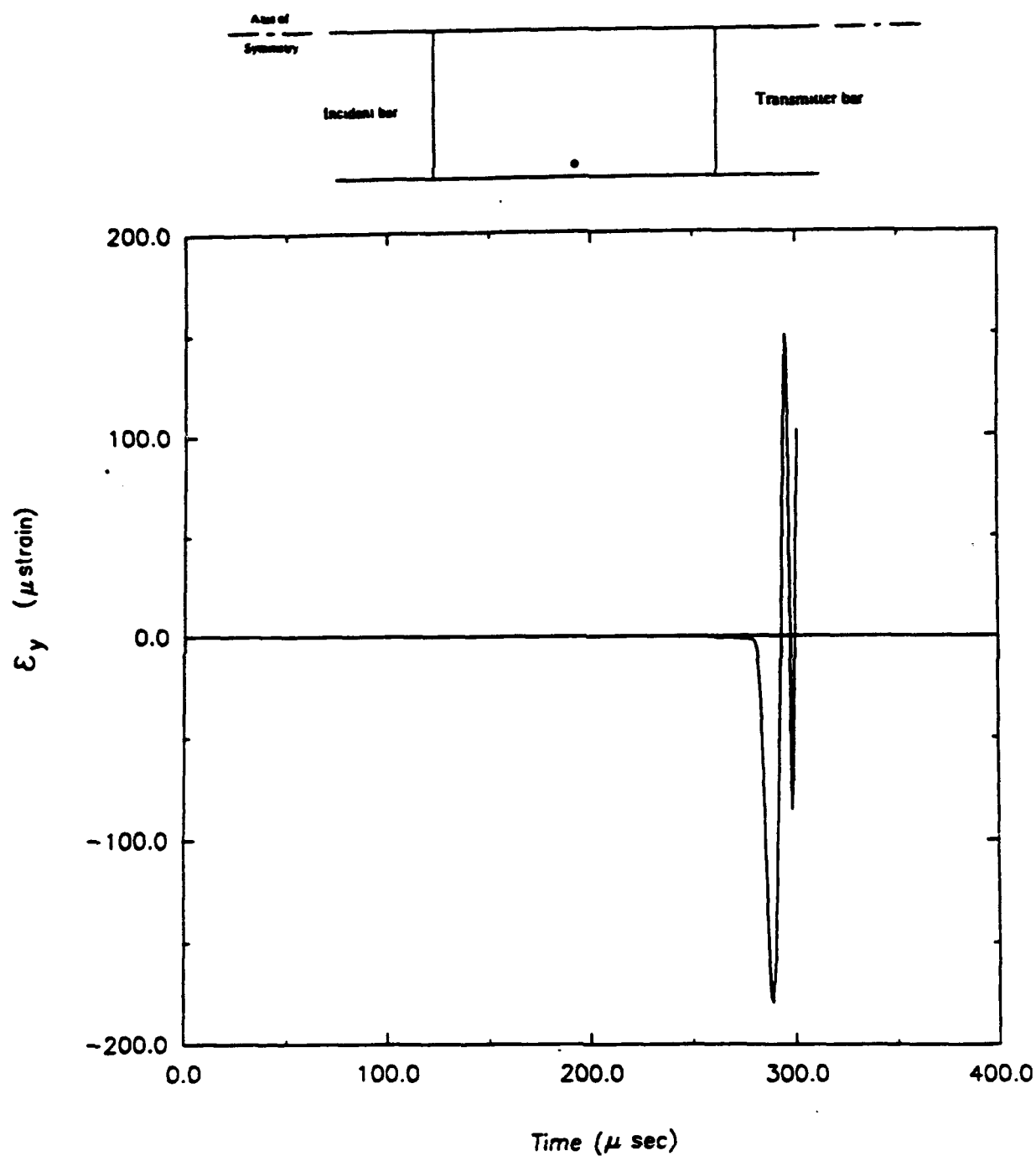


Figure 158. Time history for radial strain (direct compression, Load Case 1).

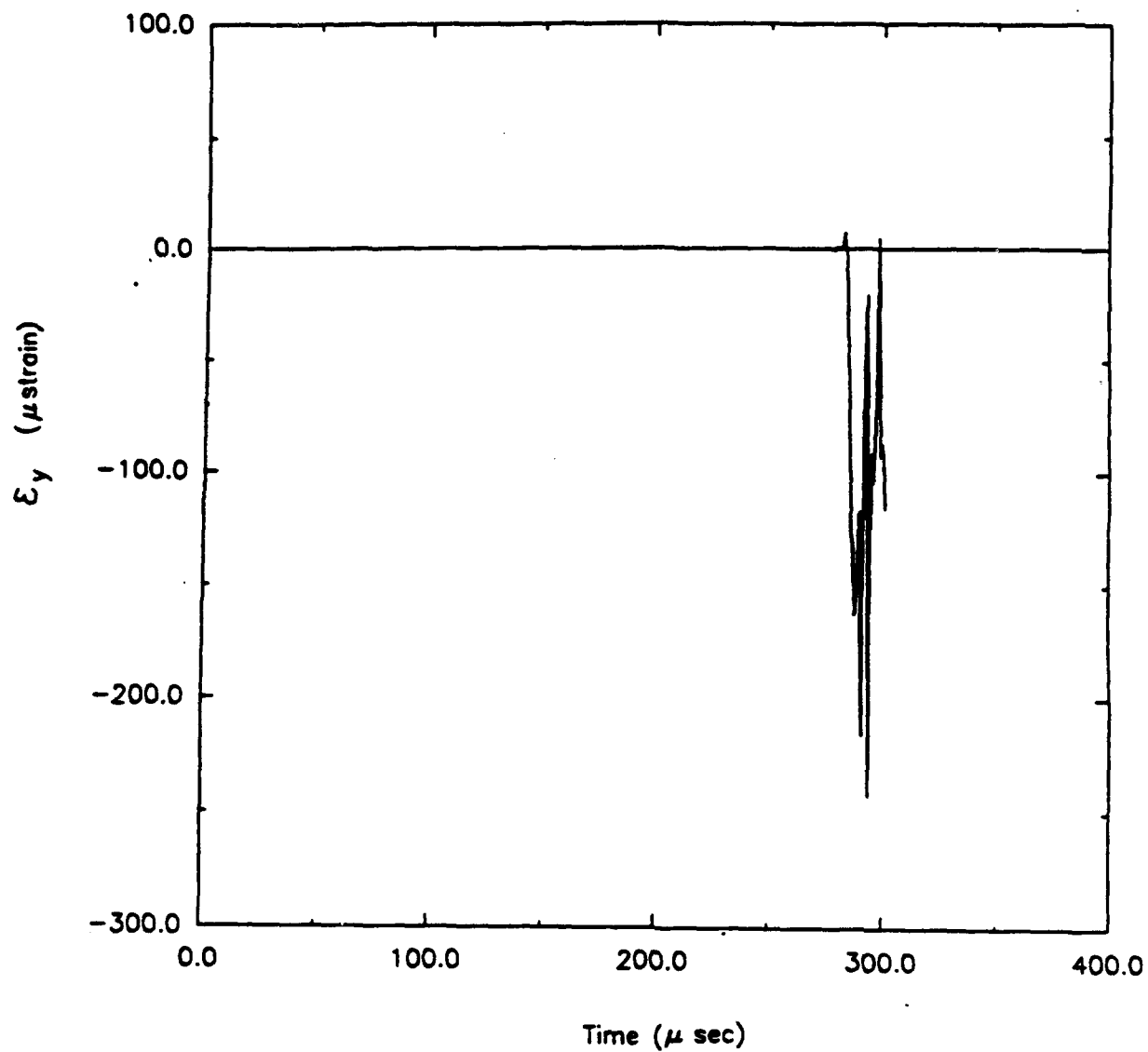
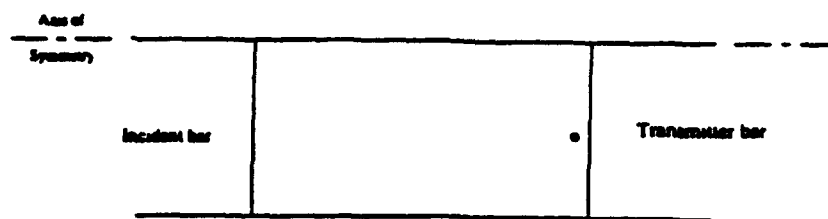


Figure 159. Time history for radial strain (direct compression, Load Case 1).

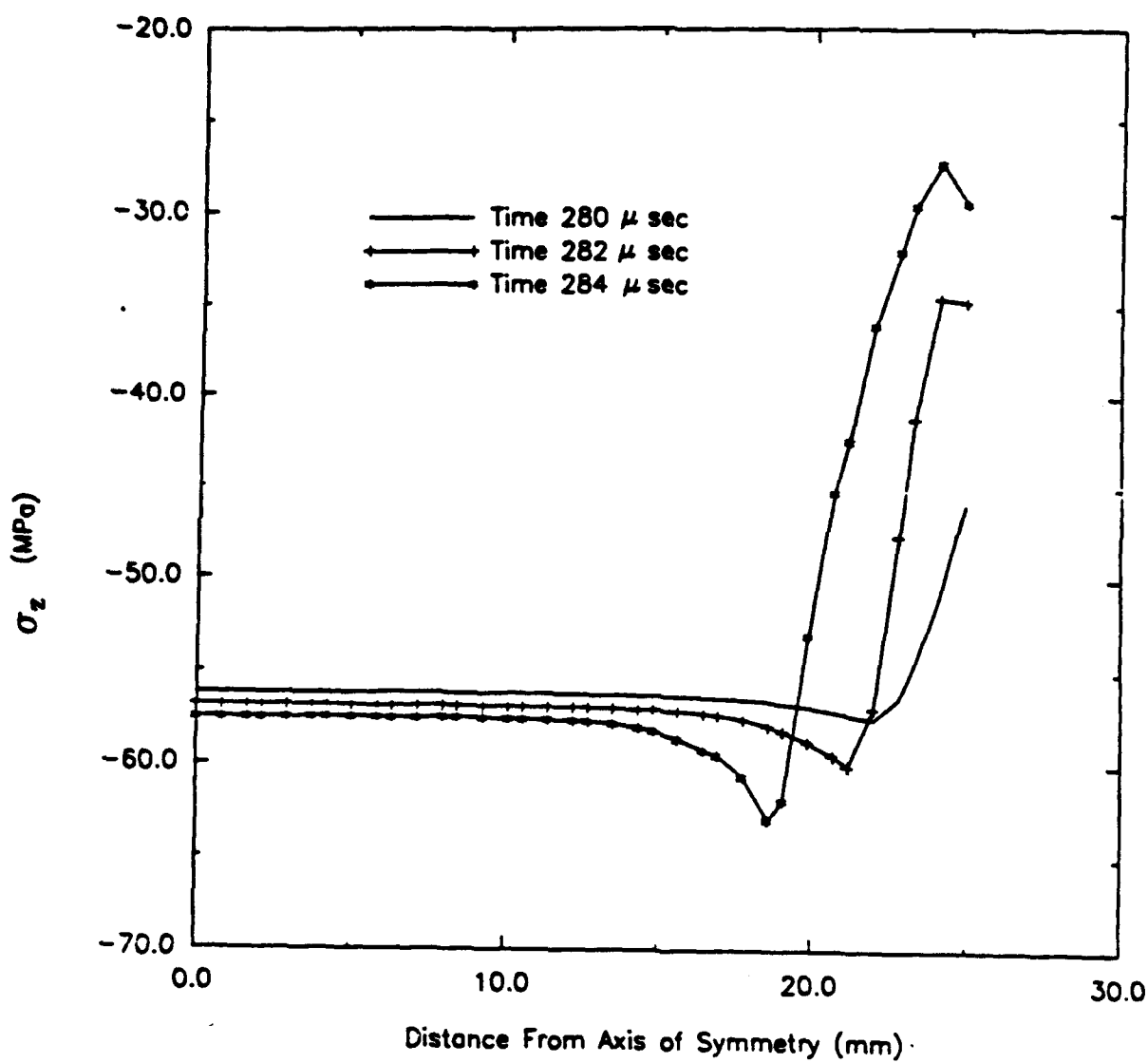
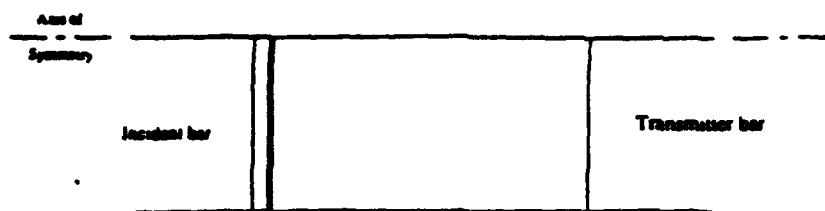


Figure 160. Profiles for longitudinal stress (direct compression, Load Case 1).

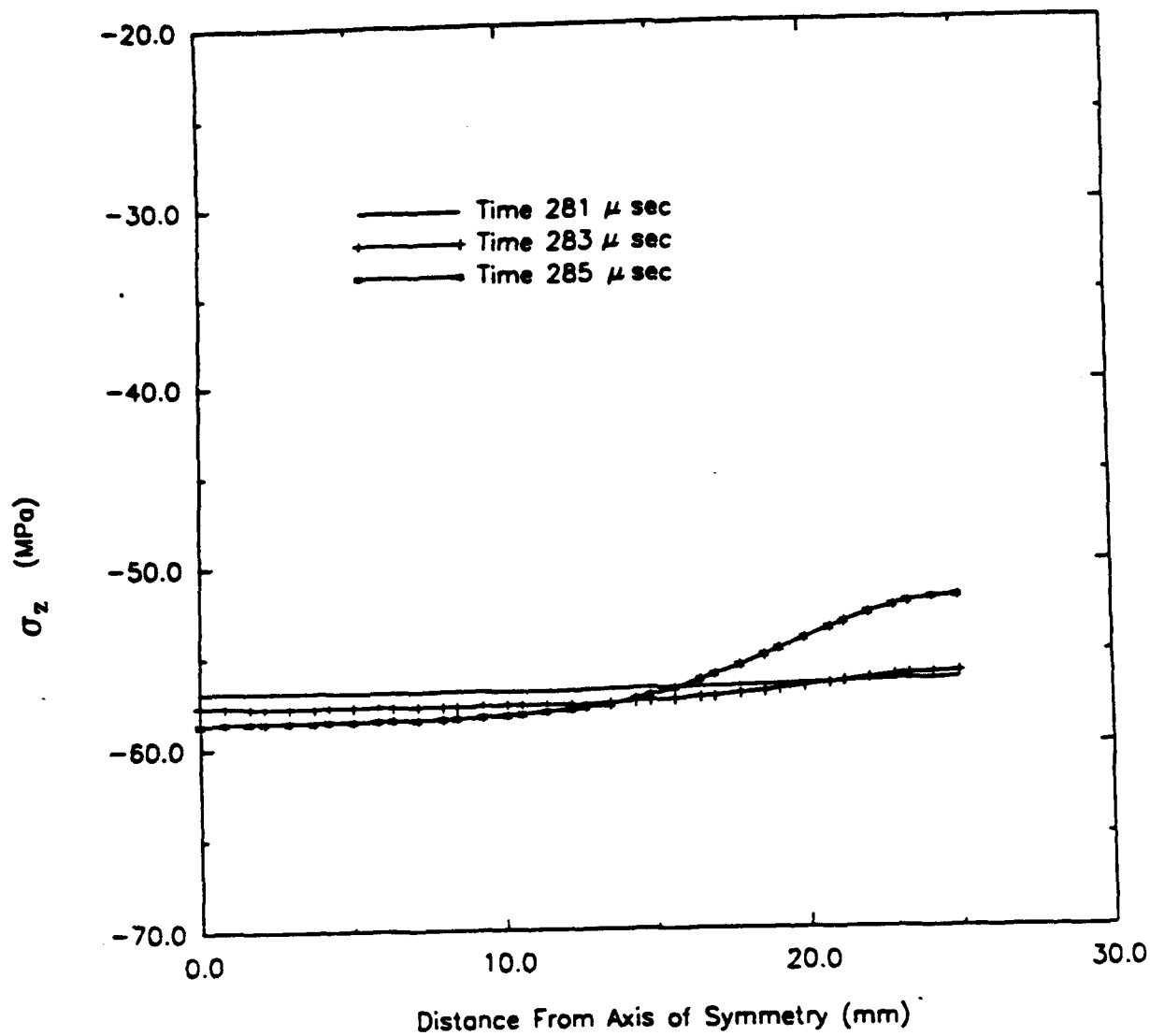
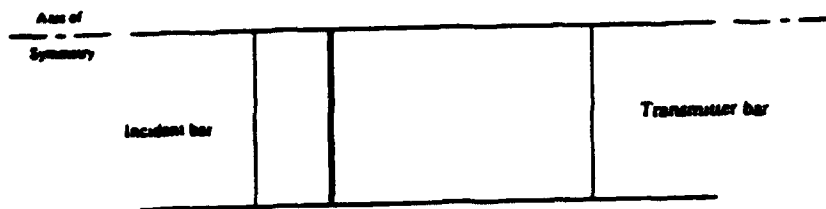


Figure 161. Profiles for longitudinal stress (direct compression, Load Case 1).

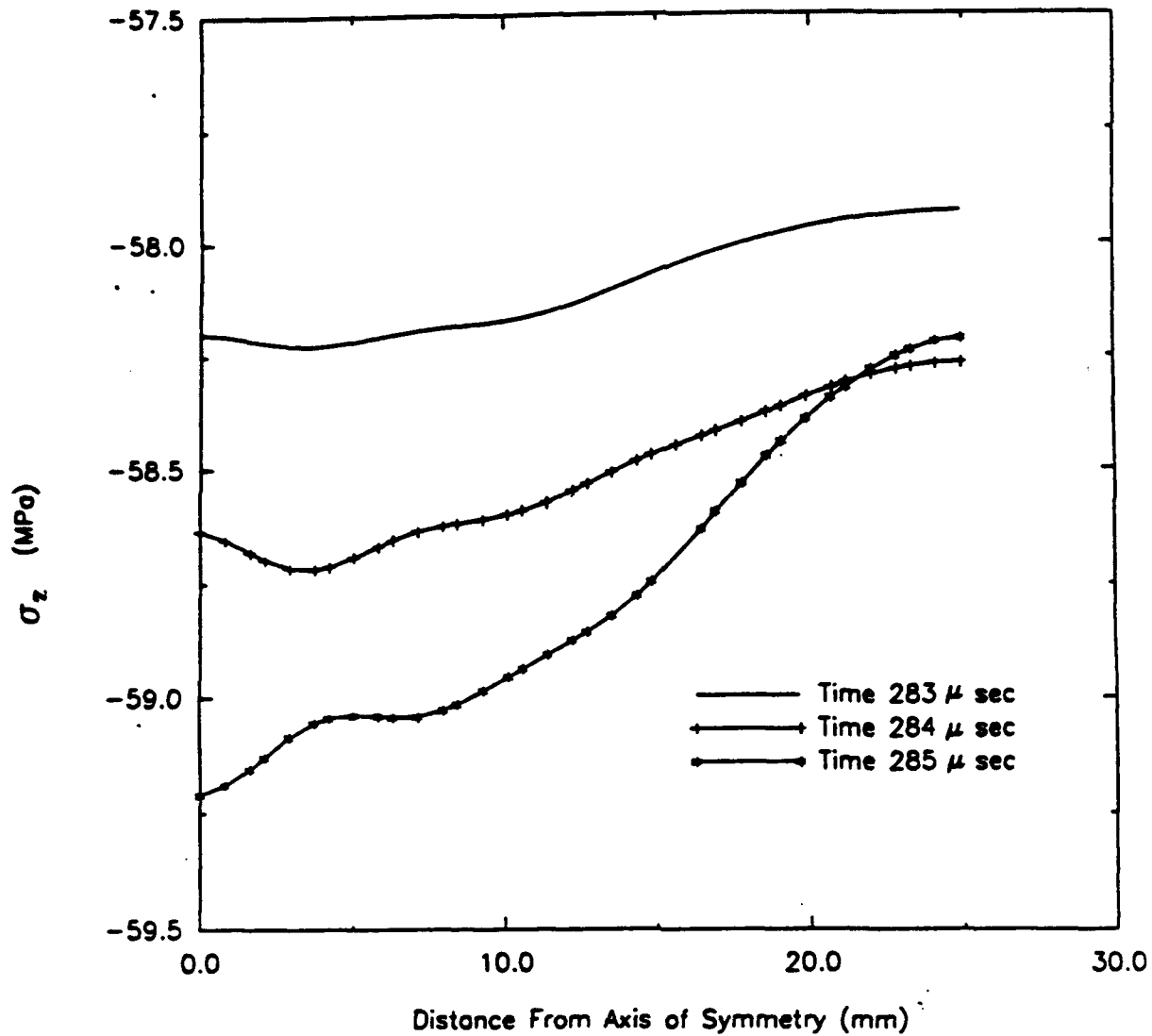
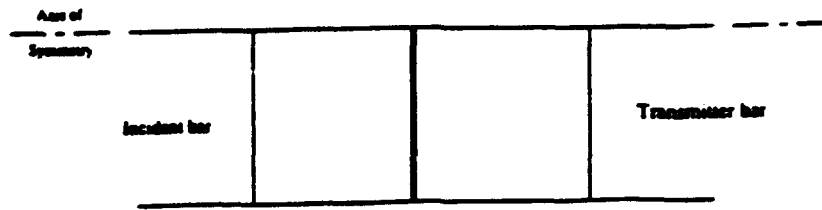


Figure 162. Profiles for longitudinal stress (direct compression, Load Case 1).

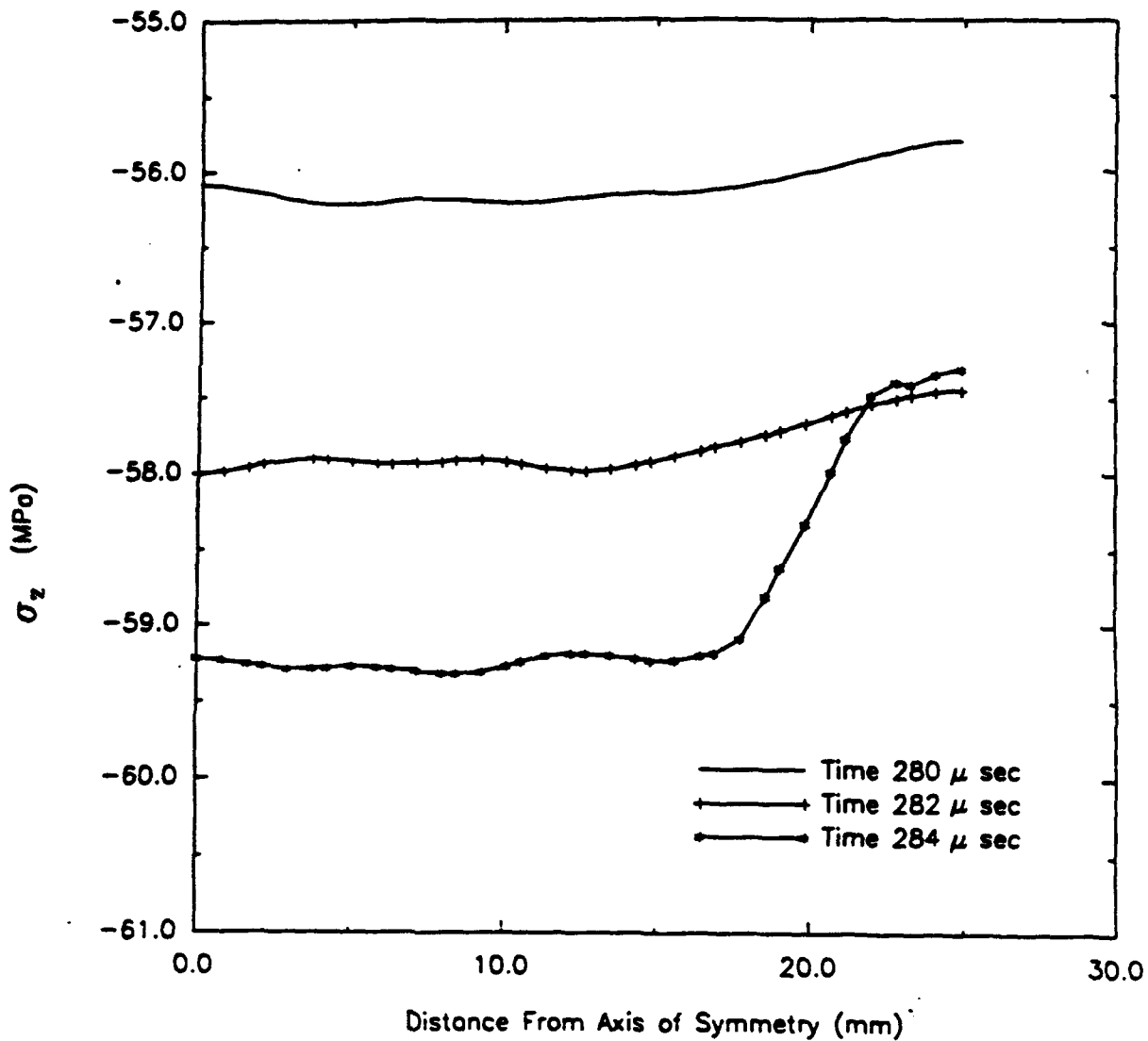
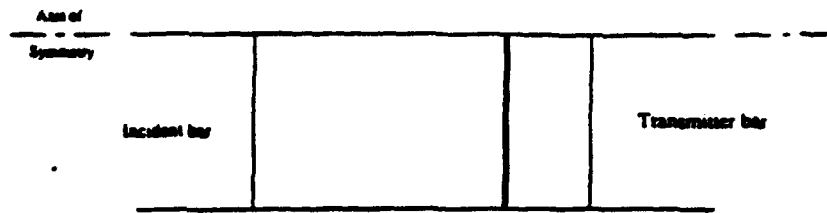


Figure 163. Profiles for longitudinal stress (direct compression, Load Case 1).

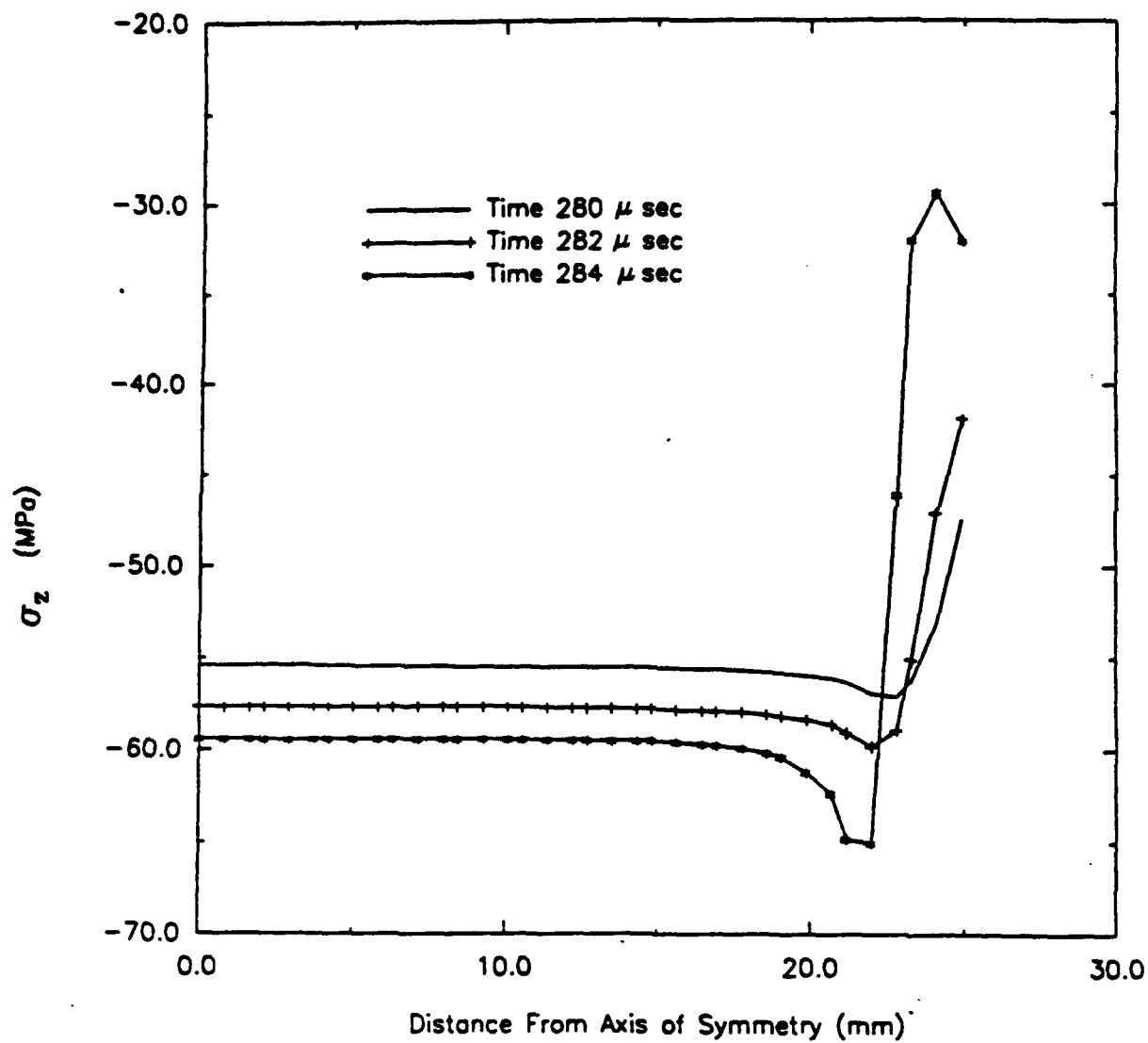
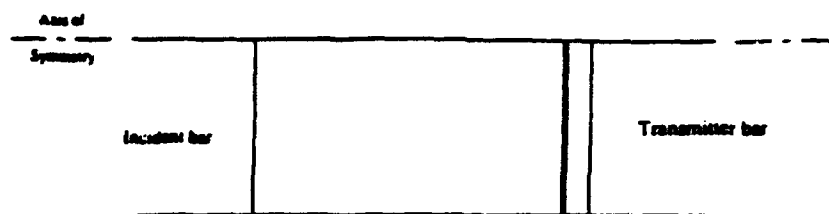


Figure 164. Profiles for longitudinal stress (direct compression, Load Case 1).

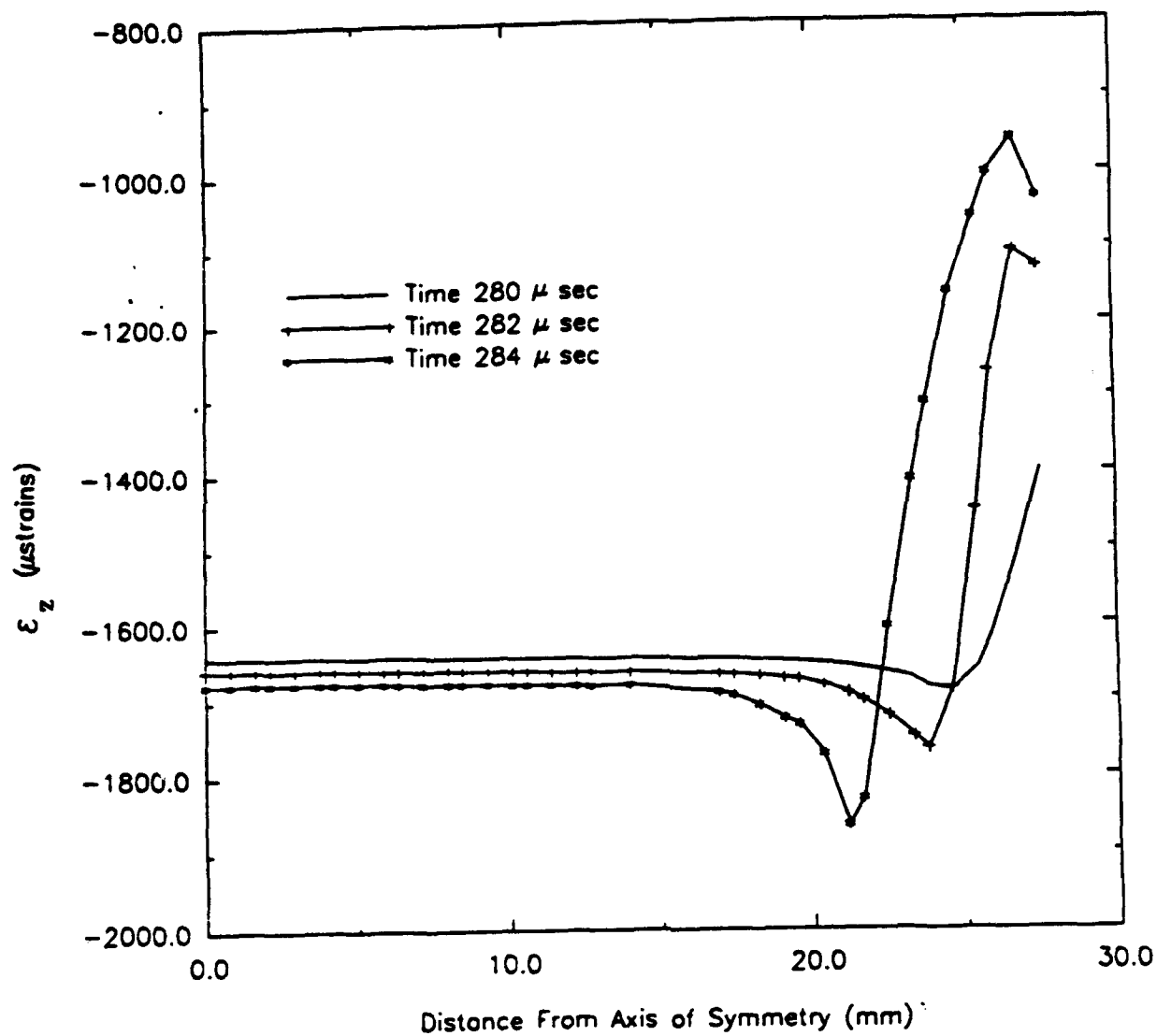
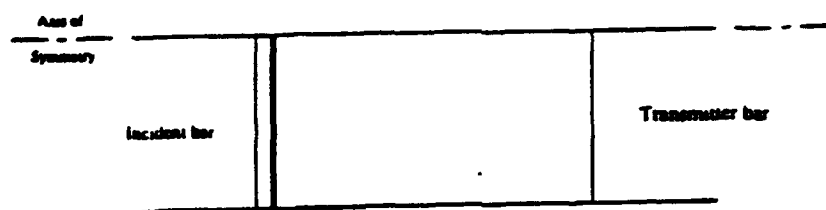


Figure 165. Profiles for longitudinal strain (direct compression, Load Case 1).

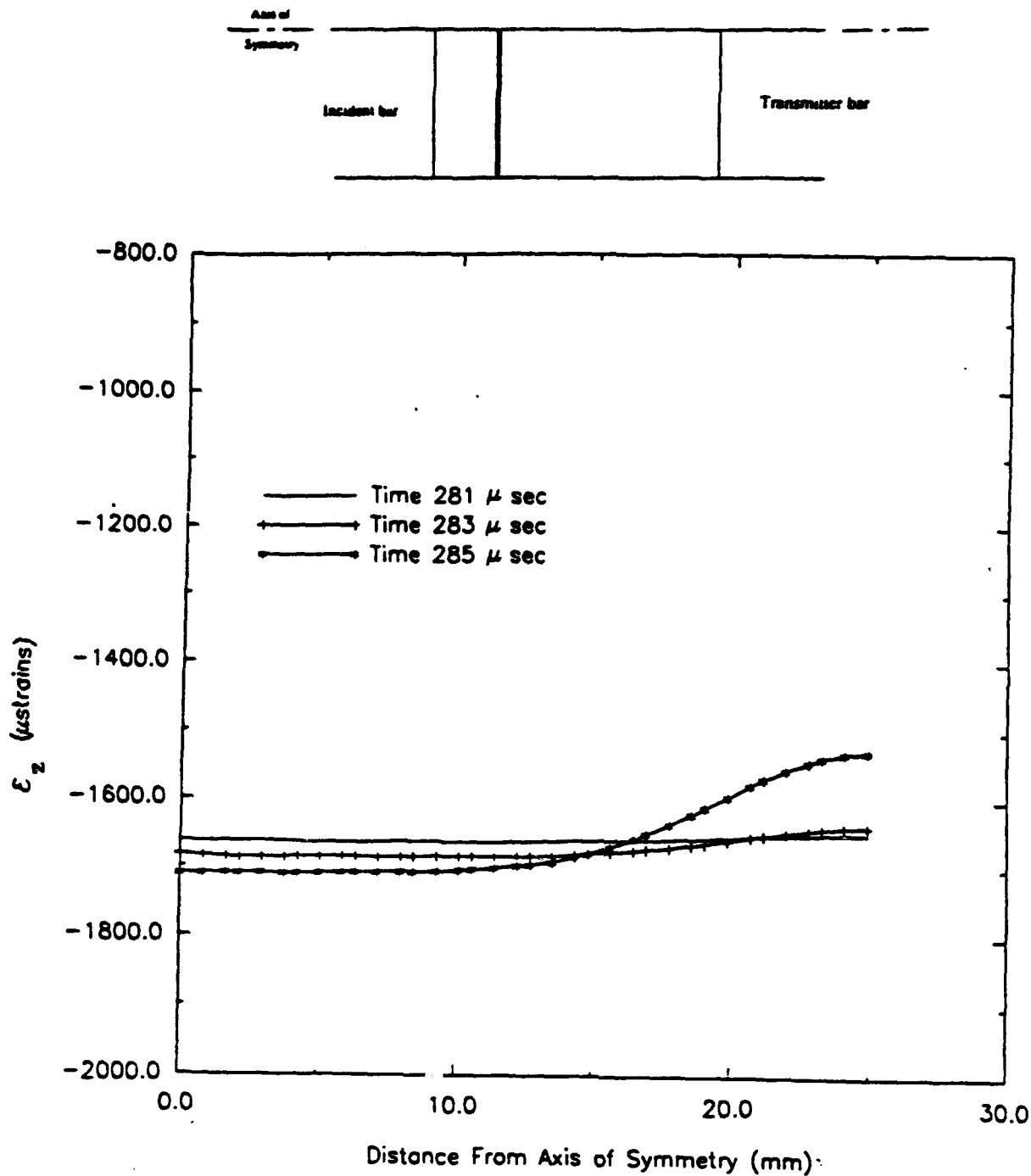


Figure 166. Profiles for longitudinal strain (direct compression, Load Case 1).

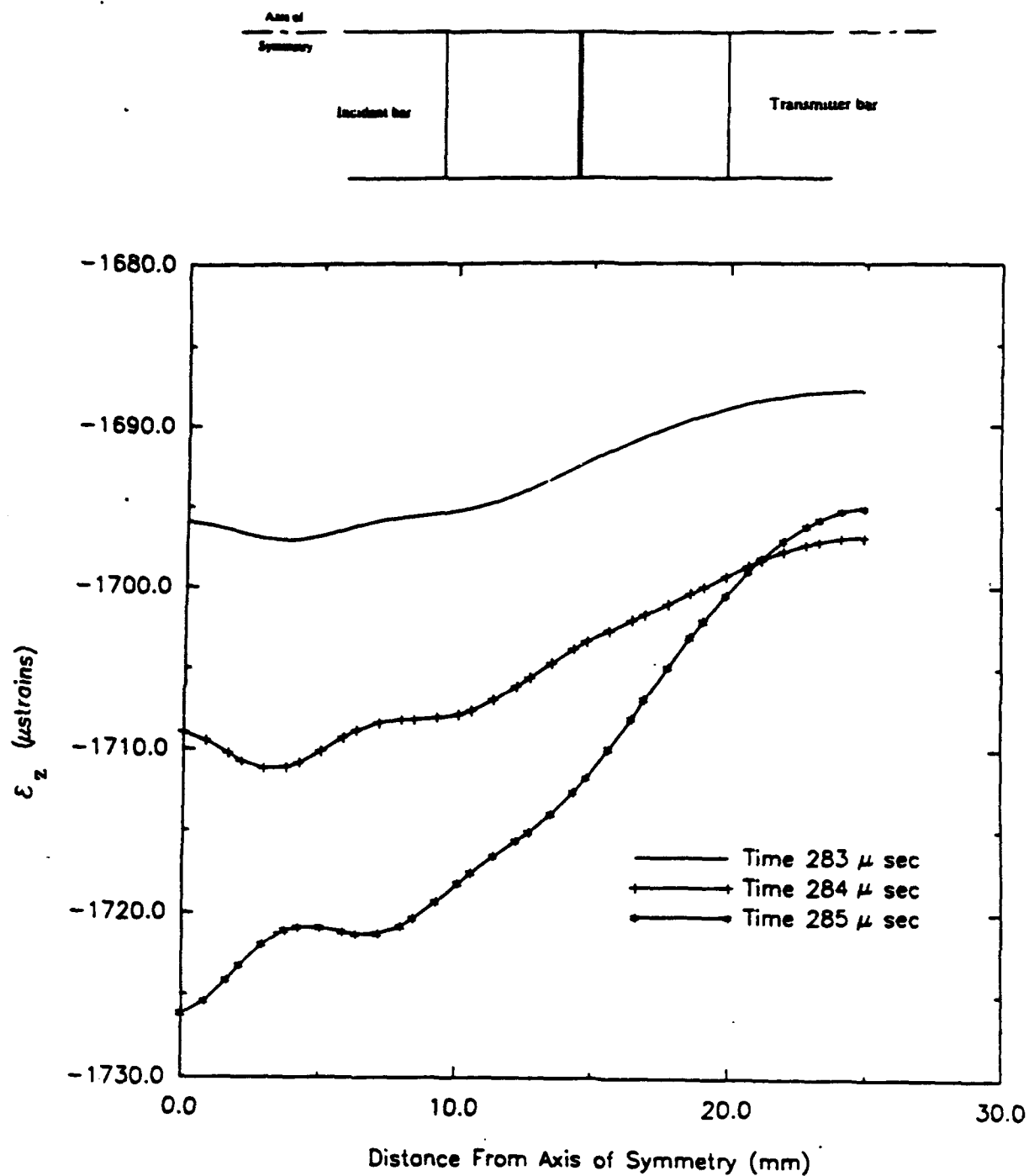


Figure 167. Profiles for longitudinal strain (direct compression, Load Case 1).

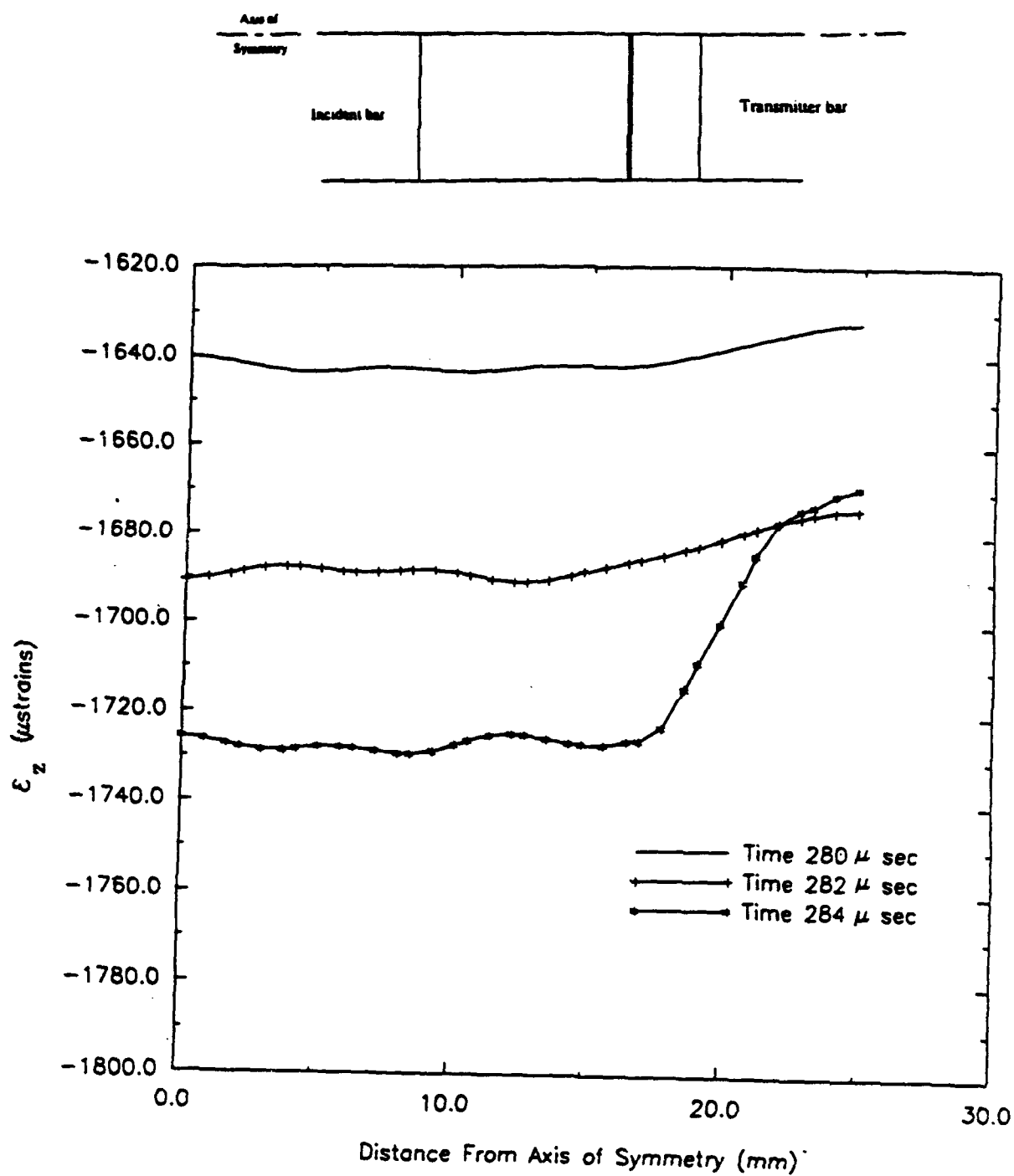


Figure 168. Profiles for longitudinal strain (direct compression, Load Case 1).

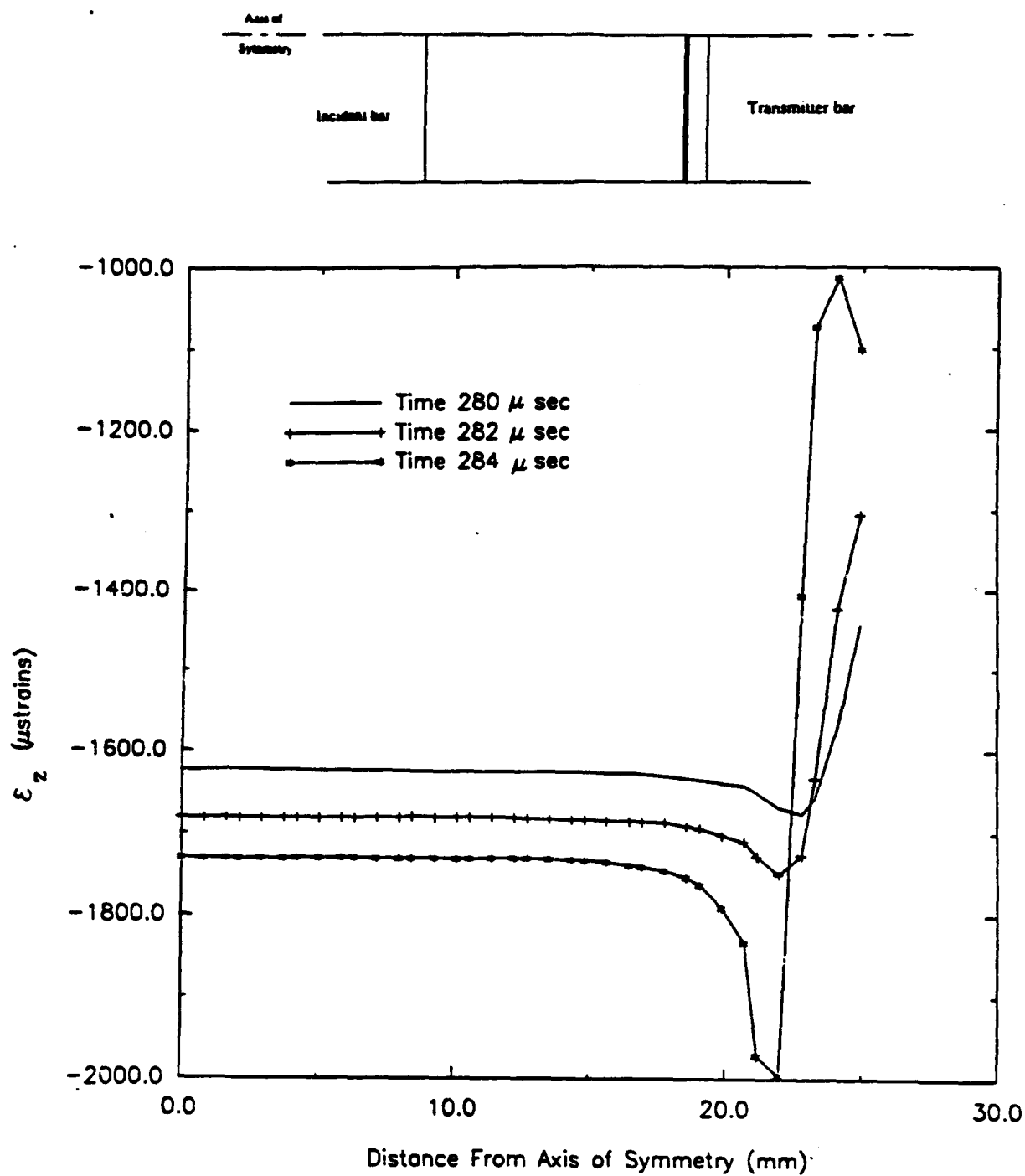
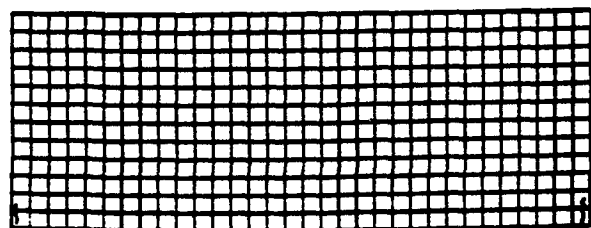
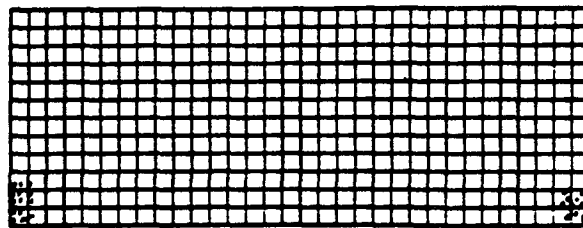


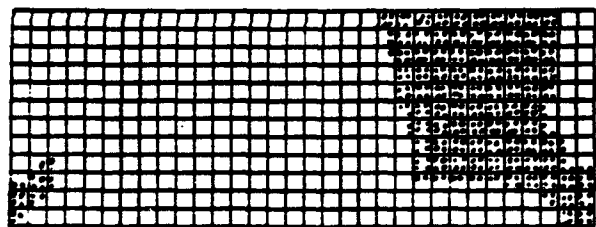
Figure 169. Profiles for longitudinal strain (direct compression, Load Case 1).



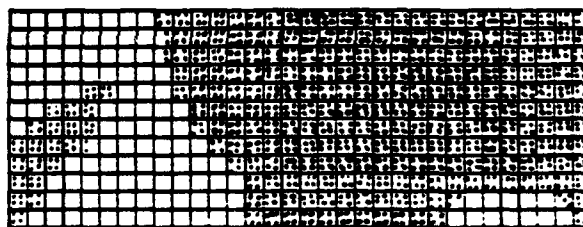
(a)



(b)



(c)



(d)

Figure 170. Cracking sequence for direct compression specimen; Load Case 1:
a) $t=279 \mu \text{ sec}$, b) $t=281 \mu \text{ sec}$, c) $t=282 \mu \text{ sec}$, d) $t=284 \mu \text{ sec}$.

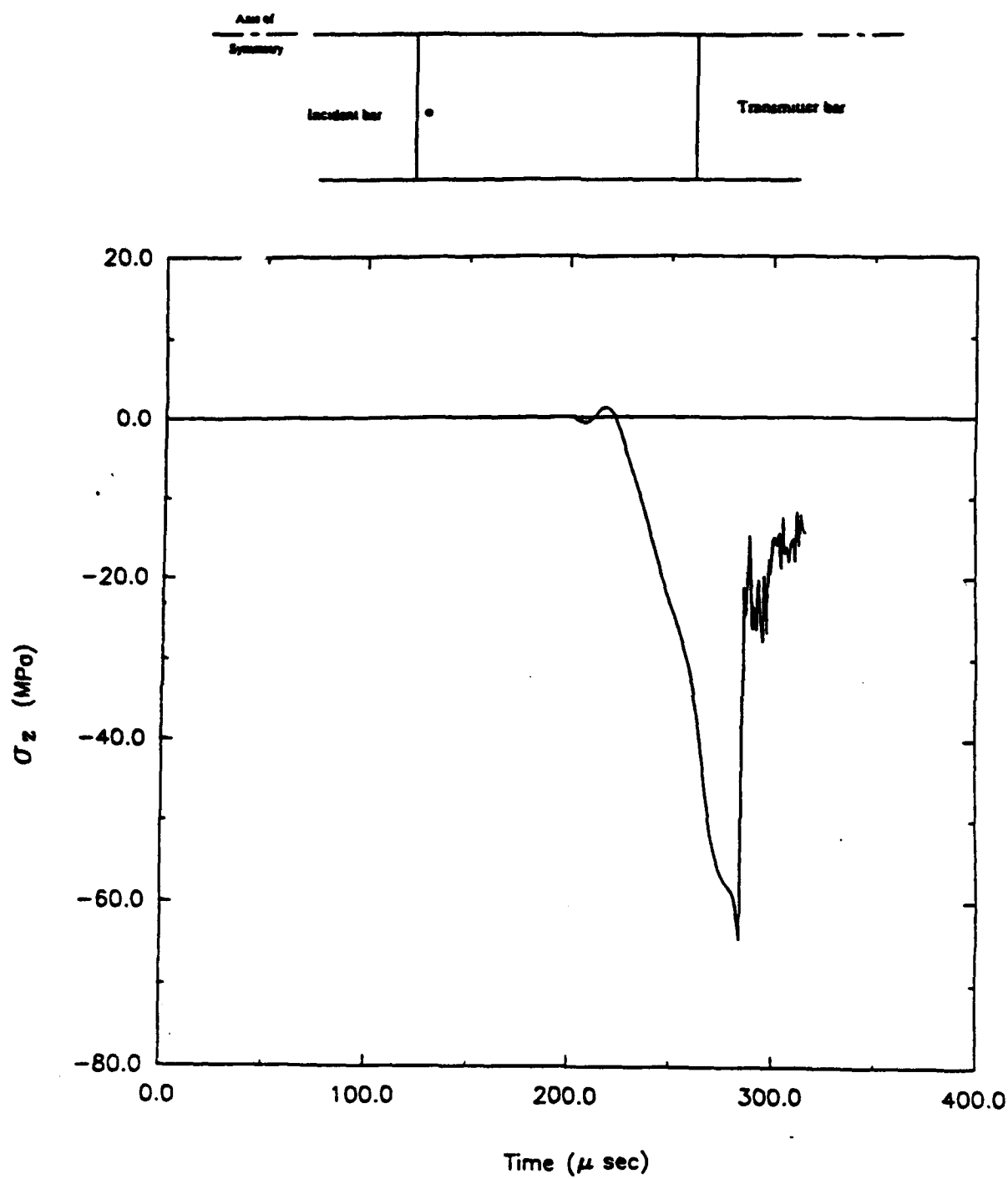


Figure 171. Time history for longitudinal stress (direct compression, Load Case 2).

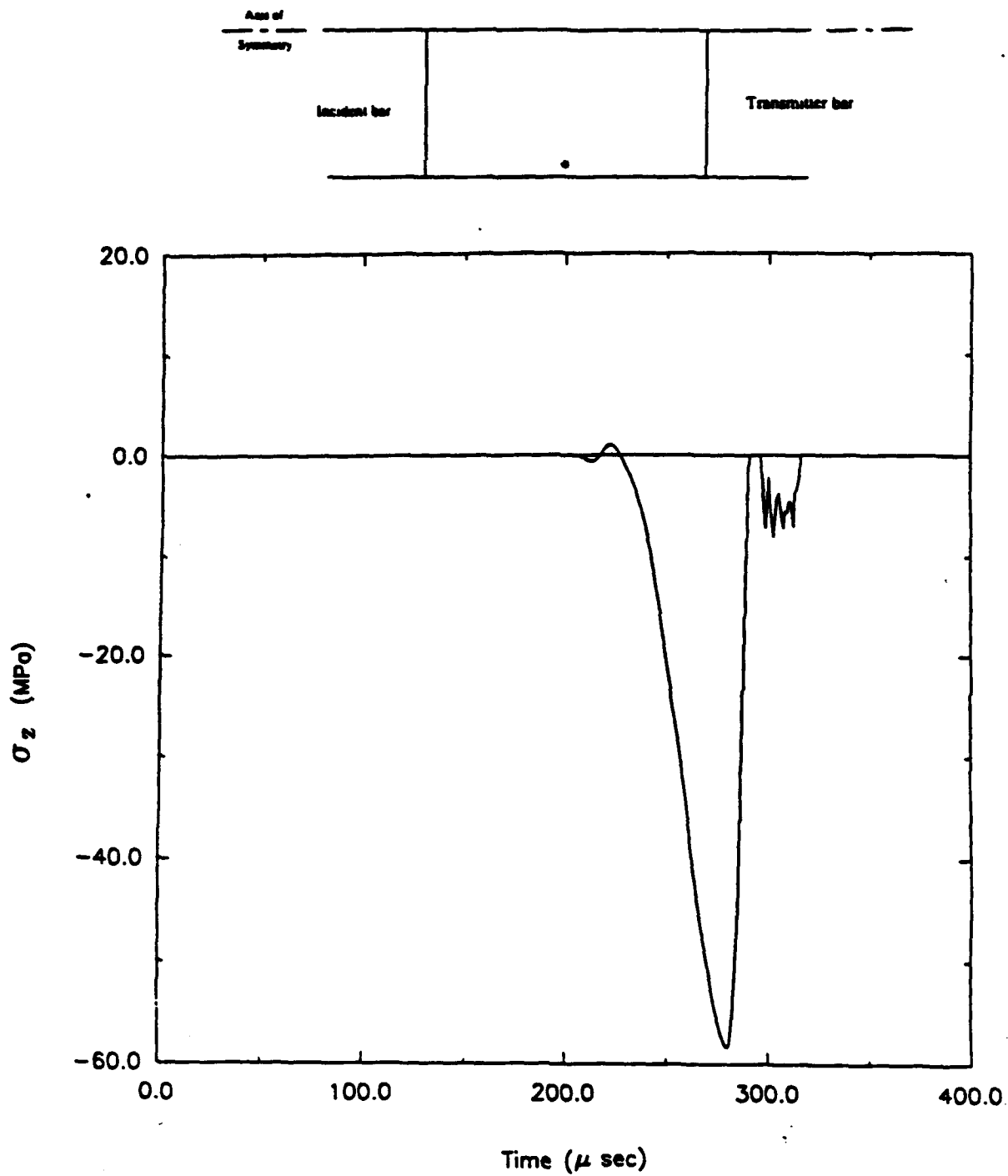


Figure 172. Time history for longitudinal stress (direct compression, Load Case 2).

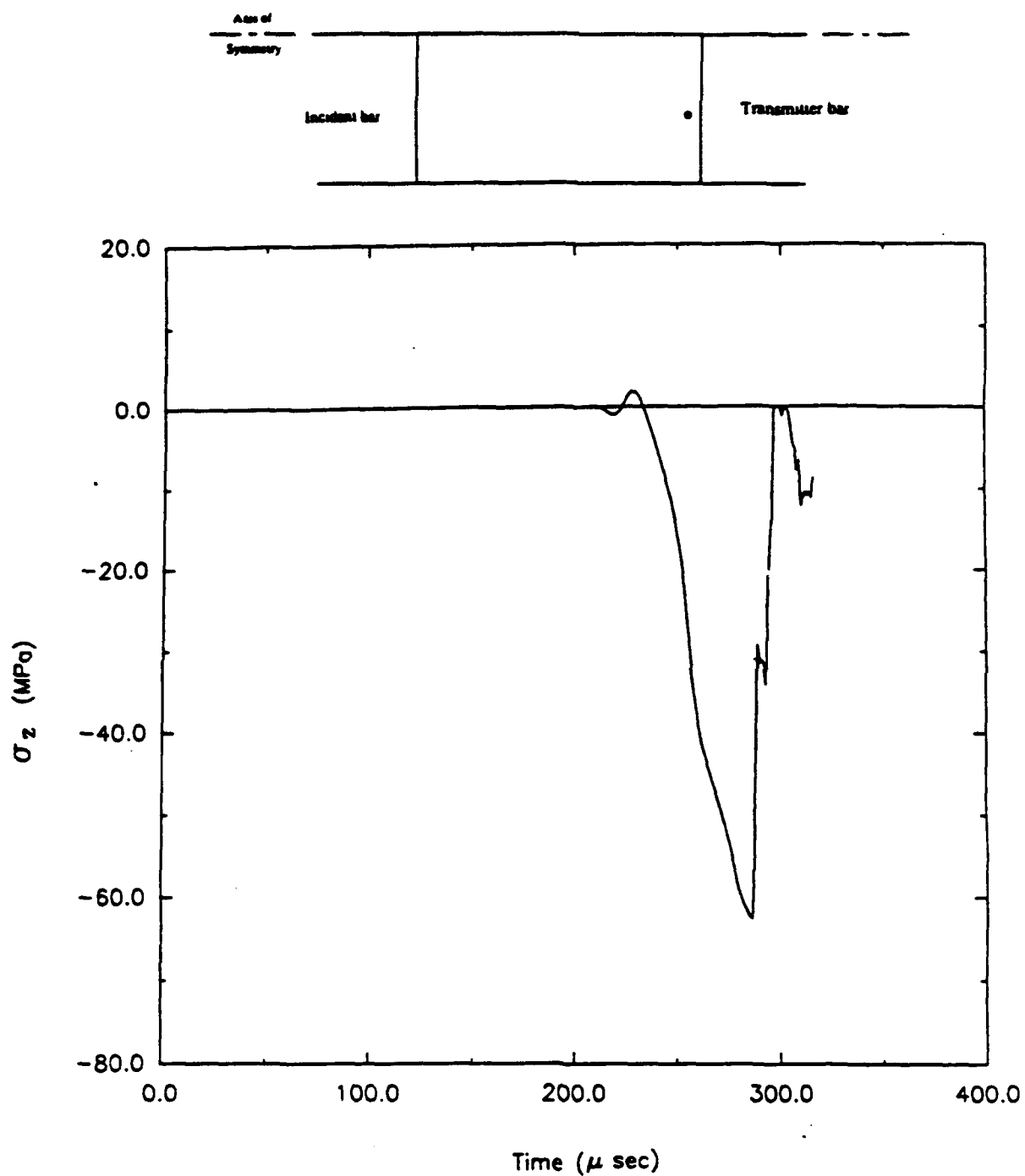


Figure 173. Time history for longitudinal stress (direct compression, Load Case 2).

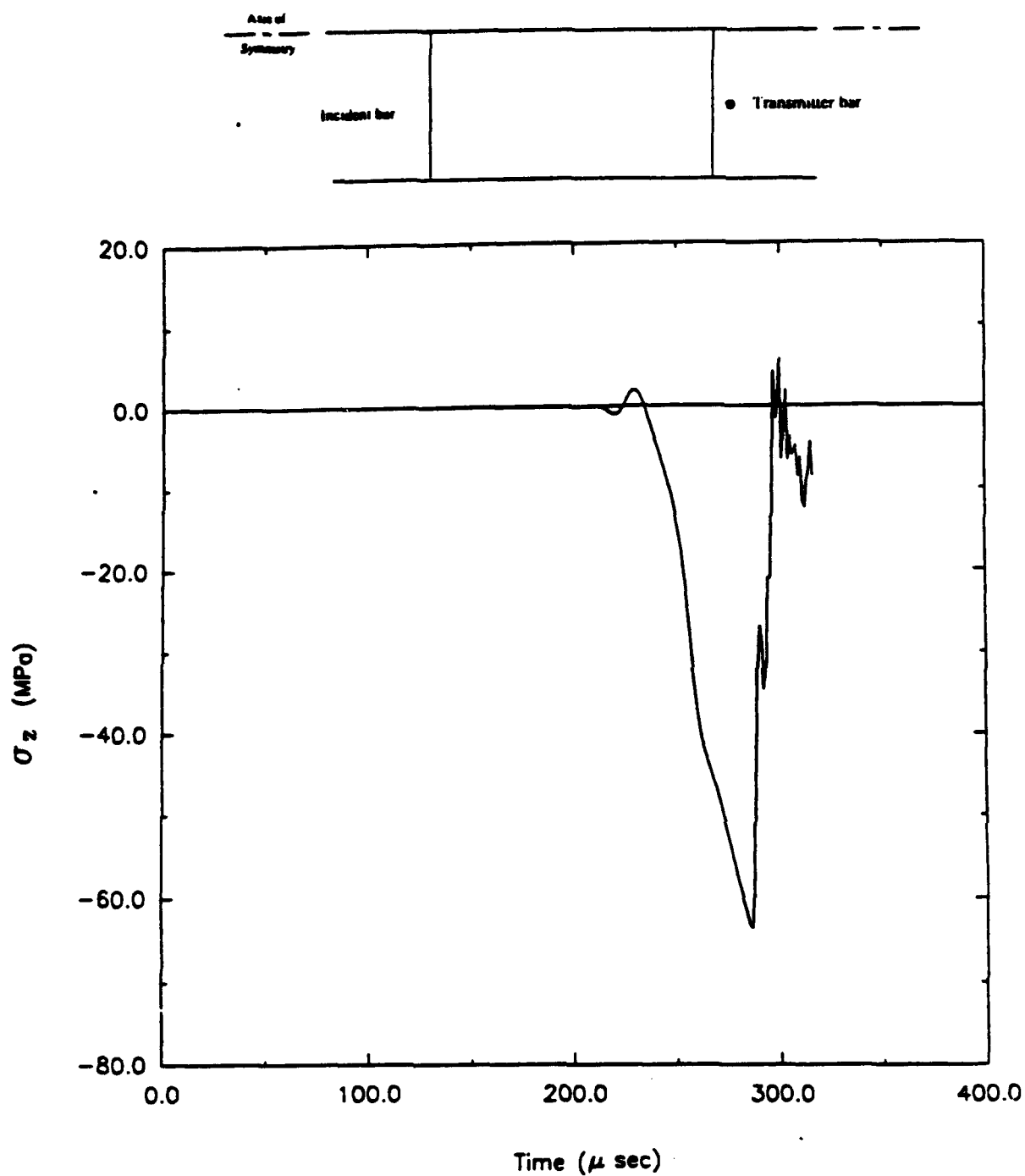


Figure 174. Time history for longitudinal stress (direct compression, Load Case 2).

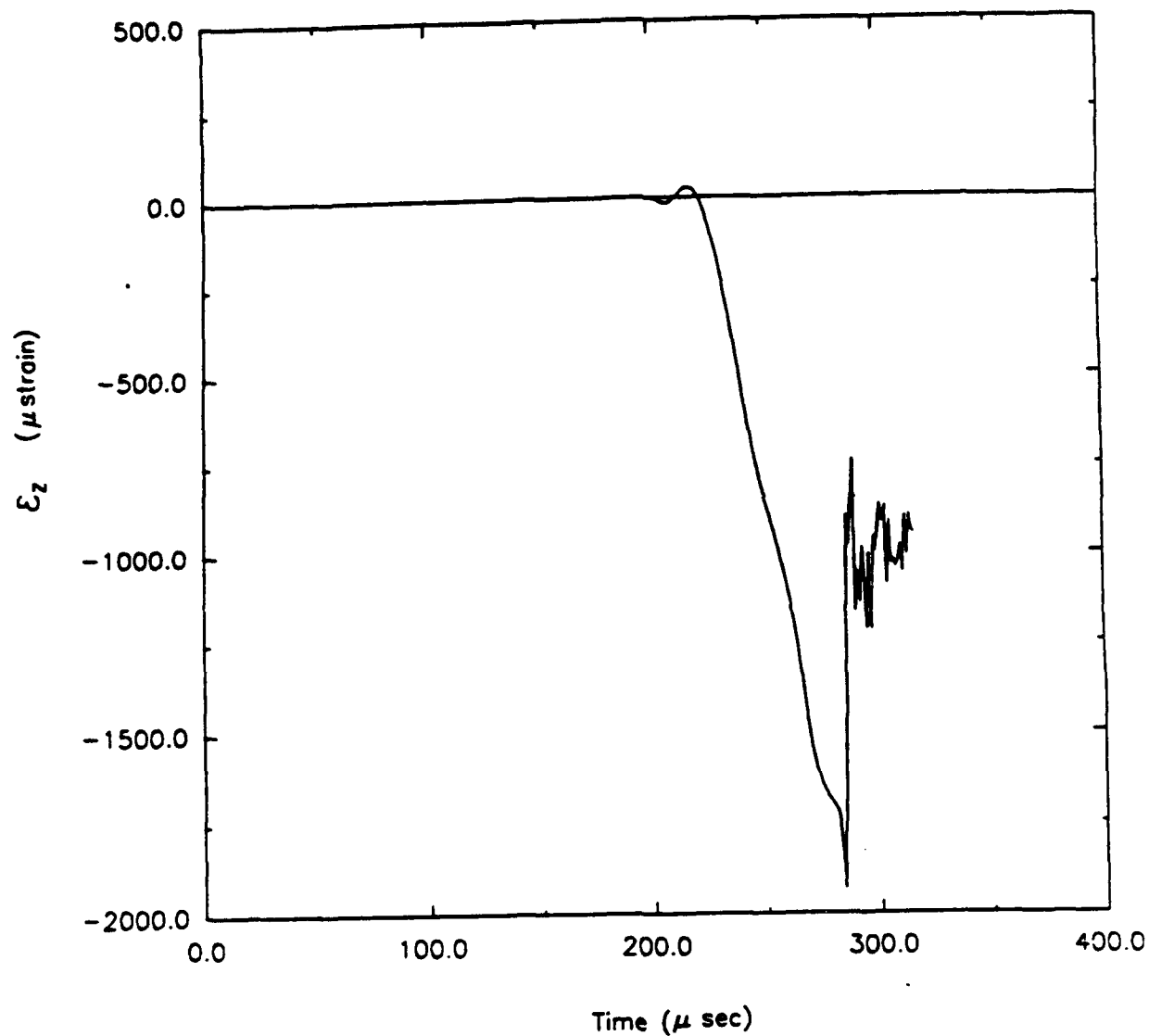
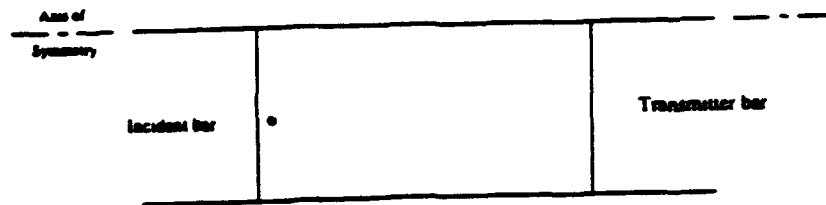


Figure 175. Time history for longitudinal strain (direct compression, Load Case 2).

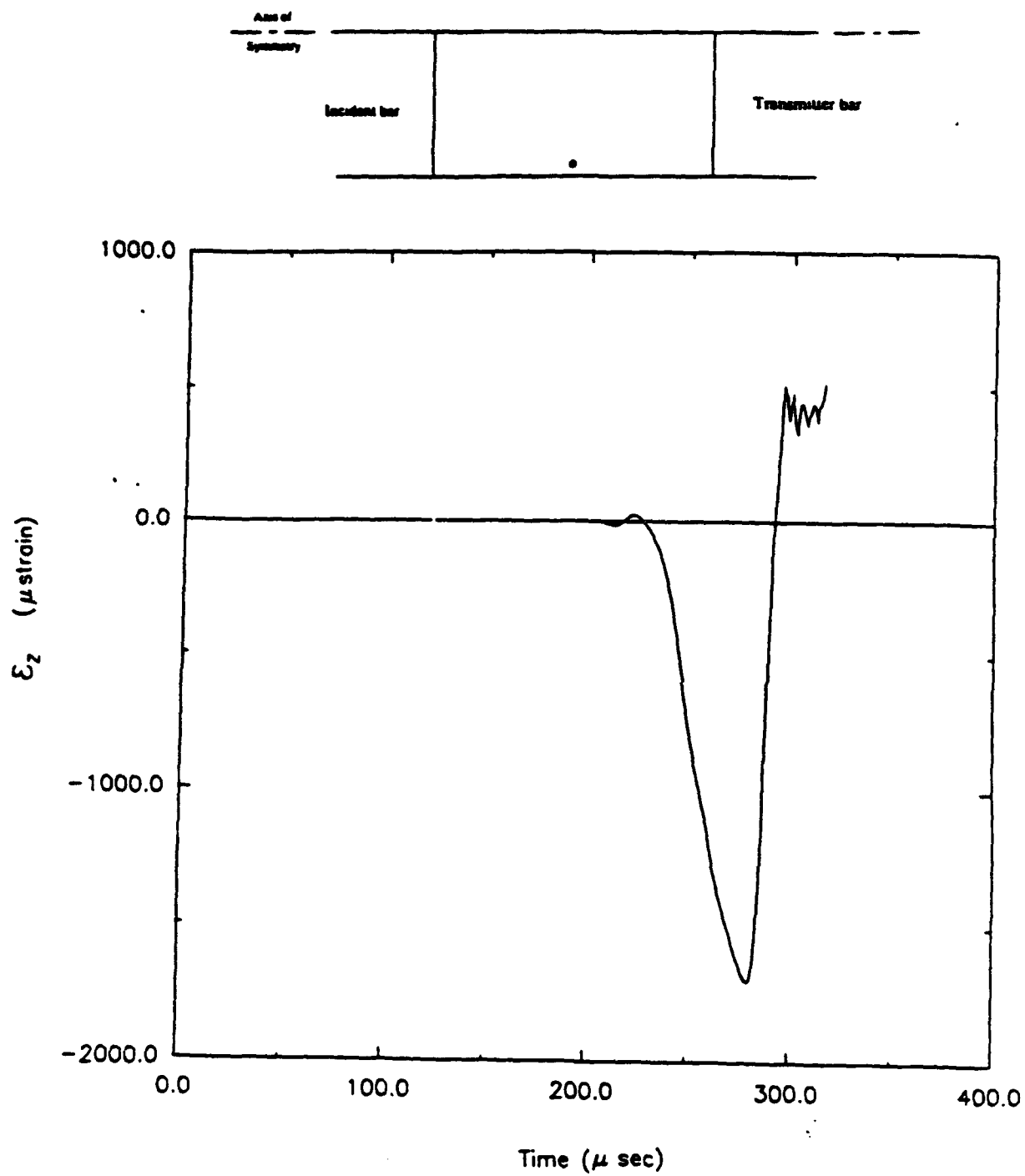


Figure 176. Time history for longitudinal strain (direct compression, Load Case 2).

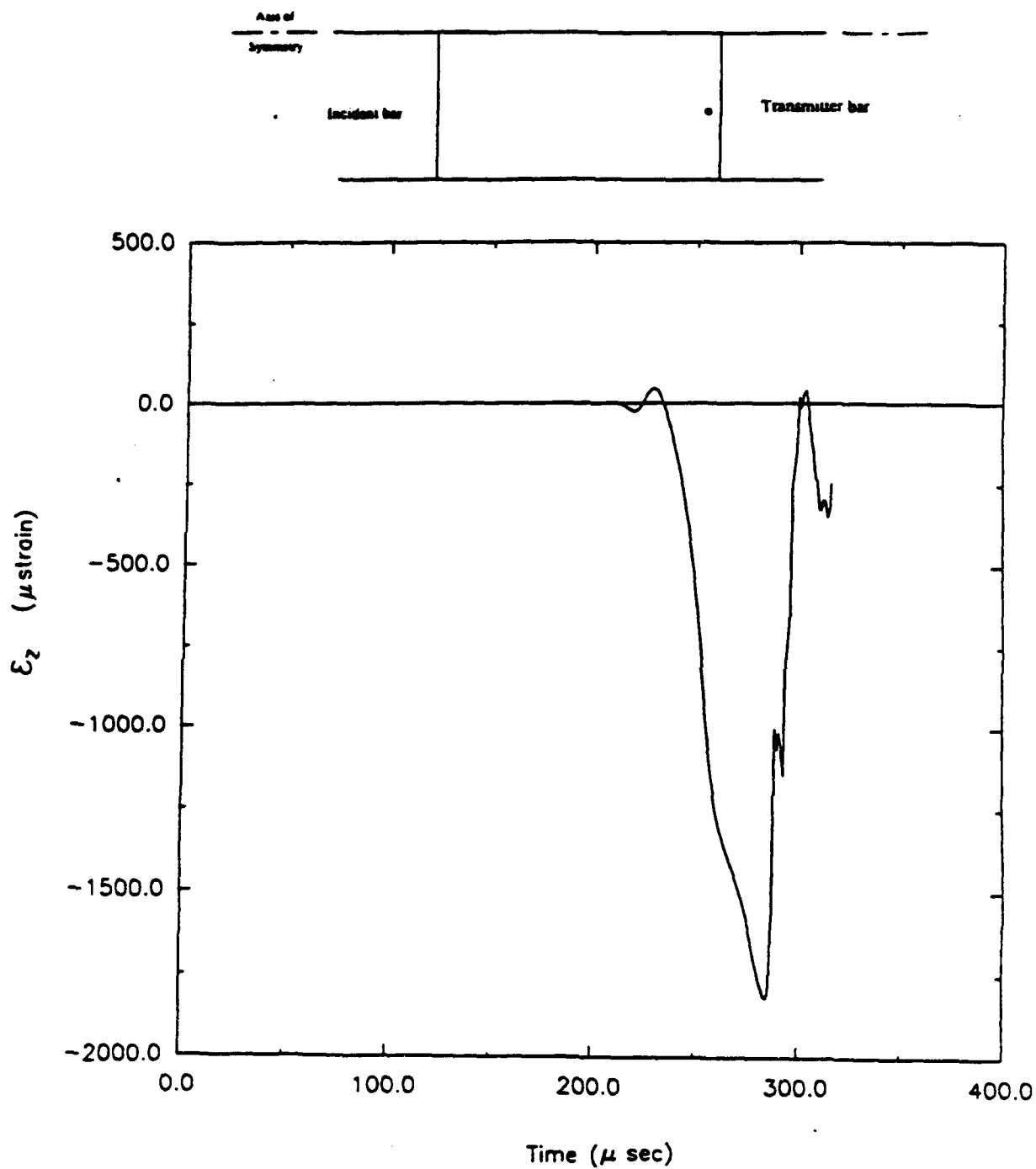


Figure 177. Time history for longitudinal strain (direct compression, Load Case 2).

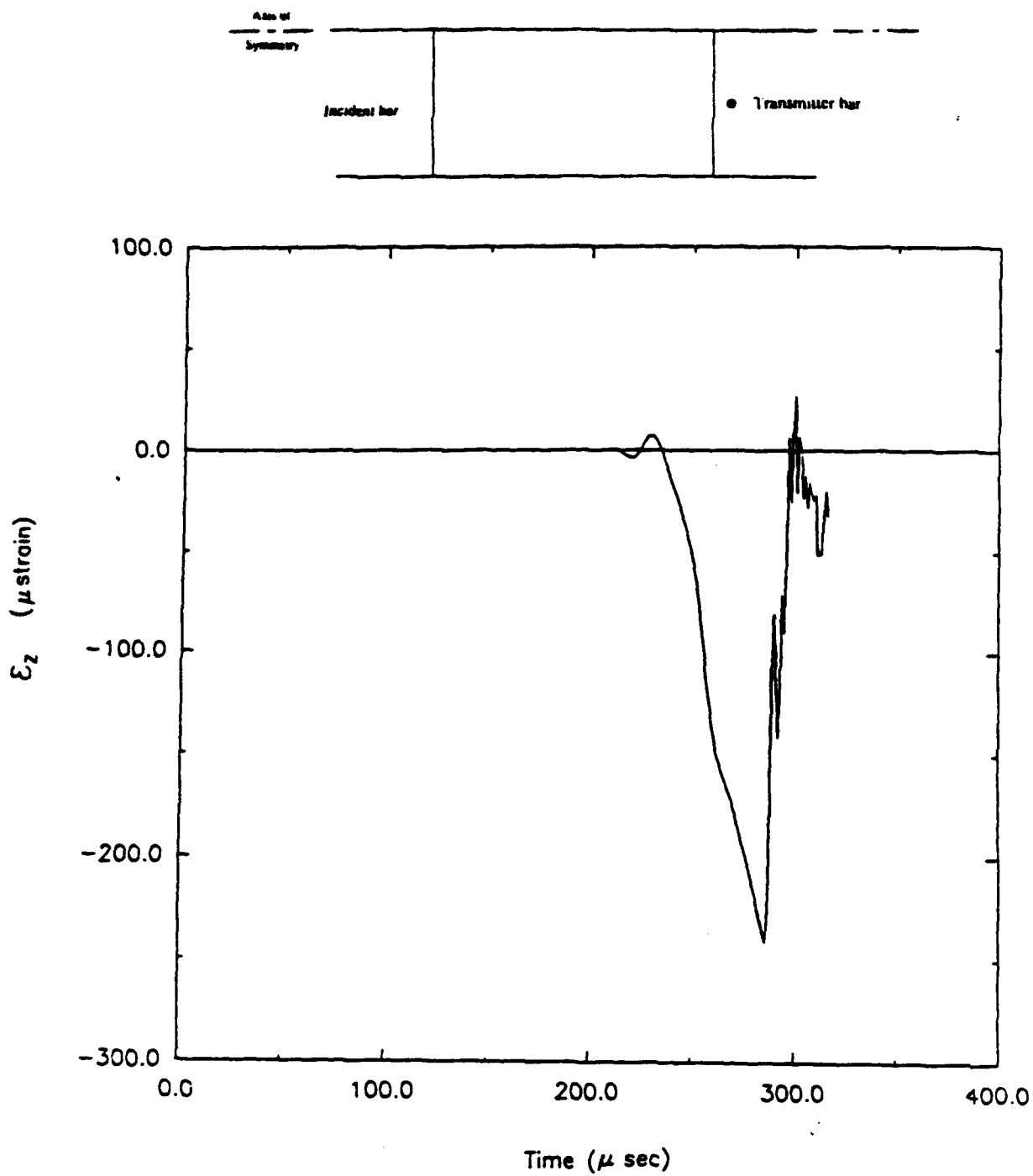


Figure 178. Time history for longitudinal strain (direct compression, Load Case 2).

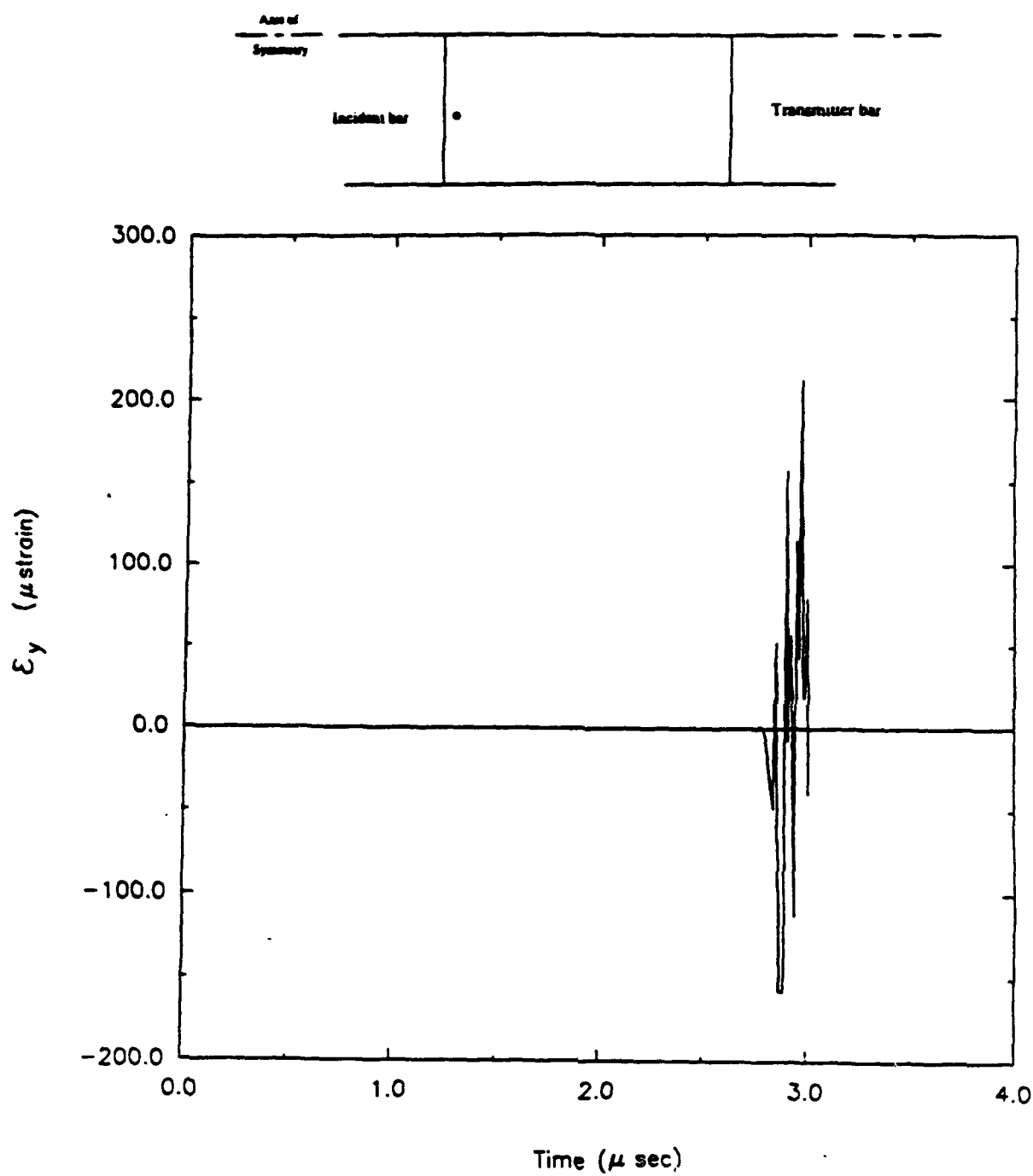


Figure 179. Time history for radial strain (direct compression, Load Case 2).

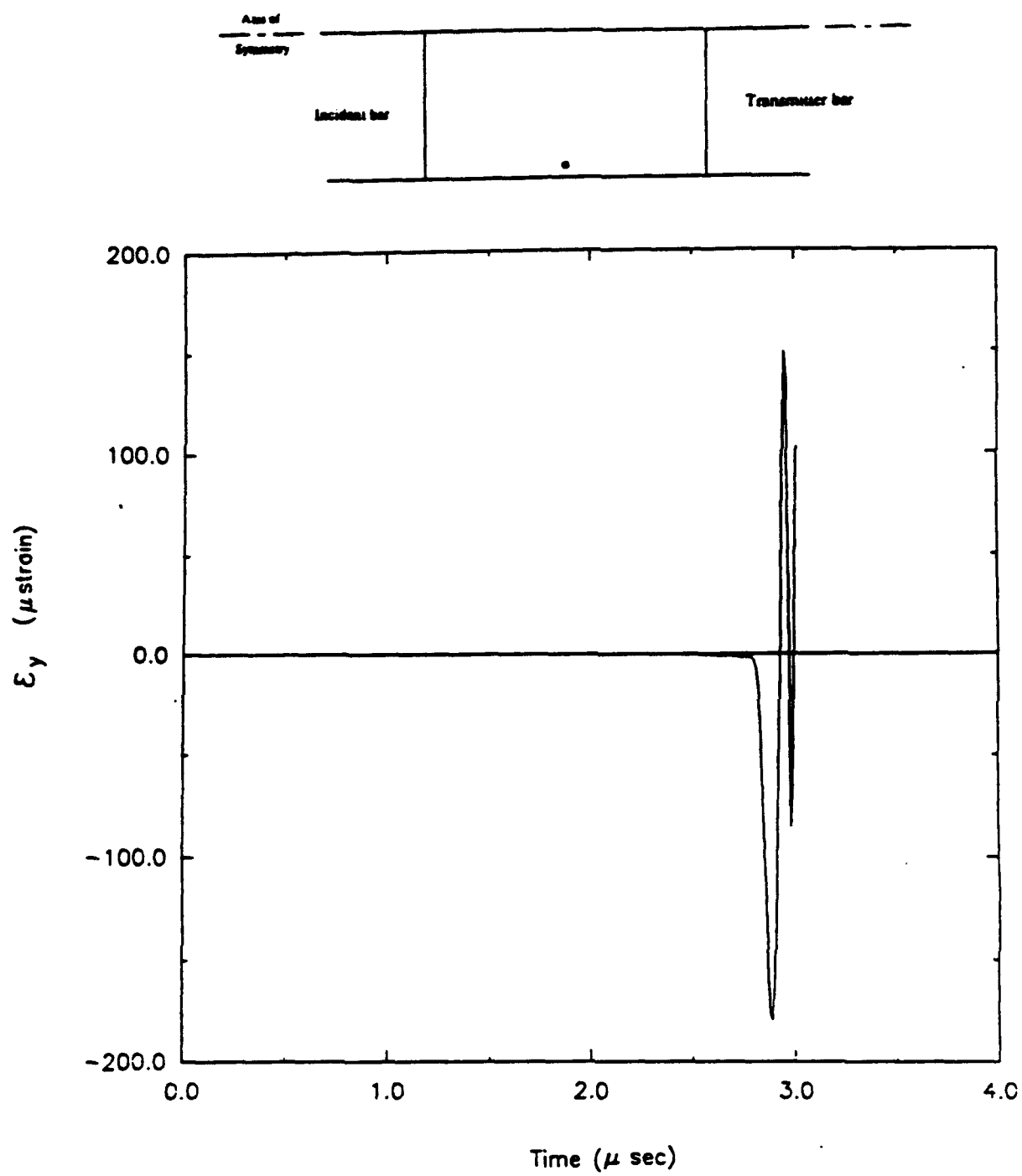


Figure 180. Time history for radial strain (direct compression, Load Case 2).

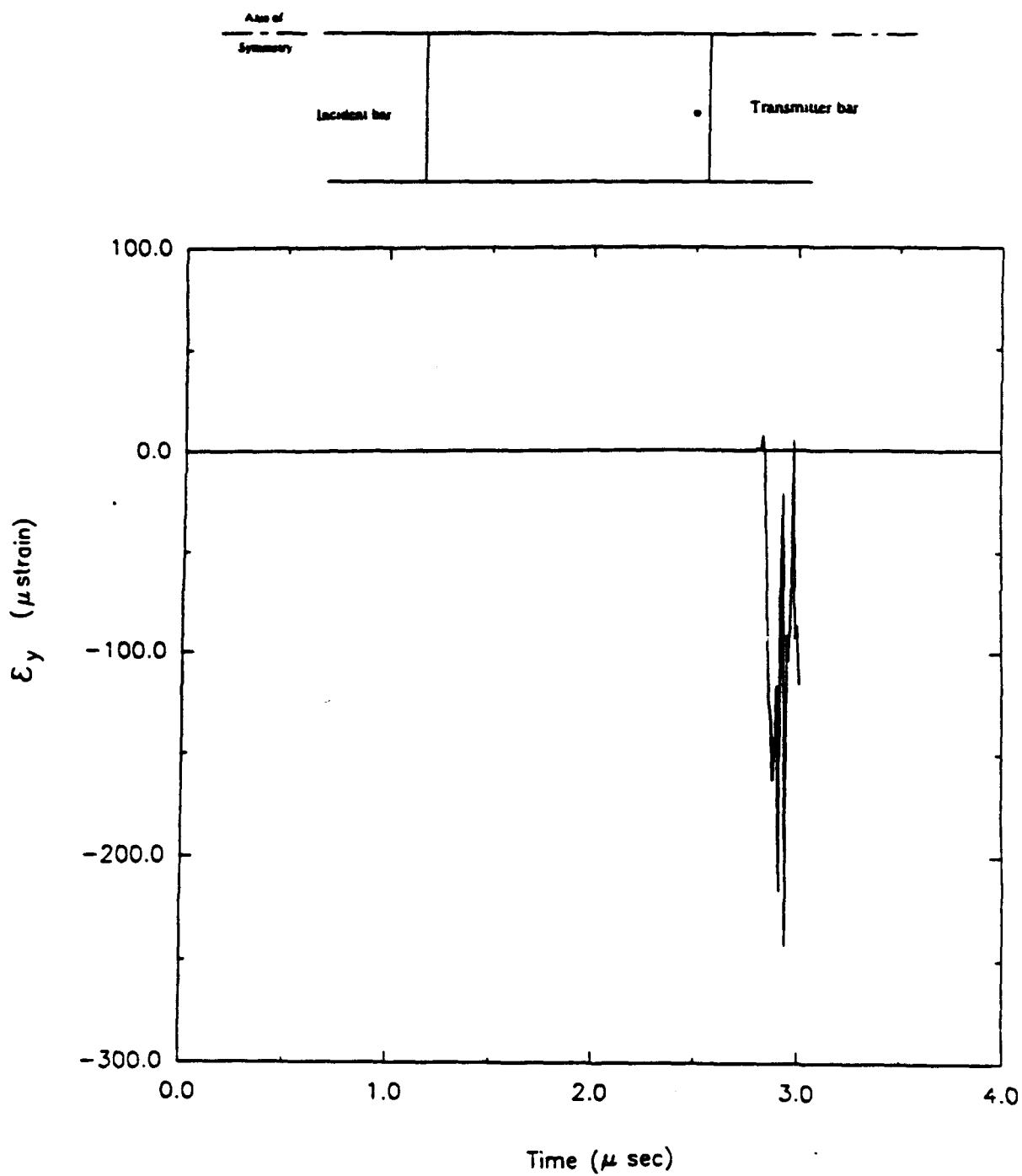


Figure 181. Time history for radial strain (direct compression, Load Case 2).

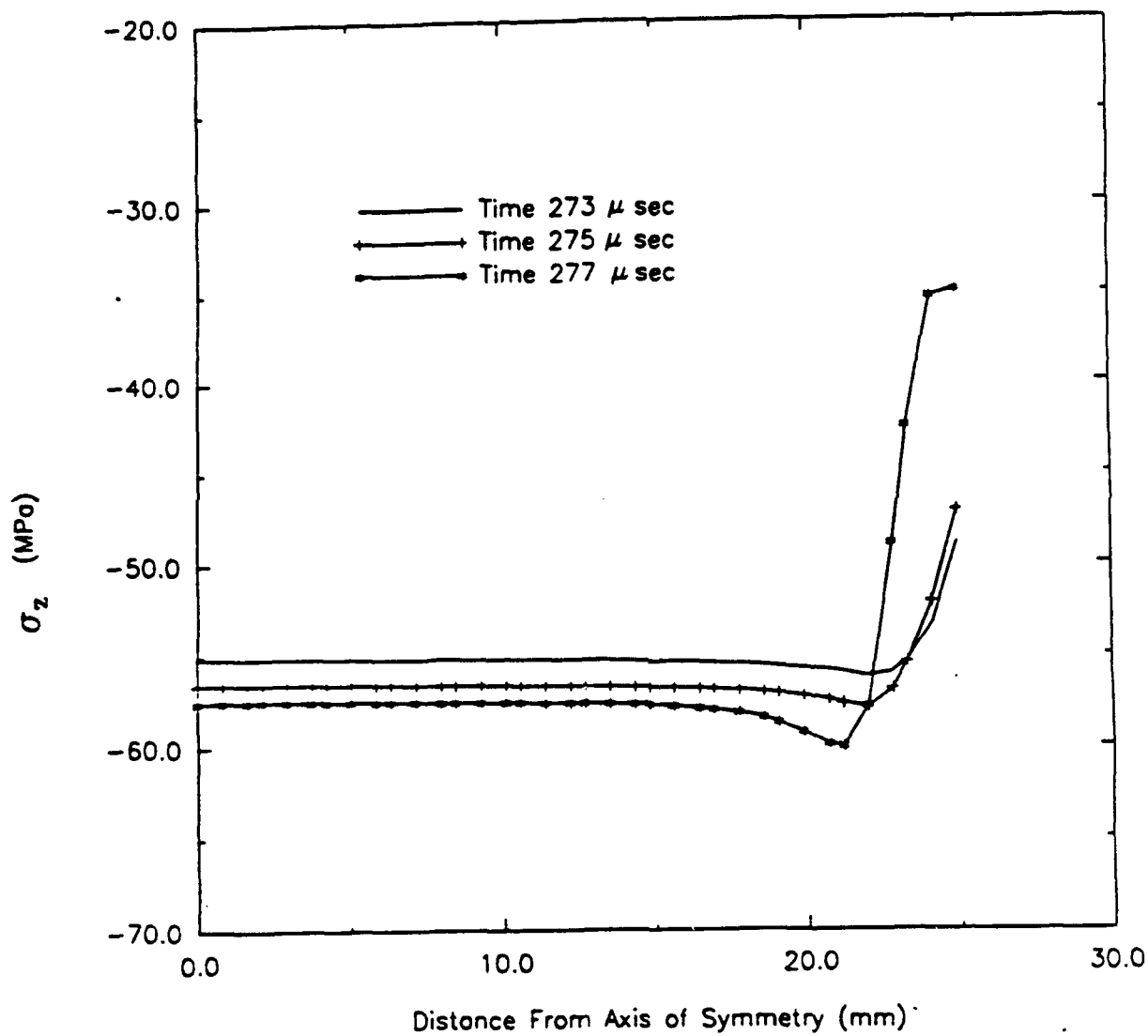
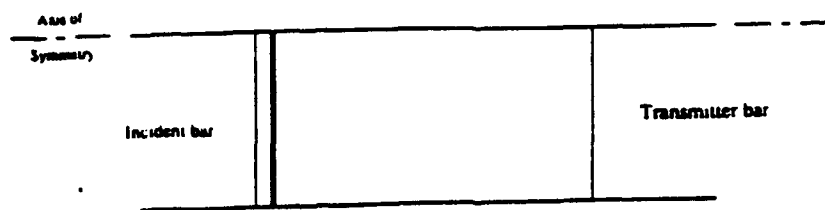


Figure 182. Profiles for longitudinal stress (direct compression, Load Case 2).

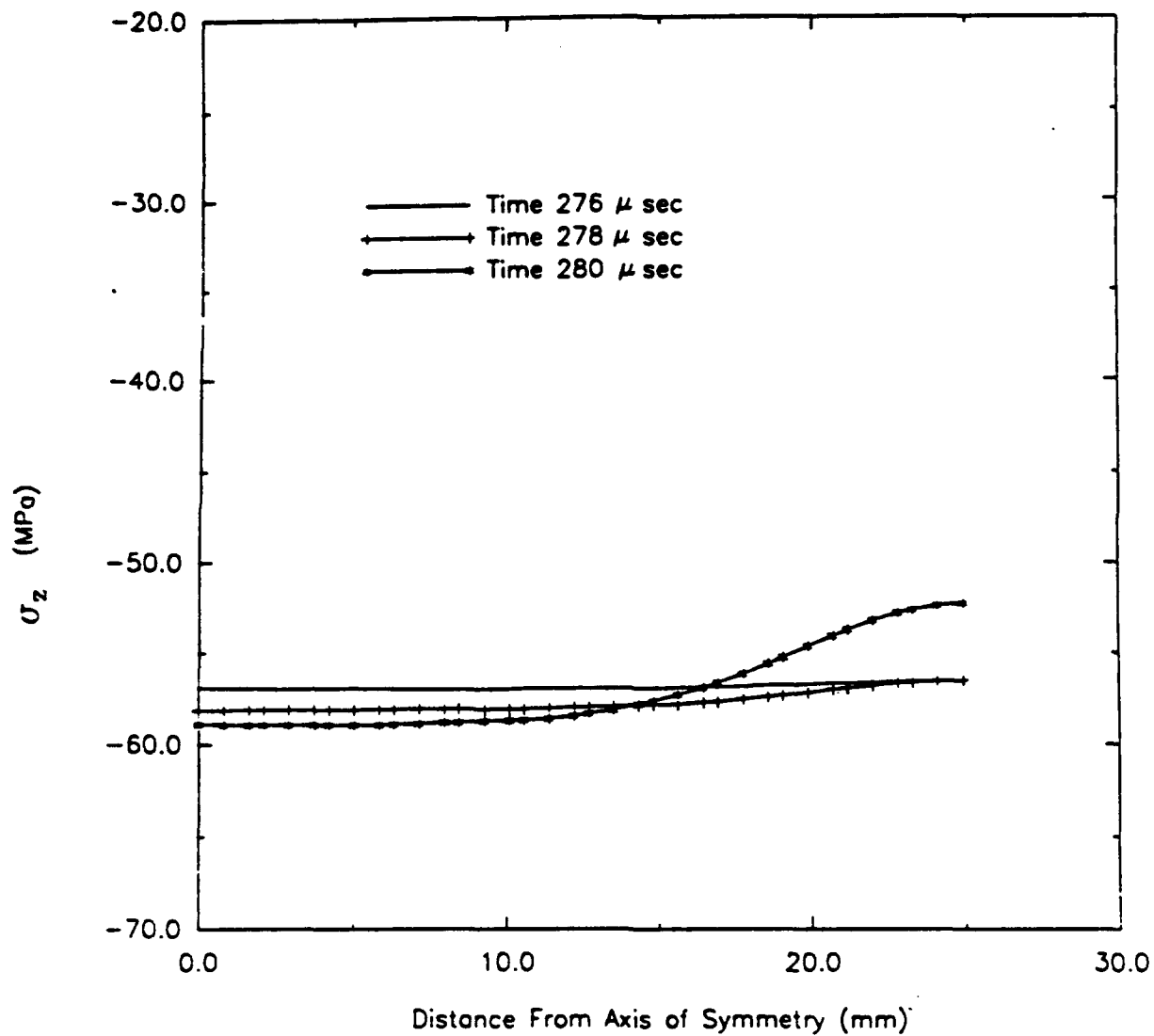
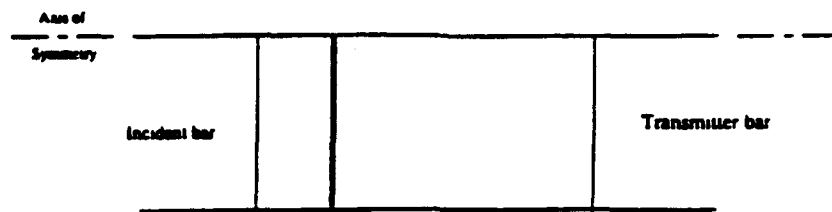


Figure 183. Profiles for longitudinal stress (direct compression, Load Case 2).

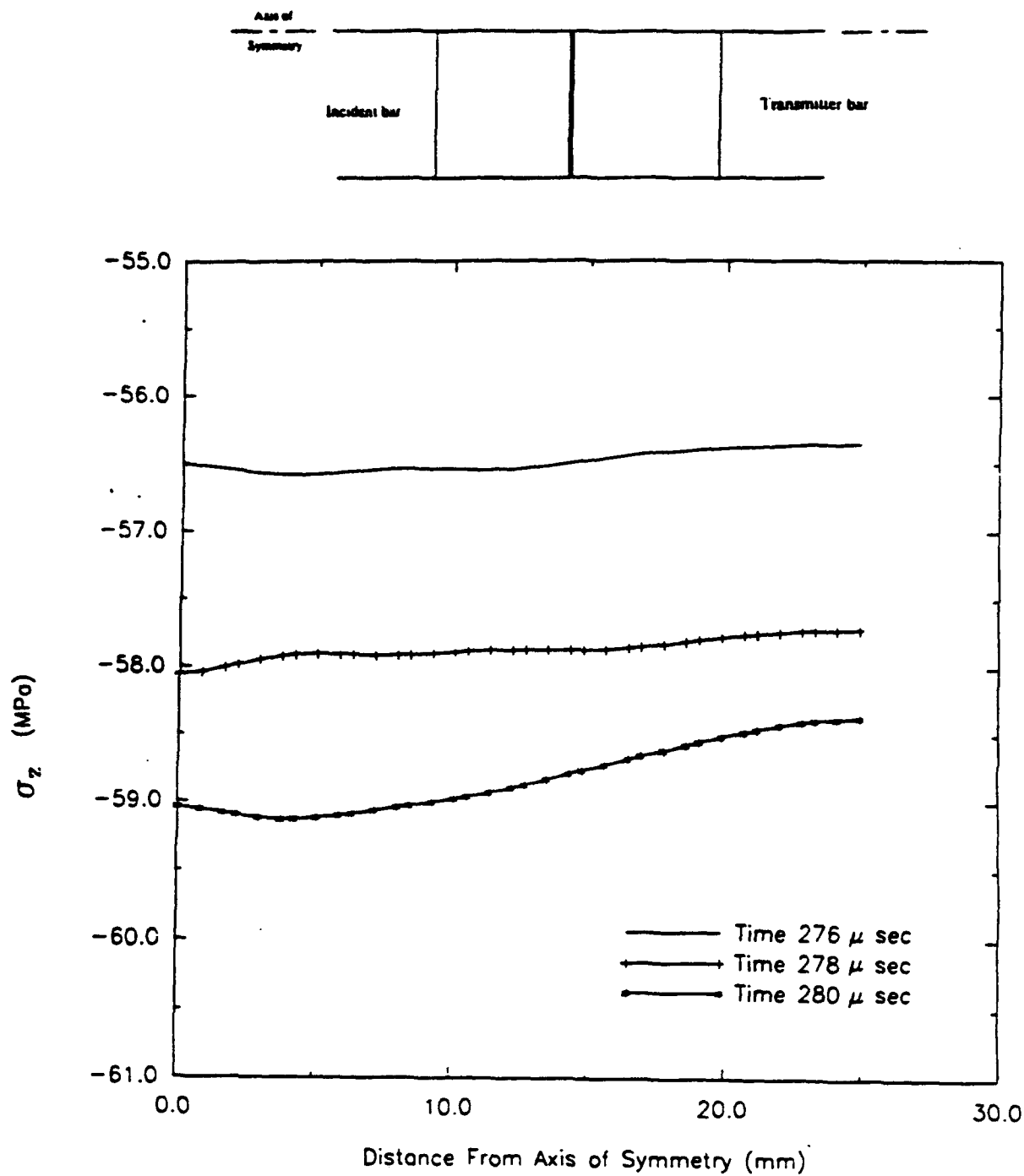


Figure 184. Profiles for longitudinal stress (direct compression, Load Case 2).

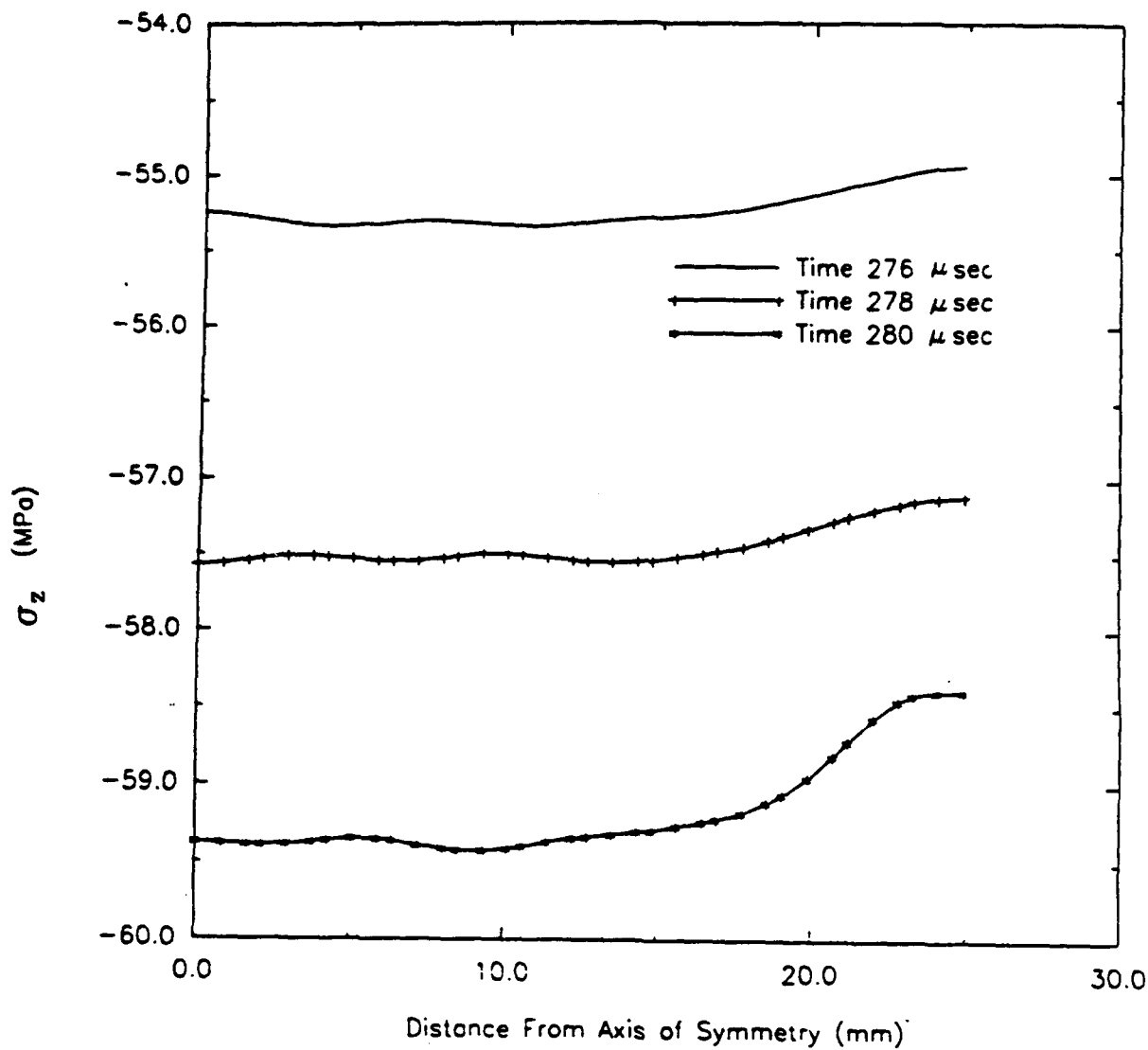
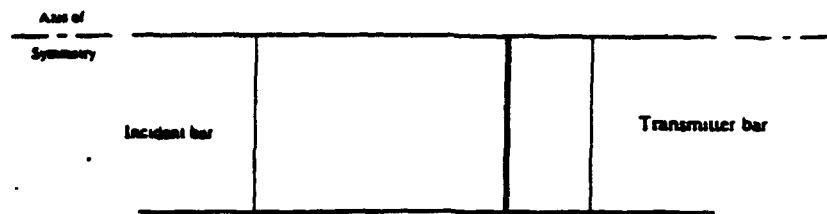


Figure 185. Profiles for longitudinal stress (direct compression, Load Case 2).

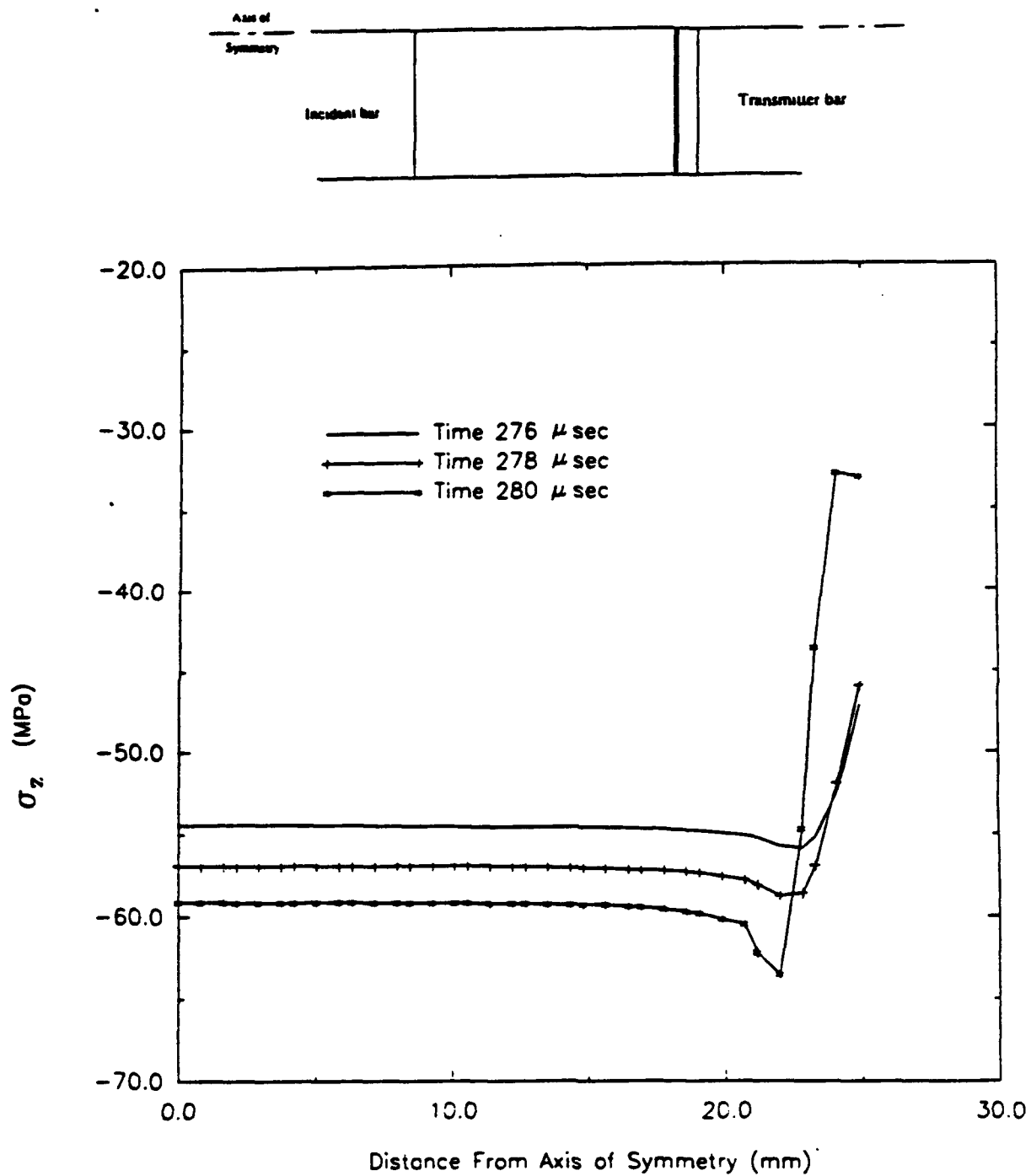


Figure 186. Profiles for longitudinal stress (direct compression, Load Case 2).

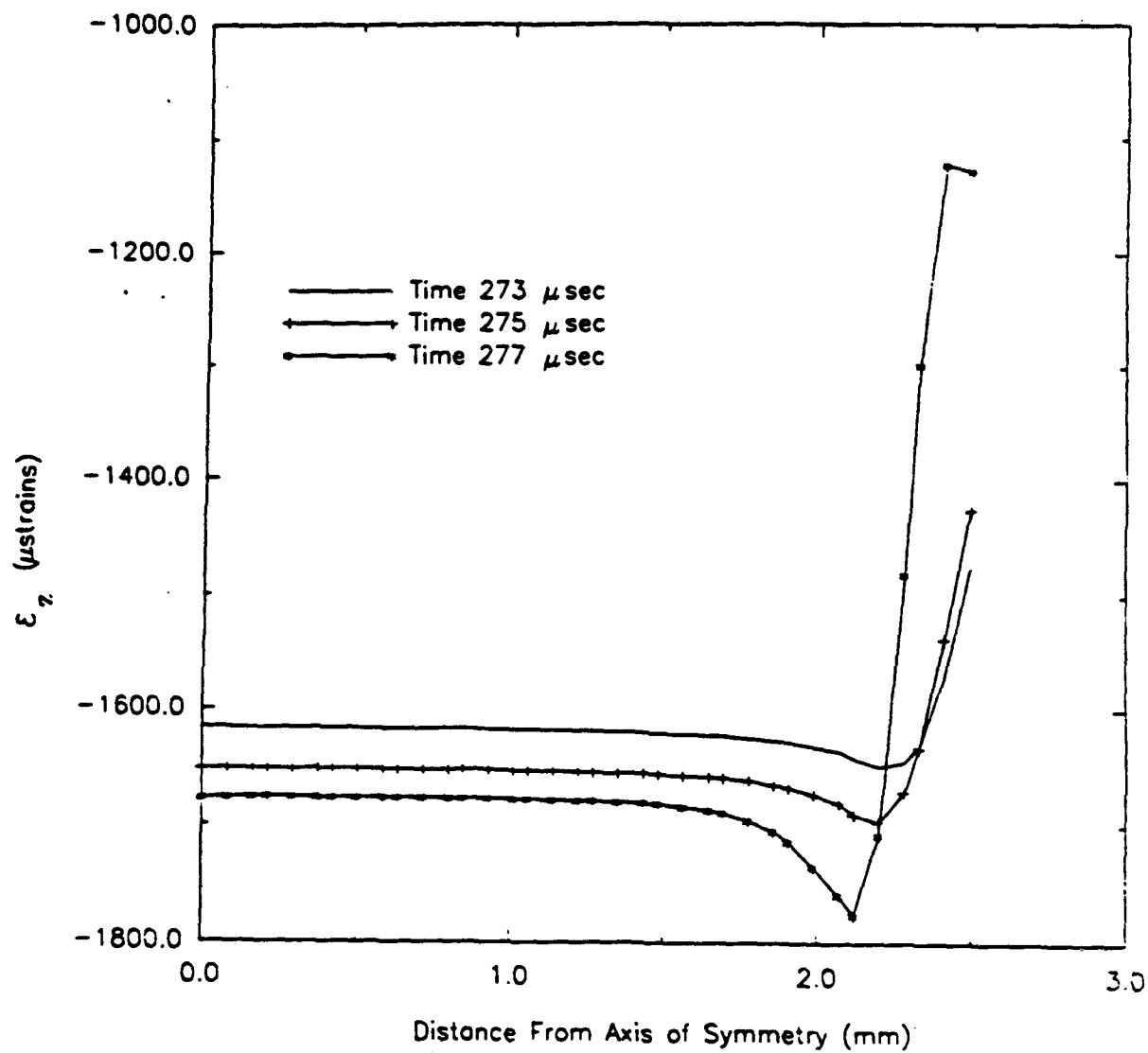
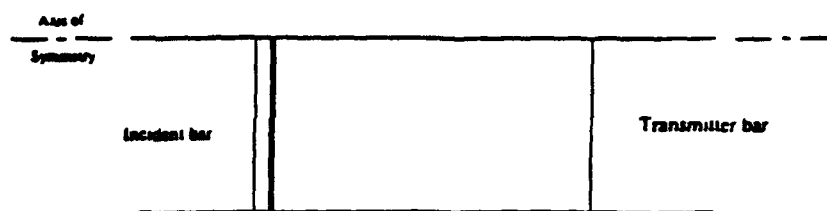


Figure 187. Profiles for longitudinal strain (direct compression, Load Case 2).

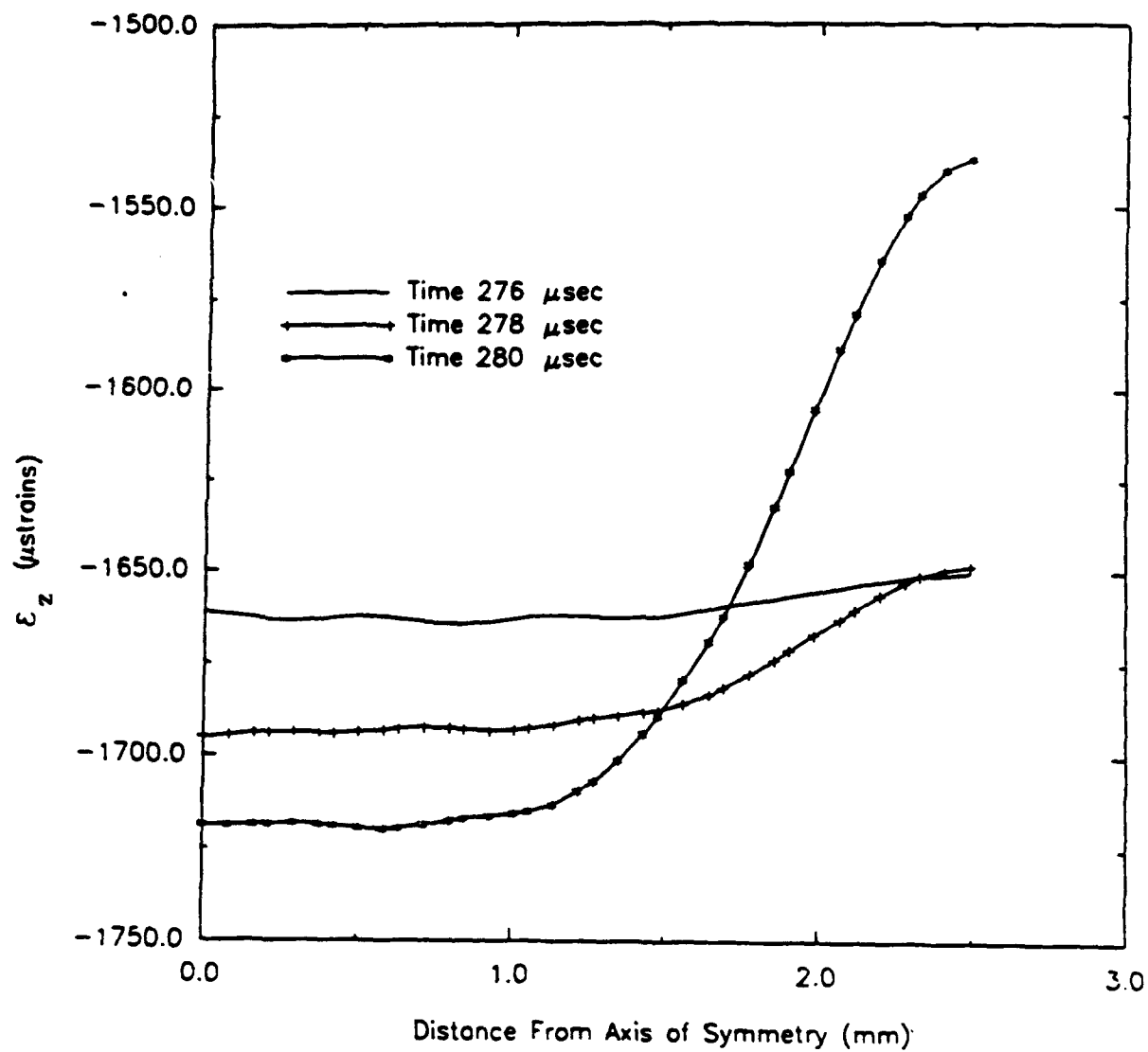
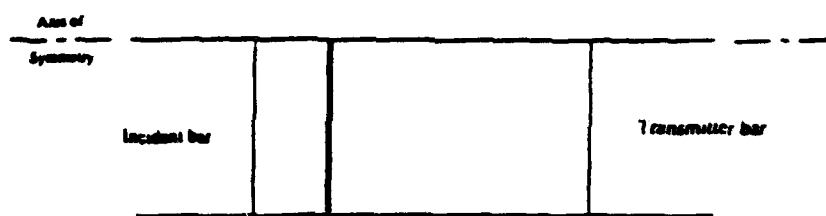


Figure 188. Profiles for longitudinal strain (direct compression, Load Case 2).

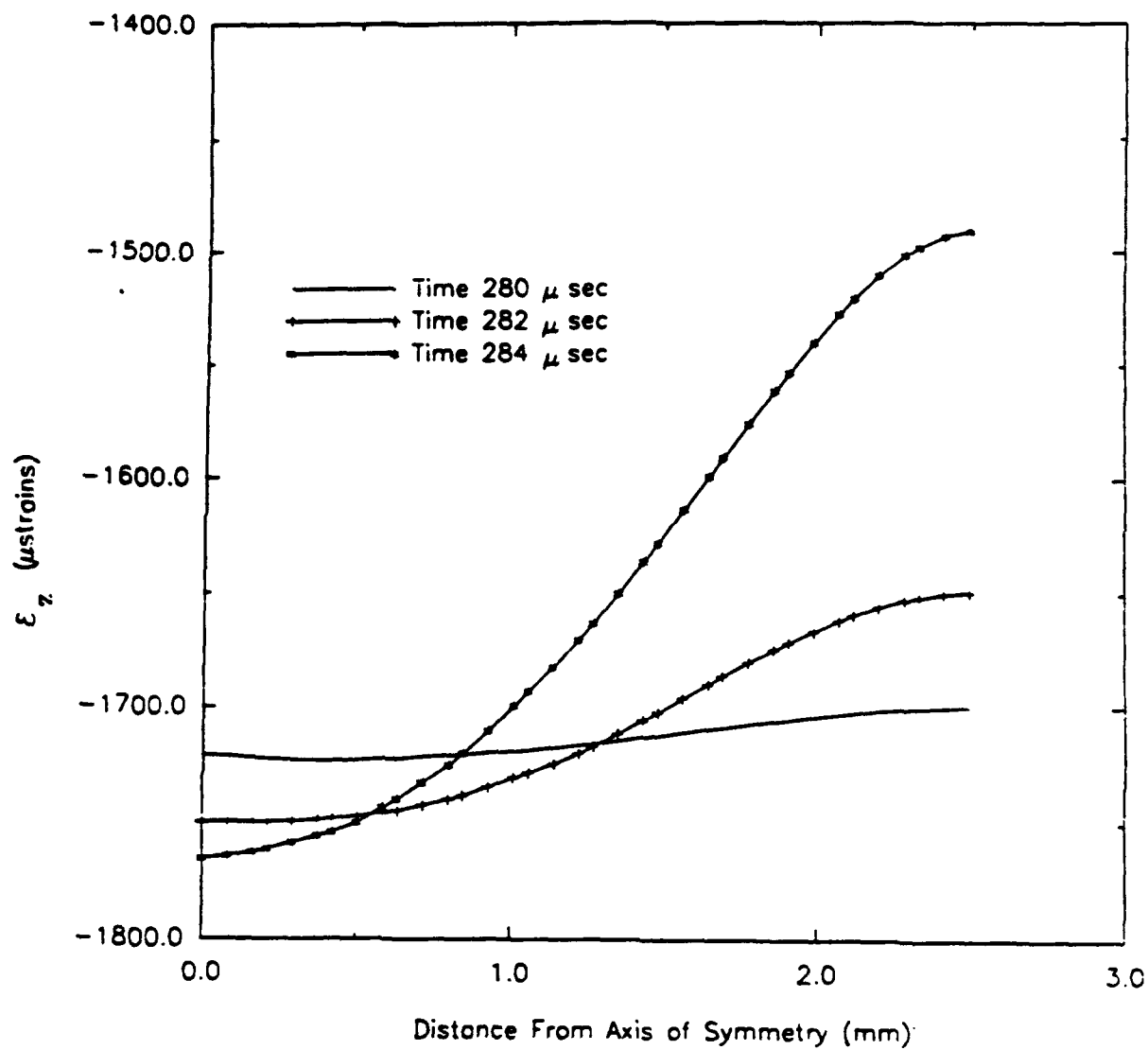
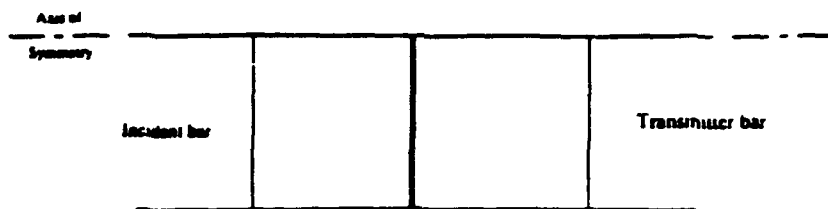


Figure 189. Profiles for longitudinal strain (direct compression, Load Case 2).

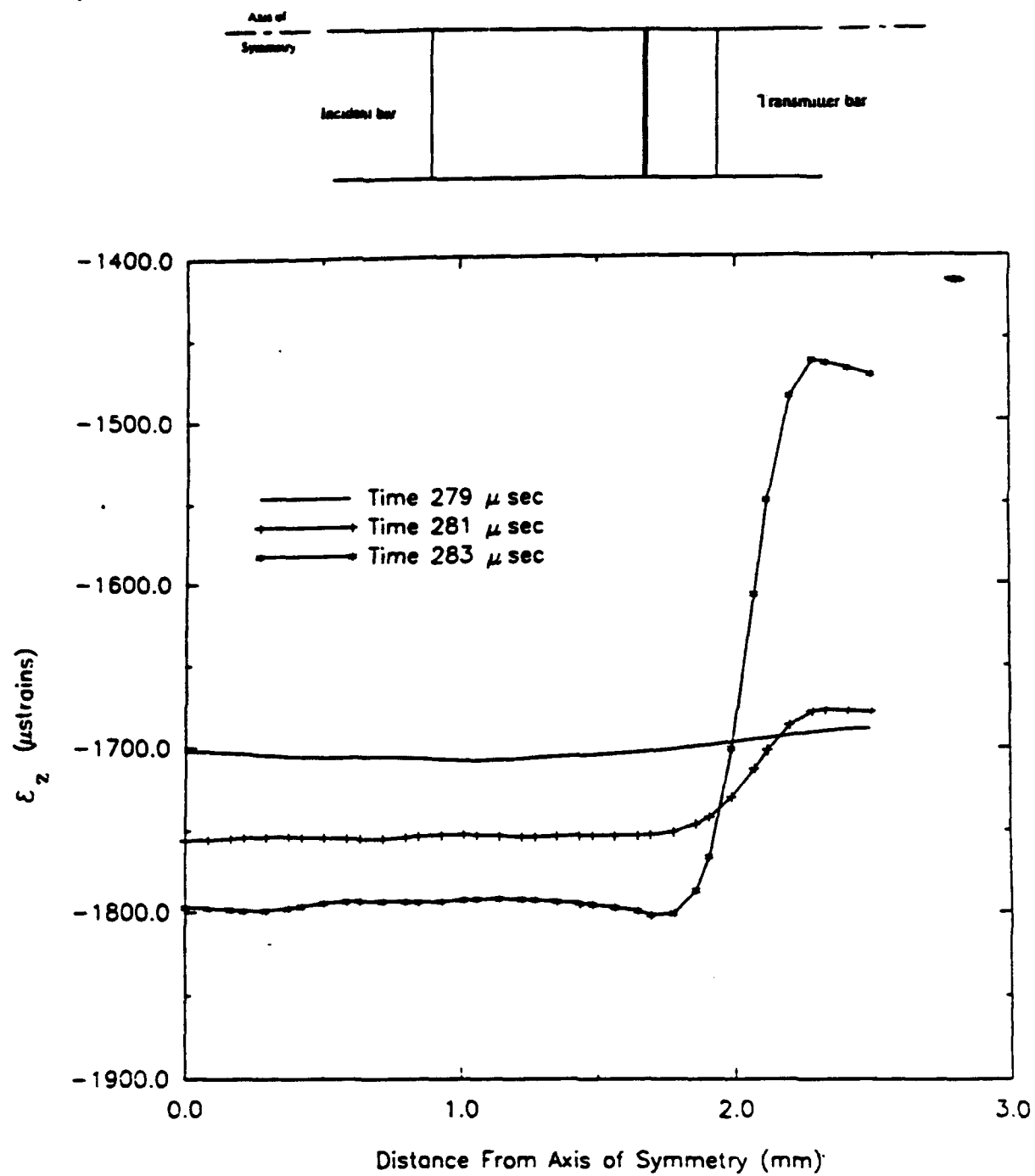


Figure 190. Profiles for longitudinal strain (direct compression, Load Case 2).

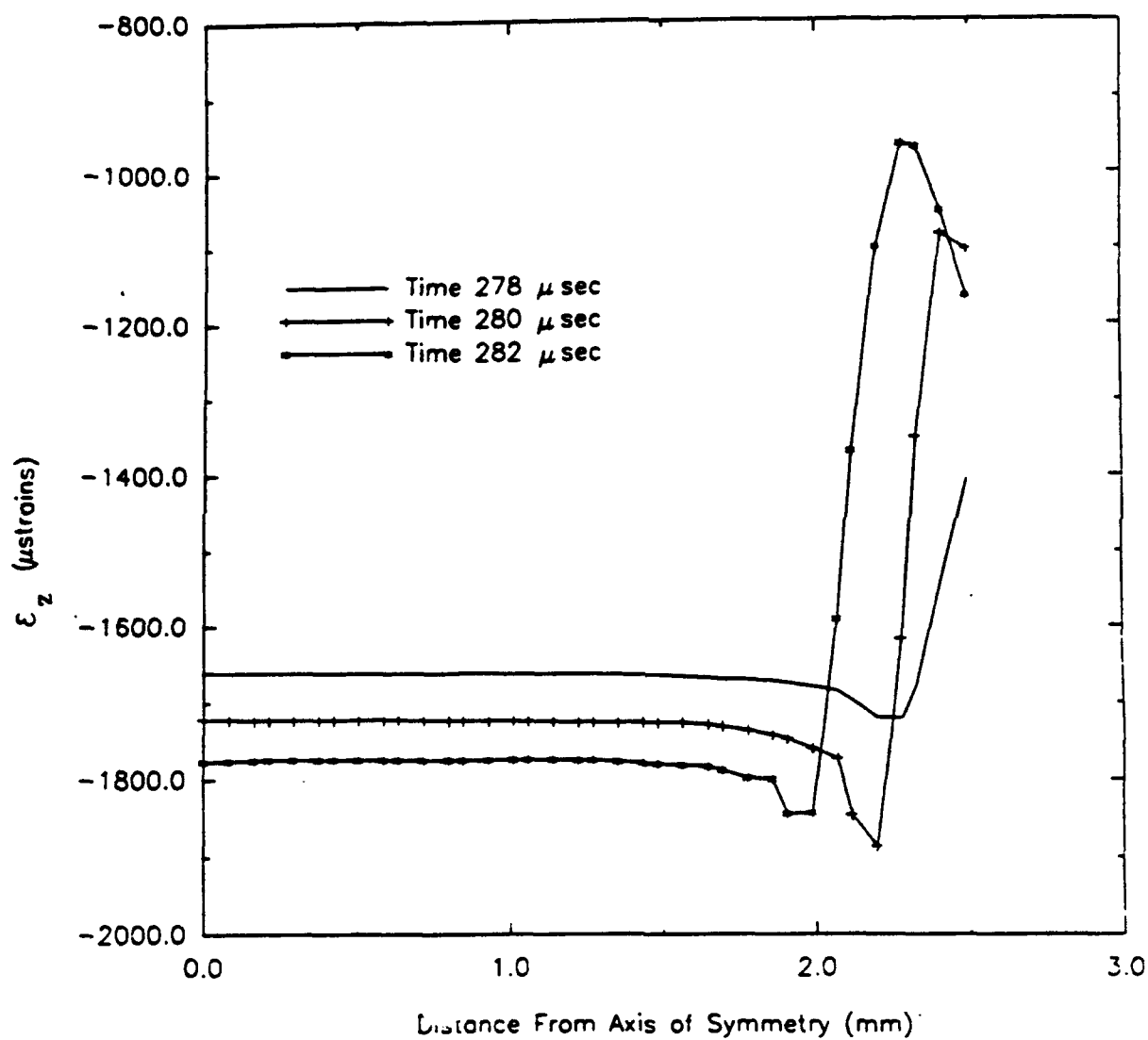
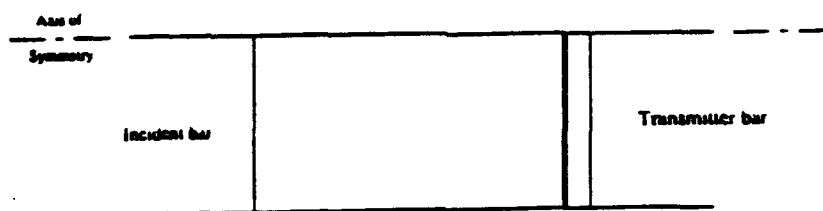
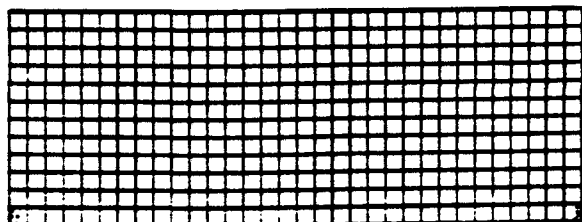
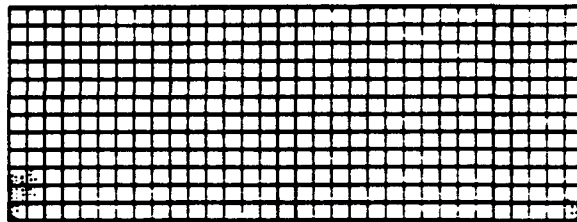


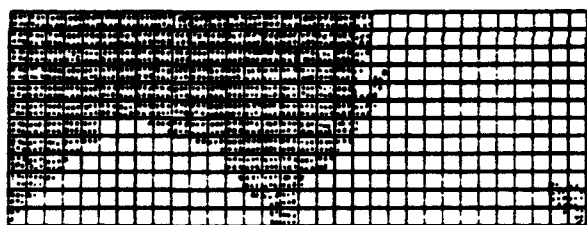
Figure 191. Profiles for longitudinal strain (direct compression, Load Case 2).



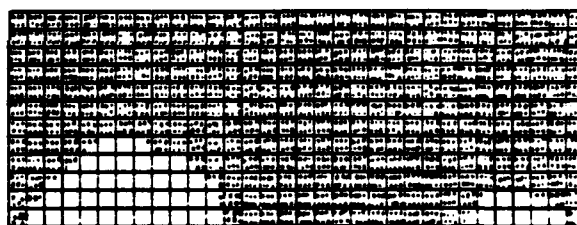
(a)



(b)



(c)



(d)

Figure 192. Cracking sequence for direct compression specimen; Load Case 2:
a) $t=272 \mu \text{ sec}$, b) $t=276 \mu \text{ sec}$, c) $t=278 \mu \text{ sec}$, d) $t=284 \mu \text{ sec}$.

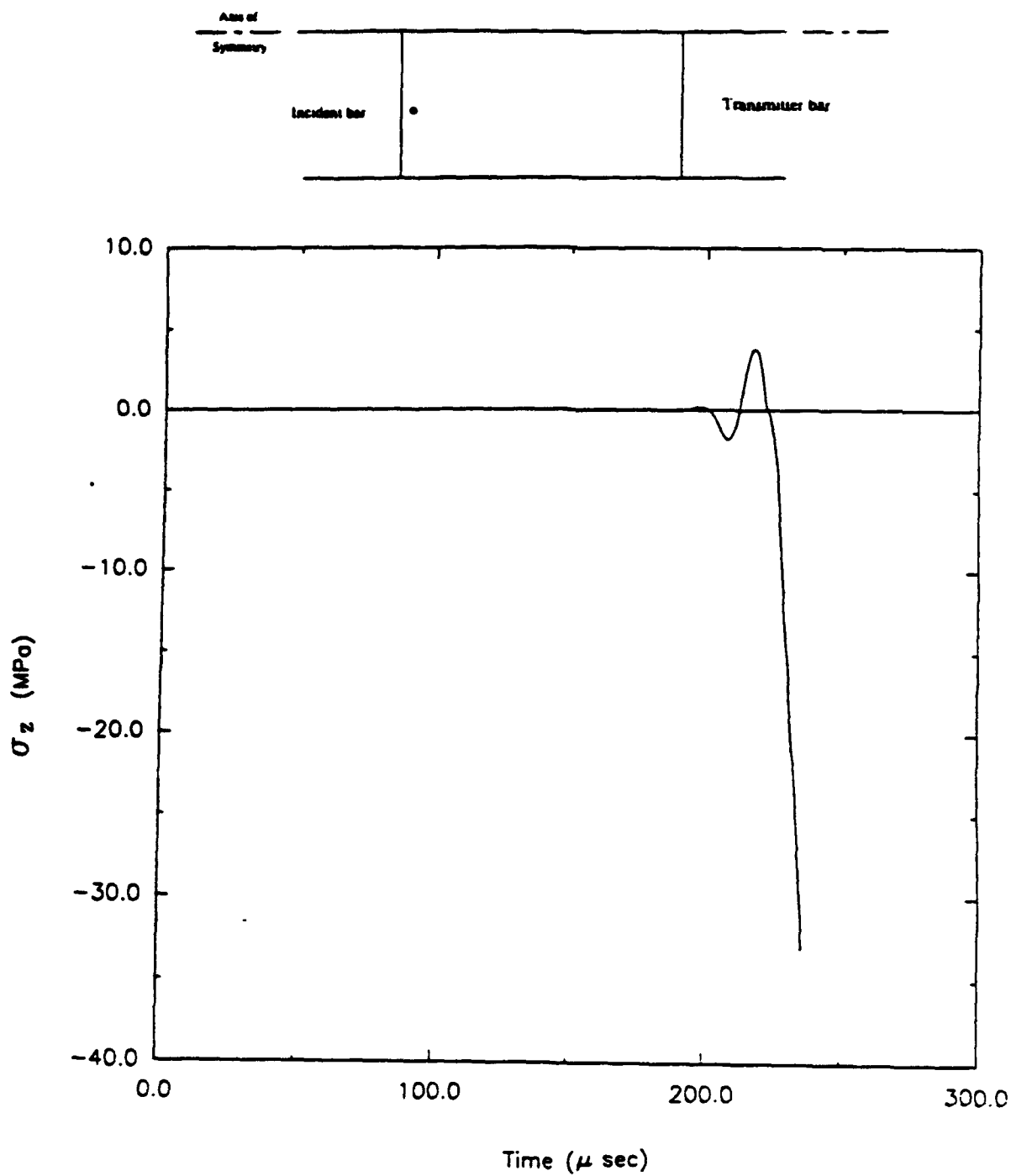


Figure 193. Time history for longitudinal stress (direct compression, Load Case 3).

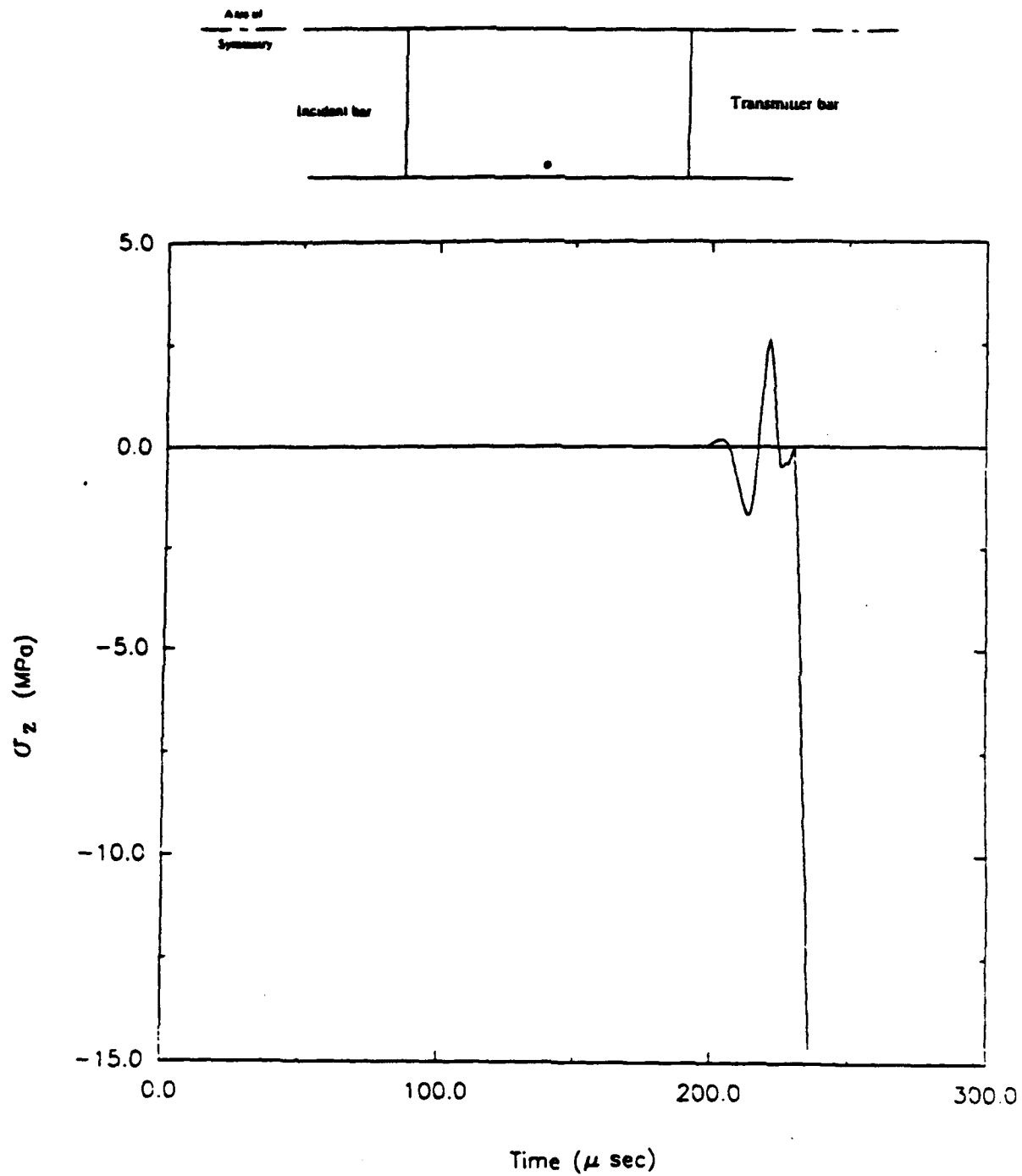


Figure 194. Time history for longitudinal stress (direct compression, Load Case 3).

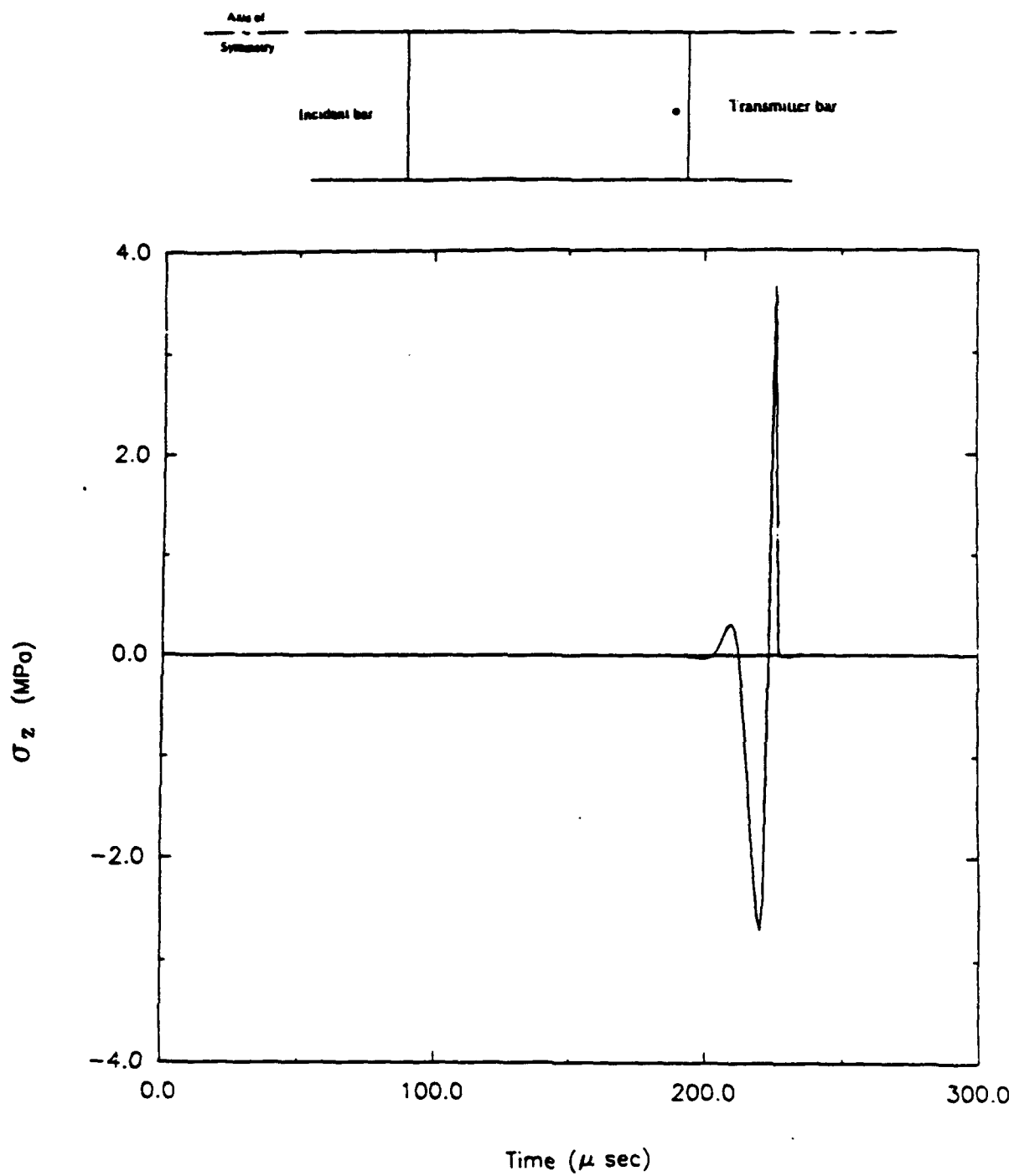


Figure 195. Time history for longitudinal stress (direct compression, Load Case 3).

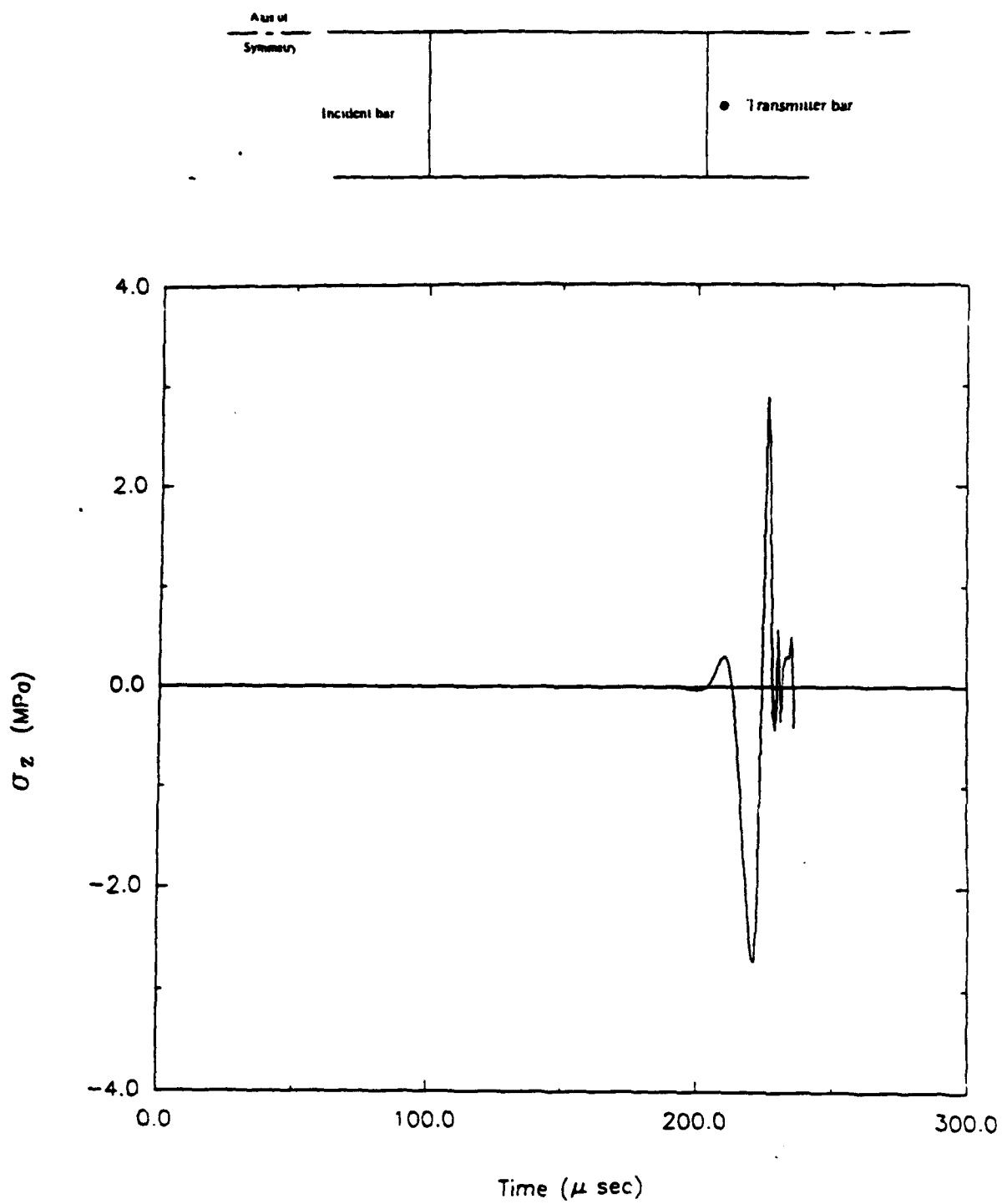


Figure 196. Time history for longitudinal stress (direct compression, Load Case 3).

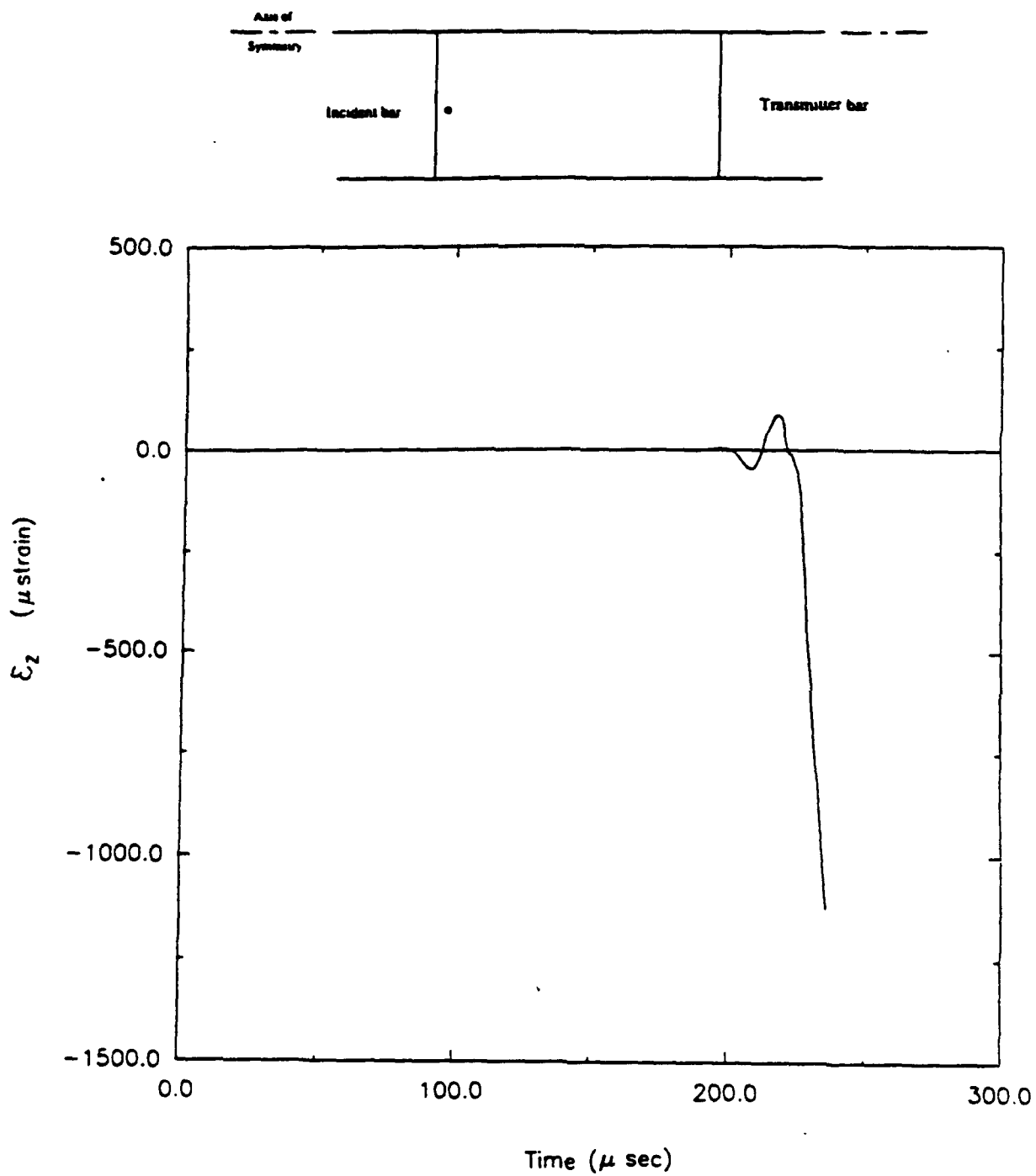


Figure 197. Time history for longitudinal strain (direct compression, Load Case 3).

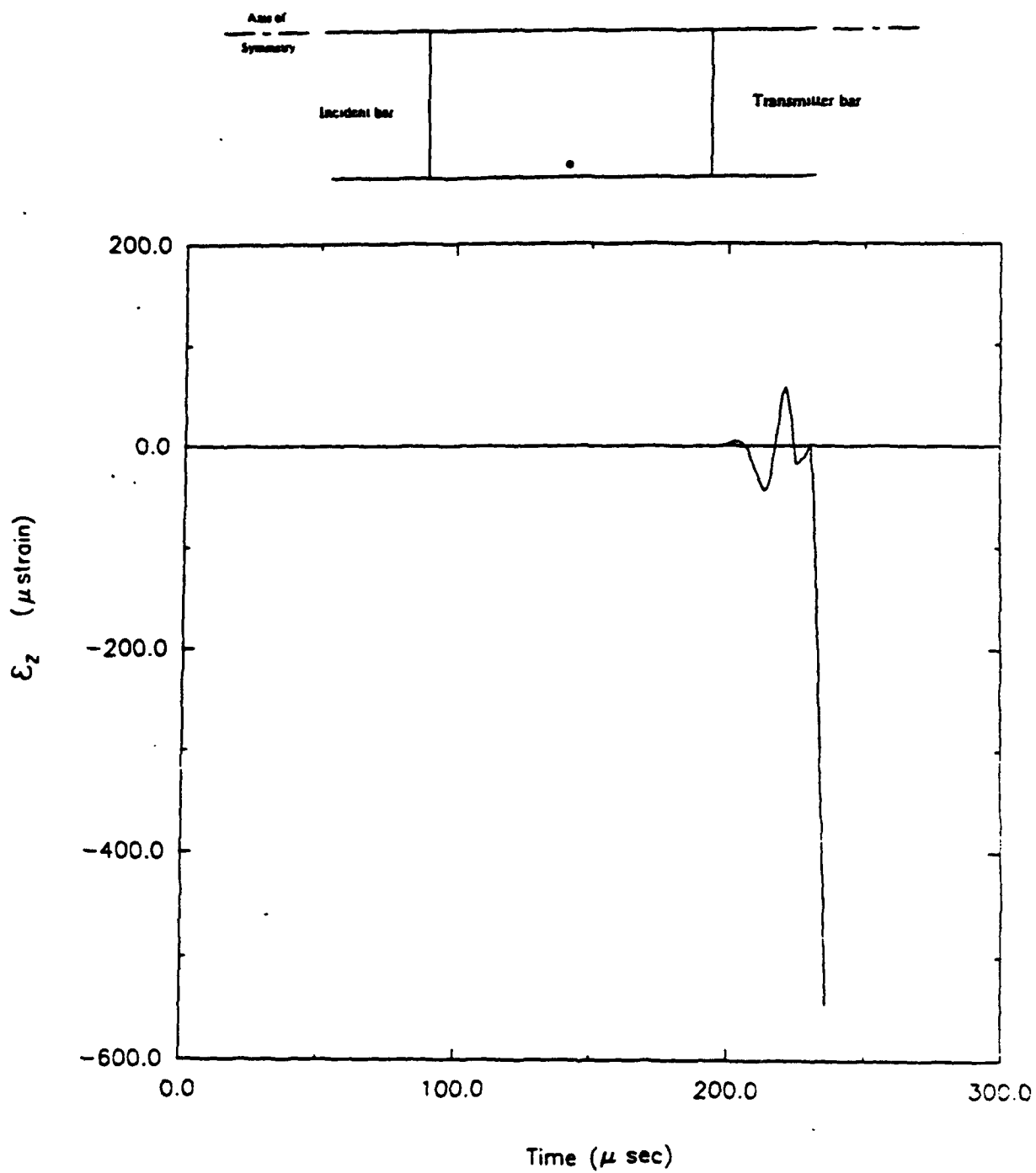


Figure 198. Time history for longitudinal strain (direct compression, Load Case 3).

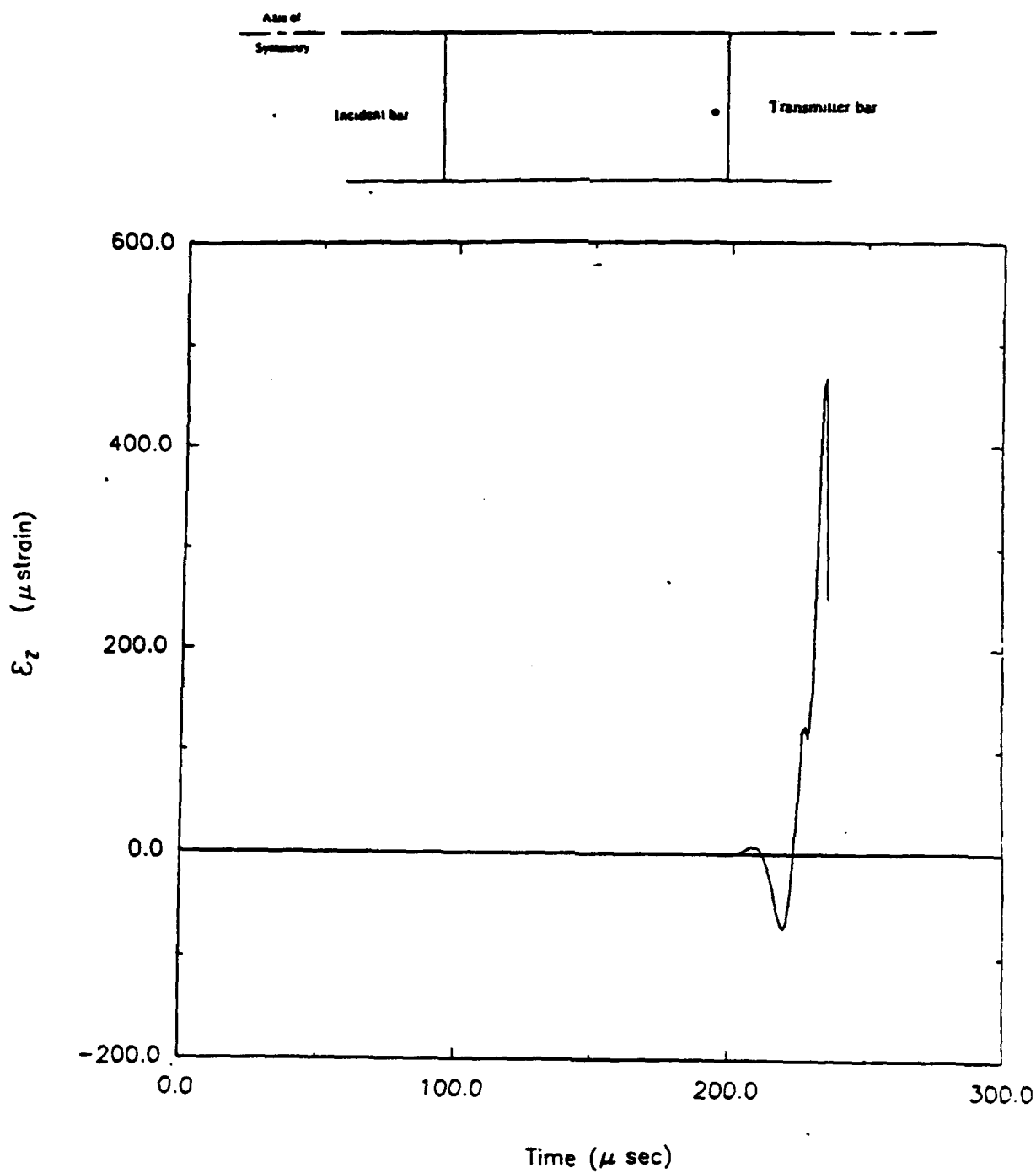


Figure 199. Time history for longitudinal strain (direct compression, Load Case 3).

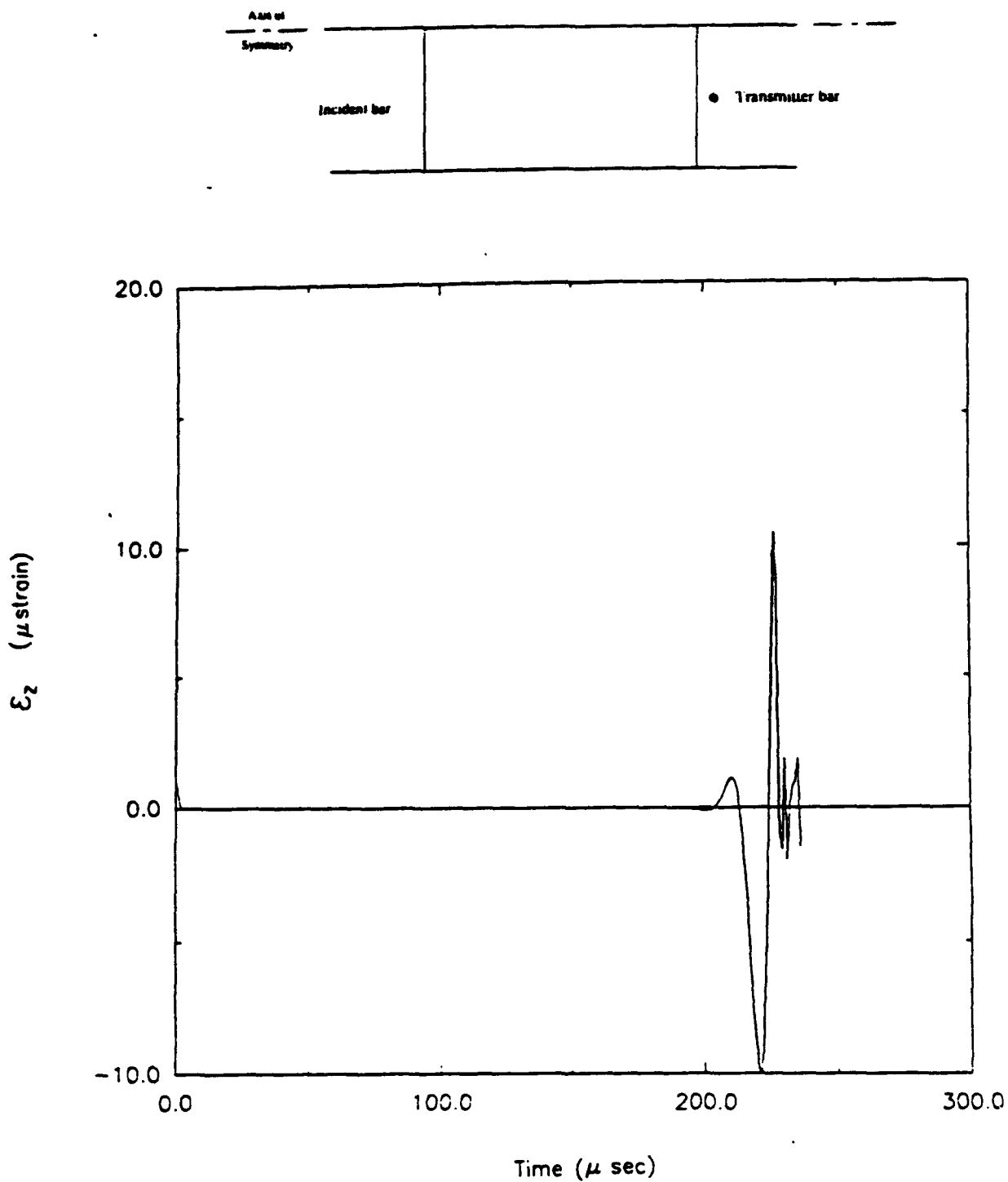


Figure 200. Time history for longitudinal strain (direct compression, Load Case 3).

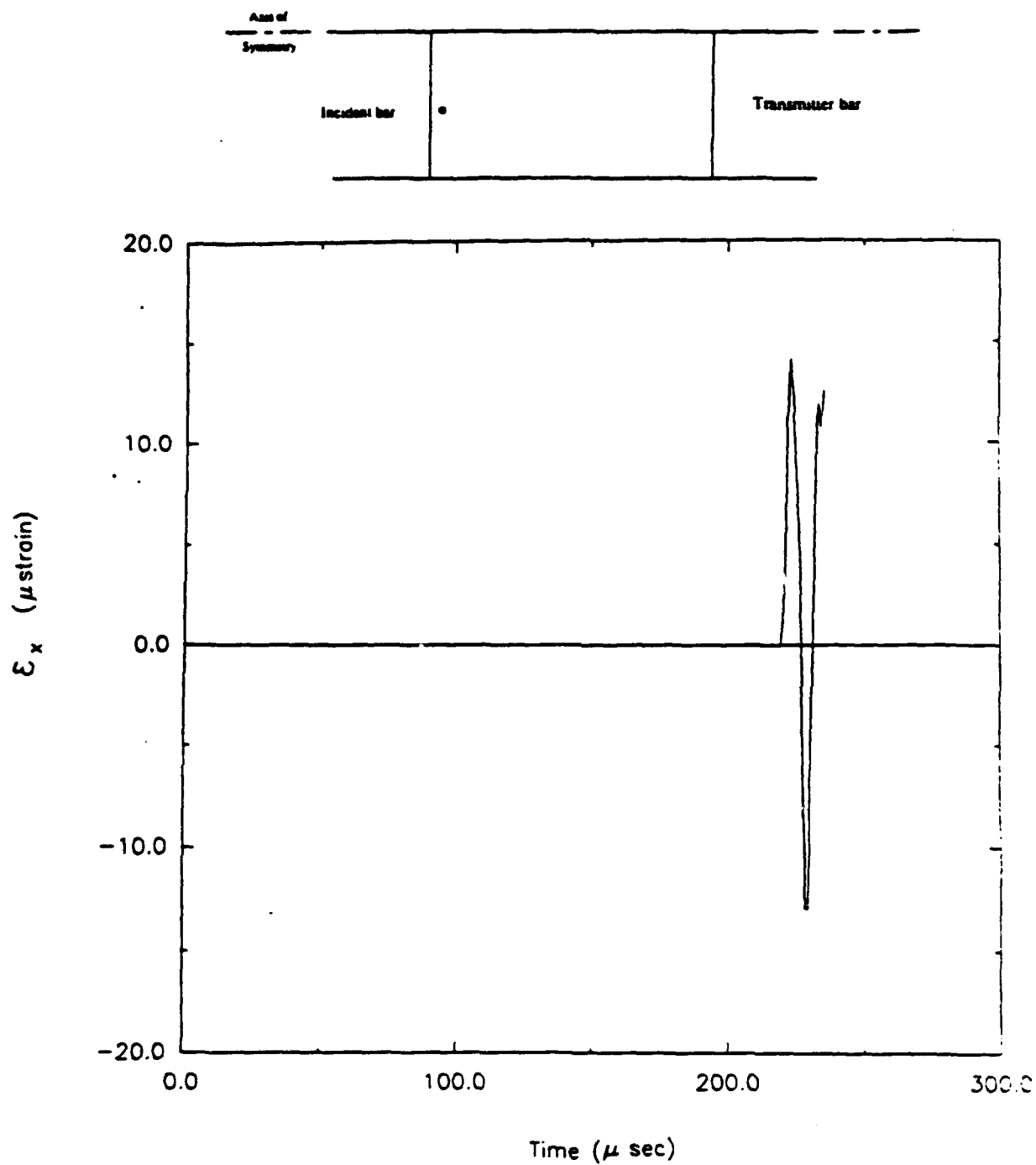


Figure 201. Time history for circumferential strain (direct compression, Load Case 3).

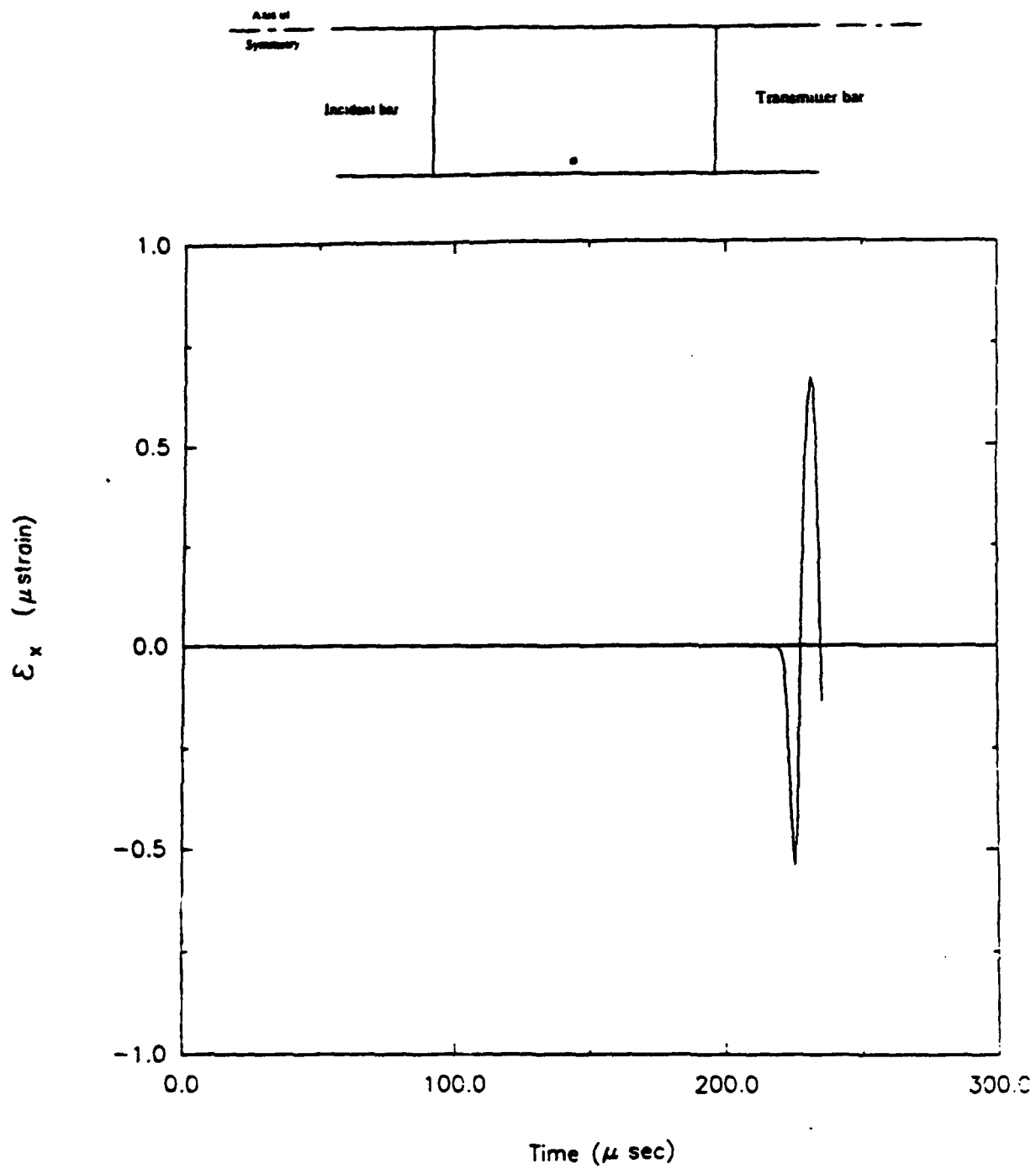


Figure 202. Time history for circumferential strain (direct compression, Load Case 3).

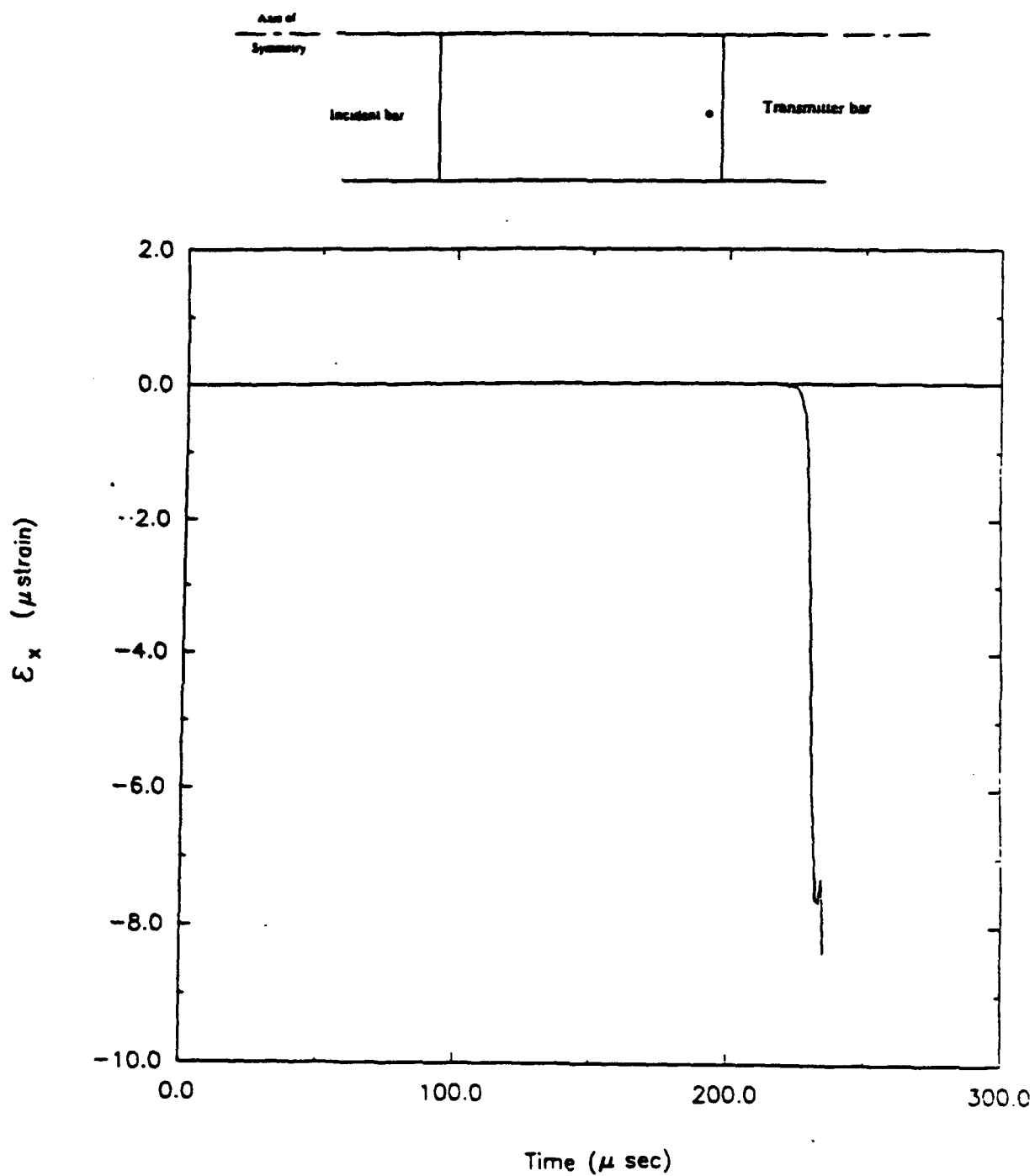


Figure 203. Time history for circumferential strain (direct compression, Load Case 3).

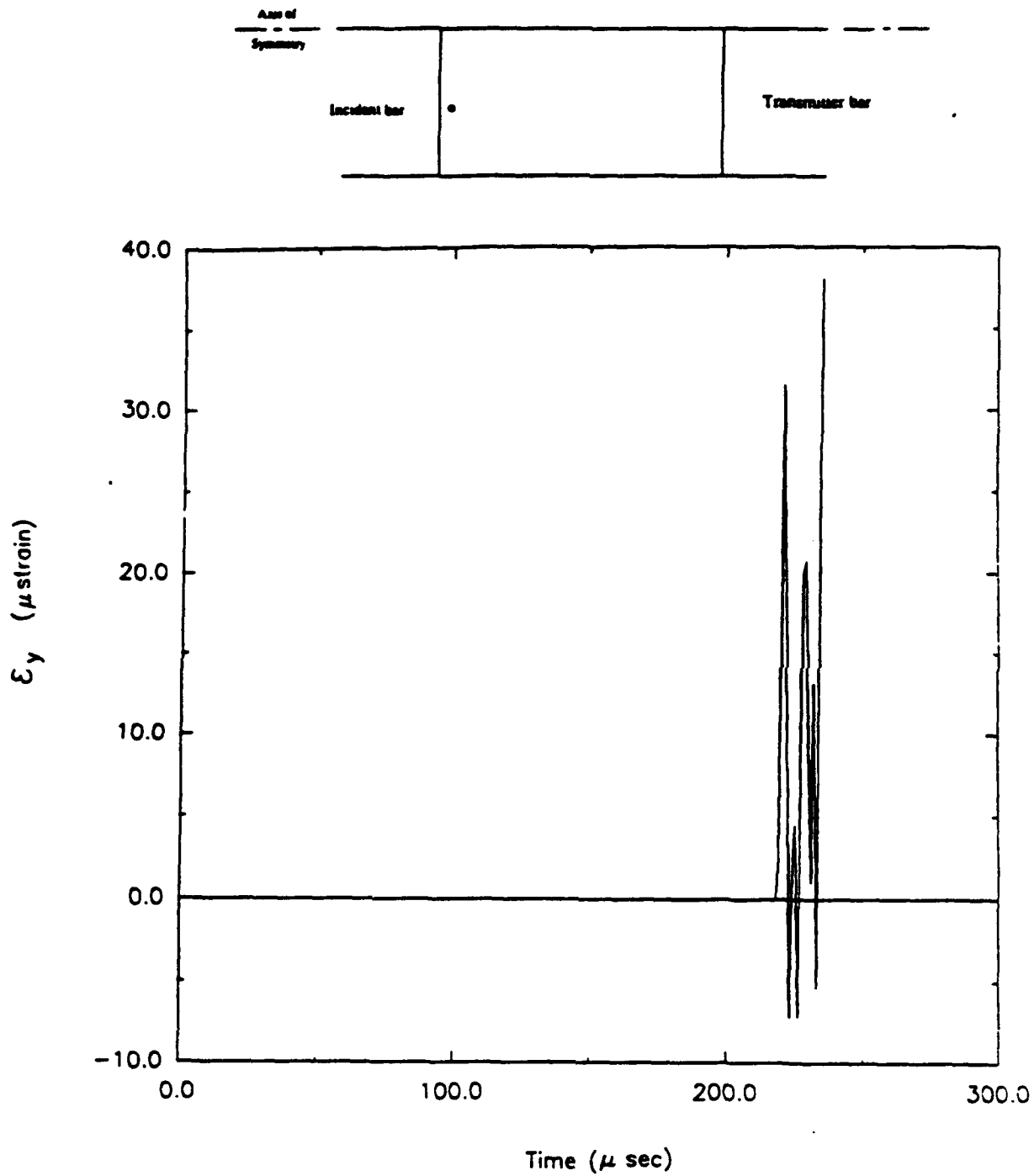


Figure 204. Time history for radial strain (direct compression, Load Case 3).

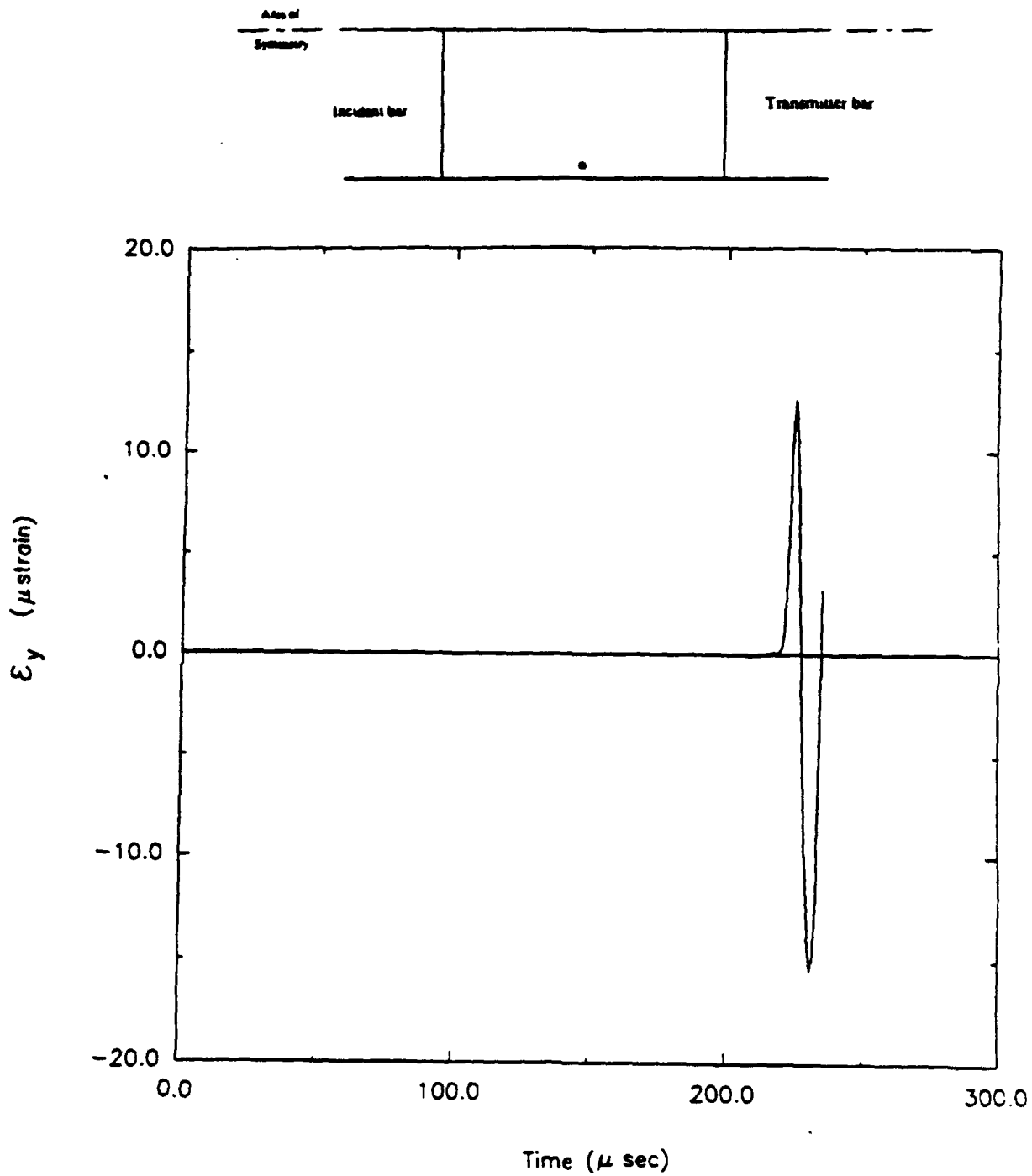


Figure 205. Time history for radial strain (direct compression, Load Case 3).

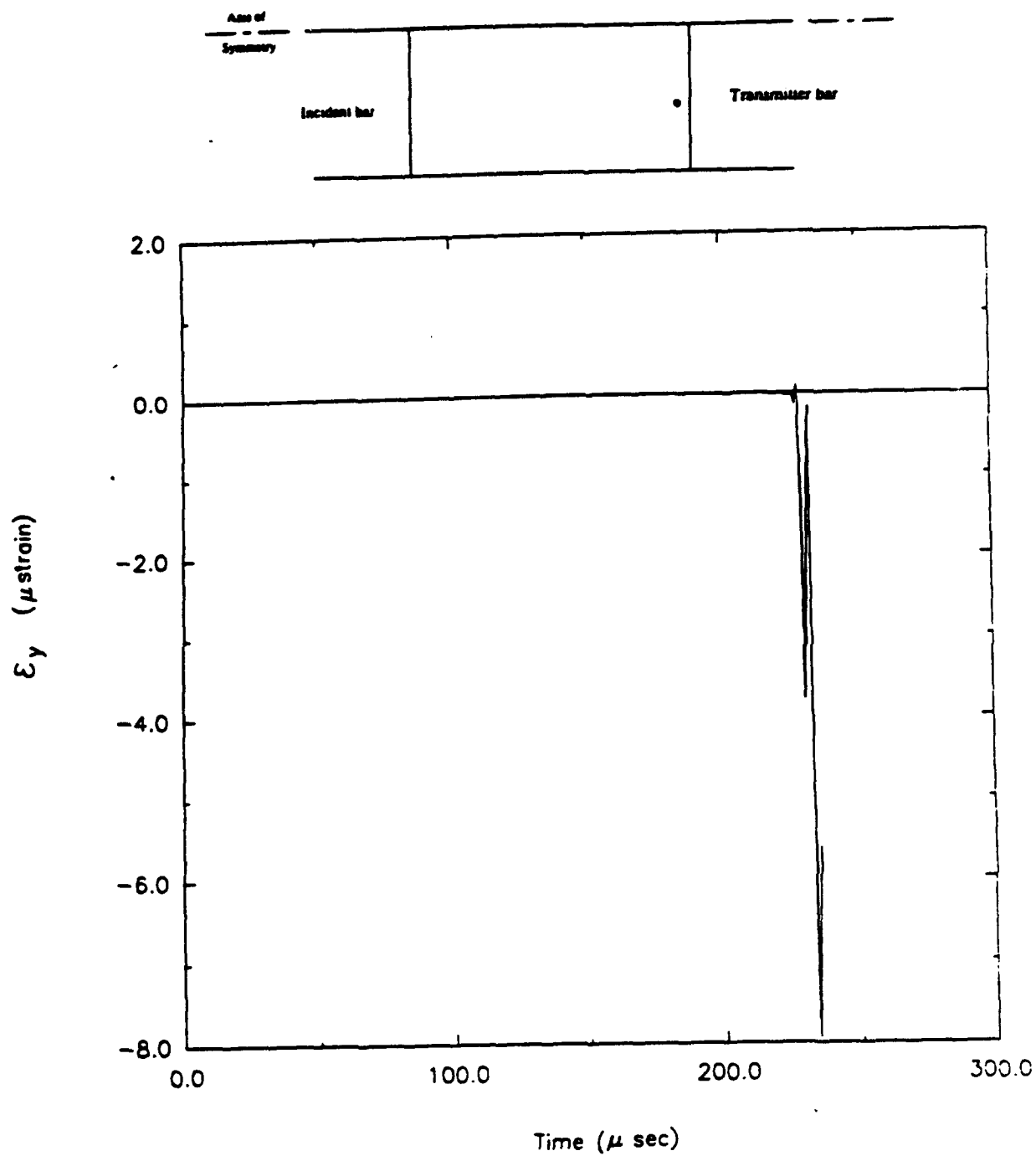


Figure 206. Time history for radial strain (direct compression, Load Case 3).

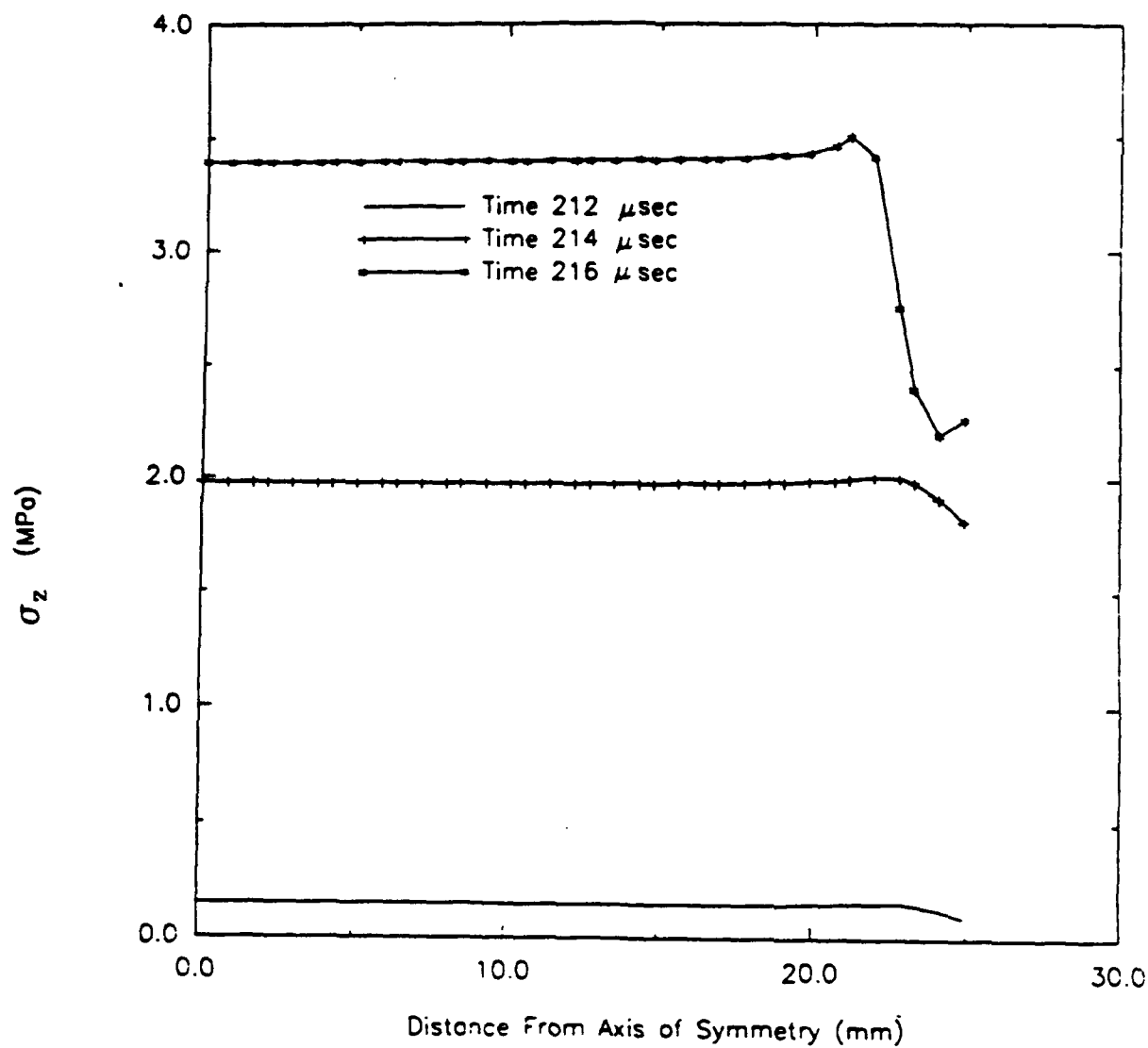
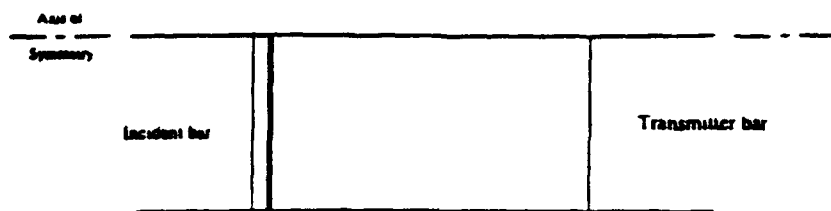


Figure 207. Profiles for longitudinal stress (direct compression, Load Case 3).

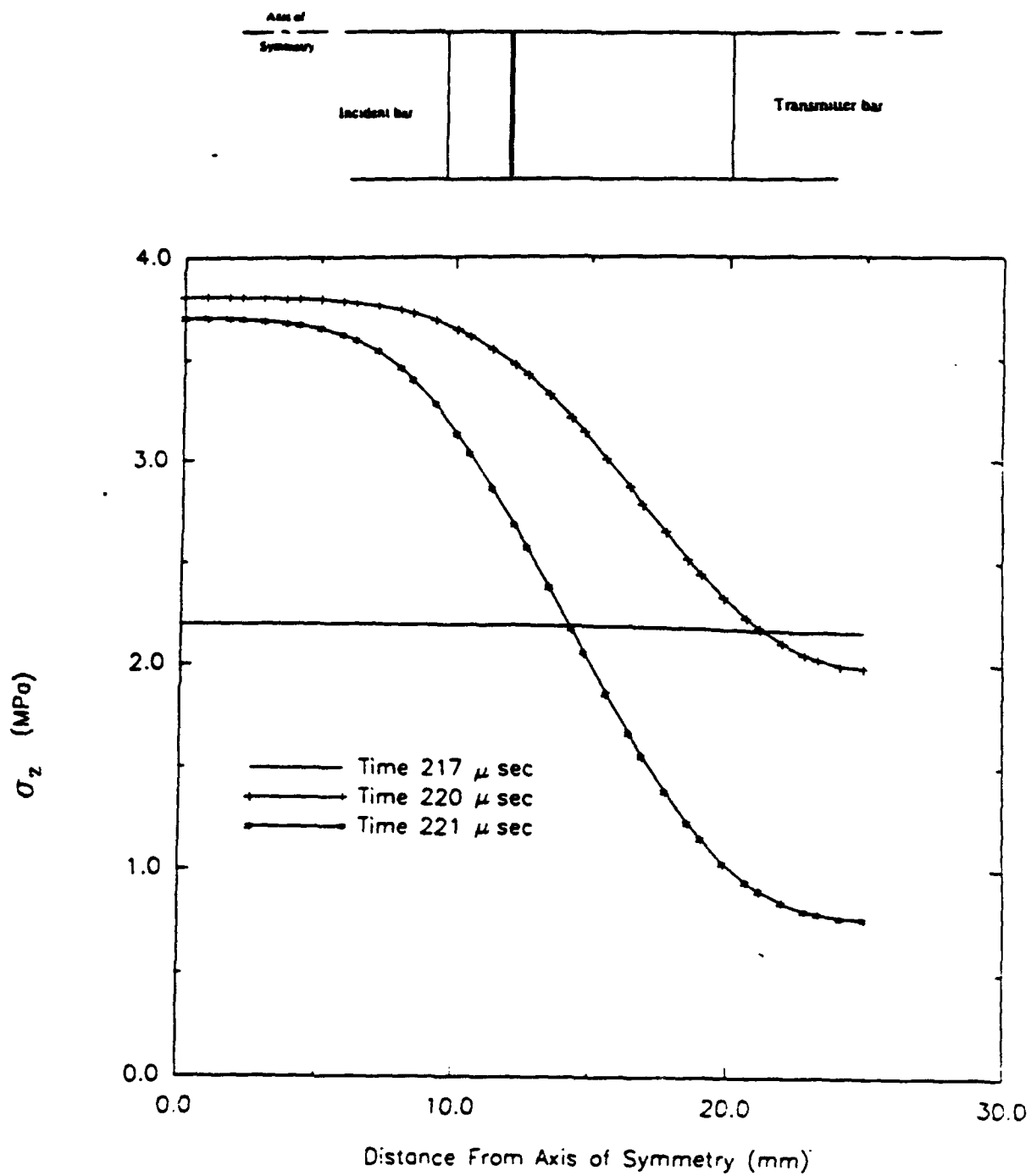


Figure 208. Profiles for longitudinal stress (direct compression, Load Case 3).

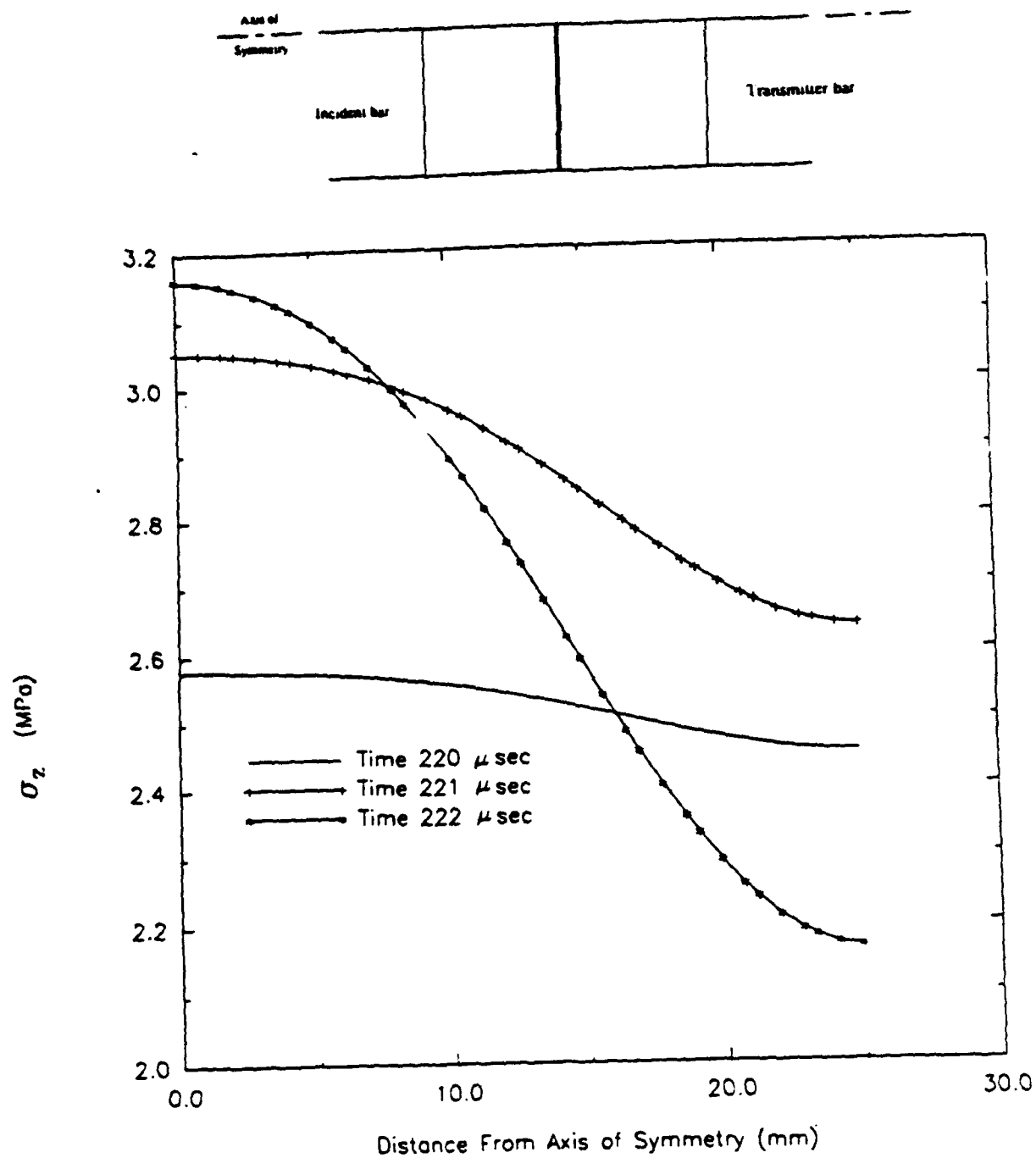


Figure 209. Profiles for longitudinal stress (direct compression, Load Case 3).

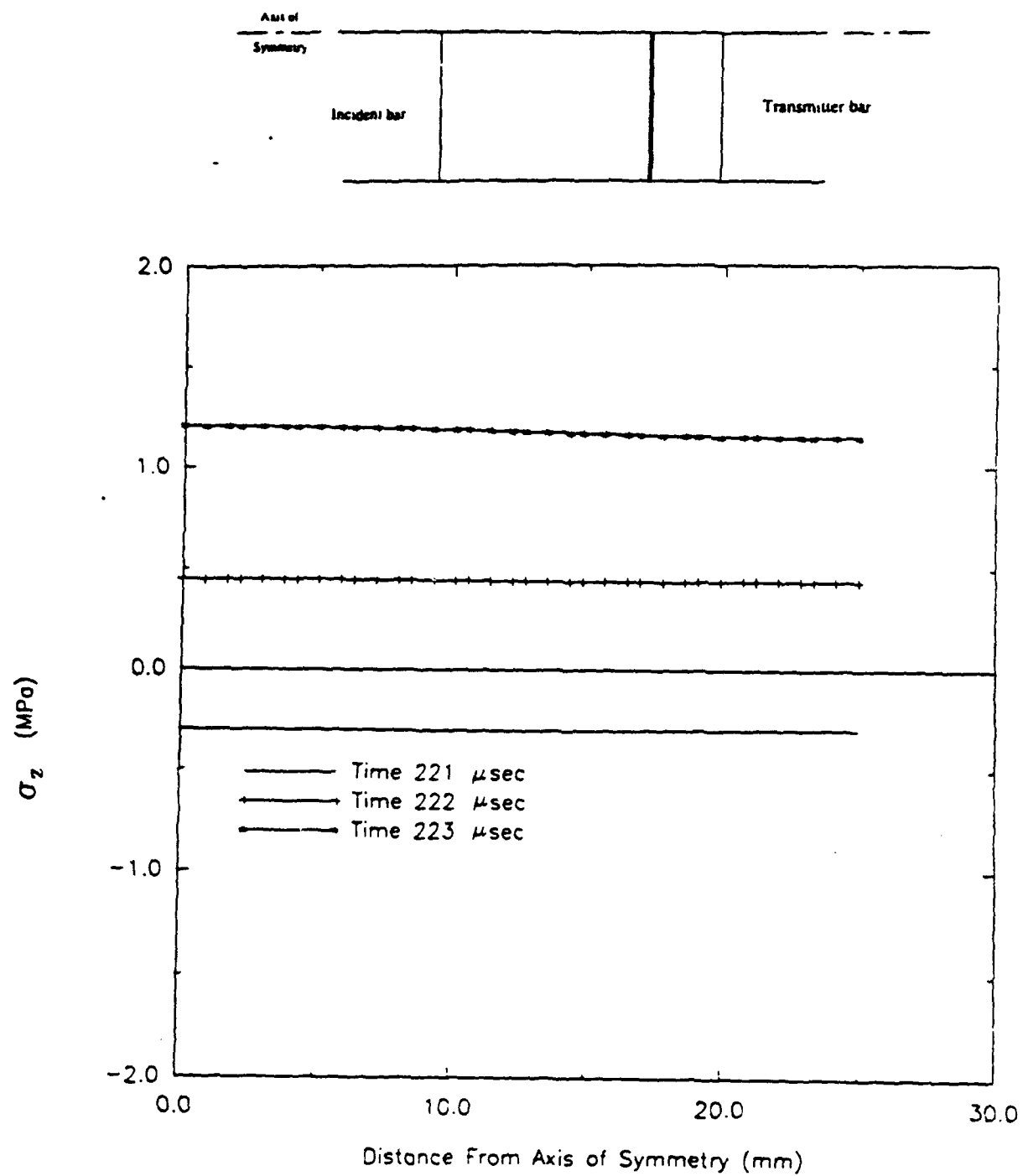


Figure 210. Profiles for longitudinal stress (direct compression, Load Case 3).

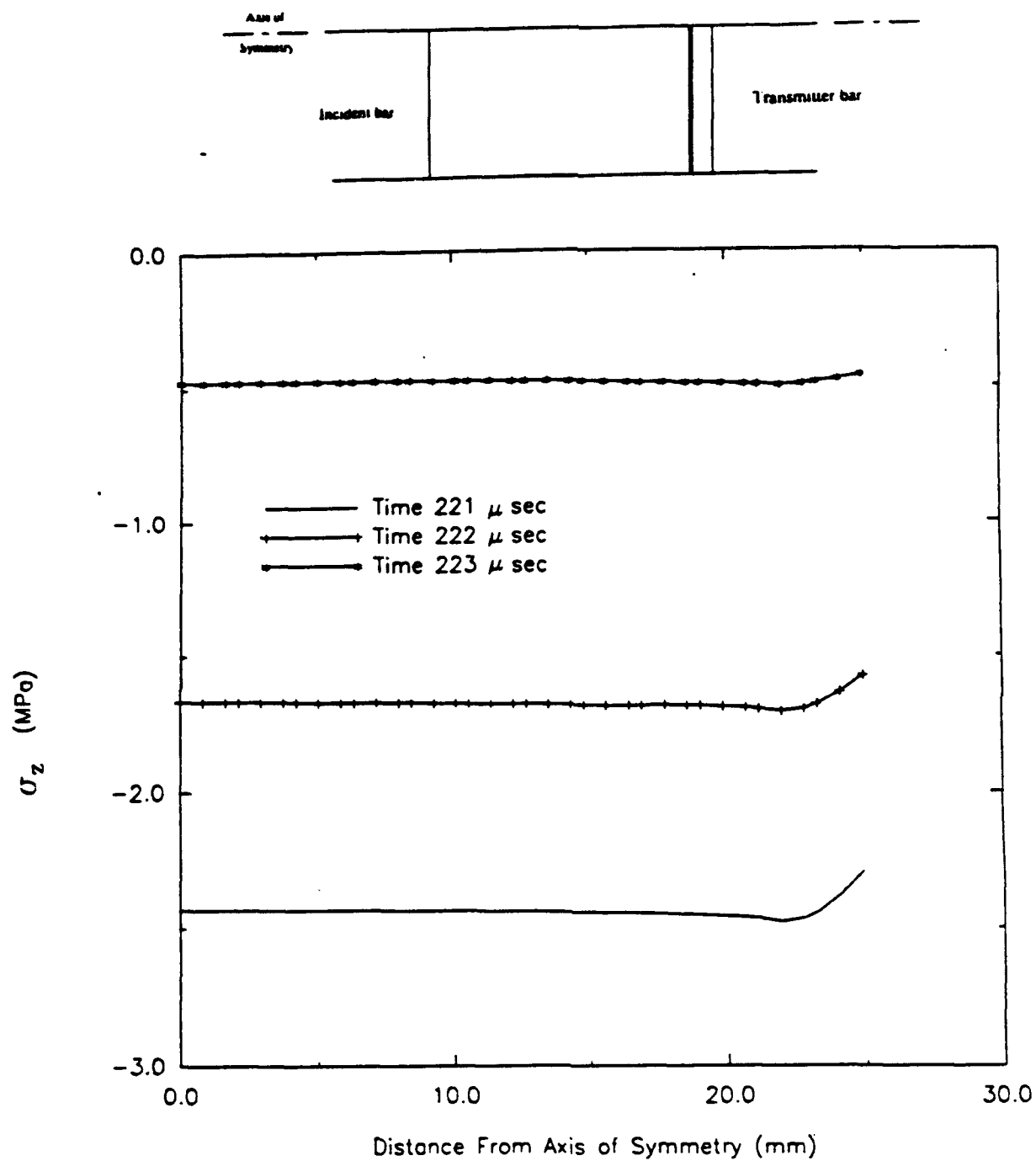


Figure 211. Profiles for longitudinal stress (direct compression, Load Case 3).

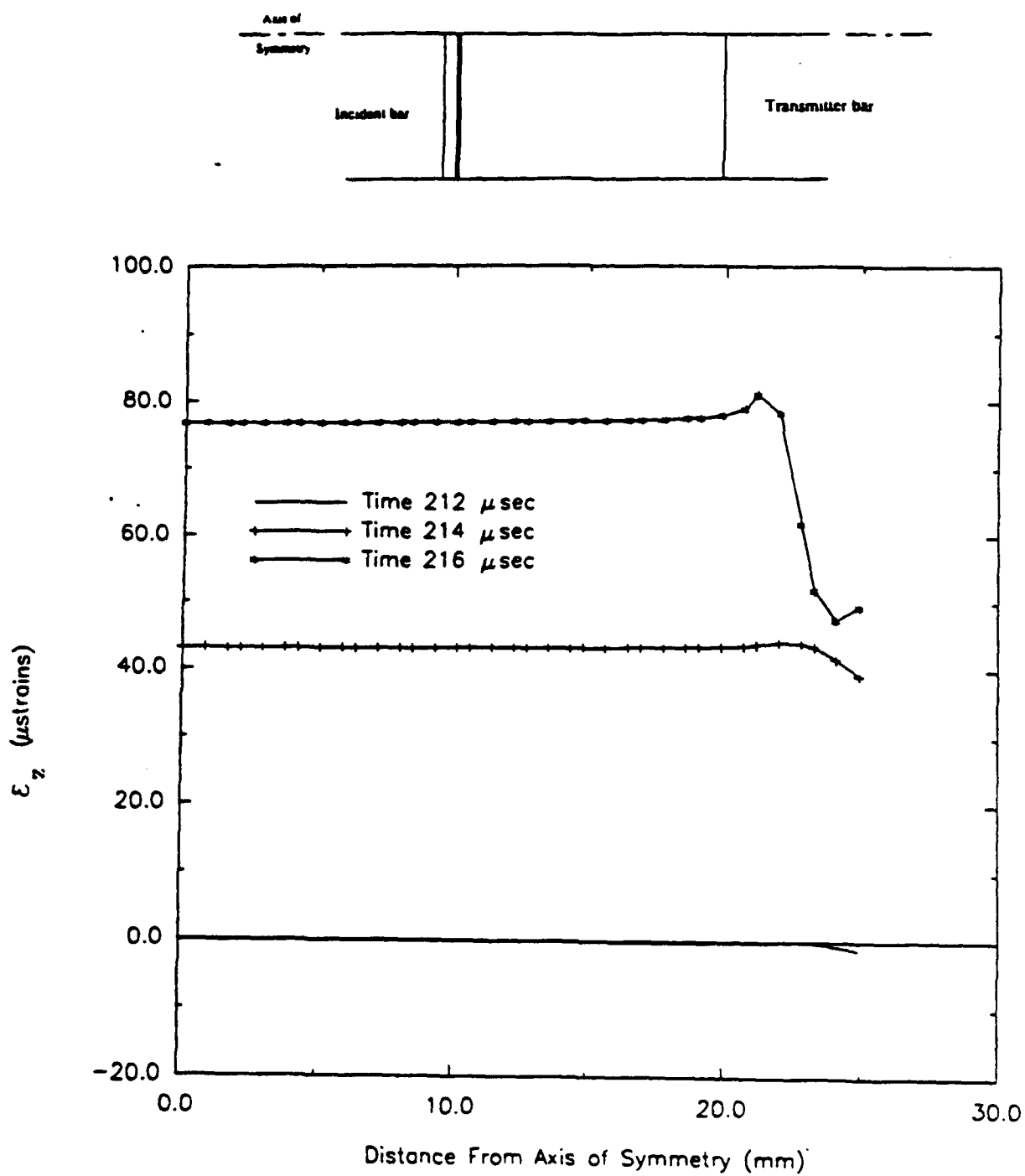


Figure 212. Profiles for longitudinal strain (direct compression, Load Case 3).

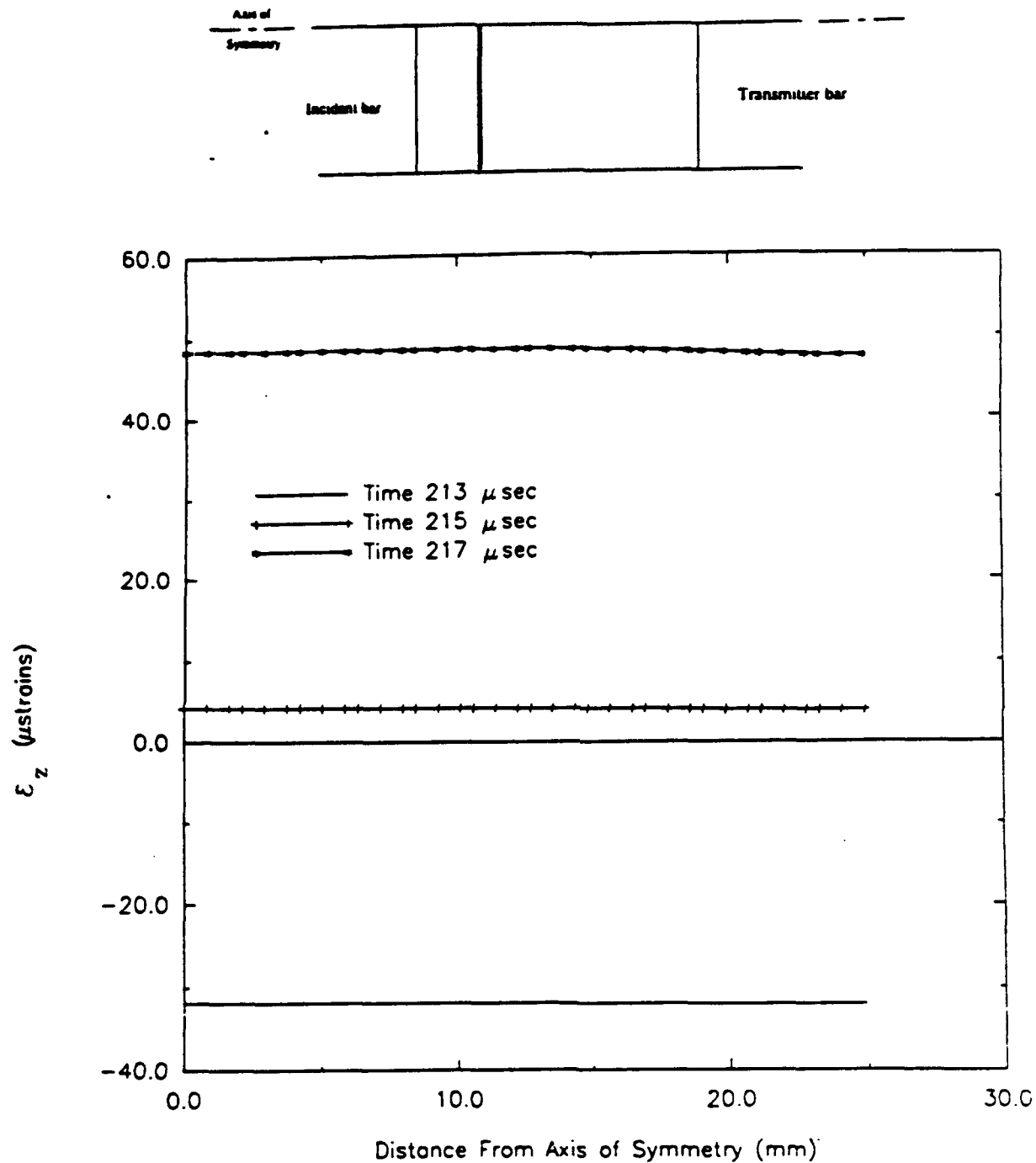


Figure 213. Profiles for longitudinal strain (direct compression, Load Case 3).

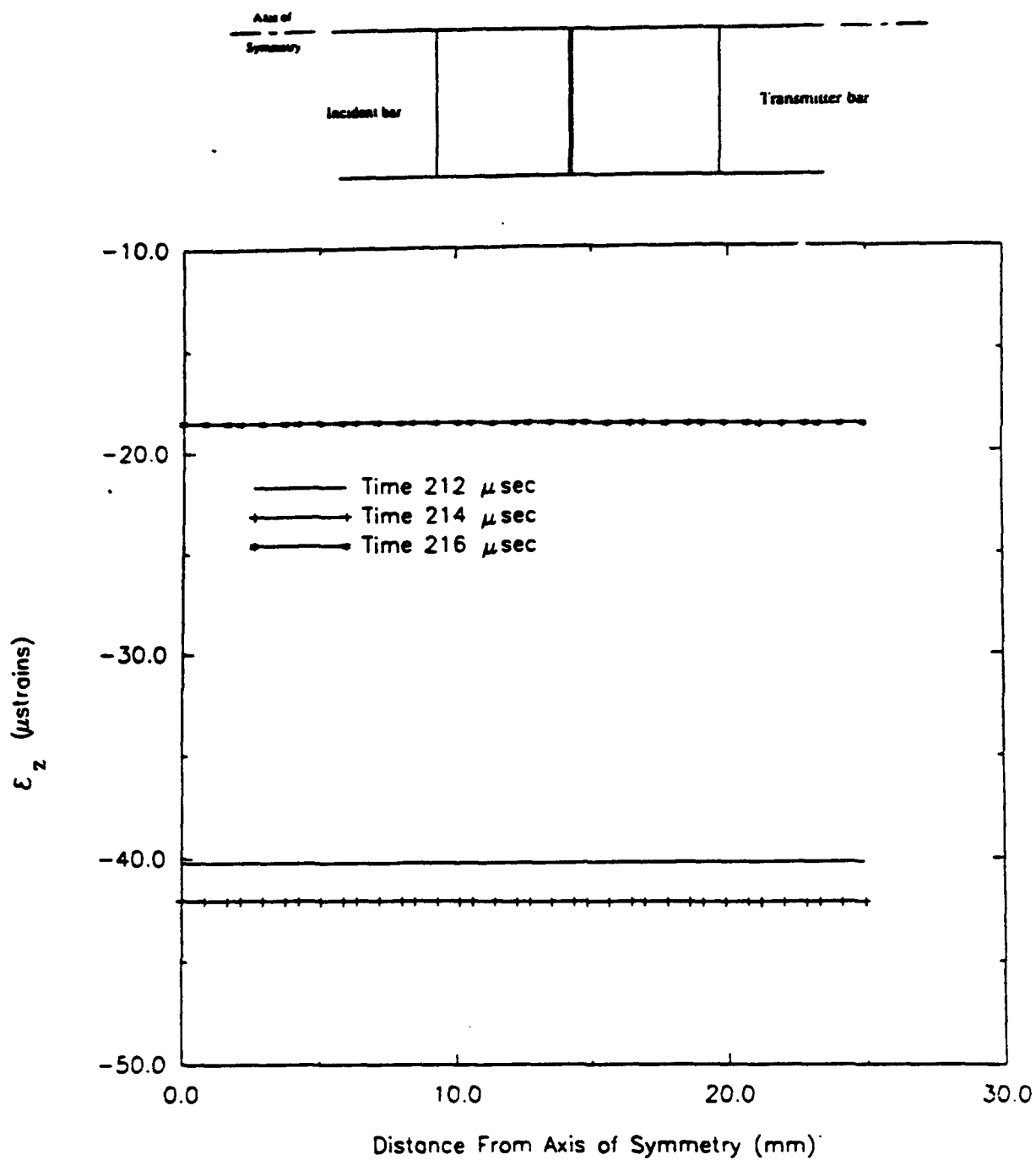


Figure 214. Profiles for longitudinal strain (direct compression, Load Case 3).

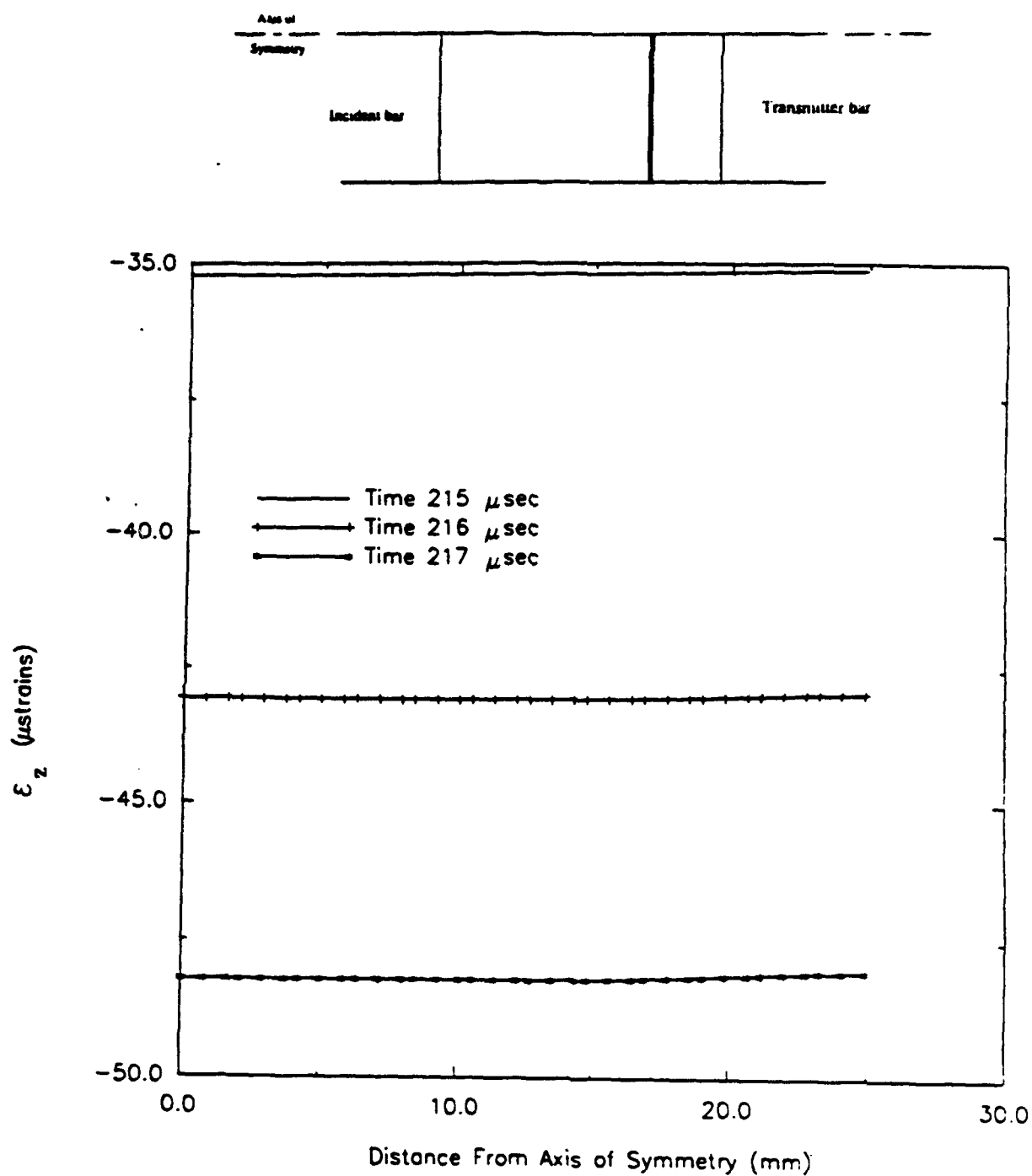


Figure 215. Profiles for longitudinal strain (direct compression, Load Case 3).

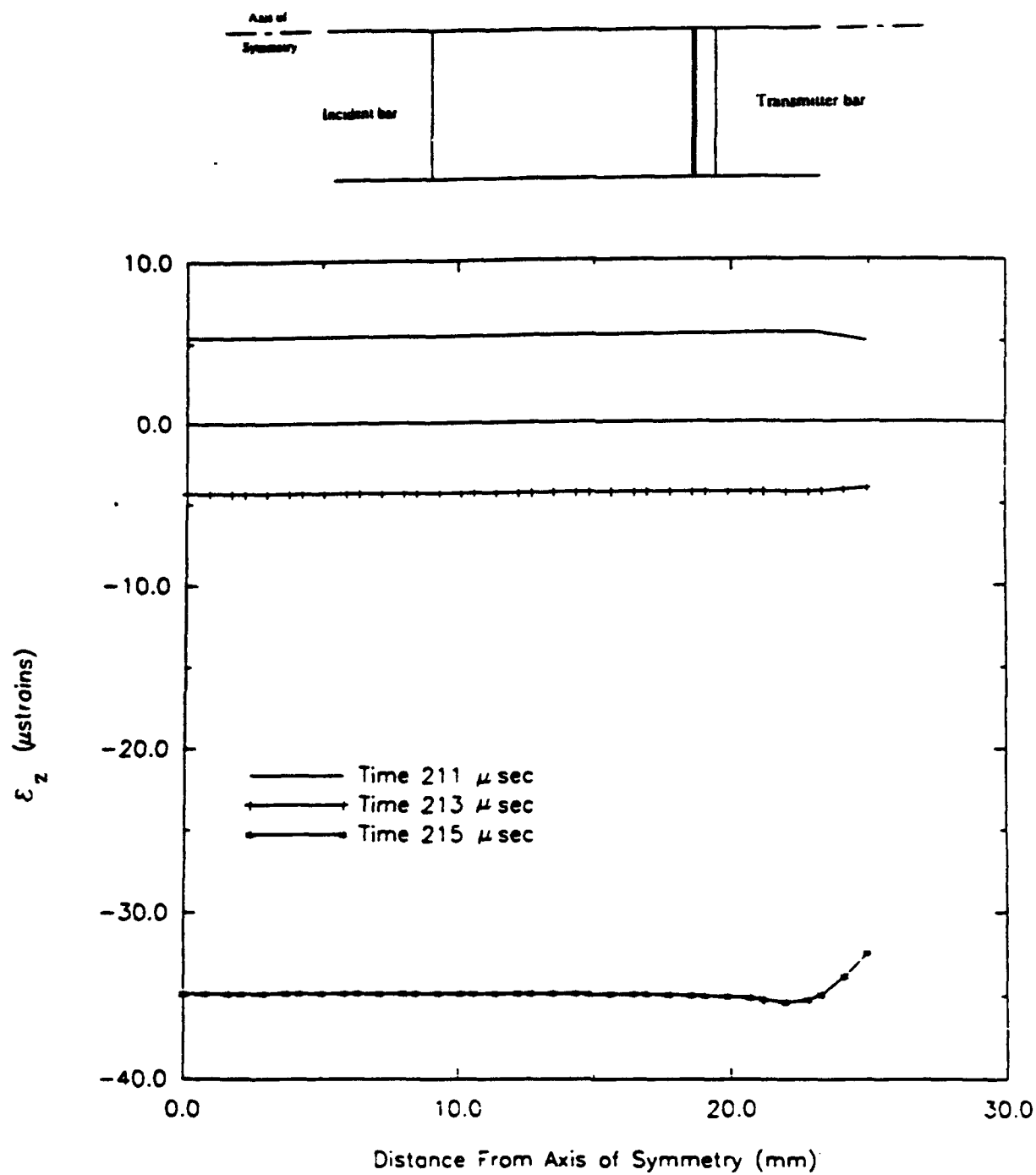
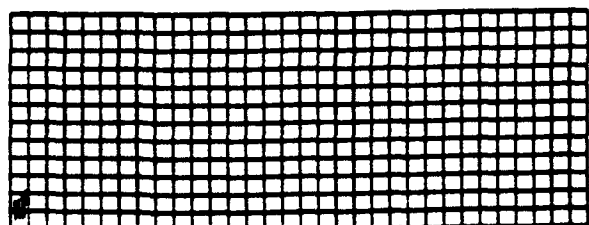
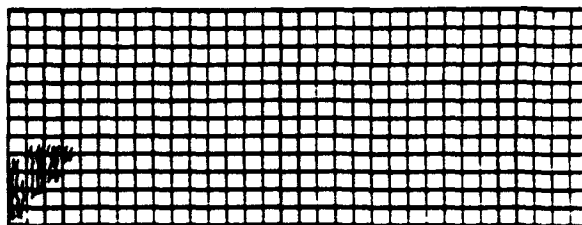


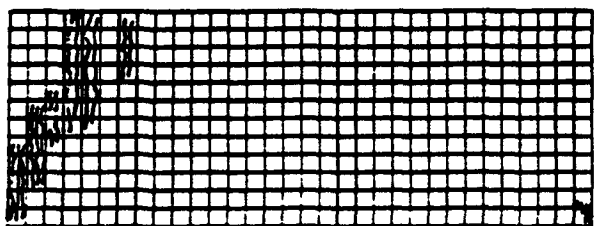
Figure 216. Profiles for longitudinal strain (direct compression, Load Case 3).



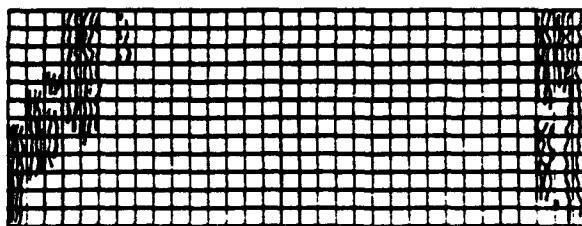
(a)



(b)



(c)



(d)

Figure 217. Cracking sequence for direct compression specimen; Load Case 3:
a) $t=216 \mu \text{ sec}$, b) $t=218 \mu \text{ sec}$, c) $t=226 \mu \text{ sec}$, d) $t=236 \mu \text{ sec}$.

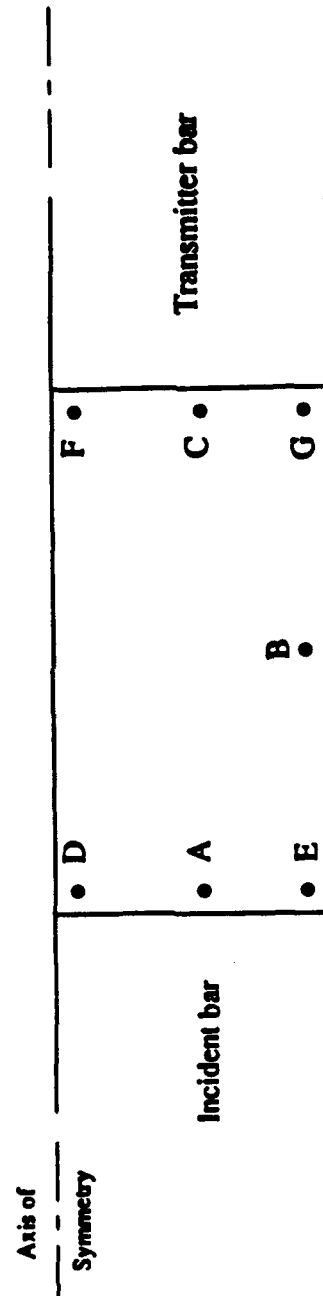


Figure 218. Definition sketch for direct compression specimen.

APPENDIX B:
REANALYSIS OF DIRECT COMPRESSION TESTS

INTRODUCTION

In the original numerical simulation of the SHPB direct compression tests, the concrete specimen and the steel pressure bars were modeled as a continuous medium. That is, the nodal points along the concrete/steel interfaces of the FEM model were "shared" or assigned the same coordinates. Because of the significant difference in Poisson's ratio between the concrete and steel, substantial resistance to radial expansion of the concrete specimen, when compressed axially, was created. This, in turn, caused significant tensile stresses to develop in the vicinity of the pressure bar/specimen interfaces, resulting in a localized tensile failure of the specimen, thus rendering the results of the analysis invalid.

To correct this modeling inaccuracy, contact surfaces were implemented into the model at the boundaries between the concrete specimen and steel pressure bars. Contact surfaces are used to model contact behavior between structural or solid elements, and can be defined as surfaces that are initially in contact or are anticipated to come into contact during the response solution. Some general conditions of the ADINA contact algorithm are: 1) the points of contact are not known apriori, 2) both frictional and frictionless sliding can be modeled, and 3) repeated contact and separation is allowed in a sequence.

When the ADINA contact surface option is employed, a coefficient of friction ranging from $\mu=0$ to $\mu=\infty$ can be specified. A nonzero frictional coefficient will render the problem much more computationally intensive because of the large number of equations required to be solved for the equilibrium condition. Also, a friction coefficient other than zero will restrain the specimen at its ends from moving radially since the effect of nonzero friction is to produce a force that opposes deformation of the specimen in the radial direction. In order to obtain a true measure of the response of the specimen to impact loads, the shear force or frictional force at the ends of the specimen should be minimized. In addition, the intent of the SHPB simulation is to determine longitudinal response of the specimen to high strain rates. The presence of shear forces would make interpretation of the results considerably more difficult because they would affect the material response of the concrete specimen. In the actual SHPB experiment conducted at AFCEA, lubricants were administered between the specimen and pressure bars. For this reason, a value

of $\mu=0.0$ was employed at the contact surfaces in the SHPB simulation.

Implementation of the contact surfaces into the SHPB model resulted in separation of the incident pressure bar from the concrete specimen during the solution response. As the incident compressive wave propagated along the incident bar and encountered the first concrete/steel interface, the contact surface acted as a free end of a beam. The compressive wave was reflected with the same magnitude but as a tensile wave. The very nature of a contact surface is to allow separation in a tension field, therefore the concrete and steel separated with very little or none of the compressive stress wave being transmitted to the specimen.

To rectify this modeling deficiency at the specimen/pressure bar boundaries, rigid links were implemented into the FEM model at both specimen/pressure bar interfaces. Rigid links are special constraint equations prescribed between two nodes, one prescribed as a master node and the other a slave node. As the master node begins to translate or rotate due to deformation, the slave node is constrained to translate and rotate in a manner such that the distance between the two nodes remains unchanged, and the rotations of the slave node are identical to the rotations of the master node. Rigid links were implemented into the FEM model at both pressure bar/specimen interfaces using the lines of nodes along the pressure bar boundaries adjacent to the concrete specimen as the slave nodes and the line of mid-nodes inside the first and last column of elements in the concrete specimen as the master nodes (refer to Figure 219). In this manner, as the compressive wave encounters the specimen and causes the concrete to expand radially, the steel pressure bars will be forced to do the same. This will create tensile strains in the steel. However, this will not prejudice the result obtained for the concrete specimen. This modified FEM model was employed to reanalyze the three direct compression simulations reported in Section III of this report.

RESULTS OF REANALYSIS

Load Case 1

Time histories for the longitudinal stress, σ_z , for one point in the incident bar, nine points in the specimen and one point in the transmitter bar are shown in Figures 220 through 230. The maximum longitudinal stresses are summarized in Table 16. A definition sketch for the location of the points

included in the time histories is presented in Figure 231. Profiles of the longitudinal stress, σ_z , at several different times along five transverse cross sections in the specimen are shown in Figures 232 through 236. A definition sketch for the profile lines is presented in Figure 237.

The crushing sequence for the specimen is illustrated in Figure 238. First cracking is observed to occur simultaneously at both the incident and transmitter ends of the specimen at time $t = 300 \mu\text{sec}$ (Figure 230 a). Further crushing of the concrete, albeit very insignificant, is observed at time $t = 525 \mu\text{sec}$ (Figure 238 b), time $t = 550 \mu\text{sec}$ (Figure 238 c), and time $t = 600 \mu\text{sec}$ (Figure 238 d). In this load case, the specimen exhibits very little cracking and remains essentially intact. In fact, the entire simulation was completed without any indication of numerical instability, suggesting that the specimen did not fail.

Table 16 Maximum Stresses, Load Case 1

Location (Refer to Figure 231)	Longitudinal Stress, σ_z , (MPa)
1	-52.2698
2	-54.9634
3	-52.5342
4	-54.7025
5	-53.2302
6	-53.3734
7	-53.5054
8	-55.3155
9	-53.3561
10	-55.1925
11	-53.0438

Load Case 2

Time histories for the longitudinal stress, σ_z , for one point in the incident bar, nine points in the specimen and one point in the transmitter bar are shown in Figures 239 through 249. Time histories for the longitudinal strain, ϵ_z , for these same points are shown in Figures 250 through 260. The maximum longitudinal stresses and strains are summarized in Table 17. A

definition sketch for the location of the points included in the time histories is presented in Figure 231.

Table 17 Maximum Stresses and Strains, Load Case 2

Location (Refer to Figure 231)	Longitudinal Stress, σ_z , (MPa)	Longitudinal Strain, ϵ_z , (μ strain)
1	-56.6701	-218.398
2	-54.7194	-15284.8
3	-57.9297	-21010.1
4	-57.1511	-1758.57
5	-57.2574	-1924.82/+1124.68
6	-56.6202	-1867.78/+747.372
7	-55.8023	-1826.42/+716.694
8	-50.8886	-1662.15
9	-57.7897	-2045.33
10	-53.2526	-1731.09
11	-57.4711	-219.891

Profiles of the longitudinal stress, σ_z , at several different times along five transverse cross section in the specimen are shown in Figures 261 through 265. Profiles of the longitudinal strain, ϵ_z , for the same times and cross sections are shown in Figures 266 through 270. A definition sketch for the profile lines is presented in Figure 237.

The failure sequence for the specimen, from initiation of the first crack until fracture, is illustrated in Figure 271. First cracking occurs at the incident end of the specimen at time $t = 265 \mu\text{sec}$ (Figure 271 a). At time $t = 289 \mu\text{sec}$, significant crushing of the concrete in the specimen ends adjacent to the transmitter and incident bars has occurred (Figure 271 b). Crushing of the concrete remains restricted to the incident and transmitter ends of the specimen at time $t = 292 \mu\text{sec}$. However, tensile cracks have also begun to appear in the specimen at this time (Figure 271 c). Finally, at time $t = 300 \mu\text{sec}$ (Figure 271 d), failure occurs. Several interesting observations are noted in this figure. First, it appears that approximately 30 to 35 percent of the concrete in the specimen has been crushed, suggesting that the specimen is not completely pulverized at failure. Second, significant tensile cracking has developed in the

interior of the specimen, suggesting that the failure was instigated by compression crushing of the concrete, but culminated in a tensile fracture.

Load Case 3

Time histories for the longitudinal stress, σ_z , for one point in the incident bar, nine points in the specimen and one point in the transmitter bar are shown in Figures 272 through 282. Time histories for the longitudinal strain, ϵ_z , for these same points are shown in Figures 283 through 293. The maximum longitudinal stresses and strains are summarized in Table 18. A definition sketch for the locations of the points included in the time histories is presented in Figure 231.

Table 18 Maximum Stresses and Strains, Load Case 3

Location (Refer to Figure 231)	Longitudinal Stress, σ_z , (MPa)	Longitudinal Strain, ϵ_z , (μ strain)
1	-79.3287	-291.268
2	-79.6066	-232017.
3	-57.5661	-250815.
4	-73.5254	-244060.
5	-57.7198	-2044.39
6	-57.7293	-2047.46
7	-57.7228	-2048.65
8	-57.9916	-282228.
9	-61.3839	-213128.
10	-68.3619	-193361.
11	-58.5673	-215.204

Profiles of the longitudinal stress, σ_z , for several different times at five transverse cross sections in the specimen are shown in Figures 294 through 298. Profiles of the longitudinal strain, ϵ_z , for the same times and cross sections are shown in Figures 299 through 303. A definition sketch for the profile lines presented in Figure 237.

The failure sequence for the specimen, from initiation of first cracking until fracture, is illustrated in Figure 304. First cracking occurs at the incident end of the specimen at time $t = 230 \mu\text{sec}$ (Figure 304 a). At time $t =$

249 μ sec (Figure 304 b), substantial crushing in the specimen is observed at both the incident and transmitter ends. At time $t = 255 \mu$ sec (Figure 304 c), approximately 75% of the specimen has been crushed. Finally at $t = 275 \mu$ sec (Figure 304 d), most of the specimen has been crushed (approximately 85%) and failure occurs. This simulation suggests that the specimen is pulverized at failure.

DISCUSSION OF RESULTS

Load Case 1

The 17/sec strain rate resulted in only localized crushing at both ends of the specimen near the surface, but the specimen did not fail. Time histories taken at points throughout the specimen indicate a uniform longitudinal stress distribution ranging from -52 to -55 MPa. The longitudinal stress histories, Figures 220 through 230, indicate that the maximum stresses at all points in the specimen fall just below the concrete compressive strength (-57.7 MPa). However, longitudinal stress profiles at various transverse cross sections indicate that on the radial surface of the specimen at the incident and transmitter ends, there is crushing. Profile lines A and E, in Figures 232 and 236, indicate stresses greater than -57.7 MPa near the surface of the concrete specimen where crushing occurs. A definition sketch for the profile lines is presented in Figure 237.

From observation of the longitudinal stress histories, it is apparent that the incident stress wave is entering the concrete, propagating through the specimen, and a portion is being reflected from the transmitter bar/concrete interface. Because crushing only occurs near the radial surface of the specimen at the incident and transmitter ends, most of the concrete is still capable of transmitting stress. The abrupt decline in the stress histories that occur at approximately 475 μ seconds is a direct result of the superposition of the incident compressive wave and the reflected tensile wave. Therefore, it can be concluded that crushing only occurs near the radial surface of the concrete at the incident and transmitter ends, but the specimen remains intact. This conclusion is corroborated by the crack plots presented in Figure 238.

Load Case 2

The 25/sec strain rate resulted in the specimen failing by crushing accompanied by tensile fracture. Every point within the specimen was stressed

in the longitudinal direction to a value equal to or just less than the compressive strength of the concrete (see Table 17). With the exception of a few points, the longitudinal strain distribution within the specimen varied very little, maintaining in the vicinity of 1700 to 2000 μ strains. (For a definition sketch of time histories, see Figure 231). Points 2 and 3 at the incident end of the specimen both exhibit very large longitudinal compressive strains. Points 4 through 10 experience longitudinal compressive strains corresponding to the minimum crushing stress. All points that exhibit drastic fluctuations in the strain histories, points 2,3,5,6 and 7, did so immediately after failure occurred, at which time the longitudinal stress fell to zero.

Observation of stress profiles at various transverse cross sections within the specimen (Figures 261 through 265) indicate that at certain times the capacity to resist longitudinal stress has vanished. Crushing of the specimen prevents the concrete from transmitting any stress. The extent of crushing in Load Case 2 is much greater than that exhibited in Load Case 1. The failure sequence crack plots presented in Figure 271 suggest that the failure is instigated by crushing of the concrete and consummated by tensile fracture. It is also apparent from the plots of the failure sequence that the specimen is not completely pulverized at failure.

Load Case 3

The 200/sec strain rate loading condition resulted in the entire concrete specimen failing by crushing. Points 2 through 4, and 8 through 10, at the incident and transmitter ends of the specimen respectively, all exhibited longitudinal stresses that were greater than or equal to the compressive strength of the concrete just prior to failure. These same six points experienced very large longitudinal compressive strains which originated immediately after the longitudinal stress fell to zero (see Table 18). The state of stress in the center of the specimen varied very little. Crushing occurred when the longitudinal stress reached the compressive strength of the concrete. Points 5, 6, and 7 in the center of the specimen also exhibited very little strain variation. The magnitude of the strain was approximately equal to that corresponding to the minimum crushing stress, (2000 μ strains).

Several interesting conclusions can be drawn from the results of the analysis. First, at the ends of the specimen, there are very large compressive stresses and strains, the magnitudes of which suggest the material has undergone some increase in strength with an increase in load and strain rate. Second, it is evident that the strength at the center of the specimen is unaffected by the increase in load and strain rate. The stress and strain in the center of the specimen at the time of failure is almost exactly equal to the minimum stress and strain corresponding to crushing. Observations of various transverse cross sections within the specimen, (Figures 294 through 298), indicate that at certain times the capacity of the concrete to resist longitudinal stress has vanished. This initially appears at profile lines A and E in the specimen (Figures 294 and 298), and propagates toward the center of the specimen, profile line C (Figure 296). From these figures, it can be seen that the failure initiates at both ends of the specimen simultaneously and moves inward. Failure finally occurs by crushing of the specimen as illustrated by the cracking sequence presented in Figure 304. These crack plots indicate that most of the specimen has been crushed and suggests small particle sizes or pulverization.

CONCLUSIONS

The magnitude of the strain rate had a significant influence on the responses predicted by the SHPB numerical simulations. In Load Case 1, 17/sec strain rate, the specimen did not fail. The concrete sample remained almost entirely intact, exhibiting very sporadic and localized crushing. In Load Case 2, 25/sec strain rate, failure was initiated by concrete crushing in approximately 30 percent of the specimen, followed by significant tensile cracking which perpetuated the failure. However, the specimen was not pulverized. In Load Case 3, 200/sec strain rate, approximately 85 percent of the specimen exhibited crushing, suggesting pulverization or small particle size. The results predicted by the numerical simulation are consistent with observed experimental results.

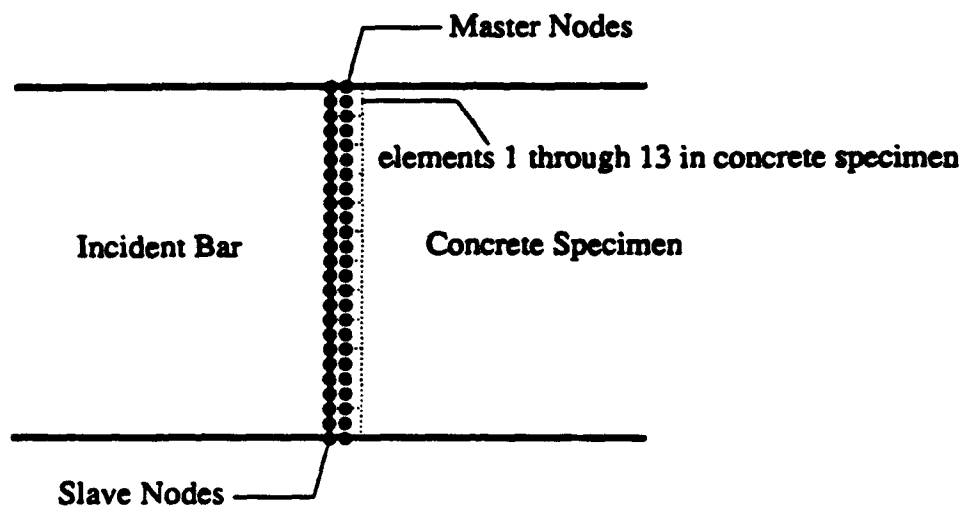


Figure 219. Illustration of rigid link (master nodes and slave nodes).

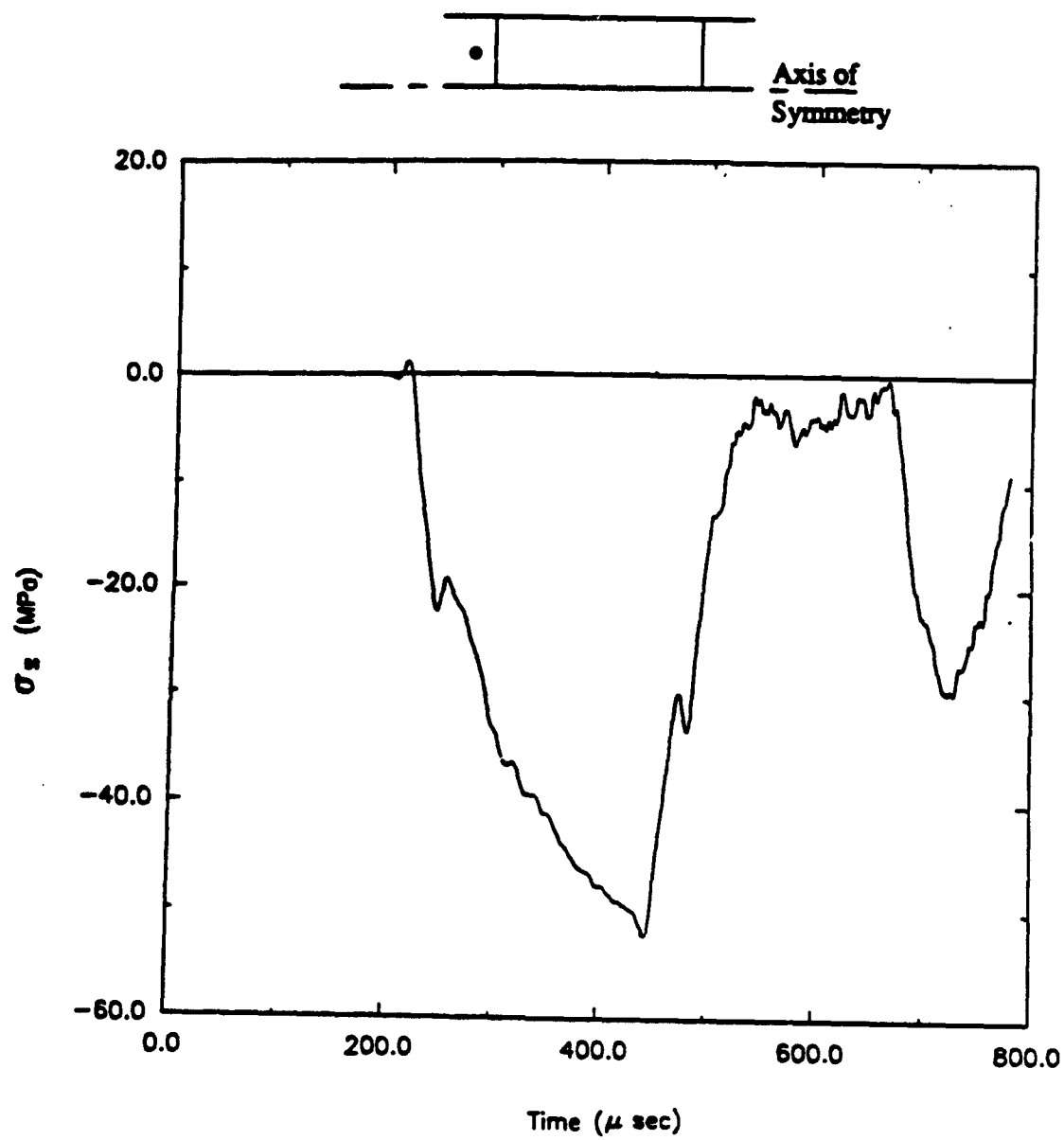


Figure 220. Time history for longitudinal stress (direct compression, Load Case 1).

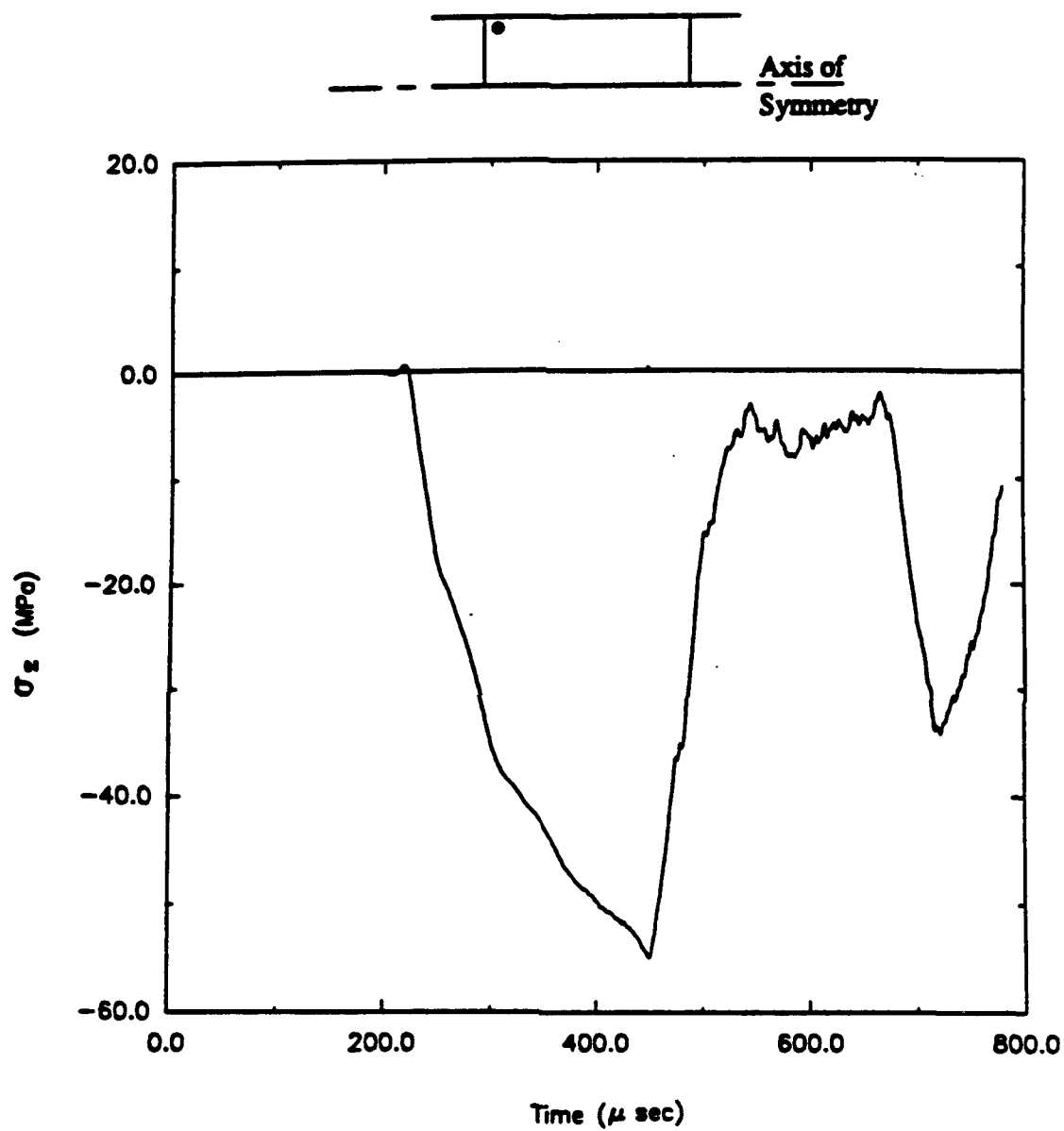


Figure 221. Time history for longitudinal stress (direct compression, Load Case 1).

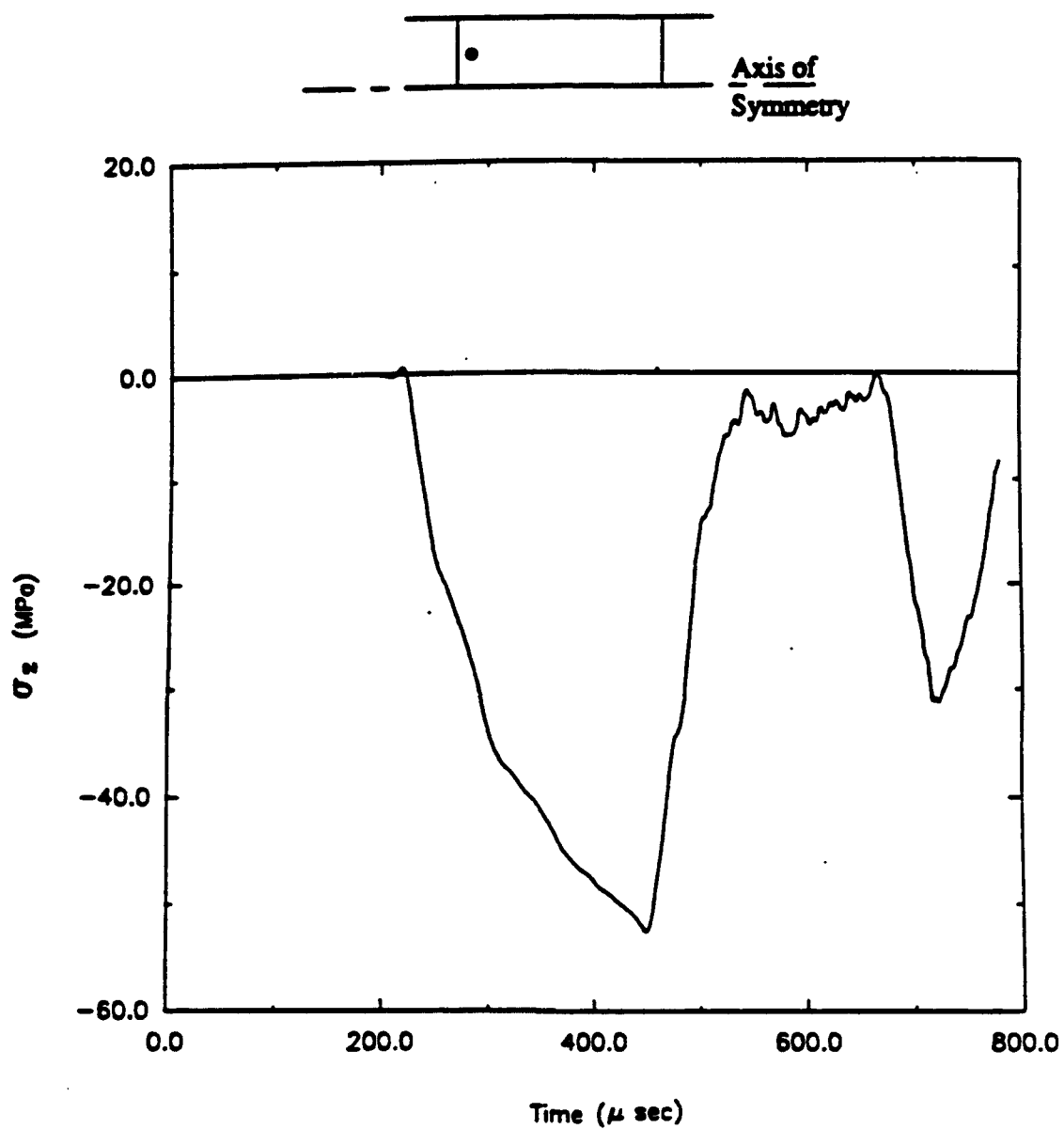


Figure 222. Time history for longitudinal stress (direct compression, Load Case 1).

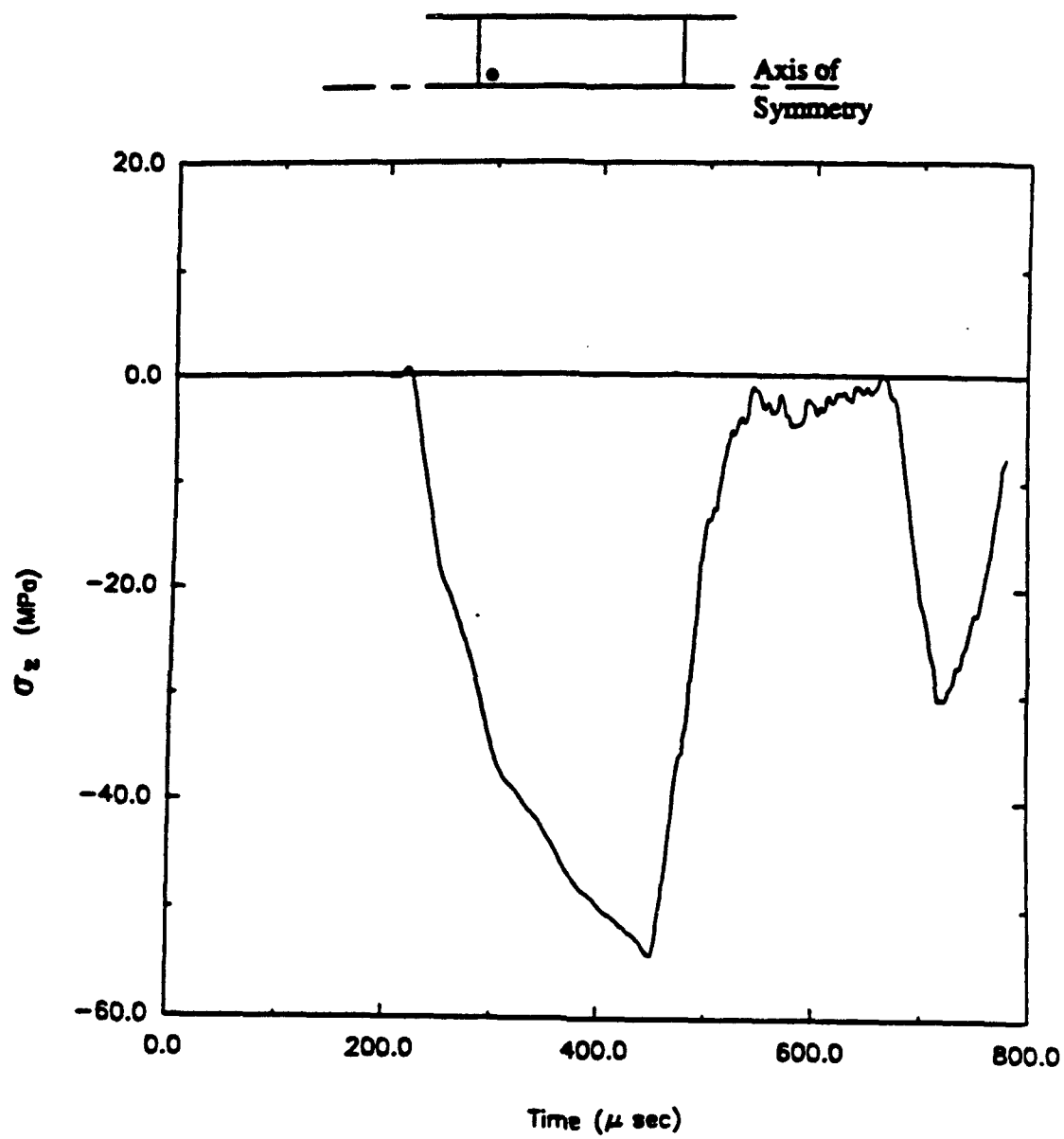


Figure 223. Time history for longitudinal stress (direct compression, Load Case 1).

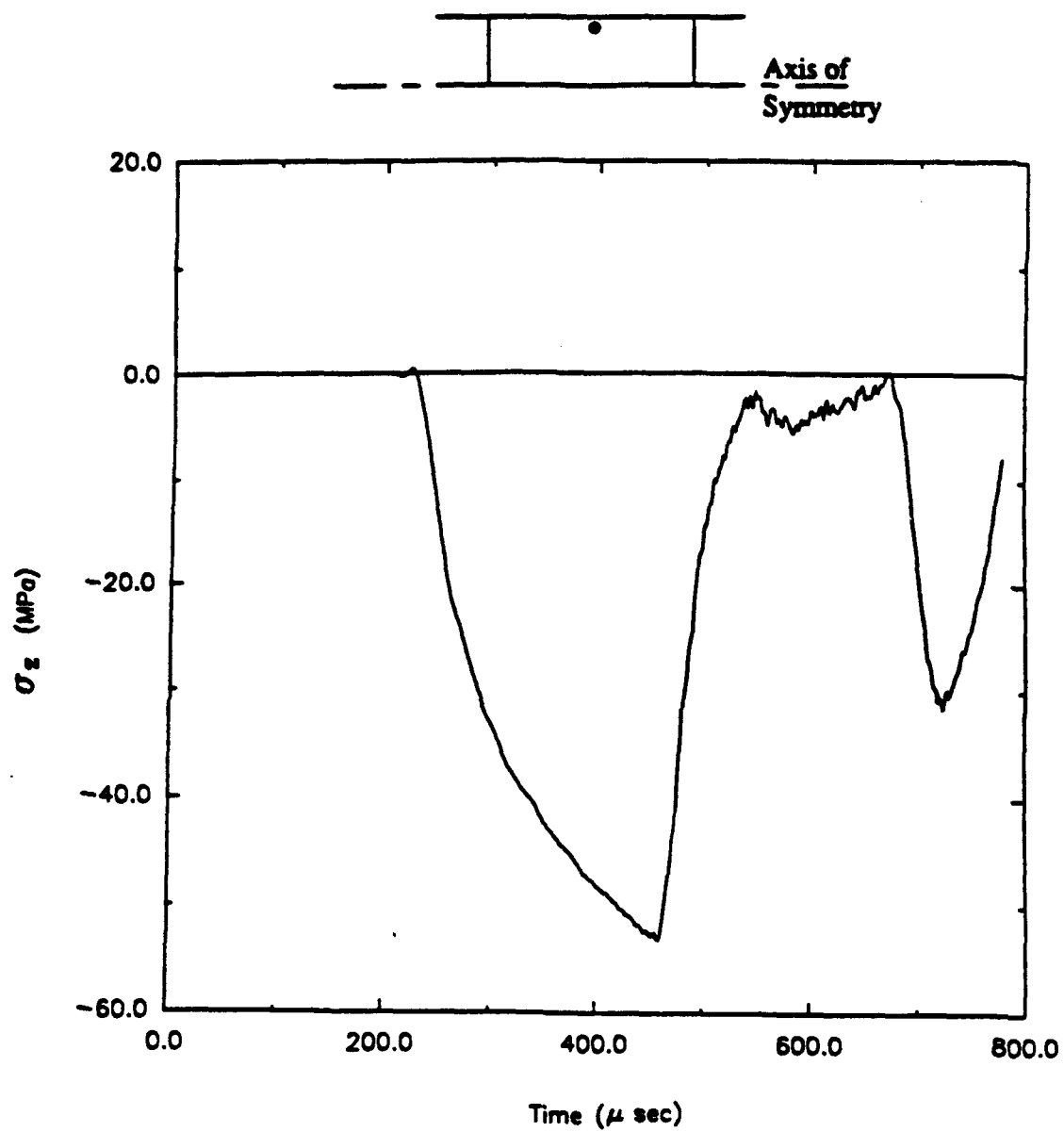


Figure 224. Time history for longitudinal stress (direct compression, Load Case 1).

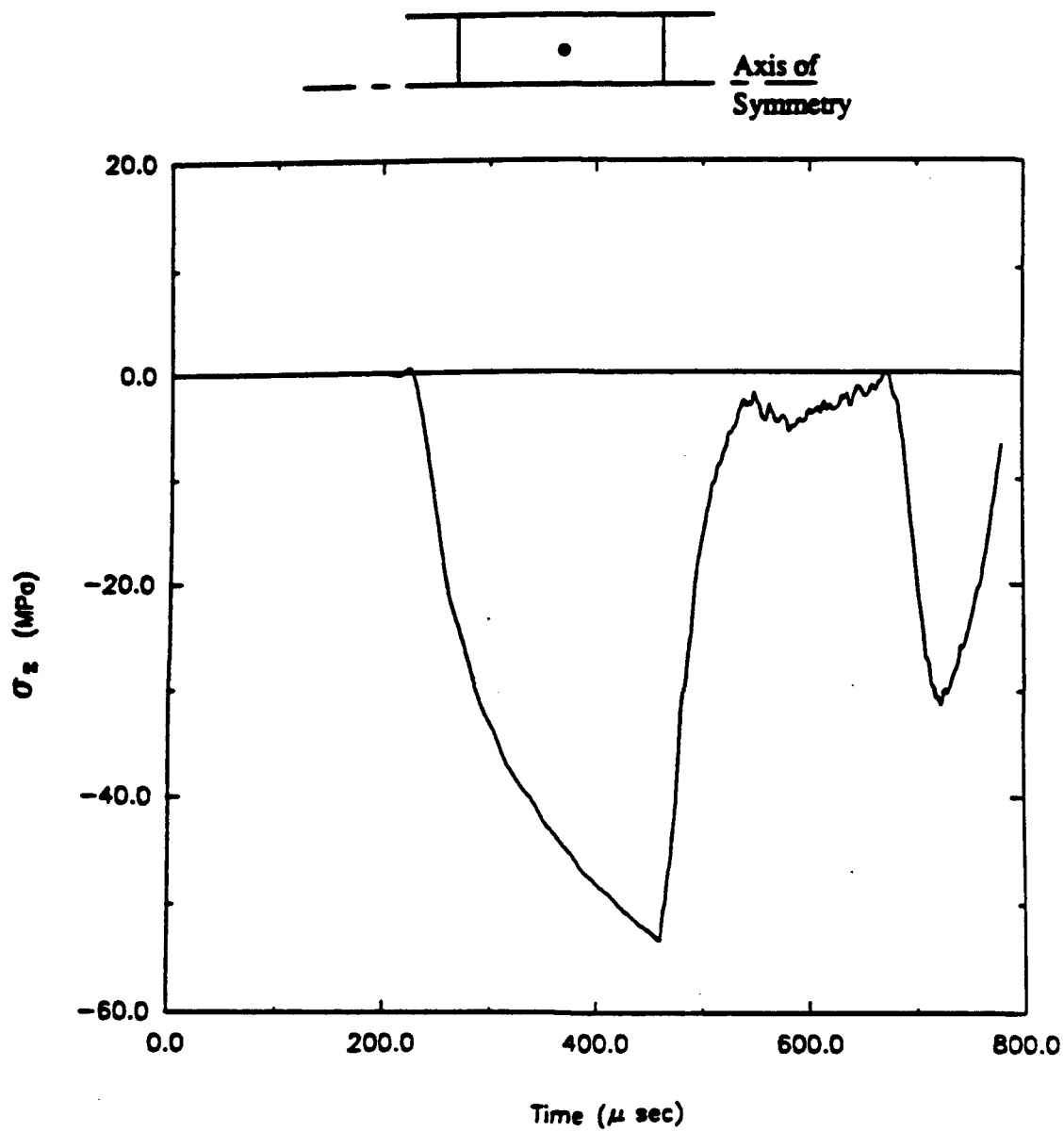


Figure 225. Time history for longitudinal stress (direct compression, Load Case 1).

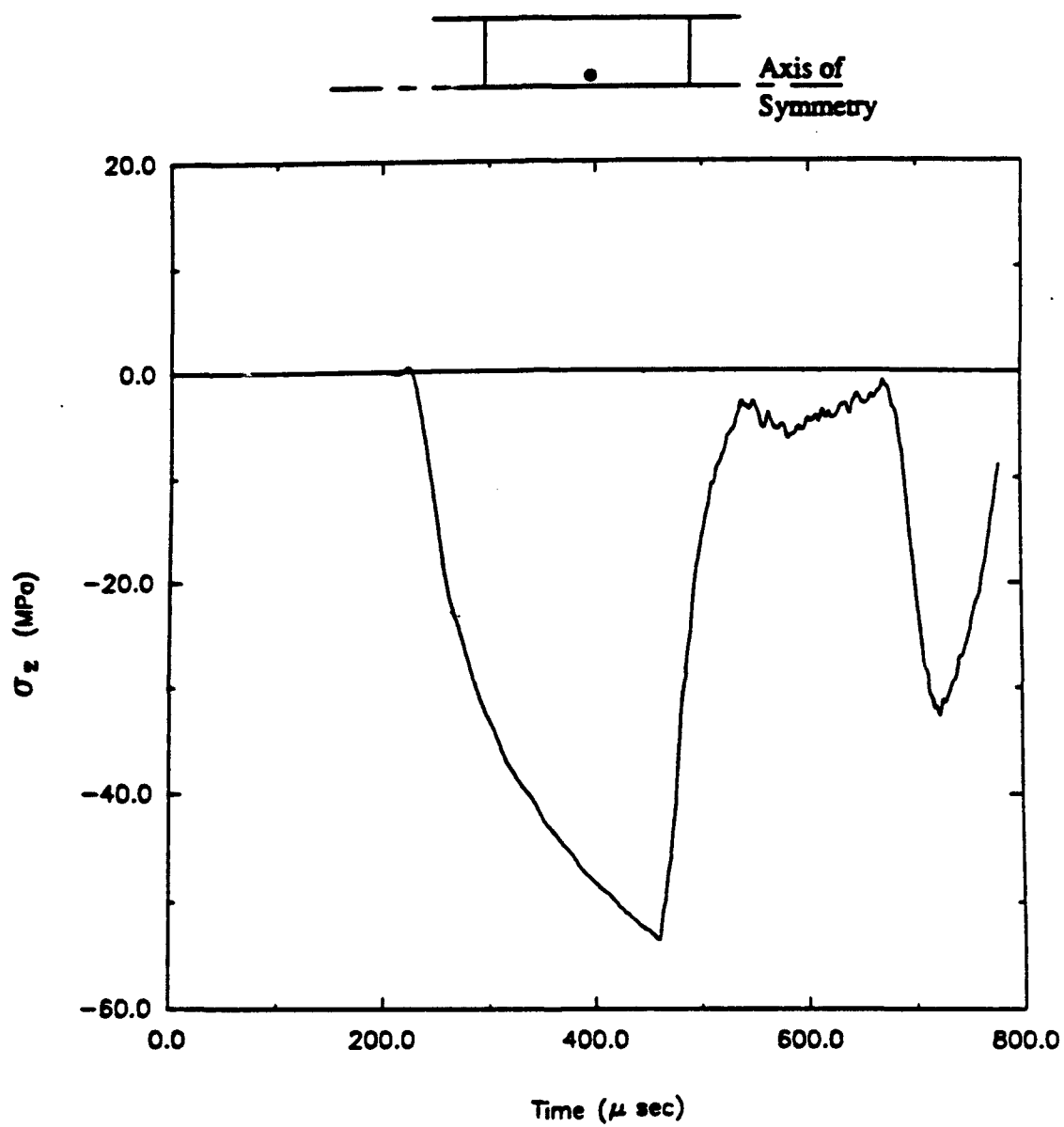


Figure 226. Time history for longitudinal stress (direct compression, Load Case 1).

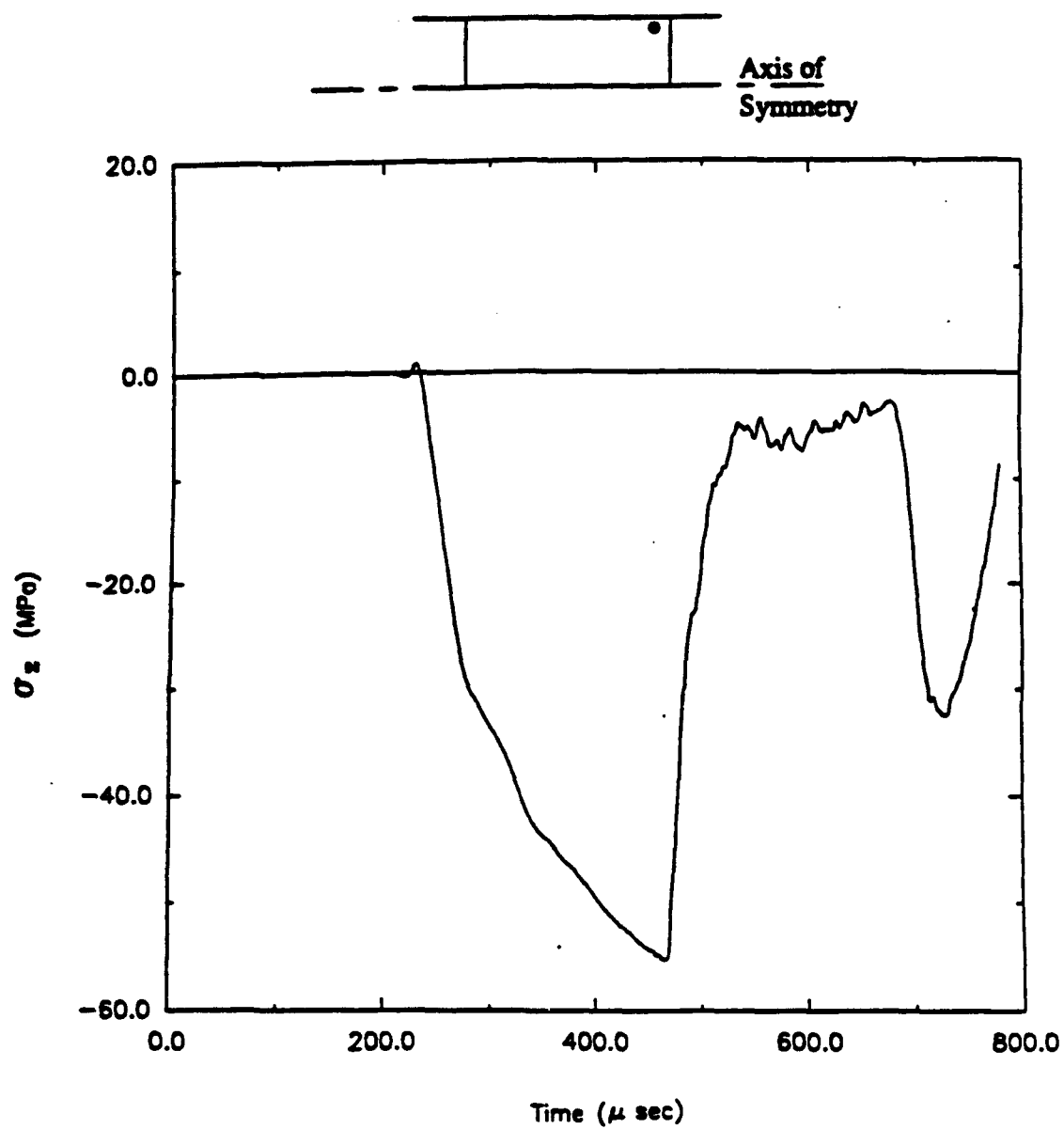


Figure 227. Time history for longitudinal stress (direct compression, Load Case 1).

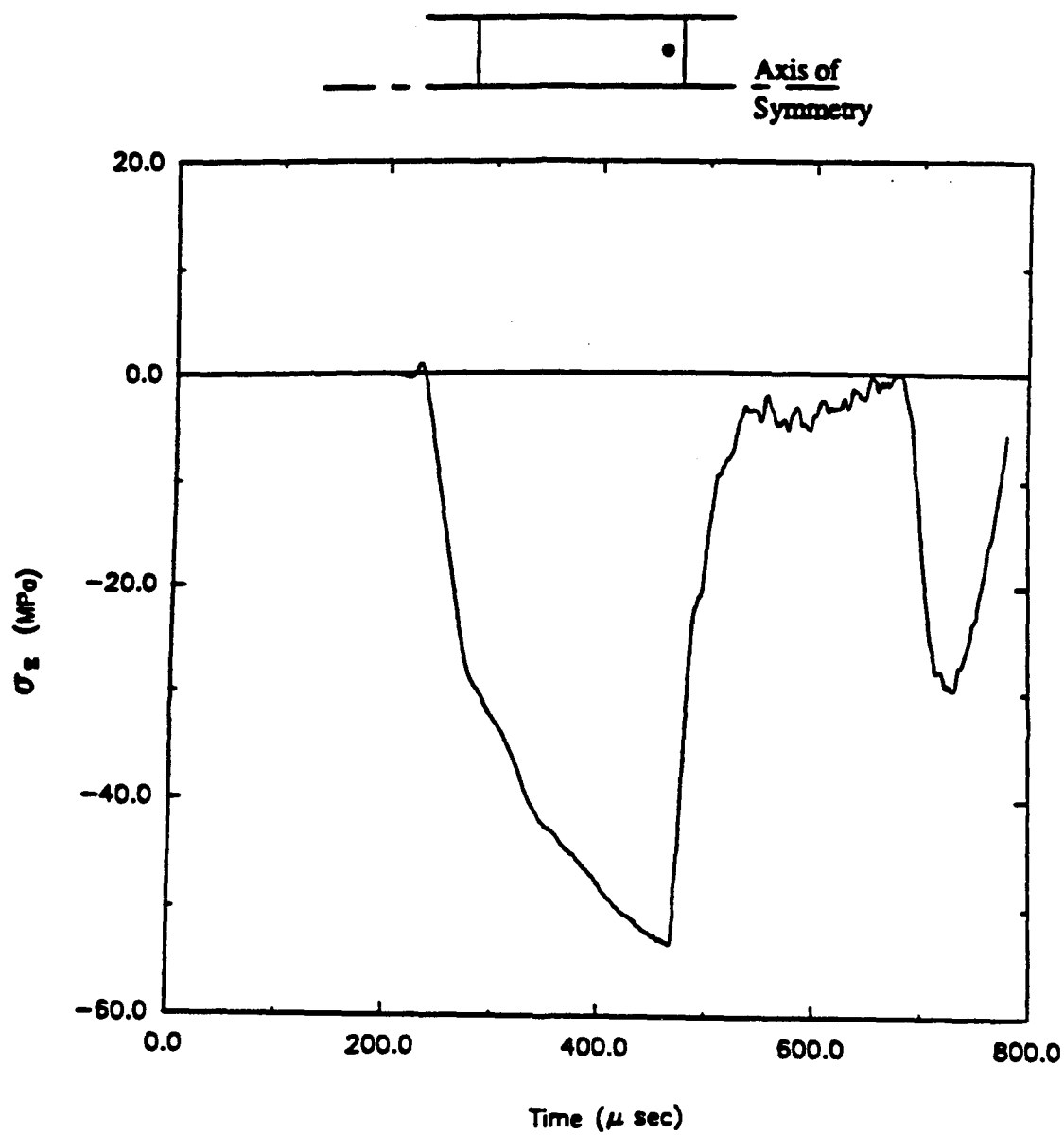


Figure 228. Time history for longitudinal stress (direct compression, Load Case 1).

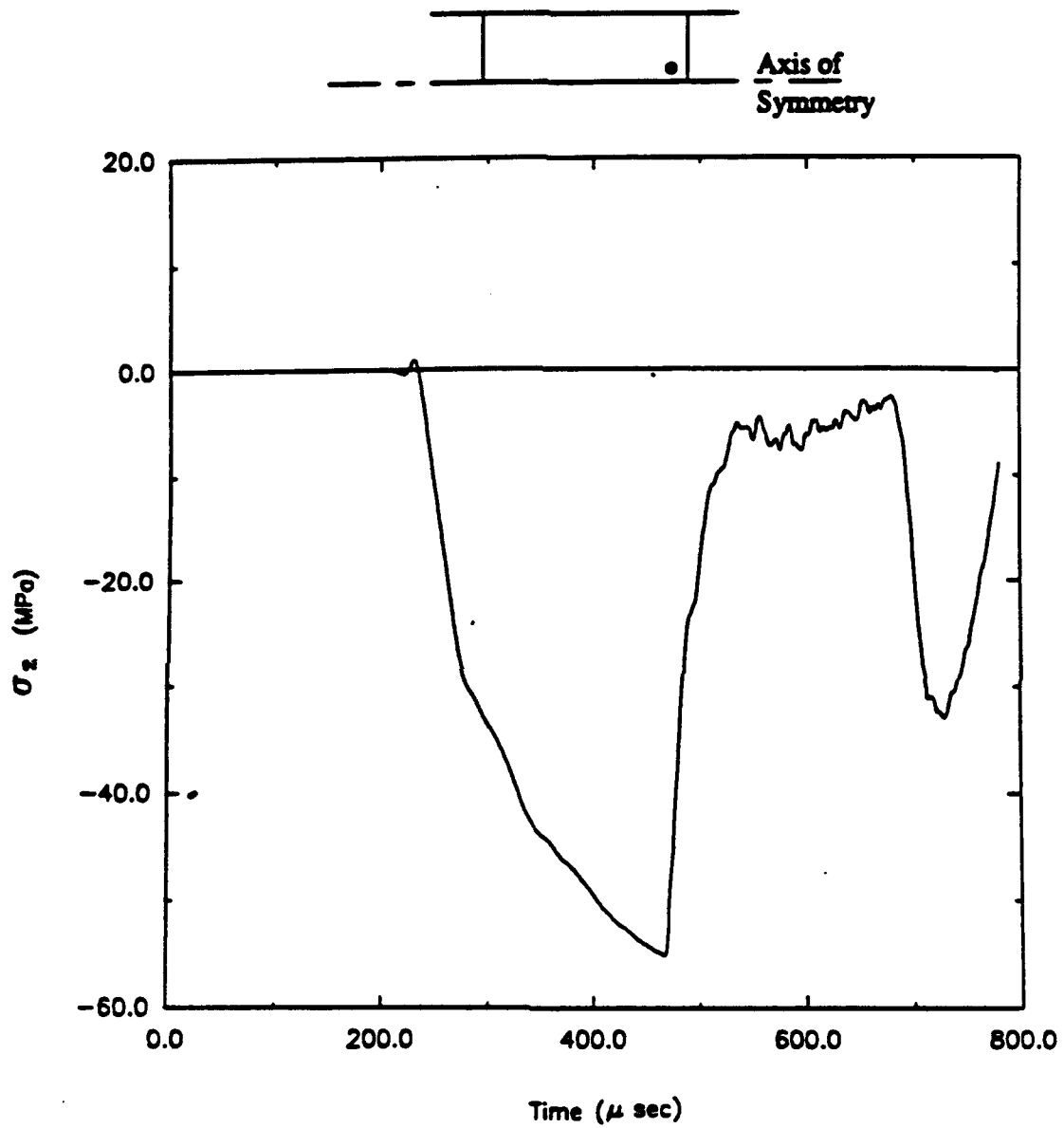


Figure 229. Time history for longitudinal stress (direct compression, Load Case 1).

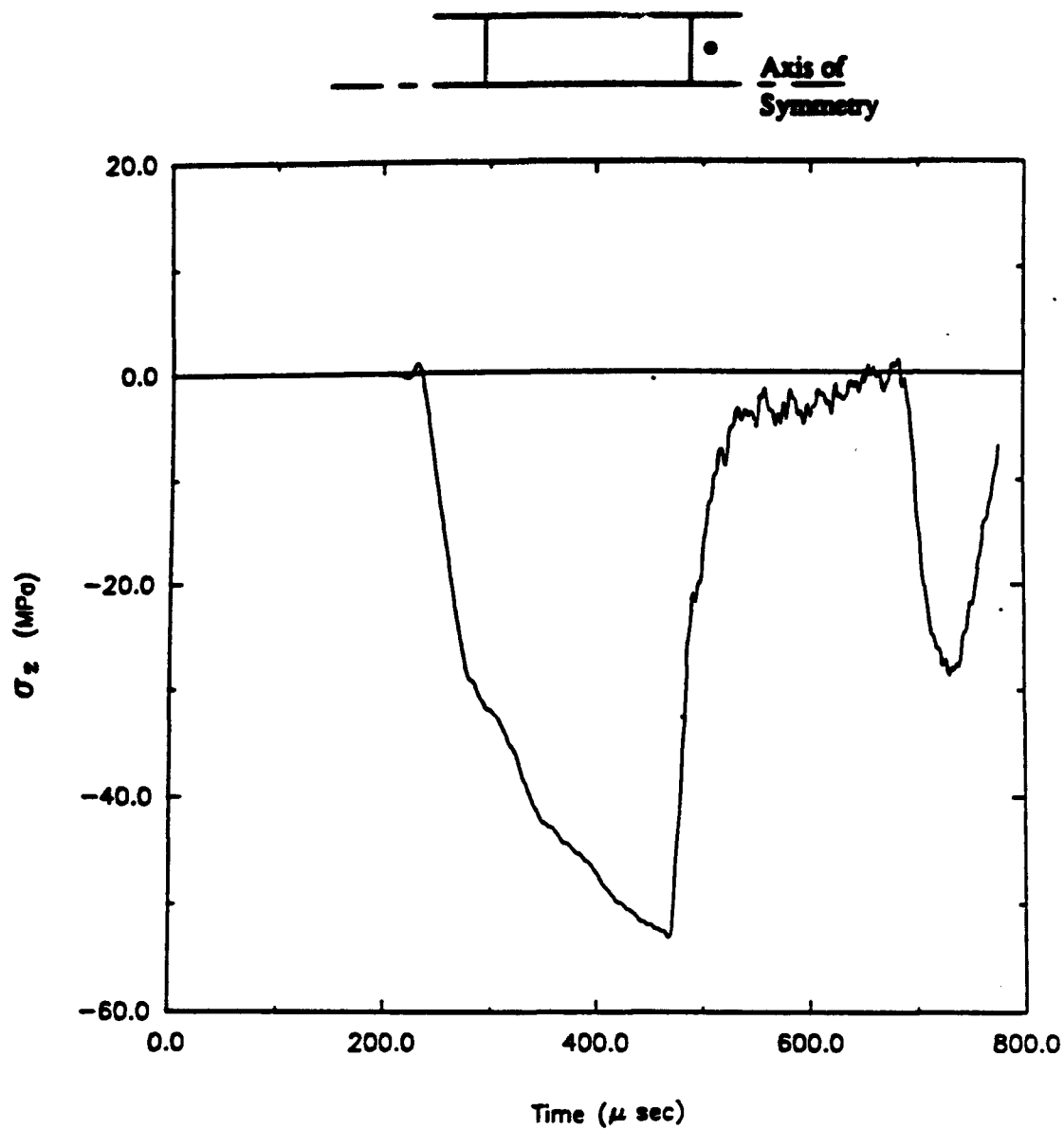


Figure 230. Time history for longitudinal stress (direct compression, Load Case 1).

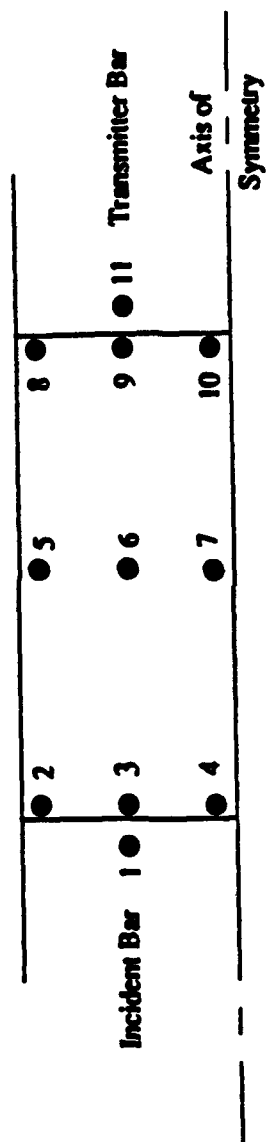


Figure 231. Definition sketch for direct compression specimen.

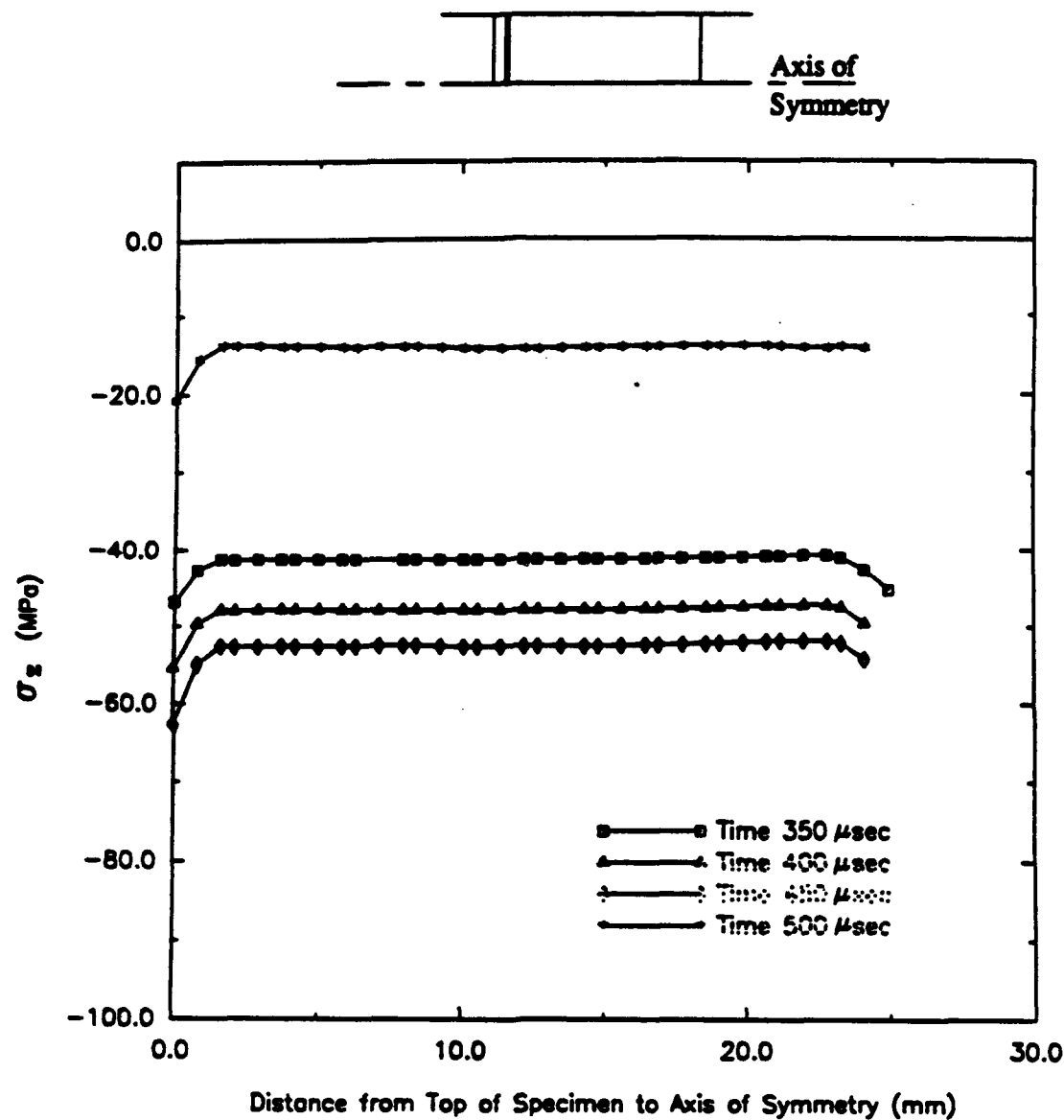


Figure 232. Profiles for longitudinal stress (direct compression, Load Case 1).

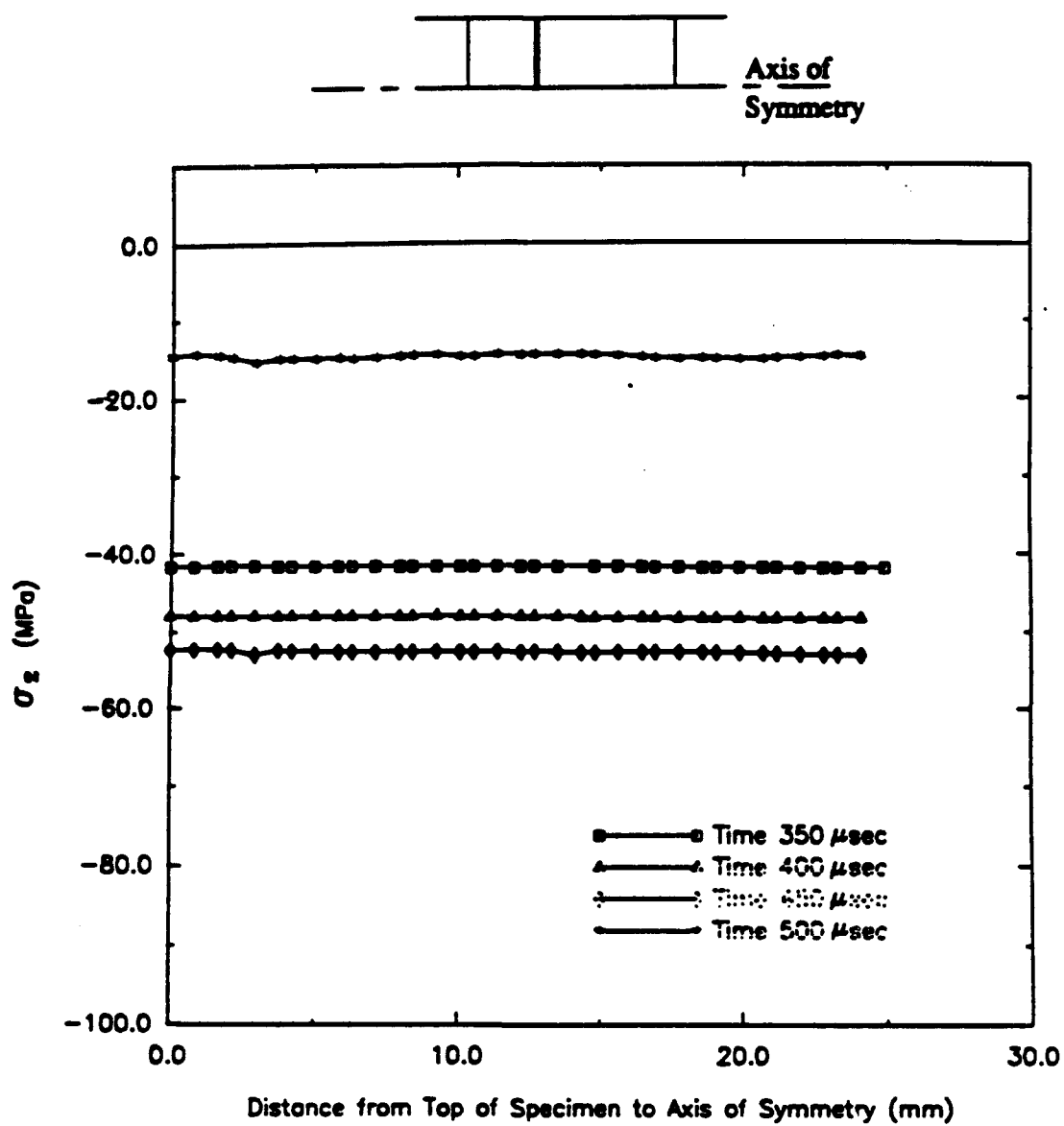


Figure 233. Profiles for longitudinal stress (direct compression, Load Case 1).

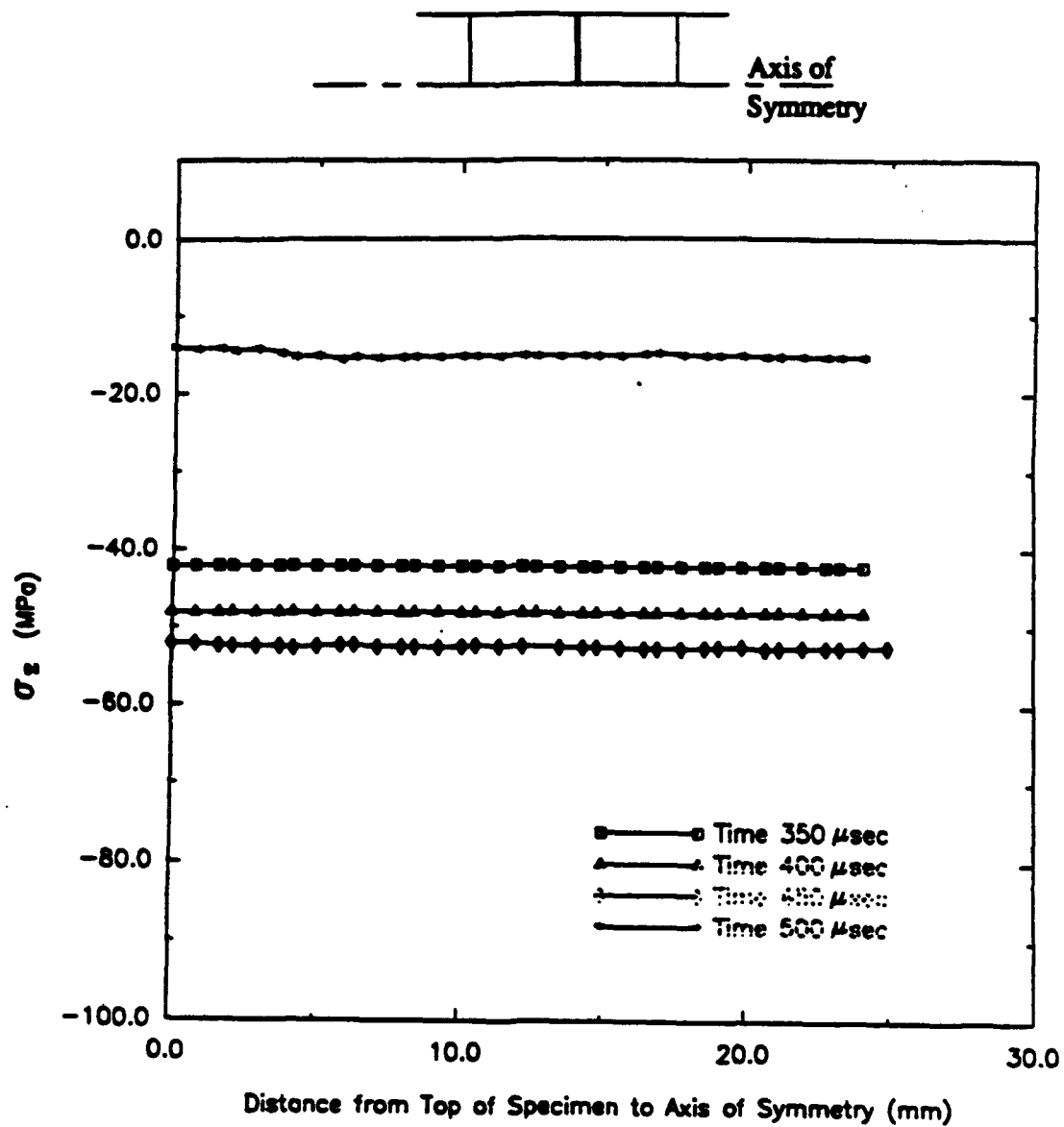


Figure 234. Profiles for longitudinal stress (direct compression, Load Case 1).

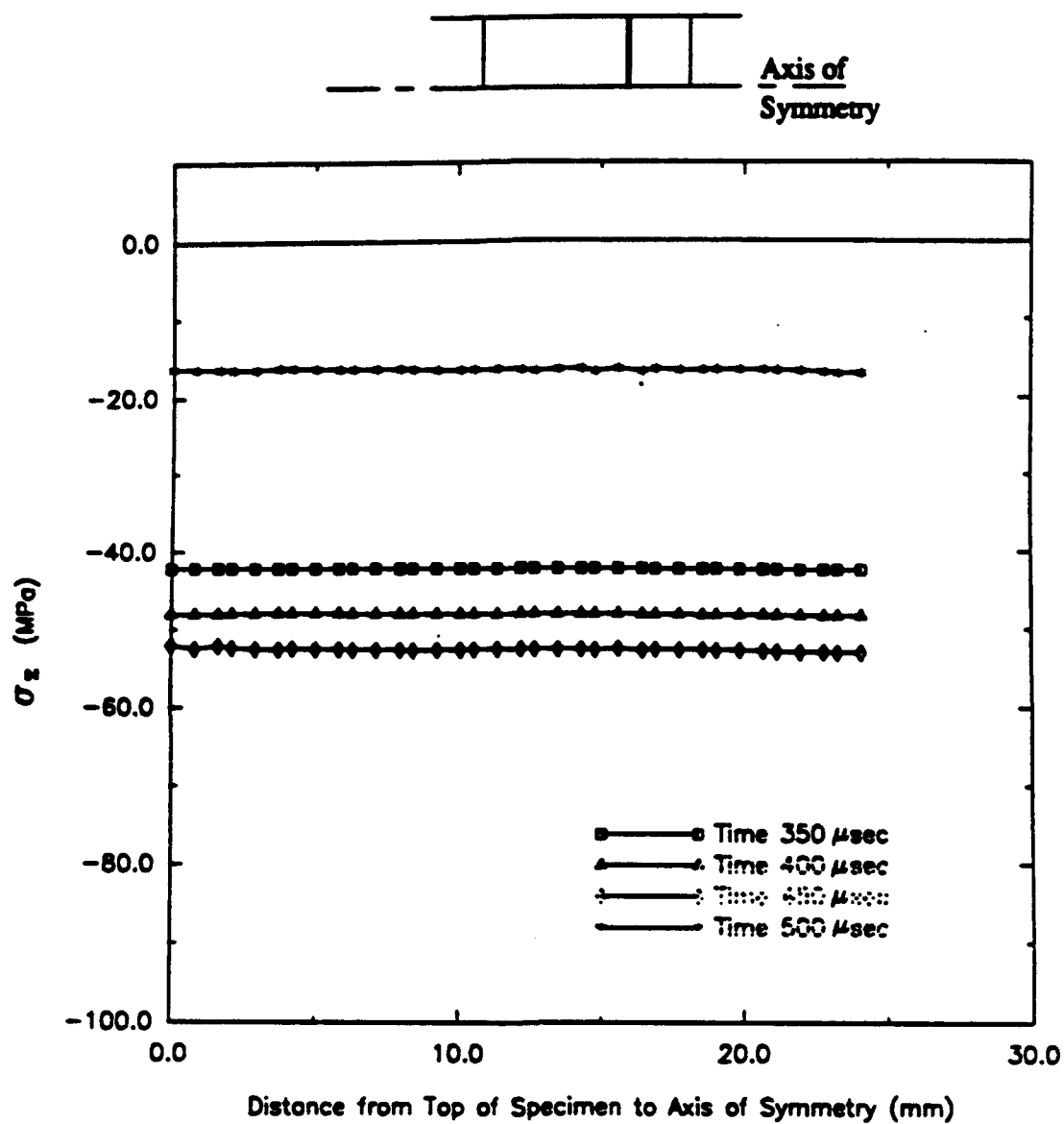


Figure 235. Profiles for longitudinal stress (direct compression, Load Case 1).

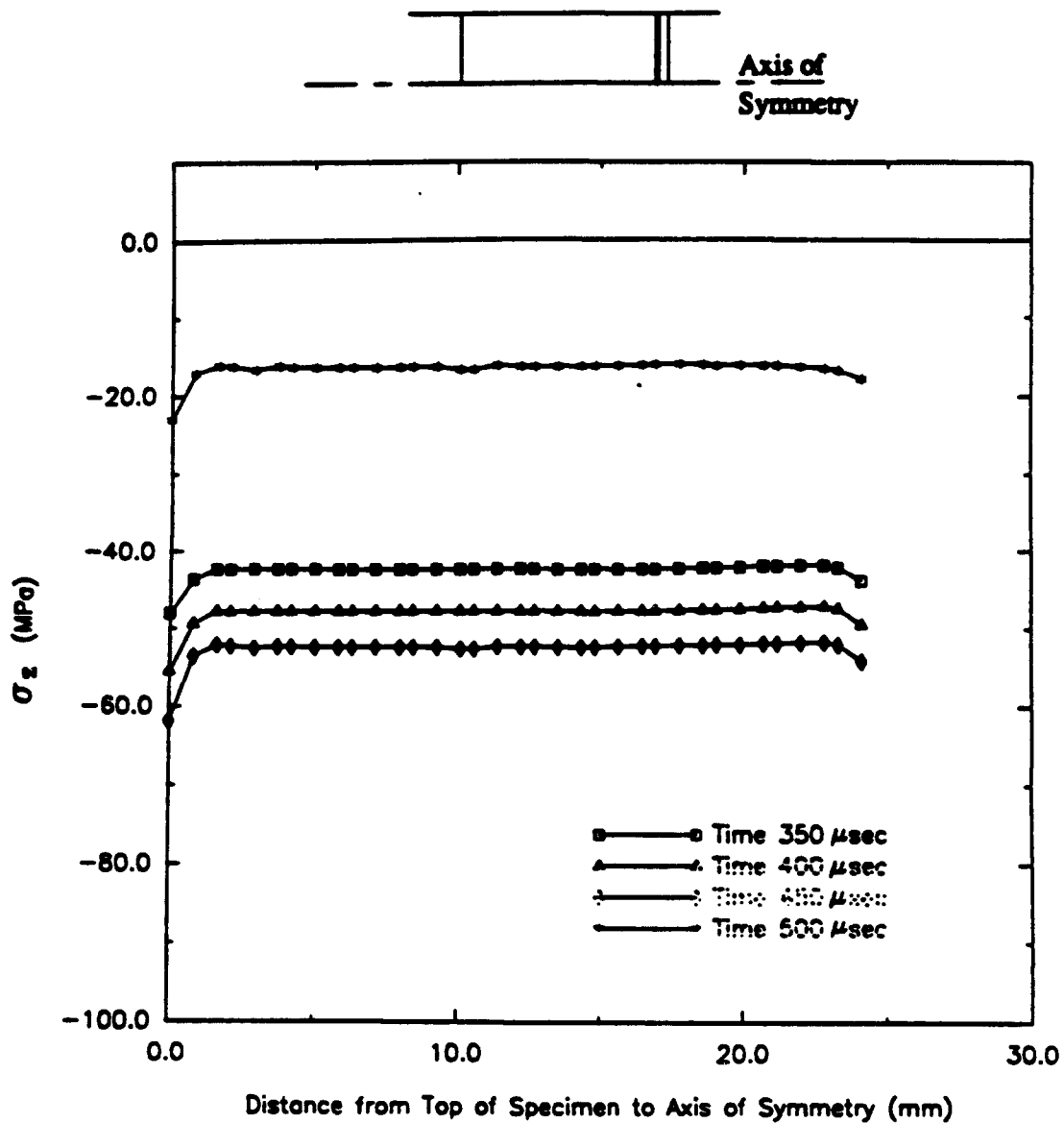


Figure 236. Profiles for longitudinal stress (direct compression, Load Case 1).

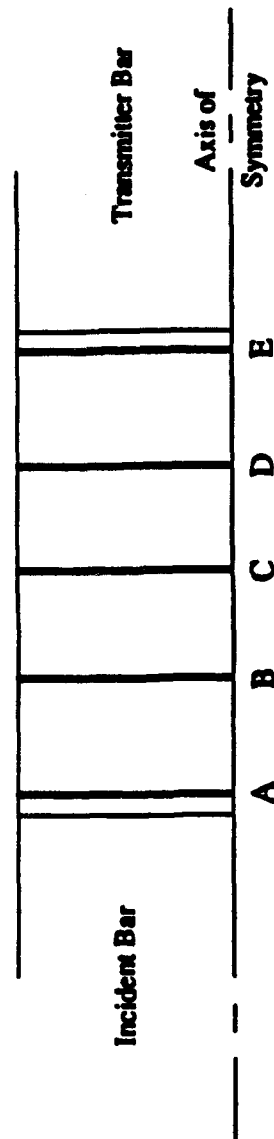
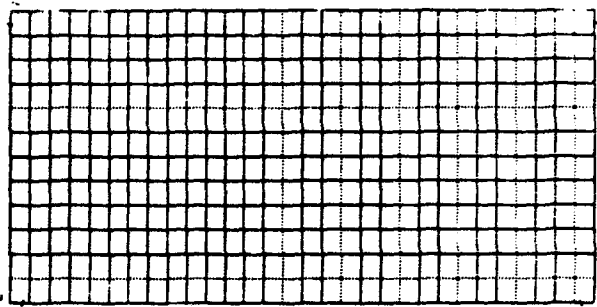
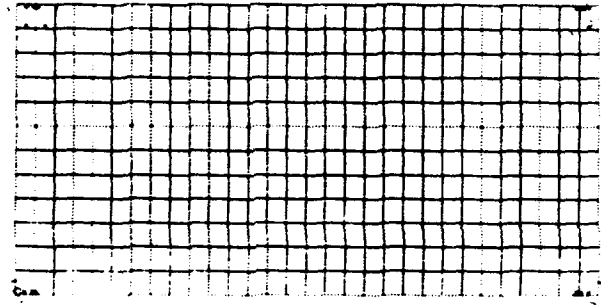


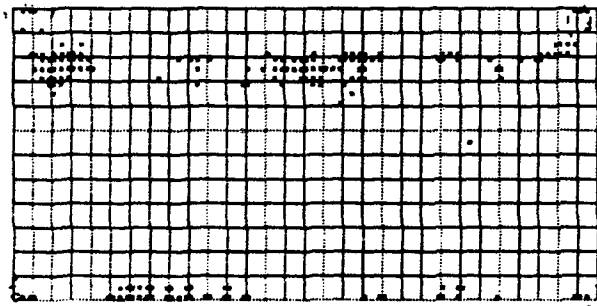
Figure 237. Definition sketch for direct compression specimen.



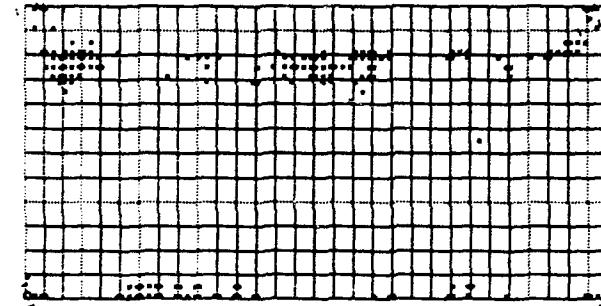
(a)



(b)



(c)



(d)

Figure 238. Cracking sequence for direct compression specimen; Load Case 1:
a) $t=300 \mu\text{sec}$, b) $t=525 \mu\text{sec}$, c) $t=550 \mu\text{sec}$, d) $t=600 \mu\text{sec}$.

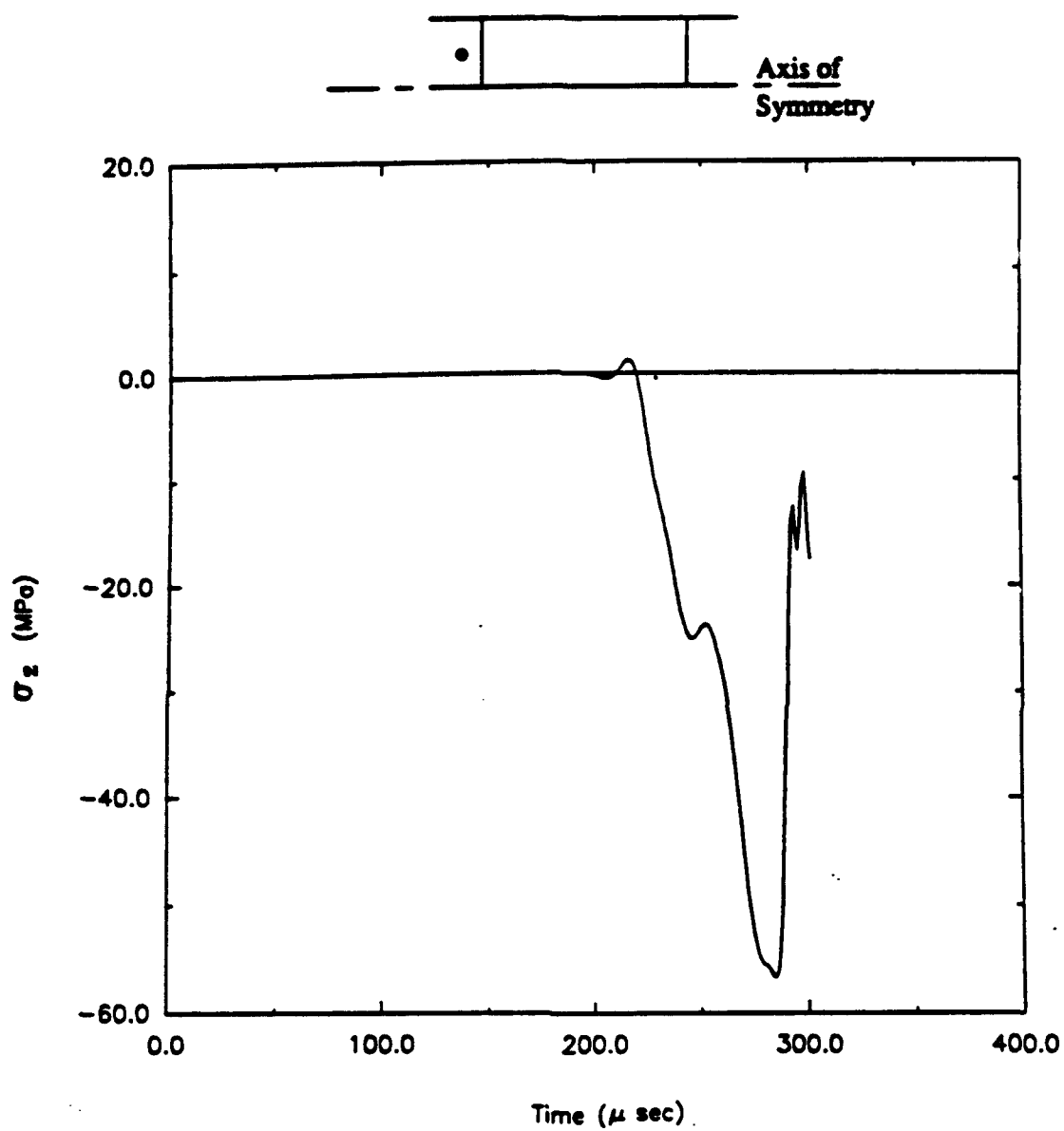


Figure 239. Time history for longitudinal stress (direct compression, Load Case 2).

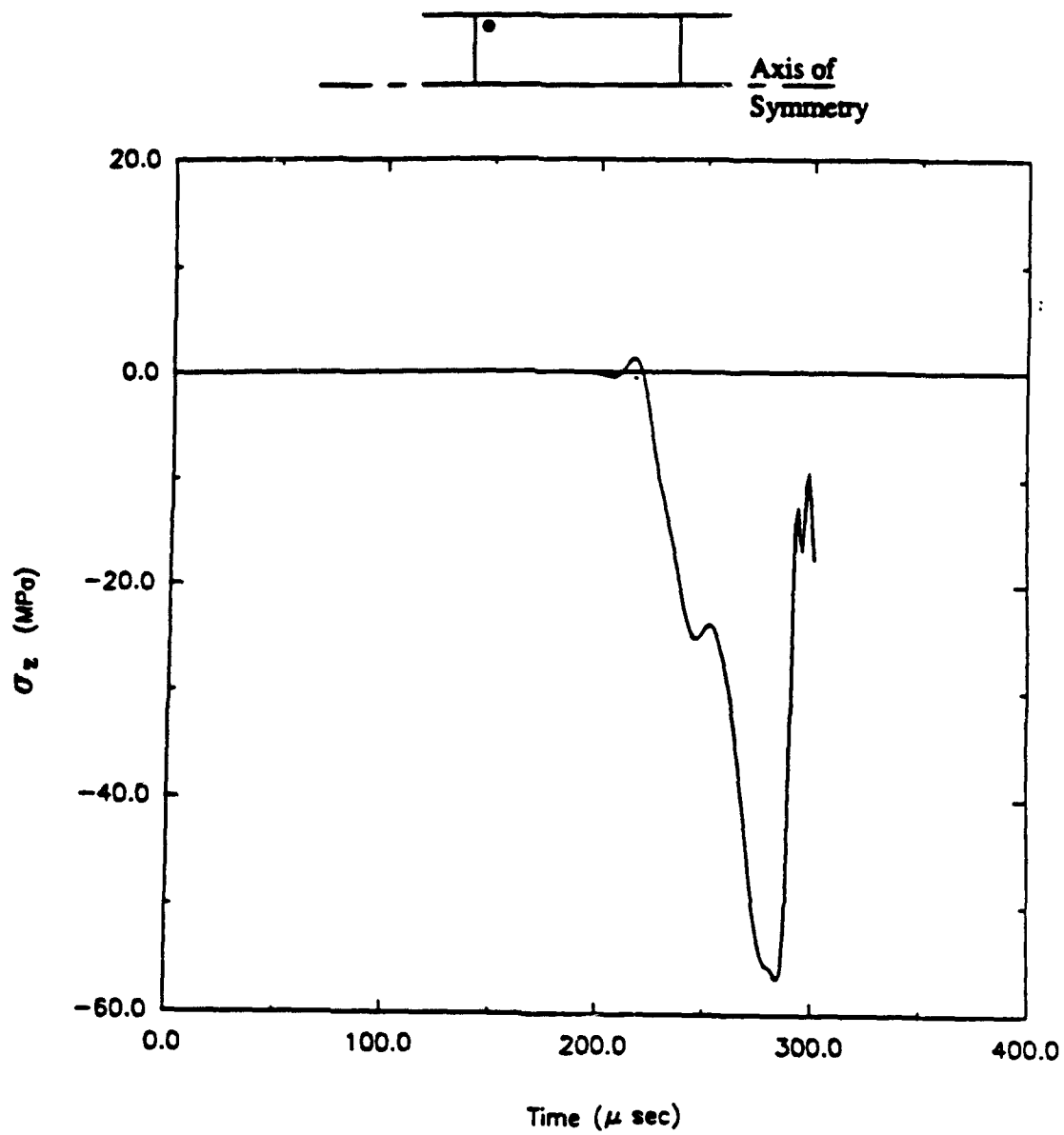


Figure 240. Time history for longitudinal stress (direct compression, Load Case 2).

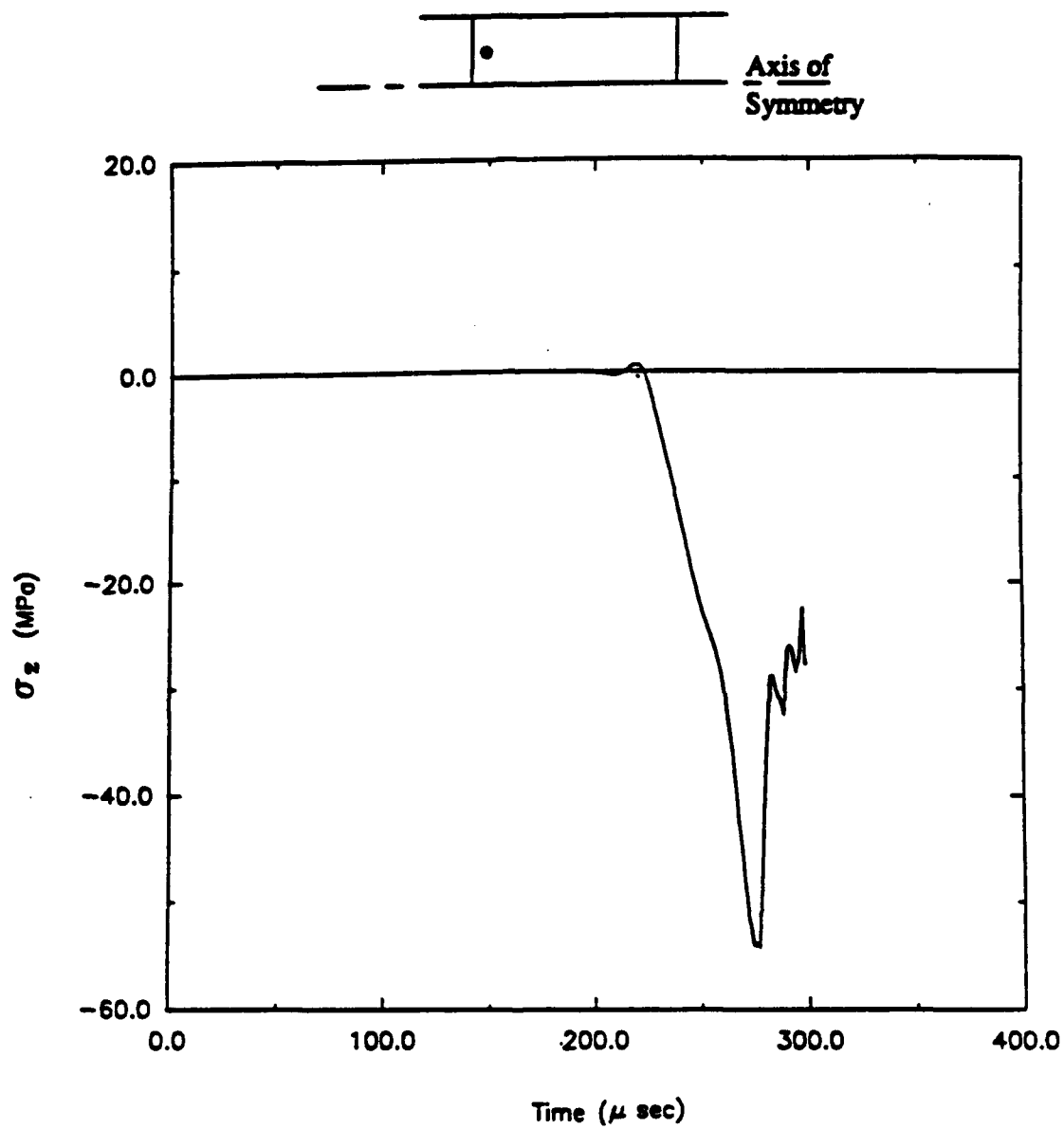


Figure 241. Time history for longitudinal stress (direct compression, Load Case 2).

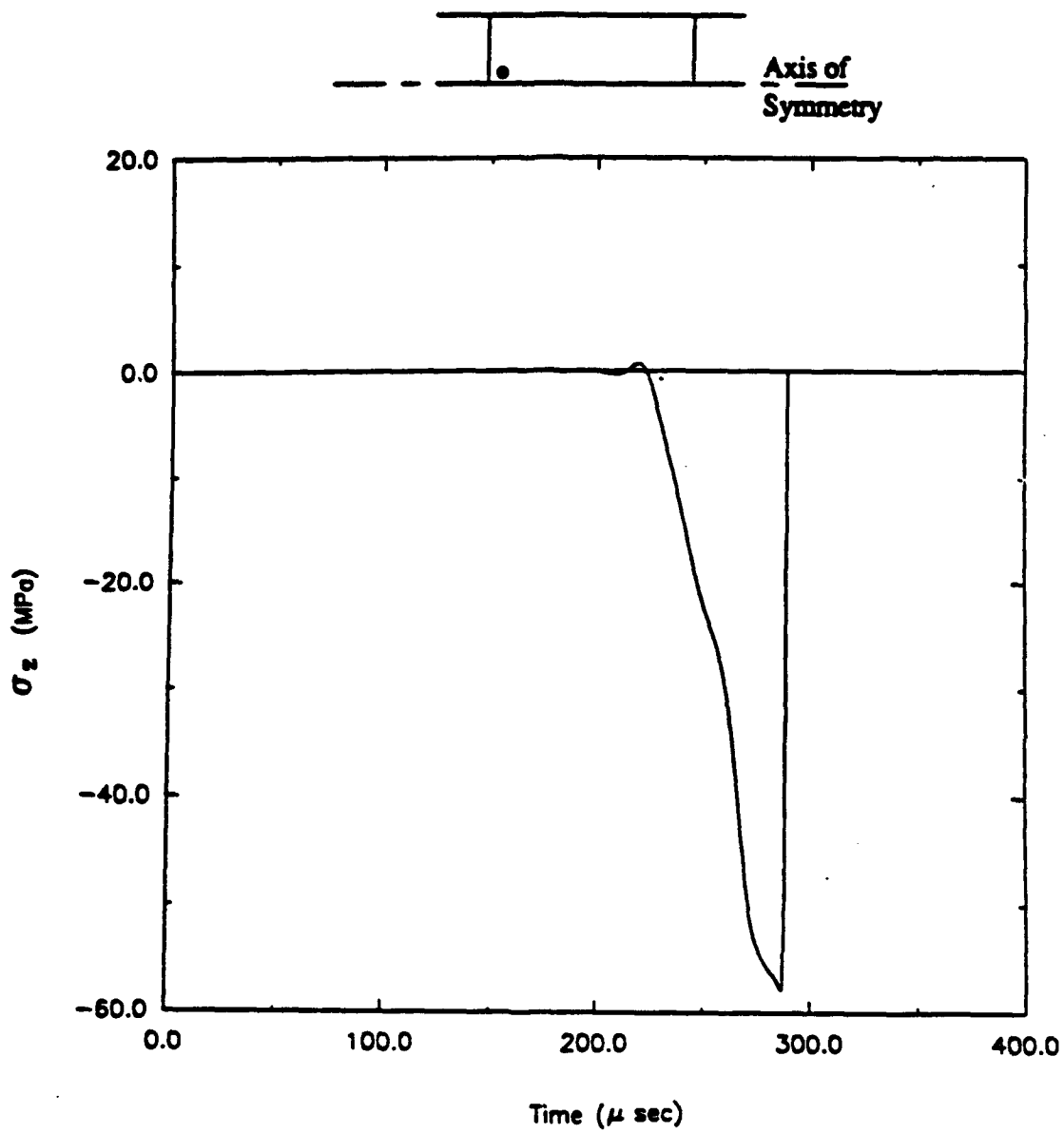


Figure 242. Time history for longitudinal stress (direct compression, Load Case 2).

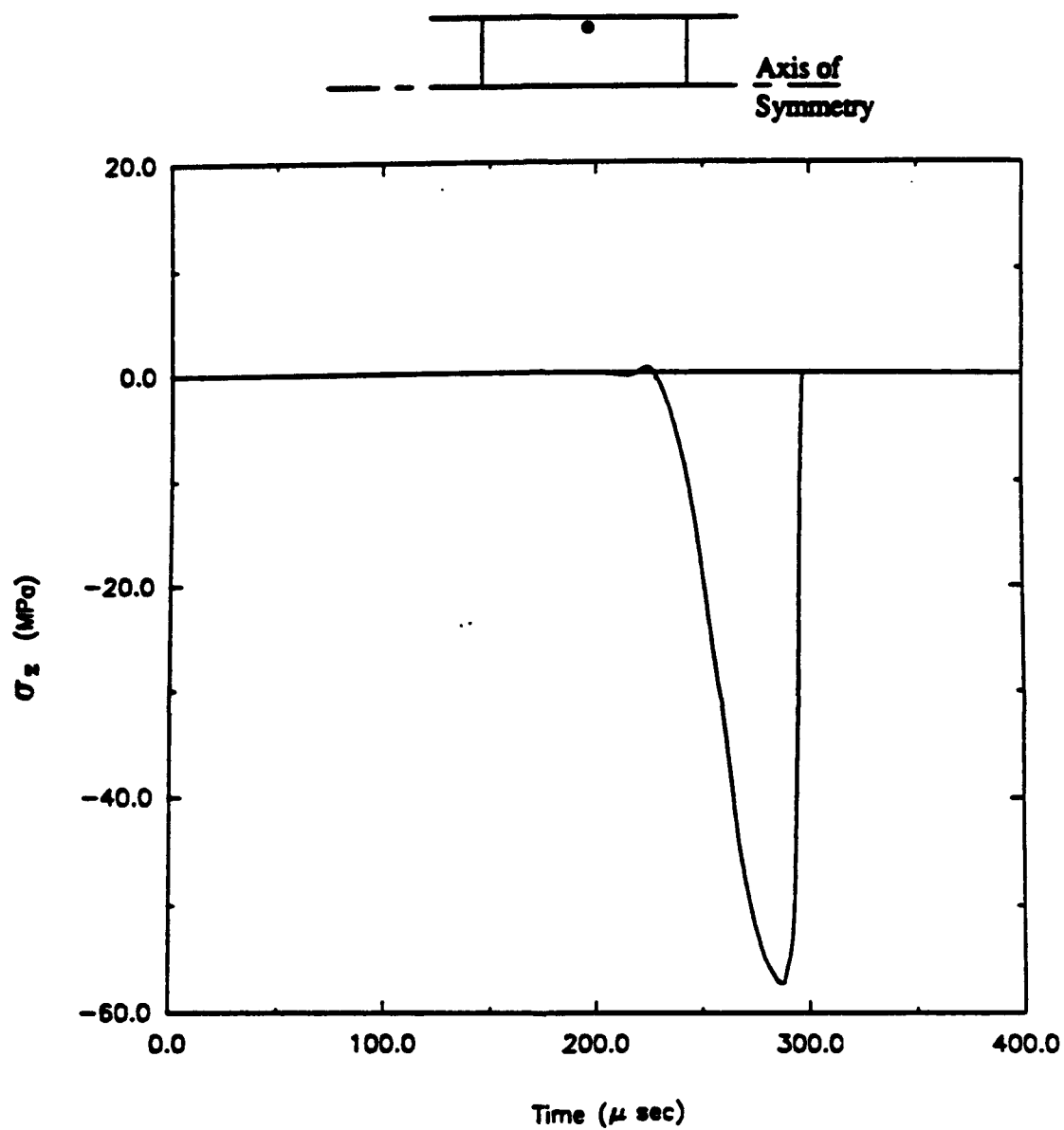


Figure 243. Time history for longitudinal stress (direct compression, Load Case 2).

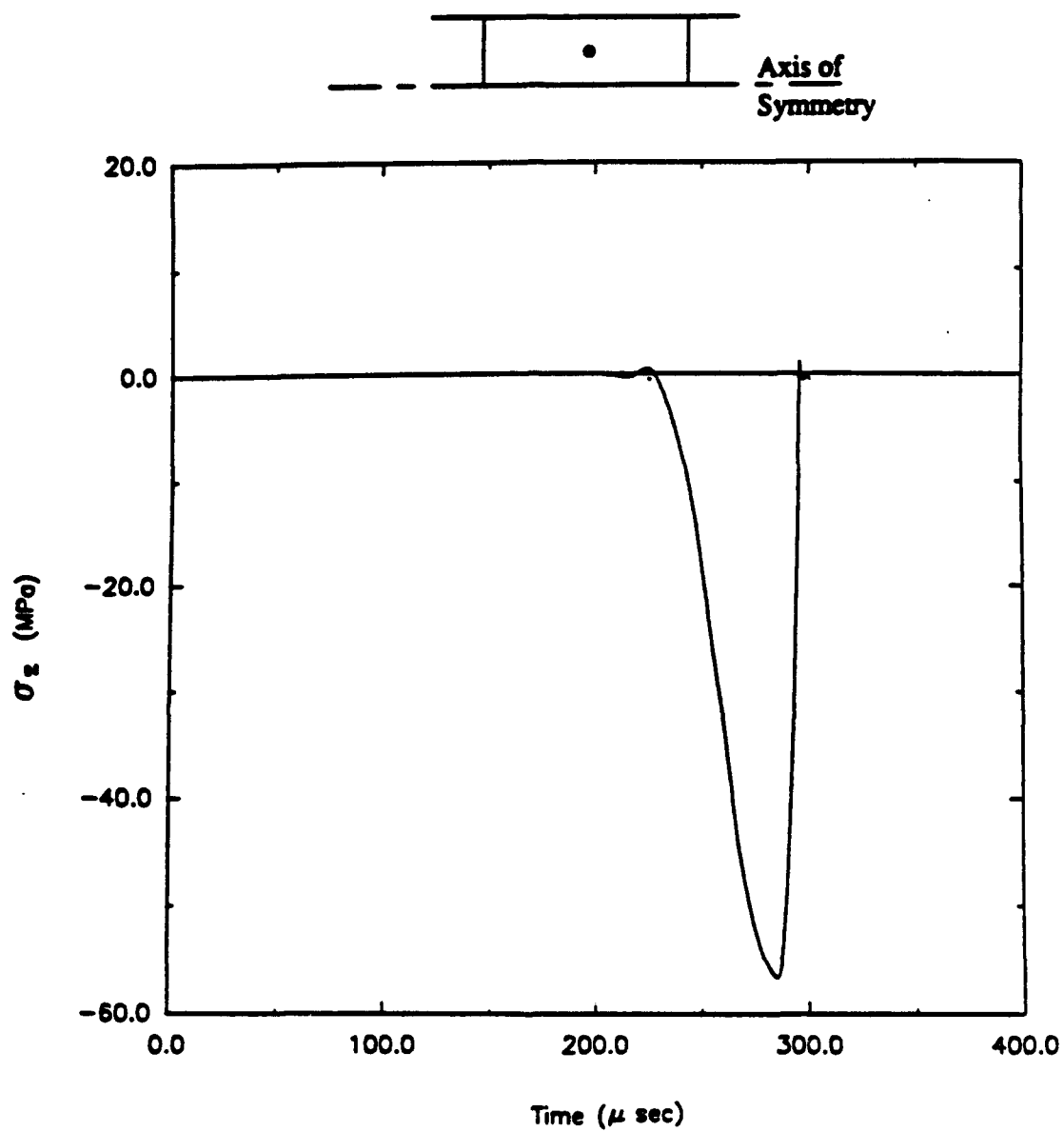


Figure 244. Time history for longitudinal stress (direct compression, Load Case 2).

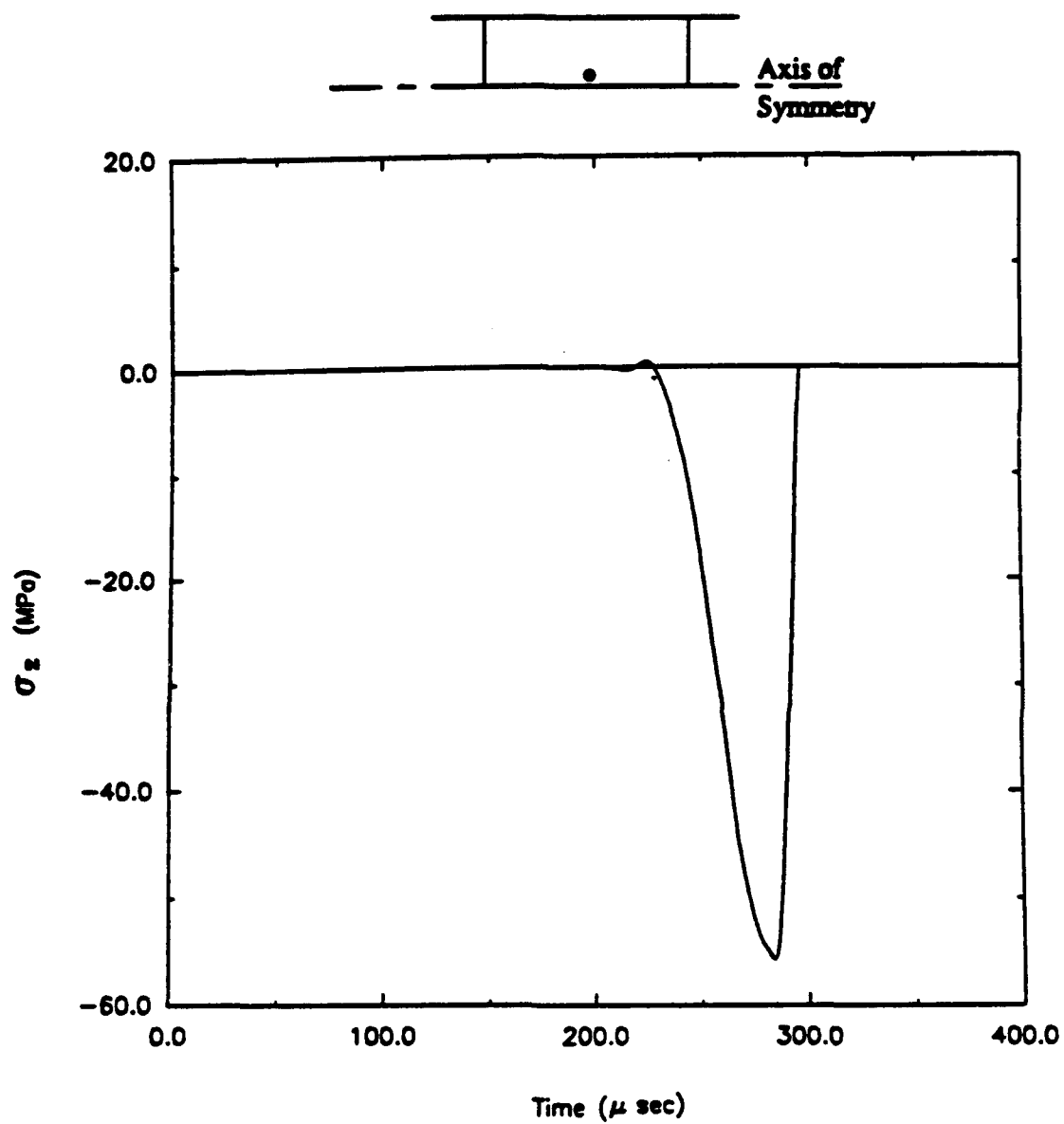


Figure 245. Time history for longitudinal stress (direct compression, Load Case 2).

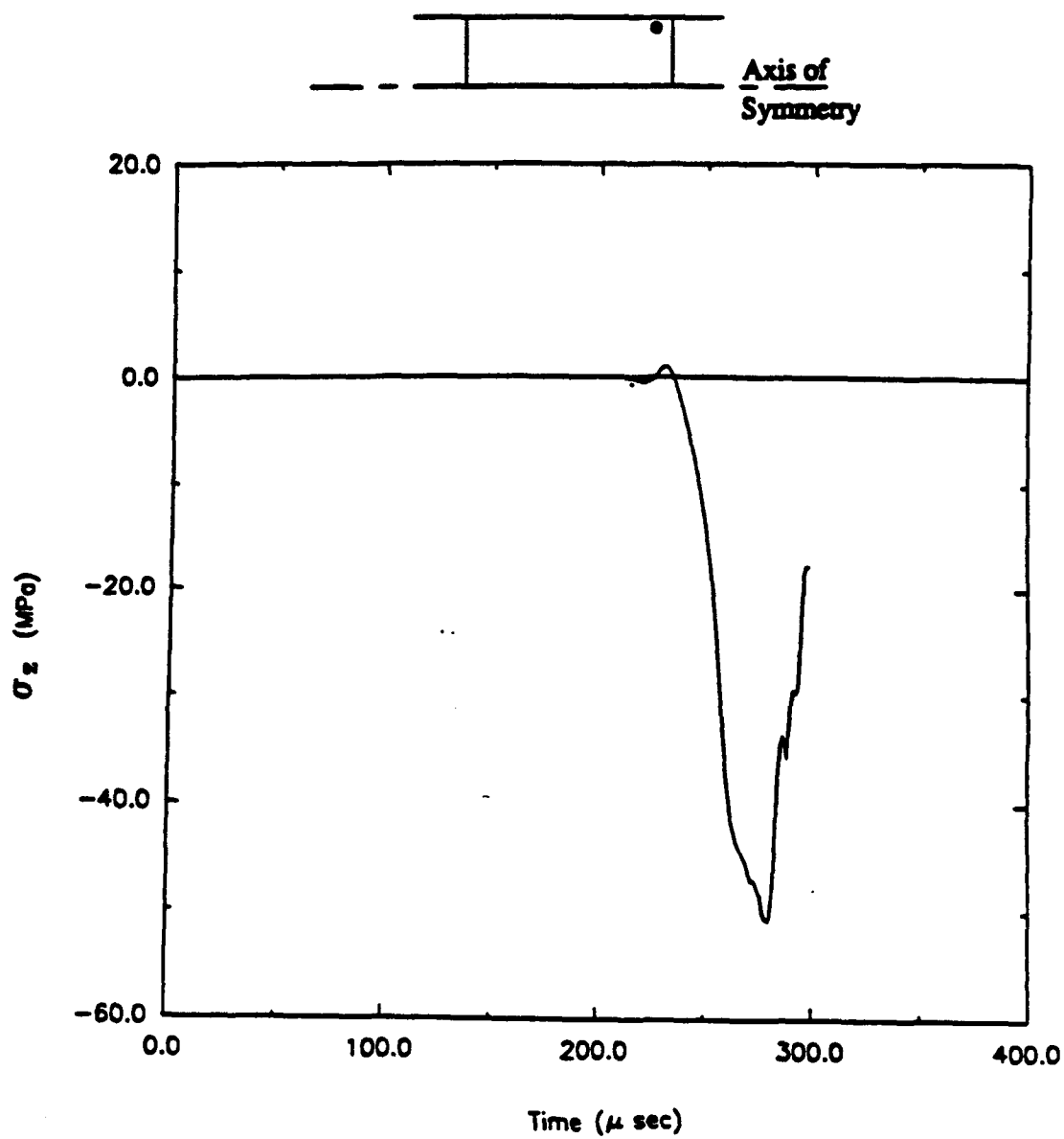


Figure 246. Time history for longitudinal stress (direct compression, Load Case 2).

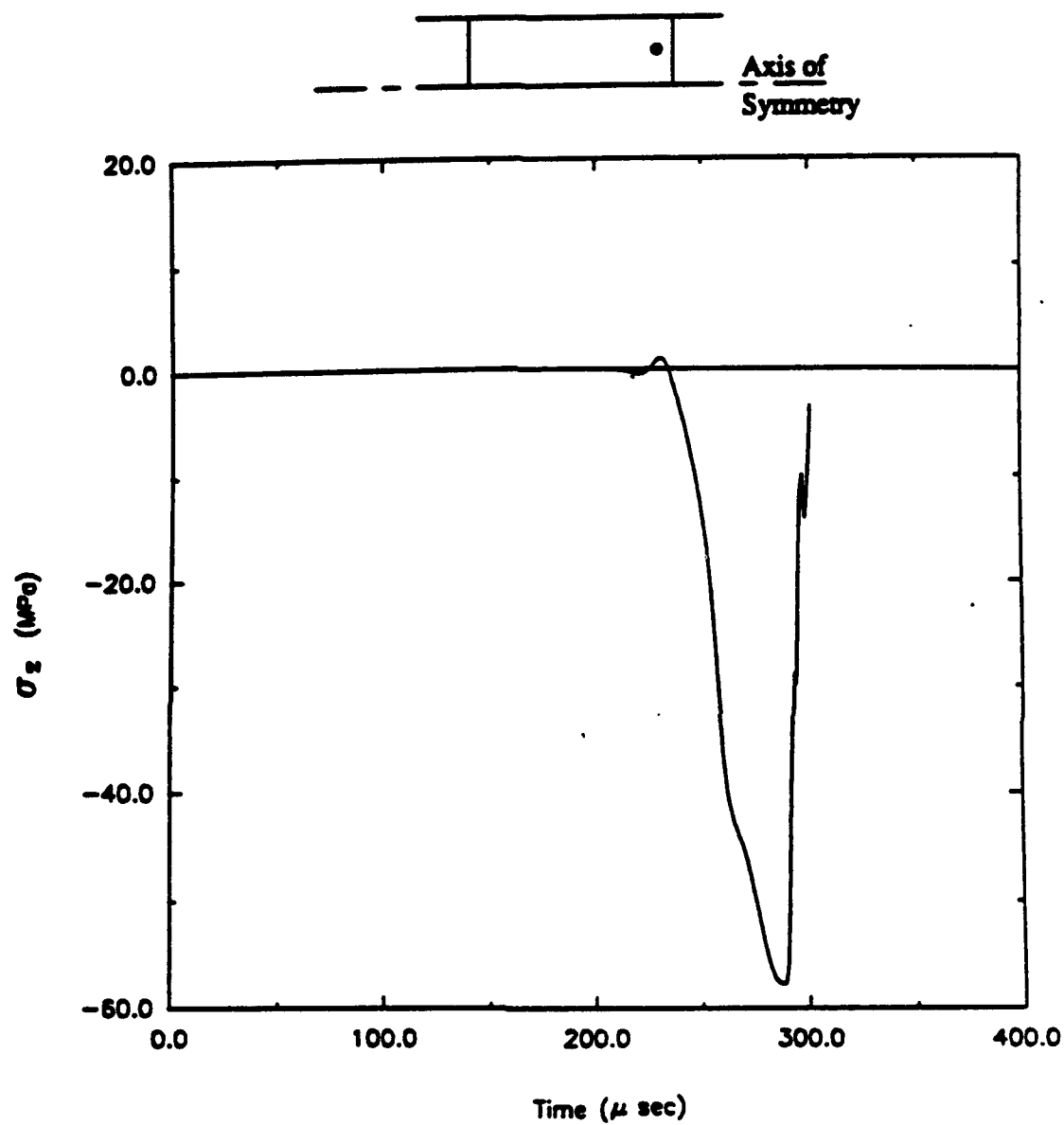


Figure 247. Time history for longitudinal stress (direct compression, Load Case 2).

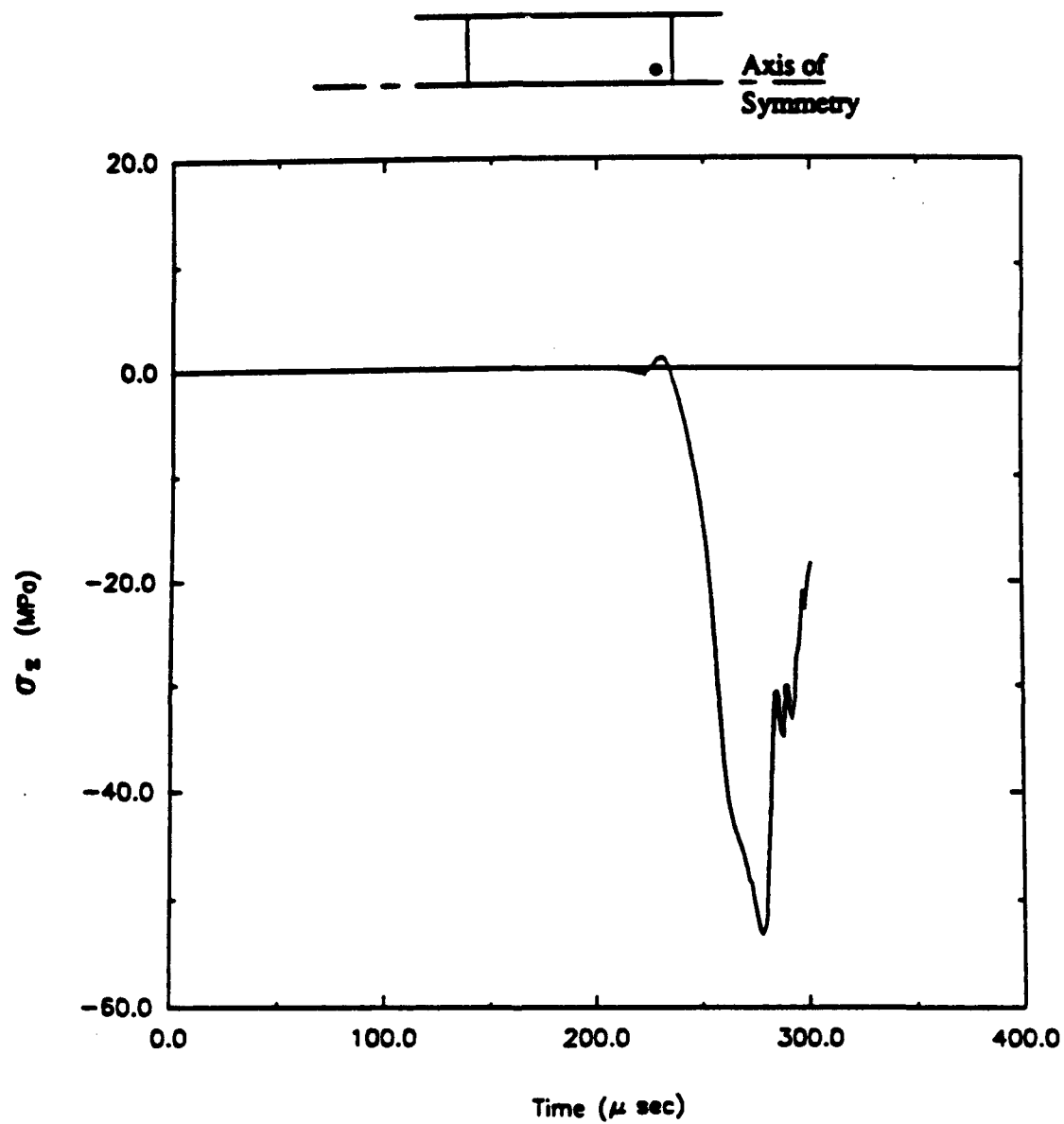


Figure 248. Time history for longitudinal stress (direct compression, Load Case 2).

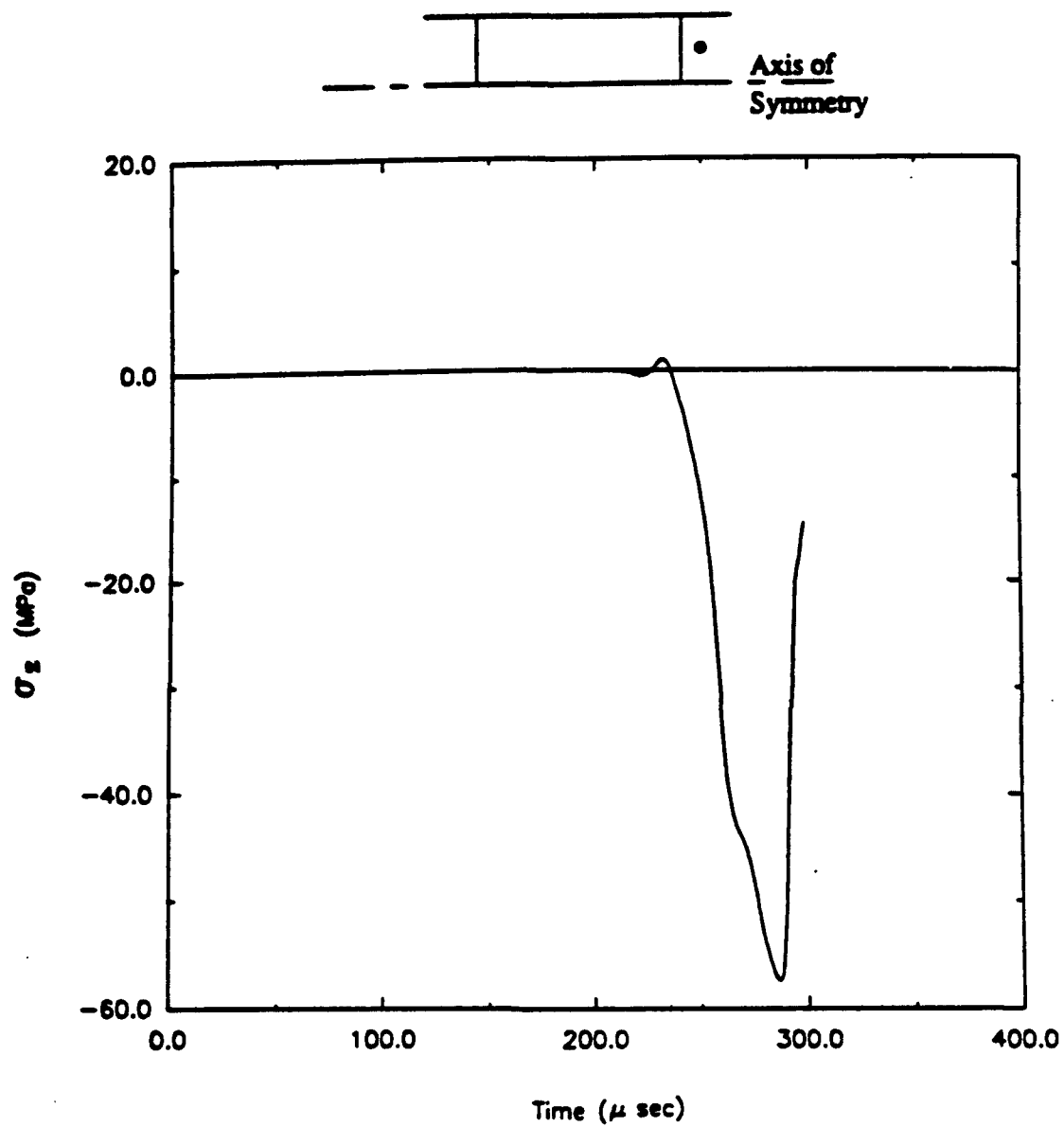


Figure 249. Time history for longitudinal stress (direct compression, Load Case 2).

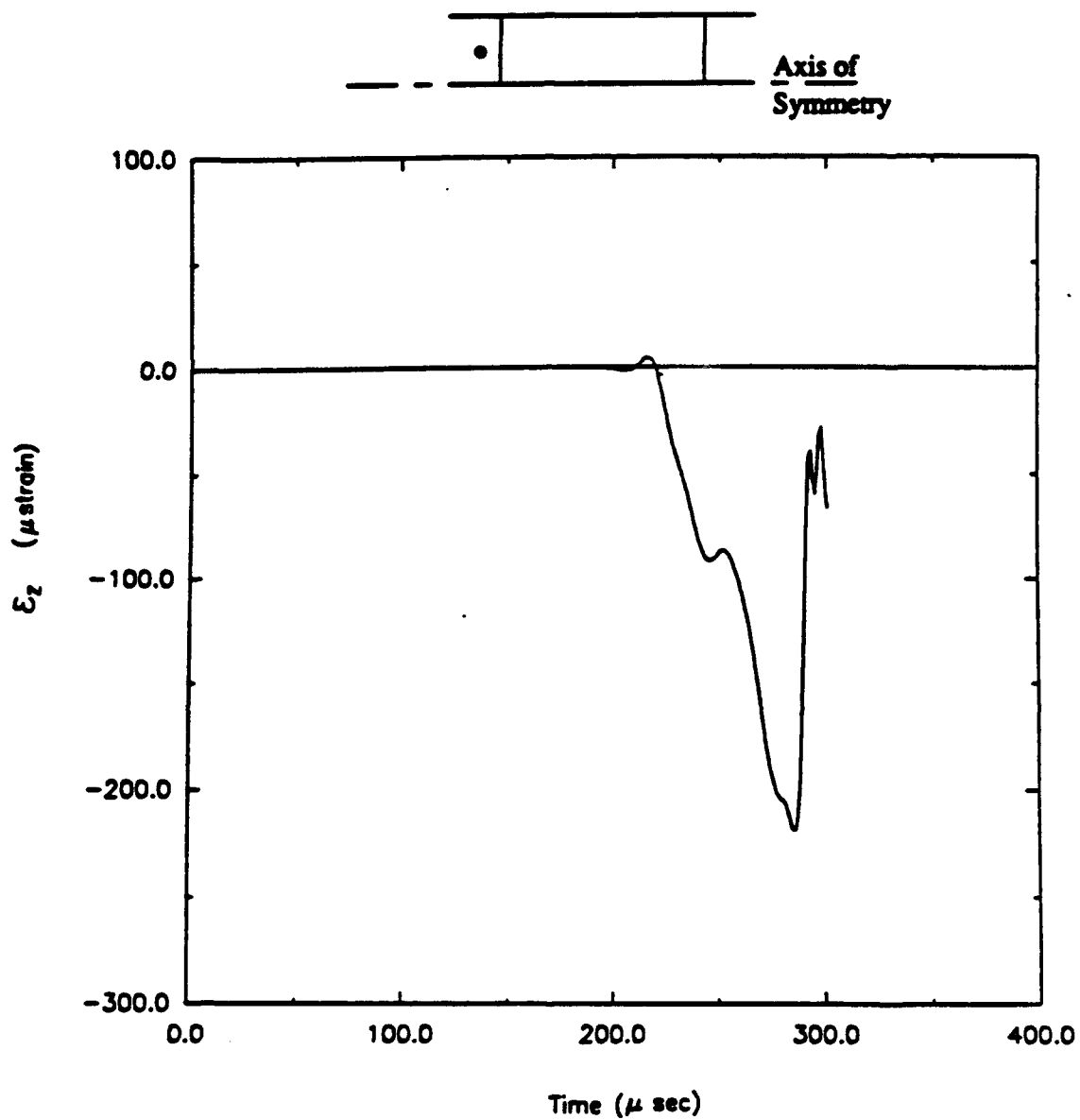


Figure 250. Time history for longitudinal strain (direct compression, Load Case 2).

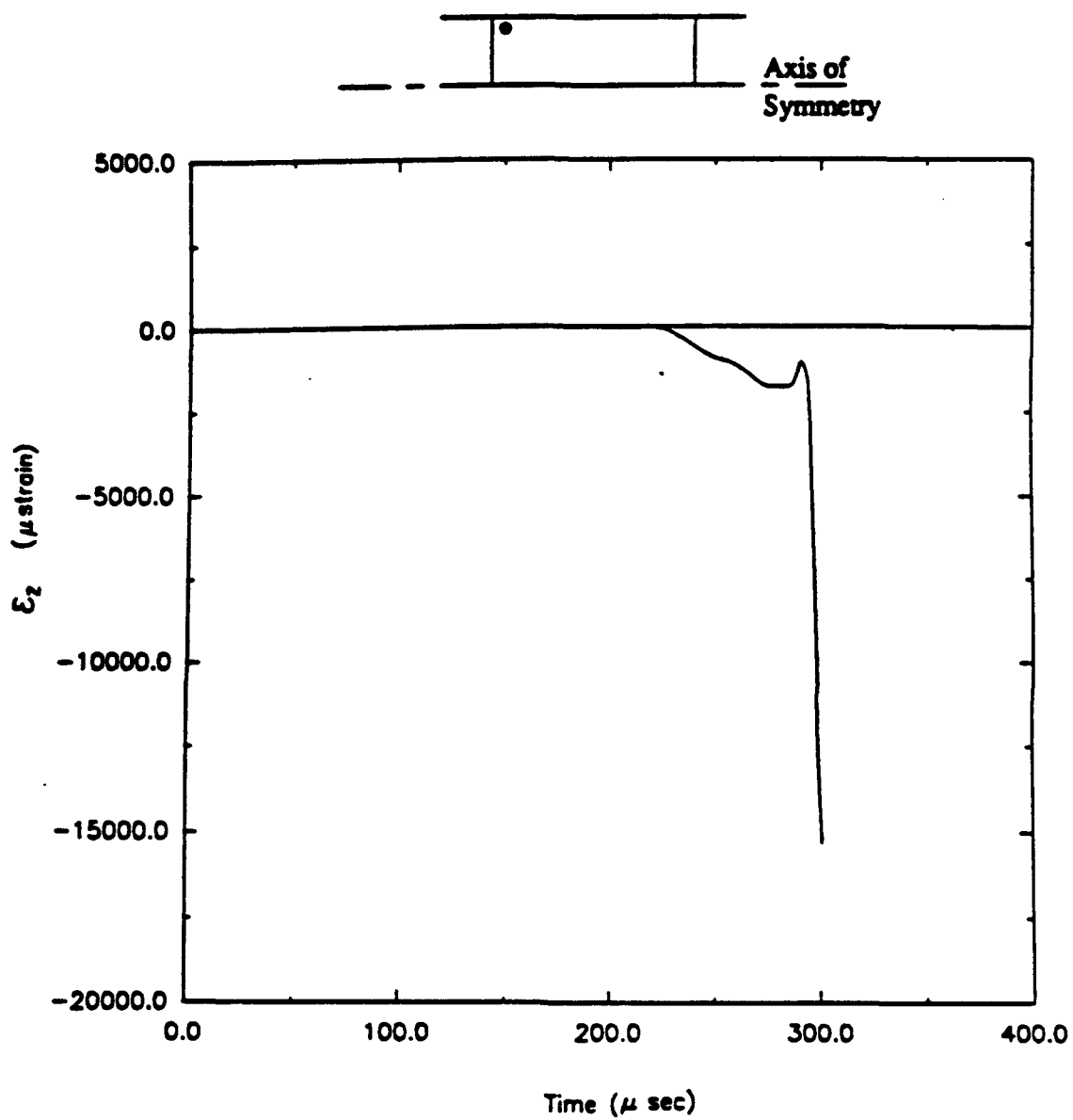


Figure 251. Time history for longitudinal strain (direct compression, Load Case 2).

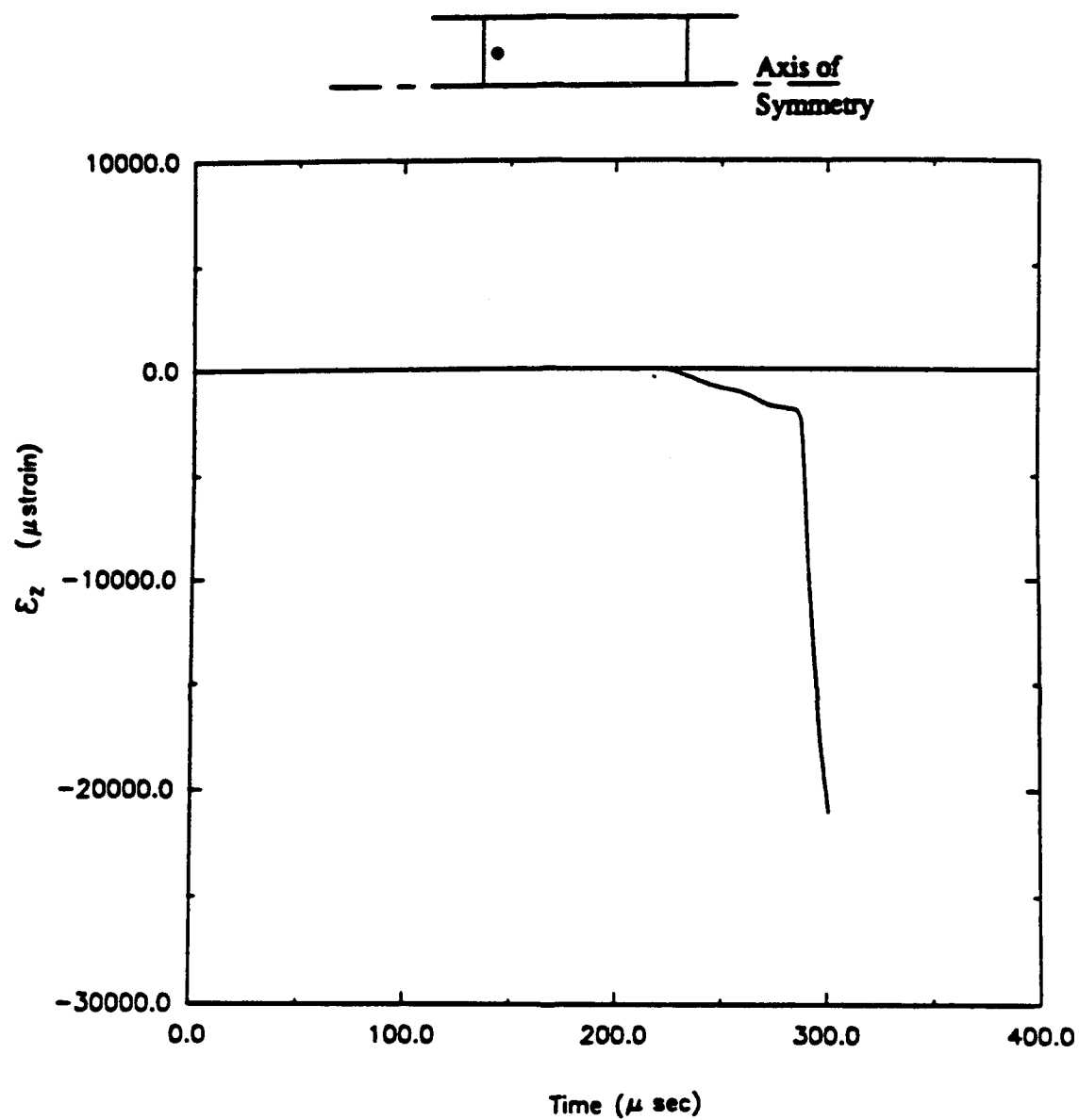


Figure 252. Time history for longitudinal strain (direct compression, Load Case 2).

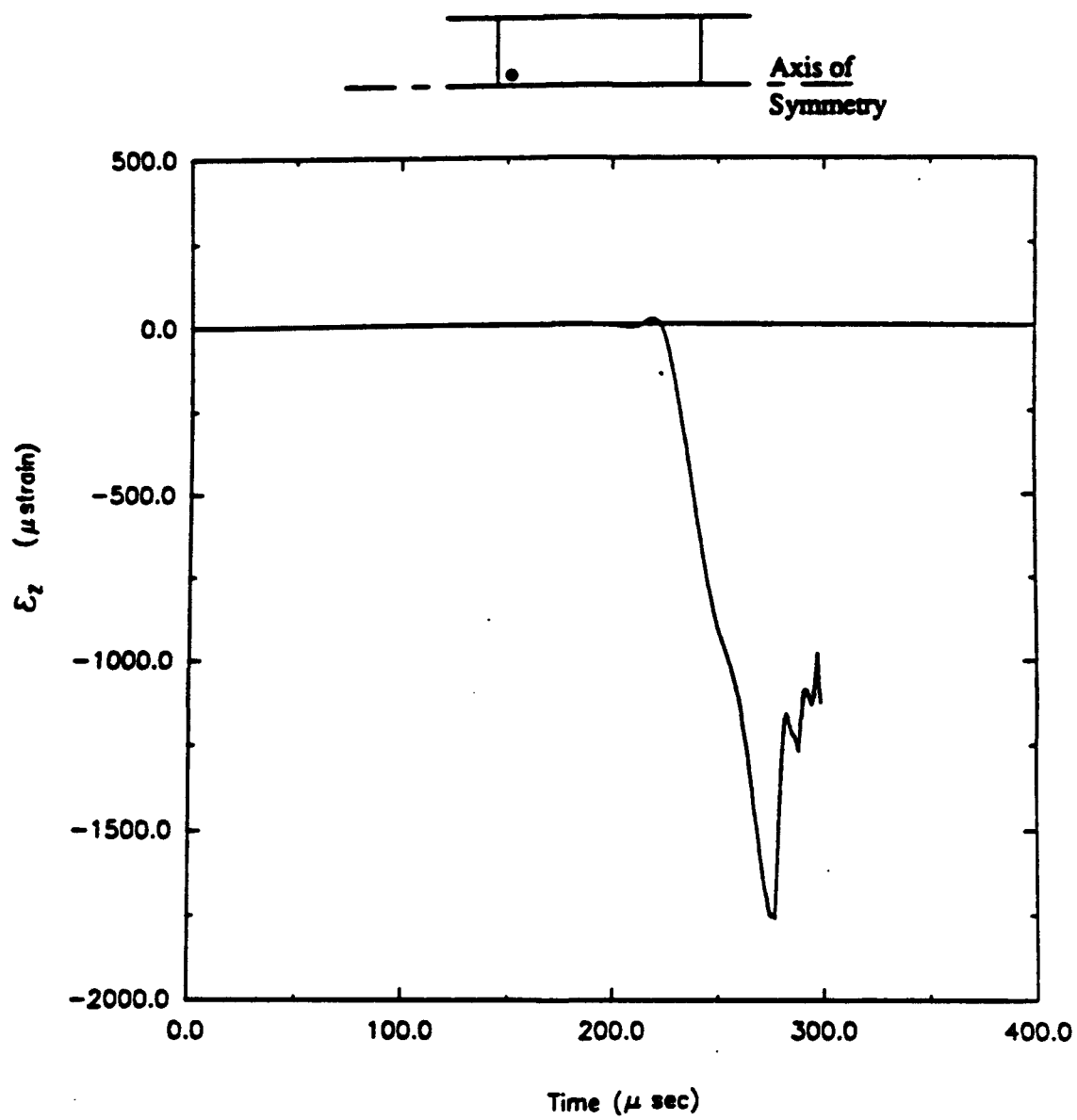


Figure 253. Time history for longitudinal strain (direct compression, Load Case 2).

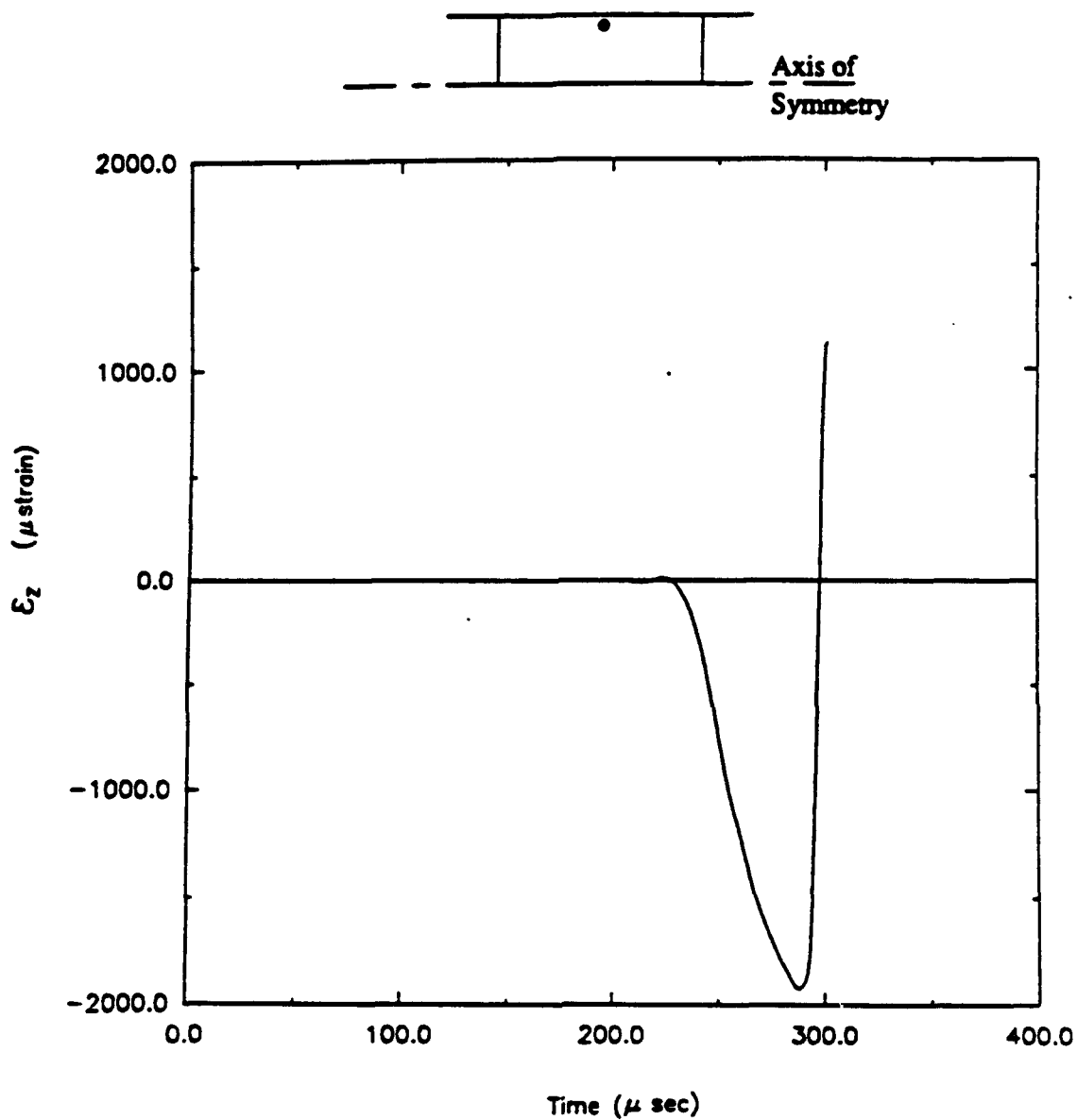


Figure 254. Time history for longitudinal strain (direct compression, Load Case 2).

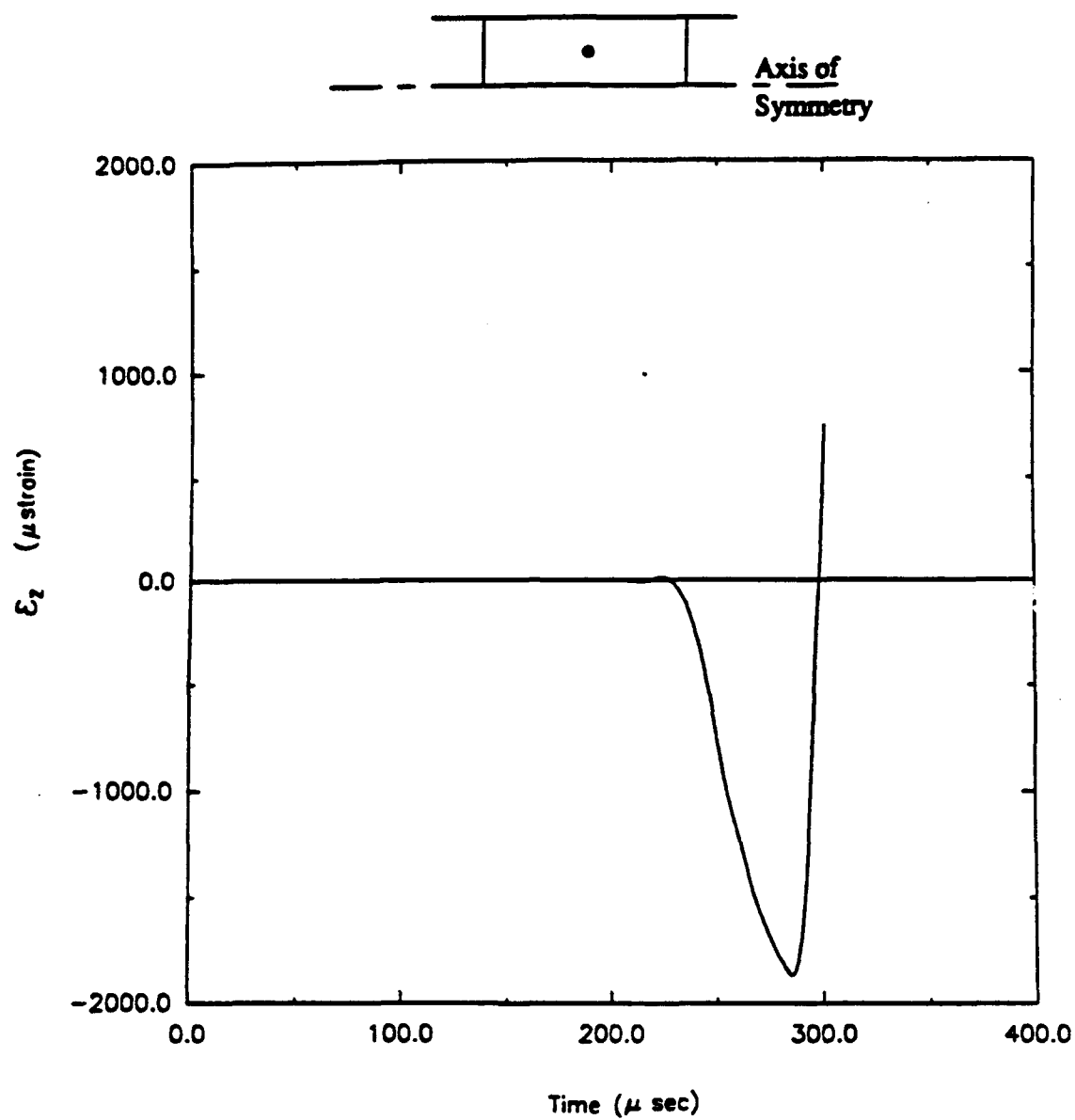


Figure 255. Time history for longitudinal strain (direct compression, Load Case 2).

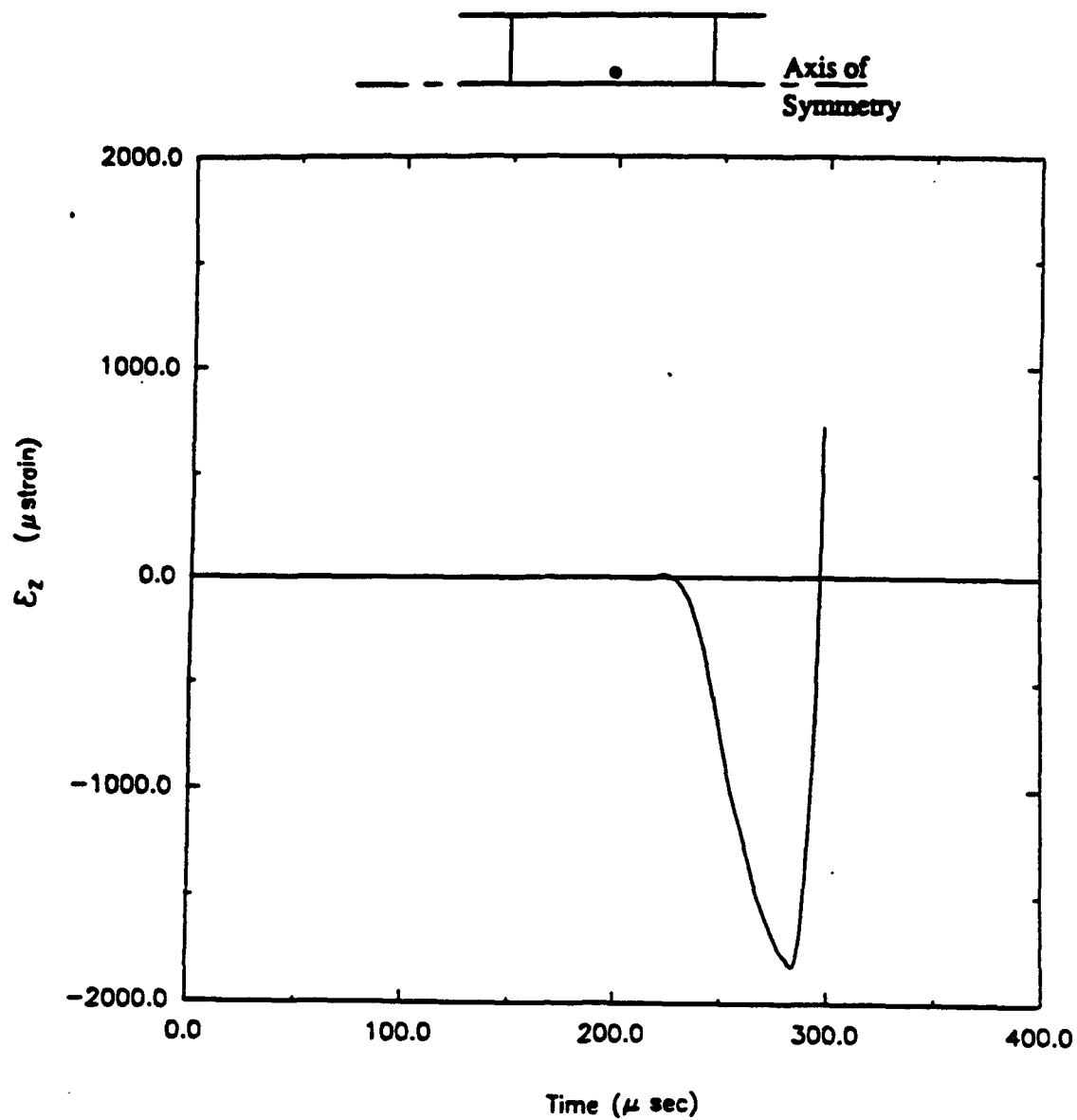


Figure 256. Time history for longitudinal strain (direct compression, Load Case 2).

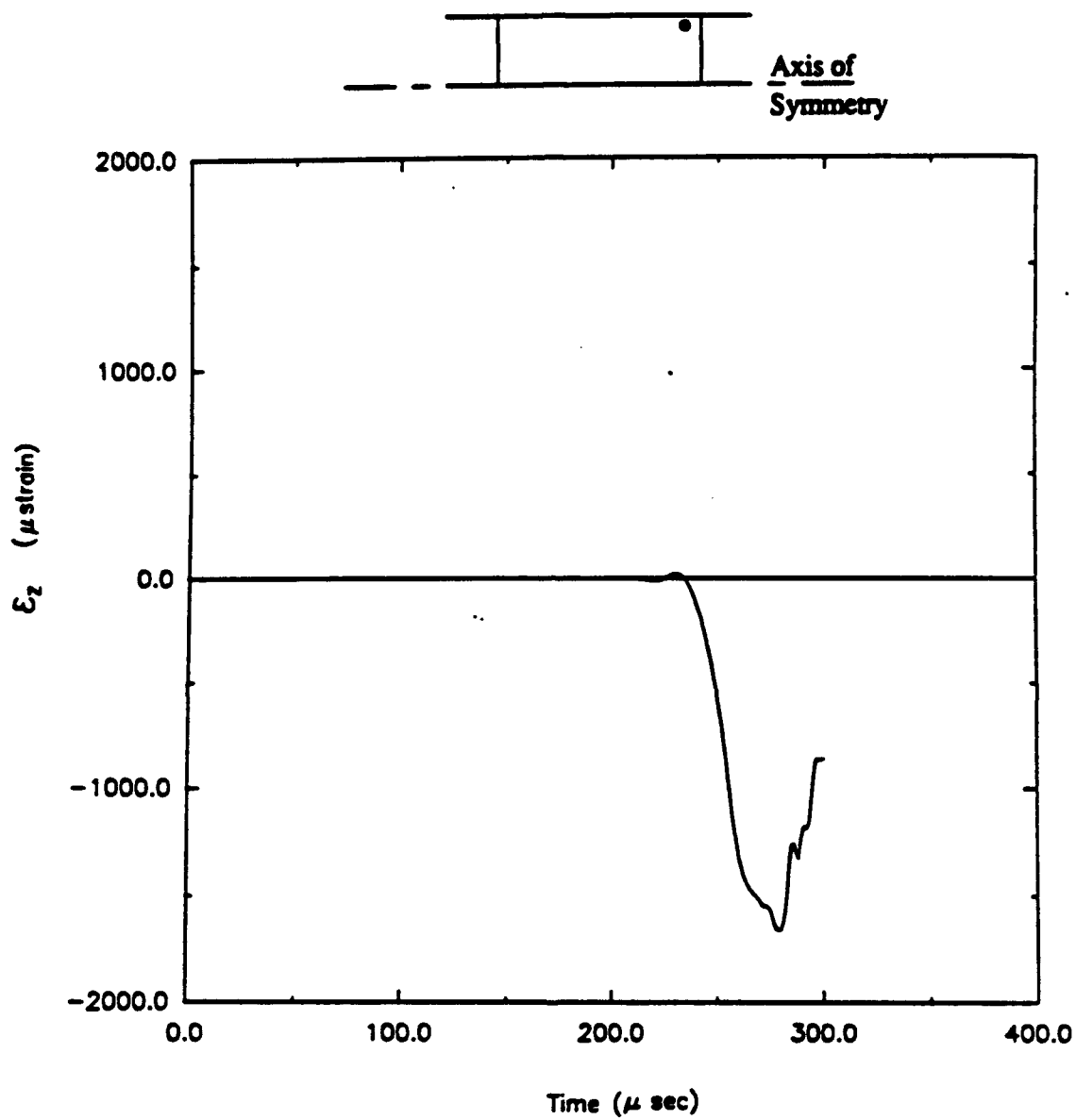


Figure 257. Time history for longitudinal strain (direct compression, Load Case 2).

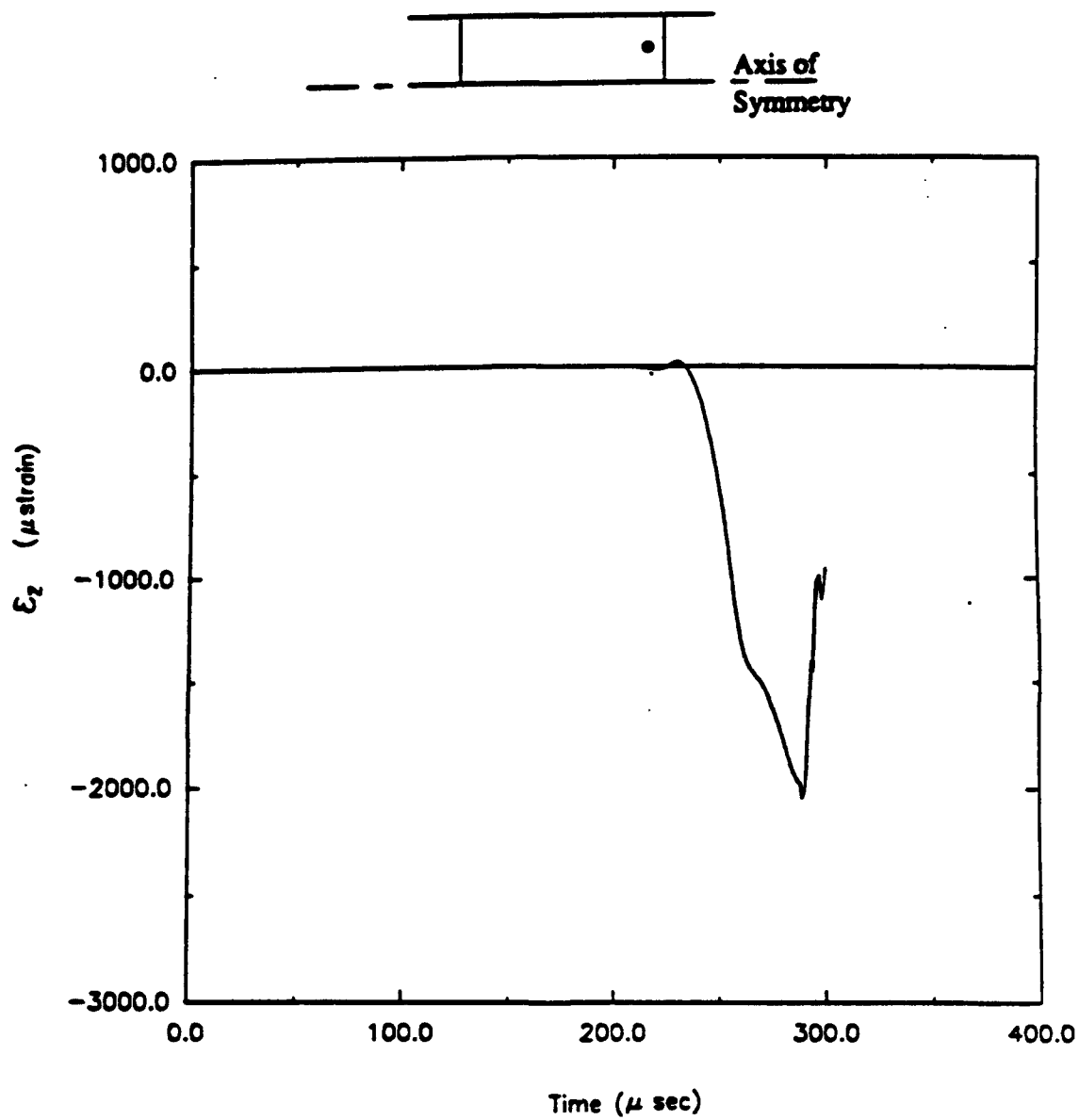


Figure 258. Time history for longitudinal strain (direct compression, Load Case 2).

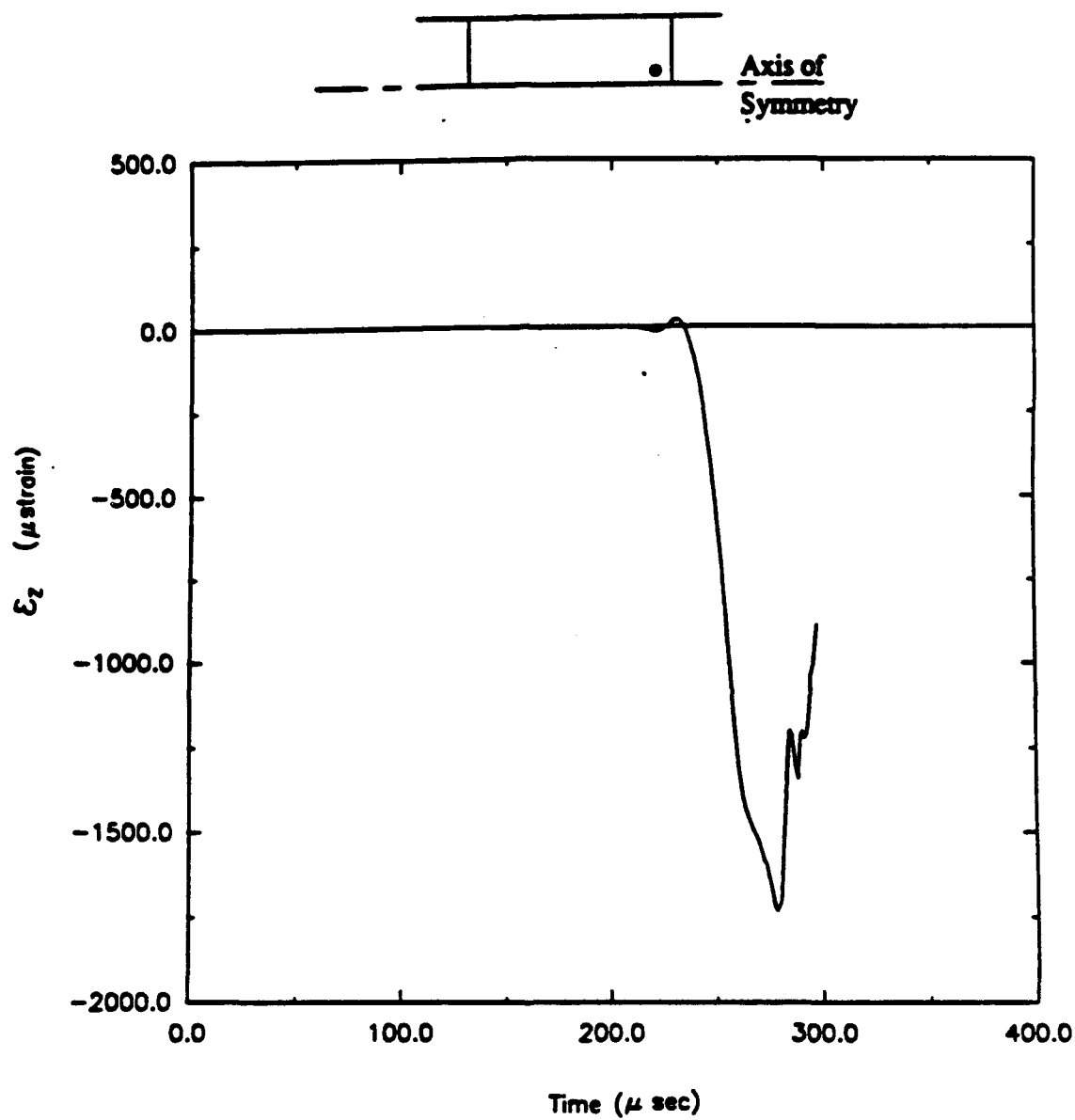


Figure 259. Time history for longitudinal strain (direct compression, Load Case 2).

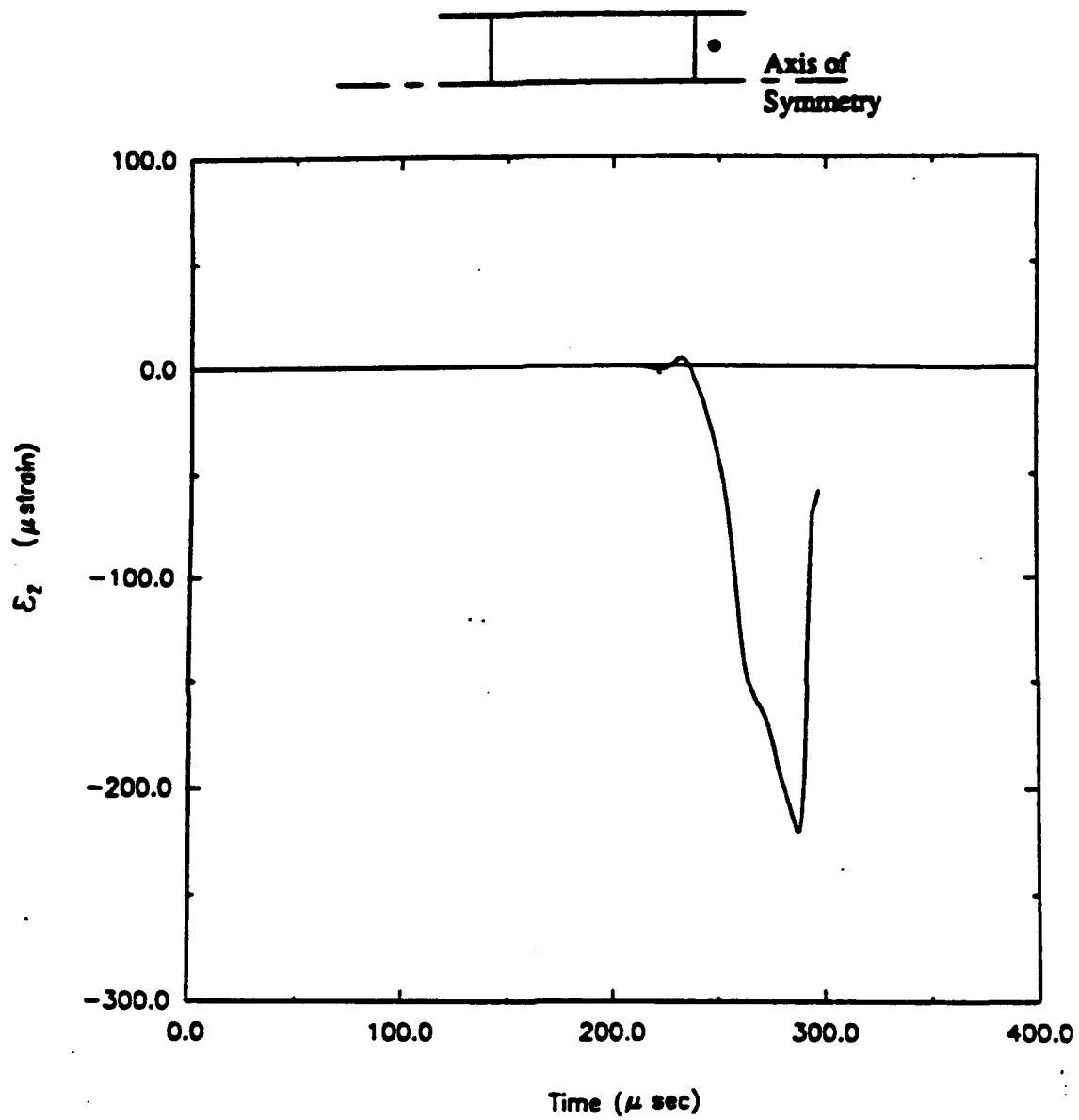


Figure 260. Time history for longitudinal strain (direct compression, Load Case 2).

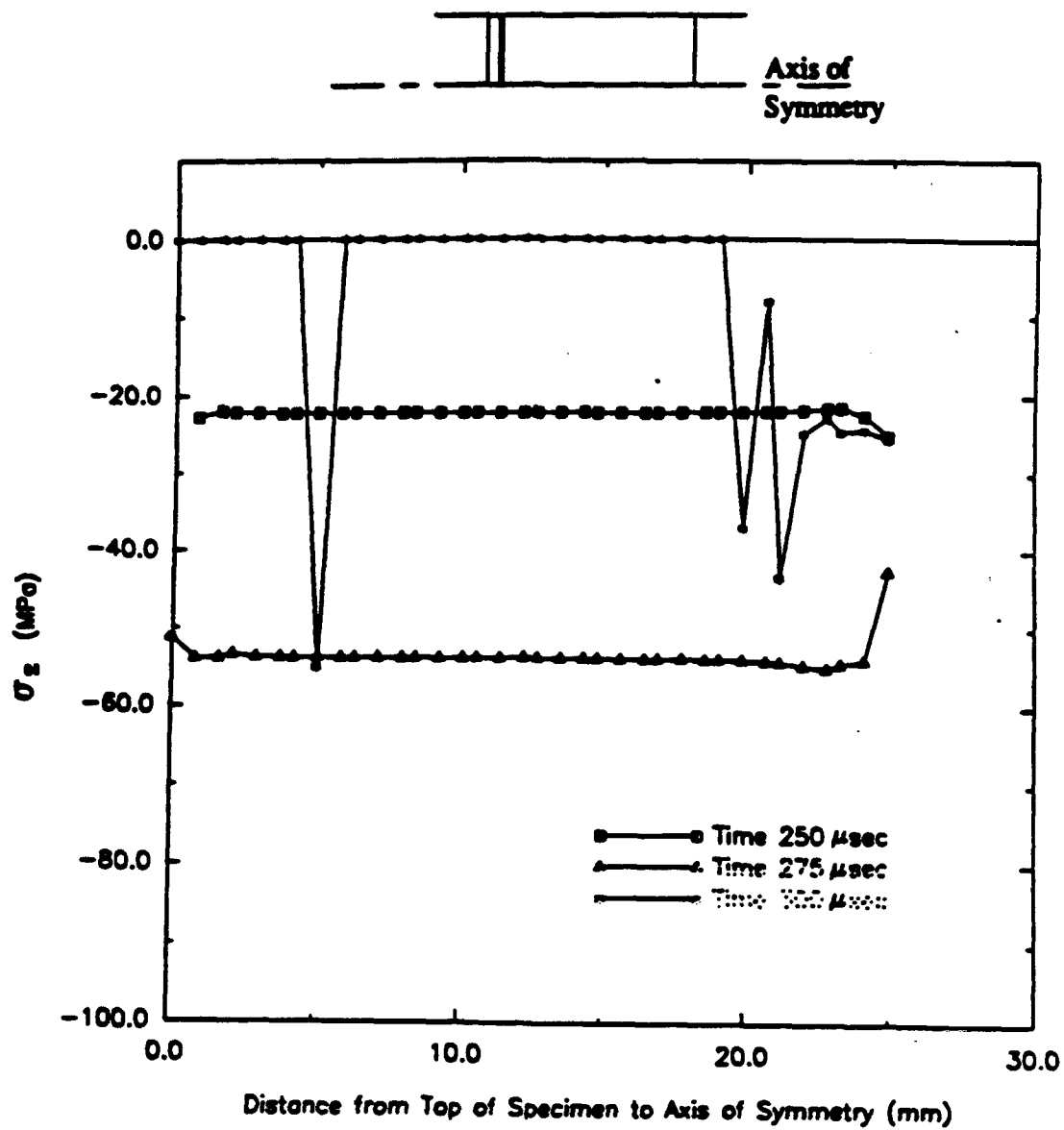


Figure 261. Profiles for longitudinal stress (direct compression, Load Case 2).

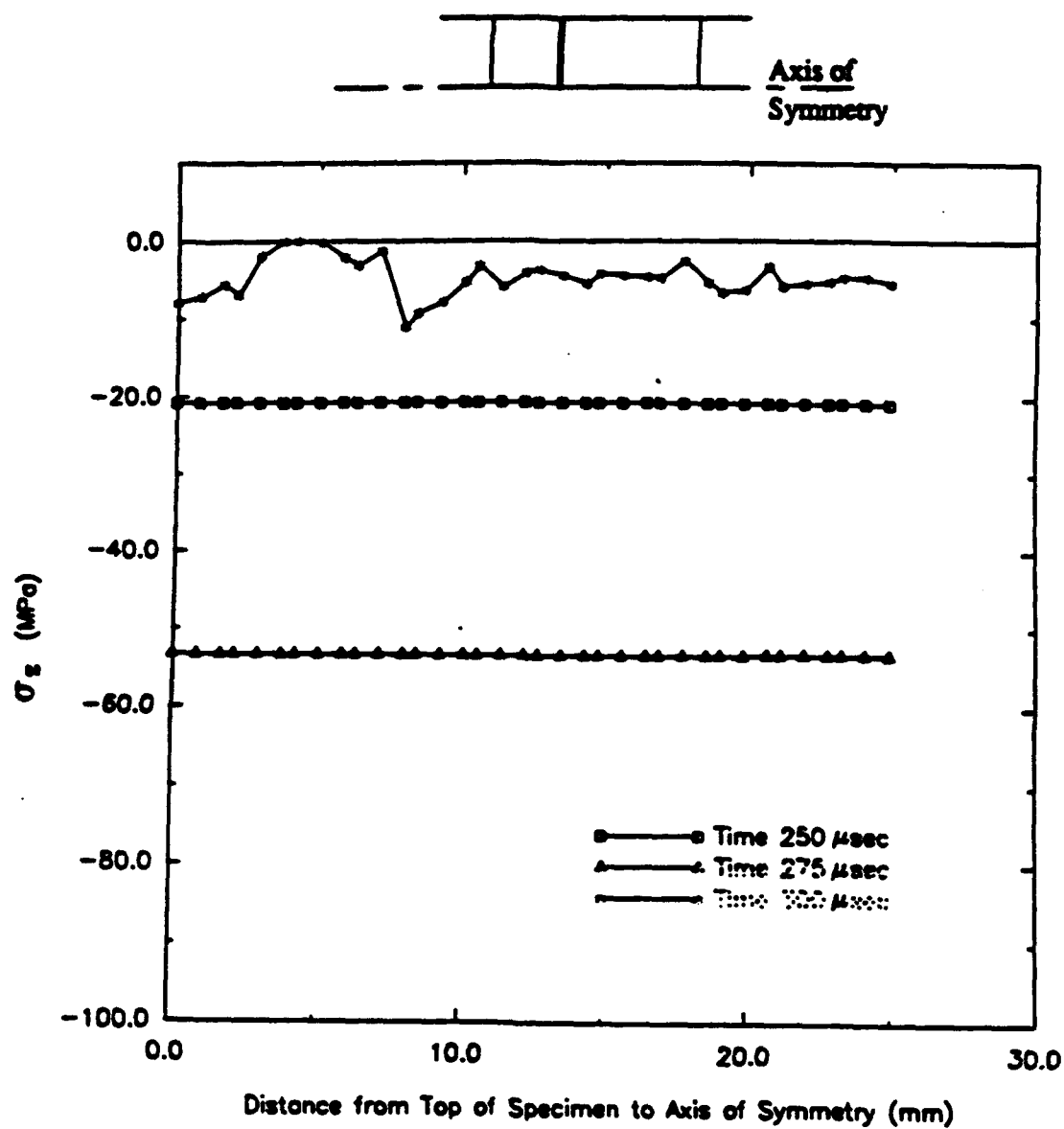


Figure 262. Profiles for longitudinal stress (direct compression, Load Case 2).

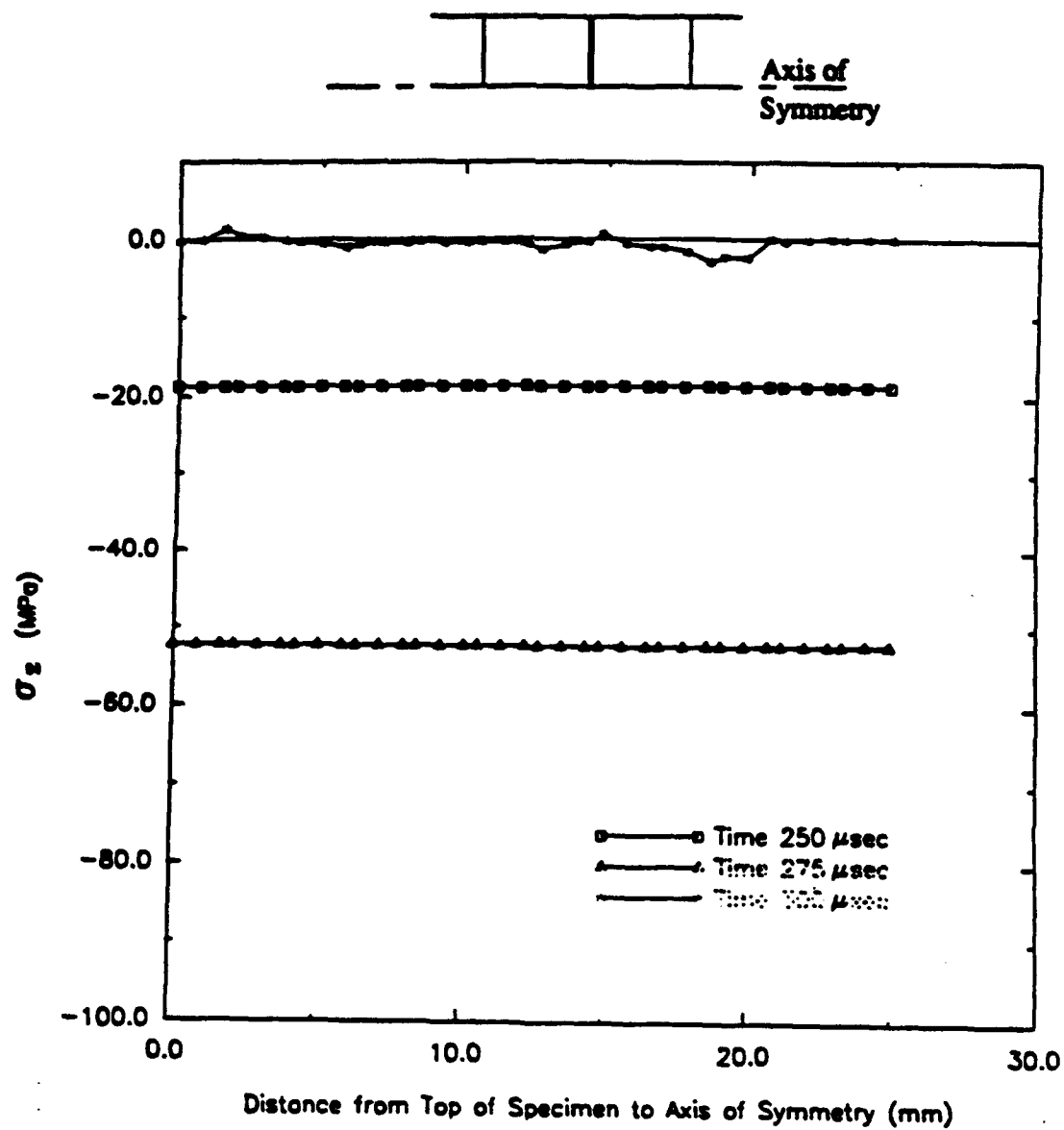


Figure 263. Profiles for longitudinal stress (direct compression, Load Case 2).

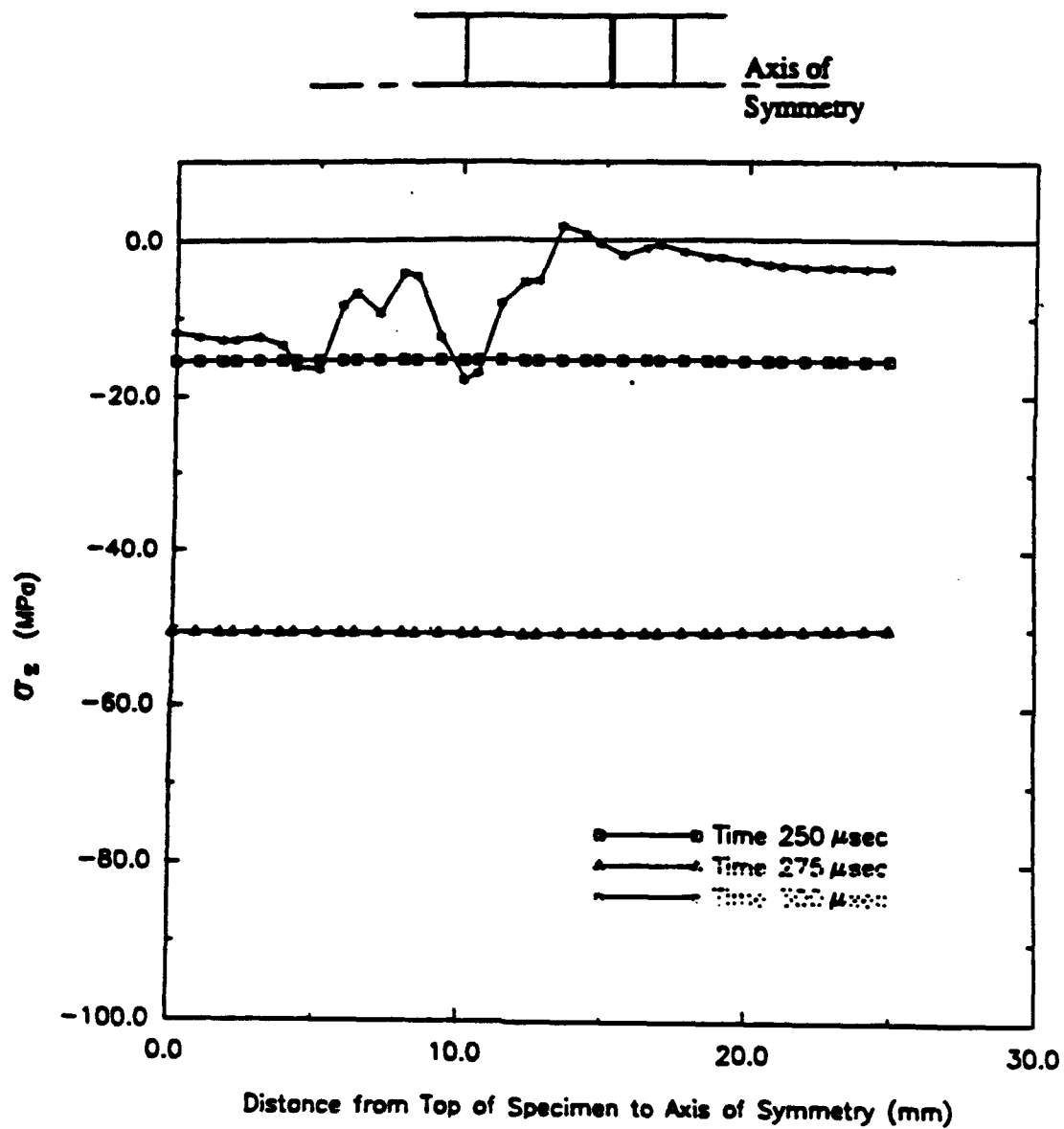


Figure 264. Profiles for longitudinal stress (direct compression, Load Case 2).

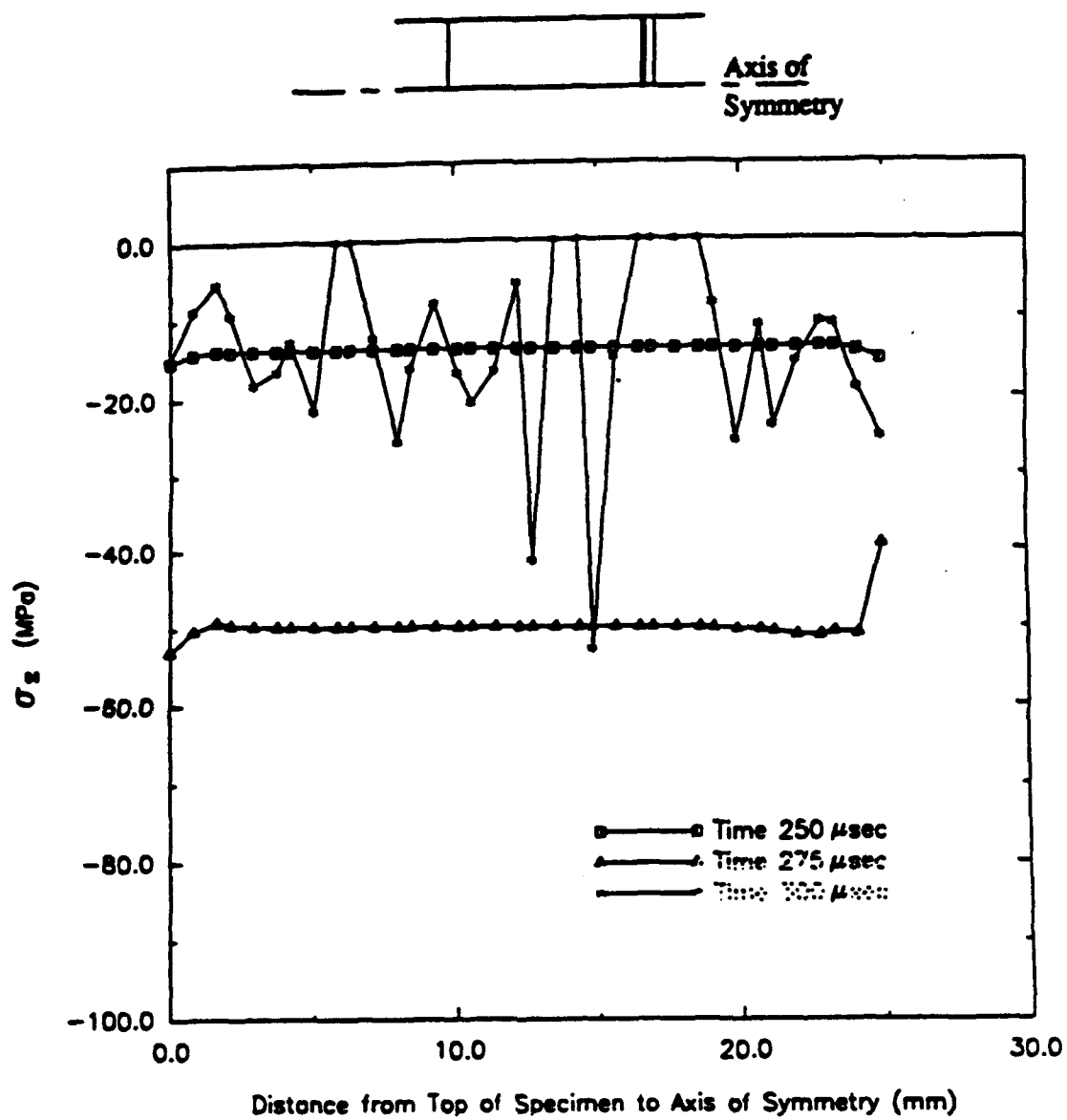


Figure 265. Profiles for longitudinal stress (direct compression, Load Case 2).

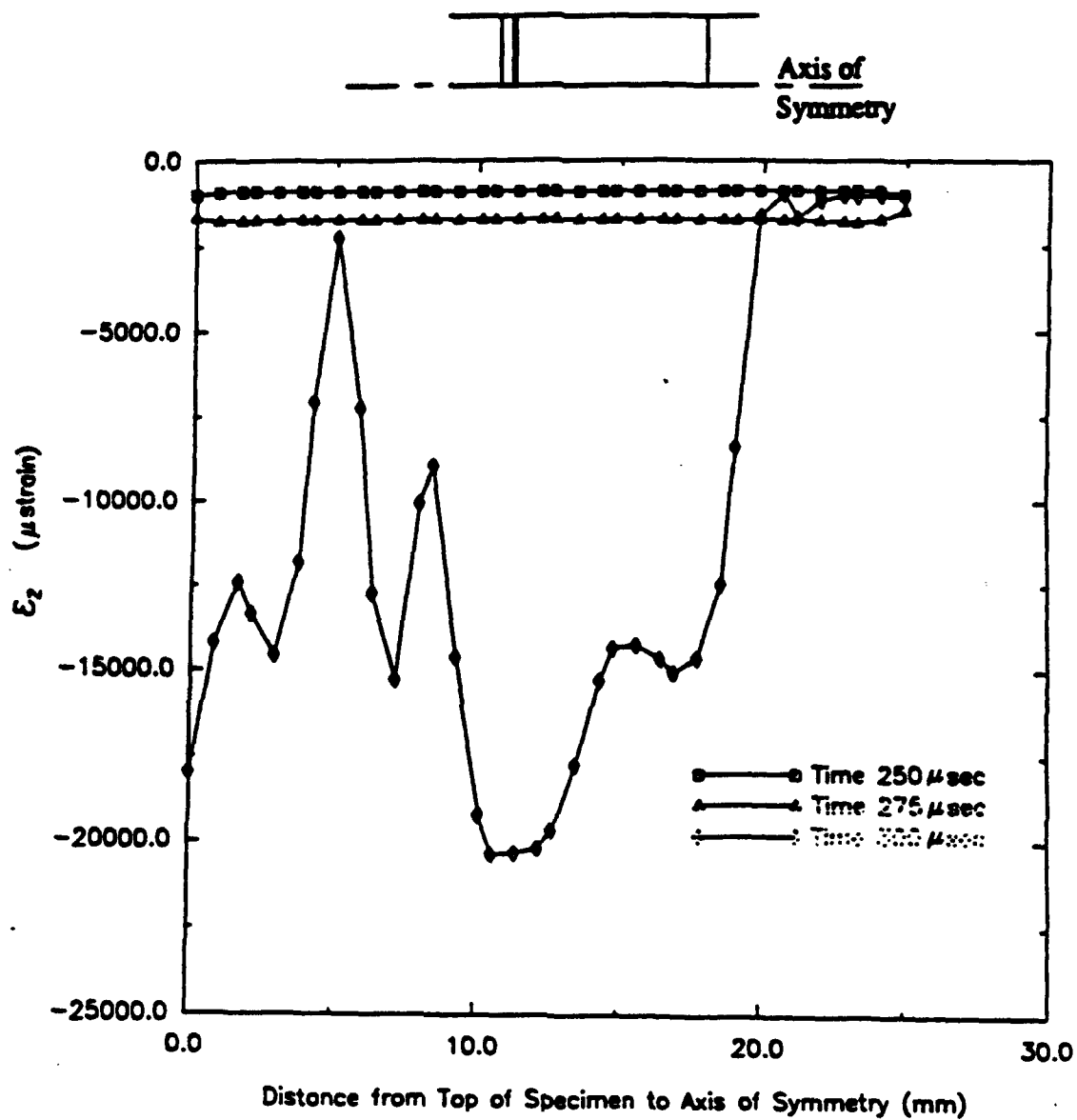


Figure 266. Profiles for longitudinal strain (direct compression, Load Case 2).

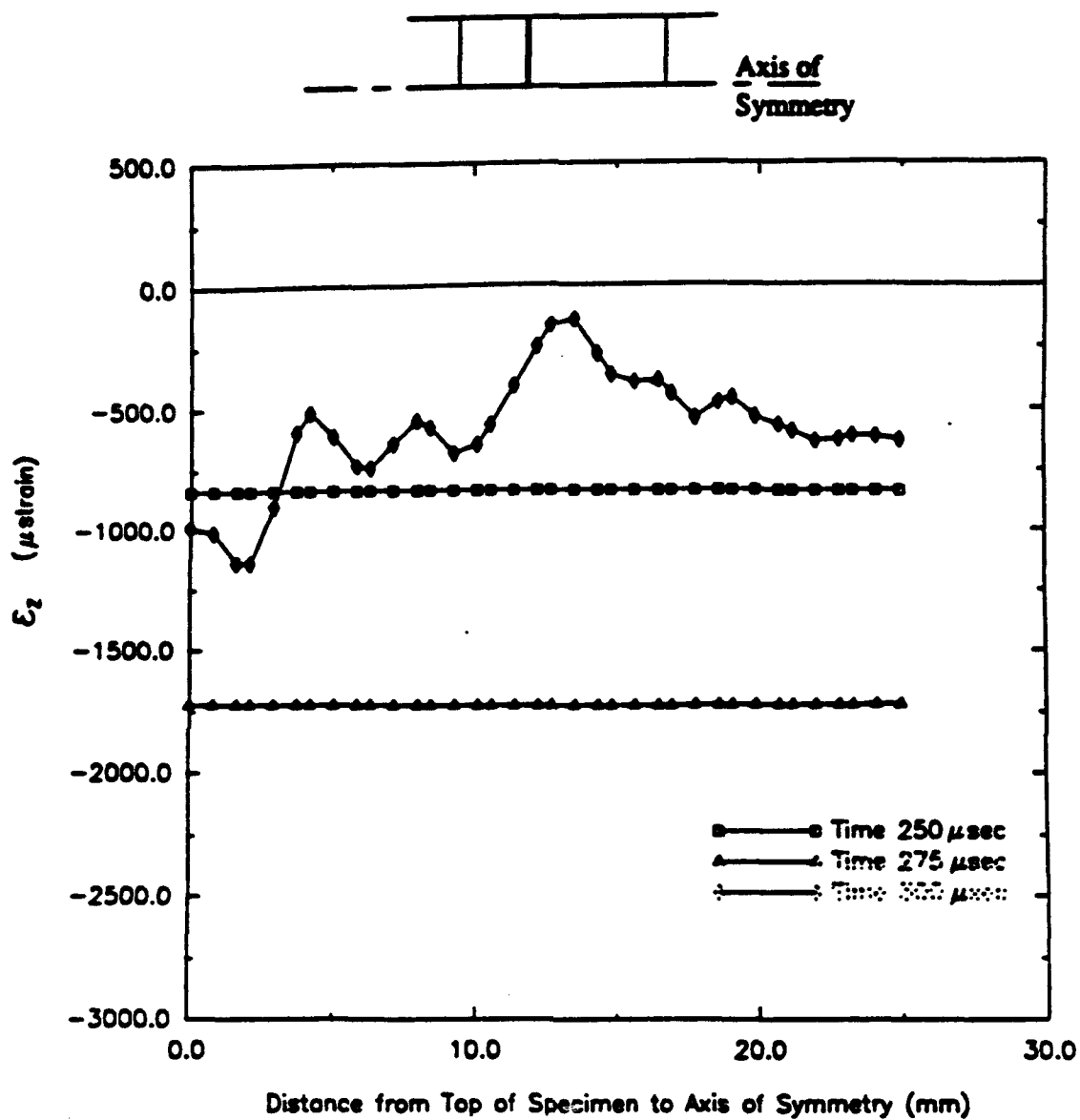


Figure 267. Profiles for longitudinal strain (direct compression, Load Case 2).

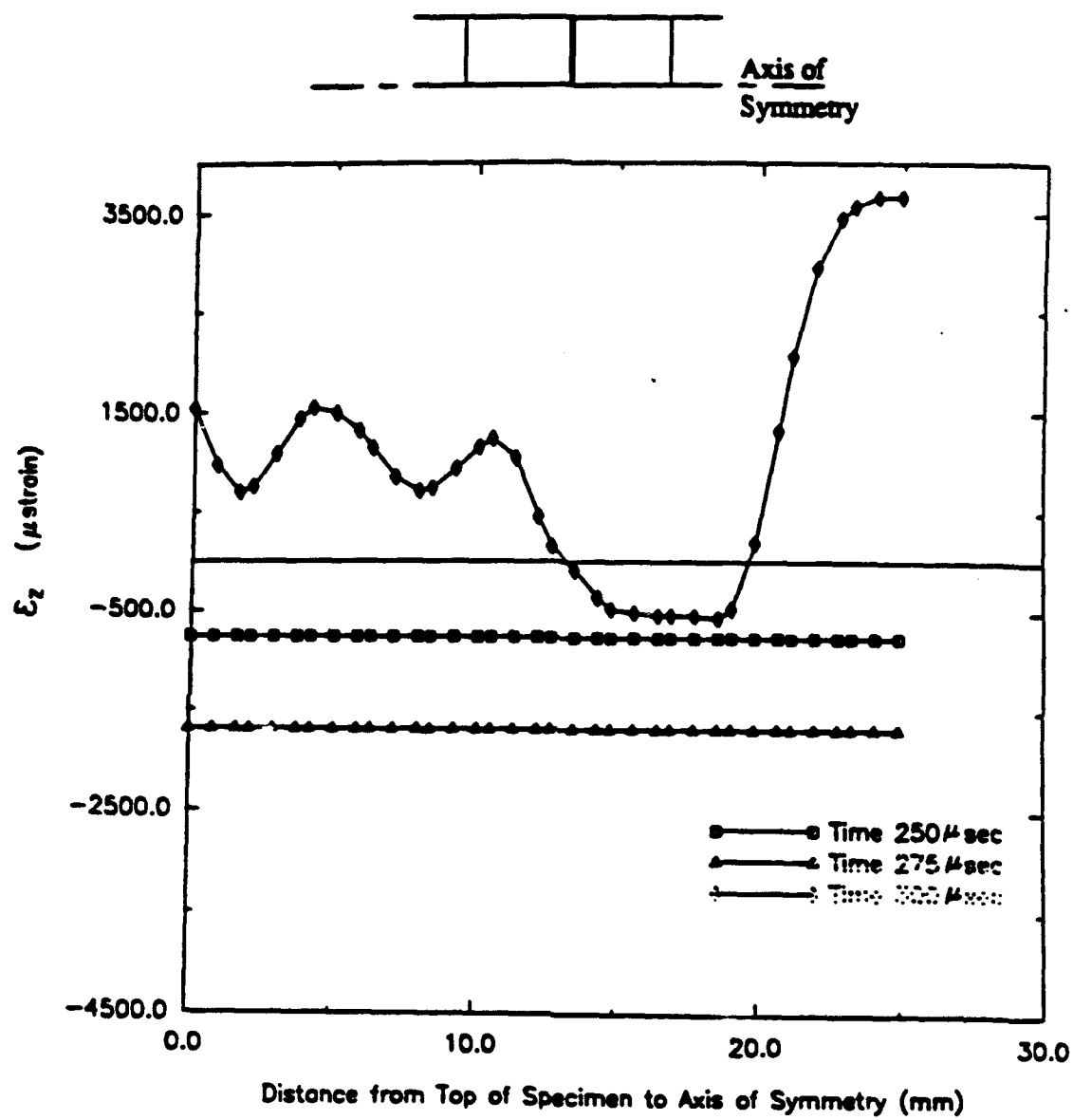


Figure 268. Profiles for longitudinal strain (direct compression, Load Case 2).

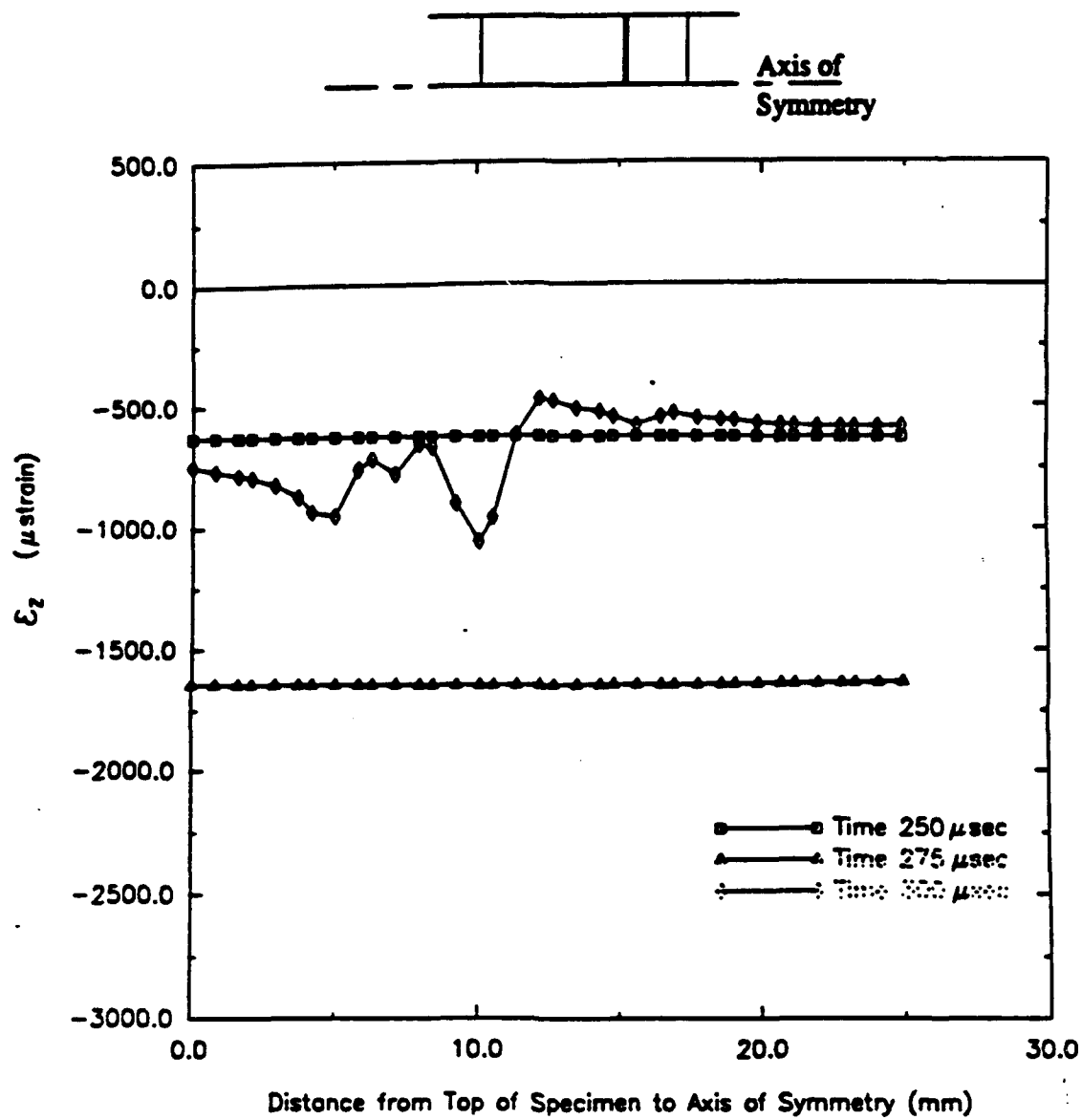


Figure 269. Profiles for longitudinal strain (direct compression, Load Case 2).

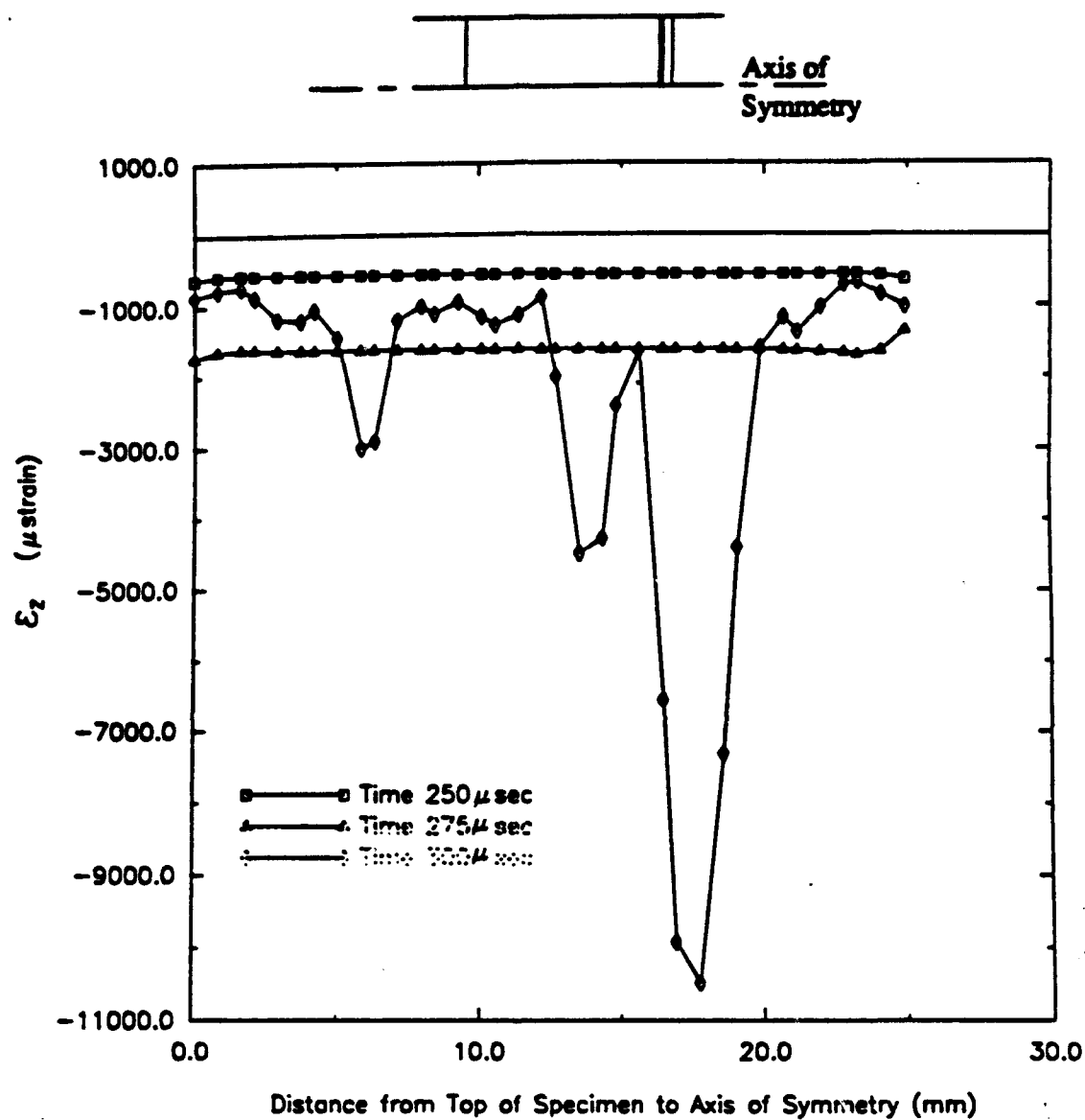
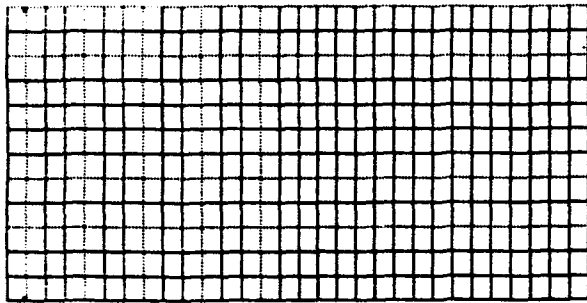
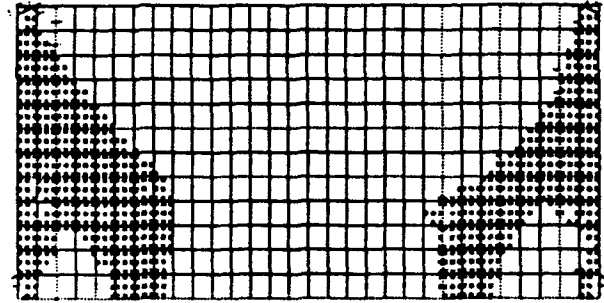


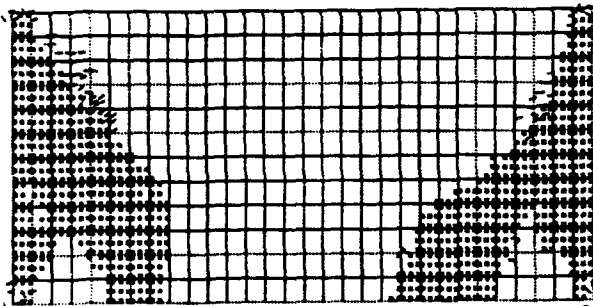
Figure 270. Profiles for longitudinal strain (direct compression, Load Case 2).



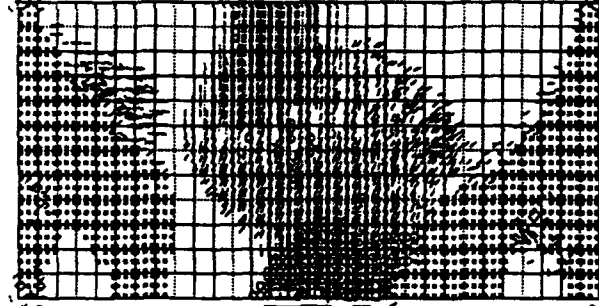
(a)



(b)



(c)



(d)

Figure 271. Cracking sequence for direct compression specimen; Load Case 2:
a) $t=265 \mu\text{sec}$, b) $t=289 \mu\text{sec}$, c) $t=292 \mu\text{sec}$, d) $t=300 \mu\text{sec}$.

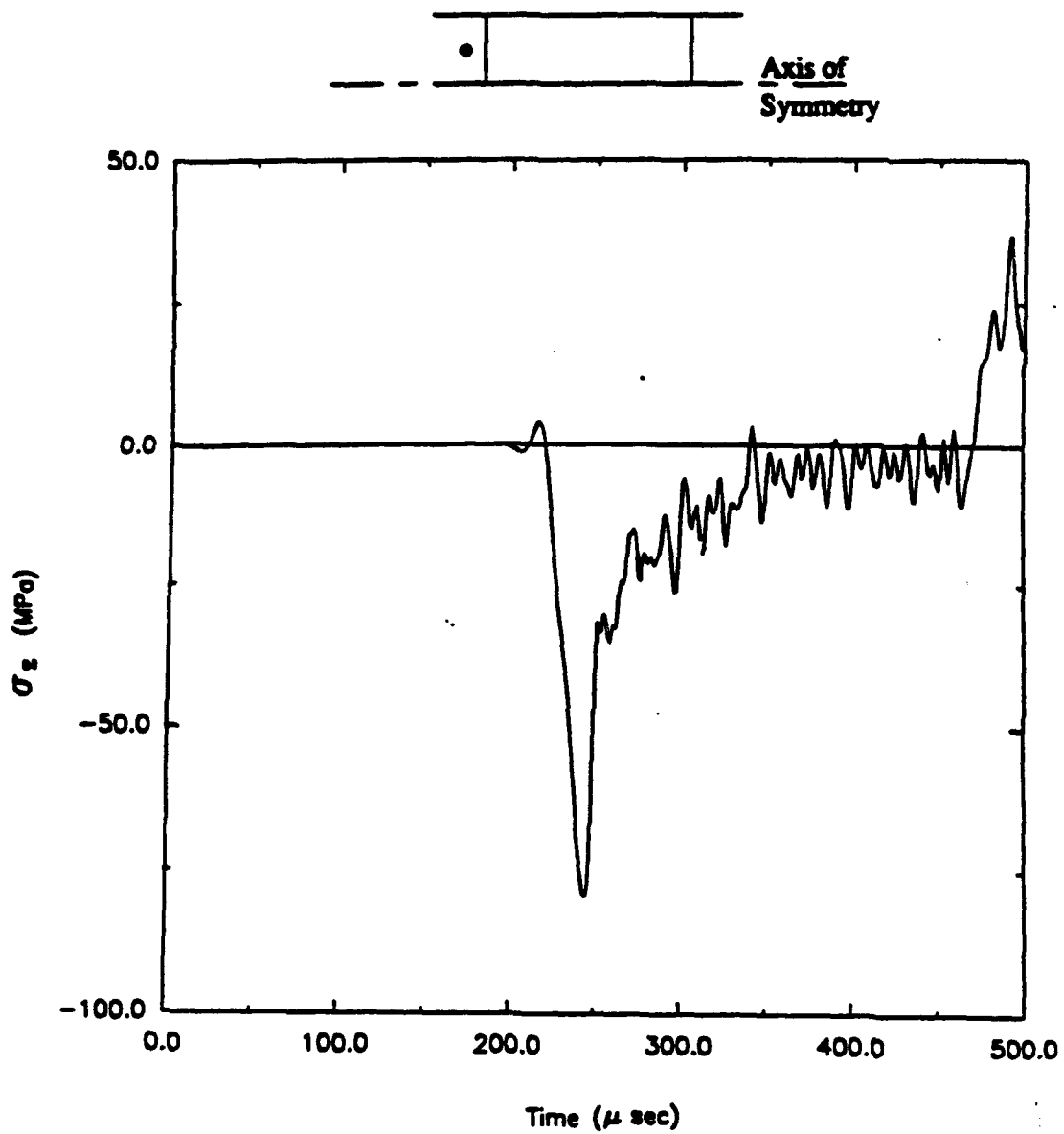


Figure 272. Time history for longitudinal stress (direct compression, Load Case 3).

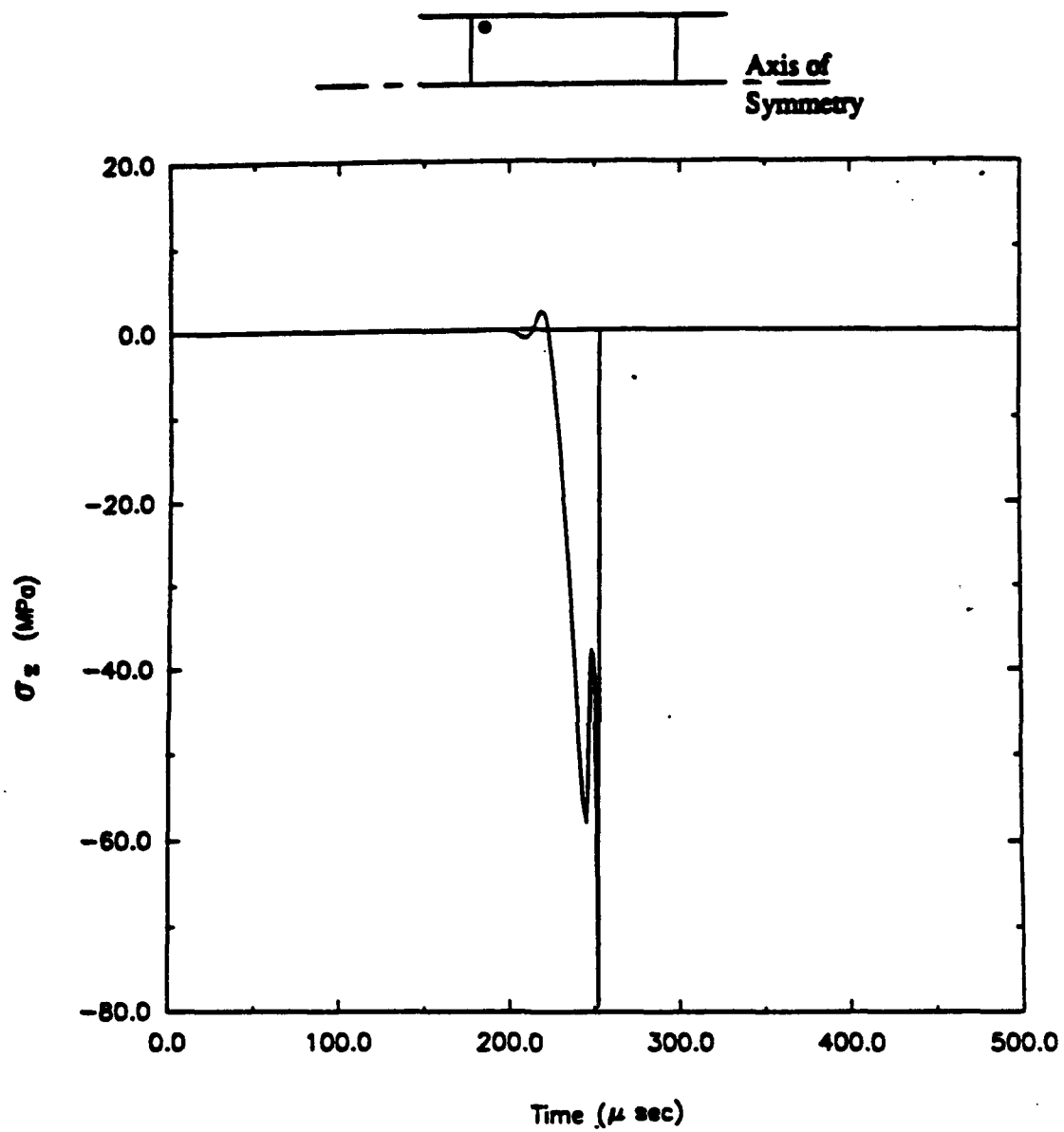


Figure 273. Time history for longitudinal stress (direct compression, Load Case 3).

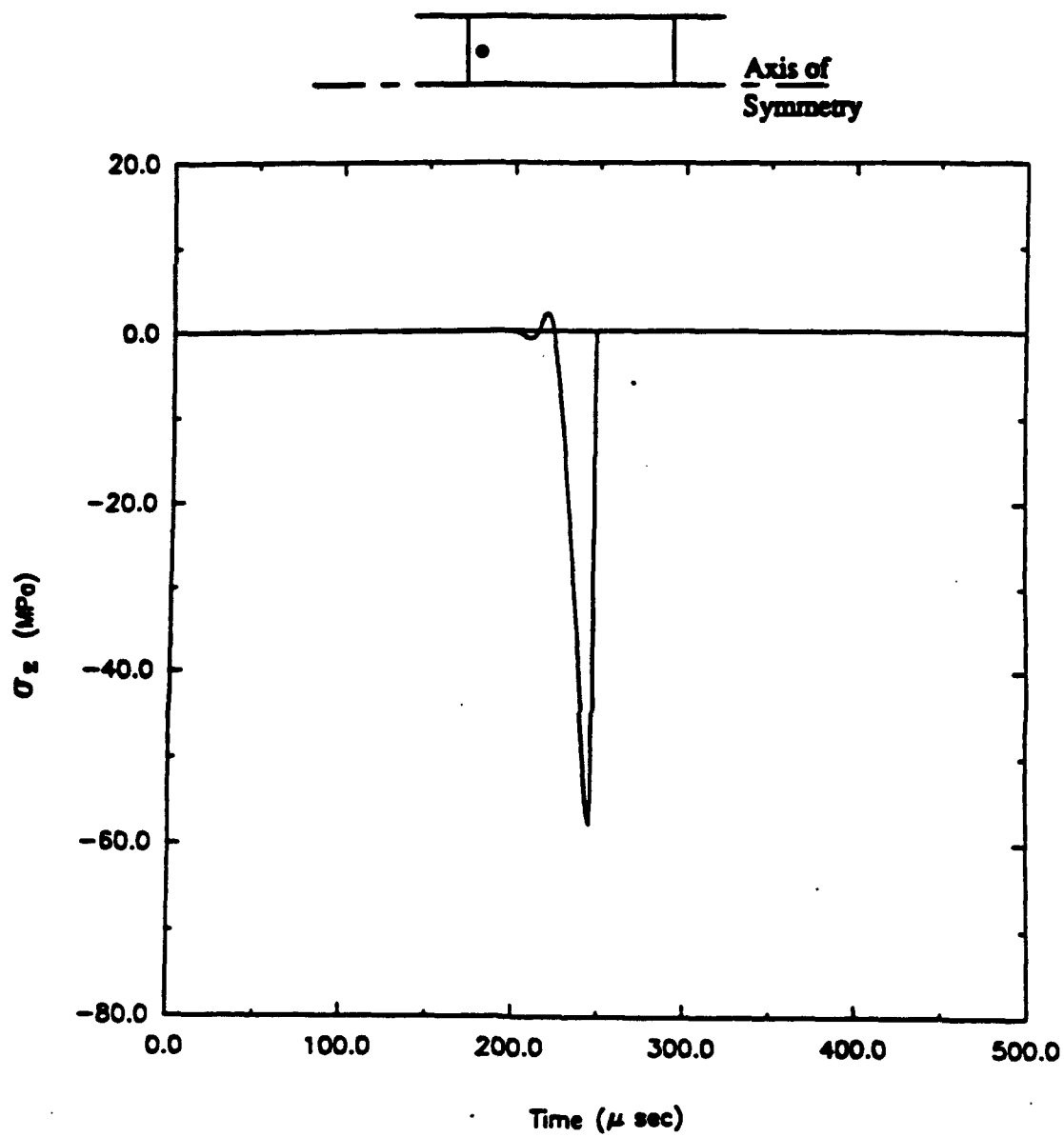


Figure 274. Time history for longitudinal stress (direct compression, Load Case 3).

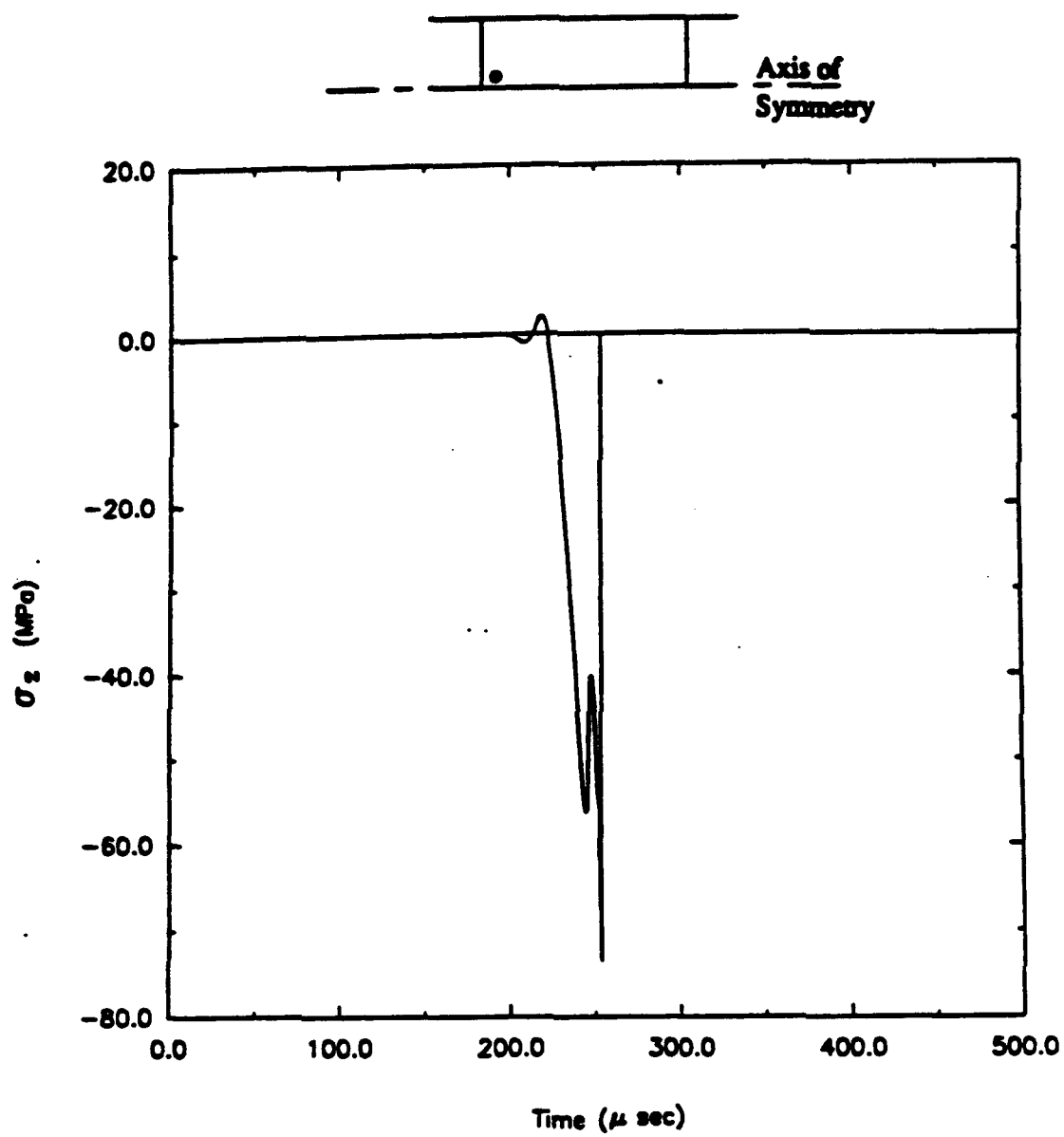


Figure 275. Time history for longitudinal stress (direct compression, Load Case 3).

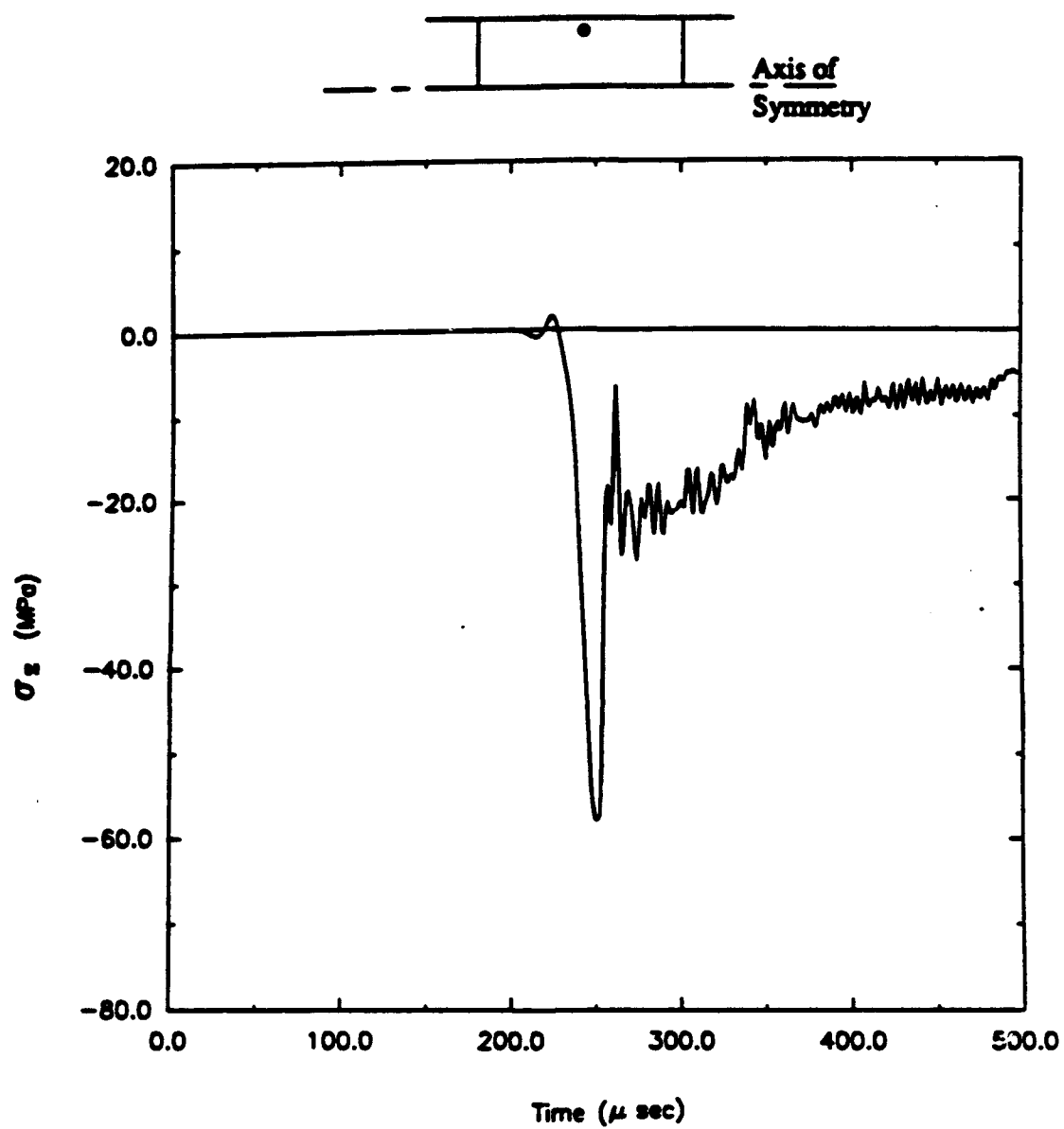


Figure 276. Time history for longitudinal stress (direct compression, Load Case 3).

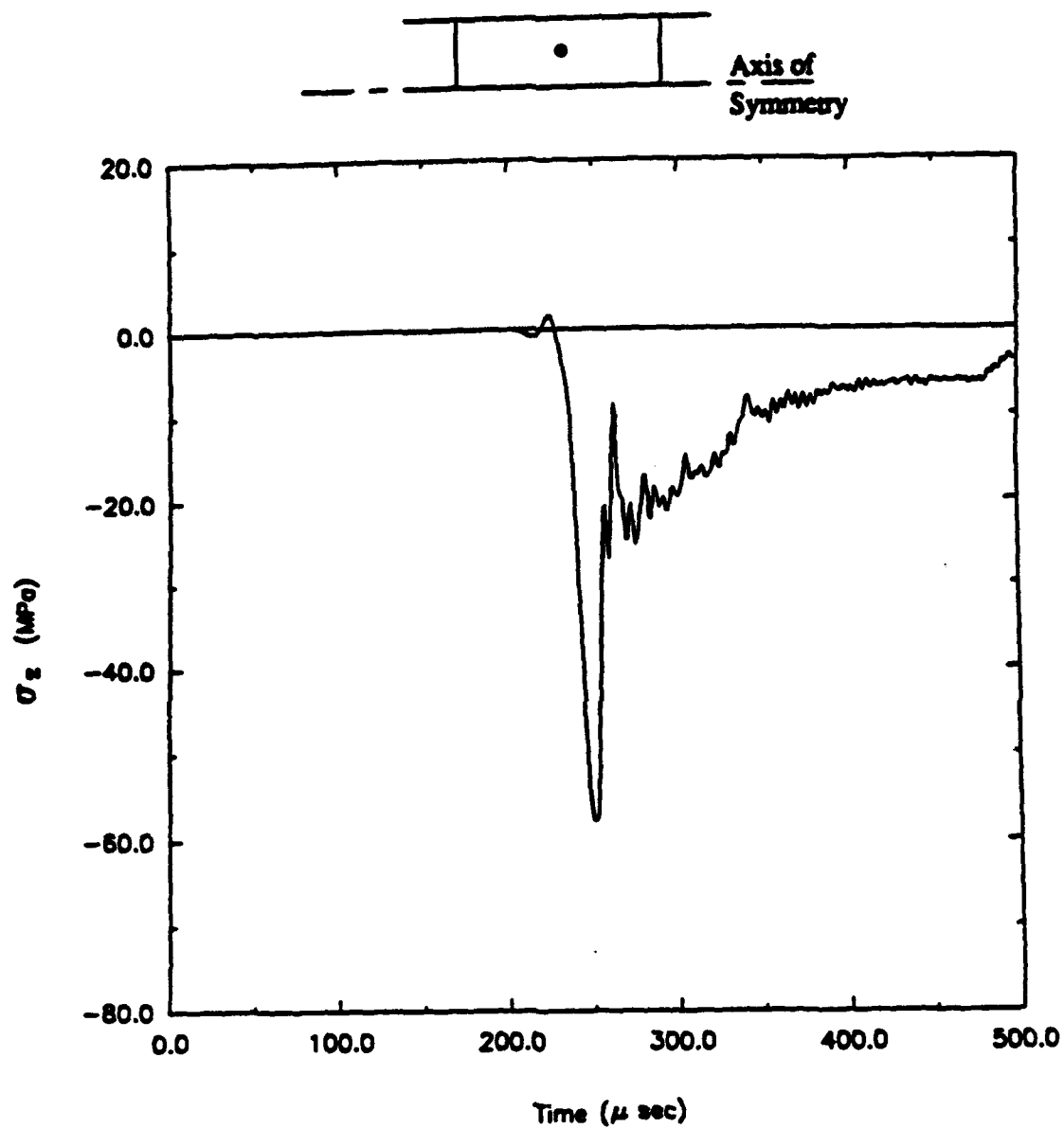


Figure 277. Time history for longitudinal stress (direct compression, Load Case 3).

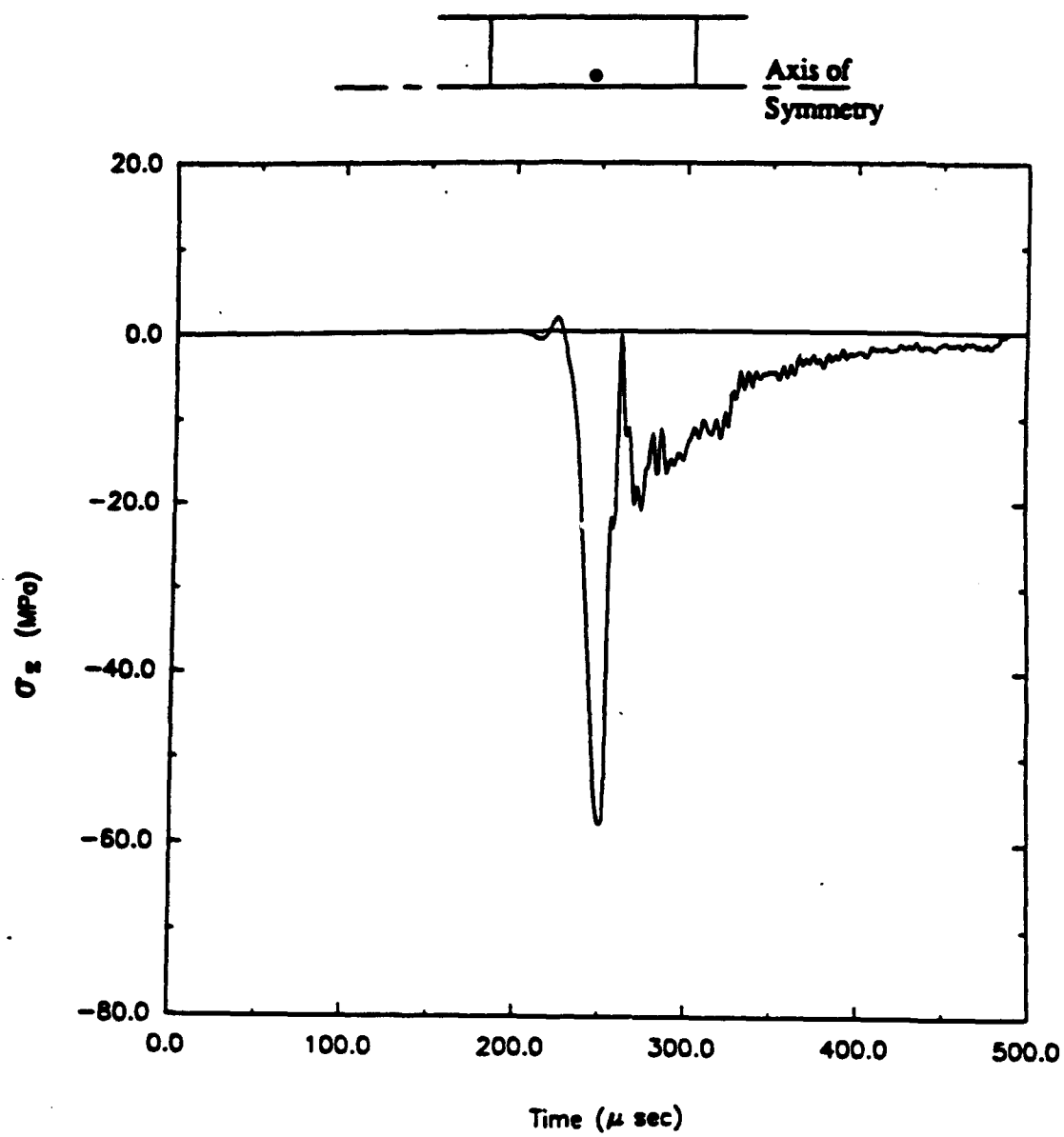


Figure 278. Time history for longitudinal stress (direct compression, Load Case 3).

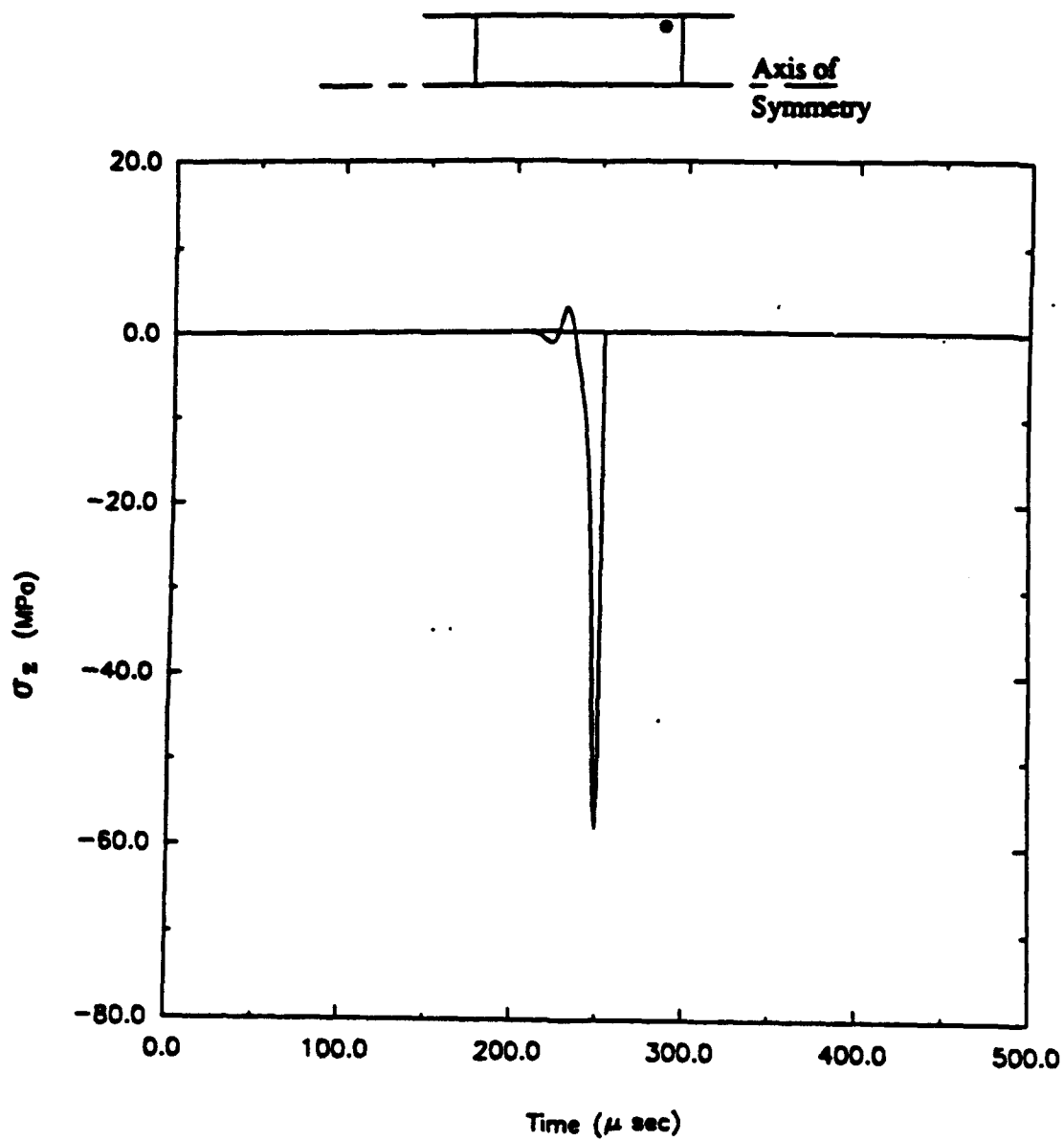


Figure 279. Time history for longitudinal stress (direct compression, Load Case 3).

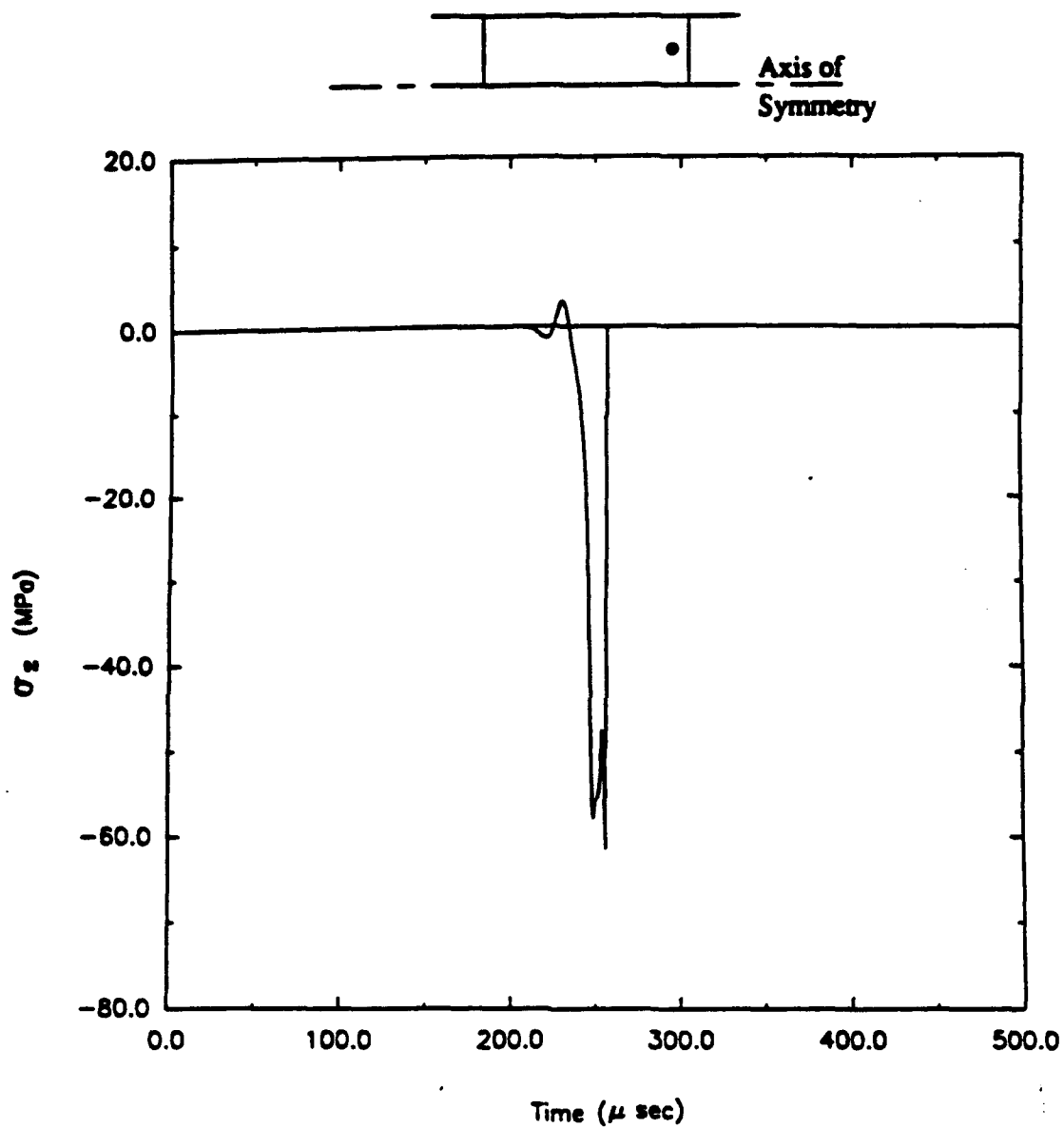


Figure 280. Time history for longitudinal stress (direct compression, Load Case 3).

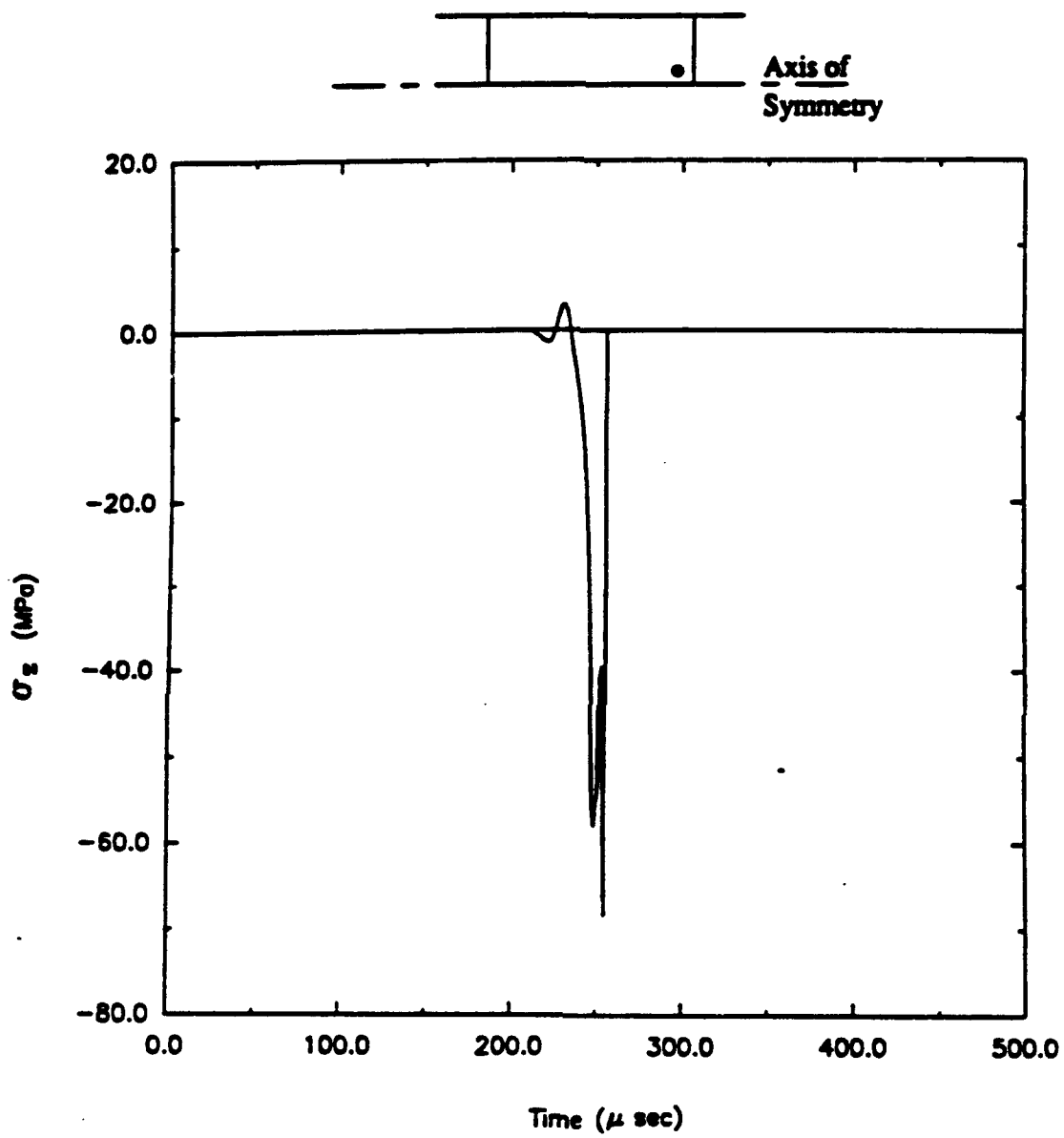


Figure 281. Time history for longitudinal stress (direct compression, Load Case 3).

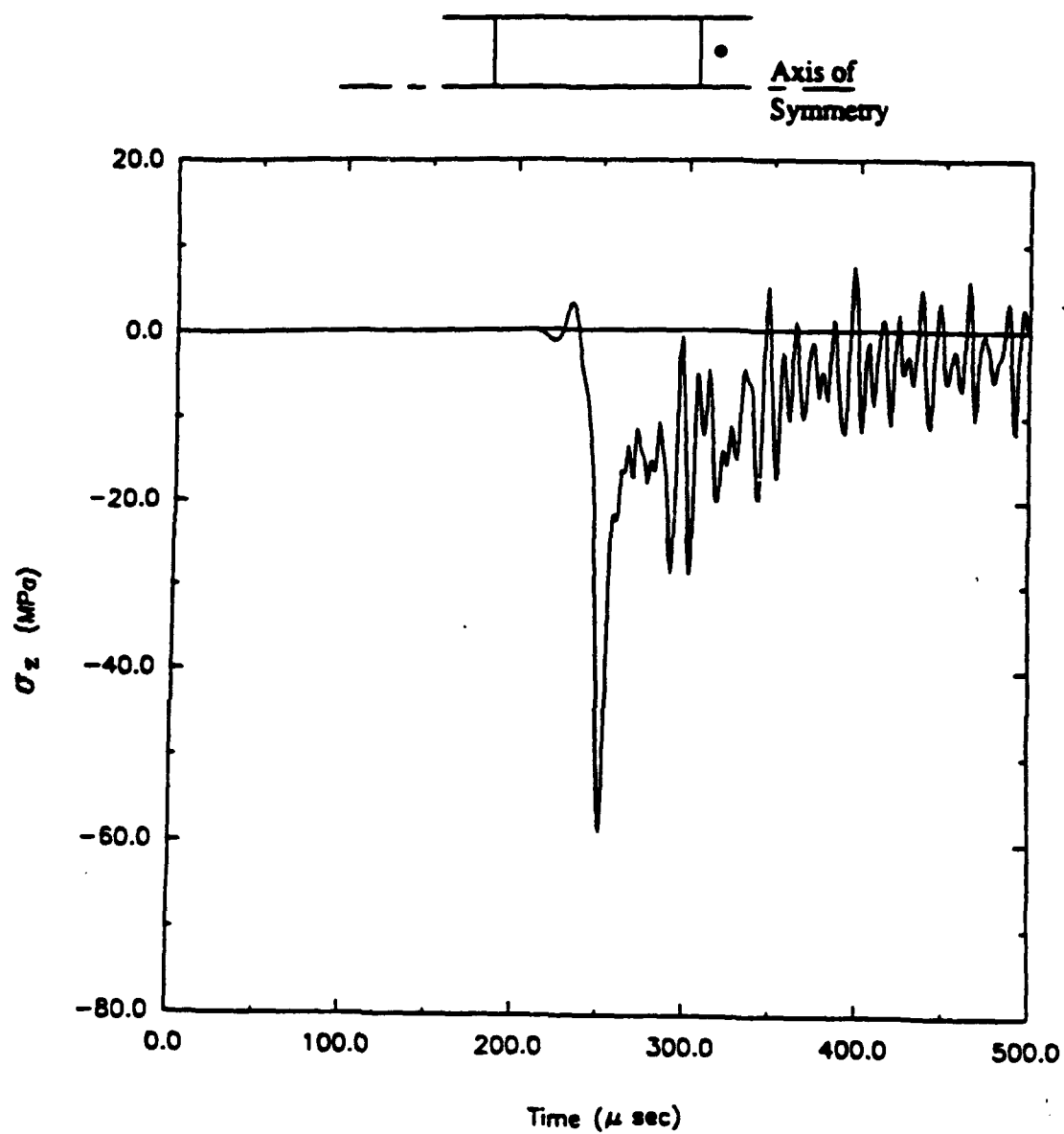


Figure 282. Time history for longitudinal stress (direct compression, Load Case 3).

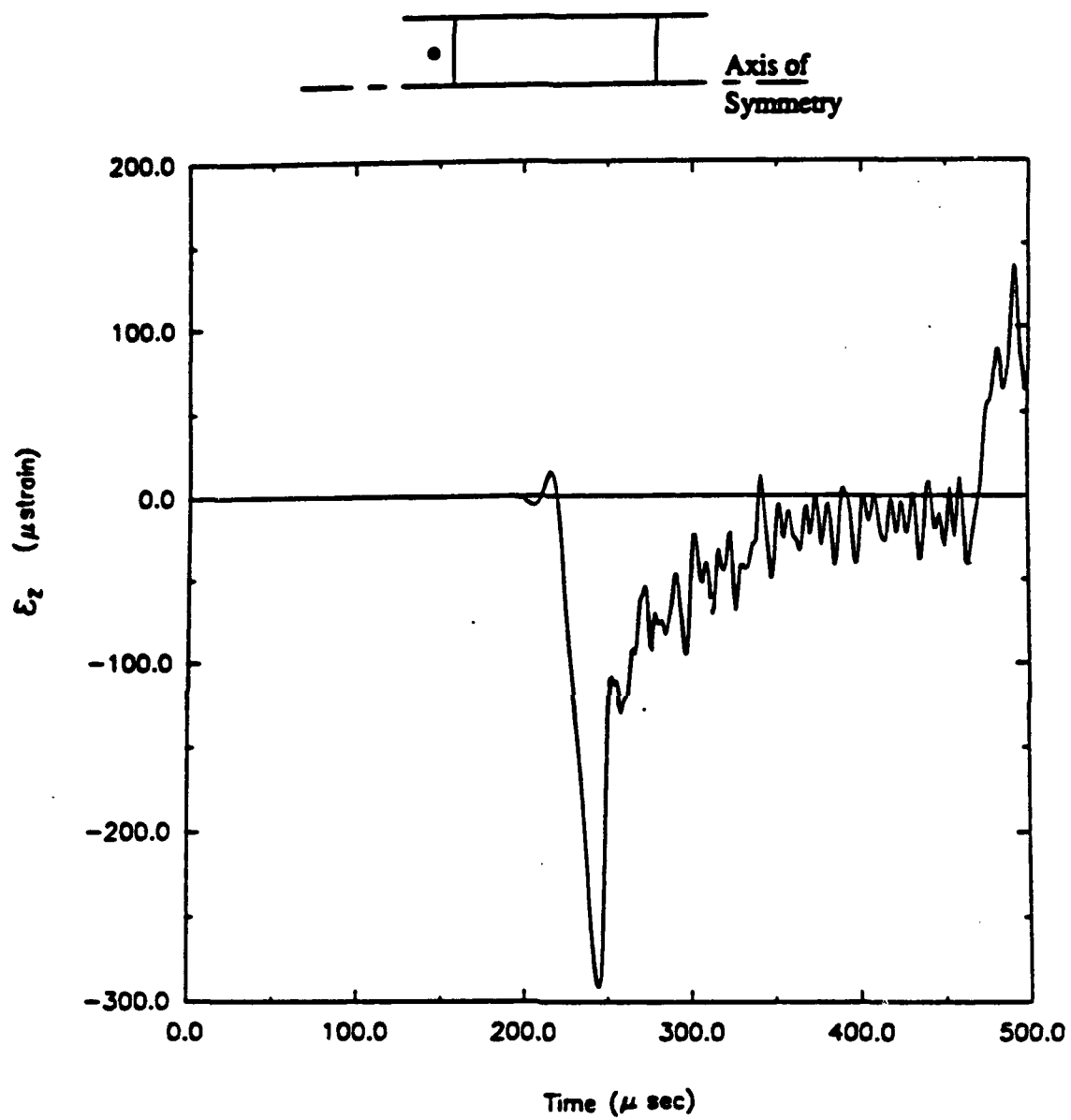


Figure 283. Time history for longitudinal strain (direct compression, Load Case 3).

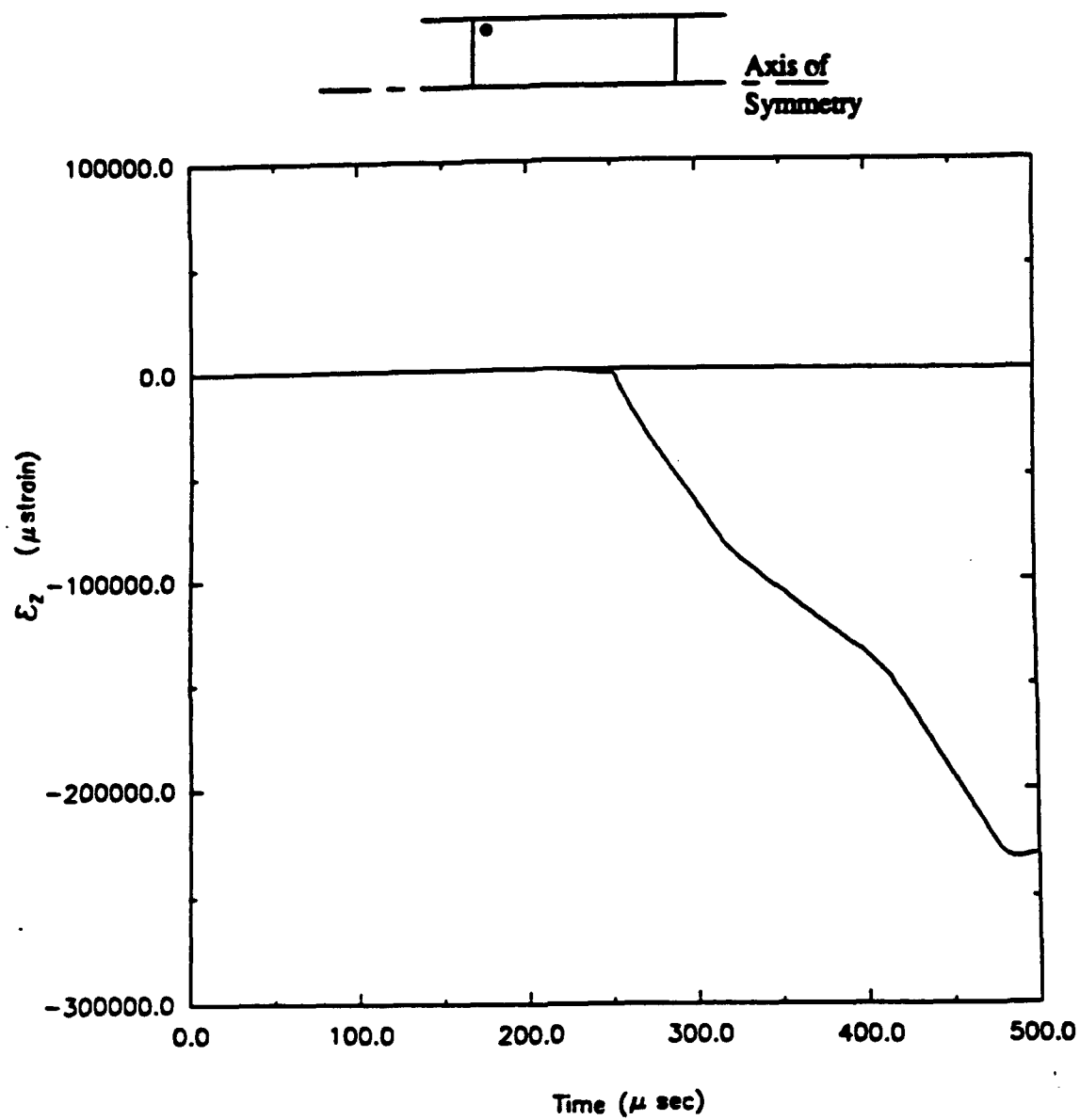


Figure 284. Time history for longitudinal strain (direct compression, Load Case 3).

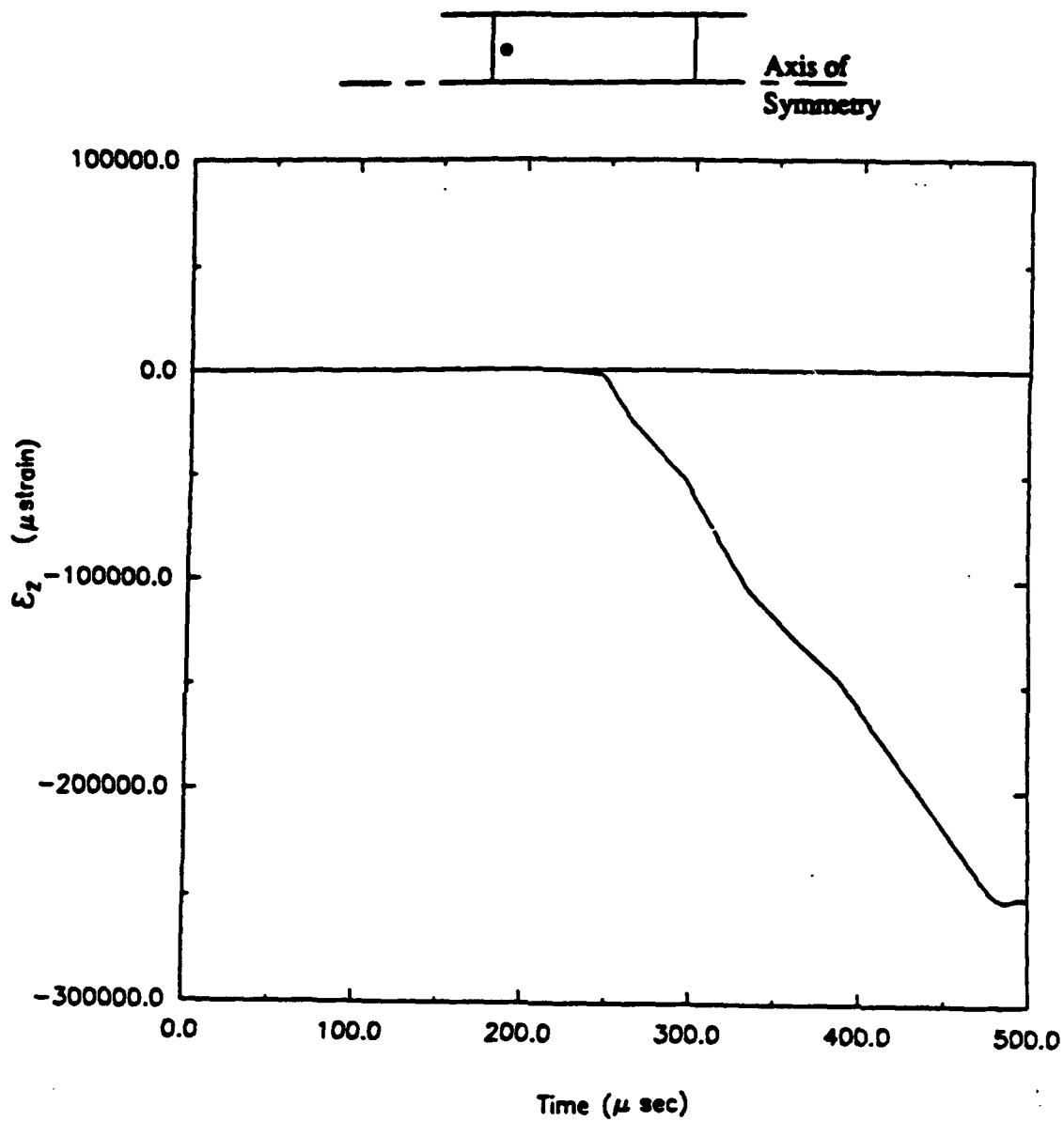


Figure 285. Time history for longitudinal strain (direct compression, Load Case 3).

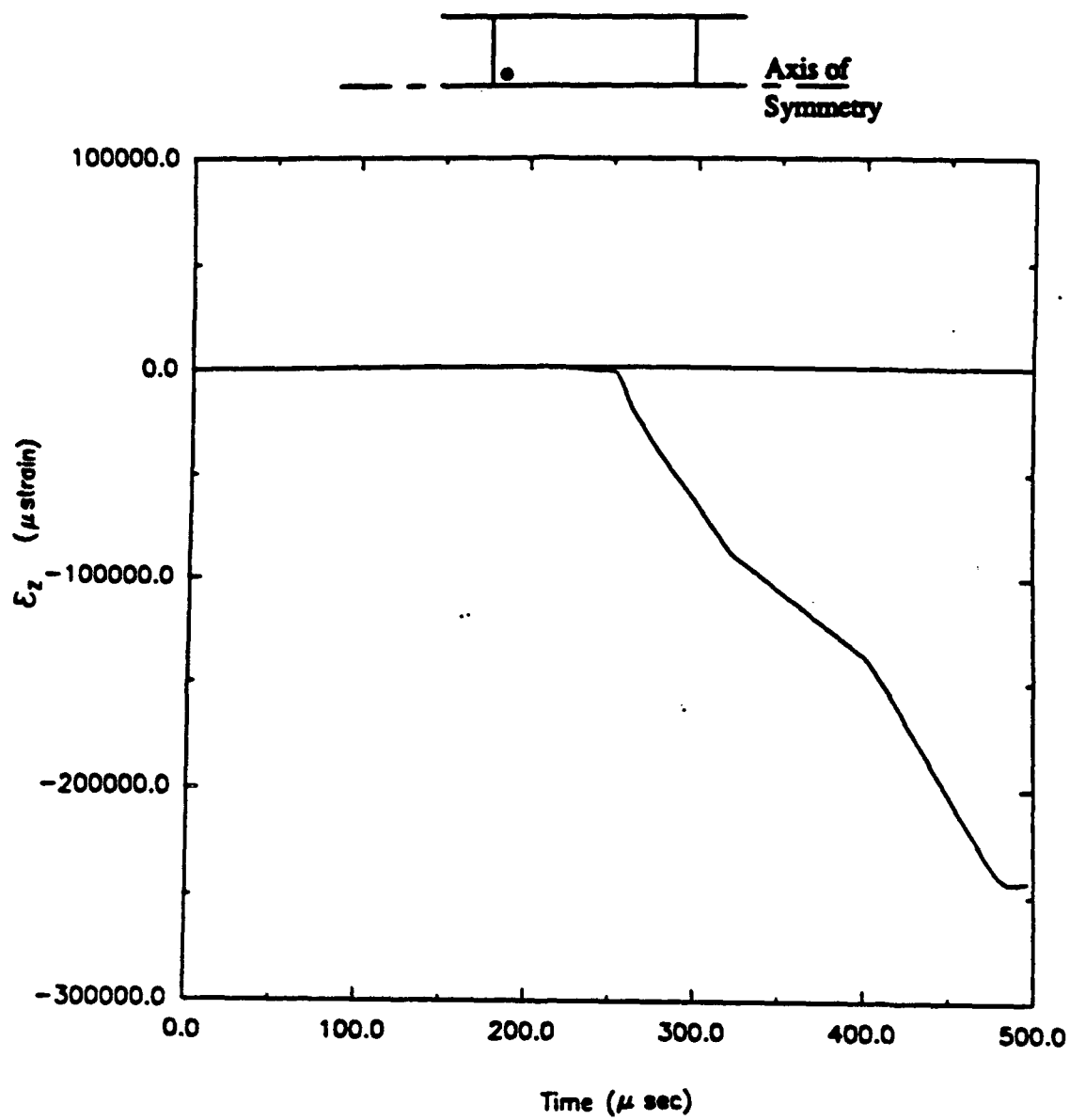


Figure 286. Time history for longitudinal strain (direct compression, Load Case 3).

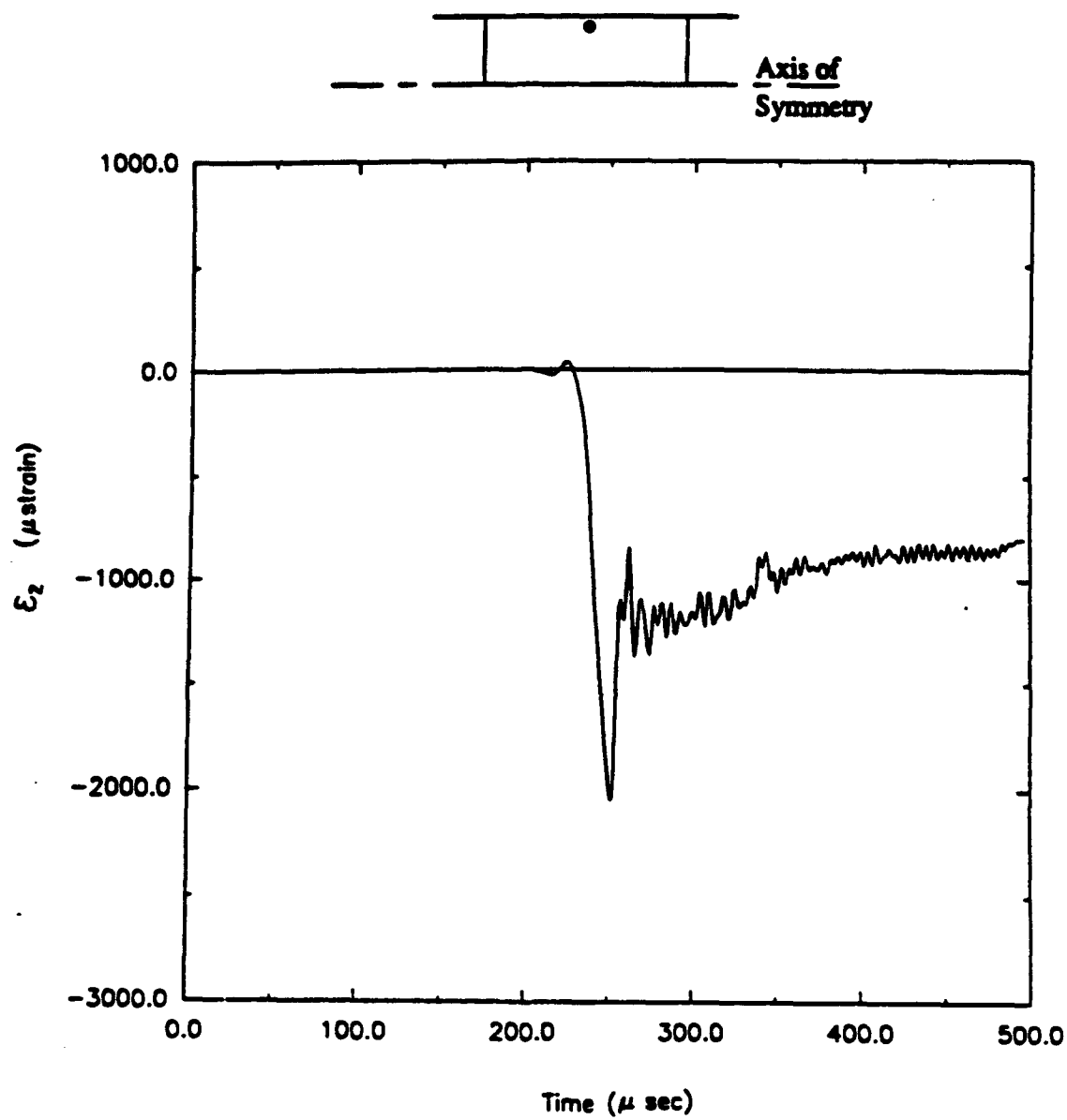


Figure 287. Time history for longitudinal strain (direct compression, Load Case 3).

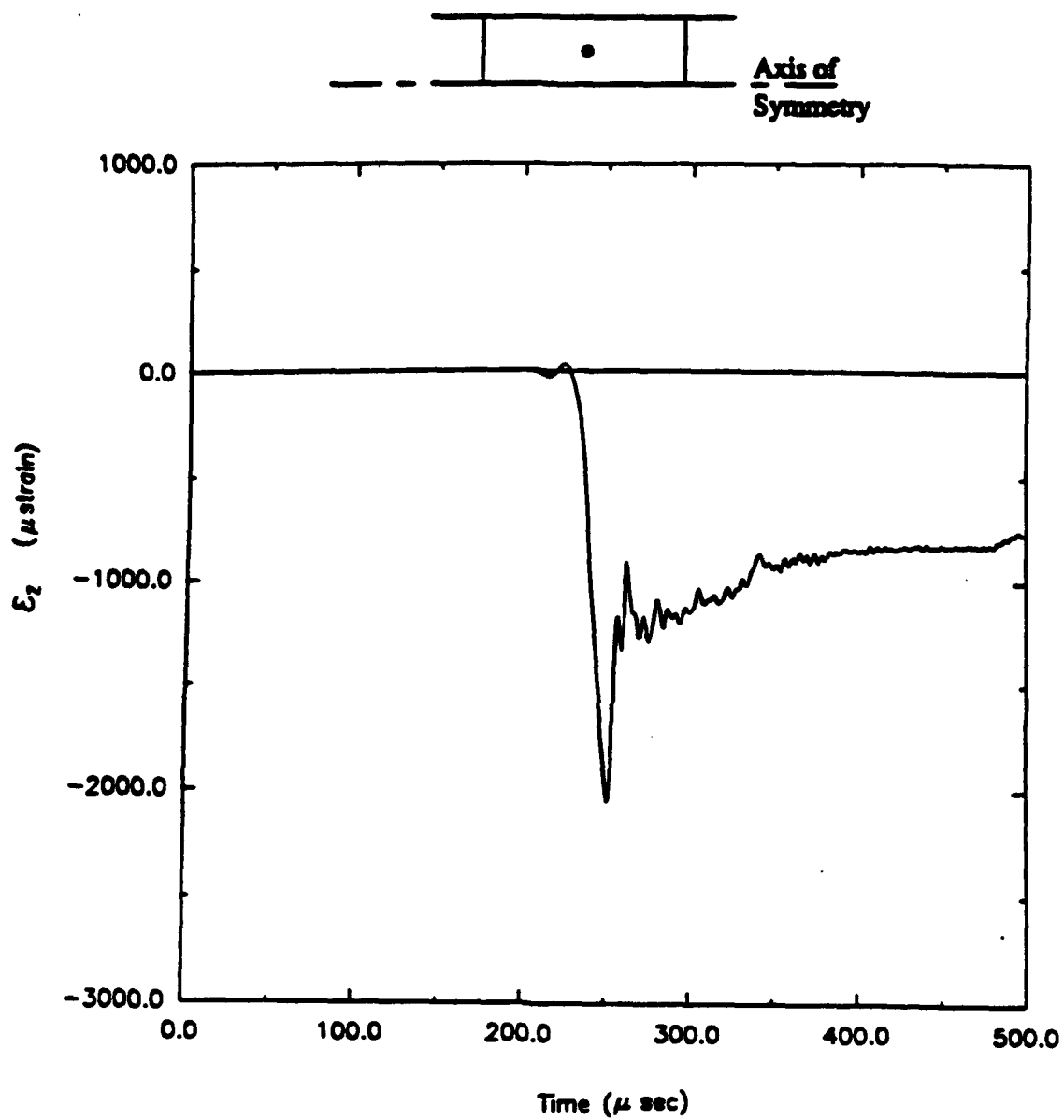


Figure 288. Time history for longitudinal strain (direct compression, Load Case 3).

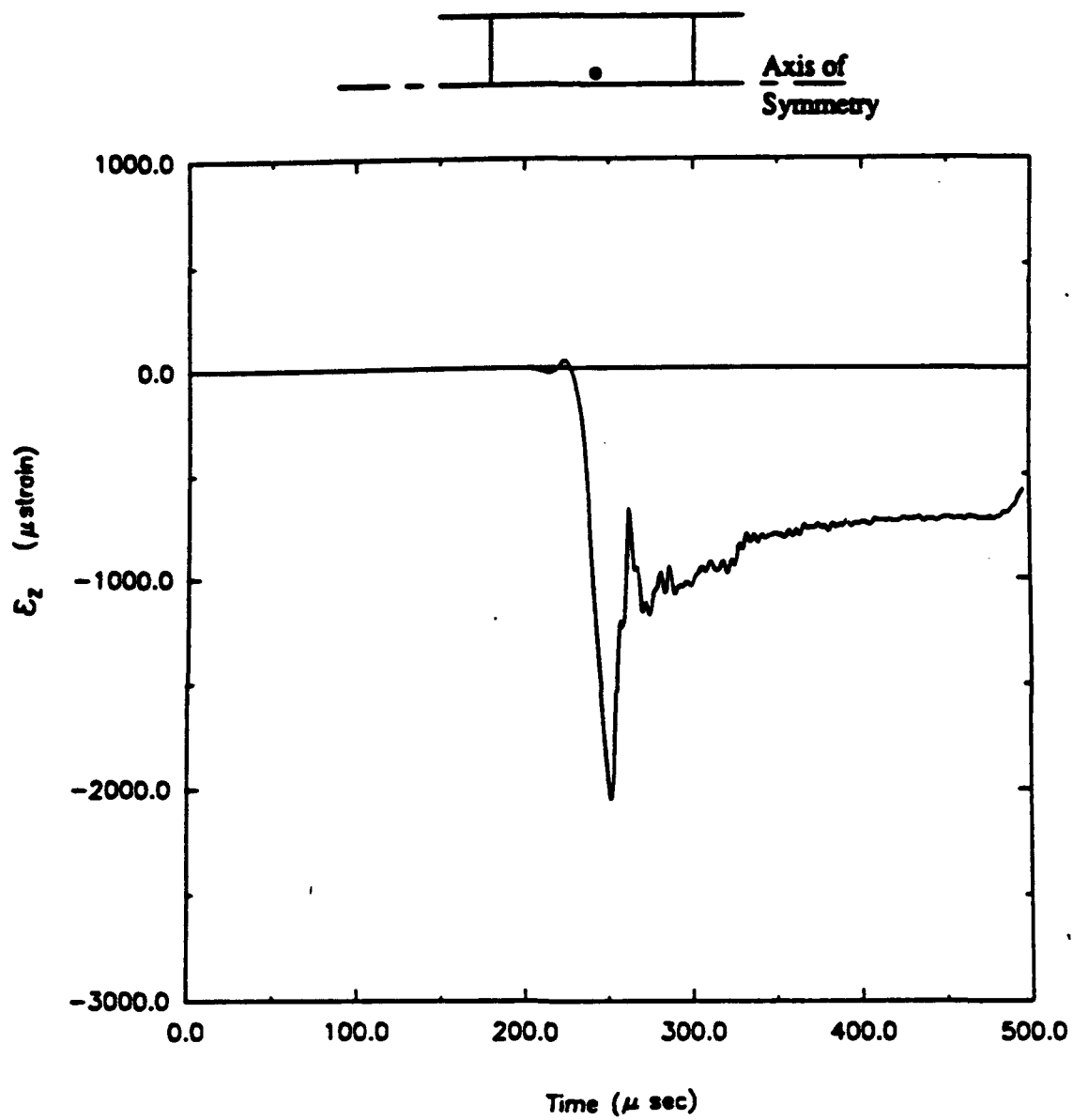


Figure 289. Time history for longitudinal strain (direct compression, Load Case 3).

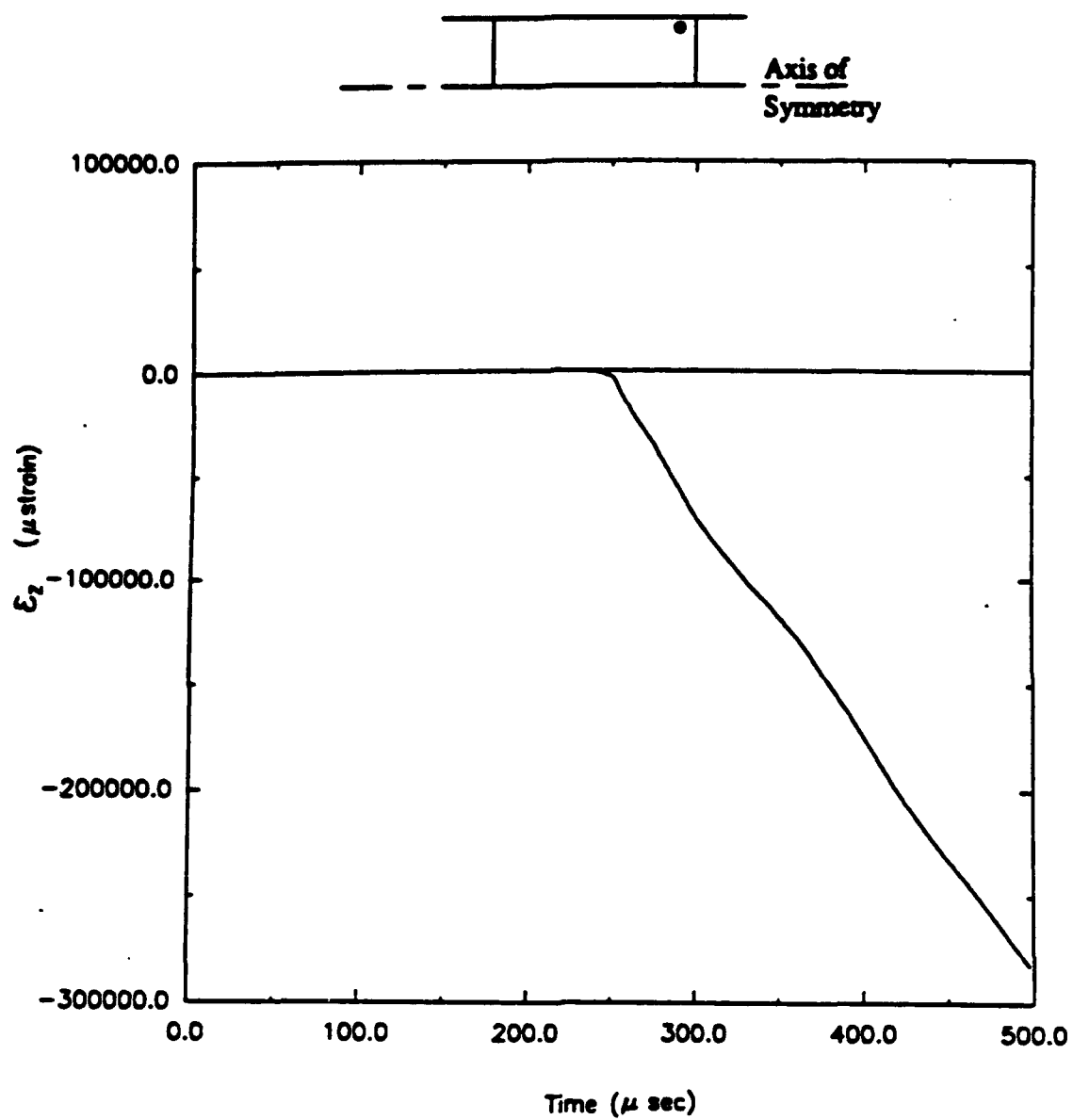


Figure 290. Time history for longitudinal strain (direct compression, Load Case 3).

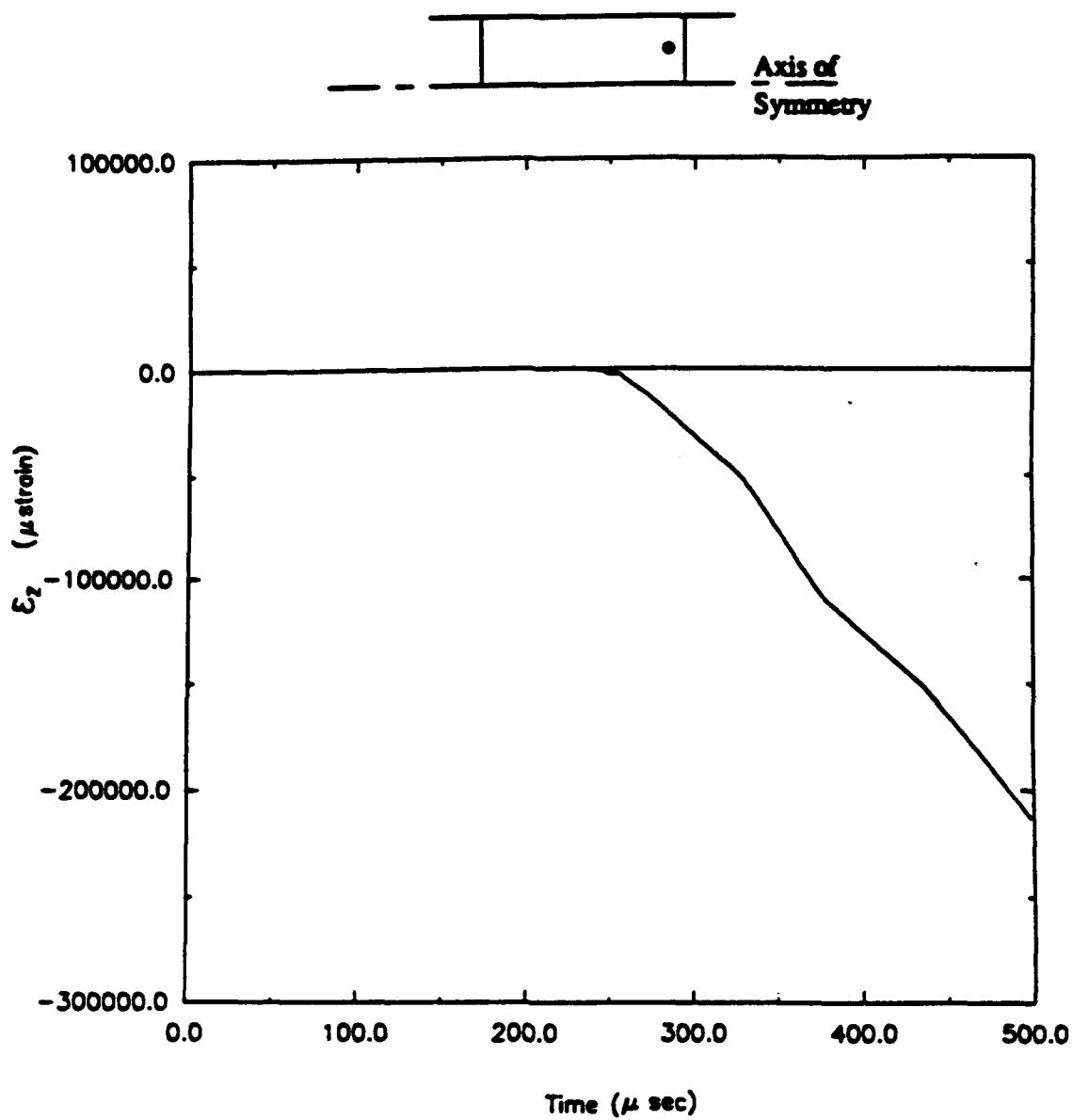


Figure 291. Time history for longitudinal strain (direct compression, Load Case 3).

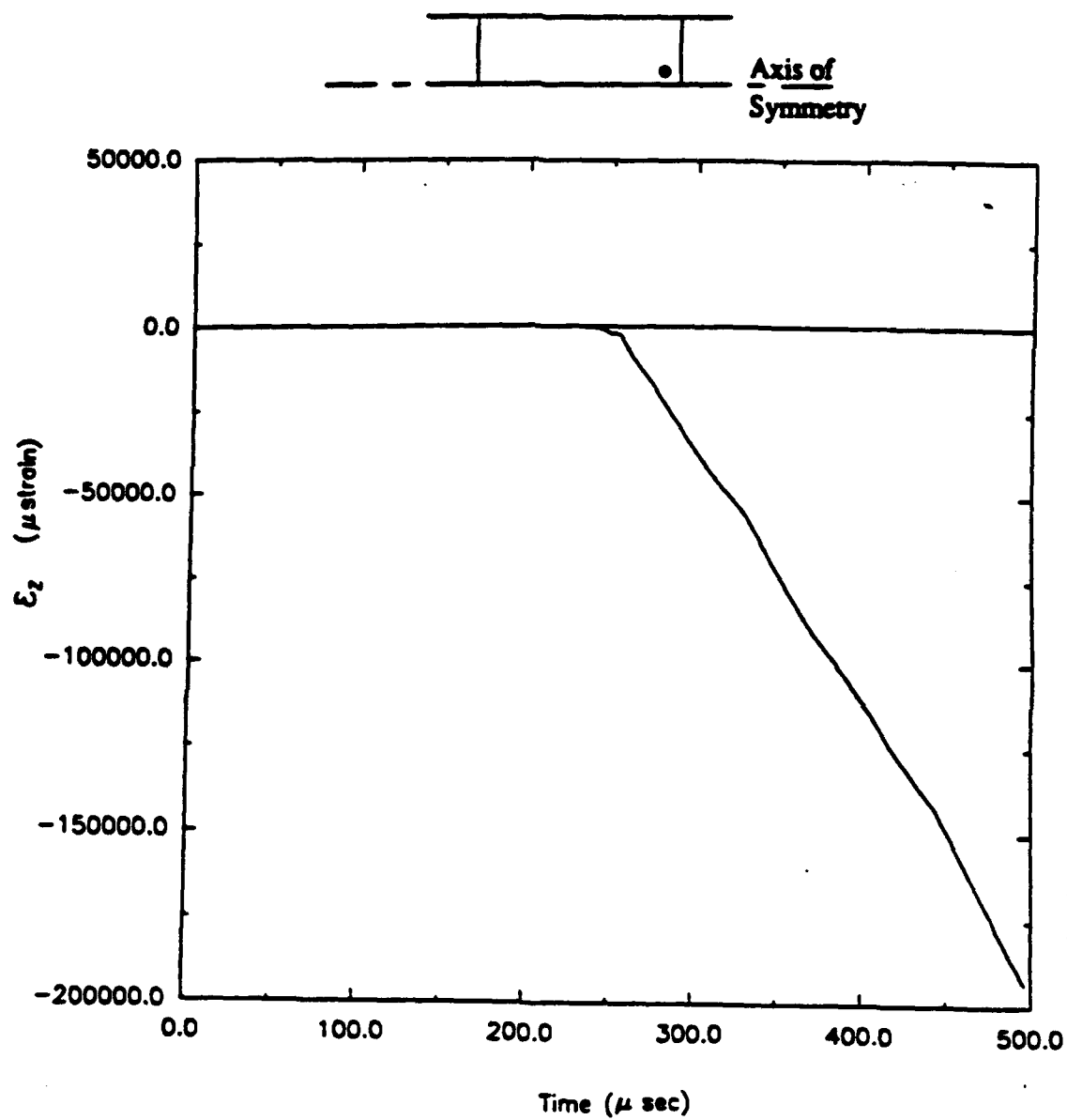


Figure 292. Time history for longitudinal strain (direct compression, Load Case 3).

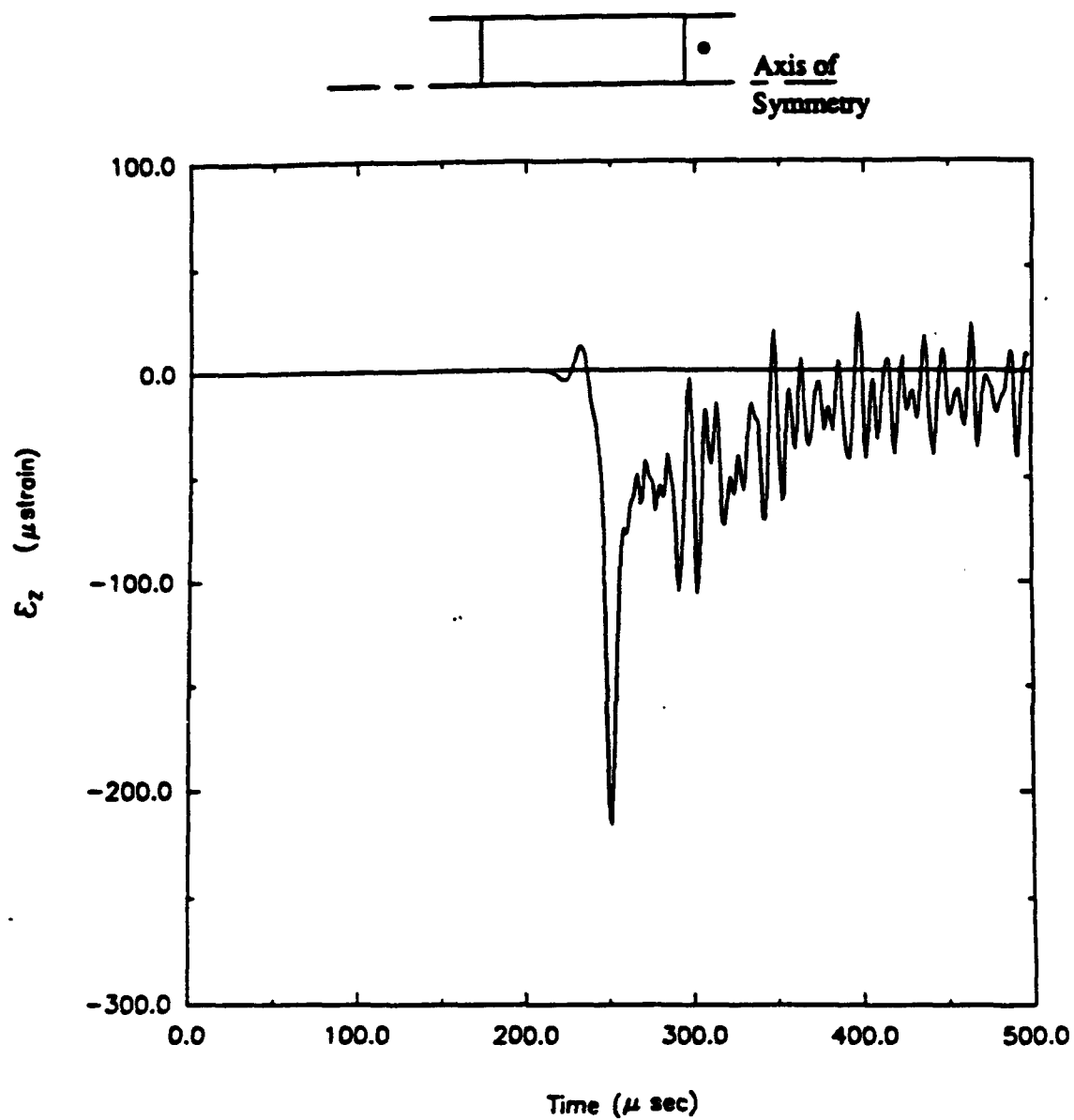


Figure 293. Time history for longitudinal strain (direct compression, Load Case 3).

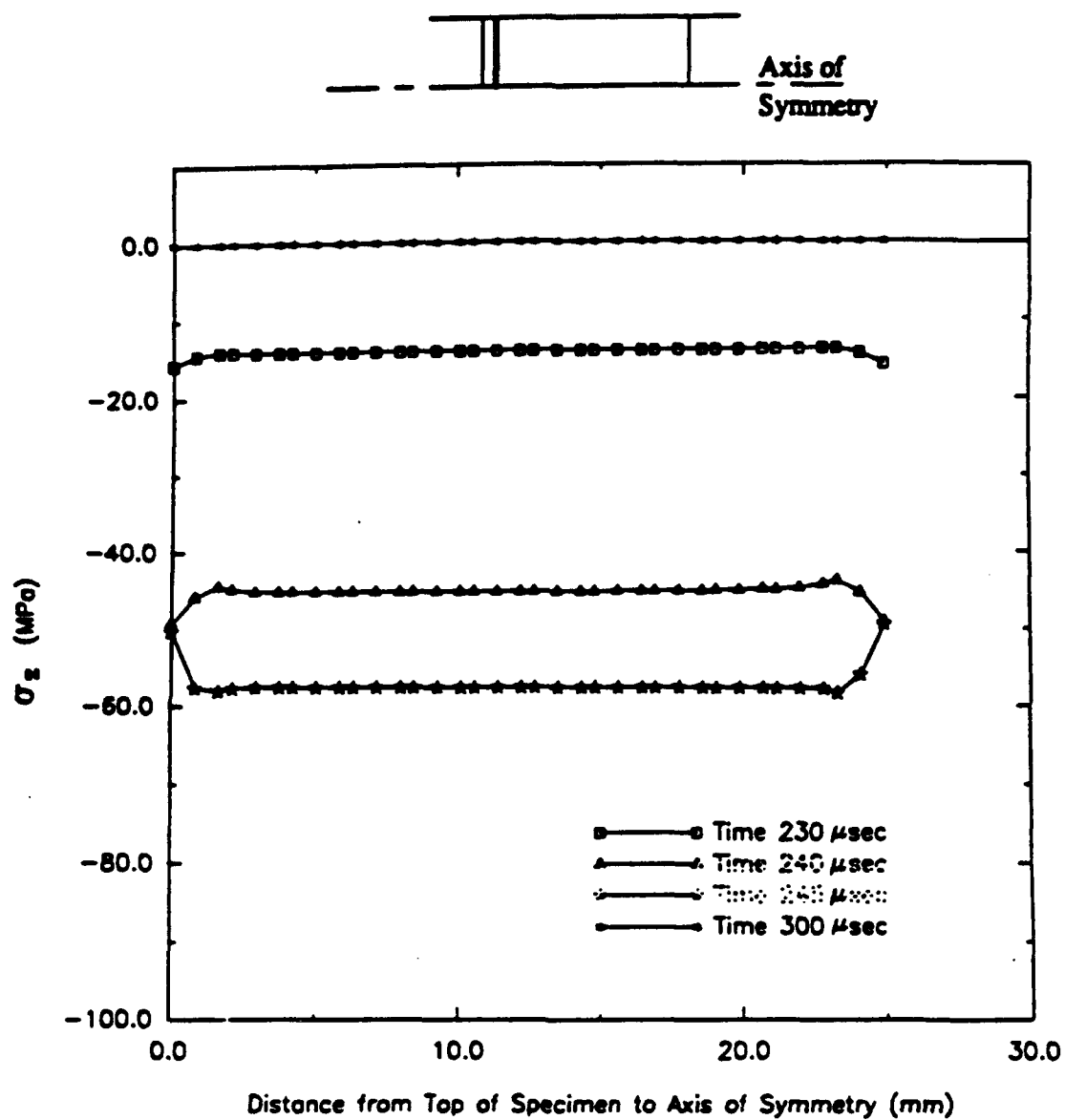


Figure 294. Profiles for longitudinal stress (direct compression, Load Case 3).

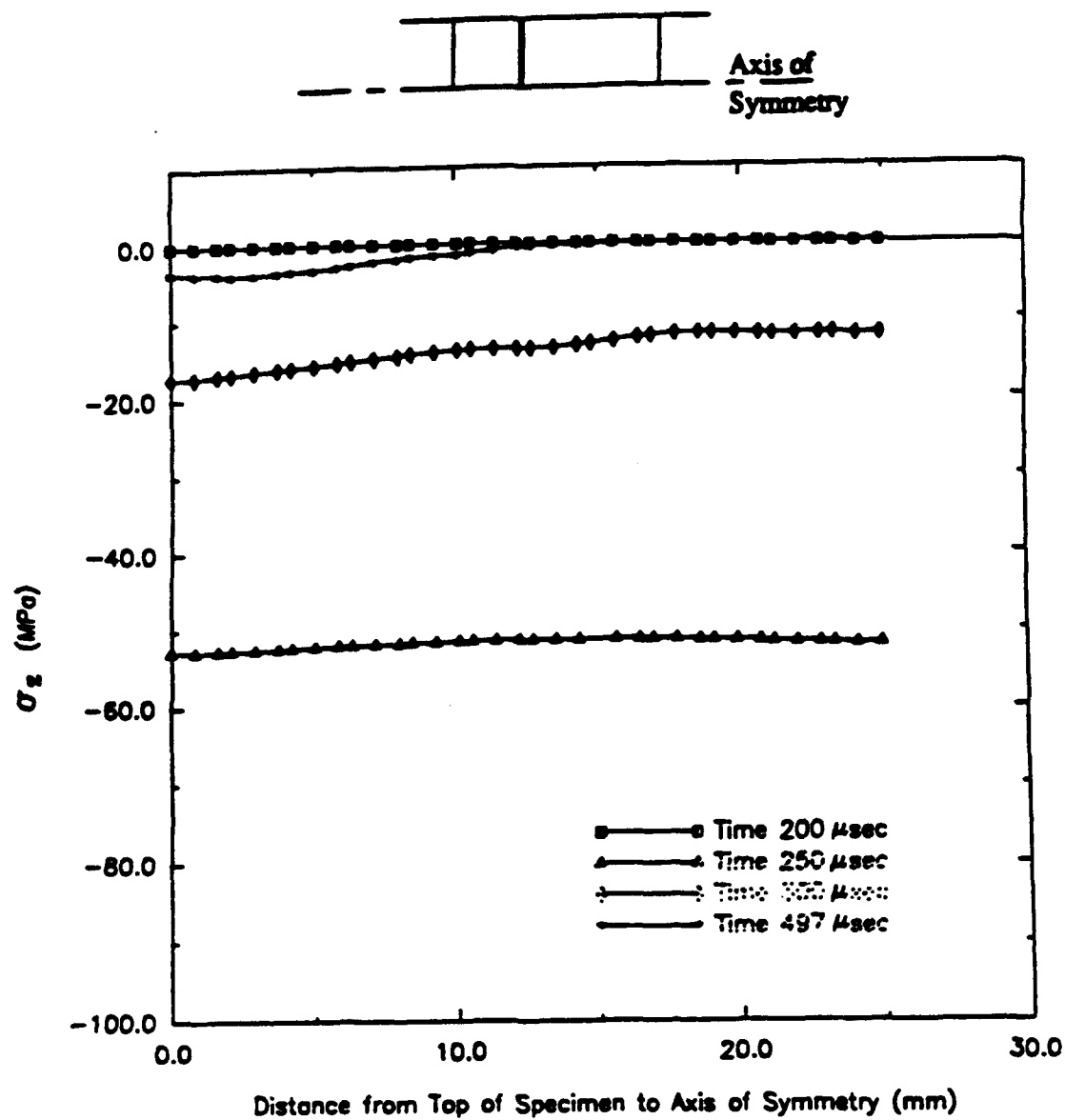


Figure 295. Profiles for longitudinal stress (direct compression, Load Case 3).

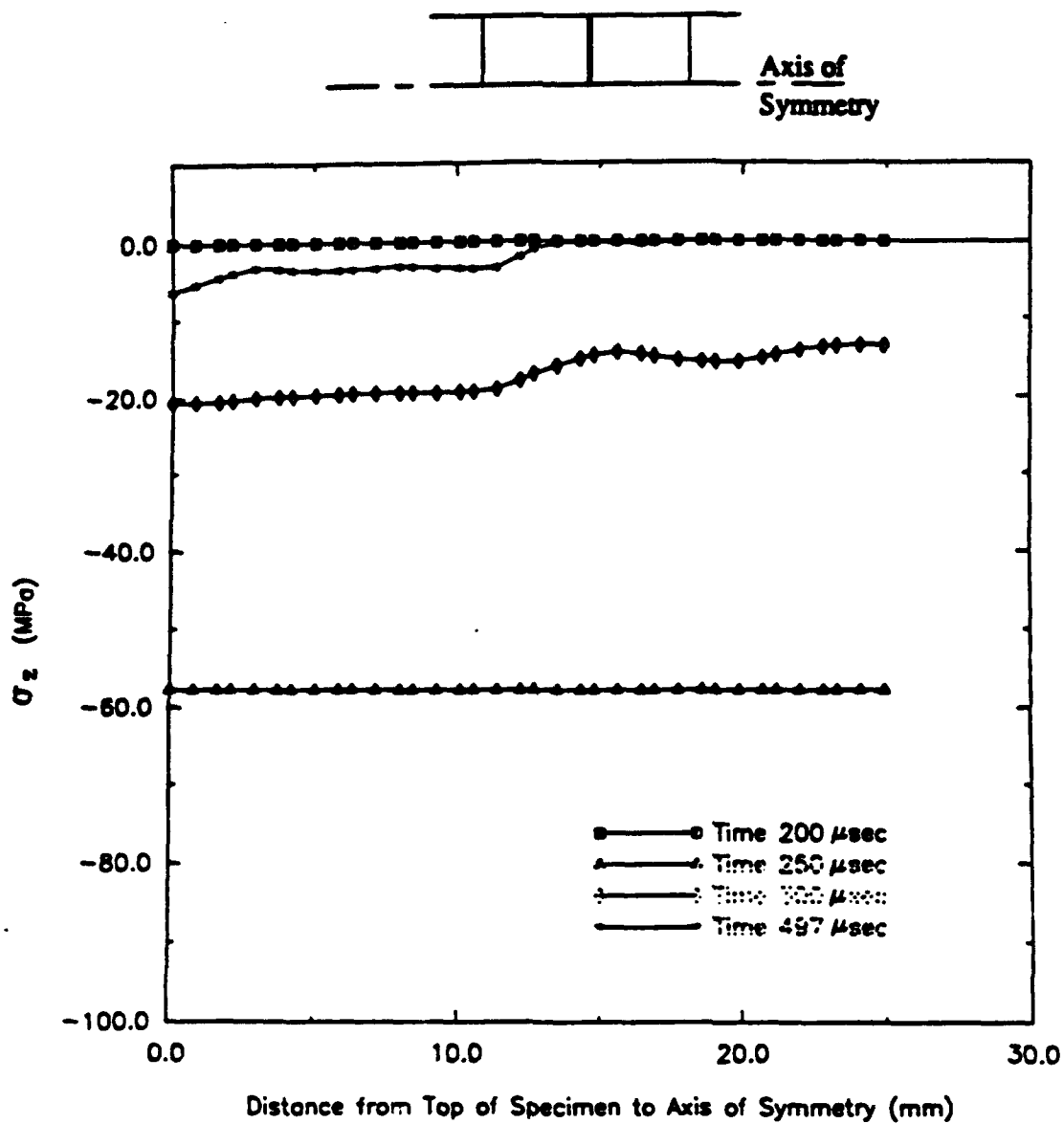


Figure 296. Profiles for longitudinal stress (direct compression, Load Case 3).

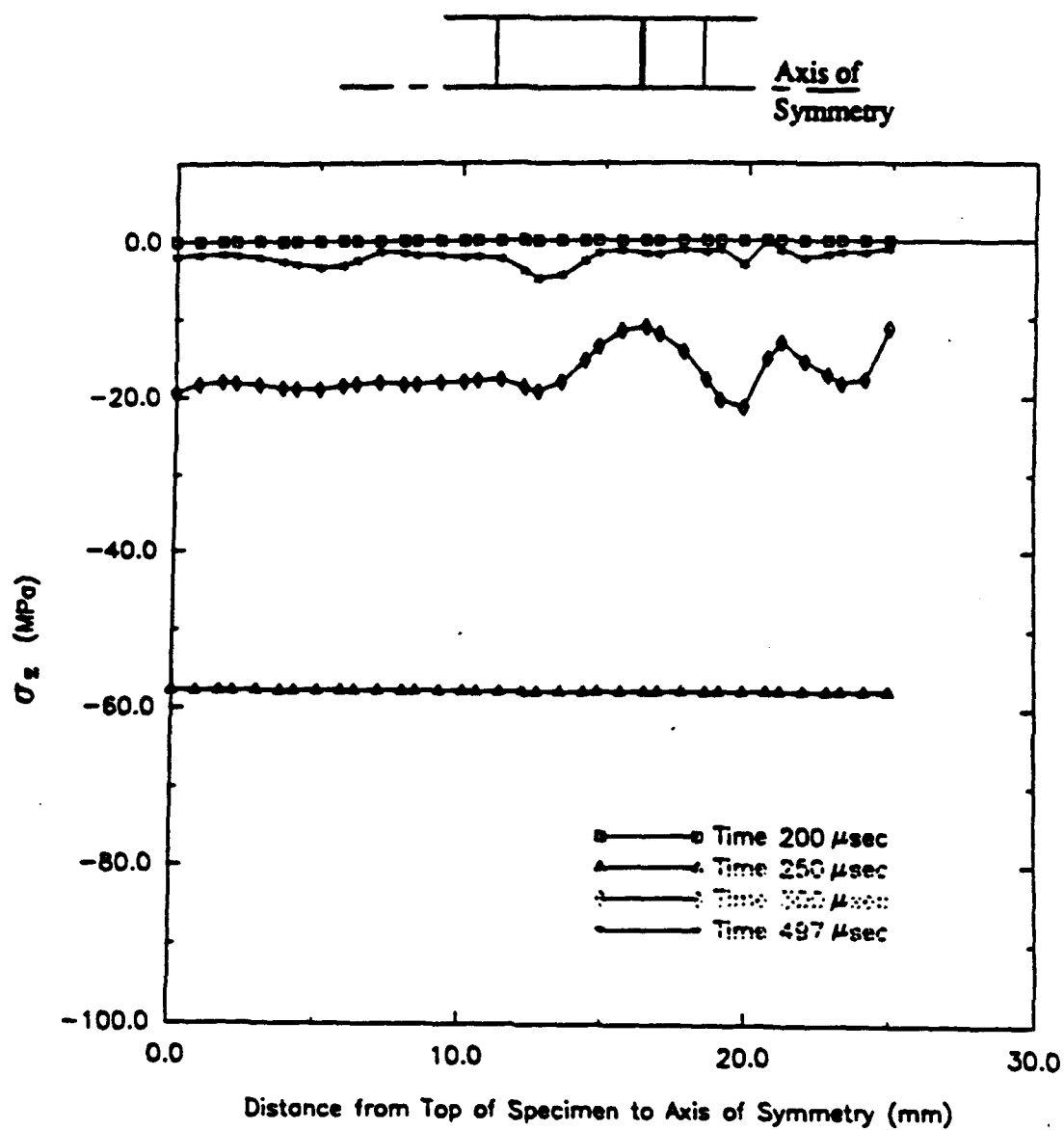


Figure 297. Profiles for longitudinal stress (direct compression, Load Case 3).

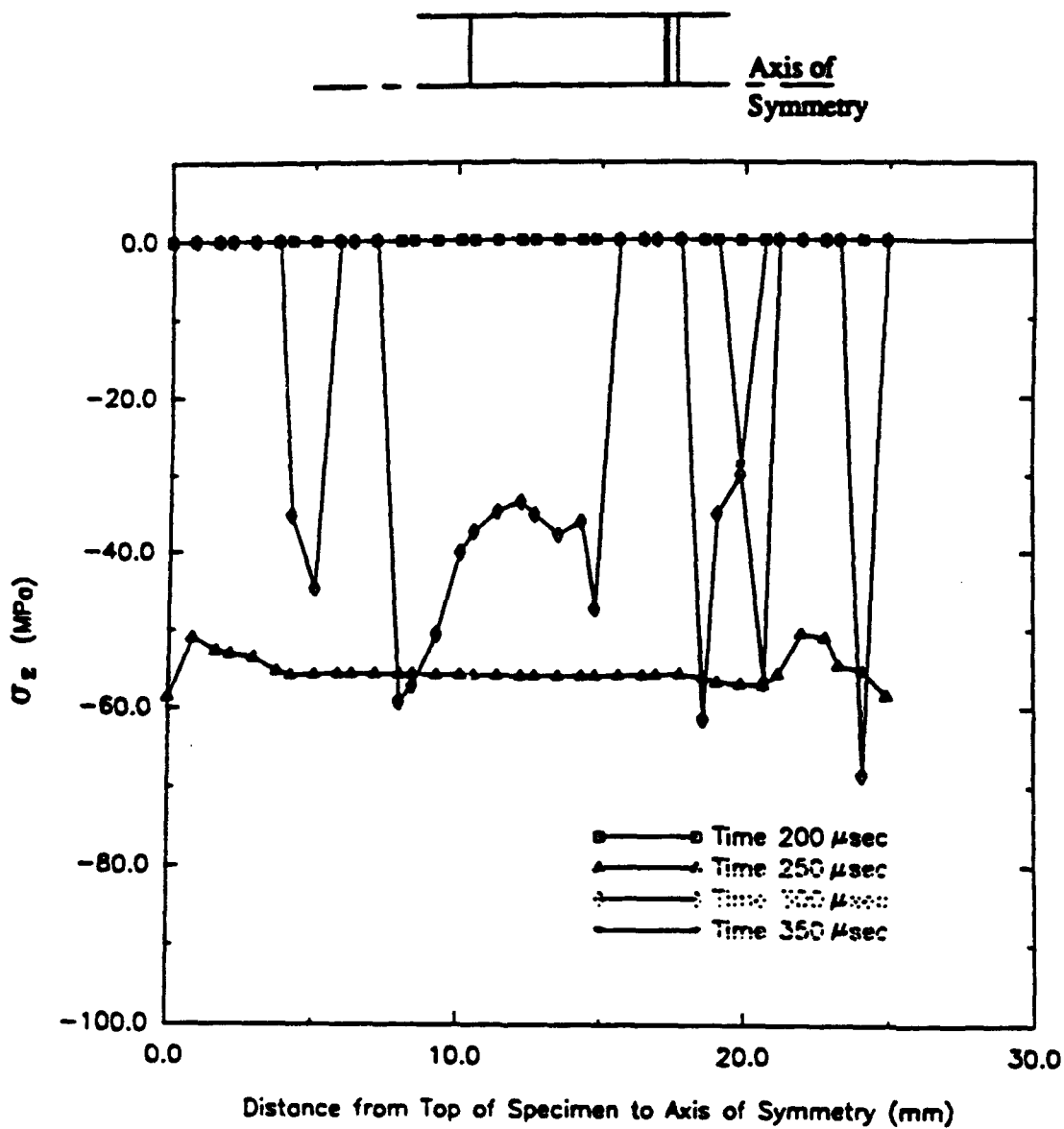


Figure 298. Profiles for longitudinal stress (direct compression, Load Case 3).

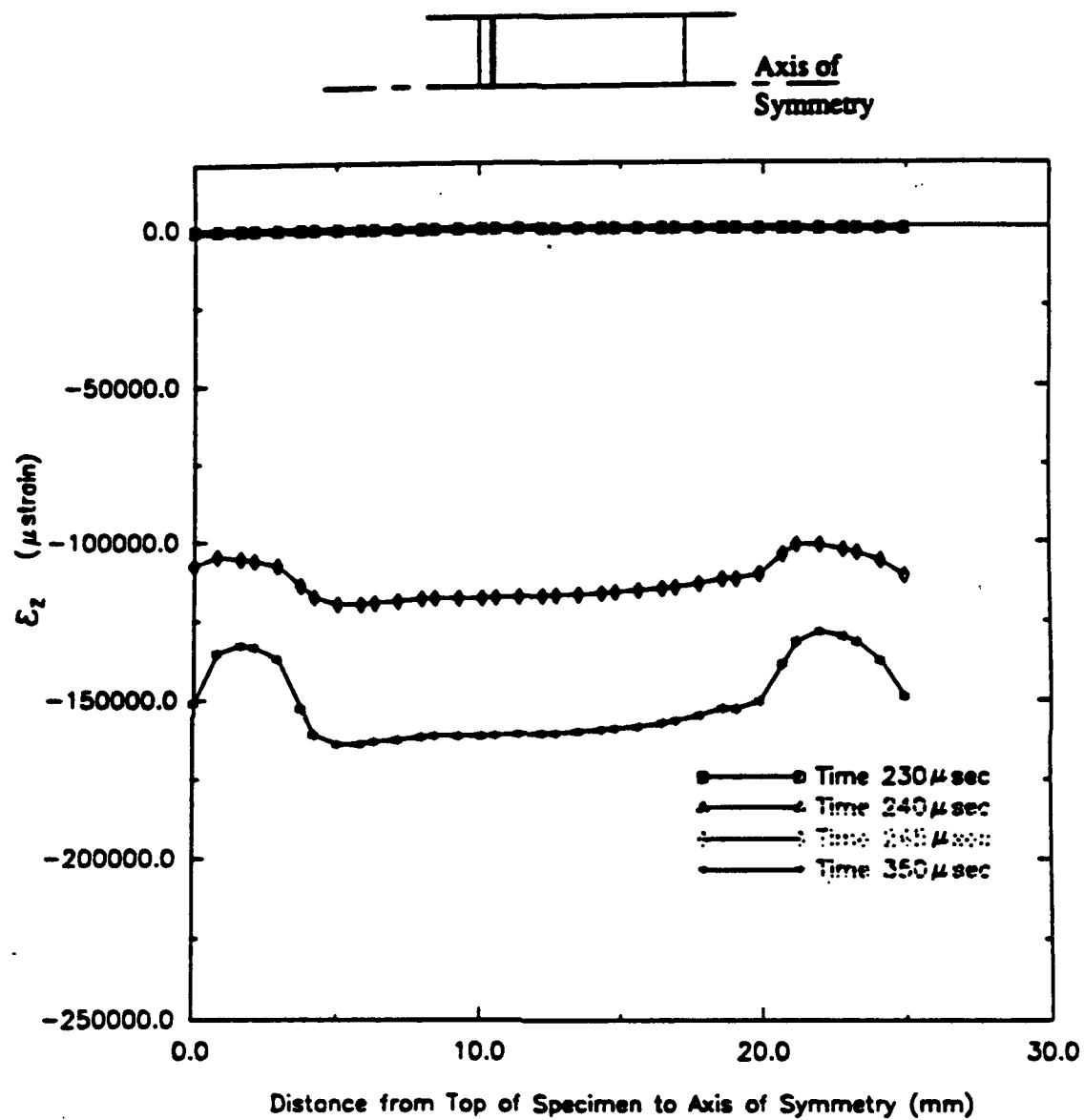


Figure 299. Profiles for longitudinal strain (direct compression, Load Case 3).

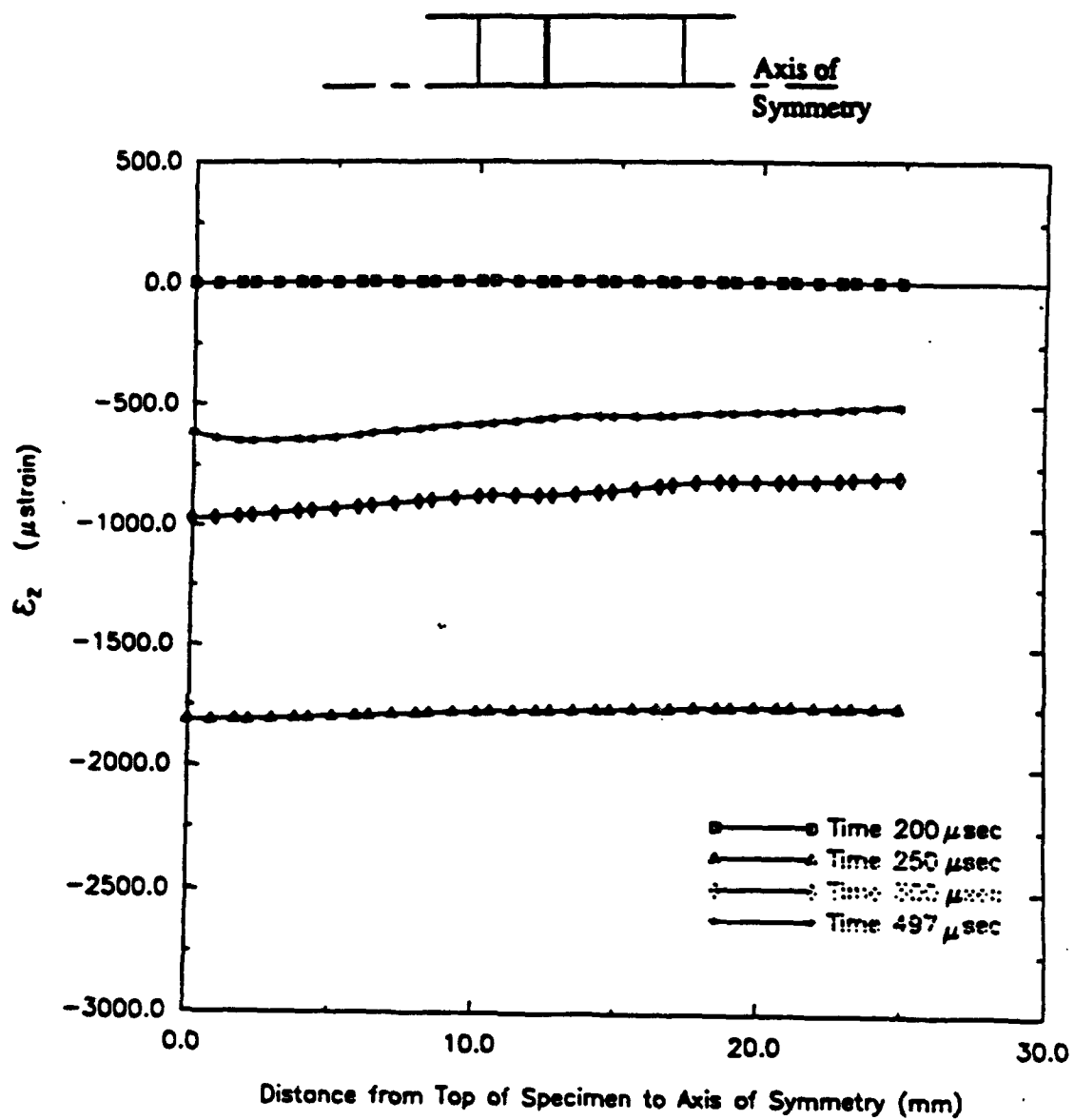


Figure 300. Profiles for longitudinal strain (direct compression, Load Case 3).

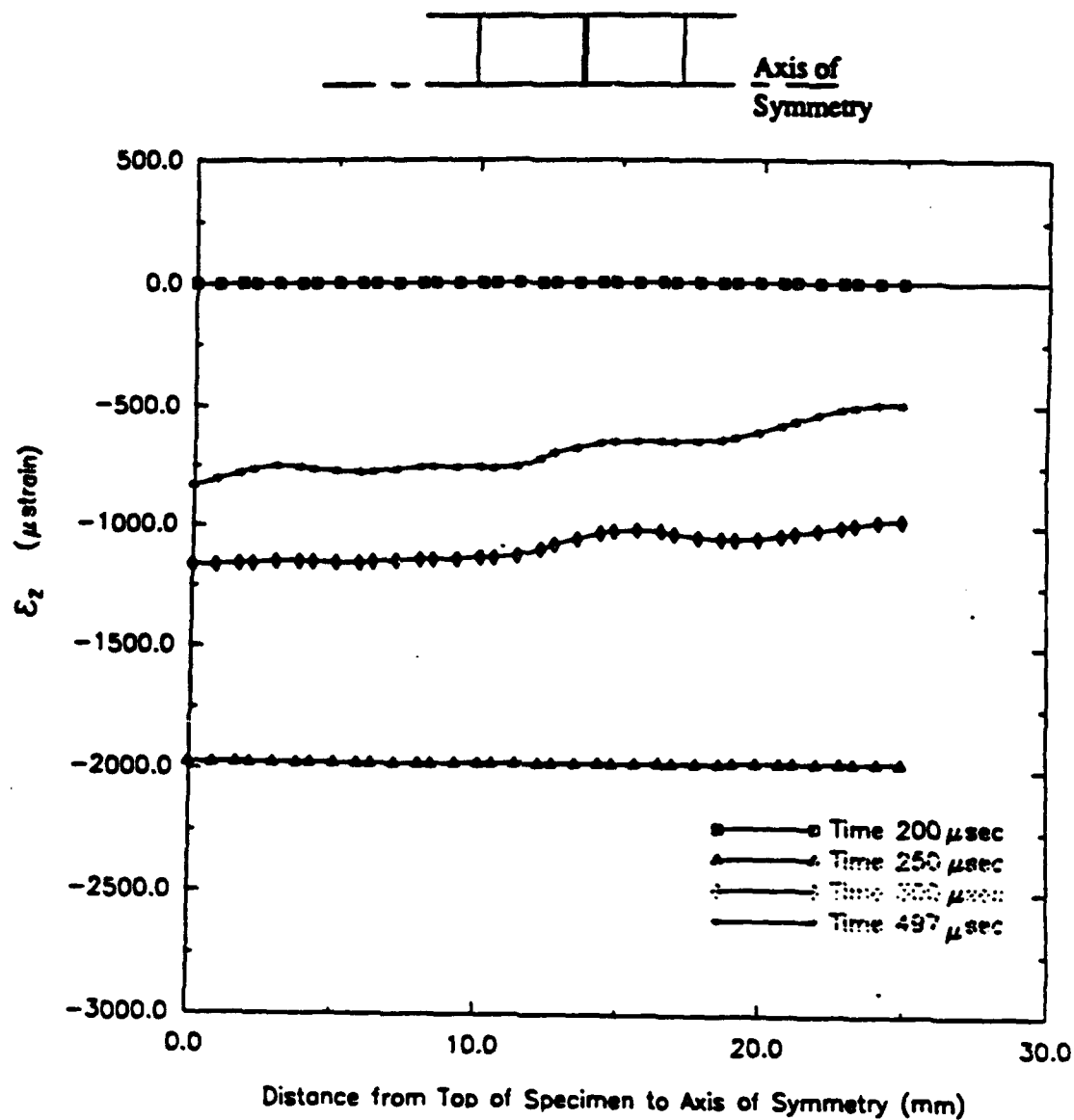


Figure 301. Profiles for longitudinal strain (direct compression, Load Case 3).

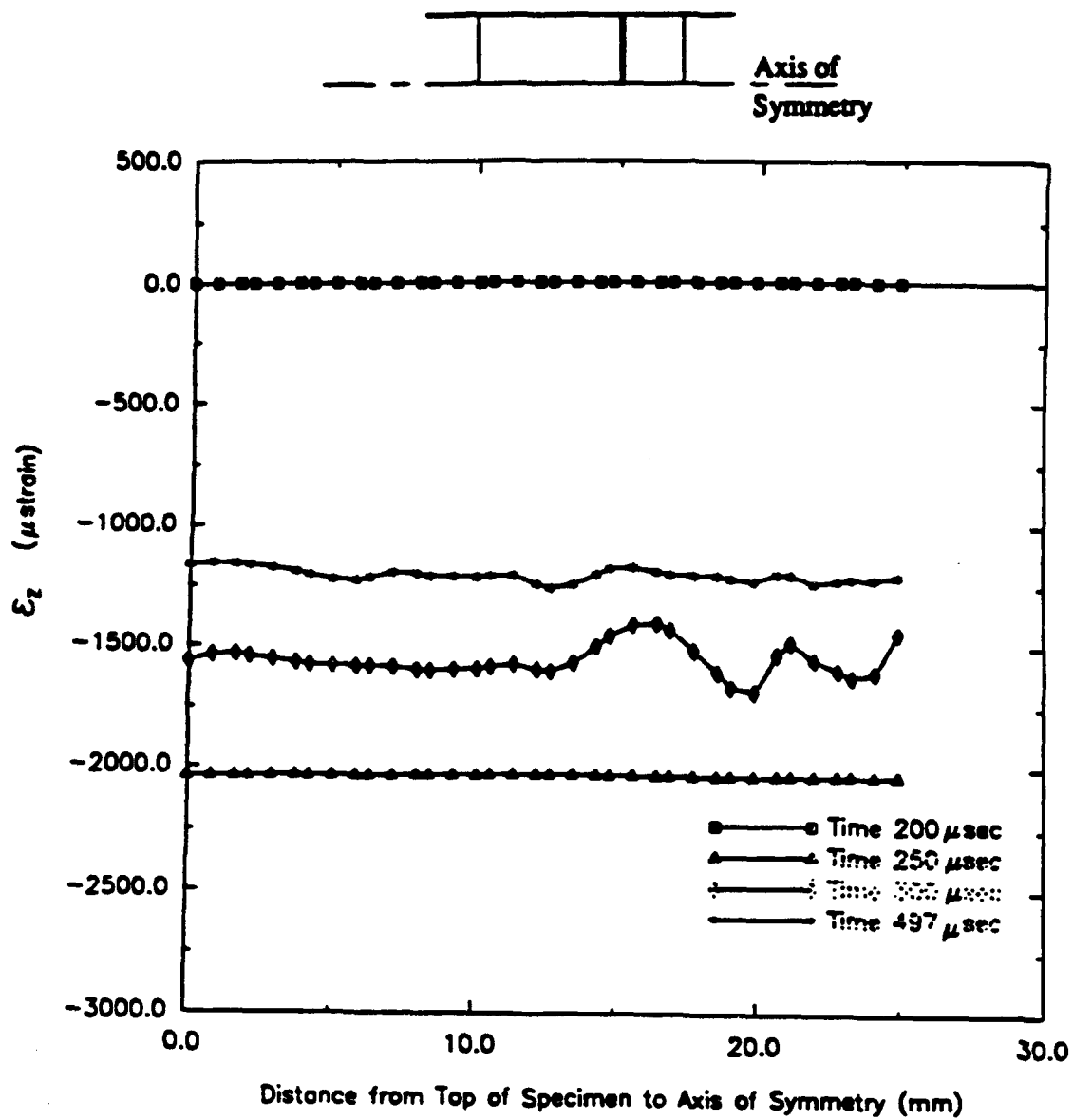


Figure 302. Profiles for longitudinal strain (direct compression, Load Case 3).

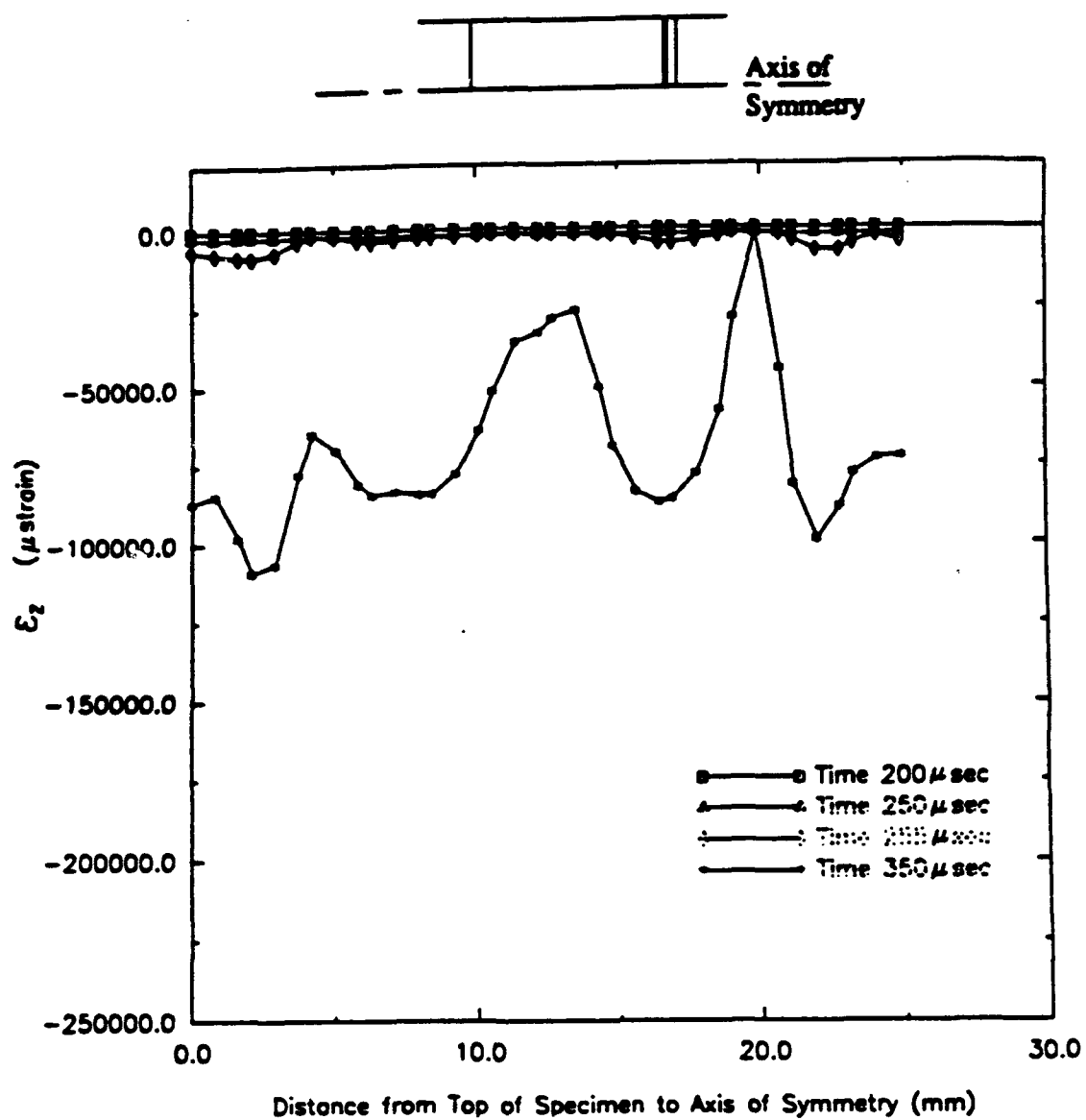
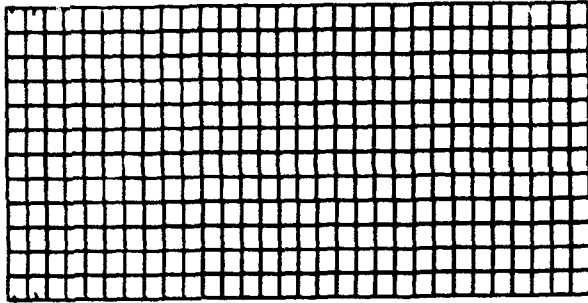
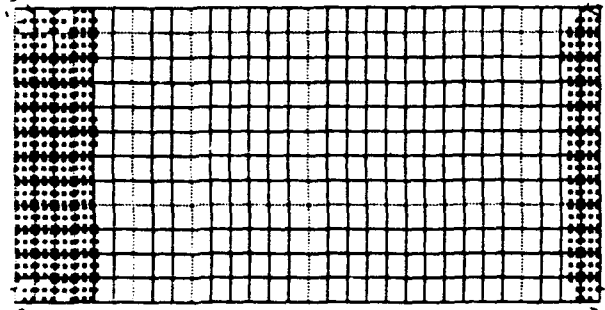


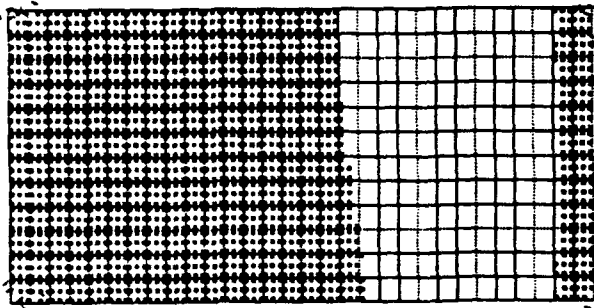
Figure 303. Profiles for longitudinal strain (direct compression, Load Case 3).



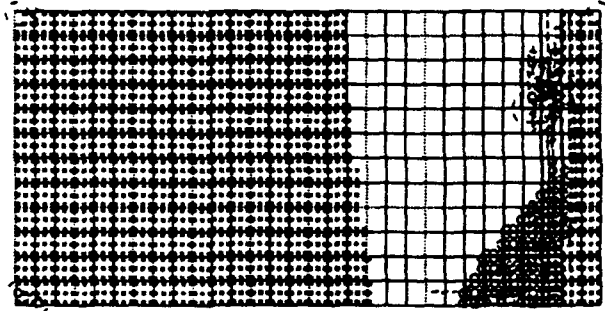
(a)



(b)



(c)



(d)

Figure 304. Cracking sequence for direct compression specimen; Load Case 3:
a) $t=230 \mu\text{sec}$, b) $t=249 \mu\text{sec}$, c) $t=255 \mu\text{sec}$, d) $t=275 \mu\text{sec}$.